

13 April 2012 | \$10

Science

COMPUTATIONAL BIOLOGY

AAAS

SPECIAL SECTION

Computational Biology

INTRODUCTION

- 171 Does It Compute?

NEWS

- 172 Virtual Hot Spots
>> *Science Podcast*

REVIEWS

- 175 Cell Polarity: Quantitative Modeling as a Tool in Cell Biology
A. Mogilner et al.
>> *Science Podcast*

- 179 Integrating Genomes
D. R. Zerbino et al.
- 183 Using Gene Expression Noise to Understand Gene Regulation
B. Munsky et al.
- 187 Computational Approaches to Developmental Patterning
L. G. Morelli et al.

>> *Editorial p. 131; Policy Forum p. 159; Perspectives pp. 163 and 164; Report p. 229; Science Express Reports by F. Bosveld et al. and P. Müller et al.; Science Signaling; and Science Careers at http://scim.ag/comp_bio*



page 144

EDITORIAL

- 131 Creativity at the Interface
Bruce Alberts
>> *Computational Biology section p. 171*

NEWS OF THE WEEK

- 136 A roundup of the week's top stories

NEWS & ANALYSIS

- 139 Research Cuts Will Cause 'Exodus' From Spain
- 140 Greece Eyes CERN, ESA Cuts to Plug Budget Gap
- 141 Ocean's Deep, Dark Trenches to Get Their Moment in the Spotlight
>> *Science Express Perspective by R. A. Lutz and P. G. Falkowski*
- 143 Sleep Study Suggests Triggers for Diabetes and Obesity
>> *Science Translational Medicine Research Article by O. M. Buxton et al.*

NEWS FOCUS

- 144 Mystery Disease Haunts Region
- 147 Sparks Fly Over Shoestring Test of 'Holographic Principle'
- 150 Lunar and Planetary Science Conference
Icy-Hot Mercury's Water Pinned Down in the Dark
Tougher Times for Any Life on an Early Mars?
Snapshots From the Meeting
The Young Solar System Took a One-Two Punch?

LETTERS

- 152 Outsourced Psychiatry: Remote Support
F. R. Ali et al.
- Outsourced Psychiatry: Experts Still Relevant
M. M. Weissman and H. Verdelli
- Sound and Fury, Clarified
D. Raoult
- Response
C. Mary
- Cultural Diversity in a Global Society
L. Cheng
- Science Statesmanship
M. D. Lowman

- 155 CORRECTIONS AND CLARIFICATIONS

BOOKS ET AL.

- 158 The Origins of Grammar
J. R. Hurford, reviewed by R. C. Berwick

POLICY FORUM

- 159 Shining Light into Black Boxes
A. Morin et al.
>> *Computational Biology section p. 171*

PERSPECTIVES

- 161 Revitalizing Remyelination—the Answer Is Circulating
S. A. Redmond and J. R. Chan
- 162 The Strangest Terrestrial Planet
W. B. McKinnon
>> *Reports pp. 214 and 217*
- 163 Beyond Turing's Machines
A. Hodges
- 164 Dusting Off the Turing Test
R. M. French
>> *Computational Biology section p. 171*
- 166 ESCRTing DNA at the Cleavage Site During Cytokinesis
M. Petronczki and F. Uhlmann
>> *Report p. 220*

CONTENTS continued >>



COVER

A series of spheres with two-dimensional patterns generated by computer simulation shows that Turing's reaction-diffusion model may be the basis for skin patterning in animals. A modulation of one parameter value in a reaction-diffusion-based model causes the pattern to change gradually from spots to labyrinths, with the range encompassing the diversity of patterns seen on animal skin. See page 171 and http://scim.ag/comp_bio.

Image: Seita Miyazawa, Osaka University

DEPARTMENTS

- 127 This Week in *Science*
- 132 Editors' Choice
- 134 *Science* Staff
- 257 New Products
- 258 *Science* Careers

- 167 **Wiping Drug Memories**
A. L. Milton and B. J. Everitt
>> *Report p. 241*
- 168 **Monkey See, Monkey Read**
M. L. Platt and G. K. Adams
>> *Report p. 245*
- 170 **Retrospective: F. Sherwood Rowland (1927–2012)**
R. J. Cicerone et al.

RESEARCH ARTICLE

- 193 **A Fine-Scale Chimpanzee Genetic Map from Population Sequencing**
A. Auton et al.
Chimpanzees show similar genetic recombination rates as humans but differ in the genomic regions involved.

REPORTS

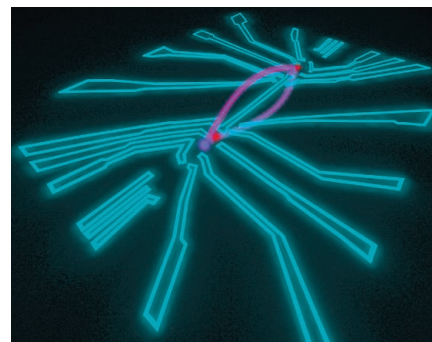
- 198 **Observation of Skyrmions in a Multiferroic Material**
S. Seki et al.
Whirlpools of spin are observed in an insulating material exhibiting both magnetic and ferroelectric order.
- 202 **Demonstration of Entanglement of Electrostatically Coupled Singlet-Triplet Qubits**
M. D. Shulman et al.
The states of two qubits residing in a pair of double quantum dots are rendered interdependent through electrical gating.
- 205 **Topological Transitions in Metamaterials**
H. N. S. Krishnamoorthy et al.
Metamaterials can undergo an optical analog of electronic phase transitions that impacts local light-matter interactions.
- 209 **Ferroelectric Columnar Liquid Crystal Featuring Confined Polar Groups Within Core-Shell Architecture**
D. Miyajima et al.
Precise positioning of polar components in a liquid crystal architecture modulates the collective electronic properties.
- 214 **Gravity Field and Internal Structure of Mercury from MESSENGER**
D. E. Smith et al.
Mercury's outer solid shell is denser than expected, suggesting a deep reservoir of high-density material, possibly iron-sulfide.
- 217 **Topography of the Northern Hemisphere of Mercury from MESSENGER Laser Altimetry**
M. T. Zuber et al.
Mercury's topography indicates sustained geophysical activity for most of the planet's geological history.
>> *Perspective p. 162*

- 220 **ESCRT-III Governs the Aurora B-Mediated Abscission Checkpoint Through CHMP4C**
J. G. Carlton et al.
The membrane scission and cytokinesis ESCRT machinery may help to protect against genetic damage.
>> *Perspective p. 166*
- 225 **Atg7 Modulates p53 Activity to Regulate Cell Cycle and Survival During Metabolic Stress**
I. H. Lee et al.
When the autophagy protein tg7 is absent, nutrient withdrawal does not stop the cell cycle.
- 229 **Mechanism of Voltage Gating in Potassium Channels**
M. Ø. Jensen et al.
Molecular dynamics simulations show how a voltage-gated channel closes.
>> *Computational Biology section p. 171*
- 233 **Ribosome Profiling Shows That miR-430 Reduces Translation Before Causing mRNA Decay in Zebrafish**
A. A. Bazzini et al.
MicroRNAs act to repress their messenger RNA targets first by blocking translation initiation and then through degradation.
- 237 **miRNA-Mediated Gene Silencing by Translational Repression Followed by mRNA Deadenylation and Decay**
S. Djuranovic et al.
MicroRNAs act to destroy their messenger RNA targets by blocking translation initiation, which leads to degradation.
- 241 **A Memory Retrieval-Extinction Procedure to Prevent Drug Craving and Relapse**
Y.-X. Xue et al.
A behavioral intervention that decreases drug seeking in rat models of relapse can decrease drug craving in heroin addicts.
>> *Perspective p. 167*
- 245 **Orthographic Processing in Baboons (*Papio papio*)**
J. Grainger et al.
Baboons discriminate words from nonwords on the basis of spelling.
>> *Perspective p. 168*

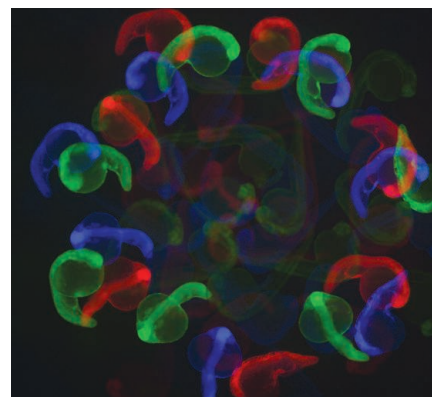
CONTENTS continued >>



pages 168 & 245



page 202



pages 233 & 237

SCIENCEONLINE

SCIENCEEXPRESS

www.sciencexpres.org

Mechanical Control of Morphogenesis by Fat/Dachsous/Four-Jointed Planar Cell Polarity Pathway

F. Bosveld et al.

Polarized protocadherin and myosin induce an anisotropic tension at cell junctions and thereby shape epithelial tissue.

10.1126/science.1221071

>> *Computational Biology section p. 171*

Differential Diffusivity of Nodal and Lefty Underlies a Reaction-Diffusion Patterning System

P. Müller et al.

The inhibitor Lefty diffuses more widely than the activator Nodal.

10.1126/science.1221920

>> *Computational Biology section p. 171*

Epigenomic Enhancer Profiling Defines a Signature of Colon Cancer

B. Akhtar-Zaidi et al.

Methylation tags at long-distance gene regulatory elements provide a signature specific to cancer cells.

10.1126/science.1217277

A Dive to Challenger Deep

R. A. Lutz and P. G. Falkowski

10.1126/science.1222641

>> *News story p. 141*

Signatures of Majorana Fermions in Hybrid Superconductor-Semiconductor Nanowire Devices

V. Mourik et al.

Theoretically predicted particles that double as their own antiparticles emerge in a superconductor-coupled indium antimonide nanowire.

10.1126/science.1222360

Growing Microtubules Push the Oocyte Nucleus to Polarize the *Drosophila* Dorsal-Ventral Axis

T. Zhao et al.

The addition of tubulin monomers to microtubules provides the force to relocate the oocyte nucleus.

10.1126/science.1219147

SCIENCENOW

www.sciencenow.org

Highlights From Our Daily News Coverage

Land Bridge Caused Wild Temperature Swings

The strip of earth connecting Asia and North America disrupted ocean circulation.

http://scim.ag/Temperature_Swings

Of Robots and Cocktails

A humanoid machine helps researchers understand how we home in on conversations.

http://scim.ag/Humanoid_Machine

Fishing for Fluid Dynamics

Movement of fishermen's nets helps untangle water-flow patterns in an Italian lake.

http://scim.ag/Fluid_Dynamics

SCIENCE SIGNALING

www.sciencesignaling.org

The Signal Transduction Knowledge Environment

10 April issue: <http://scim.ag/ss41012>

RESEARCH ARTICLE: Direct Binding Between Orai1 and AC8 Mediates Dynamic Interplay Between Ca²⁺ and cAMP Signaling

D. Willoughby et al.

A signaling complex enables the compartmentalized regulation of cyclic AMP signaling by calcium entering through a specific channel.

RESEARCH ARTICLE: Ras Stabilization Through Aberrant Activation of Wnt/ β -Catenin Signaling Promotes Intestinal Tumorigenesis

W. Jeong et al.

PERSPECTIVE: Wnt/ β -Catenin and MAPK Signaling—Allies and Enemies in Different Battlefields

D. Guardavaccaro and H. Clevers

Crosstalk between the Wnt/ β -catenin and MAPK pathways contributes to colon cancer.

PODCAST

M. Nedergaard et al.

New findings elucidate mechanisms by which astrocytes can modulate neuronal activity.

SCIENCE TRANSLATIONAL MEDICINE

www.sciencetranslationalmedicine.org

Integrating Medicine and Science

11 April issue: <http://scim.ag/stm041112>

EDITORIAL: Toward Precision Medicine—A New Social Contract?

S. Desmond-Hellmann

Patients have the power to drive development of a new taxonomy of disease and precision medicine.

RESEARCH ARTICLE: Adverse Metabolic Consequences in Humans of Prolonged Sleep Restriction Combined with Circadian Disruption

O. M. Buxton et al.

Sleep deficiency and out-of-synch circadian rhythms impair pancreatic insulin secretion, a possible precursor to metabolic syndrome and diabetes.

>> *News story p. 143*

RESEARCH ARTICLE: Model-Based Noninvasive Estimation of Intracranial Pressure from Cerebral Blood Flow Velocity and Arterial Pressure

F. M. Kashif et al.

FOCUS: From Lundberg to SIM-ICP—Computational Physiology and Modeling Intracranial Pressure

B. Goldstein et al.

A model-based, patient-specific, and calibration-free approach is used for continuous, noninvasive estimation of intracranial pressure.

RESEARCH ARTICLE: Prognostic Indicators of Life-Threatening Malaria Are Associated with Distinct Parasite Variant Antigen Profiles

G. M. Warimwe et al.

Two key clinical indicators of life-threatening malaria in African children may be associated with differential expression of parasite surface antigens on infected erythrocytes.

SCIENCE CAREERS

www.sciencereers.org/career_magazine

Free Career Resources for Scientists

Are Computational Biologists the Next Pharma Scientists?

M. Price

Drug development companies are now hiring more computational biologists, creating an abundance of high-paying jobs.

<http://scim.ag/CompBioPharma>

>> *Computational Biology section p. 171*

Going Against the Grain

E. Pain

Graduate student Denis Gebauer had to work hard to prove that his unorthodox findings on crystallization were real.

<http://scim.ag/AgainstGrain>

Swimming With SHARks

R. Kaufman

In a world where research is valued above all, how do teaching and outreach experiences influence careers?

<http://scim.ag/SHARKProject>

SCIENCEPODCAST

www.sciencemag.org/multimedia/podcast

Free Weekly Show

On the 13 April *Science* Podcast: quantitative modeling in biology, women in academia, virtual animals, and more.

SCIENCEINSIDER

news.sciencemag.org/scienceinsider

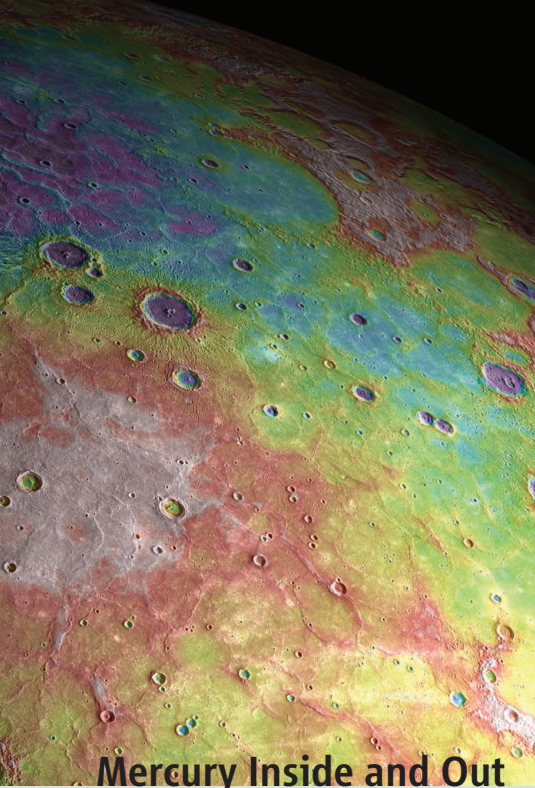
Science Policy News and Analysis

SCIENCE (ISSN 0036-8075) is published weekly on Friday, except the last week in December, by the American Association for the Advancement of Science, 1200 New York Avenue, NW, Washington, DC 20005. Periodicals Mail postage (publication No. 484460) paid at Washington, DC, and additional mailing offices. Copyright © 2012 by the American Association for the Advancement of Science. The title SCIENCE is a registered trademark of the AAAS. Domestic individual membership and subscription (\$1 issues): \$149 (\$74 allocated to subscription). Domestic institutional subscription (\$1 issues): \$990; Foreign postage extra: Mexico, Caribbean (surface mail) \$55; other countries (air assist delivery) \$85. First class, airmail, student, and emeritus rates on request. Canadian rates with GST available upon request, GST #1254 88122. Publications Mail Agreement Number 1069624. Printed in the U.S.A.

Change of address: Allow 4 weeks, giving old and new addresses and 8-digit account number. Postmaster: Send change of address to AAAS, P.O. Box 96178, Washington, DC 20090-6178. Single-copy sales: \$10.00 current issue, \$15.00 back issue prepaid includes surface postage; bulk rates on request. Authorization to photocopy material for internal or personal use under circumstances not falling within the fair use provisions of the Copyright Act is granted by AAAS to libraries and other users registered with the Copyright Clearance Center (CCC) Transactional Reporting Service, provided that \$30.00 per article is paid directly to CCC, 222 Rosewood Drive, Danvers, MA 01923. The identification code for Science is 0036-8075. Science is indexed in the Reader's Guide to Periodical Literature and in several specialized indexes.



ADVANCING SCIENCE, SERVING SOCIETY



Mercury Inside and Out

The MESSENGER spacecraft orbiting Mercury has been in a ~12-hour eccentric, near-polar orbit since 18 March 2011 (see the Perspective by McKinnon). Smith *et al.* (p. 214, published online 21 March) present the most recent determination of Mercury's gravity field, based on radio tracking of the MESSENGER spacecraft between 18 March and 23 August 2011. The results point to an interior structure that differs from those of the other terrestrial planets: the density of the planet's solid outer shell suggests the existence of a deep reservoir of high-density material, possibly an Fe-S layer. Zuber *et al.* (p. 217, published online 21 March) used data obtained by the MESSENGER laser altimeter through to 24 October 2011 to build a topographic map of Mercury's northern hemisphere. The map shows less variation in elevation, compared with Mars or the Moon, and its features add to the body of evidence that Mercury has sustained geophysical activity for much of its history.

Going Ape Over Genetic Maps

Recombination is an important process in generating diversity and producing selectively advantageous genetic combinations. Thus, changes in recombination hotspots may influence speciation. To investigate the variation in recombination processes in humans and their closest existing relatives, Auton *et al.* (p. 193, published online 15 March) prepared a fine-scale genetic map of the Western chimpanzee and compared it with that of humans. While

rates of recombination are comparable between humans and chimpanzees, the locations and genetic motifs associated with recombination differ between the species.

Harnessing the Magnetolectric Effect

Some multiferroic materials exhibit the so-called magnetolectric effect, in which an external magnetic field can cause electric polarization and an electric field can cause magnetic order. This is important because the manipulation of magnetic structures by electric means is technologically highly desirable. Seki *et al.* (p. 198) discovered spin whirlpools called skyrmions in the multiferroic material Cu_2OSeO_3 and observed a magnetolectric coupling exerted by the skyrmions. The existence of skyrmions in an insulating magnetolectric material holds promise for their future manipulation.

Manipulating Optical Topology

Phase transitions in solid-state systems are often associated with a drastic change in the properties of that system. For example, metal-to-insulator transition or magnetic-to-nonmagnetic states find wide application in memory storage technology. An exotic electronic phase transition is the Lifshitz transition, whereby the Fermi surface undergoes a change in topology and a drastic change in the electronic density of states. Krishnamoorthy *et al.* (p. 205) now show that the notion of such a phase transition can be carried over to the optical regime by the suitable design of a metamaterial structure. This effect could be used to control the interaction between light and matter.

Finessing Ferroelectric Liquid Crystals

For a material to show a ferroelectric response, it needs to have segments that can be polarized, with a net polarization that remains when the applied field is removed. However, the fluidity that allows liquid crystal molecules to easily move under an applied

force also makes it hard to create a ferroelectric response. Miyajima *et al.* (p. 209) show that a set of columnar liquid crystal molecules, with polar cyano groups tethered to amide-capped nonpolar chains, can assemble into an umbrella-shaped core-shell architecture, in which hydrogen bonding among the amides keeps the cyano groups confined. With only subtle variations in the tether chemistry, the assemblies can be tuned from having a paraelectric to a ferroelectric response, which requires only a small coercive field.

To Cut or Not to Cut

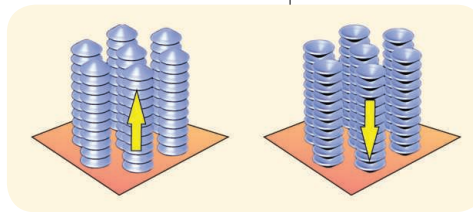
During animal cell division, the final separation of daughter cells requires ESCRT-III (endosomal sorting complex required for transport III), the core membrane scission machinery. Carlton *et al.* (p. 220, published online 15 March; see the Perspective by Petronczki and Uhlmann) report that ESCRT-III modulates abscission timing through one of its subunits, CHMP4C. Depletion of CHMP4C results in faster resolution of the midbody, the cytoplasmic bridge that connects the daughter cells at the end of cytokinesis. This phenotype correlates with a differential spatiotemporal distribution of CHMP4C at the midbody. As CHMP4C is essential for activating the Aurora B-mediated abscission checkpoint, consequently, depletion of CHMP4C results in the accumulation of genetic damage. Thus, the ESCRT machinery protects the cell against genetic damage by coordinating its cytokinetic activity with the abscission checkpoint.

Disrupting Drug Memories

In drug recovery programs, conditioned responses to drug cues can be inhibited by extinction protocols. However, extinguished behavioral responses can return after renewed exposure to the drug itself, or to drug-associated paraphernalia, and sometimes these responses reemerge spontaneously. Attempts have been made to disrupt cue-memory reconsolidation

or to strengthen extinction learning, but these efforts have often relied on pharmacological agents that either are not approved for human use or cause problematic side effects. Xue *et al.* (p. 241; see the Perspective by Milton and Everitt) have tried to circumvent the limitations of pharmacological

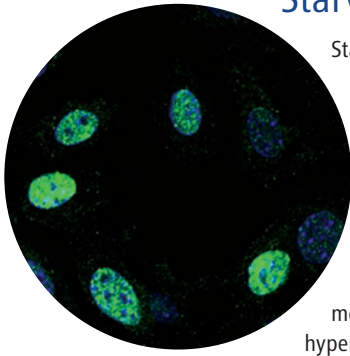
Continued on page 129



Continued from page 127

approaches in daily retrieval trials conducted in rats within the short timeframe of the “reconsolidation window” before the extinction sessions reduced drug-induced reinstatement, spontaneous recovery, and renewal of drug seeking. When translated to heroin-addicted humans, similar retrieval trials before extinction sessions impaired cue-induced heroin craving up to 6 months later. This retrieval-extinction procedure is thus a promising non-pharmacological treatment for addiction.

Starvation and Autophagy



Starvation stimulates withdrawal from the cell cycle, as well as stimulating autophagy. Are these two events connected? **Lee *et al.*** (p. 225) show a direct and nutrient-sensitive interaction between the tumor suppressor p53 and the essential autophagy gene Atg7. Further, in the absence of Atg7, the p53-dependent induction of the cyclin-dependent kinase inhibitor p21 is inhibited. This leads to Atg7-deficient cells being unable to properly withdraw from the cell cycle under starved conditions. While Atg7 deletion leads to an impairment of p53-mediated cell-cycle arrest, the Atg7-deficient cells hyperactivate p53-mediated cell-death pathways. The physiological importance of this hyperactivation is underscored by the observation that

genetic blocking of p53-mediated cell death significantly extended neonatal survival of mice in which Atg7 had been deleted.

Open and Shut Case

Voltage-sensing domains (VSDs) control the activity of voltage-gated ion channels to regulate the ion flow that underlies nerve conduction. Structural and biophysical studies have provided insight into voltage gating; however, understanding has been hindered by the lack of a crystal structure of a fully closed state. Starting from a structure of an open conducting state, a voltage-gated K⁺ channel, **Jensen *et al.*** (p. 229) used all-atom molecular dynamics simulations to show the conformational changes involved in switching to the closed, nonconducting state. Additional simulations revealed the major steps of channel activation. The computational determination of a closed state may guide development of drugs to treat channelopathies associated with this resting state.

Translation Block

MicroRNAs (miRNAs) are small, noncoding RNA genes that are found in the genomes of most eukaryotes, where they play an important role in the regulation of gene expression. Although whether gene activity is repressed by blocking translation of messenger RNA (mRNA) targets, or by promoting their deadenylation and then degradation, has been open to debate. **Bazzini *et al.*** (p. 233, published online 15 March) and **Djuranovic *et al.*** (p. 237) looked at early points in the repression reaction in the zebrafish embryo or in *Drosophila* tissue culture cells, respectively, and found that translation was blocked before target mRNAs were significantly deadenylated and degraded. Thus, miRNAs appear to interfere with the initiation step of translation.

Monkey See, Monkey Read

An orthographic object such as a set of letters, and the ability to recognize such sets as words, is a key component of reading. The ability to develop these skills has often been attributed to the prior acquisition of a complex language. For example, we learn how letters sound and thus recognize when a particular letter makes up part of a word. However, orthographic processing is also a visual process, because we learn to recognize words as discrete objects, and the ability to read may thus be related to an ability to recognize and classify objects. **Grainger *et al.*** (p. 245; see the Perspective by **Platt and Adams**) tested orthographic skills in baboons. Captive, but freely ranging, baboons were trained to distinguish real English words from combinations of similar letters that are not words, and they were able to distinguish real words with remarkable accuracy. Thus, a basic ability to recognize words as objects does not require complex linguistic understanding.

CREDIT: IN HYE LEE



Bruce Alberts is Editor-in-Chief of *Science*.

Creativity at the Interface

THE BIOCHEMISTRY THAT MAKES LIFE POSSIBLE IS BASED ON A COMPLEX NETWORK OF MANY thousands of interactions between molecules, and it presents an enormous challenge to the scientists trying to understand it. This special issue of *Science*, with its focus on computational biology, demonstrates how mathematics and computer science are being successfully harnessed to tease apart this complexity (see p. 171). But we are only at the very beginning of the process, and it is certain that reaching a true understanding of cells and organisms will require many more contributions from mathematicians, computer scientists, engineers, physicists, and chemists to complement the efforts of biologists. For this reason, graduate schools have become increasingly enthusiastic about recruiting outstanding students with strong backgrounds in these fields to address challenging problems in the biological and biomedical sciences. This is an important trend, except that too often faculty mistakenly assume that learning biology is easy, leaving these very talented young people nearly on their own to acquire the biological wisdom that they will need to explore the many mysteries in living systems. In fact, it is not at all easy to acquire the type of deep understanding of biology that is required to make wise decisions about what is, and what is not, an important problem to investigate; and a successful career in research will require much more than just a union of different expertise and tools.

Doing good science is a highly creative endeavor, much like producing a piece of art. Like an artist confronting a blank canvas, any scientist exploring biological systems is faced with an enormous number of choices. The first choice concerns exactly what problem to investigate with the tools that are available. To make this critical decision wisely, one needs to appreciate how solving any particular problem relates to clarifying other poorly understood aspects of a cell or organism, because the research problems of greatest interest will aim to fill these important gaps. Should those who mentor young scientists place more emphasis on preparing them to make such judgments? More specifically, what type of graduate courses could most efficiently address this need?

The next critical step is to design a promising strategy for attacking the chosen problem. Creativity is essential if one is to make a unique contribution, and a broad knowledge of what has previously been accomplished is key. As the French mathematician Henri Poincaré wrote more than a century ago: "To create consists precisely in not making useless combinations and in making those which are useful and which are only a small minority. Invention is discernment, choice . . . Among chosen combinations the most fertile will often be those formed of elements drawn from domains which are far apart. . . . The true work of the inventor consists in choosing among these combinations so as to eliminate the useless ones . . ."*

In biology as in other fields, the vast majority of possible investigations that could in principle be carried out are uninteresting, involving what Poincaré might have called "useless combinations of prior knowledge," and should be avoided. But how to choose? Should mentors spend more time helping students and postdoctoral fellows think broadly about research strategies, with the aim of preparing them to address the most important problems, whose solutions could fill critical gaps in our knowledge? Courses that explicitly analyze the decisions that outstanding scientists have made, emphasizing some paths not taken, could be productive here.

In biology, scientists are producing an enormous amount of data, but many creative new approaches will be needed to convert the data into the deep understandings of biological mechanisms needed for breakthroughs that benefit humanity. How to best train the next generation to meet this challenge is a fascinating question to contemplate, as we work to improve the effectiveness of the scientific enterprise and expand its role in the world.

— Bruce Alberts

10.1126/science.1223013

*H. Poincaré, *Mathematical Creation*, in J. R. Newman, *The World of Mathematics*, vol. 4 (Dover Publications, Mineola, NY, 2004) (www.ias.ac.in/resonance/Feb2000/pdf/Feb2000Reflections.pdf).



MICROBIOLOGY

Thorn in TB's Side?

Multidrug-resistant tuberculosis (TB) is increasing in prevalence worldwide and is a particular problem for the poor, the malnourished, and the immunocompromised. Despite the global and uncontrolled epidemic of tuberculosis, relatively few pathogenic mechanisms are understood for the causative mycobacterium, *Mycobacterium tuberculosis*. The best-characterized mycobacterial pathogenic systems are the ESX-1 protein secretion system and the waxy cell wall that protects the bacteria within the host. Joshi *et al.* describe EccA1, an ATPase protein whose gene is located at the periphery of the ESX-1 locus, which is required for ESX-1 protein secretion functions. The EccA1 protein was found to interact with key enzymes required for the synthesis of mycolic acids, the lipids central to the waxy cell envelope. Thus, EccA1 may be responsible for the functional coordination of the ESX-1 protein secretion system with cell wall biosynthesis. Encouragingly, interfering with EccA1 ATPase function caused mycobacterial cells to become more sensitive to antibiotics that target the mycolic acid synthesis pathways. — SMH
Chem. Biol. **19**, 372 (2012).

PHYSICS

Heat in Hiding?

Control over the propagation of electromagnetic radiation has been revolutionized by the discovery and development of transformation optics. Theoretical and experimental work has shown that the coordinate system of Maxwell's equations that governs how light propagates through a material can be manipulated at will by the careful design of metamaterial structures—giving rise to invisibility cloaks and perfect lenses. Guenneau *et al.* now show that such transformation principles could also be applicable to heat, whereby the coordinate system of the diffusion equation can be manipulated to control the flow of heat through a particular region. Numerical simulations support the design of fairly simple structures that may function as thermal cloaks or thermal concentrators. If realized, such structures could find use in thermal management systems for microelectronic circuits or stealth applications where hot objects can be hidden from view. — ISO

Opt. Express **20**, 8207 (2012).

BIOPHYSICS

A Protein's Magnetic Personality

Cryptochromes, identified in plants as blue-light photoreceptors, may have yet another function to add to their résumé. The proteins are known to help regulate circadian rhythm and development and are found in plants,

insects, and animals. Sequence similarities also link cryptochromes to bacterial DNA photolyases. Maeda *et al.* have now analyzed how redox signaling through the cofactor flavin adenine dinucleotide (FAD) can make these proteins function as magnetoreceptors. Studying a cryptochrome from *Arabidopsis* and a DNA photolyase from *Escherichia coli*, the authors spectroscopically measured microsecond radical-pair kinetics. In response to light, electron transfer from tryptophan residues generates a FAD radical anion. Imposition of a 28-mT magnetic field promoted back electron transfer (presumably by influencing spin state interconversion rates), with a consequent drop in conversion of the initial radical pair to a longer-lived intermediate via tryptophan deprotonation. Effects were apparent in magnetic fields as low as 1 mT. Although this is somewhat stronger than Earth's magnetic field, these particular *Arabidopsis* and *E. coli* proteins are not normally known for perceiving magnetic fields. The authors speculate about how cryptochrome proteins would need to be tethered and immobilized to function more efficiently as magnetic compasses in birds. — PJH

Proc. Natl. Acad. Sci. U.S.A. **109**, 4774 (2012).

EDUCATION

Getting the Question Right

An inquiry-based science curriculum requires teachers to generate scientific questions for their students. Are students studying to be teachers (preservice teachers) learning this skill?



Graves and Rutherford examined the ability of elementary preservice teachers to generate a testable question from earth science data available online. One group was given instruction on what constitutes a testable question, and the other was referred to a conclusion rubric in a laboratory manual. Generated questions were categorized as testable or nontestable, and testable questions were analyzed using

a rubric designed to evaluate the preservice teacher's ability to identify variables, state investigative parameters, and identify relationships between variables. The majority of preservice teachers from both groups wrote questions that were testable but still needed modification, suggesting that the instruction given to the test group did not improve the quality of their questions. Moreover, it highlights the need to provide preservice teachers with more opportunities to experience the nature of science by participating in research. — MM

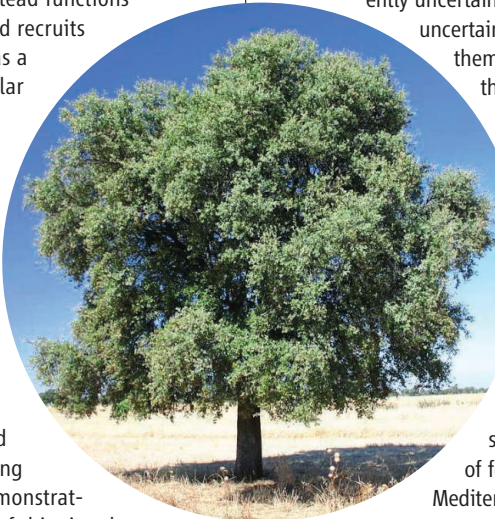
J. Coll. Sci. Teach. **41**, 46 (2012).

IMMUNOLOGY

Sorting Out Toll in Flies

Seminal studies of the Toll pathway in *Drosophila* led to the discovery of Toll-like receptors (TLRs) in mammals and paved the way toward our current understanding of innate immune signaling. In mammals, pairs of adapter proteins couple to TLRs to activate downstream signaling. In particular, a "sorting" adapter (either TIRAP or TRAM) helps to localize TLRs to a region of the cell that promotes signaling. Once sorted, a "signaling" adapter (either MyD88 or TRIF) then binds and initiates downstream signaling that culminates in changes in gene expression. Surprisingly, however, homologs for the sorting adapters have not been found in flies, and the MyD88 homolog in flies (dMyD88) does not appear to act as a signaling adapter. Marek and Kagan investigated the innate signaling mechanisms in *Drosophila* and found that dMyD88 instead functions as a sorting adapter and recruits Tube, which functions as a signaling adapter. Similar to mammalian cells, the sorting ability of dMyD88 was dependent on a C-terminal phosphoinositide-binding domain. Flies that expressed dMyD88 lacking this domain exhibited impaired immune defense, and other insect species expressed phosphoinositide-binding dMyD88 homologs, demonstrating the important role of this signaling module in immune defense. — KLM

Immunity **36**, 10.1016/j.immuni.2012.01.019 (2012).



PLANT SCIENCES

Splicing Shifts

Alternative splicing, which affects about 40% of intron-containing genes in *Arabidopsis*, is a mechanism whereby mRNA transcripts are adjusted in ways that affect the function or stability of the mRNA or the structure of the translated protein. The circadian clock is also an important regulator of many genes in the plant genome. James *et al.* have now analyzed the intersection of these two complex phenomena, and discovered even more complexity. Although the period of the *Arabidopsis* circadian clock is rather stable over a range of temperatures, the clock does respond to temperature: Low

temperatures can cause a stall, and temperature cycles can entrain the clock. The authors analyzed the handful of core clock genes and found extensive alternative splicing among these transcripts. The splicing events changed in response to temperature, often in surprising ways. For example, transcripts encoding proteins thought to have redundant functions showed divergent splicing patterns in response to temperature shifts. Thus, models of circadian clock function should incorporate the added complexity of alternative mRNA splice variants that are modulated by temperature shifts and acclimations. — PJH

Plant Cell **24**, 10.1105/tpc.111.093948 (2012).

ECOLOGY

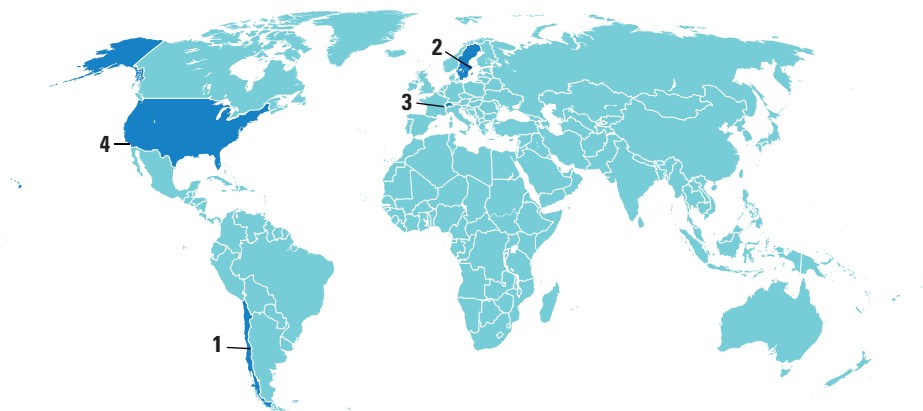
Climate Model Comparisons

Predicting the effects of climate change on the future distributions of species is an inherently uncertain exercise. There are uncertainties in climate models themselves and also in the models of species' response to climate change. To address this problem, Cheaib *et al.* compared the predictions of eight different species' response models for five dominant tree species in the flora of France, representative of the range of forest communities from Mediterranean in the south to more temperate in the north.

For the two evergreen species considered, there was generally good agreement between models. Holm oak, the dominant Mediterranean species, substantially increases its range under all model scenarios; the range of Scots pine, a species of cooler and mountainous regions, was predicted to contract under most models. However, models agreed relatively poorly in their predictions of range shifts of three temperate broad-leaved deciduous species. A principal source of uncertainty is the current limits to understanding the effects of increasing CO₂ concentrations on the physiology of these species. Such comparisons not only help foresters and conservation managers judge the probability of success (or otherwise) of management alternatives, but also help to focus future research on the areas of greatest uncertainty — AMS

Ecol. Lett. **15**, 10.1111/j.1461-0248.2012.01764.x (2012).

AROUND THE WORLD



Santiago 1

Patagonian Dam Moves Forward

A controversial \$3.5 billion hydroelectric dam project in Patagonia—Project HidroAysén—won a key legal battle last week when the Chilean Supreme Court rejected seven appeals from environmentalists and local groups seeking to stop it. Opponents had asked the Supreme Court



Protesters in Santiago oppose Project HidroAysén.

to overturn a lower court's ruling in favor of the project, which is supported by the national government.

Builders plan to erect five dams on the Baker and Pascua rivers in the pristine Aysén region, flooding about 6000 hectares. The company says the dams could produce 20% of Chile's electricity by 2020. But opponents say that the risks—including the likelihood of glacial lake outburst floods—are greater than has been acknowledged. The company has yet to win approval to build power lines for the project, which will require a 2000-kilometer-long continuous corridor from the dams to Santiago.

Stockholm 2

Life Science Lab Gets Fresh Funding

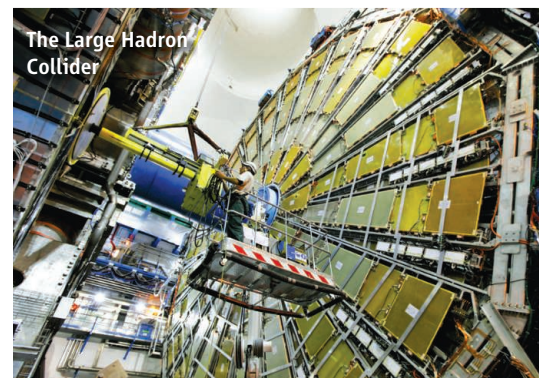
A groundbreaking Swedish life science research initiative will add lab space and nearly triple its ranks to 1000 investigators, thanks to newly announced infusions of funds. The private Knut and Alice Wallenberg Foundation will donate \$33.4 million, and pharmaceutical company AstraZeneca will add between \$5 million and \$10 million annually over the next 5 years, to Sweden's Science for Life Laboratory (SciLifeLab). The Swedish government later this year will also inject more money into the 2-year-old collaboration between four of the country's universities, according to Jan Björklund, Sweden's minister for education.

In a strategic bid to create a national life sciences powerhouse, Sweden committed \$75 million in 2010 to create SciLifeLab, whose campuses in Stockholm and Uppsala focus on proteomics studies, bioimaging, and projects such as sequencing the genomes of the Norway spruce and microbes living in the Baltic Sea (*Science*, 14 May 2010, p. 805). "We have high ambitions," Björklund said at a 3 April press conference in Stockholm. The new funds will enable SciLifeLab "to gather the sharpest brains and lay the foundation for new and major breakthroughs." <http://scim.ag/scilife>

Geneva, Switzerland 3

Beginning of End of Higgs Hunt

After its annual winter shutdown, the world's highest-energy atom smasher, the Large Hadron Collider (LHC) at the Euro-



pean particle physics lab, CERN, resumed taking data on 5 April, running at slightly higher energy than before. So begins what should be the final chapter in the decades-long hunt for the Higgs boson, the hypothetical particle that is key to physicists' explanation of how all fundamental particles get their mass. The LHC feeds two huge particle detectors, ATLAS and CMS, that are hunting the Higgs, and last year both spotted possible signs of the particle. This year, the LHC should produce three times as much data as it did in 2011, enough to clinch the discovery—or prove that the Higgs doesn't exist. "I would imagine that some time this summer, when we have collected as much data as we got last year, we'll get a hint of which way it will go," says Bruce Mellado, a member of the ATLAS team from the University of Wisconsin, Madison. "Either we'll confirm the excesses we saw in 2011 or we won't."

Pasadena, California 4

Giant Magellan Telescope Tells NSF 'No Thanks'

The organization behind the \$700 million Giant Magellan Telescope (GMT) has decided not to seek financial help from the U.S. government to build its 24.5-meter

NOTED

>A new tool is available to **help doctors detect signs of Alzheimer's disease**: On 6 April, the U.S. Food and Drug Administration (FDA) approved the radioactive drug Amyvid, which binds to telltale amyloid plaques in the brain. The drug has been used for years in research, including clinical trials, but FDA had held off on approving it pending more evidence that doctors would read the scans consistently.

telescope. Its decision leaves the \$1 billion Thirty Meter Telescope (TMT) project as the sole contender for federal support, should the government be able to afford it in the future.

In late December, the National Science Foundation (NSF) announced that it did not anticipate having money to fund either project until sometime in the next decade. At the same time, NSF said it would offer \$1.25 million over 5 years for the development of a public-private partnership plan that might lead to the building of a large telescope, if NSF were to ever have funds available.

The GMT Organization opted out, issuing a press release on 2 April that explained it would instead seek to cultivate



A blasting site in Chile for GMT.

partnerships on its own. "The partners in the project feel that they are making such rapid progress that they have chosen to press ahead at full speed, looking to link up with the NSF at a later date when the needs of both organizations are better aligned," the press release states.

http://scim.ag/_gmto

NEWSMAKERS

Morehouse Cardiologist Tapped to Head NHLBI

Gary Gibbons, a cardiologist and scientist at Morehouse School of Medicine in Atlanta, has been named director of the National Heart, Lung, and Blood Institute (NHLBI).

Gibbons, 55, founded and directs a cardiovascular research institute at Morehouse that links basic science and health in minority populations. Gibbons's own lab studies how genetic variation influences vascular biology and cardiovascular disease. He will join NHLBI this summer.

The \$3.1 billion NHLBI is the third-largest of the National Institutes of Health's 27 institutes and centers. NHLBI has not



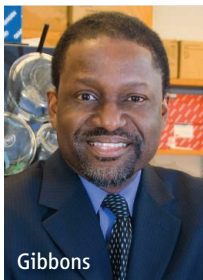
The Rebounding of the Lark

The critically endangered Raso lark (*Alauda razae*) lives on a single desert island in the Cape Verde Archipelago. Happily, the birds have undergone a remarkable boom over the past decade, according to a paper published online this week in *Animal Conservation*. Since 2004, the population of the birds has skyrocketed from 65 to 1490—including a tripling in numbers last year alone—according to a team led by ornithologist Michael Brooke of the University of Cambridge in the United Kingdom. "It's unprecedented among birds," Brooke says. The increase correlates with greater rainfall, which probably boosts the number of insects available to eat.

Andy Symes of BirdLife International, who has reviewed the conservation status of the lark, calls the finding "fantastic news." But he cautions that the population could easily fall if the island dries out again. Both he and Brooke recommend that a second population be established on a nearby island to help ensure that the species isn't wiped out by an unlucky event such as severe drought, disease, or new predators.

had a permanent director since Elizabeth Nabel left in late 2009 to head Brigham and Women's Hospital in Boston. Gibbons was interested in the job because of his "intimate" familiarity with NHLBI—he's a longtime grantee and adviser—and his commitment to "its legacy of doing discovery science that advances public health," he says.

He plans to update the institute's strategic vision "with a renewed look that's more timely and contemporary."



Gibbons

FINDINGS

Huge Dust Devil Prowling Mars

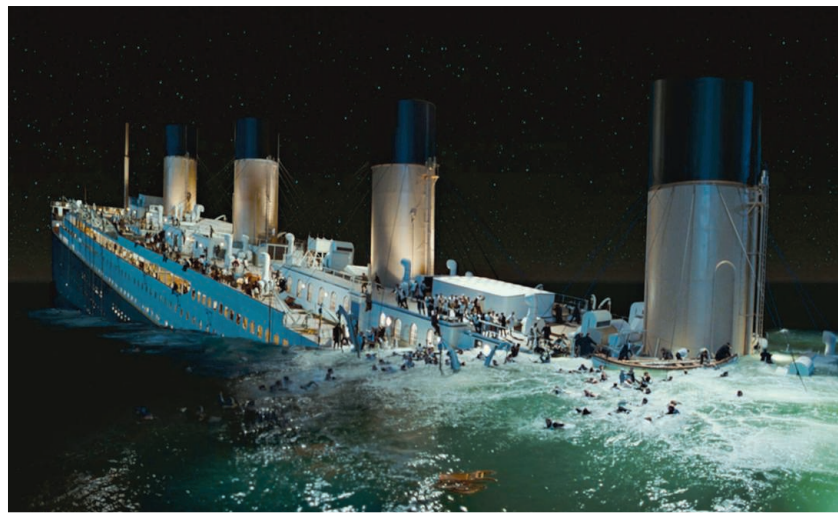
Earth may have terrifying tornadoes, but when it comes to dust devils, Mars has us beat. A camera onboard the Mars Reconnaissance Orbiter captured a swirling funnel of dust spinning up to an altitude of 20 kilometers.

On Earth, tornadoes often reach such heights, but dust devils seldom reach more than a few hundred meters. That's because dust devils only draw their energy from the solar heating of the surface; tornadoes also tap the heat energy from the condensation of water vapor in a tornadic storm.

Mars is too dry for that, but the

>>>

Random Sample



The Research Will Go On: Spring Tides, Mirages, and Star Fields

Ultimately, it was an iceberg that sank the Titanic on the night of 14 April 1912. But with the 100th anniversary of the sinking of the ocean liner looming, several ideas have popped up about how conditions on the north Atlantic Ocean might have helped set the stage for disaster.

In the April 2012 issue of *Sky & Telescope* magazine, physicists Donald Olson and Russell Doescher, both of Texas State University in San Marcos, note that a powerful spring tide may have helped push icebergs into the ocean liner's path. On 4 January 1912, the moon—within 6 minutes of being full—was at its closest approach to Earth in 1400 years. The resulting increase in tides may have not only enhanced the calving of Greenland glaciers, but also kept the icebergs from running aground along the coasts of Labrador and Newfoundland. Instead, the researchers suggest, the icebergs drifted into the Labrador Current, reaching the shipping lanes by April.

British historian Tim Maltin, meanwhile, argued in a National Geographic special that aired 8 April that an iceberg in the ship's path might have been all but invisible to a lookout—thanks to a “super-refraction,” a mirage resulting from the interaction of the cold Labrador Current and the warm Gulf Stream waters. The resulting atmospheric conditions, he argued, would have created a false horizon that hid the iceberg from view.

But at least one scientific detail has been nailed down—in last weekend's rerelease of James Cameron's 1997 blockbuster *Titanic* (in 3D). Prompted by a “snarky” note from astrophysicist Neil deGrasse Tyson, Cameron corrected the star field over the sinking ship to reflect what a passenger adrift in 1912 at that latitude and longitude would have actually seen.



A martian dust devil, 20 kilometers high.

>>FINDINGS

thinness of its air allows dust devils to soar, lofting dust high into the atmosphere between major dust storms. Some Mars scientists suspect dust devils generate enough static electricity to produce bleachlike chemicals that consume any organic matter—and any living thing—in martian soil. And dust devils can also lend NASA a hand; they occasionally blow the dust off a rover's solar cells.

BY THE NUMBERS

100% Percentage of ongoing NASA missions—nine in total—that will be extended, according to its 2012 senior review.

10 million Number of species that researchers, writing in *Systematics and Biodiversity*, say the ecological community should seek to inventory over the next 50 years.

Majorana Fermions Found

Seventy-five years after Italian physicist Ettore Majorana proposed their existence, ephemeral particles now known as Majorana fermions have been spotted by researchers.

Online this week in *Science*, Leo Kouwenhoven and colleagues at Delft University of Technology and Eindhoven University of Technology in the Netherlands report that they spotted expected signatures of Majorana fermions in specially designed transistors. In standard transistors, applying a voltage to an electrode called a gate turns on the flow of current between two other electrodes. Previous theoretical predictions suggested that if one of the secondary electrodes was a superconductor, and the current was allowed to flow through a special semiconductor nanowire under a magnetic field, the combination would force electrons in the nanowire to behave collectively as if Majorana fermions were present at opposite ends of the wire. That's exactly what Kouwenhoven's team found.

The old-yet-new particles are expected to have properties that make them ideal for constructing a quantum computer (*Science*, 8 April 2011, p. 193). When you move two Majorana fermions with respect to one another, they essentially “remember” their former position, a property that could be used to encode data at the quantum level. Kouwenhoven's group hasn't spotted that signature yet, but they're on the hunt now. <http://scim.ag/majferm>

Science LIVE

Join us Thursday, 19 April, at 3 p.m. EDT for a live chat with experts on **how deep wastewater injection is triggering earthquakes** around the country. <http://scim.ag/science-live>

EUROPEAN DEBT CRISIS

Research Cuts Will Cause 'Exodus' From Spain

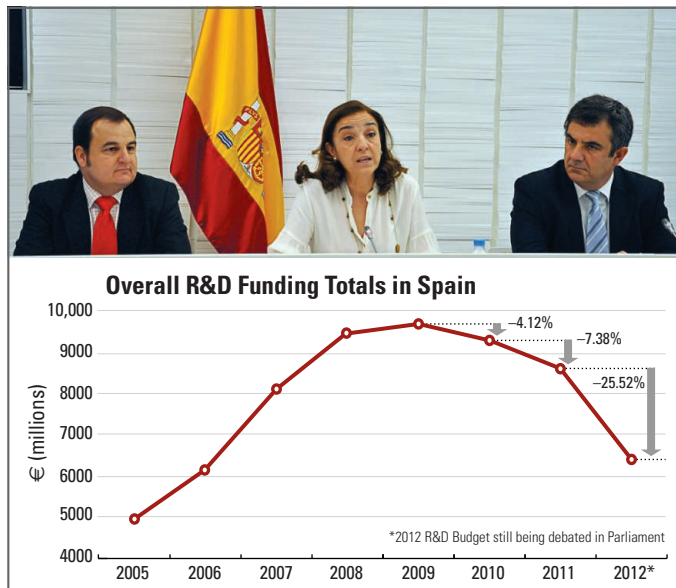
Spanish scientists had ample warning that they were facing a tough funding year ahead. But last week's announcement that the long-delayed 2012 national budget would slash the funding for science by more than 25% surpassed their worst predictions.

According to the Confederation of Spanish Scientific Societies's (COSCE's) analysis of the budget, carried out since it was presented to the Spanish Parliament on 3 April, the national government will allocate €6.40 billion to scientific investigation, development, and innovation in 2012. Of that, €5.64 billion will be for civil research—a 25.6% decrease compared with last year's budget. The remaining €757 million will be spent on military research—a 24.9% drop from 2011. The overall 25.5% cut is “the most drastic cut known” since national research programs were put in place in the late 1980s, COSCE said in a press statement. COSCE is also concerned because in recent years the government has not even paid the full amount allocated in the science budget.

The budget cut “is much worse than expected, and that is despite all the mobilizations, statements, and calls of alert from the scientific community,” says Francisco J. Hernández Heras, a Spanish neuroscience postgrad at the University of Cambridge in the United Kingdom. In January, just a few days after the government announced a package of austerity measures that anticipated a €600 million cut in the 2012 science budget, Hernández Heras initiated a petition for Spanish taxpayers to allocate part of their taxes to science as a way of making up the lost money. Protests from the scientific community culminated in an open letter to the government and Parliament on 27 March from COSCE, the Conference of Spanish University Chancellors, the grassroots organization Investigación Digna, the Federation of Young Investigators, and major trade unions.

The letter, which garnered the sup-

port of more than 50 additional organizations and 26,700 researchers, warned that the anticipated cut—which turned out to be much smaller than the actual cut—“would cause considerable long-term damage to the already weakened Spanish research system, contributing to its collapse.” By applying a 25% cut to science, compared to the 16.9% average across all ministries, “the Government has not only ignored the scientific community but tried to annihilate it,” says Amaya Moro-Martin, a spokesperson for Investigación Digna.



Past the peak. Spanish science minister Carmen Vela Olmo (center) has presented a science budget that takes funding back to nearly 2006 levels.

Secretary of State for Research, Development, and Innovation Carmen Vela Olmo tried to reassure scientists. Under the Spanish research funding system, a large sum—€2.3 billion in 2012—is earmarked for loans to companies to carry out R&D. Although this sum was cut by 28.5% compared to last year, this should be “less damaging,” Vela stated, because more than half the fund was unused last year.

But scientists are especially concerned about the €1.64 billion allocated as lump sums to public research institutes and competitive grants to research teams—down from

€2.12 billion last year. Of that money, the chunk of the competitive funding for basic research projects, scientific training, post-doctoral hiring, and scientific infrastructure is to be cut by 38% to €451 million in 2012. “This reduction of competitive funding is in my view the most dangerous evolution of the budget,” says Luis Sanz-Menéndez, director of the CSIC Institute of Public Goods and Policies in Madrid and chair of the Committee for Scientific and Technological Policy of the Paris-based Organisation for Economic Co-Operation and Development. “Such a big reduction ... is damaging the most dynamic part of the system.”

That decision has already been made for the flagship Juan de la Cierva postdoctoral fellowships and the Ramón y Cajal contracts, which are the closest equivalent to tenure-track positions in Spain. Altogether, their number will decrease by 43% to 340. Young researchers are hit especially hard, with the government also announcing in December that no new permanent positions would be created in the public research institutes, not even to fill positions left vacant by retirement. This will prompt “an exodus of several researcher generations,” warns the Federation of Young Investigators.

After absorbing deep cuts in previous years, the public research institutes are relatively spared this year with a 3.5% reduction in government funding for salaries and part of their running costs. But the large decrease in competitive grants for research teams will indirectly result in less money entering universities to pay for overhead costs, Sanz-Menéndez says. Although universities are mainly supported by the regional governments, austerity measures at the federal level will also create “serious problems,” Sanz-Menéndez adds. “We will probably witness also reductions” in the regional government funding of universities.

“The whole country is suffering a terrible financial and economic crisis, then it would be naïve to believe that [science] will be protected in an environment where you have 5 million unemployed people, ... reductions in the health system, or in other ... public services,” Sanz-Menéndez says. He encourages scientists to try to promote a more selective and competitive allocation of funds and

greater internationalization of Spanish science. “There is a chance to make reforms and change the functioning of the system.”

But most scientists are disappointed. A leitmotiv in public statements of both this and the previous government has been the need to switch from a construction and tourism-based economy toward a knowledge-based one. The budget is “illogical” because it goes

in the opposite direction and is “irresponsible because it will have lethal consequences in the short- and in the long-term, not only for Spanish science but [also] for the Spanish economy,” says Moro-Martín, who is a Ramón y Cajal researcher at the Center for Astrobiology near Madrid.

The battle is not over yet, however. Budget figures could be adjusted by amend-

ments in Parliament. “In fact, last week the [opposition party] presented a [proposal] in order to consider R&D as a strategic objective and work towards a global agreement to save R&D,” says COSCE President Carlos Andradas Heranz, a mathematician at the Complutense University of Madrid. “But the actual numbers do not invite [optimism].”

—ELISABETH PAIN

EUROPEAN DEBT CRISIS

Greece Eyes CERN, ESA Cuts to Plug Budget Gap

To plug a €10 million hole in its science budget while avoiding the closure of domestic research centers, Greece has begun renegotiating its subscriptions to and memberships in international organizations, notably the European Space Agency (ESA) and the CERN particle physics laboratory near Geneva, Switzerland. It aims to reduce, or at least partly defer, its annual payment to CERN and may leave the lab altogether if it is unable to do so.

The government announced the €10 million cut on 6 March as part of a broader reduction in Greece's debt demanded by the *troika* of the European Union, the European Central Bank, and the International Monetary Fund. The money will be sliced from the roughly €80 million budget of the education ministry's general secretariat of research and technology. That budget accounts for a big chunk of Greece's total research spending, which amounts to only 0.6% of gross domestic product—a far smaller share of national wealth than most other European Union countries (1.85% on average).

Research secretary Konstantinos Kokkinoplitis decided initially that the savings should come from the country's 11 national research centers, which together account for some €55 million of his budget. These centers, however, had already experienced a 30% cut in funding over the previous 2 years. According to Costas Synolakis, president of the Hellenic Center for Marine Research in Anavyssos, just south of Athens, any additional squeeze would mean closing centers for the last few months of the year; staff members cannot legally be fired or have their salaries reduced. Like many other Greek scientists, Synolakis believes that if cuts to research have to be made, then interna-

tional subscriptions—roughly €27 million in total—will have to be reduced.

Kokkinoplitis is negotiating with ESA to pay up to €6 million of Greece's €14 million 2012 subscription in 2013, and he hopes to secure a similar deal with CERN. He met with the directors of Greece's 11 research centers in mid-March, and most of them, Synolakis says, “agreed that Greece needs to be part of CERN.” However, Synolakis adds,

One less flag? Research secretary Konstantinos Kokkinoplitis wants to reduce Greece's subscription to CERN or pull out all together.



everyone present also agreed that “if it comes to the survival of the centers, the contribution to CERN will need to go or be substantially reduced. ... It is sad, but it came to that.” Says Kanaris Tsinganos, director of the National Observatory of Athens: “It would be weird to close the research centers and pay all of these international subscriptions.”

After meeting with the research center directors, Kokkinoplitis wrote to CERN Director General Rolf-Dieter Heuer, saying that if he cannot reduce the €14.7 million that Greece needs to pay the lab in 2012, then the

country may have to pull out entirely. He then traveled to Geneva on 27 March and, he says, discussed the possibility that Greece would defer some—perhaps 50%—of this year's payment and then pay the balance next year or the year after.

However, Petros Rapisdis, a particle physicist at the National Center for Scientific Research in Athens and Greece's scientific representative on CERN's council of member states, questions whether the country would be able to make good on any deferred payments. He points out that when in difficulty in the past, Greece has always reduced, rather than merely deferred, its contribution. Indeed, council documents show that for most of its 58-year membership in CERN (Greece was one of the founding members), the country has not paid its full dues. Like every other member state, its contribution is tied to its gross national product, but often it has paid 50% or less of its share.

Such special treatment has required repeated approvals by at least two-thirds of CERN's member states. But that may be more difficult this time, Rapisdis says. “Kokkinoplitis will have a hard time because eastern European countries such as Bulgaria, Hungary, and Slovakia are not asking for any special arrangement,” he says.

Greece is not the only country having difficulty paying its CERN membership. In 2011, Belgium, Italy, and Portugal all failed to pay up fully by the end of the year, and half of Spain's roughly €80 million contribution for 2011 is still outstanding. However, according to Carlos Pajares, a particle physicist at the University of Santiago de Compostela and the Spanish scientific representative on the CERN council, Spain should meet about 90% of its obligation for 2012, despite huge cuts in research funding in general (see p. 139), and the remainder will perhaps be diverted from separate funding on accelerator R&D.

—EDWIN CARTLIDGE

Edwin Cartlidge is a writer based in Rome.



Deep-sea feast. A baited camera attracts snailfish (left) and amphipods (above).

MARINE SCIENCE

Ocean's Deep, Dark Trenches to Get Their Moment in the Spotlight

Like Captain Ahab's white whale, deep-sea trenches have lured explorers for decades, tantalizing them with glimpses of an ecosystem shrouded in darkness. The latest to attempt to pierce the gloom, movie director James Cameron, last month took his privately built one-man submersible 10,000 meters down to the deepest point on Earth: the Challenger Deep in the Pacific Ocean's Mariana Trench. Although Cameron's journey to the abyss yielded little new scientific data, it whetted the public appetite for information about life in the otherworldly environments of deep-sea trenches. An international group of marine scientists may soon provide a feast of such data, from the first major systematic study of a deep-sea trench.

If all goes as planned, early next year a 3-year project dubbed HADES (Hadal Ecosystem Studies) will take its inaugural plunge into the Kermadec Trench, a 10,000-meter-deep gash off the northeast coast of New Zealand. There, a team headed by deep-sea ecologist Timothy Shank of the Woods Hole Oceanographic Institution (WHOI) in Massachusetts will use robotic tools to try to answer some long-standing questions about the origin, evolution, and distribution of life in the trenches. In particular, the team—which includes collaborators at universities in the United States and United Kingdom, the National Institute of Water and Atmospheric Research in New Zealand, and the U.K.'s National Oceanography Centre—will focus on the hadal zone, between 6000 and 11,000 meters down. "It's our first look at an

ecosystem," Shank says. "This is terra incognita in some ways."

Earlier trench research efforts, starting in the late 1940s, were limited to dragging nets and dredges to collect samples (see Perspective, <http://scim.ag/RALutz>). HADES scientists, however, will use a broad array of more capable tools, including WHOI's hybrid remotely operated vehicle *Nereus*, which can sample broad swaths of ocean while operating autonomously or tethered to a ship. They'll also have "hadal landers"—baited traps and cameras that freefall to the bottom, record data, and float back to the surface—and devices that can measure the physiology of deep-ocean creatures. "We're not blindly towing a net behind a ship [anymore]," says Jeffrey Drazen, a physiological ecologist at the University of Hawaii, Mānoa.

Drazen and his colleagues will need all these tools to study a habitat no longer viewed as a kind of cold storage where barely anything happens. Past studies have shown that trenches are geologically and biologically active. Formed when a denser tectonic plate sinks beneath a lighter one, they harbor seeps, seamounts, and mud volcanoes, and are even influenced by the moon. Those tidal cycles challenge "the notion that the deep sea is a constant environment," says marine biologist Alan Jamieson of the University of Aberdeen in the United Kingdom. He is studying whether and how cockroach-sized crustaceans called amphipods sense those daily pressure changes. "They may well be entrained to a tidal cycle [even though] they

don't know what the moon is," he says.

Scientists are also "learning that a lot of things accumulate in trenches: food, carbon, chemicals, and even our trash," says WHOI's Shank. Researchers have found everything from plastic raincoats to evidence of a Holstein dairy cow.

The Kermadec expedition will also examine how animals deal with the high pressures in the deep sea. Marine animal physiologist Paul Yancey of Whitman College in Walla Walla, Washington, will focus on one of these adaptations: organic compounds called piezolytes. In organisms that live in shallower seas, these molecules help regulate cellular water content. But Yancey discovered that they also defend some deep-sea animals against high pressures. So far, researchers have only studied piezolytes in fish found down to 4900 meters and crustaceans and sea cucumbers down to 2900 meters. No one knows how the molecules function, or how concentrated they are, in animals at nearly 10,000 meters.

The University of Hawaii's Drazen intends to study how food availability in the trench affects metabolism. Fine organic particles drift down from surface waters and are funneled into trenches, settling along their deepest points. That means the food supply likely increases with depth in trenches, and HADES researchers suspect that if food supply determines an organism's metabolic rate, then animals along the trench's axis will have higher rates than ones farther away. They'll test that idea by deploying respirometers, chambers that measure an organism's oxygen consumption, along the Kermadec's 1200-kilometer axis. The researchers will use *Nereus*'s "slurp gun" and robotic arm to catch creatures "and plop them into these chambers" for testing, Drazen says.

Nereus will also conduct systematic video surveys of organisms across and along the trench. The Kermadec sits in a productive ocean, researchers note, in contrast to the Mariana Trench's relatively nutrient-poor waters. That's one reason much of the past "deep work, from a biological point of view, has been done in Kermadec," Jamieson notes

—and why researchers wanted to return in force. Although scientists already “have an idea of who’s there, ... we don’t know how they interact with each other,” Shank says. Ultimately, the HADES team hopes to compare the Kermadec data with older information collected on adjacent, but shallower, habitats called abyssal plains.

Researchers also hope to figure out how

animals got into trenches in the first place. One hypothesis is that Antarctic bottom water flowed into Pacific Ocean trenches, bringing animals along with it, Shank says. Over millions of years, tectonic activity isolated the trenches, trapping animal populations and leaving them to follow their own evolutionary paths. Genetic testing of Kermadec creatures could help clarify their history.

Although HADES is currently funded for work in just one trench, researchers are hoping to dig deep into other hadal trenches. “Trenches are isolated, so what happens at one doesn’t necessarily happen at another,” Aberdeen’s Jamieson says. HADES researchers would like nothing more than to spend the next decade wandering the globe, peering into the gloom.

—JANE J. LEE

CIRCADIAN RHYTHMS

Sleep Study Suggests Triggers for Diabetes and Obesity

Late nights in the lab, early morning commutes from the suburbs, Angry Birds videogame marathons into the wee hours—the demands and distractions of modern life are stealing our sleep and perhaps robbing us of our health. The longest sleep-limitation study to date, published in *Science Translational Medicine* (<http://scim.ag/OMBuxton>), found many people are on sleep and work schedules that prime them for diabetes and obesity.

Evidence for deleterious effects of reduced sleep, including a shorter life span, has come largely from epidemiological studies. Although rarer, sleep-intervention studies have begun to suggest physiological mechanisms that might account for such findings. Two years ago, for example, neuroscientist Orfeu Buxton of Brigham and Women’s Hospital in Boston and colleagues showed that young men who underwent just a week of reduced sleep had lower responsiveness to the hormone insulin, a decline that is a hallmark of type 2 diabetes.

Our 24/7 society can disrupt our schedules in another way. Humans evolved to be active during the day. Light calibrates the central circadian pacemaker, the body’s master clock in the brain. In turn, it helps harmonize molecular clocks in individual tissues so that our physiology and behavior mesh—we get hungry in the morning, for instance, and feel drowsy at night. Studies have suggested that upsetting these circadian rhythms triggers a range of health problems. That’s potentially bad news for people who have night jobs or are on rotating shifts, which require them to change work hours frequently; they often have to contend with inadequate sleep and discom-bobulated circadian cycles.

In their latest sleep study, Buxton and colleagues gauged the physiological impact of this double whammy. For nearly

6 weeks each, 21 study subjects lived in the equivalent of a hotel suite in the hospital’s Boston research lab. After storing up on sleep, these people spent 3 weeks on a regimen in which they could sleep for only 5.6 hours in each 24-hour period. Like rotating shift workers, they went to bed at varying times. To throw off their circadian rhythms, the light-dark cycle in the facility lasted 28 hours rather than the usual 24. And to prevent these rhythms from resetting, the

weeks of scant sleep and low light levels led to another potentially harmful change: Resting metabolic rate, a measure of energy use, fell by 8%. Over a year, that decrease would translate into a weight gain of nearly 6 kilograms, the team estimated.

These new findings are important because they detail “some potential pathways by which sleep and circadian disruption can lead to obesity and diabetes,” says sleep researcher Michael Grandner of the University of Pennsylvania.

After a 10-day recovery period during which the participants stayed in the lab but slept for 10 hours a night and were on a normal light-dark cycle, insulin secretion and glucose levels returned to normal. “Happily, the effect was reversible in our study,” says clinical physiologist and co-author Steven Shea, also of Brigham and Women’s Hospital. “But if you have years of that [disruption], it may be tougher to reverse.”

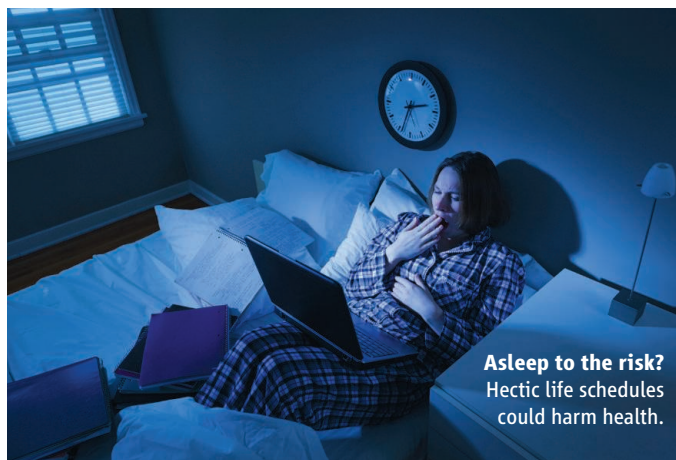
The next step, Buxton says, is to go beyond lab studies: “My interest is free-range humans.”

For example, Shea says, it might be fruitful to test blood samples from workers whose shift times change frequently to determine whether their glucose and insulin status mirror those in the sleep study.

Sleep epidemiologist James Gangwisch of Columbia University Medical Center in New York City suspects that the sleep study doesn’t reflect reality, however: “I’m not sure too many people are exposed to such extreme shifts in their circadian rhythms.”

Nevertheless, he and Grandner agree that the findings from Buxton’s team offer a cautionary message. “We live in a culture that prides itself on how little sleep we can get by on,” Grandner says. “This study provides more evidence this is not a healthy way of living.”

—MITCH LESLIE



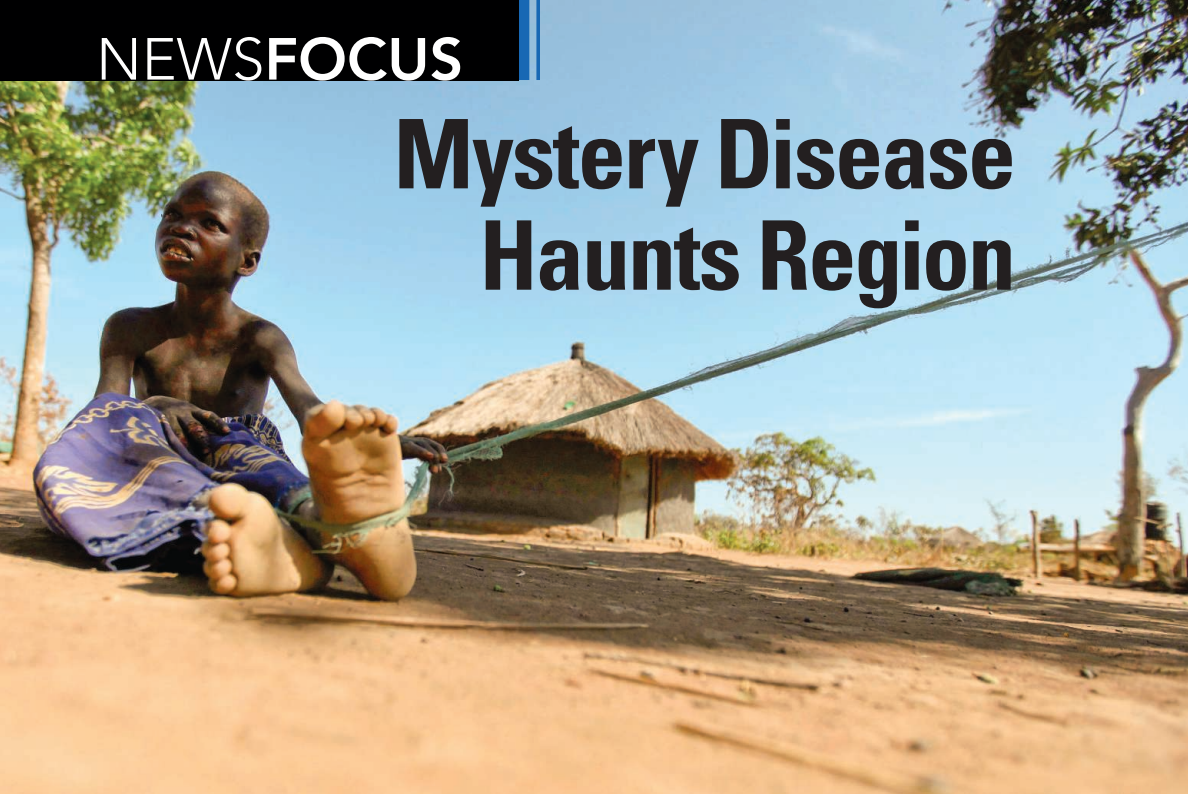
Asleep to the risk?
Hectic life schedules could harm health.

researchers kept light levels at the equivalent of twilight or dimmer.

So how did the participants, who went more than a month without Internet access, TV, or contact with anyone outside the facility, cope with these conditions? “Our general impression is that people aren’t always their kindest selves when they are sleep restricted,” Buxton tactfully notes.

Their metabolism also wasn’t at its best. The amount of glucose in each person’s blood shot up, with three people reaching levels that researchers term prediabetic. “Over time, much higher glucose levels like that would be expected to be unhealthy,” Buxton says. The team identified the likely reason: The pancreas released less insulin, the hormone that spurs cells to absorb sugar. Three

Mystery Disease Haunts Region



Could the parasite behind onchocerciasis, better known as river blindness, also explain the odd “nodding” seizures in a growing number of African children?

IN 1959, TROPICAL-DISEASE EXPERT Louise Jilek-Aall started working as a physician in Mahenge, a town in a mountainous and isolated area of southern Tanzania. She soon encountered an “astonishing” number of people suffering from epilepsy. As she investigated further, the mothers of some of the most severe cases told her their children were normal until they were around 4 or 5 years old, when they began to have seizures characterized by repeated downward movements of their heads. Jilek-Aall says the residents had a specific word for the condition, which translated literally as “nodding the head.”

Early on, children with the nodding seizures still led a somewhat typical life. They “were running around, playing with other children. They were not discriminated against at all,” recalls Jilek-Aall, who founded an epilepsy clinic in Mahenge in 1960. By the time they reached puberty, however, they grew sicker. “They became listless. They were not eating well,” and they suffered a noticeable decline in intelligence, she says. “Then one day, the usual grand mal seizures would start,” and the children would develop a form of full-blown epilepsy.

At that point, their prospects were grim. People with epilepsy were feared as possibly contagious, Jilek-Aall says: “They were shunned by the others. Some of them died of maltreatment.” The numbers were hard to determine, however. At the time, she says,

the people in Mahenge had very traditional beliefs, and it was taboo to discuss someone who had died.

Jilek-Aall, now a professor emeritus at the University of British Columbia, Vancouver, in Canada first described the nodding seizures in a 1964 paper. For many years, Western colleagues doubted or dismissed her reports, but no more. An apparent outbreak of a similar nodding syndrome in Uganda and southern South Sudan over the past few years has attracted many more researchers, including teams from the U.S. Centers for Disease Control and Prevention (CDC) and the World Health Organization (WHO), to look for possible causes. They are chasing several suspects, including a parasitic worm, but so far there’s no proven culprit.

The world media has also become fascinated, showing videos of children nodding their heads uncontrollably or staring vacantly as if in a trance, a state that often follows the head-nodding attacks. Because food seems to trigger the attacks, many can’t eat properly and quickly lose weight. Gradually, they become more and more disabled. News accounts have described how families tie their children to trees so that they don’t wander off or fall into fires or rivers. Yet many do have deadly accidents; others die of malnutrition or secondary infections.

How many children are affected in Uganda and South Sudan, as well as the exact geographic scope of the problem, are unclear.

Desperate measures. Some children with nodding disease are restrained to prevent them from injuring themselves or wandering off.

The Ugandan ministry of health has said that at least 3000 children there have nodding disease. In South Sudan, cases have been reported in six counties. The pattern of reports suggests the syndrome may be spreading, but no one has systematically surveyed the entire area, and accurate counts are difficult to achieve.

The condition has become a prominent issue in Uganda’s volatile politics, exacerbated by long-standing tensions between the northern regions and the central government in Kampala. Legislators have

had heated debates over special funds to help nodding syndrome patients. And President Yoweri Museveni made two visits in March to health centers in the north that treat nodding syndrome patients. He pledged that he would defeat the disease just as he had defeated rebel warlord Joseph Kony and his Lord’s Resistance Army, which terrorized northern Uganda for more than a decade.

But without a clear explanation of the condition’s cause or effective treatments, that will be no easy task.

A new phenomenon

Northern Uganda and the southern tip of South Sudan are notoriously difficult places to live. Both regions have been torn by decades of civil war. In northern Uganda, tens of thousands of children were kidnapped and pressed into service in Kony’s army. A series of Sudanese civil wars, which culminated in South Sudan’s independence last July, displaced an estimated 5 million people and killed 2.5 million. Malnutrition and a host of endemic diseases are widespread. Health services are scarce.

A head-nodding syndrome similar to the one Jilek-Aall had described in Tanzania in the 1960s began showing up in South Sudan in the early 1990s. Then, in 2009, increasing numbers of children with head-nodding seizures began to draw the attention of health officials in northern Uganda. Residents in the area said they had never

before seen such behavior. Ugandan officials asked CDC for help.

CDC researchers were puzzled, says Scott Dowell, a pediatric infectious disease specialist who directs CDC's Division of Global Disease Detection and Emergency Response. When the call went out for qualified groups to help, "everyone said, 'This is really fascinating, but it's definitely not one of ours,'" he recalls. Dowell's usual job is to coordinate the logistics for the experts responding to various outbreaks, but since there weren't yet any experts on nodding disease, he says, "I had the chance to go myself."

Dowell helped assemble a team that included epidemiologists, toxicologists, nutrition experts, and neurologists from CDC, WHO, and the Ugandan ministry of health. The researchers conducted a variety of studies, including electroencephalography (EEG) and magnetic resonance imaging (MRI) of patients' brains, sometimes during seizures. The team went in "with an open mind" about whether the nodding might be a muscular disorder or even a behavioral syndrome, Dowell says. But patients' brain-wave activity on the EEGs "made it quite clear that [head nodding] was a seizure," and that most patients had ongoing seizure activity typical of epilepsy. The MRI scans added more evidence. "Something is badly wrong with the brains of these kids, and it's physiological," he says.

The researchers came together two more times in Uganda, and in May last year they visited South Sudan to investigate recent cases there. But they haven't yet figured out what is causing the condition. When WHO experts investigated a cluster of nodding disease cases in southern Sudan between 2001 and 2003, their early guesses for a cause included leftover munitions, measles, donated seeds treated with pesticides that were eaten instead of planted, donated food that might have been contaminated with toxic fungus, and even consumption of monkey meat. None of those turned out to be a clear culprit, says Abdinasar Abubakar, head of communicable disease surveillance and response for WHO in South Sudan. The region affected by nodding syndrome has actually received less food aid than other areas. "This is the bread basket of the country," he says. And comparisons of children with nodding syndrome and their healthy peers found no association with eating donated food, Dowell says.

Exposure to munitions doesn't seem to be the cause, either. There were other regions where fighting and bombardments were much heavier, Abubakar says, and "they have no sign of nodding disease." The South Sudan and Ugandan cases of the syndrome do seem



Geographic puzzle. Areas affected by nodding disease.

to have a geographic component, however. They are concentrated in a few relatively small areas. And previously healthy children who are forced to move to those areas by fighting suddenly become vulnerable to the syndrome. An influx of displaced families into affected locales is one likely reason the number of cases has gone up recently, Abubakar says.

The researchers have tested for a host of viruses, says CDC neuroepidemiologist James Sejvar, another team member. All tests have turned up negative. And although prion-triggered brain damage, perhaps due to eating monkey meat, has been floated as a possibility, the condition doesn't look like a typical prion disease, Sejvar says.

One environmental factor still on the table

is vitamin B-6 deficiency. A recently discovered genetic condition that prevents the body from processing B-6 causes a particularly severe form of epilepsy that doesn't respond to the usual antiepileptic drugs, Dowell says. The association with nodding syndrome isn't perfect: It isn't always children with the lowest levels of B-6 who have the symptoms, he says. But the clue is strong enough that the CDC team plans to distribute high-dose vitamin B-6 supplements as part of a proposed clinical trial to find a treatment. That trial still needs approval from ethical oversight committees in the United States and Uganda, Sejvar says, but the researchers aim to start recruiting participants this summer, ultimately enrolling 80 children. One group would receive the high-dose B-6 supplement; other participants would receive one of two antiseizure medications or a placebo.

Fear the worm

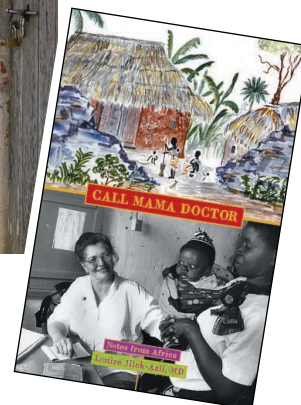
What that clinical trial won't address is the other leading hypothesis for the cause of nodding disease: an infection with the parasitic worm *Onchocerca volvulus*. The parasite is endemic in the regions that report nodding disease, and studies in Uganda and South Sudan have found that infection with the parasite is significantly more common in people with nodding syndrome than in their unaffected peers. Still, the *O. volvulus* connection isn't clear-cut. "The puzzling thing is that [the parasite] is widespread, but nodding is not," Dowell says. However, he says, the association "won't go away, even though people keep saying it doesn't make sense."

O. volvulus is no stranger to tropical-disease experts. It causes onchocerciasis, more commonly known as river blindness.

Black flies, which breed in fast-flowing rivers, transmit *O. volvulus*'s larval worms, which take up residence under the skin of black fly bite victims and grow to adulthood. The adult



Ray of hope. Louise Jilek-Aall and her colleagues have treated thousands of epilepsy patients at the clinic she founded in Mahenge, Tanzania. Her autobiography, *Call Mama Doctor*, describes her half-century of work in the region.



worms produce microfilariae, which reside mostly in the skin and connective tissue but are also sometimes found in blood, urine, and the eye. Microfilariae can damage eye tissue so severely that untreated infections can cause blindness. An international eradication campaign launched in 1974 has eliminated the parasite from large swaths of west Africa, but it persists in 27 countries in sub-Saharan Africa and six in Latin America.

Those who study river blindness have had a long-running debate over whether infection with the parasite might also cause epilepsy. Jilek-Aall says she suspected for years that the region's unusually high rate of epilepsy and onchocerciasis were connected, but it took 10 years before she and Erich Schmutzhard, a neurologist and tropical-medicine specialist at the University of Innsbruck, were able to address the question directly. Given the international efforts to eradicate river blindness, Schmutzhard says, many grant reviewers asked, "Why should we fund studies of a dying disease?"

Finally, in 2005, armed with funds from the Savoy Epilepsy Foundation in Canada and private donations, the researchers carefully categorized 62 Tanzanians with head-nodding seizures—the most thorough study to date of the disorder. Some had only head nodding; others had more severe epilepsy with other types of seizures. They analyzed blood and cerebrospinal fluid (CSF) from most of the patients. A subset traveled the 16-hour journey to Dar es Salaam, where they underwent MRI and EEG analysis.

The researchers reported in 2008 in *Epilepsia* that 43 of 51 patients tested either had microfilariae in their skin or tested positive for *O. volvulus* DNA using PCR. A positive PCR test was also weakly associated with brain lesions that showed up on the MRI scans. However, PCR tests on the CSF showed no traces of the parasite's DNA. The researchers concluded that the parasite could be involved in the head nodding but probably wasn't invading the central nervous system directly.

The hypothesis took a blow, however, when a follow-up study involving 300 individuals in Tanzania, published in 2010 in *Parasitology*, found no correlation between the intensity of *O. volvulus* infection and epilepsy. (About a third of the epilepsy patients in the study had head-nodding seizures.) That was enough to persuade Schmutzhard that nodding disease remains unexplained. Based on current evidence, he says, "onchocerciasis does not cause epilepsy."

But Jilek-Aall is not so sure. The studies failed to find a definitive link between onchocerciasis and nodding, but they don't rule it out either, she says: "I am convinced that somehow it is connected." Andrea Winkler, a neurologist at the Technical University of Munich in Germany who was corresponding author on both studies, agrees that the issue isn't settled. "We have not eliminated the possibility" that *O. volvulus* plays an indirect role, she says.

Other researchers who have seen similar cases of head nodding also suspect the worm. In 1998, pediatric neurologist Christoph Kaiser, now based in Baden-Baden, Germany, and his colleagues reported that at least 15 of the 91 epilepsy patients they studied in the Kabarole district in Western Uganda had head-nodding seizures. The evidence that



Inexplicable. James Sejvar (left) of CDC and Abdinasir Abubakar of WHO examine a child with nodding syndrome in South Sudan.

onchocerciasis can trigger epilepsy is persuasive, Kaiser says, but proving the connection has been difficult, in part because many studies simply check for microfilariae in the skin. Ivermectin, the drug distributed as part of the ongoing treatment campaigns, eliminates microfilariae, he says, but "the damage to the brain persists."

There are several ways that *O. volvulus* infections could damage the brain. In especially intense infections, the microfilariae reach the bloodstream, says parasitologist Michel Boussinesq, who studies onchocerciasis at the University of Montpellier in France, and in Cameroon. From the bloodstream, he says, they could enter the brain and cause damage directly. The lack of evidence for the parasite in the Tanzanian patients' spinal fluid argues against that, Boussinesq admits, but he says a definitive answer would come from autopsies of those who die with nodding disease. Although autopsies are difficult in

hot climates and many places in Africa have local taboos against disturbing the dead, such patient autopsies "are being attempted" in northern Uganda, Sejvar says.

Another possibility is that infection with *O. volvulus* triggers an autoimmune reaction. Antibodies produced to fight the parasite could also attack brain cells. There is evidence, Winkler notes, that antibodies for *O. volvulus* can cross-react with retinal cells. It is also possible that subtypes of the parasite could explain why head-nodding seizures seem to affect only certain regions. Winkler notes that it is widely accepted that the "savanna type" *O. volvulus* causes blindness more often than the "forest type," which primarily causes skin symptoms.

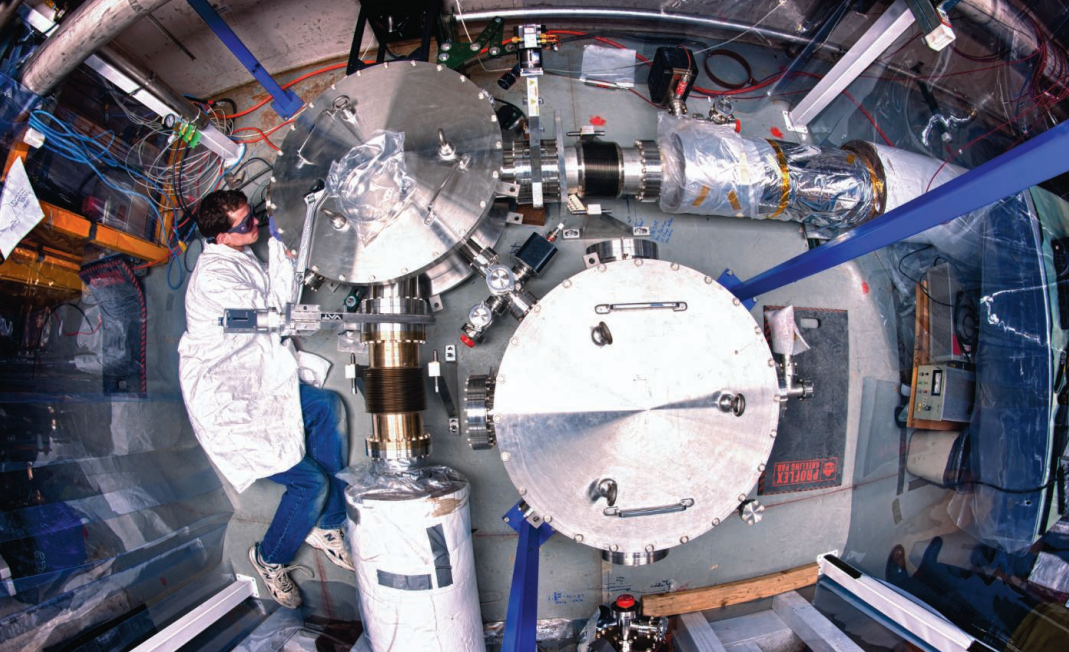
The most likely explanation for the disease, say several of the scientists chasing the disorder, is a combination of factors. Malnourished children deficient in vitamin B-6 might be particularly susceptible to neurological symptoms when they are infected with *O. volvulus*, for example. "Epilepsy is very often multifactorial," Boussinesq says. "Onchocerciasis could be a needed factor but not sufficient to provoke the condition."

New clues could come from blood and urine samples that the CDC team collected from patients in South Sudan and Uganda. They are almost done assessing vitamin levels, possible heavy-metal exposure, traces of thiocyanates (a sign of low-level cyanide poisoning due to eating improperly prepared cassava), and genetic markers among patients and healthy controls. More comprehensive surveys of

where and how many children have nodding syndrome are also planned in both Uganda and South Sudan. That should give a better picture of whether and how the syndrome is spreading.

One crucial problem, Abubakar says, is that nodding syndrome, as terrible as it is for the people and communities that are affected, is only one of many competing health emergencies in the region. In South Sudan, already overstretched health workers are also dealing with ongoing armed clashes and an acute outbreak of kala azar, or leishmaniasis, which has infected at least 22,000 people and killed nearly 1000 since late 2009. He says he hopes the recent publicity surrounding nodding syndrome will attract more researchers to the region. "I hope the advocacy and media might inspire some more institutions who might want to come and help figure out what is going on."

—GRETCHEN VOGEL



Hands-on. Student Benjamin Brubaker tinkers with the Fermilab holometer.

PHYSICS

Sparks Fly Over Shoestring Test Of 'Holographic Principle'

A team of physicists says it can use lasers to see whether the universe stores information like a hologram. But some key theorists think the test won't fly

BATAVIA, ILLINOIS—The experiment looks like a do-it-yourself project, the scientific equivalent of rebuilding a 1983 Corvette in your garage. In a dimly lit, disused tunnel here at Fermi National Accelerator Laboratory (Fermilab), a small team of physicists is constructing an optical instrument that looks like water pipes bolted to the floor. Three scientists huddle within a makeshift tent—really a plastic sheet the size of a tablecloth—to install a high-precision mirror. Nitrogen from a tank flows under the plastic to keep the mirror clean. “It doesn’t look very impressive, but it’s the equivalent of a class 100 clean room—the best you can buy,” says Craig Hogan, a theorist at Fermilab and the University of Chicago in Illinois.

A ratchet clicks as a physicist inside the tent tightens a bolt. Another shouts, “The front one, not the back one! The front one, not the back one!” As implausible as it seems, the homey experiment could revolutionize scientists’ conception of the fabric of the universe—if Hogan is right.

Known as the Fermilab holometer, the experiment aims to test one interpretation of the so-called holographic principle. The principle states that the amount of information that can be crammed into a region of space and time, or spacetime, is proportional to the region’s surface area. That’s odd, as after all, the number of computer hard drives that fit

in a room increases with the room’s volume, not the area of its walls. If the holographic principle holds, then the universe is a bit like a hologram, a two-dimensional structure that only appears to be three-dimensional. Proving that would be a big step toward formulating a quantum theory of spacetime and gravity—perhaps the single biggest challenge in fundamental physics.

The principle implies a kind of information shortage that, in Hogan’s interpretation, makes it impossible to say precisely where an object is. “Think back to kindergarten; you know that something is either here or it’s there,” Hogan says. “It’s so obvious that it’s not clear that [position] is a mystery.” In fact, Hogan says, position is inherently uncertain, and the holometer aims to prove that point.

All the experiment takes is a couple of million bucks, two lasers, and a few months of work. That makes the holometer an unusual project for Fermilab, a particle physics lab where scientists typically work on huge accelerators and hundred-million-dollar experiments that run for years. “The beauty of it is that we have the people who can come up with this low-risk, high-reward experiment,” says Fermilab’s Raymond Tomlin. “It’s one shot, and if you discover something you go to Stockholm [to collect a Nobel Prize]. And if you don’t see anything, you set a limit.”

Not everyone cheers the effort, however. In fact, Leonard Susskind, a theorist at Stanford University in Palo Alto, California, and co-inventor of the holographic principle, says the experiment has nothing to do with his brainchild. “The idea that this tests anything of interest is silly,” he says, before refusing to elaborate and abruptly hanging up the phone. Others say they worry that the experiment will give quantum-gravity research a bad name.

Black holes and causal diamonds

To understand the holographic principle, it helps to view spacetime the way it’s portrayed in Einstein’s special theory of relativity. Imagine a particle coasting through space, and draw its “world line” on a graph with time on the vertical axis and position plotted horizontally (see top figure, p. 148). From the particle’s viewpoint, it is always right “here,” so the line is vertical. Now mark two points or events on the line. From the earlier one, imagine that light rays go out in all directions to form a cone on the graph. Nothing travels faster than light, so the interior of the “light cone” contains all of spacetime that the first event can affect.

Similarly, imagine all the light rays that can converge on the later event. They define another cone that contains all the spacetime that can influence the second event. The cones fence in a three-dimensional, diamond-like region. According to special relativity, all observers will agree about which points are inside or outside the diamond, no matter how they are moving. The holographic principle states that the amount of information that such a “causal diamond” can hold varies with its surface area.

That might seem like a perverse idea, but it follows from physicists’ analysis of black holes. A black hole is a region of extremely strong gravity produced when, for example, a star collapses to a point, cramming an enormous mass into an infinitesimally small volume. Within a certain distance of the point, gravity grows so strong that even light cannot escape.

That distance defines a sphere in space called the “event horizon.” In the 1970s, theorists deduced that the amount of information contained in a black hole depends on the surface area of its horizon. One bit of information—which can be 0 or 1—can be encoded in each “Planck area,” an area smaller than 10^{-69} square meters. Jacob

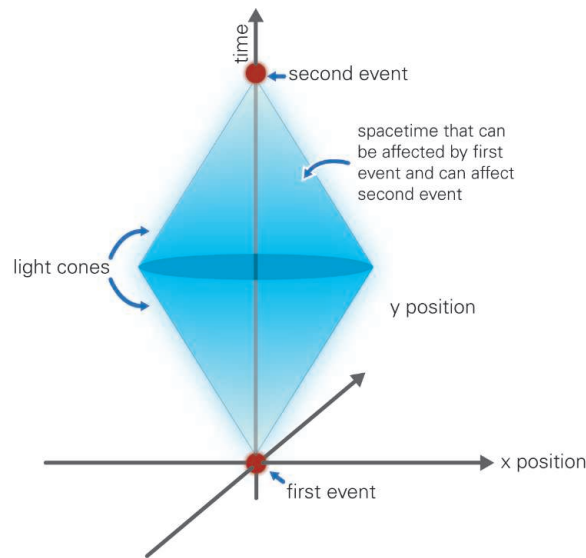
Bekenstein of the Hebrew University in Jerusalem and, independently, Stephen Hawking reached that conclusion when they realized that a black hole must have an entropy—a measure of how disordered it is inside—that grows with the surface area of its event horizon. The more disordered something is, the more information it takes to fully describe it, so the information-area link follows in step.

Known as the Bekenstein bound, that entropy limit would serve as a cornerstone for any theory of quantum gravity, which theorists expect to kick in at length scales shorter than the so-called Planck length—roughly 10^{-35} meters—and time scales shorter than the Planck time, about 10^{-43} seconds. It might have implications far beyond the event horizons of black holes, too. In the 1990s, Susskind and Gerard t'Hooft, a theorist at Utrecht University in the Netherlands, argued that any properly defined region of spacetime will obey the same information-area link, a conjecture that Susskind dubbed the holographic principle.

No one has proved that the principle holds. However, no one has come up with a scenario in which it doesn't, says Raphael Bousso of the University of California, Berkeley, who showed how to make the principle jibe with special relativity. For example, suppose you try to exceed the bound by encoding information in individual photons and cramming ever more of them into a region. You'll end up creating a black hole well before you break the limit, Bousso says.

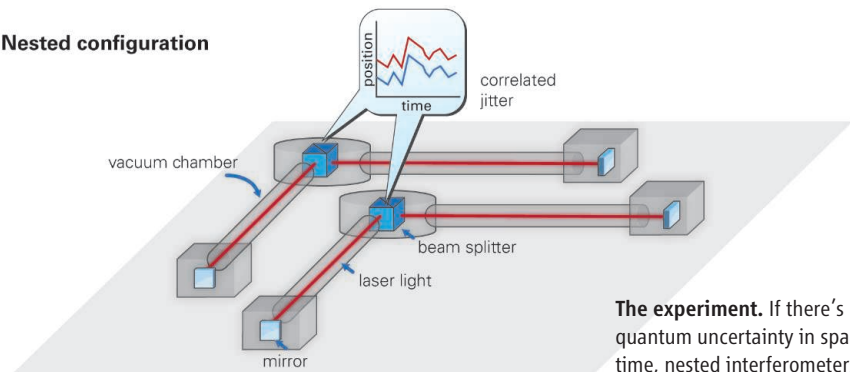
Hogan's interpretation takes matters a long step further. If the area-information link holds, then a region of spacetime can hold less information than it could if the amount of information grew with its volume. The shortage implies that positions in perpendicular directions are no longer independent variables, Hogan argues. The more precisely experimenters measure an object's position in one direction, the less precisely they can know its position in a perpendicular direction. That tradeoff resembles the one imposed by the famous Heisenberg uncertainty principle, which limits an observer's ability to measure both the position and the momentum of a quantum particle.

Specifically, Hogan argues, if researchers know precisely how far away a thing is, then they can't know exactly where it is side to side. That uncertainty should produce a sideways jiggling that grows with the distance to the object, he predicts. That jitter is precisely what physicists hope to observe with the holometer.



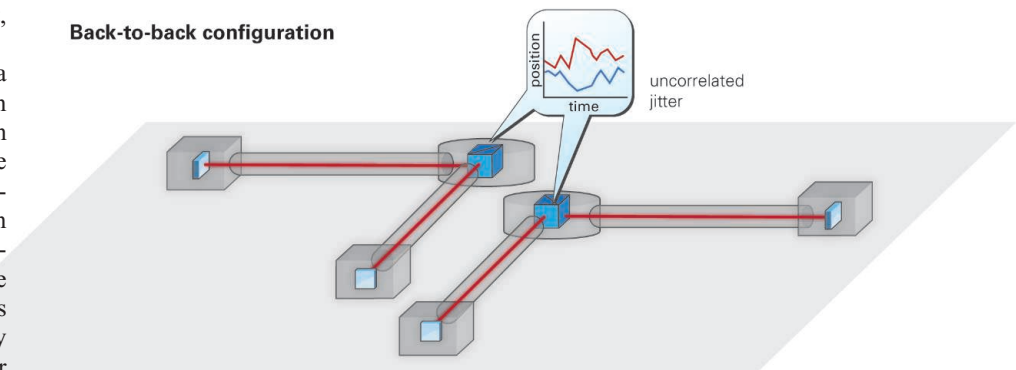
The idea. Together, light rays emanating from an earlier event and those converging on a later one form a “causal diamond.” The holographic principle says that such a region can hold an amount of information proportional to its surface area.

Nested configuration



The experiment. If there's quantum uncertainty in space-time, nested interferometers should jitter in unison; back-to-back ones, independently.

Back-to-back configuration



Playing with the LEGO LIGO

Physicists at Fermilab plan to measure the jitter using store-bought technology, spare lab space, and a \$2.5 million grant from the Department of Energy won for the project by Fermilab's Aaron Chou. That's a mere pittance at a lab that's planning billion-dollar projects. “These huge projects take a long time to design and a longer time to fund, and I worry that by the time one gets built it might not be the most interesting thing in the field,” Chou says. “I try to keep an eye out for things that might be done more easily.”

To spot the predicted jiggling, physicists are building a pair of L-shaped instruments called interferometers. An interferometer splits an incoming beam of laser light in two using a cube of glass called a “beam splitter.” The two beams race down the interferometer's perpendicular arms and reflect off mirrors at the ends. If the lengths of the arms are set just right, then the returning light waves will overlap and interfere so that all the light exits through the same face of the beam splitter that it entered. But if the relative lengths of the arms change, then some light will leak

out of the perpendicular face, or “dark port,” allowing physicists to compare the arms’ lengths to a fraction of an atom’s width.

An interferometer can also measure the sideways motion of the beam splitter. If the beam splitter moves sideways relative to one of the mirrors, it must necessarily move either toward or away from the mirror in the perpendicular arm, changing that arm’s length and letting light leak out of the dark port. So in principle, experimenters can test Hogan’s prediction by monitoring the output of a single interferometer for “holographic noise,” an unquenchable jitter in the beam splitter’s position at frequencies of millions of cycles per second.

Actually, the team will monitor two interferometers, Chou says. Nested side by side like spoons, the devices will sample the same region of spacetime (see bottom figure, p. 148). That’s because in the time that it takes light to bounce through the devices, the causal diamonds of the two beam splitters will overlap. As it is spacetime itself that is fluctuating, the jiggling of the two beam splitters should then be correlated, making it easier to detect a tiny signal—a standard trick from the processing of radio signals. If researchers do see correlated jitter, they can also reconfigure the two devices to sit back to back and sample different regions of spacetime. Any signal from holographic noise should then go away. In the search for a signal, “we’ll get a yes or a no,” says Stephan Meyer, an experimental cosmologist at the University of Chicago. “There won’t be a maybe.”

The setup should be incredibly sensitive, Hogan says. If, for any reason, the two beam splitters move in concert by roughly a Planck length per Planck time, then experimenters should be able to detect the motion that accumulates in the fraction of a microsecond it takes light to pass through the apparatus. So the experiment will be able to search for effects on the so-called Planck scale, regardless of their origins. “That’s why experimentalists love it,” Hogan says.

For a particle physics lab, the holometer experiment is a string-and-sealing-wax affair. Only one of each interferometer’s two 40-meter arms will fit in the tunnel. To house the other two arms, researchers have run plastic pipes through the side of the tunnel and the earthen berm that covers it to a wooden shed that resembles an outhouse. The experiment runs out of trailers that may have been new when Ronald Reagan was president.

The holometer team is also borrowing technology. Team members Rainer Weiss and

Samuel Waldman of the Massachusetts Institute of Technology in Cambridge also work on the Laser Interferometer Gravitational-Wave Observatory (LIGO), which comprises interferometers in Hanford, Washington, and Livingston, Louisiana, each with 4-kilometer-long arms. They’ve advised their Fermilab colleagues how to build their instruments with store-bought parts, says Fermilab’s Chris Stoughton. “The LEGO LIGO was our catch phrase,” he says. “You didn’t need to build a big experiment; you just needed to buy the parts and reconfigure them differently.”

The holometer project also gives the particle physicists a rare treat: a chance to work in a small team. “This is one of the few experi-



Undaunted. At the least, the experiment will probe the Planck scale, originator Craig Hogan says.

ments where you can get your hands on—and your head around—every part of the experiment,” says Robert Lanza, a graduate student at the University of Chicago.

Wanna bet?

But will the holometer really test the holographic principle? Aptly enough, uncertainty is high.

Even Hogan acknowledges that his prediction of an observable jittering isn’t airtight. He assumes that the uncertainty relationship applies to the position of a macroscopic object. But it could apply just to the subatomic particles within the object, which would produce a much smaller effect. In that case, failure to spot the quivering wouldn’t torpedo the basic holographic principle, Hogan says. “If we don’t see a signal, nobody is going to abandon these ideas of holography,” he says. “On the other hand, if we do see a signal, it will make the whole idea of holography more concrete.”

But some experts on the holographic principle think the experiment is completely

off-target. “There is no relationship between the argument [Hogan] is making and the holographic principle,” Bousso says. “None whatsoever. Zero.” The problem lies not in Hogan’s interpretation of the uncertainty relationship, but rather in “the first step of his analysis,” Bousso contends.

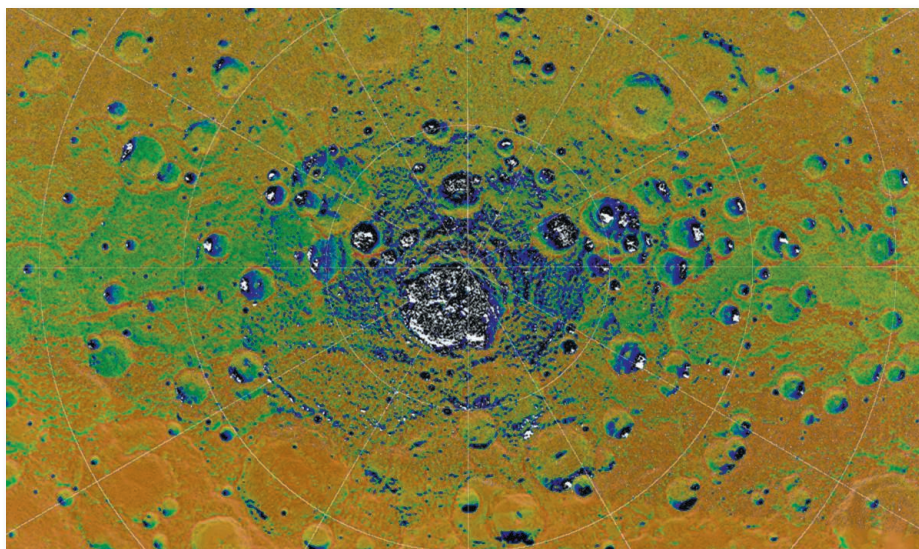
Bousso notes that a premise of special relativity called Lorentz invariance says the rules of physics should be the same for all observers, regardless of how they are moving relative to one another. The holographic principle maintains Lorentz invariance, Bousso says. But Hogan’s uncertainty formula does not, he argues: An observer standing in the lab and another zipping past would not agree on how much an interferometer’s beam splitter jitters. So Hogan’s uncertainty relationship cannot follow from the holographic principle, Bousso argues.

The experiment can do no good in testing the holographic principle, Bousso says, but running it could do plenty of harm. The holometer has garnered an inordinate amount of attention in the blogosphere and in press accounts, he says, raising unrealistic expectations. “They’re not going to have a signal and then there is going to be a backlash saying that the holographic principle isn’t valid, and we’ll look like we’re on the defensive,” Bousso says. “That’s why I’m trying to get the word out [that the experiment won’t test the principle] without appearing to make excuses.”

Hogan is unruffled. He sticks by his claim that the holographic principle implies an uncertainty in position that may be observable. This uncertainty relationship violates Lorentz invariance, he acknowledges, but the bigger issue is how Lorentz-invariant spacetime itself emerges from deeper physics at the Planck scale. In any case, Hogan says, debating this experiment can only benefit the field of quantum-gravity research, which has remained essentially theoretical. “If we can actually have an argument about an experiment and whether or not we’re doing a test of something, I think that’s helpful,” he says.

At the least, the experiment will probe the Planck scale in some way, Hogan says. “What I would love is for theorists to predict that we won’t see anything,” he says. “They haven’t done that.” Then again, they don’t have to. Within a year, Hogan and his team will have their data. It would make a thrilling, feel-good story if they scored a huge discovery that served as the basis for a real theory of quantum gravity. In science, however, long shots pay out even less often than they do at the racetrack.

—ADRIAN CHO



Good fit. Radar reflections (white) from water ice coincide with cold, shadowed regions (black).

Icy-Hot Mercury's Water Pinned Down in the Dark

Lead may melt in Mercury's noontime sun, but for 2 decades, planetary scientists have suspected that the polar nooks and crannies of the innermost planet harbor eons-old stores of water ice. At the meeting, researchers heard that signs from the MESSENGER spacecraft orbiting Mercury strongly support that claim.

Water ice had been the leading explanation for the spotty but bright radar reflections from the polar regions of Mercury since Earth-based radar first detected the reflections in 1991. Radar beams reflected from the spots the way they do from the water-ice cap of Mars. And the bright reflections came from inside large, high-latitude craters—places where perpetual shadows might chill the ground enough to preserve water ice for eons.

To detect any possible water ice, MESSENGER carried the first neutron spectrometer to probe Mercury. Cosmic rays striking the planet's surface send neutrons flying into space. But the hydrogen of water ice could keep some neutrons from reaching MESSENGER. Planetary scientist David Lawrence of The Johns Hopkins University Applied Physics Laboratory (APL) in Laurel, Maryland, and his colleagues reported that MESSENGER's neutron spectrometer had detected 1% fewer fast neutrons streaming from the north polar region than from the equator. Nearly pure water ice buried under a few tens of centimeters of insulating rocky soil could be responsible for the neutron decrease, Lawrence said.

As the first Mercury orbiter, MESSENGER is also getting the closest look ever at the shadows cast near the north pole. As planetary scientist Nancy Chabot of APL and her colleagues reported, MESSENGER imaging has revealed that near the north pole, nearly every crater wider than 10 kilometers strongly reflects radar, as water ice does, and the radar brightness essentially coincides with permanent shadow. "That's really striking," she said.

Perhaps the most striking support for the water-ice theory was the combination of the newly determined shape of Mercury's surface and a model that keeps track of incoming solar energy. MESSENGER's laser altimeter revealed the north polar region's crater-strewn topography in fine detail. Planetary scientist David Paige of the University of California, Los Angeles, and his colleagues folded that topographic map into their model, which calculates the amount of heating by sunlight. It computes surface and subsurface temperatures by gauging where permanent shadows are cast and how much sunlight is reflected into those shadows, among other processes.

The model's calculated temperatures alone are "fairly conclusive" evidence that water ice dominates Mercury's radar-bright deposits, Paige said. Model temperatures beneath 10 centimeters of insulating soil in permanent shadow typically run about 100 K. That is just the temperature needed to preserve water ice for billions of years against

sublimation to space, Paige noted. Other candidates for radar-bright deposits, such as sulfur, would survive at higher temperatures, but the modeling indicates that those temperatures are rare in the deposits.

Considering all lines of evidence, "I think the case is strong now" for water ice on Mercury, says planetary scientist Dana Hurley of APL, who was not involved in any of the analyses. In fact, "it could be that Mercury is in the sweet spot" for retaining the water of impacting comets.

Inside Mercury's permanent shadows, it is cold enough that water vapor from impacting comets will freeze to the surface but warm enough that some of the surface ice will diffuse downward before it is lost. Under some insulating soil, it is colder still, just cold enough to preserve the ice for eons. The moon's cold shadows are actually too cold for much deep storage, making Mercury the more productive icemaker.

Tougher Times for Any Life on an Early Mars?

James Head is looking to dry out and freeze up the planet Mars. While his fellow planetary scientists have been haltingly moving away from visions of a "warm and wet" early Mars conducive to the origin of life, Head has been building a case that Mars has been bitterly cold and hyper-arid for almost all of its 4 billion years. A few splashes of cold running water lightly carved the surface several billion years ago, he allows, but otherwise the surface, at least, of the Red Planet has most likely never been a place for life.

In the meeting's sole plenary lecture, Head, a planetary geologist at Brown University, marched back in martian time. He drew from the geologic climate record revealed by orbiting cameras and roving instruments, supplemented by global models of martian climate. The past 3.5 billion years of Mars climate was straightforward enough. On the surface, most researchers agree, ice moved back and forth between the poles and lower latitudes as the planet's wobbly rotation axis let the sun alternately warm the poles and the equator. But there was no rain and only rare trickles of glacial meltwater.



Earthly dampness. Water flowing in the soil of Antarctica leaves Mars-like surface markings.

Snapshots From the Meeting >>

A wet Antarctic link to Mars. At last year's conference, Mars Reconnaissance Orbiter team members presented some intriguing images. They appeared to show where water had just dribbled down martian slopes, dampening and darkening as it went (*Science*, 15 April 2011, p. 303). This year, planetary scientist Joseph Levy of Oregon State University in Corvallis compared how fast those martian dark streaks progressed downhill with how fast water from melting ice and snow in Antarctica's Taylor Valley oozed through the ground and wicked to the surface to create a lengthening dark streak. The martian features behaved just like those terrestrial

features known to be watery. Even the calculated martian soil permeability was much the same, like that of very fine sand. Any implications for life on Mars? An Antarctic wet streak "is a tough place to make a living," Levy says, "but something does": bacteria and hardy algae.

A lucky shot at the moon? After a precisely targeted impactor plowed into the moon in October 2009, the first *Science* headline was "The Moon Is Wet!" True enough: The LCROSS spacecraft did detect abundant water in the impact's debris (*Science*, 19 March 2010, p. 1448). But "I think LCROSS got lucky," LCROSS team member Richard Elphic of NASA's Ames Research Center in Mountain View, California, said at the meeting. In the 1990s, the Lunar Prospector orbiter measured lunar hydrogen in water by detecting neutrons flying off the moon. If all of the moon's permanently shadowed, deeply chilled areas harbor as much ice as LCROSS found, Elphic and his colleagues calculated, Lunar Prospector would have detected 10 times as much water hydrogen as it actually did. Although the LCROSS impactor was indeed guided to a broad area enriched in water, Elphic says, it most likely struck a particularly wet spot by chance.

—R.A.K.

Next, Head argued that the martian climate of the eon before 3.5 billion years ago was probably much the same: almost always cold and dry. No one has found a satisfactory way that early Mars could have warmed above the freezing point for hundreds of millions of years at a time, he noted. And he pointed to emerging signs that Mars was, in fact, quite cold. For example, from glacial landforms, Head and colleagues have deduced a mean annual temperature at mid-latitudes of less than 0°C about 4 billion years ago. That's well back into what has been considered warm and wet, or at least continuously damp.

Of course, many of the ancient terrains of Mars look as though they were once awash, but those watery markers could have been created without persistent surface warmth and wetness, Head said. True, clays now commonplace on the surface require prolonged contact of liquid water with rock. But researchers have lately found that at least some clays likely formed well below the surface, he said. Surface features like lakebeds and networks of branching river valleys now appear to have formed geologically quickly during brief episodes warm enough to melt snow and ice. And Mars might have warmed briefly about the same time, when humongous but episodic volcanic eruptions spewed greenhouse gases.

Head and the rest of the planetary science community could soon have a chance to test his perpetually-cold-and-dry scenario. The Curiosity rover will plunge into the martian atmosphere 5 August to land by a neatly exposed geologic record of the traditionally interpreted shift from a warm and wet to a cold and dry Mars.

The Young Solar System Took a One-Two Punch?

How violent were the early days of the solar system? For 40 years, scientists have debated when and how badly the rocky inner planets were battered in their youth. Some think any pounding recorded in the early geologic record was just the dwindling away of the solar system's violent birth pangs. But others, sometimes called catastrophists, see evidence that a brief "late heavy bombardment" by mountain-size bodies shook things up again about 4 billion years ago. At a pre-conference workshop, planetary dynamicist William Bottke suggested that each group might be partly right.

Bottke models orbital dynamics at the Southwest Research Institute (SwRI) in Boulder, Colorado. Drawing on numerous

At the conference, Bottke, with SwRI colleague Simone Marchi and others, reported that part of the problem may be that there are two kinds of impacts. "Slow" impacters hit at about 18,000 kilometers per hour, a speed typical of collisions in today's asteroid belt. Fast impacters move at 65,000 kilometers per hour, delivering 1000 times the impact energy of slow impacters. Because only high-speed impacts have the energy to reset the argon-argon isotopic "clock" often used to date impacts, the group noted, the argon-argon method lets most slow impacts go unrecorded.

At the conference, Bottke presented a blend of the competing bombardment histories that takes account of the spotty impact record produced by a mix of fast and slow impacters. As all agree, a few hundred million years after solar system formation, the lower-energy tail end of debris left over from planet formation thudded slowly through the solar system. But then, starting roughly 4.2 billion years ago, Jupiter and Saturn plowed inward through the young solar system, gravitationally stirring up high-energy impacters, Bottke said. That planetary migration is the leading candidate for triggering any late bombardment.

Bottke thinks the resulting late bombardment was longer and less intense than many catastrophists have proposed. That's because the planetary migration created a bunch of high-energy impacters that were slow to escape the asteroid belt and hit the inner planets (*Science*, 15 April 2011, p. 302). Although harder to detect today, Bottke said, the stretched-out "spike" would have been "pretty heavy" and catastrophic. —RICHARD A. KERR



The beginning. Debris left from planetary formation later pummeled the solar system, possibly twice.

presentations at the earlier 75-attendee bombardment workshop, which he co-organized, he tried to understand why dating impacts on the moon, Earth, and asteroids has been so confusing. Some dating techniques seem to show a 4-billion-year-old spike; others don't.

LETTERS

edited by Jennifer Sills

Outsourced Psychiatry:
Remote Support

IN HIS NEWS FOCUS STORY “WHO NEEDS PSYCHIATRISTS?” (16 MARCH, p. 1294), G. Miller highlights the burgeoning psychiatric morbidities in regions left devastated by conflict. Social media can now provide access to an additional conduit of expertise, which can offer remote support and help in constructing virtual healthcare architecture in politically fragile nations. In Somaliland, with a population of 3.5 million people, United Kingdom-based organizations are already using social networking portals to support continuing medical education for interns (*I*) and to provide real-time mentoring for doctors managing challenging psychiatry cases. This support is crucial in a country with no psychiatrists in the public sector and in which chaining affected patients to the floor is common. With an unpredictable political climate limiting interventions by foreign agencies, social networks provide a practical means of offering regular, intercontinental support to doctors who would otherwise be isolated. Such technology could further be deployed to gather electronic healthcare workforce records, augment coordination of clinical trials, and monitor health economies. The disparities in medical capacity between Northern and

Southern partners are already narrowing. If security and identity verification are safeguarded, social media could rapidly accelerate progress.

FAISAL R. ALI,^{1*} ADAM M. ALI,²
ALEXANDER E. T. FINLAYSON³

¹Department of Dermatological Sciences, University of Manchester, Manchester, M6 8HD, UK.

²Green-Templeton College, University of Oxford, Oxford, OX2 6HG, UK. ³Centre for Global Health, King's College, London, SE1 8UB, UK.

*To whom correspondence should be addressed.
E-mail: f.r.ali.01@cantab.net

References and Notes

1. A. E. Finlayson *et al.*, *J. Telemed. Telecare* **16**, 181 (2010).
2. All authors are affiliates of medicineafrica.com, a social enterprise providing a platform for healthcare educational partnerships.

Looking for help. An overcrowded mental hospital in Banda Aceh, Indonesia.

Outsourced Psychiatry:
Experts Still Relevant

THE NEWS FOCUS STORY ON GLOBAL MENTAL health, “Who needs psychiatrists?” (G. Miller, 16 March, p. 1294), implied that the answer is “no one.” This is not the case.

It is true that clinical trials have demonstrated the efficacy of talking therapies for depression, anxiety, and other common mental disorders, when delivered by nonpsychiatrist health workers trained by professionals. Severely ill individuals (such as those with refractory depression, bipolar disorder, or schizophrenia) require medication, which can be administered safely by nurses, family doctors, and even health workers supervised by medical personnel. Investing in community health workers as mental health gatekeepers

is the safest national strategy for sustainable mental health programs, for the reasons mentioned in the News Focus story as well as an additional one: Community health workers are not as susceptible to “brain drain”—the emigration of skilled workers for better working conditions—as health professionals.

For quality care, however, psychiatrists are needed for overall direction/supervision and training in differential diagnosis and medication management, especially when addressing complex comorbidities (mental as well as physical). Psychiatrists play a crucial role as consultants in these international projects.

MYRNA M. WEISSMAN^{1,2*} AND HELEN VERDELI³

¹Department of Psychiatry, College of Physician and Surgeons, Columbia University, New York, NY 10027, USA.

²Division of Epidemiology, New York State Psychiatric Institute, New York, NY 10032, USA. ³Counseling and Clinical Psychology, Teachers College, Columbia University, New York, NY 10027, USA.

*To whom correspondence should be addressed. E-mail: mmw3@columbia.edu¹

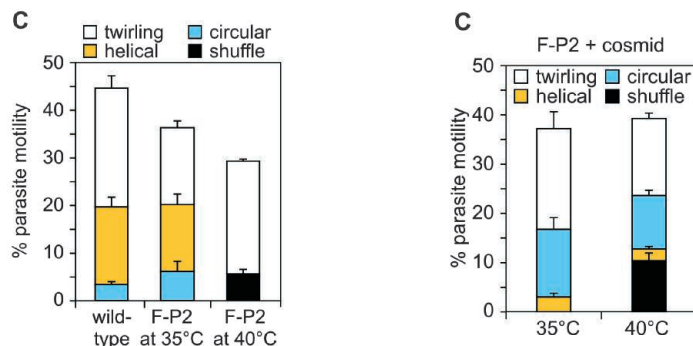
Sound and Fury, Clarified

IT WAS AN HONOR TO HAVE MY PROFILE PUBLISHED in *Science* (“Sound and fury in the microbiology lab,” C. Mary, News Focus, 2 March, p. 1033). However, I was surprised that 20% of the article is devoted to the American Society for Microbiology (ASM) story, in which I was a collateral victim of a collective sanction (there has been no collective liability in France since World War II). I did not manage the paper and did not even check the last version. The mistake by C. Capo consists of a single figure inversion (not four, as stated in the *Science* profile). This paper has since been published (*I*). In January 2007, I was awarded one of

CORRECTIONS AND CLARIFICATIONS

News Focus: “Sound and fury in the microbiology lab” by C. Mary (2 March, p. 1033). The article said that a reviewer for *Infection and Immunity* raised concerns about four figures in a revised manuscript by Raoult and colleagues. The article should have made clear that at issue were panels within a single figure of the revised manuscript. As the article stated, one author acknowledged he had made a mistake, but only two panels were in error.

Reports: “A DOC2 protein identified by mutational profiling is essential for apicomplexan parasite exocytosis” by A. Farrell *et al.* (13 January, p. 218). There were labeling errors in Figs. 1C and 3C. In Fig. 1C (left), the y axis should run from 0 to 50%, not 0 to 100%. In Fig. 3C (right), the labels on the x axis, 35°C and 40°C, should be transposed. The corrected figure panels are presented here.



the highest ASM honors—the ICAAC lecture—thus clearing doubts about my scientific integrity.

I find it interesting that the Web site (2) of the profile’s author, C. Mary, states that she works for Danone, a Paris-based food products company. My recent work on the putative role of probiotics in obesity (3–5) [reported in my book (6)] led to bad press for Danone and forced them to review their marketing strategy [e.g., (7)].

DIDIER RAOULT

Rickettsies Research Unit, University of Medicine, Marseille, 13005, France. E-mail: didier.raoult@gmail.com

References

1. Y. Bechah, C. Capo, G. Grau, D. Raoult, J. L. Mege, *Microbes Infect.* **9**, 898 (2007).
2. European Medical Writers Association, Catherine Mary (www.emwa.org/Freelance/Catherine-Mary.html).
3. D. Raoult, *Nat. Rev. Microbiol.* **7**, 616 (2009).
4. D. Raoult, *Nature* **454**, 690 (2008).
5. S. D. Ehrlich, *Nat. Rev. Microbiol.* **7**, 901 (2009).
6. D. Raoult, *Dépasser Darwin* (Plon, Paris, ed. 1, 2010).
7. MarketingAttitude.net, Activia ou le Scandale de Danone (www.marketingattitude.net/2012/01/activia-ou-le-scandale-de-danone/) [in French].

Letters to the Editor

Letters (~300 words) discuss material published in *Science* in the past 3 months or matters of general interest. Letters are not acknowledged upon receipt. Whether published in full or in part, Letters are subject to editing for clarity and space. Letters submitted, published, or posted elsewhere, in print or online, will be disqualified. To submit a Letter, go to www.submit2science.org.

Response

RAOULT IS REFERRING TO A WEB SITE THAT IS out of date. My collaboration with Danone is limited to writing two newsletters in 2002 and 2003; I have had no contact with Danone representatives for more than 9 years.

CATHERINE MARY

Cultural Diversity in a Global Society

IN HER EDITORIAL “THE GLOBAL KNOWLEDGE society” (3 February, p. 503), N. V. Fedoroff argues that “creating a truly global knowledge society” would empower humanity to solve its common problems. However, she neglects to acknowledge that humanity’s problems, although shared, are inextricable from local cultural and ecological contexts. Knowledge may be empowering as a solution to these problems, but it often empowers inequitably. With these disparities, a “global knowledge society” could harm certain cultures and cause loss in the world’s cultural diversity. For example, the globalization of the knowledge of traditional Chinese medicine has escalated demands for medicinal materials to beyond local ecological capacities, putting thousands of wild Chinese herbs at risk of extinction (1), and consequently damaging this treasured cultural practice.

Preserving the world’s cultural diversity at a time of globalization—of both knowledge and economy—is in humanity’s own interest of future viability. The world needs not one homogenized global knowledge society, as

the Editorial suggests, but a global mosaic of multiple, pluralistic knowledge societies, each rooted in its own unique cultural identity. This latter view reflects the idea of “knowledge societies” espoused by the United Nations Educational, Scientific, and Cultural Organization (UNESCO)—“the plural here,” the organization asserts in a report, “sanctions the need for an accepted diversity” (2).

LIKWAN CHENG

Department of Physical Science and Engineering, Truman College, City Colleges of Chicago, Chicago, IL 60640, USA. E-mail: lcheng6@ccc.edu

References

1. S. Cao, Q. Feng, *Science* **335**, 1168 (2012).
2. UNESCO World Report, “Towards knowledge societies” (UNESCO Publishing, Paris, 2005), p. 5; <http://unesdoc.unesco.org/images/0014/001418/141843e.pdf>.

Science Statesmanship

THE NATIONAL ACADEMY OF SCIENCES HAS reported the decline in U.S. science, technology, engineering, and mathematics (STEM) education time and time again (1, 2). Despite these findings, the federal government has not substantially increased its funding of science education.

North Carolina has found a creative solution by leveraging its own (albeit limited) state budget. The state science museum has been transformed into a hub for science research, education, and outreach technologies. Called the Nature Research Center (NRC), a new 24,000-m² wing of the existing museum was funded through public-private partnerships, creating a statewide “one-stop shop” for all facets of science education. All K-12 classrooms in North Carolina are linked through the Internet to the NRC’s multimedia technology theater, where scientists will broadcast their discoveries. Technology platforms in the NRC foster science communication to diverse audiences throughout the state (and beyond), including K-12, citizens, educators, and policy-makers.

STEM education is a responsibility for everyone—federal, state, and local governments, as well as parents and students themselves. By creating a hub for cutting-edge science research, education, and communication, North Carolina is ensuring a strong pipeline of exceptional STEM students into the workforce.

MARGARET DALZELL LOWMAN

Nature Research Center, North Carolina Museum of Natural Sciences/North Carolina State University, Raleigh, NC 27601, USA. E-mail: canopymeg@gmail.com

References

1. National Academy of Sciences, *Rising Above the Gathering Storm* (National Academies Press, Washington, DC, 2007).
2. National Academy of Sciences, *Rising Above the Gathering Storm, Revisited* (National Academies Press, Washington, DC, 2010).



Learn how current events are impacting your work.

ScienceInsider, the new policy blog from the journal *Science*, is your source for breaking news and instant analysis from the nexus of politics and science.

Produced by an international team of science journalists, *ScienceInsider* offers hard-hitting coverage on a range of issues including climate change, bioterrorism, research funding, and more.

Before research happens at the bench, science policy is formulated in the halls of government. Make sure you understand how current events are impacting your work. Read *ScienceInsider* today.

www.ScienceInsider.org

*Science***Insider**

Breaking news and analysis from the world of science policy



LANGUAGE

Me Tarzan, You Jane

Robert C. Berwick

In *The Descent of Man*, Darwin advanced a “Caruso” scenario for language’s origin: sexier singers got more mates, leading to language’s use for both communication and, crucially, thought (1). More than 140 years on, have we made any progress? Judging by *The Origins of Grammar*, not so much. James Hurford, an eminent Edinburgh University linguist, has been at the forefront of a recent revival of evolutionary thinking regarding the origin of language. The overarching principles of gradualism and continuity guide his account. He clearly means to stand on Darwin’s shoulders—evolution by natural selection via “numerous, successive, slight modifications.”

Hurford’s evolutionary story parallels the book’s three parts. First, from primate calls, prehumans pitched up with pairings of vocalized words and meanings; this “first shared lexicon” grew, word by word. Second, a burgeoning stock of single word-meaning pairs led to two-word constructions (including “Me Tarzan, you Jane”) along with an ability to learn new words and sentence constructions. Third, driven by expansions in computational capacity and the pressure of cultural needs for communication, the steady drumbeat of two-word constructions led to three-word constructions and on to Shakespeare.

Hurford insists that virtually every aspect of human language is, at heart, a cultural construct—reinvented anew as each child grows up in a particular language community, with very little in common from language to language aside from our shared language-learning capacity. Many linguists and cognitive scientists would disagree, arguing that our brain comes predisposed to eliminate as a potential human language a large range of otherwise logical possibilities.

Wide-ranging and often entertaining, Hurford’s three-part account is nonetheless just a story. Crucially, despite his unflagging commitment to Darwinism, he has missed even Darwin’s own solution to the problem of novelty, one readily applicable to language. For Hurford, gradualism and continuity entail changes of both form and function. But Darwin appreciated that there had to be discontinuities of function maintaining con-

tinuity of form. In *Origin of Species*, he singled out the transformation of swim bladders of fish into air-breathing lungs as a clear case of novel functions appearing as “wonderful metamorphoses” repurposing old forms (2).

Indeed, a relatively rapid emergence of language seems to square much better with the paleoarchaeological record. Whereas Hurford’s account demands a long, slow trek from symbolic activity and single words to language, unequivocal evidence of symbolic activity first appears associated with *Homo sapiens* (e.g., the engraved shells in Blombos cave, 77,000 years ago). Going back that far takes only 2600 generations, too little time for a slow trek.

In addition, Hurford repeatedly presents interpretations without providing data to support them: “It is quite possible that *Homo erectus*, perhaps for over a million years, had symbolic pre-syntactic communicative behaviour.” “The first evolutionary rudiments of language permitted somewhat larger group size.” “It is conceivable that the combined effects of increased group size, increased cooperation within groups, increased trust, and shared intentionality permitted some relaxation of genetic control.... Thus the first learned arbitrary symbols.” Doubtless, any of these claims could be correct. The real questions are whether any of them are true and how we might ever determine that.

To support his view that today’s complex languages evolved from simple ones, he discusses three extant “linguistic fossils”: Creole languages; a pair of hypersimplified languages (Pirahã, with fewer than 500 speakers in the Amazonian basin, and Riau, spoken by some 5 million urban Indonesians); and the trajectory of child language acquisition (adopting Haeckel’s “ontogeny recapitulates phylogeny”). However, the empirical basis for his accounts is questionable. Take Creoles: They have articles (e.g., “the” and “a”), whereas “more complex” languages such as Chinese or Russian lack them. Creole articles have a more irregular, complex distribution than those in “complex” French, Italian, or German. And questions in Creoles are formed roughly as in English, with question words (e.g., what) at the front of the sentences—another complexity not found in Chinese (3).

Biologists expecting a worked-out evolutionary model will walk away disappointed. Despite its subtitle, the book lacks explicit fitness calculations, survival and reproduction schedules, generation times, and, indeed, anything resembling the basics of population or behavioral genetics. Hurford reveals what does count for him as an evolutionary argument while explaining why prehuman vocabularies should get larger:

“Couching it in evolutionary terms, one would presumably assume there is some advantage to individuals in a group in having a large vocabulary.” However, evolutionary explanations typically demand far more than just an unproven assumption about advantage to individuals.

Tellingly for such an inherently historical science as evolution, the book contains very little about established hominin prehistory. There isn’t even an illustration of perhaps the single most striking fact about hominin evolution: whereas this clade once formed a bushy tree with many coexisting species, now there is only one lineage left, us. To be sure, Hurford does not seek to provide a historical explanation—he identifies his concern as “the ‘Why?’ and ‘How?’” of the origins of syntax. But history does matter. The available evidence points to a relatively recent appearance of symbolic activity in the human lineage, the adventitious convergence of old forms brought together for a new function just as Darwin suggested, roughly at the time of the last push of *Homo sapiens* out of Africa, 70,000 years ago. We can shed all of Hurford’s speculative baggage: There is no need for “symbolic behavior” in Australopithecines or even Neanderthals; no necessity for special pleading about Creole “simplicity” or eccentric “living fossil” languages; no call for language development to recapitulate phylogeny; and no difficulty reconciling the paradoxically long periods of apparent stasis in the paleoanthropological record with the observed bursts of functional innovation. All these empirical problems fade away, leaving us with a story altogether different from the one told in *The Origins of Grammar*.

References

1. C. Darwin, *The Descent of Man and Selection in Relation to Sex* (John Murray, London, 1871).
2. C. Darwin, *On the Origin of Species* (John Murray, London, 1859).
3. E. O. Aboh, N. Smith, Eds., *Complex Processes in New Languages* (John Benjamins, Philadelphia, 2009).

The reviewer is at the Department of Electrical Engineering and Computer Science, Massachusetts Institute of Technology, Cambridge, MA 02139, USA. E-mail: berwick@csail.mit.edu

The Origins of Grammar

Language in the Light of Evolution

by James R. Hurford

Oxford University Press, Oxford, 2012. 807 pp. \$65, £35. ISBN 9780199207879.

10.1126/science.1220733

RESEARCH PRIORITIES

Shining Light into Black Boxes

A. Morin,¹ J. Urban,² P. D. Adams,³ I. Foster,⁴ A. Sali,⁵ D. Baker,⁶ P. Sliz^{1*}

Funders, publishers, and research institutions must act to ensure that research computer code is made widely available.

The publication and open exchange of knowledge and material form the backbone of scientific progress and reproducibility and are obligatory for publicly funded research. Despite increasing reliance on computing in every domain of scientific endeavor, the computer source code critical to understanding and evaluating computer programs is commonly withheld, effectively rendering these programs “black boxes” in the research work flow. Exempting from basic publication and disclosure standards such a ubiquitous category of research tool carries substantial negative consequences. Eliminating this disparity will require concerted policy action by funding agencies and journal publishers, as well as changes in the way research institutions receiving public funds manage their intellectual property (IP).

Disparity Without a Cause

In publicly funded research outside of computational science, the creation and dissemination of new tools, techniques, and methods requires detailed publication and disclosure of information necessary to satisfy peer review, experimental reproduction, and the ability to build upon another's work. Research tools created using public funds, such as animal models or cell lines, even those intended for commercialization, must fulfill disclosure and publication requirements (1).

Disclosure practices among scientist-programmers often do not meet these standards. Computer programs created in the course of research can range from single-command line scripts to multigigabyte code repositories. Many scientist-created programs are ad hoc efforts never intended for distribution or release, but all can be equally critical to research outcomes. Although it is typical to publish general conceptual and

POLICY ACTIONS TO ELIMINATE SOURCE CODE WITHHOLDING IN RESEARCH COMPUTATION	
Institutional support	Publicly funded research institutions and university TTOs must remove organizational impediments to OSS licensing of computer code and embrace a wider variety of methods for exploiting and sharing their intellectual property. Creating a “standard set” of open software licensing tools within and across institutions that includes established OSS licenses would be an important step toward that goal.
Funding policy	Public funding and policy-setting agencies must explicitly and clearly state their strong preference for open dissemination, sharing, and publication of scientist-created software and source code. Although not an absolute requirement in recognition of the enormous diversity of research receiving public funds, the burden of justifying proprietary research products would be left to the applicant.
Publishing requirement	Scientific journal publishers must enact editorial policies requiring, as a condition of publication, that researchers make available new computer source code generated in the course of the research and necessary to reproduce the published research findings. Policies in place at journals already meeting this requirement (16–18, 36) could provide guidance for wider implementation.

functional descriptions of new, major pieces of scientist-created software, it is not uncommon to withhold the program source code and instead release only the binary (executable) version of a program. Source code is the human readable form of a programming language and contains the complete set of instructions for how a computer processes input data. In the absence of source code, the inner workings of a program cannot be examined, adapted, or modified.

The consequences of relying on these black boxes in research computation can be far-reaching. Common implementation errors in programs, such as failing to convert units correctly or assigning missing values as zero, can be difficult to detect without access to source code (2). Recent retractions, resignations, and canceled clinical drug trials at Duke University involved unreleased and unreproducible code (3). Calls for greater focus on reproducibility in scientific research have mounted in recent years (4, 5), and the inability to reproduce many published computational results or to perform credible peer review in the absence of program source code has contributed to a perceived “credibility crisis” for research computation (6, 7). Source code withholding causes duplication of efforts by preventing sharing and reuse of validated computer code (8) and is incompatible with the stated goals of science funding agencies and policy advisory bodies (9).

How and why this unique disparity in disclosure practices persists within research

computation is complex and goes beyond simple protectionism. Contributing factors may include the informal means by which most scientist-programmers attain their programming skills (10, 11). It is not uncommon for self-taught programmers to be insecure about publishing “ugly” code: programs that work but do not conform to accepted best practices, are inefficient, or are aesthetically lacking (12). Lack of awareness and education around issues of code dissemination among scientist-programmers may also contribute. Among the small number of programming courses geared toward scientists, issues of code publishing or software licensing are seldom addressed.

Systems of attribution and citation, frequently relied on as metrics for career evaluation and achievement, which have evolved to accommodate publication of traditional scientific methods and techniques, may not adequately assure authorship credit when source code is adapted by other researchers. Tendencies toward traditional IP protection regimes at institutional technology transfer offices (TTOs) can result in proprietary licensing and distribution schemes that discourage release of source code (13).

Public-funding and policy-setting agencies have yet to enumerate clear, comprehensive, and universal policies promoting the publishing and dissemination of computer source code. Some specific funding initiatives evaluate applicants, in part, on software sharing and dissemination plans

¹Harvard Medical School, Boston, MA 02115, USA. ²School of Law, University of California, Berkeley, Berkeley, CA 94720, USA. ³Lawrence Berkeley National Laboratory, Berkeley, CA 94720, USA. ⁴Argonne National Laboratory and University of Chicago, Argonne, IL 60439, USA. ⁵University of California, San Francisco, San Francisco, CA 94158, USA. ⁶University of Washington and Howard Hughes Medical Institute, Seattle, WA 98195, USA.

*Author for correspondence. E-mail: piotr_sliz@hms.harvard.edu

[e.g., (14)]. Such grants are typically for, or specifically include, large software development projects, however, and thus fail to address the large majority of scientist-created code.

Most significant may be the absence of a universal disclosure requirement by the gatekeepers of scientific publishing. Of the 20 most-cited journals in 2010 from all fields of science (15), only three (16–18) (including *Science*) have editorial policies requiring availability of computer source code upon publication. This stands in stark contrast to near-universal agreement among the 20 on policies regarding availability of data and other enabling materials.

Mechanisms of Code Dissemination

Source code can be made available through a variety of mechanisms. Posting code for download on laboratory Web sites, deposition in public code repositories, or making use of publisher facilities for supplemental materials are just a few existing options (6). Because of the complexity and unique characteristics of computer source code, however, preserving the systems of attribution and citation that have evolved to accommodate traditional channels of scientific publishing (e.g., data sets, journal articles, and lecture materials) requires additional measures. Fortunately, a variety of software licensing tools exist to help scientist-programmers retain the benefits of authorship, as well as protect IP rights, when disseminating their code.

Beyond allowing others to inspect and understand the inner workings of a computer program, open source software (OSS) licenses encourage the free adoption, reuse, and adaptation of computer source code while also assuring the attribution and citations customary in scientific research. For the scientist-programmer, disseminating software under an OSS license can be a simple method for enabling community participation in development, use, and adoption of a program and can lead to enhanced influence, reputation, and increased rates of citation for the author (19). Numerous types of OSS licenses exist to meet the diverse needs of academic environments, many of which were developed by and for academics working at research institutions [e.g., Berkeley Software Distribution (20), MIT (21), and Educational Community License (22)]. OSS licenses are also fully compatible with commercialization of scientist-created software (23) and Bayh-Dole requirements that allow the patenting of inventions created using public funds (24).

Although OSS licensing options are well suited to the open access and dissemination goals of publically funded research (25–28), not every research software development effort will find OSS licensing an appropriate vehicle for source code dissemination. Many large, publicly funded research software development projects (29, 30) have found a mixture of standard OSS and custom licensing to be appropriate means of achieving source code disclosure while also generating commercial licensing revenue.

Eliminating the Disclosure Disparity

As reliance on scientist-created software grows across scientific fields, the common practice of source code withholding carries significant costs, yields few benefits, and is inconsistent with accepted norms in other scientific domains. Changing this practice will require concrete and unambiguous policy action (see the table). Less definitive disclosure policies are unlikely to achieve desired results. For example, a recent article (31) makes a persuasive case for the necessity of source code release in reproducing scientific results, but fails to lay out efficacious policy recommendations likely to achieve significant and timely change in withholding practices.

Calls for change in disclosure practices from within the scientific community are not new. Similar actions, initiated by the research community and with the cooperation of publishers, have proven successful in the past. In the late 1980s, a group of structural biologists petitioned journal editors to help end then-common data-withholding practices by making the deposition of protein structure data into public databases a condition of publication (32). As a result, today, the Worldwide Protein Data Bank (33) is a vital enabling resource for the biomedical research community that has helped fuel the emergence of multiple fields.

More recently, the field of genomics underwent a community-driven consensus process on data publication and availability. The resulting “Bermuda principles” (34) state that data should be publicly released prior to publication, within 24 hours of generation. Similar principles have since been adopted by other publicly funded ‘omics initiatives, including structural genomics (35).

The parallels between past and current debates over data withholding and the agreed solutions in favor of disclosure and publication are striking. Requiring that source code be made available upon publication would also be expected to yield substantial benefits—including improved code

quality, reduced errors, increased reproducibility, and greater efficiency through code reuse and sharing. Achieving this would bring disclosure and publication requirements for computer codes in line with other types of scientific data and materials.

References and Notes

1. D. Weitz, *High Tech L. J.* (1993); http://heonlinebackup.com/hol/cgi-bin/get_pdf.cgi?handle=hein.journals/berktech8§ion=13.
2. G. Wilson, *Am. Sci.* **94**(1), 5 (2006).
3. R. S. Tuma, *Oncology Times*, 7 January 2011 [blog]; <http://journals.lww.com/oncology-times/blog/FRESHSCIENCEforClinicians/pages/post.aspx?PostID=10>.
4. J. P. Mesirov, *Science* **327**, 415 (2010).
5. J. P. A. Ioannidis, M. J. Khoury, *Science* **334**, 1230 (2011).
6. R. D. Peng, *Science* **334**, 1226 (2011).
7. V. Stodden, *Comput. Sci. Eng.* **11**, 35 (2009).
8. V. Stodden, MIT Sloan School Working Paper 4773-10 (2010); http://papers.ssrn.com/sol3/papers.cfm?abstract_id=1550193.
9. NSF, *National Science Foundation*; www.nsf.gov/pubs/2011/oi11003/.
10. S. M. Baxter et al., *PLoS Comput. Biol.* **2**, e87 (2006).
11. Z. Merali, *Nature* **467**, 775 (2010).
12. N. Barnes, *Nature* **467**, 753 (2010).
13. R. Litan et al., *Yale Law Econ. Res. Paper no. 426*; 10.2139/ssrn.1757982.10.2139/ssrn.1757982.
14. PAR-10-266, <http://grants.nih.gov/grants/guide/pa-files/PA-10-266.html>.
15. Thomson Reuters, *2010 Journal Citation Reports*, Science Edition (Thomson Reuters, Philadelphia, 2012).
16. B. Hanson, A. Sugden, B. Alberts, *Science* **331**, 649 (2011).
17. Editors, *J. Biol. Chem.*; www.jbc.org/site/misc/edpolicy.xhtml.
18. Editors, *Proc. Natl. Acad. Sci. USA*; www.pnas.org/site/misc/iforc.shtml.
19. H. A. Piwowar, R. S. Day, D. B. Fridsma, *PLoS ONE* **2**, e308 (2007).
20. The BSD License, www.opensource.org/licenses/bsd-license.php.
21. The MIT License, www.opensource.org/licenses/MIT.
22. D. Greenstein, B. Wheeler, *Open Source Collaboration in Higher Education* (Indiana Univ., Indianapolis, IN, 2007).
23. F. Hecker, *IEEE Softw.* **16**, 45 (1999).
24. B. N. Sampat, *Nature* **468**, 755 (2010).
25. 32006R1906—Regulation (EC) Official Journal L 391, 30/12/2006 P. 0001; <http://eur-lex.europa.eu/LexUriServ/LexUriServ.do?uri=CELEX:32006R1906:EN:HTML>.
26. National Science Foundation, www.nsf.gov/pubs/policy-docs/pappguide/nsf11001/aag_6.jsp#VID4.
27. National Institutes of Health, *Fed. Regist.* **64**(246), 72090 (1999).
28. T. R. Cech et al., *Plant Physiol.* **132**, 19 (2003).
29. Phenix, www.phenix-online.org/.
30. RosettaCommons, www.rosettacommons.org/.
31. D. C. Ince et al., *Nature* **482**, 485 (2012).
32. F. M. Richards et al., http://hkl.hms.harvard.edu/si/disclosure_letter.pdf.
33. H. Berman, K. Henrick, H. Nakamura, *Nat. Struct. Biol.* **10**, 980 (2003).
34. E. Birney et al., *Nature* **461**, 168 (2009).
35. A. Edwards, *Nat. Struct. Mol. Biol.* **15**, 116 (2008).
36. Editors, *PLoS Comput. Biol.* (2008); www.ploscompbiol.org/static/policies.action.
37. We thank K. Keating and P. Suber for discussions, and S. K. Burley for providing the document in (32).

NEUROSCIENCE

Revitalizing Remyelination—the Answer Is Circulating

Stephanie A. Redmond and Jonah R. Chan

Walled off by bone and the blood-brain barrier, the central nervous system (CNS) is protected from many physical and chemical dangers that threaten more exposed tissues. But while many tissues heal and regain function after injury or disease, the nervous system is notoriously poor at repair, even more so as we age. Because the CNS operates in near isolation from other systems, its failure to repair and regenerate has long been attributed to cell-intrinsic shortcomings that become more limited over time. But Ruckh *et al.* (1) suggest that cells of the CNS may not be so intrinsically limited in repair and that enhancing exposure of the damaged brain or spinal cord to beneficial factors in the blood could aid recovery in injury and disease.

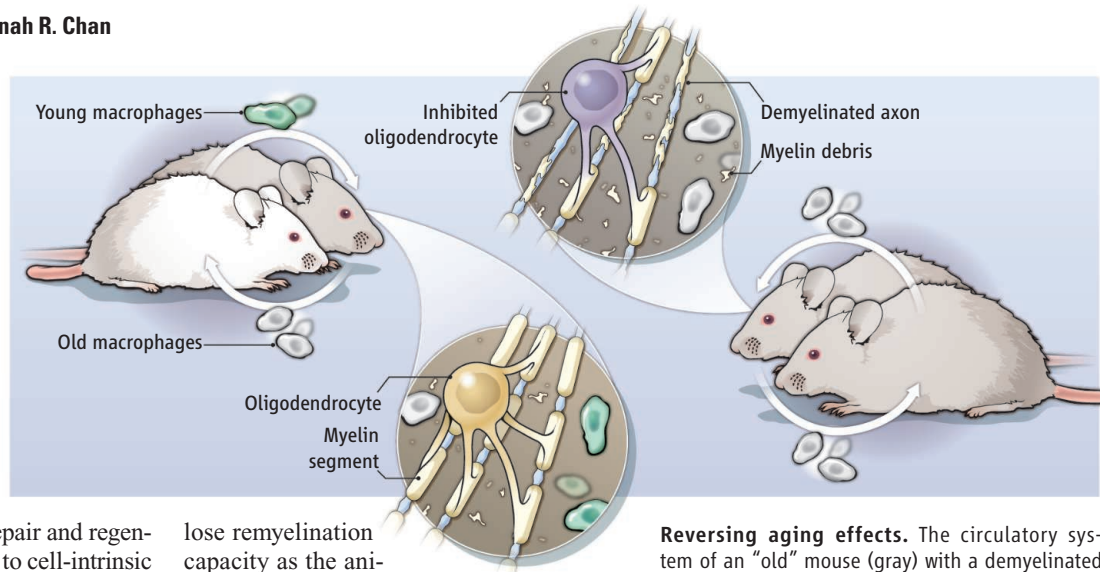
Why does the capacity for CNS repair degenerate with age? In the autoimmune disease multiple sclerosis, for instance, it is thought that remyelination of neuronal axons is painfully slow and incomplete in adults because oligodendroglia (myelin-producing cells of the CNS) are increasingly less sensitive to promyelinating cues (2). But Ruckh *et al.* show that the remyelination potential of oligodendroglia in demyelinated spinal lesions of old mice is boosted by recruitment of peripheral circulating innate immune cells (macrophages) from young mice. The authors induced a demyelinated lesion in an old mouse to assess remyelination over time. They uncoupled oligodendroglial cell-intrinsic factors from systemic factors in blood that may affect remyelination by using heterochronic parabiosis, a surgical technique that joins the circulatory system of an old wild-type mouse with that of a young mouse (genetically engineered to ubiquitously express green fluorescent protein). If adult-derived oligodendroglia intrinsically

lose remyelination capacity as the animal ages, exposing the lesion to circulating blood from a young mouse would not affect the extent of remyelination. Surprisingly, the old-young mouse pairs exhibited enhanced remyelination that depended on the recruitment of circulating macrophages from the young mouse. Exposure to the young mouse circulation is also required, as genetically preventing “young” macrophage recruitment only partially prevented the effect. These results suggest that resident “old” oligodendroglia retain considerable potential to proliferate, differentiate, and remyelinate even as they age, but age-related changes in the systemic milieu and reductions in resident and/or recruited macrophage phagocytic capacity restrict this reparative potential (see the figure).

Little is known about aging effects on the immune system, but it has been suggested that macrophages become less efficient with age and their decreased activity may contribute to age-related chronic inflammation (2, 3). This, combined with lower efficacy of pathogen clearance, could result in prolonged exposure of CNS cells to harmful amounts of detrimental cytokines. Recently, similar heterochronic parabiosis experiments identified increased concentrations of the cytokine CCL11 in healthy aged mice as sufficient to inhibit adult neurogenesis in young mice and induce cognitive deficits (4).

Additionally, the accumulation of cellular debris and/or plaques (insoluble fibrous protein aggregates) in the CNS is thought

Aged oligodendroglia in the mouse central nervous system are competent to repair neural injury when exposed to “youthful” circulatory factors.



Reversing aging effects. The circulatory system of an “old” mouse (gray) with a demyelinated lesion was surgically joined with that of a healthy “young” mouse (white) (1). The old mouse exhibited enhanced remyelination relative to the control, an old-old mouse pair. Remyelination depended on the recruitment of circulatory factors from the young mouse, including macrophages. Resident “old” oligodendroglia retain remyelination potential even as they age, but macrophage-mediated clearance of inhibitory myelin debris from the lesion may become impaired.

to inhibit neuronal repair and regeneration, as well as promote degeneration. For example, the accumulation of brain β -amyloid plaques in Alzheimer’s disease leads to neuronal death and cognitive deficits. Consistent with the findings by Ruckh *et al.*, stimulating phagocytic clearance of β -amyloid protects against neuronal death and facilitates cognitive recovery (5). Ruckh *et al.* suggest a link between age-related accumulation of damaged-myelin debris and remyelination failure. Such debris may be wrongly interpreted as healthy myelin, which might attenuate oligodendroglial proliferation, migration, and/or differentiation, resulting in a shortage of remyelinating oligodendrocytes (6–8).

Maximizing macrophage recruitment to demyelinated lesions may be one avenue to support remyelination. Both CNS microglia (resident macrophages of the brain) and recruited macrophages are polarized to the anti-inflammatory, highly phagocytic “M2” activation state in demyelinated lesions, releasing cytokines that may also directly support remyelination (3, 9). “Young” mac-

rophages recruited to “old” lesions may rescue age-related decreases in the phagocytic capacity of “old” macrophages or in their secretion of cytokines that promote repair.

The study by Ruckh *et al.* suggests that the age-related deficits in remyelination are not solely attributable to the cell-intrinsic capacity of “old” oligodendroglia, but are influenced by extrinsic factors outside the brain and spinal cord. Whether remyelination-promoting serum factors are contributed by the young mouse or remyelination-inhibitory serum factors from the old mouse are sufficiently diluted as a result of parabiosis to allow for enhanced remyelination

remains to be determined. The nature of the effect of the youthful macrophages (if any) on the activation of endogenous older microglia, and the cytokine(s) involved, also should be clarified. Such further characterization would provide valuable insight into the aging immune system.

The findings of Ruckh *et al.* suggest that maximizing intrinsic oligodendroglial myelinogenic potential by altering the local lesion environment could be a promising therapeutic target to promote repair in diseases such as multiple sclerosis. Whereas research concerning myelin repair has traditionally focused on dampening the immune

system and promoting differentiation of oligodendroglia, it may be that the keys to efficient remyelination reside in the circulation.

References

1. J. M. Ruckh *et al.*, *Cell Stem Cell* **10**, 96 (2012).
2. S. Shen *et al.*, *Nat. Neurosci.* **11**, 1024 (2008).
3. B. A. Durafour *et al.*, *Glia* **60**, 717 (2012).
4. S. A. Villeda *et al.*, *Nature* **477**, 90 (2011).
5. P. E. Cramer *et al.*, *Science* **335**, 1503 (2012).
6. R. J. Franklin, *Nat. Rev. Neurosci.* **3**, 705 (2002).
7. S. Y. Chong *et al.*, *Proc. Natl. Acad. Sci. U.S.A.* **109**, 1299 (2012).
8. M. R. Kotter, W. W. Li, C. Zhao, R. J. Franklin, *J. Neurosci.* **26**, 328 (2006).
9. R. Shechter *et al.*, *PLoS Med.* **6**, e1000113 (2009).

10.1126/science.1221689

PLANETARY SCIENCE

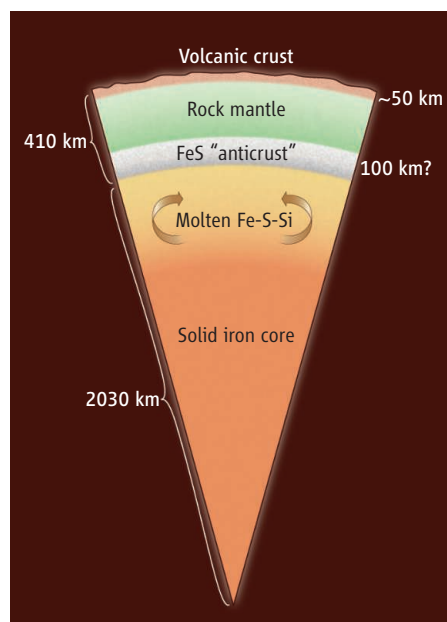
The Strangest Terrestrial Planet

William B. McKinnon

Every great planetary mission makes surprising discoveries, and NASA's MESSENGER mission has made more than its share (1–3). Now new reports on Mercury's gravity field and topography, by Smith *et al.* on page 214 (4) and by Zuber *et al.* on page 217 (5), respectively, up the ante, showing Mercury to be utterly unique among the terrestrial planets. The combination of detailed gravity measurements and high-precision topography is even more powerful, yielding the first views of Mercury's inner layering and mechanical structure.

MESSENGER has been orbiting Mercury for just over a year. Each elliptical polar circuit brings the spacecraft swooping low over the planet's northern hemisphere and then, to reduce the heat load from the broiling surface, allows the spacecraft to retreat to a safe distance at its southernmost excursion. Correspondingly, measurements of the gravity field (derived from radio tracking) and the topography (derived from laser altimetry) are most accurate over the northern hemisphere. But the implications are global.

The global gravity field, specifically its second-degree components (in a spherical harmonic sense), measures the differences between Mercury's principal moments of inertia. Although such findings are interesting in their own right, what inquiring planetary scientists really want to know is the actual moment of inertia, which is a major



constraint on Mercury's interior construction (especially because seismic data, in hand for Earth and the Moon, are quite a ways off for Mercury). A remarkable series of Earth-based radar measurements have precisely located Mercury's spin pole as well as detected a libration or oscillation in Mercury's spin rate (6). When used in combination (7), Smith *et al.* are able to determine both the normalized moment of inertia for Mercury (0.353 ± 0.017) and the ratio of the moment of inertia of Mercury's solid outer shell to that of the planet as a whole (5). By “solid outer shell” they mean that Mercury's spin libration has confirmed that the outer “rocky”

NASA's MESSENGER mission previously revealed that Mercury has a volcanic crust; now it finds evidence for an inner “anticrust.”

Inside Mercury. Recent measurements suggest a rather unusual interior structure for Mercury. The rocky mantle is comparatively thin and is sandwiched between a surface volcanic crust and an underplated iron-sulfide “anticrust.” The size of Mercury's likely inner core of solid iron (plus dissolved metallic silicon) is poorly constrained, as are possible immiscible zones in the molten outer core. How much of Mercury's crust is volcanic, and how much (if any) may be a primitive flotation crust, is also unknown.

mantle of Mercury floats on a layer of molten iron-nickel; convection in such a liquid, electrically conducting layer has long been suspected as being the cause of Mercury's magnetic dipole field (8).

Mercury's moment-of-inertia factor can be usefully compared with those of Earth and Mars—0.331 and 0.366, respectively (9)—and with that of a uniform sphere (0.40). That Mercury's value is so large implies, given the planet's high overall density (5430 kg m^{-3}), that its iron core is much larger than previously thought and much richer in lighter alloying elements. The most recent cosmochemical thinking suggests that these light elements could include both sulfur and silicon (10, 11), and possibly calcium and magnesium as well (12). For decades since the Mariner 10 flybys of Mercury in 1974 and 1975, the internal structure of Mercury has been imagined to consist of a rocky shell 600 km thick overlying an iron-nickel core with an 1800-km radius. Now Smith *et al.* find that Mercury's solid outer shell may be no more than 400 km thick (see the figure). If true, all of Mercury's geological activity across the

Department of Earth and Planetary Sciences and McDonnell Center for the Space Sciences, Washington University, St. Louis, MO 63122, USA. E-mail: mckinnon@wustl.edu

past 4.5 billion years would be due to and contained within this modest carapace. For example, the limited dynamic range of mercurian topography, detailed in Zuber *et al.*, may stem from the lack of a deep mantle and deep-mantle processes.

But there's more. The moment of inertia of the outer solid layer is also high, giving an average density near 3650 kg m^{-3} for the layer, appreciably higher than that of Earth's upper mantle (about 3400 kg m^{-3}). This is all the more remarkable given the paucity of iron and titanium in Mercury's surface volcanic rocks (13, 14) [rocks whose elemental compositions have at long last been revealed by MESSENGER's x-ray spectrometer (14), now that the Sun has become active again]. Low-iron volcanic rocks imply low-iron, and thus low-density, mantle source rocks, making it very difficult to explain the overall high density. Smith *et al.* appeal to experimental results on highly chemically reduced metallic melts (15) and the compositions of the highly reduced enstatite chondrite meteorite clan (10, 11). Cooling sulfide liquid, if sufficiently sulfur-rich, may not freeze out an inner core of solid iron (as thought to be occurring on Earth), but may plate out a layer of less dense

iron sulfide to the base of the rock mantle (see the figure). The thickness of this "anticrost" may rival or exceed that of the traditional surface crust (lower-density rocks) (4).

Smith *et al.* rightly point out that such a basal sulfide layer, if real, could profoundly affect the external expression of Mercury's magnetic field. It may also have important (if subtle) geological and geophysical effects, especially if it is of nonuniform thickness (which might be generated by impact basin formation or mantle convection). Using the topography in Zuber *et al.*, Smith *et al.* apply their gravity data to show that Mercury's surface crust likely thins toward the north pole. Mercury's northern polar region is also low-standing and a site of particularly extensive (but ancient) lava flooding. Although the present outline of the northern polar plains is ragged, such expanses of smooth plains on other planets (Procellarum on the Moon and Borealis on Mars) have inspired speculations of formative mega-impacts. In Mercury's case, and whatever their origin, the low-lying northern plains may now sit close to the geographic pole because of polar wander of Mercury's outer shell (4). Planetary scientists will begin to consider how the anticrost might

have affected this and other processes. And they will have help—the MESSENGER mission has been extended, and the BepiColombo mission will be launched in a few years.

References

1. B. Hanson, *Science* **321**, 58 (2008).
2. S. C. Solomon, L. M. Prockter, D. T. Blewett, *Earth Planet. Sci. Lett.* **285**, 225 (2009).
3. R. A. Kerr, *Science* **333**, 1812 (2011).
4. D. E. Smith *et al.*, *Science* **336**, 214 (2012); 10.1126/science.1218809.
5. M. T. Zuber *et al.*, *Science* **336**, 217 (2012); 10.1126/science.1218805.
6. J.-L. Margot, S. J. Peale, R. F. Jurgens, M. A. Slade, I. V. Holin, *Science* **316**, 710 (2007).
7. S. J. Peale, R. J. Phillips, S. C. Solomon, D. E. Smith, M. T. Zuber, *Meteorit. Planet. Sci.* **37**, 1269 (2002).
8. G. Schubert, M. N. Ross, D. J. Stevenson, T. Spohn, in *Mercury*, F. Vilas *et al.*, Eds. (Univ. of Arizona Press, Tucson, AZ, 1988), pp. 429–460.
9. W. M. Folkner, C. F. Yoder, D. N. Yuan, E. M. Standish, R. A. Preston, *Science* **278**, 1749 (1997).
10. V. Malavergne, M. J. Toplis, S. Berthet, J. Jones, *Icarus* **206**, 199 (2010).
11. K. Keil, *Chem. Erde Geochem.* **70**, 295 (2010).
12. B. Charlier, T. L. Grove, M. T. Zuber, *43rd Lunar Planet. Sci. Conf.*, abstract 1400 (2012); www.lpi.usra.edu/meetings/lpsc2012/pdf/1400.pdf.
13. J. W. Head *et al.*, *Science* **333**, 1853 (2011).
14. L. R. Nittler *et al.*, *Science* **333**, 1847 (2011).
15. G. Morard, T. Katsura, *Geochim. Cosmochim. Acta* **74**, 3659 (2010).

10.1126/science.1220825

COMPUTER SCIENCE

Beyond Turing's Machines

Andrew Hodges

In marking Alan Turing's centenary, it's worth asking what was his most fundamental achievement and what he left for future science to take up when he took his own life in 1954. His success in World War II, as the chief scientific figure in the British cryptographic effort, with hands-on responsibility for the Atlantic naval conflict, had a great and immediate impact. But in its ever-growing influence since that time, the principle of the universal machine, which Turing published in 1937 (1), beats even this.

When, in 1945, he used his wartime technological knowledge to design a first digital computer, it was to make a practical version of that universal machine (2). All computing has followed his lead. Defining a universal machine rests on one idea, essential to Turing's mathematical proof in 1936, but quite counter-intuitive, and bearing no resemblance to the large practical calculators of the 1930s.

It put logic, not arithmetic, in the driving seat. This central observation is that instructions are themselves a form of data. This vital idea was exploited by Turing immediately in his detailed plan of 1945. The computer he planned would allow instructions to operate on instructions to produce new instructions. The logic of software takes charge of computing. As Turing explained, all known processes could now be encoded, and all could be run on a single machine. The process of encoding could itself be automated and made user-friendly, using any logical language you liked. This approach went far beyond the vision of others at the time.

Even more fundamental than the universal machine is the concept of computability that Turing defined in 1936. His first step was to ask for a precise definition of "mechanical process," and he proceeded by analyzing what it means for someone to follow a rule. In modern terms, "anything that can be done by a computer program" was his answer, with the invention of the computer as a by-product.

Whether all types of computation—including that of our own minds—can be modeled as computer programs remains an open question.

This leaves open the question of whether such an analysis would include absolutely everything that a material system (including brains) might be able to achieve. Ever since 1936, this nagging question has been on the agenda, and it is still there.

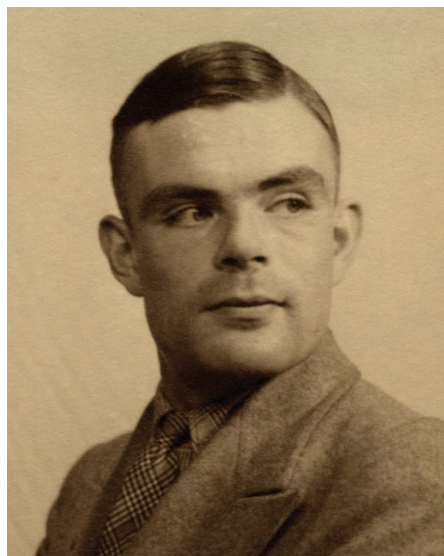
In 1939, Turing suggested that mathematical steps that are not rule-following, and so not computable, could be identified with mental "intuition" (3). However, he gave no discussion of whether the human brain was actually embodying uncomputable physical processes. Wartime experience led Turing in a different direction. His brilliant codebreaking algorithms, outdoing human guessing, stimulated the conviction that all mental operations must be computable, including those functions of the mind not apparently following methodical rules. His 1950 paper (4), most famous for the wit of the Turing test of intelligence (5), also included a careful discussion of computability. It set out a basic argument that if the brain's action is computable, then it can be implemented on a computer, this

Wadham College, University of Oxford, Oxford, OX1 3PN, UK. E-mail: andrew.hodges@wadh.ox.ac.uk

being a universal machine. In defending this point of view, Turing referred to what would now be called chaotic effects in the brain and argued that these did not prevent computer simulation. Notably, at this time Turing was also founding a new branch of mathematical biology: He was applying the insights of an applied mathematician who was also one of the first to use a computer for simulating physical systems.

In 1951, however, Turing gave a radio talk with a different take on this question, suggesting that the nature of quantum mechanics might make simulation of the physical brain impossible. This consideration can be traced back in Turing's thought to 1932, when he first studied the axioms of quantum mechanics [see (6)]. Turing then took up renewed interest in quantum theory and noted a problem about the observation of quantum systems (now known as the quantum Zeno effect). With his death, this train of thought was lost, but the serious question of relating computation to fundamental physics has remained.

Since the 1980s, quantum computing has given a practical technological arena in which computation and quantum physics interact excitingly, but it has not yet changed Turing's picture of what is computable. There are also many thought-experiment models that explore what it would mean to go beyond the limits of the computable. Some rather trivi-



ally require that machine components could operate with boundless speed or allow unlimited accuracy of measurement. Others probe more deeply into the nature of the physical world. Perhaps the best-known body of ideas is that of Roger Penrose (7). These draw strongly on the very thing that motivated Turing's early work—the relationship of mental operations to the physical brain. They imply that uncomputable physics is actually fundamental to physical law and oblige a radical reformulation of quantum mechanics.

Superficially, any such theory contradicts the line that Turing put forward after 1945. But more deeply, anything that brings together the fundamentals of logical and physical description is part of Turing's legacy. He was most unusual in disregarding lines between mathematics, physics, biology, technology, and philosophy. In 1945, it was of immediate practical concern to him that physical media could be found to embody the 0-or-1 logical states needed for the practical construction of a computer. But his work always pointed to the more abstract problem of how those discrete states are embodied in the continuous world. The problem remains: Does computation with discrete symbols give a complete account of the physical world? If it does, how can we make this connection manifest? If it does not, where does computation fail, and what would this tell us about fundamental science?

References

1. A. M. Turing, *Proc. London Math. Soc.* **52-42**, 230 (1937).
2. M. Davis, *The Universal Computer: The Road from Leibniz to Turing* (Taylor & Francis, Boca Raton, FL, Turing Centenary edition, 2012).
3. A. M. Turing, *Proc. London Math. Soc.* **52-45**, 161 (1939).
4. A. M. Turing, *Mind* **49**, 433 (1950).
5. R. M. French, *Science* **336**, 164 (2012).
6. A. Hodges, *Alan Turing: The Enigma* (Princeton Univ. Press, Princeton, NJ, Turing Centenary edition, 2012).
7. R. Penrose, *The Emperor's New Mind* (Oxford Univ. Press, Oxford, 1989).

10.1126/science.1218417

COMPUTER SCIENCE

Dusting Off the Turing Test

Robert M. French

Hold up both hands and spread your fingers apart. Now put your palms together and fold your two middle fingers down till the knuckles on both fingers touch each other. While holding this position, one after the other, open and close each pair of opposing fingers by an inch or so. Notice anything? Of course you did. But could a computer without a body and without human experiences ever answer that question or a million others like it? And even if recent revolutionary advances in collecting, storing, retrieving, and analyzing data lead to such a computer, would this machine qualify as “intelligent”?

Just over 60 years ago, Alan Turing published a paper on a simple, operational test for

machine intelligence that became one of the most highly cited papers ever written (1). Turing, whose 100th birthday is celebrated this year, made seminal contributions to the mathematics of automated computing, helped the Allies win World War II by breaking top-secret German codes, and built a forerunner of the modern computer (2). His test, today called the Turing test, was the first operational definition of machine intelligence. It posits putting a computer and a human in separate rooms and connecting them by teletype to an external interrogator, who is free to ask any imaginable questions of either entity. The computer aims to fool the interrogator into believing it is the human; the human must convince the interrogator that he/she is the human. If the interrogator cannot determine which is the real human, the computer will be judged to be intelligent.

Revolutionary advances in data capture, storage, retrieval, and analysis revive questions raised by the Turing test.

In the early days of artificial intelligence (AI), the Turing test was held up by many as the true litmus test for computational intelligence (3, 4). However, workers in AI gradually came to realize that human cognition emerges from a web of explicit, knowledge-based processes and automatic, intuitive, “subcognitive” processes (5), the latter deriving largely from humans' direct interaction with the world. It was argued, therefore, that by tapping into this subcognitive substrate—something a disembodied computer did not have—a clever interrogator could unfailingly distinguish a computer from a person (6). By 1995, most serious researchers in AI had stopped talking about machines passing Turing's original, teletype-based test (7), let alone harder versions involving testing visual, auditory, and object-manipulation abilities (8). The Turing

LEAD-CNRS, Université de Bourgogne, Dijon, France.
E-mail: robert.french@u-bourgogne.fr

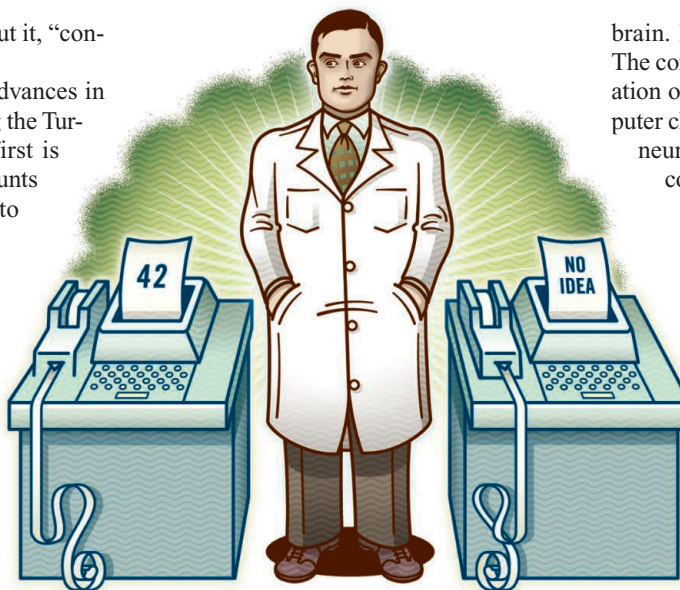
test had been, as one researcher put it, “consigned to history” (9).

However, two revolutionary advances in information technology may bring the Turing test out of retirement. The first is the ready availability of vast amounts of raw data—from video feeds to complete sound environments, and from casual conversations to technical documents on every conceivable subject. The second is the advent of sophisticated techniques for collecting, organizing, and processing this rich collection of data. Two deep questions for AI arise from this new technology. The first is whether this wealth of data, appropriately processed, could be used by a machine to pass an unrestricted Turing test.

The second question, first asked by Turing, is whether a machine that had passed the Turing test using this technology would necessarily be intelligent.

Suppose, for a moment, that all the words you have ever spoken, heard, written, or read, as well as all the visual scenes and all the sounds you have ever experienced, were recorded and accessible, along with similar data for hundreds of thousands, even millions, of other people. Ultimately, tactile, and olfactory sensors could also be added to complete this record of sensory experience over time. Researchers at the cutting edge of today’s computer industry think that this kind of life-experience recording will become commonplace in the not-too-distant future (10). Recently, a home fully equipped with cameras and audio equipment continuously recorded the life of an infant from birth to age three, amounting to ~200,000 hours of audio and video recordings, representing 85% of the child’s waking experience (11, 12).

Assume also that the software exists to catalog, analyze, correlate, and cross-link everything in this sea of data. These data and the capacity to analyze them appropriately could allow a machine to answer heretofore computer-unanswerable questions that tap into facts derived from our embodiment or from our subcognitive associative networks, like the finger experiment that began this article or like asking native English speakers whether the neologism “Flugblogs” would be a better name for a start-up computer company or for air-filled bags that you tie on your feet for walking across swamps (6). Someone, somewhere has almost certainly done the finger experi-



ment and may well have posted their observations about it to the Internet—or will do so after reading this article—and this information would be accessible to a data-gathering Web crawler. By extension, if a complete record of the sensory input that produced your own subcognitive network over your lifetime were available to a machine, is it so far-fetched to think that the machine might be able to use that data to construct a cognitive and subcognitive network similar to your own? Similar enough, that is, to pass the Turing test.

Computers are already extremely good at collecting and analyzing data from 8 billion (and counting) Web pages, document databases, TV programs, Twitter feeds, etc. (13). In early 2011, IBM’s Watson (14), a 2880-processor, 80-teraflop (i.e., 80 trillion operations/s) computing behemoth with 15 terabytes of RAM, won a *Jeopardy* challenge against two of the best *Jeopardy* players in history. Watson’s success was attributable, at least in part, to its meticulous study of *Jeopardy*-like answers and questions, but its performance was nevertheless astounding (15). How much would be required to retool Watson for a no-holds-barred Turing test?

The real challenge is not to store countless petabytes (1 million gigabytes) of information, but to selectively retrieve and analyze that information in real time. The human brain processes data in a highly efficient manner, requiring little energy and relying on a densely interconnected network of ~100 billion relatively slow and imprecise neurons. It is still not known to what extent the mechanisms of neuronal firing and the patterns of neuronal interconnectivity are optimal for the analysis of the data stored in the

brain. IBM is betting that it just might be. The company recently unveiled a new generation of experimental “neurosynaptic” computer chips, based on principles that underlie neurons, with which they hope to design cognitive computers that will “emulate the brain’s abilities for perception, action and cognition” (16).

Yes, you say, but data-crunching computers will never be able to think about their own thoughts, which in the final analysis is what makes us human. But there is nothing stopping the computer’s data-analysis processes, themselves, from also being data for the machine. Programs already exist that self-monitor their own data processing (17).

All of this brings us squarely back to the question first posed by Turing at the dawn of the computer age, one that has generated a flood of philosophical and scientific commentary ever since. No one would argue that computer-simulated chess playing, regardless of how it is achieved, is not chess playing. Is there something fundamentally different about computer-simulated intelligence?

References and Notes

1. A. Turing, *Mind* **59**, 433 (1950).
2. A. Hodges, *Science* **336**, 163 (2012).
3. H. Dreyfus, *What Computers Still Can’t Do* (MIT Press, Cambridge, MA, 1992).
4. J. Haugeland, *Artificial Intelligence, the Very Idea* (MIT Press, Cambridge, MA, 1985).
5. D. R. Hofstadter, *Metamagical Themas* (Basic Books, New York, 1985), pp. 631–665.
6. R. M. French, *Mind* **99**, 53 (1990).
7. R. M. French, *Trends Cogn. Sci.* **4**, 115 (2000).
8. S. Harnad, *Minds Mach.* **1**, 43 (1991).
9. B. Whitty, in *Machines and Thought: The Legacy of Alan Turing*, P. Millican, A. Clark, Eds. (Oxford Univ. Press, Oxford, 1996), pp. 53–63.
10. G. Bell, J. Gemmell, *Total Recall: How the E-Memory Revolution Will Change Everything* (Dutton, New York, 2009).
11. D. Roy et al., in *Proceedings of the 28th Annual Conference of the Cognitive Science Society*, R. Sun, N. Miyake, Eds. (Erlbaum, Mahwah, NJ, 2006), pp. 2059–2064.
12. www.media.mit.edu/research/groups/1446/human-speechome-project
13. D. Talbot, “A Social-media decoder,” *Technol. Rev.* (Nov/Dec. 2011); www.technologyreview.com/computing/38910/.
14. D. Ferrucci et al., *AI Mag.* **31**, 59 (2010).
15. R. Kurzweil, “Why IBM’s *Jeopardy* victory matters,” *PC Mag.* (2011); www.pcmag.com/article2/0,2817,2376035,00.asp.
16. See www-03.ibm.com/press/us/en/pressrelease/35251.wss, posted on 18 August 2011.
17. J. Marshall, *J. Exp. Theor. Artif. Intell.* **18**, 267 (2006).
18. This work was supported in part by ANR grant 10-065-GETPIMA. Thanks to D. Dennett, M. Weaver, and especially M. Mitchell for comments on an early draft of this article.

10.1126/science.1218350

CELL BIOLOGY

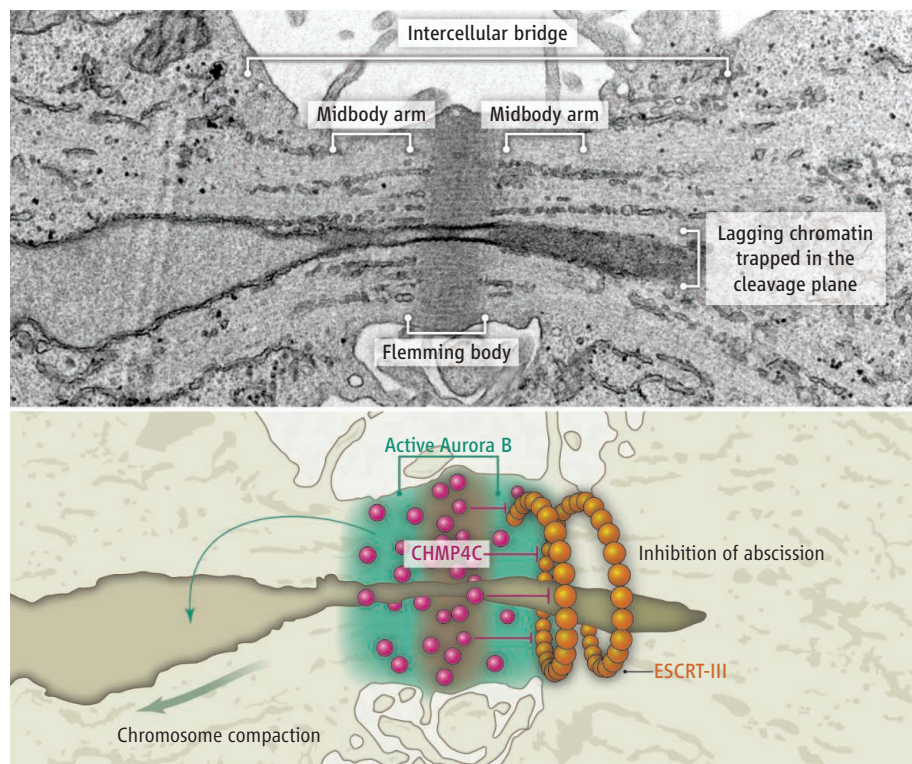
ESCRTing DNA at the Cleavage Site During Cytokinesis

Mark Petronczki¹ and Frank Uhlmann²

Collisions are only good business for insurance companies. During cell division, collisions between separating chromosomes and the cytokinetic apparatus, which physically divides the two daughter cells, must be avoided to prevent catastrophic consequences for genome stability (1). Cytokinesis follows the separation of sister genomes, which are pulled to opposite cell poles, and involves splitting the cytoplasm by the ingression of a cleavage furrow followed by a terminal membrane fission event called abscission (2). Recent work has identified a monitoring system that prevents cell separation while chromatin lingers in the division plane (3, 4). At the heart of it lies a conserved protein kinase, Aurora B. On page 220 in this issue, Carlton *et al.* identify CHMP4C, a subunit of the ESCRT-III (endosomal sorting complex required for transport) complex, as a key target of Aurora B that delays abscission and prevents DNA damage if chromatin bridges persist in human cells (5).

Cytokinesis is initiated by a contractile ring of actin and myosin filaments that drive the ingression of the cleavage furrow at the cell equator. Constriction proceeds until the membrane forms an intercellular bridge covering the midbody, a dense proteinaceous structure that emerges from the anaphase spindle (see the figure). The midbody now serves as a recruitment platform for abscission factors including the ESCRT-III complex. ESCRT-III forms filaments around the abscission site that might eventually contract and break the connection between nascent daughter cells (6, 7). The midbody region is also where Aurora B resides during cytokinesis. As part of the NoCut pathway in budding yeast, Aurora B promotes association of two anillin-like proteins with the contractile ring to delay abscission in response to chromatin at the cleavage site (3, 8). How Aurora B controls the timing of abscission

¹Cell Division and Aneuploidy Laboratory, Cancer Research UK London Research Institute, Clare Hall Laboratories, Blanche Lane, South Mimms, Hertfordshire, EN6 3LD, UK.
²Chromosome Segregation Laboratory, Cancer Research UK London Research Institute, Lincoln's Inn Fields Laboratories, 44 Lincoln's Inn Fields, London WC2A 3LY, UK. E-mail: mark.petronczki@cancer.org.uk (M.P.); frank.uhlmann@cancer.org.uk (F.U.)



Caught in the middle. Thin-section electron micrograph of a HeLa cell cytokinetic furrow shows chromatin trapped in the cleavage plane (provided by Sergey Lekomtsev). Schematic model depicts how Aurora B kinase at the midbody arms, activated by lagging chromatin, phosphorylates CHMP4C to cause its localization to the Flemming body where it delays abscission. Aurora B also activates condensin to compact chromosomes in order to clear the cleavage plane.

in human cells was not known.

Carlton *et al.* have now made big strides toward explaining the mechanism by which Aurora B achieves this (5). They investigated the role of an ESCRT-III subunit called CHMP4, which exists in three isoforms. One of these isoforms, CHMP4C, was found to act as a negative regulator of cytokinesis by delaying abscission if chromosome bridges persist. Aurora B targets a unique short C-terminal insertion in CHMP4C, and, upon phosphorylation, CHMP4C localizes to the central region of the midbody known as the Flemming body (see the figure), where it delays abscission in response to chromatin bridges and thus prevents DNA damage (5). These findings suggest that Aurora B puts a brake on abscission in human cells by promoting recruitment of CHMP4C to the Flemming body. The mechanism by which CHMP4C

During cell division, Aurora B prevents collisions between chromatin and the cytokinetic apparatus by targeting the ESCRT-III subunit CHMP4C.

delays abscission merits future investigation. Does CHMP4C prevent ESCRT-III filament assembly or contraction? Another important question is whether additional mechanisms exist that promote longevity of the intercellular bridge to prevent furrow regression and cytokinesis failure, an error with devastating consequences for genome stability (9, 10).

In addition to controlling abscission, Aurora B also prevents collisions between chromosomes and the cytokinetic apparatus by helping to move chromosomes out of the cleavage plane. Normally, the chromosomal condensin complex shortens chromosome arms to prevent them from becoming trapped in the cleavage furrow during anaphase. The condensin complex accumulates on chromatin bridges if they persist, and phosphorylation of condensin by Aurora B enhances chromosome compaction (11–13). This should

help to clear chromosomes from the cleavage plane. Thus, Aurora B lies at the heart of at least two pathways that coordinate chromosome segregation with cytokinesis in yeast and mammalian cells.

How does Aurora B sense trailing chromatin? The NoCut pathway in budding yeast can be activated by ectopically bringing Aurora B into contact with chromatin, which suggests that spatial proximity with chromatin generates the signal to delay abscission (8). Another important open question is how collision of the contractile machinery

with chromatin causes DNA damage. Is this simply because of physical forces exerted by the contractile machinery or other biochemical processes that are linked to cytokinesis? The mechanism uncovered here (5) reveals one way that cells avoid becoming a case for the insurance.

References

1. A. Janssen, M. van der Burg, K. Szuhai, G. J. Kops, R. H. Medema, *Science* **333**, 1895 (2011).
2. F. A. Barr, U. Gruneberg, *Cell* **131**, 847 (2007).
3. C. Norden *et al.*, *Cell* **125**, 85 (2006).
4. P. Steigemann *et al.*, *Cell* **136**, 473 (2009).
5. J. G. Carlton, A. Caballe, M. Agromayor, M. Kloc, J. Martin-Serrano, *Science* **336**, 220 (2012); 10.1126/science.1217180.
6. J. G. Carlton, J. Martin-Serrano, *Science* **316**, 1908 (2007).
7. J. Guizetti *et al.*, *Science* **331**, 1616 (2011).
8. M. Mendoza *et al.*, *Nat. Cell Biol.* **11**, 477 (2009).
9. Q. Shi, R. W. King, *Nature* **437**, 1038 (2005).
10. T. Fujiwara *et al.*, *Nature* **437**, 1043 (2005).
11. N. Nakazawa, R. Mehrotra, M. Ebe, M. Yanagida, *J. Cell Sci.* **124**, 1795 (2011).
12. K. Tada, H. Susumu, T. Sakuno, Y. Watanabe, *Nature* **474**, 477 (2011).
13. F. Mora-Bermúdez, D. Gerlich, J. Ellenberg, *Nat. Cell Biol.* **7**, 822 (2007).

10.1126/science.1221832

NEUROSCIENCE

Wiping Drug Memories

Amy L. Milton and Barry J. Everitt

The tendency to relapse in individuals who are trying to remain abstinent is a major, but as yet unrealized, treatment target for drug addiction. On page 241 in this issue, Xue *et al.* (1) suggest that the memories elicited by drug cues and contexts can be diminished, thereby reducing their impact on relapse in both animals and people addicted to drugs.

Memories persist through the process of reconsolidation (2). When retrieved, a previously consolidated memory can enter a labile state in which new information can be introduced, before the memory restabilizes to persist in the brain, in its new updated form (3). By reexposing addicts to drug cues, a process similar to “cue-exposure therapy” (4), Xue *et al.* have manipulated the memory-updating process to overwrite the original memory and thereby reduce the risk of relapse in the long term. Rather than solely inducing memory extinction—the formation of a new “cue–no drug” memory that competes with the original “cue–drug” memory—the authors have used “extinction within the reconsolidation window” to reduce drug-seeking. A similar procedure for cue-fear memories has been shown to reduce fear in rats and humans (5, 6).

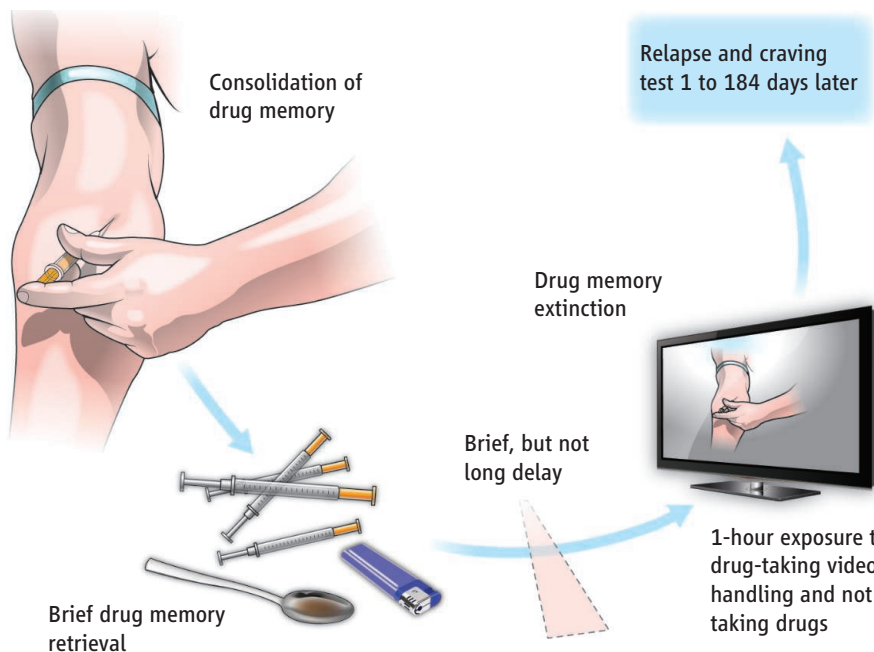
The authors used two models of drug use in rats that allow associations to form between stimuli (cues) and contexts, and two addictive drugs, cocaine and heroin. In the acute model, rats received injections of either cocaine or heroin in a specific envi-

ronment or control injections in another environment. Subsequently, their preference for the drug-paired environment, tested when the rats were drug-free, provided a measure of their drug memory. Animals were reexposed to the drug-paired environment to reactivate the cue–drug memory and after a delay of 10 min, 1 hour, or 6 hours, they were exposed continuously to the same

A nonpharmacological approach alters the memory of drug exposure in rats and has implications for treating relapse in human addicts.

drug environment (but given no drug) to engage memory extinction processes. Only in the 10-min and 1-hour groups was subsequent preference for the drug environment abolished, and it did not return even after “reminder” injections of the drug.

This apparent loss of drug memory was also observed in a more complex drug self-administration model, which more



Decreasing craving and relapse. A nonpharmacological method that weakens original cue–drug memories can decrease drug craving and relapse in abstinent heroin addicts (1). Heroin addicts associate drug cues and contexts with the addictive drug effect, establishing a drug memory. If a heroin addict (who has undergone detoxification) is shown images of drug-associated cues (such as drug paraphernalia) over an extended time period, this engages memory extinction processes, but this procedure does not erase the original cue–drug memory and the cravings can return. However, if the addict undergoes a brief “memory reactivation session” 10 min before extinction, this engages a memory reconsolidation process, which updates the old memory. The result is a greatly diminished “drug memory” later on, and drug cravings are reduced.

closely approximates addictive behavior in humans. Rats were trained to self-administer either cocaine or heroin, in the presence of drug-associated cues, over an extended period during which cue-drug memories were formed (7, 8). The animals then either underwent only extinction training or received a brief cue-drug memory-reactivation session 10 min before extinction training. When assessed 1 month later, only the group that had received the reminder and extinction showed a reduced tendency to resume drug-seeking behavior following exposure to either drug-associated cues or a reminder injection of cocaine or heroin. Furthermore, although extinction training occurred in a different environment to that of self-administration training, the resumption of drug seeking was reduced in the original self-administration environment. Thus, the usual context specificity of extinction (9) was overcome, suggesting that it may be possible to treat individuals in the clinic, with the beneficial effects of the treatment realized in the now-abstinent drug user's environment.

Remarkably, the authors successfully translated the approach of manipulating reconsolidation and extinction to a population of heroin addicts (see the figure). Three groups of patients, having undergone heroin detoxification, were briefly exposed to either a drug-relevant video or a control video followed, 10 min or 6 hours later, by 60 min of heroin cue extinction (they were exposed to imagery and drug paraphernalia, but given no drugs). Subjective craving and physiological responses (heart rate and blood pressure) were measured from 1 to 184 days later. Only the group that had the 10-min delay between the heroin video and extinction showed a marked reduction in craving and blood pressure after presentation of heroin-associated cues at every time point tested.

Although an increasing amount is known about the cellular and molecular mechanisms underlying reconsolidation (10, 11) and extinction (12)—e.g., both depend upon activation of *N*-methyl-D-aspartate (NMDA) receptors and intracellular signaling pathways—little is known about the nature of the interaction between reconsolidation and extinction that would explain why the extinction observed in this procedure is so profound and escapes its usual context specificity (9). Xue *et al.* point to a possible involvement of the atypical protein kinase C isoform PKM ζ , a scaffold protein that maintains α -amino-3-hydroxy-5-methyl-4-isoxazolepropionic acid (AMPA)

receptors in potentiated synapses (13) and so may reflect the structural changes in neurons that support a stabilized memory (14). Extinction training increased PKM ζ expression in the infralimbic cortex, which has long been implicated in the extinction of drug memories (12), and this increase was further enhanced by a memory reminder session before extinction training, perhaps strengthening extinction. Likewise, extinction reduced the expression of PKM ζ in the basolateral amygdala, an area critical for the reconsolidation of cue-drug memories (11), and this was further reduced by a memory reminder session before extinction training, perhaps suggesting impaired reconsolidation. How these changes occur, how they relate to each other, and whether they are causal in the apparent, subsequent amnesia remain to be investigated.

Perhaps the most remarkable aspect of these findings is that the effects of a purely behavioral manipulation in rats that in no sense were “addicted” translate so readily to patients who have been addicted to heroin for more than 9 years. This is especially so considering that even in the animal model with longer, 10-day drug self-administration histories, drug-taking behavior itself was explicitly extinguished, although no analogous process occurs either in the real-world

environment of those addicted to drugs, or in the clinical study, in which there was only passive exposure to drug memory-eliciting stimuli. With these conundrums in mind and the obscure molecular mechanism, the findings nevertheless encourage the view that targeting maladaptive memories that play an important role in the persistence of addictive behavior may provide a new avenue for treatment interventions (15).

References

1. Y.-X. Xue *et al.*, *Science* **336**, 241 (2012).
2. K. Nader, *Trends Neurosci.* **26**, 65 (2003).
3. J. L. C. Lee, *Trends Neurosci.* **32**, 413 (2009).
4. C. A. Conklin, S. T. Tiffany, *Addiction* **97**, 155 (2002).
5. M. H. Monfils, K. K. Cowansage, E. Klann, J. E. LeDoux, *Science* **324**, 951 (2009).
6. D. Schiller *et al.*, *Nature* **463**, 49 (2010).
7. A. L. Milton, B. J. Everitt, *Eur. J. Neurosci.* **31**, 2308 (2010).
8. M. M. Torregrossa, P. R. Corlett, J. R. Taylor, *Neurobiol. Learn. Mem.* **96**, 609 (2011).
9. M. E. Bouton, *Biol. Psychiatry* **52**, 976 (2002).
10. J. L. C. Lee, B. J. Everitt, K. L. Thomas, *Science* **304**, 839 (2004).
11. A. L. Milton, J. L. C. Lee, V. J. Butler, R. Gardner, B. J. Everitt, *J. Neurosci.* **28**, 8230 (2008).
12. K. M. Myers, W. A. Carlezon Jr. M. Davis, *Neuropsychopharmacology* **36**, 274 (2011).
13. Y. Yao *et al.*, *J. Neurosci.* **28**, 7820 (2008).
14. R. Shema, T. C. Sacktor, Y. Dudai, *Science* **317**, 951 (2007).
15. A. L. Milton, B. J. Everitt, *Neurosci. Biobehav. Rev.* **36**, 1119 (2012).

10.1126/science.1221691

PSYCHOLOGY

Monkey See, Monkey Read

Michael L. Platt and Geoffrey K. Adams

Baboons can distinguish between written words and nonwords.

Reading great literature provides a humanistic approach to understanding one's nature and place in history. Likewise, the scientific study of the biological bases of reading may provide insights into the origins of human cognition. On page 245 of this issue, Grainger *et al.* (1) show that these biological mechanisms may be rooted much deeper in human evolutionary history than previously supposed (see the first figure).

Biological approaches to cognition propose that specialized neural modules evolved to solve specific problems encountered in the physical or social environment, such as identifying and remembering the faces of the members of one's group. However, read-

ing and writing appeared too recently and spread too rapidly within and between populations to have required genetic changes to support it. In a striking example, the writing system for Cherokee, a previously unwritten language, was invented in the early 19th century, and was widely learned and used in Cherokee society within one generation (2). Clearly, reading is supported by neural mechanisms that are much older than the behavior itself and that presumably evolved before the human diaspora from Africa.

Ultimately, reading depends on language. But at what stage in the process of translating written symbols into meaning is language necessary? Some insight is provided by the observation that animals can learn to discriminate letters from one another; pigeons even seem to do so in a manner resembling

Duke Institute for Brain Sciences, Duke University, Durham, NC 27710, USA. E-mail: platt@neuro.duke.edu

letter discrimination by humans. Presumably, then, the identification of letters is a visual problem, not a linguistic one (3). In languages like English that are written with an alphabet, letters represent the sounds that make up words; the processing of a sequence of letters into a word builds on the processing of a sequence of sounds in speech. By contrast, in pictographic writing systems like Chinese, symbols directly (and often iconically) represent specific words or ideas. In either case, orthographic processing of individual elements would appear to be the first, critical speech-dependent step in reading.

The evidence reported by Grainger *et al.* challenges this speech-based model of reading. The authors developed a task to assess whether baboons can successfully perform orthographic processing. To receive a food pellet reward, the baboons had to discriminate four-letter English written words from nonwords of the same length. Nonwords were constructed of letter combinations that were rare in the sample of English words. The baboons were able to learn not only a specific list of words, but also to predict whether a new letter sequence was a real English word or not. Presumably, the baboons learned the statistics of letter combinations in the four-letter English words and used this information to perform the task. Because baboons do not speak any human language, this finding strongly suggests that the speech-based model of reading may be at best incomplete and possibly wrong.

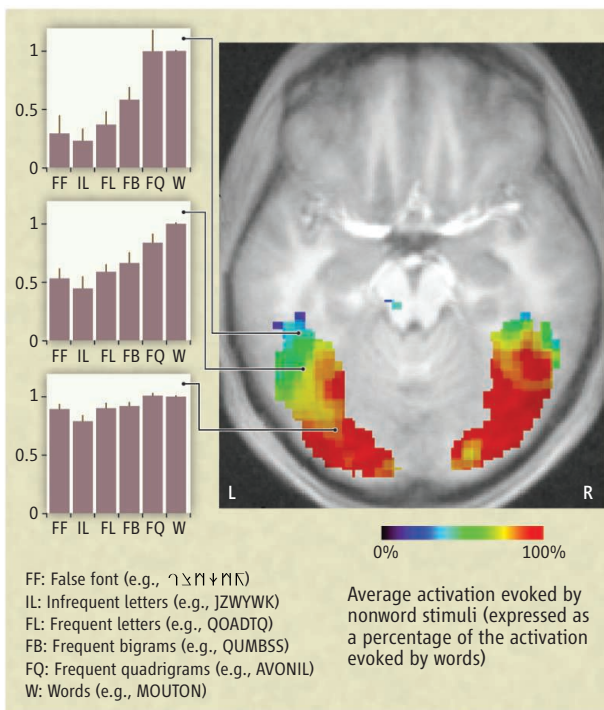
An alternative is that reading taps into neural circuits that evolved to support other functions found in humans and our primate cousins. Recent brain imaging studies indicate that a specific, reproducible set of brain areas is activated during reading (see the second figure) (4). Some of these are also activated by spoken language, but the visual word form area (VWFA), in the left

Selective activation. As human subjects view stimuli that more closely approximate words, brain activity increases in left but not right anterior occipitotemporal cortex, the VWFA (4). The color scale reflects brain response to nonwords normalized to brain response to words; cooler colors indicate greater selectivity for words. The bar plots record average brain response to each class of stimuli.



occipitotemporal sulcus region, is selectively activated by reading written characters and not by recognizing spoken words or simple visual stimuli. The VWFA appears to develop with experience; activation levels in this area in children and adolescents (7 to 18 years old) predict word-phoneme decoding abilities (5).

Given that until recently, few people learned to read, the VWFA cannot have evolved specifically to support reading. Dehaene and Cohen (6) have argued that brain circuits that evolved to serve one purpose are often “recycled” in humans to support new, culturally specified functions. Such neuronal recycling places strong constraints on which neural circuits come to mediate new behaviors, such as reading, through experience.



Another story? Grainger *et al.* show that humans and nonhuman primates share a basic visual capacity for orthographic processing.

Support for this idea comes from the observation that in all alphabets, letters are made up of roughly three strokes; this might be related to the physiological architecture of neurons in the primate visual system. At successively higher levels of visual cortex, neurons reassemble the visual scene from simple fragments into elementary shapes that can be combined to form any object (7). Some of these neurons respond to the intersection of lines that resemble letters like T or Y. By matching the appearance of letters to the inherent structure of the neurons involved in recognizing elementary objects, writing systems could be more easily learned and were thus more likely to survive and spread through a culture.

Grainger *et al.*'s finding that baboons can learn to parse English words from nonwords has important implications for human health and education. Dyslexia, a neurological disorder characterized by difficulties in reading not caused by problems with vision, hearing, or poor education, affects between 2 and 20% of any literate population; up to 40 million persons in the United States struggle with difficulties in reading (8). Given that reading and writing were invented at most 5400 years ago, and many millions of people in various cultures never learn to read, it is puzzling that dyslexia is considered a neurological disorder with biological causes. The observation that the neural circuits involved in reading and writing are not hard-wired may explain why most people with dyslexia can learn to read, albeit sometimes more slowly and with less fluidity than people without dyslexia. The very plasticity that enabled humans to invent reading and writing can be harnessed to overcome dysfunctions in the underlying neural circuitry.

References and Notes

1. J. Grainger, S. Dufau, M. Montant, J. C. Ziegler, J. Fagot, *Science* **336**, 245 (2012).
2. W. Walker, J. Sarbaugh, *Ethnohistory* **40**, 70 (1993).
3. D. S. Blough, *Science* **218**, 397 (1982).
4. F. Vinckier *et al.*, *Neuron* **55**, 143 (2007).
5. S. E. Shaywitz *et al.*, *Proc. Natl. Acad. Sci. U.S.A.* **95**, 2636 (1998).
6. S. Dehaene, L. Cohen, *Neuron* **56**, 384 (2007).
7. M. A. Changizi, S. Shimojo, *Proc. Biol. Sci.* **272**, 267 (2005).
8. Dyslexia information page, National Institute of Neurological Disorders and Stroke; see www.ninds.nih.gov/disorders/dyslexia/dyslexia.htm.

Acknowledgment: Reprinted by permission of Houghton Mifflin Harcourt Publishing Company.

10.1126/science.1221402

RETROSPECTIVE

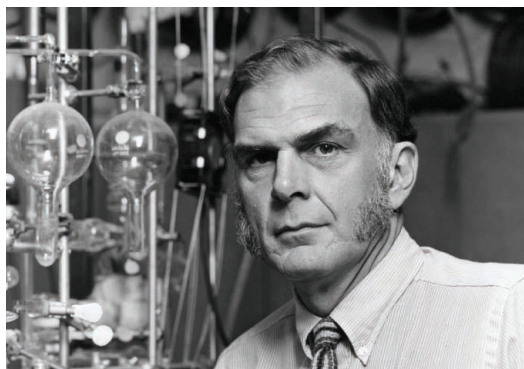
F. Sherwood Rowland (1927–2012)

Ralph J. Cicerone,¹ Mario J. Molina,² Donald R. Blake³

F Sherwood (“Sherry”) Rowland died on 10 March at age 84. He was a distinguished scientist, first in physical chemistry and radiochemistry as a hot-atom chemist and later as an atmospheric chemist (*1*). He was also famous for his leadership in discovering and publicizing the danger to the ozone layer posed by continued human release of chlorofluorocarbons (CFCs).

The research that led Sherry Rowland to become a public figure began with curiosity. In the early 1970s, CFCs were an industrial success story as near-ideal refrigerants and as propellants in many aerosol-spray products. At a 1972 Atomic Energy Commission conference, Rowland heard that James Lovelock had detected CFC-11 in air over the North and South Atlantic Ocean. Rowland wondered what would eventually happen to this synthetic chemical in the atmosphere. In 1973, one of us (M.J.M.) joined Rowland at the University of California (UC) at Irvine. As chemists, Rowland and Molina knew that CFCs had been designed to be inert and nonsoluble and were, thus, unlikely to be decomposed by common atmospheric processes. However, they realized from laboratory data and chemical insight that the CFCs would be decomposed by ultraviolet light (wavelengths below 220 nm) in the upper atmosphere, above much of the ozone layer.

Rowland and Molina continued their detective work, asking what would become of the fragments of CFCs: carbon, chlorine, and fluorine atoms. They discovered that chlorine attacks ozone catalytically and that continued release of CFCs into the atmosphere could destroy substantial amounts of the global ozone layer. After confirming that there were no errors in the calculations, they publicized these results at a press conference in September 1974, soon after their first paper on the topic was published. In his many subsequent interviews and public appearances, Rowland was unfailingly



polite and clear, and he never exaggerated. Consequently, his credibility grew.

A great deal of media and public attention in CFCs ensued, especially between 1974 and 1978, including hearings in state legislatures, city councils, and the U.S. Congress. While Cicerone and Molina testified at a number of these hearings, Rowland was particularly generous with his time when asked for comments or advice by legislators who were considering laws or regulations concerning the production, sale, and distribution of CFCs.

During this time of intense public debate, Rowland and Molina discovered a complication to the originally proposed chemical mechanism by which chlorine would destroy ozone: It became clear that chlorine nitrate would form in the atmosphere, thereby linking reactions of chlorine oxides and nitrogen oxides. This insight led to a brief period of uncertainty about the impact of CFC-derived chlorine on ozone, due to two factors: The three-molecule reaction rate to form chlorine nitrate in the lower stratosphere was not known with sufficient accuracy, and the mathematical techniques in use at the time in some mathematical models were unsuitable. Both issues were resolved within a few months. It was extremely important that this modification to the originally proposed reaction scheme was introduced by Rowland and a colleague (M.J.M.), not by a critic of the theory.

By the time the Antarctic ozone hole was discovered in 1985, Rowland had already raised the idea that hydrogen chloride and chlorine nitrate were unlikely to undergo only gas-phase reactions; laboratory studies had shown them to be “sticky,” surface-

A Nobel Prize–winning atmospheric chemist instrumental in discovering and publicizing the role of chlorofluorocarbons in ozone destruction.

reactive chemicals. Later, surface reactions of these two chlorine-containing species were shown to be responsible for releasing active chlorine into the Antarctic stratosphere and destroying ozone.

In many public appearances, Rowland presented his case that continued use of CFCs would greatly diminish the ozone layer, thereby increasing the intensity of biologically damaging ultraviolet light at Earth’s surface. He was always up-to-date scientifically, and he showed his data: Those who opposed him had few easy opportunities to discredit him. He also became very active in evaluating atmospheric ozone data, searching for the predicted decreasing trends. With his students, including one of us (D.R.B.), he published analyses of air samples from all over the world, showing that atmospheric methane concentrations were rising.

Sherry Rowland contributed enormously to the public understanding and credibility of science. Along the way, he was President of the American Association for the Advancement of Science (1993 to 1994); the AAAS building reflects his work with its designers. He insisted on a human-friendly design and no CFC-based refrigerants. He also served as foreign secretary of the U.S. National Academy of Sciences (1994 to 2002), was instrumental in starting the field of atmospheric chemistry, and was a founding faculty member of UC Irvine. In 1995, he was awarded the Nobel Prize in Chemistry (with Paul J. Crutzen and Mario J. Molina). His many friends treasured his affinity for operatic music, his interest in sports (he had played semiprofessional baseball and basketball), and his occasionally memorable jokes.

Sherry Rowland’s engaging personality was obvious, but nowhere more so than in a tense 1986 U.S. Senate hearing. Asked what he would do, if he were king, about the widespread usage of CFCs in light of their threat to stratospheric ozone, he replied, turning to his wife, Joan: “I would ask the queen.”

References and Notes

1. See www.uci.edu/features/2012/03/feature_rowlandobit_120311.php for a slideshow in memory of Sherry Rowland’s life and work.

10.1126/science.1222108

¹National Academy of Sciences, 500 5th St., NW, Washington, DC 20001, USA. ²Department of Chemistry and Biochemistry, University of California, San Diego, La Jolla, CA 92093–0356, USA. ³Department of Chemistry, University of California, Irvine, CA 92697–2025, USA. E-mail: rcicerone@nas.edu; drblake@uci.edu; mjm Molina@ucsd.edu

INTRODUCTION

Does It Compute?



A DISCUSSION OF COMPUTATIONAL BIOLOGY HAS TO START WITH A PIONEER OF THE field, Alan Turing, especially in this centennial year of his birth. He introduced us to the digital computer and proposed that much biology could be described by mathematical equations—the number of spirals in a sunflower is a Fibonacci number and pattern formation in animal skins can be described by a reaction diffusion model. Turing lacked the data and the computing power to substantiate his models. Today, the availability of vast quantities of new data, together with striking advances in computing power, is promising to give us new insights into the mechanisms of life. This special section, together with related content in *Science Signaling* and *Science Careers*, highlights recent advances and outstanding challenges.

Models that simulate biological processes can be characterized both by their level of biological detail and by their mathematical complexity. Mogilner *et al.* (p. 175) describe these different classes of computer models, using the example of cell polarity mechanisms to show that diverse models are required to fit different experimental studies in an iterative loop of modeling and experimentation. In a News Focus, Pennisi (p. 172) illustrates this loop, describing how researchers have combined modeling and experimentation to understand how lizards, turtles, and other animals cope with heat stress and potentially global warming (videos of some of these models can be found at http://scim.ag/comp_bio).

Advances in sequencing technology have resulted in a barrage of genomic information. Zerbino *et al.* (p. 179) review the development of computational methods and algorithms to efficiently analyze these data, from the initial genome reconstruction to their use in comparing individuals and organisms, reconstructing phylogenies, and tying genotype to phenotype. Munsky *et al.* (p. 183) note that phenotypic variation can occur even in genetically identical cells. They discuss stochastic gene expression as the likely source of this variability and describe how the analysis of variability can give insight into the mechanisms of gene regulation. At the level of morphogenesis that so fascinated Turing, Morelli *et al.* (p. 187) describe how a combination of theory and experiment is being used to investigate developmental processes. They describe how patterning can arise from molecular gradients, from coupled biological oscillations, or from mechanical deformations of cells and tissues. Underlying all of this analysis is computer code, and in a Policy Forum, Morin *et al.* (p. 159) call for this code to be made widely available and suggest how this might be implemented.

Turing not only sought mathematical rules that govern biology, as described in Perspectives by Hodges (p. 163) and French (p. 164); he also questioned whether there were fundamental differences between how machines and biological organisms compute. There is much more work to be done in exploring such questions, and we look forward to the many new insights that will be gained along the way.

— VALDA VINSON, BEVERLY A. PURNELL, LAURA M. ZAHN, JOHN TRAVIS

Computational Biology

CONTENTS

News

172 Virtual Hot Spots

Reviews

175 Cell Polarity: Quantitative Modeling as a Tool in Cell Biology
A. Mogilner et al.

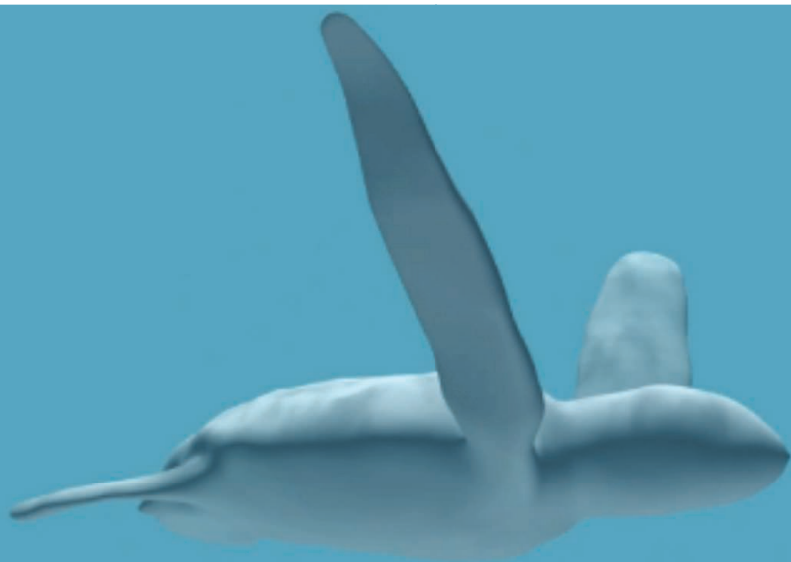
179 Integrating Genomes
D. R. Zerbino et al.

183 Using Gene Expression Noise to Understand Gene Regulation
B. Munsky et al.

187 Computational Approaches to Developmental Patterning
L. G. Morelli et al.

See also Editorial p. 131; Policy Forum p. 159; Perspectives pp. 163 and 164; Report p. 229; Science Express Reports by F. Bosveld et al. and P. Mueller et al.; and Science Signaling, Science Careers, and Science Podcast at http://scim.ag/comp_bio.

Science



Virtual Hot Spots

Physiological ecologists who design computer models to predict how animals handle heat are forecasting the effects of climate change

When he was a graduate student in ecology, Warren Porter spent a year in the field watching desert iguanas. Yet a simple question continued to puzzle him: Why did the color of this lizard's skin get lighter during the day? After Porter landed a position in the zoology department of University of Wisconsin, Madison, as an assistant professor, he looked outside his field for answers. He started taking engineering courses to learn about heat transfer and other physical principles that affect animals, and eventually teamed up with two mechanical engineers to build a computer model to test how differently colored lizards would fare as the sun made its way across the sky.

"We found that brightening would extend their activity by 2 to 3 hours a day or more," Porter recalls. The lighter skin absorbed less heat, reducing the likelihood of overheating, and that translated into extra time for foraging. The result sold Porter on the value of computer modeling.

Thirty years later, this biophysical ecologist still sits down at the keyboard to predict how animals make their way through the world. His models are much more sophisti-

cated, but the goal is the same: to understand energy transfer between an animal and its environment and how that affects the organism's behavior, survival, and distribution. Humans can use clothing, heating, and air-conditioning to extend the limits of what they can do at extreme environmental conditions. But other animals are not so lucky. They can seek food and mates only when their bodies fall within a certain temperature range. They may have adaptations, such as changing the color of their skin, that can help, or they can move into the shade or sun depending on the time of day. Yet in the end, temperature still constrains most creatures, whether they are warm- or cold-blooded.

To predict where and when animals will function, "the place to start is temperature," says Raymond Huey, an evolutionary physiologist at the University of Washington, Seattle. It's "better than any other environmental factor." Temperature constraints affect the survival of individual animals, specific populations, and even whole species. "There is a growing awareness of the valuable role that physiological knowledge can play in understanding organism-environment interactions," says Michael Kearney, a

Test case. This virtual sea turtle is helping computer modelers determine where oceans might become too warm for the real leatherbacks.

physiological ecologist at the University of Melbourne in Australia.

Such knowledge has become increasingly important given the threat of climate change. While some researchers compare historical and current records to assess how warming might affect the range of a species, modelers such as Porter make predictions in silico. "The models allow a direct connection to be made between what we measure about the physiology of an organism and climatic data," Kearney says. "It's an exciting area, and it's a relevant area because of the focus and awareness of environmental change," adds Huey.

For every hour they work at the computer running a model, researchers may spend days in the field taking measurements to validate or refute their virtual animal. Early versions of animal models needed many simplifying assumptions on matters such as the shape of the animal and straightforward scenarios to make them computationally tractable. But researchers can now incorporate many more details, making simulations much more realistic and meaningful, says Michael Sears, an ecologist at Bryn Mawr College in Pennsylvania.

The virtual animals represented by these models still have their skeptics. All models make assumptions, each of which can introduce inaccuracies that some argue add up to be significant. But more decision-makers are making use of them, says Donald DeAngelis, a U.S. Geological Survey ecologist at the University of Miami in Florida. "Models let us put the information that we have together in a rational, orderly way to make predictions about the future," he says. "Without them, all we can do is guess."

Humble beginnings

When Porter began experimenting with computer models, his goal was simply to predict the body temperature of a lizard of a given size, weight, and color in a particular environment. His first challenge was to convert local temperature, wind speed, and sunlight data into information relevant to the lizard itself—conditions on the ground,

Online
sciencemag.org
Related video
and podcast
interview (http://scim.ag/media_6078).

and even underground. For that, Porter and his colleagues developed a microclimate model and combined its results with lizard physiological and morphological data to predict the animal's temperature under particular conditions.

To see if this crude first model reflected reality, Porter built casts of real lizards using dental wax, plaster of Paris, and aluminum and painted them to reflect sunlight just like the real animals. He placed the casts outdoors with temperature sensors and found that they were within 2°C of what the virtual lizards in his model experienced. "Warren Porter and some of his colleagues were the first people to try to do modeling really looking at the balance of energy in individual organisms," DeAngelis says. "It was a new approach at the time."

Through the years, Porter has refined and adapted his model to different animals and new situations. He gave the virtual lizards the ability to be active when their body temperature allowed it and incorporated food and water requirements to better determine how a lizard would fare under a given condition. To make the model more general, he came up with a version that had a virtual layer of insulation, akin to fur and feathers, thereby letting him study birds and mammals.

At its core, his model incorporates three aspects of energy transfer. Based on the animal's size and color, it calculates the heat loss for a particular microclimate and, consequently, what temperatures the animal experiences. Other researchers have figured out the temperature range at which many species can be active, and the model uses that information to determine how much time an animal might spend eating and drinking. This determines how many calories the virtual animal takes in and burns and the amount of water it consumes and loses, a mix of numbers that adds up to its so-called mass balance. And finally, the model looks at what Porter calls momentum balance, the energy costs of moving.

The models keep getting more sophisticated. In Porter's early work, for example, the bodies of lizards were treated as simple cylinders by the computer programs; now the simulations take into account the real shapes of organisms.

His recent look at leatherback turtles offers further evidence of how far the field has come. As these 2.5-meter-long sea turtles swim, the exertion causes their overall body temperatures to rise, so the animals need to be in water cool enough to keep them from

overheating. Porter has begun to determine where in the ocean these lumbering giants are likely to be found. He starts with off-the-shelf 3D modeling and computational fluid dynamics software programs that let him simulate a 3D virtual turtle swimming through water. That simulation enables him and his colleagues to calculate the drag on the animal, which helps them formulate the energy expended by the turtle and the excess heat produced. His model calculates heat loss in different ocean temperatures and from there, the simulation spits out where the seas are cool enough for the leatherbacks.

Porter and his colleagues have applied his computer programs to many species: diving birds, tsetse flies, polar bears, whoop-



On the rocks. Plastic models of mussels provide temperature information important for simulations of how the bivalves fare at a particular site.

ing cranes, elk, an extinct Hawaiian honeycreeper, a rare viper in Taiwan, and tuatara, a living fossil reptile found in New Zealand. "We're in the position to design any kind of animal and put it in any place in the world and find out how much food and water it needs," Porter says. The models "are extremely detailed and work remarkably well," Huey notes.

Using Porter's research as a starting point, Melbourne's Kearney has recently broadened the scope of such modeling efforts. Working with Brian Helmuth of the University of South Carolina in Columbia, he has linked Porter's model to theories about how animals use energy and food and

water for all aspects of their life history, including development, growth, and reproduction. "I can use the integrated models to understand climatic constraints on the entire life cycle and [on] population-level phenomena," Kearney says.

Helmuth studies intertidal organisms, in particular mussels and sea stars, with similar goals. "What we've been doing with terrestrial animals, he's doing with marine animals," Porter says. For Helmuth, a big challenge has been ground-truthing the models. To do that, he's developed "robomussels"—plastic devices shaped and colored like mussels to handle heat the same way—with temperature sensors inside. He's planted them at 40 intertidal zones around the world.

His goal is to find those places where mussels are being, or will be in the near future, pushed to their limits. And although there may not be much that people can do in the short term to stem rising temperatures globally, Helmuth says, "we may be able to ameliorate other stresses," such as pollution or overfishing, that might push mussels at a particular location over the edge. He is now trying to determine just how fine-scale he must model wind speed, cloud cover, and other factors to get the model's predictions to reflect reality. Can remote-sensing data suffice, or are on-site weather stations necessary? "How do you get the local detail that you need without getting so mired in [it] that you don't see the broad pattern," he wonders.

Getting down to spatial details

With his own biophysical models, Bryn Mawr's Sears has found that it's very important to look on the fine scale. Like Porter, he started out as a field biologist with a puzzle: Lizards living at lower elevations were smaller than lizards higher up, even though conventional wisdom held that the cooler climate at high elevations should retard physiological growth. Suspecting that the more desertlike environment lower down constrains the lizards' growth, he and Michael Angilletta Jr., a physiological ecologist at Arizona State University, Tempe, decided to determine how lizards might cope with the heat.

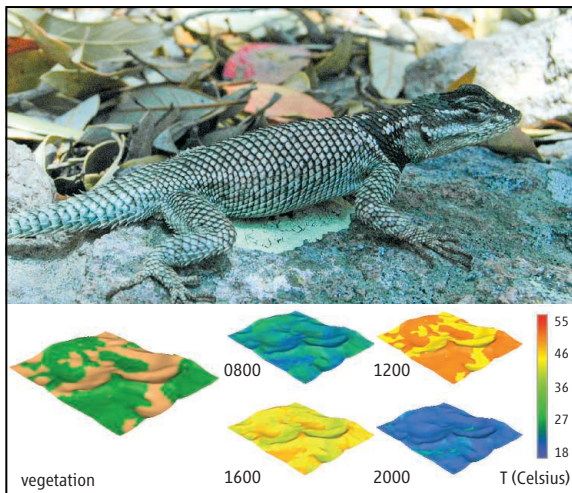
Their simulations and subsequent field studies showed that the hot sun did limit lizard activity, but in a more complex way than researchers had assumed. The limitations imposed by heat depended significantly on the distribution of shade in the particular

lizard's environment. "The pattern of [shade] variation has a huge impact on their ability to thermoregulate," Huey says. "They've done a really nice simulation and analysis to show that."

Sears started by creating a realistic simulation of the lizard's desert habitat, which required a visit to sand dunes in central New Mexico to obtain fine-scale temperature measurements. He and his colleagues then wrote a computer program that could specify how hot each 0.5-meter-square spot would be at different times of the day, depending on where the sun was. It's a computationally intense simulation, taking nearly 24 hours to factor in all the shadowing for a 100-square-meter plot with a bumpy, complex landscape—the vegetation coverage incorporated into the model was provided by aerial photos. "They were the first to really factor in spatial [heterogeneity] on a small scale," Huey says.

Next, Sears plops a virtual lizard of a particular size into various versions of his landscape model. In some, there are big patches of shade, as if there are few big trees; in others there are many small patches, the equivalent of small bushes. He gives the virtual animal the goal of maintaining an optimum temperature for finding food. The lizard initially finds shade, but eventually has to move on to another location because of the shifting sunlight, for example. "What our models have done is focus on where those temperatures are available in space and whether animals can actually use them," Angilletta explains.

To see if their models were valid,



Daily struggle. The Yarrow spiny lizard (*top*) must move around quite a bit to stay cool, according to simulations of how temperature changes throughout the day in its vegetation-covered landscape (*bottom, left*).

Angilletta and Sears spent almost 2 summers in the Chihuahuan desert in New Mexico building fenced-in 400-square-meter plots, arrayed with different configurations of shade cloth. They then released about 80 lizards into these plots and carefully monitored the lizards' movements. Their data from these plots support what the models are predicting: Lots of small patches of shade and sun are better for the animals than a few big patches.

Knowing that heterogeneity of a habitat makes a difference can matter. Conservationists working to protect the dune sagebrush lizard are trying to decide where to set aside land and how to manage these conservation areas. Sears's modeling work shows that the threatened species should be able to be active

20% to 50% longer in complex habitats. "The more complex habitats are probably the ones you should focus on preserving," he says.

While Sears and other animal modelers are typically trying to simulate the current reality, when they tweak their computer programs to plug in temperature changes due to global warming, the situation can become dire for some species. "You're going to have a change in the number of places an animal can find its preferred temperature, but you are also going to have a change in where those are in space and how connected they are," Angilletta explains. For example, lizards may not be as able to reach a preferred place because they would heat up too much as they travel from one to another.

Angilletta and Sears next plan to add other aspects of lizard ecology—such as predators or rivals—to their models to see how that affects the animal's ability to keep its temperature right. And Angilletta is working on other modeling projects to come up with predictions for how an entire species can be affected by climate change. Through such modeling, "the biological consequences of environmental change are addressable, probably for the first time," Huey says.

That's a long way from simply explaining why a desert iguana changes color, but Porter says the underlying principles of the research are the same. "The computational biology is just a tool to understand what it is that makes animals work," he concludes.

—ELIZABETH PENNISI



Shade arrays.

Large areas covered with different patterns of shade cloth, as seen in the aerial photo (*left*), helped researchers evaluate simulations showing the importance of diverse shading in hot environments.

REVIEW

Cell Polarity: Quantitative Modeling as a Tool in Cell Biology

Alex Mogilner,^{1*} Jun Allard,¹ Roy Wollman²

Among a number of innovative approaches that have modernized cell biology, modeling has a prominent yet unusual place. One popular view is that we progress linearly, from conceptual to ever more detailed models. We review recent discoveries of cell polarity mechanisms, in which modeling played an important role, to demonstrate that the experiment-theory feedback loop requires diverse models characterized by varying levels of biological detail and mathematical complexity. We argue that a quantitative model is a tool that has to fit an experimental study, and the model's value should be judged not by how complex and detailed it is, but by what could be learned from it.

Four hundred years ago, Galileo observed that “Nature’s great book is written in mathematical language.” Since that time, physical phenomena have been described by mathematical equations, yet biology has remained qualitative. A possible explanation is that complex behavior in physics emerges from relatively simple interactions between many copies of few elements, whereas biological complexity results from nonlinear interactions of many heterogeneous species. In this sense, biological systems are similar to engineered machines (1): Inventories of both airplane parts and animal cell proteins consist of tens of thousands entries; cell interactomes look similar to machine blueprints; and performances of both engineering and biological structures are characterized by robustness and noise resistance (2). This analogy has limitations: Biological systems are built from stochastic and unreliable parts; are evolved rather than designed; and are subject to reverse, not direct, engineering. Nevertheless, in the last two decades, the mathematics usually applied to engineering and physics has been often used in cell biological studies where quantitative models serve as a guide for failing intuition (3).

The foundation for this surge was laid by two seminal papers that appeared 60 years ago. One was the biologically abstract and mathematically simple manuscript by Alan Turing (4) proposing that a pattern can emerge in an initially homogeneous mixture of two chemicals. Turing used two linear partial differential equations (PDEs) (Box 1) with few parameters to demonstrate that two chemicals, a slowly diffusing “activator” and a rapidly diffusing “inhibitor,” could concentrate in different regions of space. Untested and unsubstantiated at the time, this conceptual model has served as a basis for many studies of polarity, chemotaxis, and development. Another work

by Hodgkin and Huxley (5) was mathematically complex, grounded in experimental data and very detailed: Many ordinary differential equations (ODEs) (Box 1) with many parameters and

nonlinearities were used to describe ion currents through voltage-gated channels in the axon membrane. The parameters and nonlinearities were measured, and the model reproduced the observed electric bursts in nerve cells, which revolutionized our understanding of excitable systems.

These two papers symbolize the opposite ends of “modeling space” (Fig. 1A). It is tempting to pronounce that we will be describing cells in ever more accurate terms and minute detail, moving from focused and conceptual (like ODEs describing three-node motifs in regulatory networks) to accurate and broad models (6), perhaps ending with a “whole-cell model” that completely recapitulates cell behavior on a computer, substitutes for wet laboratory experiments and makes personalized medicine possible. This is an appealing, if distant, goal. Meanwhile, this view subtly puts broad models above focused ones and suggests that there is a modeling “Road to Valhalla.” Note, however, that our understanding of the nerve impulse progressed from the

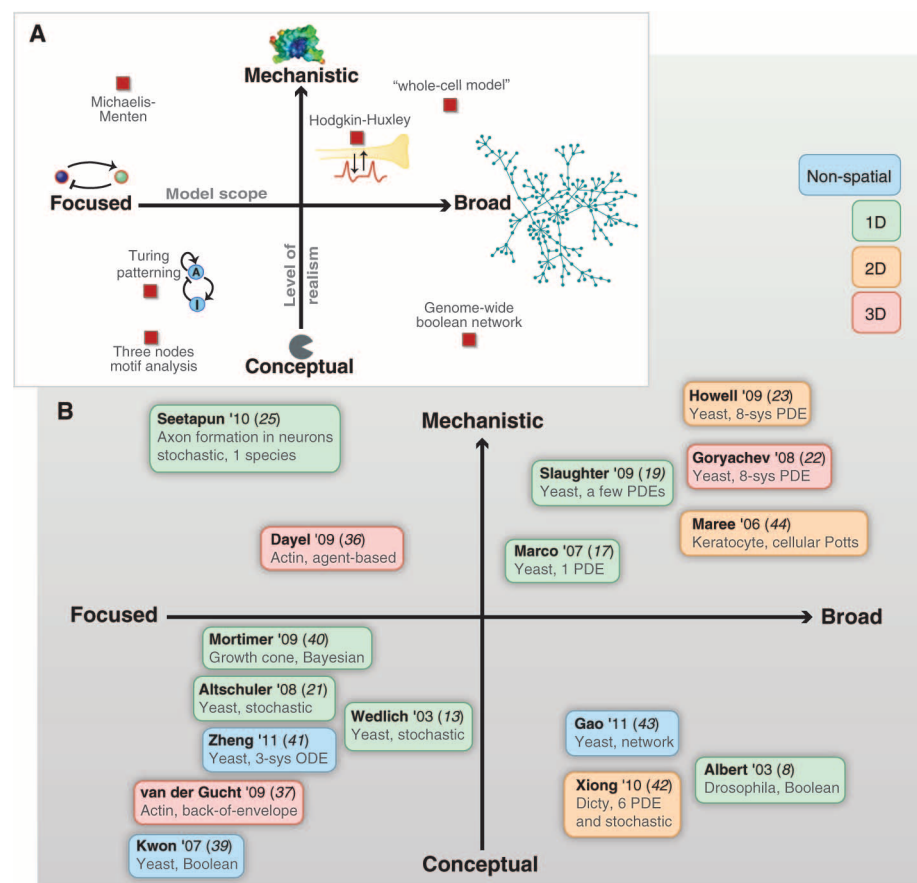


Fig. 1. Modeling space. (A) Computational models can be characterized by their scope and level of realism. Mathematically, focused models are simple, whereas broad ones are complex. Biologically, the models range from conceptual, offering mainly qualitative insight, to accurate and mechanistic, making many quantitative predictions. (B) Polarity models in modeling space marked by the first author, year in which the model was published, biological system the model applied to and mathematical method. Color corresponds to physical dimensionality of the model. Mathematical scope and level of realism do not correlate with dimensionality, type of math, or biological system.

¹Department of Neurobiology, Physiology, and Behavior and Department of Mathematics, University of California, Davis, CA 95616, USA. ²Department of Chemical and Systems Biology, Stanford University, Stanford, CA 94305, USA.

*To whom correspondence should be addressed. E-mail: mogilner@math.ucdavis.edu



Box 1. MODELING TOOLS

In mathematical biology, an **ODE** normally expresses the time derivative of a dynamic variable in terms of a function, usually nonlinear, of this variable. More frequently, a system of ODEs (dynamical system) appears. For example, if $[E]$, $[S]$, and $[C]$ are concentrations of enzyme, substrate, and complex, respectively, then the dynamical system

$$\frac{d[E]}{dt} = -k_1[E][S] + k_2[C], \quad \frac{d[S]}{dt} = -k_1[E][S], \quad \frac{d[C]}{dt} = k_1[E][S] - k_2[C]$$

describes Michaelis-Menten kinetics. In this system, rates k_1 and k_2 are model parameters. ODEs are an extremely powerful tool as (i) vast mathematical apparatus (bifurcation diagrams and phase portraits, perturbation theory, and numerical analysis) has been developed to solve them; (ii) solving ODEs is almost trivial with much available user-friendly software; and (iii) their solutions provide very detailed mechanistic insight. The caveats of using ODEs for modeling are (i) chemicals have to be well mixed in the cell or their spatial gradients have to be neglected, (ii) detailed information about molecular interactions has to be available, and (iii) many data are necessary to validate the model.

A **PDE** is a generalization of an ODE: concentrations of chemicals (or distributions of molecular players, in general) can change not only in time, but in space as well, so not only time derivatives, but also (so-called “partial”) derivatives with respect to spatial coordinates appear in the equations. For example, Michaelis-Menten kinetics in a 3D cell in the presence of diffusion will have the form:

$$\frac{\partial[E]}{\partial t} = -k_1[E][S] + k_2[C] + D_E \Delta[E], \quad \frac{\partial[S]}{\partial t} = -k_1[E][S] + D_S \Delta[S], \\ \frac{\partial[C]}{\partial t} = k_1[E][S] - k_2[C] + D_C \Delta[C]$$

where D 's are diffusion coefficients, and $\Delta = \partial^2/\partial x^2 + \partial^2/\partial y^2 + \partial^2/\partial z^2$. These PDEs constitute a so-called reaction-diffusion system. Instead of diffusion, other transport processes (e.g., directed motor-driven transport) can be represented mathematically as well. PDEs have to be accompanied by boundary conditions that have to be chosen carefully. Similar to ODEs, PDEs are great for mechanistic insight. Solving PDEs is far from trivial. ODEs' caveats (ii) and (iii) apply to PDEs as well.

Unlike deterministic models, **stochastic simulations** usually describe molecules not as concentrations, but as random numbers. These numbers change in time with certain probabilities that are functions of random variables (numbers of these and other molecules) in the system. Many different types of stochastic models exist, for example: (i) direct Monte Carlo simulations, in which the computer generates random changes in the random variables at equal time increments; (ii) Gillespie simulations, in which computer calculates random time intervals at which the state of the system changes; (iii) Langevin equations that allow the addition of random steps to deterministic changes; (iv) Smoluchowski equations

that introduce a probability density for system states and transform random equations into deterministic PDEs, and so on. The great advantage of stochastic simulations is that they expose the effects of fluctuations and noise that are often enormous in cells because of the relatively small number of molecules involved. The caveat is that usually stochastic simulations produce but a single random trajectory of the system (Smoluchowski equations are a notable exception, but these are often very hard to solve), so multiple, computationally expensive simulation runs and nontrivial statistical tools are needed for thorough investigation.

Agent-based simulations that are sometime deterministic, but more often stochastic, rely on explicitly tracking all essential molecules so that, on the basis of the current positions and states of these molecules, all interactions (chemical and mechanical) are computed and movements and states of every molecule are calculated based on the rules of physical chemistry and classical mechanics. Usually, thousands of such molecule-agents are simulated, the numerical codes are very involved, and computational expense is enormous. Often, these simulations suffer from limited qualitative insight—in a way, they substitute a computational “black box” for the live cell—but these problems are usually more than offset by two benefits: life-like resulting movies that can be compared directly with time-lapse microscopy and the ability to perform lifelike perturbation experiments on the computer. Other useful modeling techniques, such as cellular automata and Potts models, are midway between PDEs and agent-based simulations.

Boolean networks are well suited to reproduce the qualitative behavior of extensive networks when the amount of quantitative experimental data is limited. In a Boolean representation, the biological active or inactive state of a species are represented by the on-off states of nodes in an “interactome” network. Logical rules based on qualitative insight prescribe switches between states of each node, depending on the state of the nodes to which the node is connected in the network. Boolean models are useful for a fast quantitative look at the dynamics of large biological networks, but because of the difficulties of treating physical time and some mathematical artifacts, such models are gradually falling out of favor.

Bayesian models use the rules of probability theory (Bayes' formula for conditional probabilities) and experimental multivariate data that depict causal relationships between biological variables to uncover statistical (and/or causal) relations among these variables. These models lack a time dimension and therefore cannot include feedback loops that are prevalent in biology.

Network analysis uses the sophisticated methods of graph theory, topology, statistics, and combinatorics to find modules, motifs, and other building blocks representing small standard dynamic systems in large biological networks. The methods of network analysis are extremely useful for large networks, and relevant software is becoming better and more widely available.

complex Hodgkin-Huxley model through the FitzHugh-Nagumo model (7) that reduced the system radically to two PDEs and few parameters. Although simplistic, the FitzHugh-Nagumo model was amenable to deeper mathematical analysis, by building intuition that could be applied to full biophysical reality. Besides, increasing a model's realism does not necessarily mean more difficult math: There are simple and accurate models, like

Michaelis-Menten kinetics equations (Fig. 1A) (Box 1). There are also broad and detailed, yet conceptual models, such as the Boolean description (Fig. 1A) (Box 1) of segment polarity gene expression (8). Here, we review recent studies of budding yeast to illustrate how a variety of modeling approaches advanced our understanding of cell polarity (Fig. 2). We argue that quantitative modeling is a versatile tool that has to fit the biological

problem and can be judged by its usefulness rather than its comprehensiveness or sophistication.

Modeling Yeast Polarity

Many cells polarize in response to external cues such as preexisting landmarks, chemoattractants, or contact with other cells (9). In budding yeast cells, cortical landmark proteins inherited from previous division cause localized activation of the

guanosine triphosphatase (GTPase) Rsr1, leading to recruitment of the polarization machinery components, including the key GTPase Cdc42 (Fig. 2A) and, ultimately, to symmetry breaking and switching from isotropic growth to growth along a polarized axis (10). However, landmark proteins are not essential for the emergence of the Cdc42 cluster that marks future growth site: When the landmark is bypassed by Rsr1 removal or constitutive activation of Cdc42^{Q61L} (in which glutamine at position 61 is replaced by leucine and which cannot hydrolyze guanosine triphosphate and respond to upstream signals), clusters of concentrated Cdc42 still form, albeit at random locations, so the cell is able to self-polarize (Fig. 2A). This phenomenon is arguably the best understood paradigm of cell polarity, in no small measure owing to the power of yeast genetics and many studies that judiciously combined microscopy and modeling to allow detailed mechanistic insights.

Turing's pioneering paper and several models it inspired (11, 12) predict that locally acting positive-feedback loops and globally acting negative regulators can lead to self-polarization. [The models we review below share the general philosophy of Turing's mechanism, but in a narrower, mathematical sense they differ from Turing system; see (12) for details.] Immediate questions arise from this prediction: Is it indeed the Turing mechanism that is responsible for self-polarization? What are the molecular identities of the activators and inhibitors? What are the transport mechanisms underlying the process? How are complex, specific combinations of regulatory pathways wired to achieve polarity?

Less than a decade ago, Wedlich-Soldner *et al.* (13) started to answer these questions quantitatively by using mutants to establish that actin-myosin-directed vesicle transport and fusion were essential for Cdc42^{Q61L} polarization. They proposed that Cdc42 molecules would be recruited to a localized cap on the membrane through transport along actin cables, whereas deposition of Cdc42 to the cap would stimulate further actin accumulation at this site (Fig. 2B). As it was hard to prove experimentally that such a positive-feedback circuit is sufficient to induce polarization, Wedlich-Soldner *et al.* performed simple stochastic simulations (Box 1) in which actin cables nucleated at a rate proportional to the local membrane Cdc42 concentration, Cdc42 was delivered along each cable at a rate proportional to Cdc42 cytoplasmic concentration, and Cdc42 settled on the plasma membrane in a bell-shaped distribution around the cable. Multiple caps were often observed in a single cell, and the model predicted, correctly, that the cap number increases with initial membrane Cdc42 concentration.

Two years later, Ozbudak *et al.* (14) studied the dynamics of this symmetry breaking with Rsr1 deleted, rather than by expressing higher levels of activated Cdc42. To their surprise, they found that the single Cdc42 peak moved around the cell. When actin was inhibited, the Cdc42 peak re-

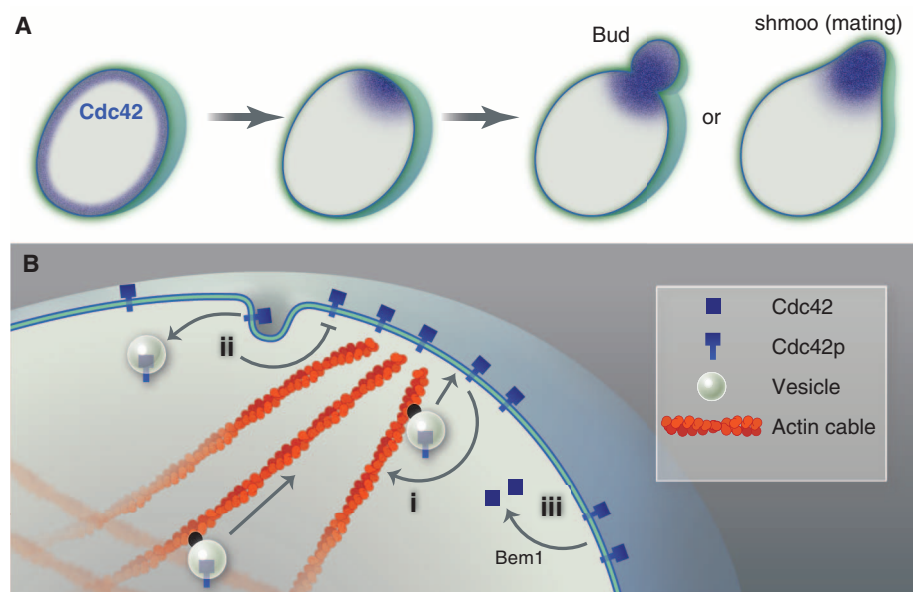


Fig. 2. Budding yeast polarization. (A) Initially symmetric cell with uniform distribution of Cdc42 becomes polarized, either in response to an extracellular cue or spontaneously. Polarization of Cdc42 distribution leads to polarized growth, either for budding or mating. (B) Feedback loops leading to Cdc42 polarization: (i) positive, actin-dependent feedback, (ii) endocytosis, and (iii) positive feedback via autocatalytic Cdc42 membrane recruitment mediated by Bem1.

mained, but its movement ceased. To explain this phenomenon, Ozbudak *et al.* turned to the experimental finding that the scaffold protein Bem1 is an essential component in an actin-independent self-polarization pathway (15) and to the theoretical finding that certain negative-feedback loops can result in traveling waves (16). They assumed that actin cables deliver molecules initiating an actin patch on the membrane causing a dispersal, rather than concentration of Cdc42, which ultimately means that Cdc42 molecules on the membrane inhibit further local accumulation of Cdc42 with a time delay dependent on the actin dynamics. A PDE with respective negative feedback and a time-delayed term, in addition to a hypothetical autocatalytic reaction term describing Bem1-dependent accumulation of Cdc42 on the membrane and Cdc42 diffusion term, mathematically explained the traveling wave. This conceptual model, besides making sense of the data, proposed that actin dynamics are part of a negative-, not positive-, feedback loop.

Marco *et al.* proposed an alternative solution (17) based on data showing that endocytosis and lateral diffusion in the membrane are essential for yeast polarization (18). They suggested that a combination of three processes—actin-Cdc42-positive accumulation, Cdc42 lateral diffusion, and removal by endocytosis, together, could maintain the polarized state (Fig. 2B). By combining three respective mathematical terms in a simple PDE and solving this equation, Marco *et al.* found that both emergence and maintenance of the polarization cap could be explained. The model made a nontrivial prediction: There is an optimal rate of endocytosis in terms of how “sharp” the Cdc42

polarization is, because slower endocytosis causes spreading of the Cdc42 cap over the surface, whereas faster endocytosis depletes the Cdc42 cluster. Measurements of the rates of transport, endocytosis, and geometric parameters indeed resulted in the predicted optimal rate. Compared with the previous model, this one was more accurate and detailed, with parameters fitted from the data.

The model of Marco *et al.* was based on the measurements of a mutant, Cdc42^{Q61L}, which is stably associated with the membrane. A couple of years later, Slaughter *et al.* (19) took their model to the next level of accuracy by trying to explain how cells maintain the dynamic distribution of the wild-type Cdc42, which transitions between the membrane and cytoplasm at higher rates than Cdc42^{Q61L}. Slaughter *et al.* based their model on data indicating that actin-dependent and independent pathways play redundant but essential roles in maintaining Cdc42 polarization. By assuming that these two pathways work in parallel to control Cdc42 recycling at the polar cap and by adding respective mathematical terms [making the model in (17) more detailed and precise], Slaughter *et al.* found that, depending on the data-supported model parameters, the shape of the Cdc42 peak resembles either a bud that the cell grows to enter the mitotic cycle or a shmoo that grows as a mating projection (Fig. 2A). Thus, the model made a provocative prediction that parameters of Cdc42 recycling in yeast are adapted not to achieve maximum polarity but to fulfill specific morphogenetic outcomes.

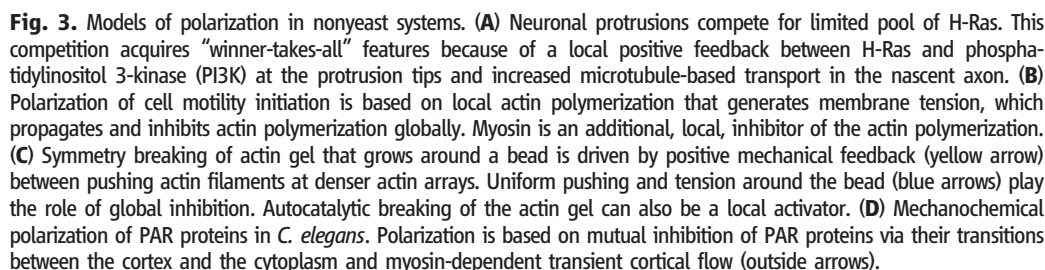
A recent study (20) carefully examined the assumptions used in (17) and noticed that the

In the same year, another mathematical model investigated the actin-independent pathway (22) on the basis of a very different philosophy. All previous models were top-down, based on coupling “modules,” with molecular details left to be clarified later, by assumed nonlinear interactions. In contrast, Goryachev and Pokhilko (22) built a bottom-up model by describing simple mass-action reactions and diffusion for all known components of the actin-independent pathway in mathematical terms, solving respective equations and confirming that this fine-grained model predicts self-polarization without any additional assumptions. Then,

All these models inspired a recent powerful study (23) in which Howell *et al.* tested the redundant polarization mechanisms by creating a fusion protein that effectively tethered Bem1 to the membrane. This effectively weakened the diffusion-mediated mechanism and validated actin-mediated positive feedback. They noted that the synthetically rewired cells often polarized to two sites simultaneously. Combined experimental-theoretical analysis of both wild-type and rewired cells led to the understanding that yeast cells polarize to a single “front” because of competition of membrane Cdc42p clusters for a limiting pool

A power of conceptual modeling is that ideas that arise in one model are often applicable to other phenomena. Polarization plays an important role in a wide variety of systems from neurons (Fig. 3A) (24–26) to *Caenorhabditis elegans* development (Fig. 3D) (27–29) to cell migration (Fig. 3B) (30–34) to mechanical symmetry breaking in actin gels (Fig. 3C) (35–38). In all these cases, a critical role in the establishment of polarity is played by the intricate interplay of positive- and negative-feedback loops, understanding of which is impossible without modeling.

Much progress has been made in understanding cell polarity by using models that not only summarized experimental findings but inspired further experiments by forcing researchers to think rigorously about what can be assumed and motivating more accurate observations. As the history of the yeast polarization modeling illustrates, modelers did not simply increase the models'



complexity but rather moved nimbly within quadrants of the two-dimensional (2D) modeling space charted by two orthogonal axes characterizing model scope and level of realism (Fig. 1B).

A look at this space illustrates that to achieve qualitative insight, simple Boolean (39), Bayesian (40) (Box 1), ODE (41), or stochastic (13, 21) models or physical estimates (37) that are focused and conceptual may include few details and make few predictions, but these predictions can be important. A model can be “bigger” and its scope more broad, but the level of realism can stay similar to that of the focused conceptual models. For example, broad and conceptual PDE (42), Boolean (8), or network (43) models can describe mathematically very large interacting systems but use only causal links between genes and/or proteins and so predict just qualitative features of emergent spatial-temporal patterns. However, focused models with relatively few mathematical details (25, 36) can be accurate and mechanistic when precise numbers matter as well as qualitative insight. The broad and mechanistic models (17, 19, 22, 23, 44) are useful when there is a need to mathematically integrate detailed quantitative data and to test precisely formulated hypotheses.

Outlook

Cell biology is transitioning into a quantitative science characterized by increasing integration of modeling into experiment. In this transition, we have to proceed with numerous, often arbitrary, assumptions about the nature of processes and parameter values governing cell systems. One great future challenge is to improve quantitative experimental methods with an eye toward synchronizing modeling and experiments. Then, frequent back-

and-forth between theory and experiment using models of varying scope and level of realism will allow us to overcome the arbitrariness and uncertainty. Another significant challenge is to make switching from one type of model to another a more standard, less ad hoc procedure, to ease modeling use and integration between theory and experiment. Models along this course should be considered impermanent and should be judged by how useful they are and what we can learn from them, not by how close we are to the elusive whole-cell model.

References and Notes

1. G. T. Reeves, S. E. Fraser, *PLoS Biol.* **7**, e21 (2009).
2. A. D. Lander, *Cell* **144**, 955 (2011).
3. J. M. G. Vilar, C. C. Guet, S. Leibler, *J. Cell Biol.* **161**, 471 (2003).
4. A. M. Turing, *Philos. Trans. R. Soc. Lond. B* **237**, 37 (1952).
5. A. L. Hodgkin, A. F. Huxley, *J. Physiol.* **117**, 500 (1952).
6. S. J. Vaytaden, S. M. Ajay, U. S. Bhalla, *ChemBioChem* **5**, 1365 (2004).
7. R. FitzHugh, *Biophys. J.* **1**, 445 (1961).
8. R. Albert, H. G. Othmer, *J. Theor. Biol.* **223**, 1 (2003).
9. W. J. Nelson, *Nature* **422**, 766 (2003).
10. J. M. Johnson, M. Jin, D. J. Lew, *Curr. Opin. Genet. Dev.* **21**, 740 (2011).
11. M. D. Osum, C. V. Rao, *Curr. Opin. Cell Biol.* **21**, 74 (2009).
12. A. Jilkine, L. Edelstein-Keshet, *PLOS Comput. Biol.* **7**, e1001121 (2011).
13. R. Wedlich-Soldner, S. Altschuler, L. Wu, R. Li, *Science* **299**, 1231 (2003).
14. E. M. Ozbudak, A. Becskei, A. van Oudenaarden, *Dev. Cell* **9**, 565 (2005).
15. J. E. Irazoqui, A. S. Gladfelter, D. J. Lew, *Nat. Cell Biol.* **5**, 1062 (2003).
16. H. Meinhardt, *J. Cell Sci.* **112**, 2867 (1999).
17. E. Marco, R. Wedlich-Soldner, R. Li, S. J. Altschuler, L. F. Wu, *Cell* **129**, 411 (2007).
18. J. Valdez-Taubas, H. R. B. Pelham, *Curr. Biol.* **13**, 1636 (2003).
19. B. D. Slaughter, A. Das, J. W. Schwartz, B. Rubinstein, R. Li, *Dev. Cell* **17**, 823 (2009).
20. A. T. Layton *et al.*, *Curr. Biol.* **21**, 184 (2011).
21. S. J. Altschuler, S. B. Angenent, Y. Wang, L. F. Wu, *Nature* **454**, 886 (2008).
22. A. B. Goryachev, A. V. Pokhilko, *FEBS Lett.* **582**, 1437 (2008).
23. A. S. Howell *et al.*, *Cell* **139**, 731 (2009).
24. M. Fivaz, S. Bandara, T. Inoue, T. Meyer, *Curr. Biol.* **18**, 44 (2008).
25. D. Seetapun, D. J. Odde, *Curr. Biol.* **20**, 979 (2010).
26. N. Inagaki, M. Toriyama, Y. Sakumura, *Dev. Neurobiol.* **71**, 584 (2011).
27. N. W. Goehring *et al.*, *Science* **334**, 1137 (2011).
28. F. Tostevin, M. Howard, *Biophys. J.* **95**, 4512 (2008).
29. A. T. Dawes, E. M. Munro, *Biophys. J.* **101**, 1412 (2011).
30. M. M. Kozlov, A. Mogilner, *Biophys. J.* **93**, 3811 (2007).
31. F. Ziebert, S. Swaminathan, I. S. Aranson, *J. R. Soc. Interface* (2011).
32. D. Shao, W.-J. Rappel, H. Levine, *Phys. Rev. Lett.* **105**, 108104 (2010).
33. D. Kabaso, R. Shlomovitz, K. Schloen, T. Stradal, N. S. Gov, *PLOS Comput. Biol.* **7**, e1001127 (2011).
34. A. R. Houk *et al.*, *Cell* **148**, 175 (2012).
35. K. Sekimoto, J. Prost, F. Jülicher, H. Boukellal, A. Bernheim-Grosswasser, *Eur. Phys. J. E* **13**, 247 (2004).
36. M. J. Dayel *et al.*, *PLoS Biol.* **7**, e1000201 (2009).
37. J. van der Gucht, C. Sykes, *Cold Spring Harb. Perspect. Biol.* **1**, a001909 (2009).
38. J. S. Bois, F. Jülicher, S. W. Grill, *Phys. Rev. Lett.* **106**, 028103 (2011).
39. Y.-K. Kwon, K.-H. Cho, *Biophys. J.* **92**, 2975 (2007).
40. D. Mortimer *et al.*, *Proc. Natl. Acad. Sci. U.S.A.* **106**, 10296 (2009).
41. Z. Zheng, C.-S. Chou, T.-M. Yi, Q. Nie, *Math. Biosci. Eng.* **8**, 1135 (2011).
42. Y. Xiong, C.-H. Huang, P. A. Iglesias, P. N. Devreotes, *Proc. Natl. Acad. Sci. U.S.A.* **107**, 17079 (2010).
43. J. T. Gao *et al.*, *Proc. Natl. Acad. Sci. U.S.A.* **108**, 7647 (2011).
44. A. F. M. Marée, A. Jilkine, A. Dawes, V. A. Grieneisen, L. Edelstein-Keshet, *Bull. Math. Biol.* **68**, 1169 (2006).

Acknowledgments: We thank R. Li and D. Lew for helpful discussions. This work was supported by NIH grant 2R01GM068952 and NSF grant DMS-1118206 to A.M.

10.1126/science.1216380

REVIEW

Integrating Genomes

D. R. Zerbino,¹ B. Paten,¹ D. Haussler^{1,2*}

As genomic sequencing projects attempt ever more ambitious integration of genetic, molecular, and phenotypic information, a specialization of genomics has emerged, embodied in the subdiscipline of computational genomics. Models inherited from population genetics, phylogenetics, and human disease genetics merge with those from graph theory, statistics, signal processing, and computer science to provide a rich quantitative foundation for genomics that can only be realized with the aid of a computer. Unleashed on a rapidly increasing sample of the planet's 10^{30} organisms, these analyses will have an impact on diverse fields of science while providing an extraordinary new window into the story of life.

Since the first genome sequences were obtained in the mid-1970s (1, 2), computers have been necessary for processing (3) and

archiving (2, 4) sequence data. However, the discipline of computational genomics traces its roots to 1980, when Smith and Waterman developed an algorithm to rapidly find the optimal comparison (alignment) of two sequences of length n among the more than 3^n possibilities (2, 5), and Stormo *et al.* built a linear threshold function to search a library of 78,000 nucleotides of *Escherichia coli* messenger RNA sequence for ribosome binding sites (6). What

seemed large data sets for biology then don't seem so today, as high-throughput, short-read sequencing machines churn out terabytes of data (2, 7). We have seen a 10,000-fold sequencing performance improvement in the past 8 years, far outpacing the estimated 16-fold improvement in computational power under Moore's law (8). Using genomics data to model genome evolution, mechanism, and function is now the heart of a lively field.

Every genome is the result of a mostly shared, but partly unique, 3.8-billion-year evolutionary journey from the origin of life. Diversity is created mostly by copy errors during replication. These create single-base changes, which are known as substitutions if spread to the whole population (fixed) or single-nucleotide polymorphisms (SNPs) if not uniformly present in the population (segregating). Replication errors also create insertions and deletions (collectively, indels), as well as tandem duplications where a short sequence is repeated sequentially. Chromosomes often exchange long similar segments through the process of homologous recombination. Specific sequences of DNA, known as transposable elements, have the

¹Center for Biomolecular Sciences and Engineering, University of California, Santa Cruz, CA 95064, USA. ²Howard Hughes Medical Institute, University of California, Santa Cruz, CA 95064, USA.

*To whom correspondence should be addressed. E-mail: haussler@soe.ucsc.edu



capacity to replicate themselves within the cell, using machinery analogous to that found in certain viruses, leaving many copies (9). Rearrangements lead to patterns such as inversions, segmental deletions and duplications (causing copy number variants), chromosome fusion and fission, and translocations between chromosomes (10). At the largest scale, occasionally the whole genome is duplicated, greatly increasing its gene content (11). The present diversity of life was created gradually through these edits and is manifest in the germline genotype of each living individual. Starting from the germline genotype, the genomes of the somatic cells continue to experience similar edits during the lifetime of every individual, some undergoing a kind of evolutionary process called somatic selection that plays a role in cancer and immunity (2, 12).

Genomes are the core of the molecular mechanisms of cells, and of the physical properties (or phenotype) of organisms. They contain recipes of the active molecules of the cell, proteins, and their messenger RNAs, as well as other functional RNAs. Sequencing technology is used to determine RNA abundance (13), subcellular location (14), splicing isoforms (15), secondary structure (16), and rates of engagement with molecular complexes such as the ribosome (17). It is used to assay the epigenetic mechanisms that regulate RNA and protein production and function, including methylation (2, 18), histone modifications (19), transcription factor binding (20), chromatin accessibility (21), and chromatin three-dimensional interactions (2, 22). When applied to these data, computational genomics builds models of epigenetic mechanisms and gene regulatory networks (2, 23), articulating with the broader models of molecular systems biology such as protein signaling cascades, metabolic pathways, and regulatory network motifs (24).

Combining evolutionary, mechanistic, and functional models, computational genomics interprets genomic data along three dimensions. A gene is simultaneously a DNA sequence evolving in time (history), a piece of chromatin that interacts with other molecules (mechanism), and, as a gene product, an actor in pathways of activity within the cell that affect the organism (function). Molecular phenotypes from epigenetic state and RNA expression levels are the first stations on the road from genotype to organismal phenotype, where evolutionary selection acts. Beyond the basics of storing, indexing, and searching the world's genomes, the three fundamental, interrelated challenges of computational genomics are to explain genome evolution, model molecular phenotypes as a consequence of genotype, and predict organismal phenotype.

Obtaining Genomic Sequences

Current methods in genome analysis start with genome assembly (2), the process of reconstructing an entire genome from relatively short random DNA fragments, called reads. Given sufficient read redundancy, or coverage depth, it is possible to detect read overlaps and thereby progressively re-

constitute most of the genome sequence (2). However, this ideal scenario is complicated by the fact that genomes commonly contain large redundant regions (repeats), or regions where the statistical distribution of bases is significantly biased (low-complexity DNA), leading to coincidental, spurious read overlaps. These create complex networks of read-to-read overlaps that do not all reflect actual overlaps in the genome. The most persistent difficulty of assembly is to determine which overlaps are legitimate and which are spurious. This problem is NP-hard, which means that it is at least as hard as any problem in the class of problems that can be solved in nondeterministic polynomial time (2). Therefore, we expect that the only efficient solutions will be heuristic methods that are not guaranteed to find the optimal solution. For this reason, difficult regions of genomes are left as undeter-

mined by repeats (2), and both mappers and reference-based assemblers tend to bias toward the reference genome, occasionally treating genuine variants as noise (2). As technology improves toward longer reads, we expect improvements here too.

Modeling the Evolution of Genotype

Genomes are compared by alignment: The bases of DNA are partitioned into sets (columns) that are putatively derived from a suitably recent common ancestor. From this, we can analyze what was conserved or changed during the evolution of the genomes from their common ancestor. At a large scale, alignments can indicate changes in segment order and copy number, and at a small scale they can indicate specific base substitutions (see Fig. 1).

As in genome assembly, the primary challenge is to distinguish spurious sequence similarities



Fig. 1. Assembly and alignment. (A) Assembly of a number of reads, grouped by pairwise sequence overlap. Because the genomic sequence contains a repeated sequence, the reads coming from the two copies of the repeat overlap and must be separated by the assembly software to produce a linear assembly. **(B)** Alignment of five sequences and an outgroup. Each row is a sequence; each column is a set of bases that descend from a common ancestral base. Six columns are highlighted. Column 4 contains a base that is fixed among the five sequences, whereas the other columns contain segregating SNPs. The trees on the sides represent two alternative ways of representing the phylogeny between the sequences. The left tree is optimal in terms of substitution complexity for columns 1, 2, and 3; the right tree is optimal for columns 4, 5, and 6. Given the difference between the two trees, a recombination event may have occurred between columns 3 and 5.

mined gaps (2), prone to errors (2), or costly to finish (2). Newer sequencing technologies, producing longer reads (2), may alleviate this problem.

After the first complete genome from a species is assembled (the reference genome), new genomes from that species or closely related species are generally not assembled de novo but are assembled using the reference genome as a template, exploiting similarities derived from the common evolutionary ancestor. Reads from the new genome are mapped (aligned) onto the reference genome (2), and systematic discordances are detected (2). This process may be used simply to enumerate the variants present in the new genome, or to guide the complete assembly of the new genome (called reference-based assembly) (2). However, with short reads, mapping algorithms may also be

from those due to common ancestry. Regions of genomes that are subject to purifying selection in which similarity of sequence is conserved, such as orthologous protein-coding regions, can often be reliably aligned across great evolutionary distances, such as between vertebrates and invertebrates. Regions that are neutrally drifting (i.e., not under positive or negative selection) diverge much more quickly, and can be reliably aligned only if they diverged recently (e.g., within the past 100 million years for two vertebrate genomes) (2). It is therefore common to distinguish alignments of subregions (local alignments) (2) from alignments of complete sequences (global alignments) (2) or even complete genomes (genome alignments) (2). Local alignments are typically used between conserved functional regions of more

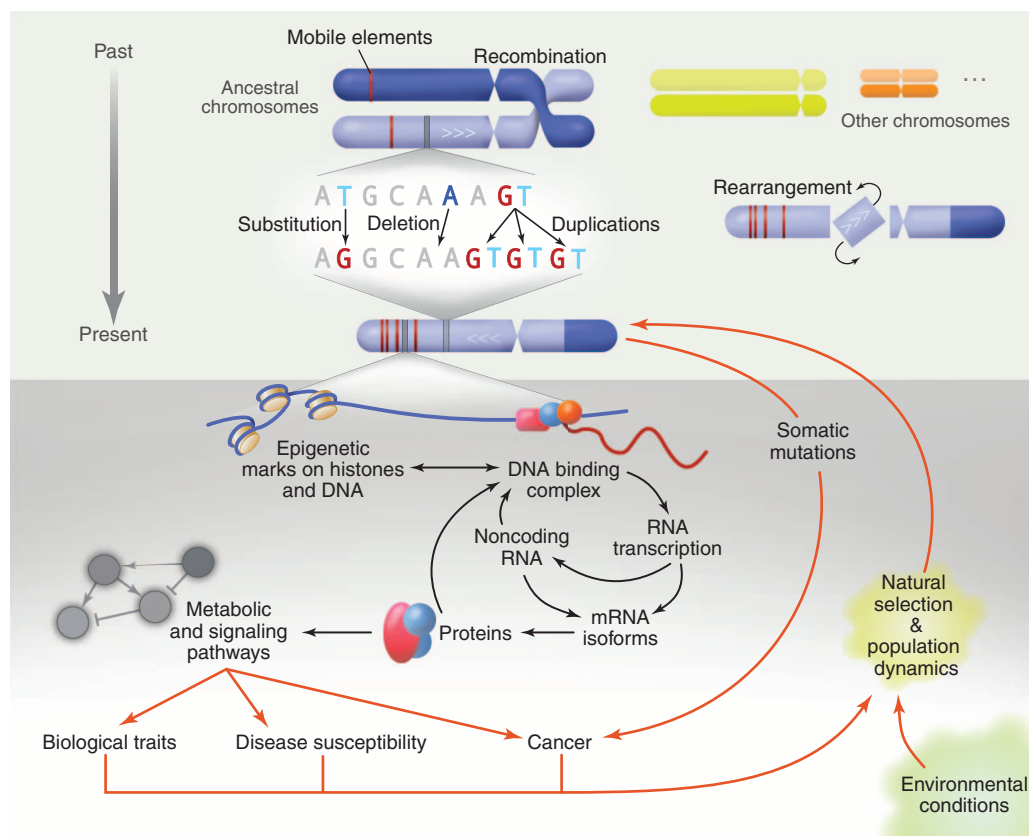


Fig. 2. The dynamic processes that affect and are affected by the genome. **Top:** The genome changes as it is modified by random mutations. At the larger scale, homologous recombination events swap equivalent pieces of DNA, rearrangements reconnect different regions of DNA, and transposable elements can self-reproduce. At the finer scale, small modifications such as substitutions and insertion/deletion events occur. **Bottom:** The genome affects the molecular processes in the cell, namely the transcription of genes and functional RNA, which through pathways affect the phenotype of the organism by causing phenotypes such as disease and other specific traits. Through natural selection, the phenotypes condition the selective pressure on the genome favoring or disfavoring specific mutations.

distantly related genomes (2). Conversely, full genome alignments become practical when comparing genomes from closely related species.

When applied to more than two species or to multiple gene copies within a species, phylogenetic methods provide an explicit order of gene descent through shared ancestry. When the model of evolution is restricted to consider only indels and substitutions (the most common events), the phylogeny is represented by a single tree in which the terminal (leaf) nodes represent the observed (present-day) sequences, the branches represent direct lines of descent, and the internal nodes represent the putative ancestral sequences (2). Finding the optimal phylogeny under probabilistic or parsimony models of substitutions (and also of indels) is NP-hard (2), and considerable effort has been devoted to obtaining efficient and accurate heuristic solutions.

Phylogenetic analysis is complicated by homologous recombination, which creates DNA molecules whose parts have different evolutionary histories (Fig. 2). The coalescent model with recombination (2) models the evolutionary history of a gene with both substitutions and homologous

recombination. Individual histories of parts are represented in an alignment with a separate phylogenetic (coalescent) tree for each base (2).

Evolutionary relationships between DNA sequences may also include balanced structural rearrangements that change the order and the orientation of the bases in the genome, as well as segmental duplications, gains, and losses that alter the number of copies of homologous bases (2). Unfortunately, these processes are usually modeled and treated separately from one another, and separately from substitutions and short indels. The construction of a mathematically and algorithmically tractable unified theory of genome evolution, in which stochastic processes jointly describe base substitution, recombination, rearrangement, and the various forms of duplication, gain, and loss, remains a major challenge for the field (2). With incomplete knowledge of the mathematical difficulties inherent in such a model, it is hard to predict when, if ever, such a model will be forthcoming. The only thing we are assured of is that projects such as the 1000 Genomes Project (2) will be producing massive amounts of data from which to build and

test (via likelihood methods) a variety of approximate models.

From Genotype to Phenotype

Geneticists have correlated genomic mutations to phenotypic differences for many years, but today they do so at an unprecedented scale. Sequencing surveys across vertebrates [Genome 10K (2)], insects [i5K (2)], plants (2), microorganisms (2), cell lineages (2), and “metagenomes” (obtained by sequencing DNA from environmental samples containing an unknown collection of organisms) (2) present us with tens of thousands of genomes and challenge us to rework and deepen our methods. To date, such studies have given us concrete examples of the unfolding history and diversity of life, explored the ties between the body’s microbial populations and our health, and investigated the response of species to current environmental changes such as climate shift, disease, and competitors (2). Future studies could be coupled with experimental data derived from an expansion of cell culture resources for diverse species and tissues (2) and newer single-cell assay methodologies (2), allowing deeper comparisons.

When studying the population genetics of a single species, the recombination rate determines how likely it is that proximal sequence variants share the same coalescent tree (2). Lack of recombination leads to linkage disequilibrium, in which nearby segregating variants are correlated. This phenomenon is exploited in correlating specific segregating variants with phenotypic traits or diseases—for example, in genome-wide association studies conducted with microarrays or incomplete sequencing data (2). However, this same phenomenon limits the resolution of these approaches in finding the actual causal variant. Genome-wide association studies are also blind to the patterns of allele segregation in close relatives. Future genotype-phenotype studies using complete genomes will increasingly use genotypic context in related as well as unrelated cases and controls, combined with better prediction of the possible effects of genome variants, to identify causal variants (2).

Large projects such as ENCODE (2), modENCODE (2), and the Epigenomics Roadmap (2) are providing data on the epigenome and the transcriptional machinery needed to construct models of molecular phenotypes involving epigenetic state, RNA expression, and (inferred) protein levels, requiring specialized analysis tools. Genome browsers such as Ensembl (2) and the UCSC Genome Browser (2) provide an integrated view

of these data, along with background knowledge and various modeling results. Because many key elements of epigenetics, RNA expression, and protein production cannot be directly measured and therefore must be inferred, the mathematical models of these processes contain numerous latent (hidden) variables, often one for every site in the genome. Approaches include hidden Markov models (2), factor graphs (2), Bayesian networks (2), and Markov random fields (2). Model inference (parameter estimation) and model application (computation of conditional and marginal probabilities) are large-scale computational tasks.

Genotype determines phenotype via epigenetic, transcriptional, and proteomic state. Classification and regression methods that are used to predict phenotype from genotype can take advantage of estimates of these intermediate states as additional or alternate inputs (2). These methods include general linear models, neural networks (2), and support vector machines (2), preferred in part because of their ability to cope with very high-dimensional input feature spaces (i.e., with many measured variables). There is currently more to be gained in predicting phenotype by incorporating biological knowledge to improve the input feature space—for example, by substituting inferred transcript levels or inferred protein activity levels for raw gene expression measurements (2)—than by using yet more sophisticated techniques of classification and regression.

Looking Ahead to Applications

Understanding the shared evolutionary history of life starts by storing, indexing, and comparing genomes. It requires tools to rapidly produce evolutionarily related segments of DNA according to a model of genome evolution when prompted with a query segment. How will this be accomplished as we collectively grow from petabytes (10^{15} bytes) of genome data today to exabytes (10^{18} bytes) tomorrow? One possibility may be to use differential compression based on the inferred evolutionary trajectory of genomes, where each sequence is represented as a set of differences from its inferred parent (2). This may allow us to create a new web of genetic information that is compact, rapidly searchable, and directly reflects the natural origin of genomic relatedness.

Genomics has had a profound effect on medicine and will continue to do so. Cancer therapeutics are expected to advance as a result, because genomic modifications are the source of nearly all cancers (2). Within the body's somatic cells, genomic changes occur at random, from environmental impacts, or as a result of treatment; subpopulations of genetically distinct cancer cells expand and compete (2). Sequencing a sample of a cancer patient's noncancerous tissue reveals the patient's genome at birth (i.e., germline genome). Comparing this to the genome obtained from a tumor biopsy then reveals the mutations that have occurred subsequently in the patient's cancer cells. Tracking tumor genomes in this manner from early disease through

each stage of treatment will become the norm and will inform therapeutic decisions (2). Changes that are readily detectable only through computational methods in genotype, epigenetic state, gene expression pattern, and activated pathway structure will provide crucial information on the state of the tumor during initial tumor growth and during the emergence of resistance to therapy (2). Recurring tumor-specific genomic variants and intermediate molecular phenotypes that drive cancer and determine patient response to therapy will come more clearly to light (2) and will be translated into better-targeted cancer diagnosis and treatment (2).

Other fields of medicine will also benefit from computational methods and findings. For example, immune cells undergo specific mutations through rounds of somatic selection (2), accompanied by changes in epigenetic state, gene expression pattern, and activated pathway structure. Deep sequencing of T cell receptors and B cell antibodies (2), coupled with genome-wide measurements of genetic variation, epigenetic state, and gene expression pattern in immune cells, will be used to model immune cell function and correlate immune response with antigen. High-throughput genomics data will be used in vaccine design (including cancer immunotherapy) and the treatment of infectious diseases (2), autoimmune diseases, and compromised immune systems resulting from chemotherapy, transfusions, transplants, and stem cell therapies (2).

Genomic variants, epigenetic state, and expression pattern play key roles in stem cell therapies and basic science applications of stem cells that can only be discerned through the use of computational tools (2). Induced pluripotent stem (iPS) cells and lineage-specific directly reprogrammed cells are made from somatic cells (2) that have already incurred somatic mutations and are cultured in conditions that may select for further mutations (2). These mutations will soon be assessed with whole-genome analysis. Measurements of epigenetic modification and gene expression will confirm the pluripotent or lineage-specific status of the reprogrammed cells and verify that the epigenetic memory of the tissue from which they were derived is erased. Because every batch of reprogrammed cells will show some unexpected genetic mutations, epigenetic changes, and expression differences on a genome-wide level, some with consequences, the interpretation of these data will be of critical importance. In summary, the future of research into cancer, immunology, and stem cells involves all three key challenges of computational genomics: explaining (somatic) evolution, modeling molecular phenotype, and predicting organismal phenotype.

In addition to other medical applications, similar scenarios are playing out in applications of genomics in a wide range of fields, such as agriculture (2) and the study of human prehistory (2). The increasing availability of data is leading to the development of elaborate multidimensional analysis tools incorporating DNA sequences, alignments, phylogenetic trees, lists of variants, epigenomic

and functional assays, phenotypic changes, etc. To face the challenges of obtaining the maximum information from every sequencing experiment, we must borrow advances from a spectrum of different research fields and tie them together into foundational mathematical models implemented with numerical methods. There is a tension between the comprehensiveness of models and their computational efficiency. As this plays out, a comprehensive but computable model of genome evolution and its functional repercussions on organisms is taking shape, embodied in computational genomics. Yet we still await a formulation that is both simple and expressive enough to compare models, store information, and communicate results in an exabyte age. As a common language develops, shaped by our increasing knowledge of biology, we anticipate that computational genomics will provide enhanced ability to explore and exploit the genome structures and processes that lie at the heart of life.

References and Notes

1. W. Fiers *et al.*, *Nature* **260**, 500 (1976).
2. For a full list of references by subject, see table S1 in the supplementary materials.
3. T. R. Gingeras, J. P. Milazzo, D. Sciaky, R. J. Roberts, *Nucleic Acids Res.* **7**, 529 (1979).
4. G. H. Hamm, G. N. Cameron, *Nucleic Acids Res.* **14**, 5 (1986).
5. T. F. Smith, M. S. Waterman, *J. Mol. Biol.* **147**, 195 (1981).
6. G. D. Stormo, T. D. Schneider, L. Gold, A. Ehrenfeucht, *Nucleic Acids Res.* **10**, 2997 (1982).
7. E. R. Mardis, *Trends Genet.* **24**, 133 (2008).
8. L. D. Stein, *Genome Biol.* **11**, 207 (2010).
9. C. Feschotte, *Nat. Rev. Genet.* **9**, 397 (2008).
10. L. Feuk, A. R. Carson, S. W. Scherer, *Nat. Rev. Genet.* **7**, 85 (2006).
11. P. Dehal, J. L. Boore, *PLoS Biol.* **3**, e314 (2005).
12. L. M. F. Merlo, J. W. Pepper, B. J. Reid, C. C. Maley, *Nat. Rev. Cancer* **6**, 924 (2006).
13. A. Mortazavi, B. A. Williams, K. McCue, L. Schaeffer, B. Wold, *Nat. Methods* **5**, 621 (2008).
14. J. C. Simpson, R. Willenreuther, A. Poustka, R. Pepperkok, S. Wiemann, *EMBO Rep.* **1**, 287 (2000).
15. C. Trapnell *et al.*, *Nature* **28**, 511 (2010).
16. J. G. Underwood *et al.*, *Nat. Methods* **7**, 995 (2010).
17. N. T. Ingolia, S. Ghaemmaghami, J. R. S. Newman, A. J. Weissman, *Science* **324**, 218 (2009).
18. A. L. Brunner *et al.*, *Genome Res.* **19**, 1044 (2009).
19. T. S. Mikkelsen *et al.*, *Nature* **448**, 553 (2007).
20. G. Robertson *et al.*, *Nat. Methods* **4**, 651 (2007).
21. A. P. Boyle *et al.*, *Cell* **132**, 311 (2008).
22. M. J. Fullwood *et al.*, *Nature* **462**, 58 (2009).
23. P. J. Mitchell, R. Tjian, *Science* **245**, 371 (1989).
24. U. Alon, *Nat. Rev. Genet.* **8**, 450 (2007).

Acknowledgments: We thank D. A. Earl for designing the figures, and E. Green, M. Häussler, J. Ma, D. Earl, H. Zerbino, R. Kuhn, G. Hickey, T. Pringle, K. Pollard, A. Krogh, R. Shamir, M. Waterman, and R. Durbin for their corrections and comments. Supported by the Howard Hughes Medical Institute (D.H.), National Human Genome Research Institute Data Analysis Center for the Encyclopedia of DNA Elements grant U01 (B.P.), and the American Association for Cancer Research (Stand Up To Cancer/An Integrated Approach to Targeting Breast Cancer Molecular Subtypes and Their Resistance Phenotypes) (D.R.Z.).

Supplementary Materials

www.sciencemag.org/cgi/content/full/336/6078/179/DC1
Table S1

10.1126/science.1216830

REVIEW

Using Gene Expression Noise to Understand Gene Regulation

Brian Munsky,^{1*} Gregor Neuert,^{2*} Alexander van Oudenaarden^{2,3}

Phenotypic variation is ubiquitous in biology and is often traceable to underlying genetic and environmental variation. However, even genetically identical cells in identical environments display variable phenotypes. Stochastic gene expression, or gene expression “noise,” has been suggested as a major source of this variability, and its physiological consequences have been topics of intense research for the last decade. Several recent studies have measured variability in protein and messenger RNA levels, and they have discovered strong connections between noise and gene regulation mechanisms. When integrated with discrete stochastic models, measurements of cell-to-cell variability provide a sensitive “fingerprint” with which to explore fundamental questions of gene regulation. In this review, we highlight several studies that used gene expression variability to develop a quantitative understanding of the mechanisms and dynamics of gene regulation.

Identical genotype and environmental exposure are not sufficient to guarantee a unique phenotype. Consider a single mother cell dividing into two daughter cells of equal volume. During the division process, all the molecules in the mother cell are in Brownian motion according to the laws of statistical mechanics. The probability that each daughter cell inherits the same number of molecules is infinitesimally small. Even in the event that the two daughter cells receive exactly one copy of a particular transcription factor, each transcription factor will perform a Brownian random walk through its cellular volume before finding its target promoter and activating gene expression. Because Brownian motion is uncorrelated in the two daughter cells, it is statistically impossible for both genes to become activated at the exact same time, further amplifying the phenotypic difference between the two daughter cells. These are just two examples of the many sources of gene expression variability that arise in isogenic cells exposed to the same environment.

The origins and consequences of stochastic gene expression, or gene expression “noise,” have been studied extensively during the last decade and have recently been reviewed in detail (1–6). Here we focus on recent works that integrate experimental and computational analyses of gene expression noise to systematically test and refine our understanding of regulation in dif-

ferent genes, regulatory pathways, and organisms. We discuss how combining single-cell measurements and stochastic analyses can reveal qualitative and quantitative features of gene regulation that are hidden by bulk assays or deterministic analyses. In the first part of this review, we discuss how the cell-to-cell variability in gene

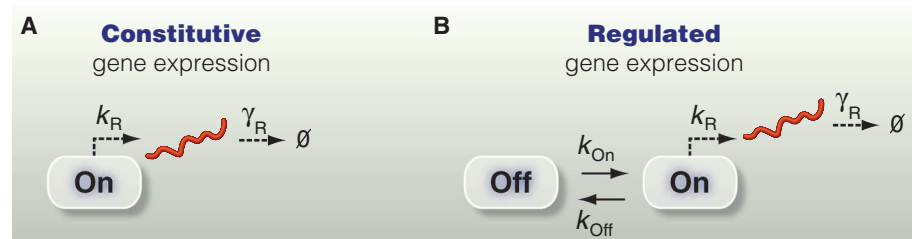


Fig. 1. Constitutive versus regulated gene expression. **(A)** Schematic of a constitutive gene expression model with transcription rate k_R and mRNA degradation rate constant γ_R . **(B)** Schematic of a two-state (On, Off) model with transition rates k_{On} and k_{Off} .

expression of a particular transcript or protein has been used to develop a quantitative understanding of the underlying gene regulation. In the second part, we cover how statistical correlations in the fluctuations of different transcripts and/or proteins can be used to infer gene regulatory interactions.

Inferring Models of Gene Regulation from Variability in Gene Expression

Poisson expression statistics. In the simplest possible model of constitutive gene expression (Fig. 1A), a transcript is produced at a constant rate k_R and destroyed in a first-order reaction with rate constant γ_R . If the total number of a particular transcript m is large, the kinetics can be approximated by the following deterministic differential equation:

$$\frac{dm}{dt} = k_R - \gamma_R m \quad (1)$$

This approximation breaks down in cells when the copy numbers of transcripts are small. For example, the average transcript copy numbers of the constitutive housekeeping genes *MDN1*, *KAP104*, and *DOA1* in budding yeast are 6.1, 4.9, and 2.6, respectively (7). These low copy numbers suggest a probabilistic reformulation of Eq. 1. In the constitutive expression model, transcript births and deaths occur as uncorrelated events, such that in any short time interval, dt , the probability of one transcript production is $k_R dt$, and the probability of one transcript degradation is $\gamma_R m dt$. For equilibrium to be possible, the probability of having m transcripts, $\text{Prob}[m]$, and producing another must be equal to the probability of having $(m + 1)$ transcripts, $\text{Prob}[m + 1]$ and having one degrade. That is, $k_R \text{Prob}[m] = \gamma_R (m + 1) \text{Prob}[m + 1]$ for any m , which is only possible if the copy-number distribution follows a Poisson distribution (8).

It is possible to quantify the variability in transcriptional regulation at the mRNA level using single-molecule fluorescent in situ hybridization (smFISH) (9, 10). In this technique, endogenous mRNA transcripts are labeled with a large number of fluorescently modified DNA oligonucleotides. As a result, a fluorescence microscope can detect the precise location of each individual mRNA molecule as a diffraction-limited spot.

Zenklusen *et al.* (7) used smFISH to count specific mRNA molecules in intact fixed yeast cells and found that the constitutive gene expression model offers surprisingly good quantitative matches to transcriptional behaviors for the housekeeping genes *MDN1*, *KAP104*, and *DOA1* in budding yeast. The measured numbers of mRNA transcripts per cell were well described by Poisson distributions for all three genes. By measuring the number of partially formed nascent mRNA in each nucleus, Zenklusen *et al.* also determined that subsequent transcript production events were uncorrelated (7), again consistent with the constitutive expression model.

Two-state model of gene regulation. Although the constitutive gene expression model captures the fluctuations of several housekeeping genes in budding yeast (7), it does not perform as well when gene expression is regulated. Because deviations

¹Center for Nonlinear Studies, the Information Sciences Group, and the National Flow Cytometry Resource, Los Alamos National Laboratory, Los Alamos, NM 87545, USA. ²Departments of Physics and Biology, Massachusetts Institute of Technology, Cambridge, MA 02139, USA. ³Hubrecht Institute, Royal Netherlands Academy of Arts and Sciences and University Medical Center Utrecht, Uppsalalaan 8, 3584 CT, Utrecht, Netherlands.

*These authors contributed equally to this work. To whom correspondence should be addressed. E-mail: munsky@lanl.gov (B.M); gneuert@mit.edu (G.N.)

from Poisson behavior indicate regulation, can quantifying these deviations reveal the mechanism of regulation? A key parameter to quantify the deviation from Poisson statistics is the Fano factor, which is the ratio between the variance, σ^2 , and the mean, \bar{m} , of the mRNA copy-number distribution, σ^2/\bar{m} (8). For a Poisson distribution, the Fano factor equals 1. Golding *et al.* (11) determined a Fano factor of 4.1 for a synthetic transcript driven by the $P_{LAC/ARA}$ promoter in *Escherichia coli*, indicating that the transcript distribution was significantly wider than a Poisson distribution. A two-state model of gene expression (12–16) can fit these data much better. This model considers two promoter states: an Off state, in which no transcription occurs, and an On state, which has transcription rate k_R . The constants k_{On} and k_{Off} define the transition rates between the two states, and γ_R is a first-order rate constant for transcript degradation (Fig. 1B). The Off state is usually associated with a closed chromatin state in which the binding sites for transcription factors are inaccessible, whereas the On state is associated with the open active chromatin state (14).

According to the two-state model, the average fraction of cells in the On state is $f_{On} = k_{On}/(k_{On} + k_{Off})$, and the average number of mRNA molecules in each cell is $\bar{m} = f_{On}k_R/\gamma_R$. The expression for the Fano factor in steady state can be written as (12):

$$\sigma^2\bar{m} = 1 + \frac{(1-f_{On})k_R}{(k_{On} + k_{Off} + \gamma_R)} \quad (2)$$

Figure 2A uses a heat map to illustrate the Fano factor's dependence upon k_{Off} and k_{On} for a fixed transcription rate k_R . To compare the variability at equal expression levels, the three dashed lines denote parameter combinations that produce an average of 2, 25, and 75 mRNAs per cell. Although the average expression level is constant along these lines, the Fano factor varies significantly, as does the qualitative shape of the mRNA distribution. For example, Fig. 2B shows the distributions corresponding to the filled squares on the $\bar{m} = 25$ line in Fig. 2A. Although each parameter set yields an average of 25 molecules per cell, they exhibit three distinctly different behaviors for the variability of m between cells. On the basis of differences in the mean, Fano factor, and qualitative shapes of distributions, we can dissect the parameter space into three different “phenotype” classes (14, 17). In class I, both k_{On} and k_{Off} are slow, and cells separate into distinct On and Off populations, yielding a bimodal mRNA distribution (Fig. 2B, left) and resulting in a large Fano factor. In class II, k_{On} is slow and k_{Off} is fast, and therefore most cells are Off. In this case, the low value of f_{On} contributes to low means and Fano factors, but occasional mRNA bursts give rise to long exponential tails in the mRNA distribution (Fig. 2B, middle). Finally, in class III, k_{On} is fast in comparison to either γ_R or k_{Off} , and the system spends very short periods in the Off state. The

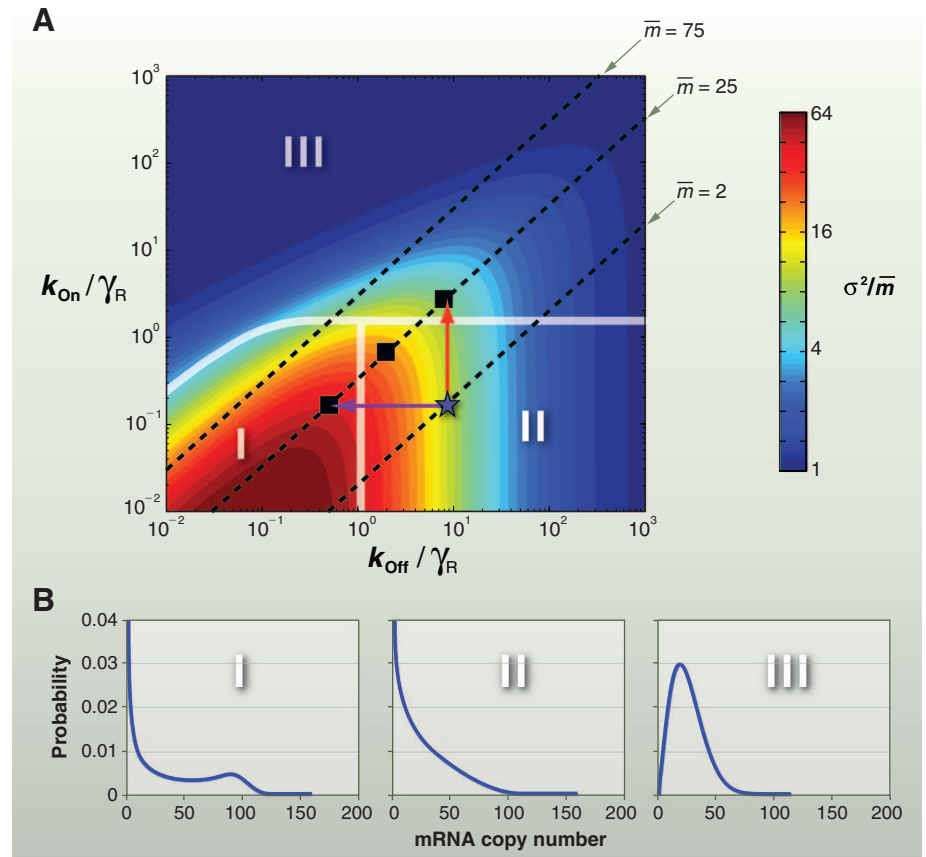


Fig. 2. Effects of transcriptional control on mRNA distributions. **(A)** Heat map of the cell-to-cell variability (Fano factor, σ^2/\bar{m}), versus normalized gene activation rate k_{On}/γ_R and normalized deactivation rate k_{Off}/γ_R with fixed production and degradation rates ($k_R = 100$, $\gamma_R = 1$). Lines of equal average mRNA expression are shown for 2, 25, and 75 molecules. The parameter space is separated into three classes (I, II, III) that exhibit different types of cell-to-cell variability. **(B)** Representative distributions from each class: Class I corresponds to systems with long Off and On periods, giving rise to bimodal distributions with clearly delineated On/Off populations. Class II corresponds to populations with short On and long Off periods, giving rise to occasional mRNA bursts and long distribution tails. Class III includes systems with short Off periods, giving rise to continuous production and more graded unimodal distributions. All three distributions have the same average of 25 mRNAs and correspond to the squares in (A). Distributions were computed with the finite state projection approach (34).

dynamics of this special case collapses down to that of the constitutive expression model, with an effective transcription rate $k_R^{eff} = k_R f_{On}$ and a Poisson-like mRNA distribution (Fig. 2B, right).

A cell can increase the average mRNA copy number \bar{m} from 2 (indicated by the blue star in Fig. 2A) to 25 by either decreasing k_{Off} (purple arrow in Fig. 2A) or increasing k_{On} (red arrow in Fig. 2A). Increasing k_{On} converts a class II phenotype into a class III phenotype, resulting in more Poisson-like expression. Conversely, decreasing k_{Off} shifts the system to class I, corresponding to bimodal expression. Thus, although both modulation mechanisms yield the same change in average mRNA levels, their single-cell statistics are quantitatively and qualitatively different. Below we highlight several studies that exploit these differences to learn more about the gene regulatory control mechanisms.

As in studies of constitutive expression, single-cell responses of regulated genes have been examined at the mRNA level. Raj *et al.* (15) used smFISH to study gene expression variability in mammalian cells. They integrated an inducible *tetO* promoter into the genome and quantified mRNA numbers and locations. The measured mRNA distributions had long exponential tails that closely matched those of the class II phenotype, corresponding to bursts of mRNA that were short, infrequent, and intense. Furthermore, Raj *et al.* observed that On cells exhibited extra-bright clusters of nascent transcripts and elevated levels of nuclear mRNA, whereas Off cells lacked these transcription site spots and had far fewer nuclear mRNAs. In this context, spatial variability provided quantitative insight into transcriptional dynamics. More recent smFISH studies have also discovered mRNA distributions from

all three classes for a myriad of other genes in several model organisms, including bimodal distributions of class I in cell-cycle and inducible genes in yeast (18); long exponential distribution tails corresponding to class II in *E. coli* (19), ribosomal RNA (20), and coding and long non-coding RNA (21) transcription in yeast; and unimodal Poisson-like distributions of class III in yeast (7).

Single-molecule FISH has also been used to explore how transcriptional regulation changes between conditions (15, 19). Raj *et al.* (15) showed that an increase in the transcriptional activator tTA or in the number of activator binding sites increased the transcriptional activity of the *tetO* promoter in mammalian cells. Quantitative comparisons of measured mRNA distributions with the two-state model revealed that activation was consistent with either k_{off} modulation (purple arrow in Fig. 2A) or k_R modulation. In a recent study, So *et al.* also integrated experimental and computational analyses to find that k_{off} modulation is a common motif, which regulates mRNA expression in 20 independent *E. coli* genes, whose mRNA expressions span four orders of magnitude (19). Using smFISH (10), they measured mRNA distributions in 150 different combinations of genes and growth conditions that modulate those genes. After correcting for different gene copy numbers and mRNA lifetimes, the mRNA mean and Fano factor were computed and plotted for every gene and experimental condition, and the resulting scatter plot was closely fit by Eq. 2, where k_{on} and k_R were constant, and k_{off} was selected to match the mean expression.

Although the former studies explored gene regulation at the mRNA level (7, 15, 18–21), similar conclusions have been reached through single-cell analyses at the protein level. Raser and O'Shea (14) used single-cell measurements of fluorescent protein concentrations to show that induction of the *PHO5* promoter in budding yeast increases the expression level while reducing the cell-to-cell variability. This trend was explained as the system starting in class II and increasing k_{on} to switch toward class III (red arrow in Fig. 2A). Similarly, Octavio *et al.* (22) explored the regulation of the *FLO11* gene in yeast. Using inducible promoters to control the regulatory proteins Flo8, Sfl1, Tec1, Ste12, Phd1, Msn1, and Mss1, they pushed the system into each of the three phenotypes. Then, by elucidating how each transcription factor altered the variability in gene expression, they determined the mechanisms by which each factor modulated transitions between an Off state, an intermediate “competent” state, and the fully active On state.

Inferring Gene Regulatory Interaction from Correlations Between Fluctuating Genes

The examples above illustrate how the expression distribution of a particular transcript or flu-

orescent protein reporter can be used to quantify the transitions between active and inactive transcription states and to determine the mechanism by which regulators modulate this process. In many of these studies, the analysis of regulatory behavior required the application of an external input or a change in environmental conditions. It is not always easy to introduce such a perturbation, but what if they already existed in nature? As discussed above, most cellular proteins undergo stochastic fluctuations, which can activate or repress downstream processes and thereby introduce valuable perturbations. As a result, when multiple transcript or protein species are monitored in the same cell, important additional information can be extracted by analyzing how different species correlate with one another. This correlation analysis was used in experiments focused on synthetic gene networks in *E. coli*, where expression levels of several genes were monitored in the same cell with fluorescent reporters. By analyzing the pairwise correlation between the different fluorescent reporters, the major fluctuation sources could be determined (23, 24).

In a recent study, Stewart-Ornstein *et al.* (25) used fluorescent proteins to examine the pairwise correlations of hundreds of different yeast genes, whose expression levels varied over three orders of magnitude. Even without using exogenous perturbations, single-cell steady-state measurements could reveal clear groups of genes whose stochastic fluctuations were strongly coordinated. These collections of genes, which they labeled “noise regulons,” corresponded to functional groups related to stress response, mitochondrial regulation, and amino acid biosynthesis. Furthermore, Stewart-Ornstein *et al.* showed that steady-state correlations were strongly predictive of the proteins' dynamic response to heat shock.

Using a two-color RNA fluorescent in situ hybridization assay, Gandhi *et al.* (18) measured pairwise correlations between RNA species regulated by the same promoter or by two different promoters. The Gal4-regulated genes *GAL1*, *GAL7*, and *GAL10* were induced with 2% galactose, and their distributions were measured at steady state. As expected, single-cell correlation analyses showed strong correlations between *GAL1* and *GAL7*, as well as between *GAL1* and *GAL10*. mRNA correlations were also found in other regulatory genes. Transcripts of the genes *SWI5* and *CLB2*, which are expressed in the G₂/M stages of the cell cycle, were strongly correlated with each other, but weakly anticorrelated with *NDD1*, which dominates during the S phase. By contrast, constitutive genes such as *MDN1* (ribosome biogenesis), *PRP8* (pre-mRNA splicing), and *KAP104* (nucleocytoplasmic transport) exhibited much less coordination.

Although correlations at a single time point can reveal static relationships among different mRNA and protein species, this view lacks information about the system's history and causal relationships. If two proteins X and Y are cor-

related, the questions remain: Does X activate Y; does Y activate X; or does a third protein W control them both? To illustrate this situation, Fig. 3A shows simple motifs by which proteins W, X, and Y could relate to one another, and Fig. 3B shows typical scatter plots of the single-cell expression for proteins X and Y for these motifs. When static correlations cannot discriminate between these motifs, dynamic correlations in single-cell fluctuations may help (26). Such analyses make use of the cross-correlation function (26), $R_{XY}(\tau) = \langle X(t + \tau)Y(t) \rangle / \sigma_X \sigma_Y$, which measures how fluctuations in Y at time t relate to those in X at time $t + \tau$. Here, $\langle \dots \rangle$ denotes the covariance of two variables, and σ_X and σ_Y are the standard deviations of X and Y, respectively. The magnitude of $R_{XY}(\tau)$ reveals positive or negative regulation, and the timing of peaks in $R_{XY}(\tau)$ reveals causality in this regulation. As examples, Fig. 3C plots the cross-correlation functions between proteins X and Y for each of the motifs in Fig. 3A. For the first motif, where X activates Y, the blue line in Fig. 3C (left) shows that $R_{XY}(\tau)$ has a maximum, and because X is upstream of Y, this peak occurs at a negative delay time. Conversely, when protein Y is a repressor of X, $R_{XY}(\tau)$ has a minimum at a positive τ (Fig. 3C, second column, red line). If both X and Y were controlled by W, the maximum or minimum would occur at $\tau = 0$, and its sign would be positive or negative depending upon whether W has the same or different effects on X and Y (Fig. 3C, right two columns).

Dunlop *et al.* (26) tested this dynamic correlation approach in live cells by inserting three fluorescent protein reporters of different colors into the *E. coli* genome. Yellow fluorescent protein (YFP) was fused to the λ CI repressor, which controlled expression of red fluorescent protein (RFP). Cyan fluorescent protein (CFP) was placed on a separate constitutive promoter. With the use of fluorescence time-lapse microscopy, all three colors could be monitored simultaneously over several hours. Dynamics of the YFP-RFP pair were anticorrelated with a delay of about 120 min, clearly revealing that CI-YFP repressed RFP (similar to Fig. 3C, second column, blue line). Conversely, the unregulated YFP-CFP pair exhibited a delay-free correlation characteristic of common upstream regulators (extrinsic noise) that affect both YFP and CFP in a similar fashion (similar to Fig. 3C, third column). Thus, the causal relationships of all three reporters were uniquely determined. Extending and applying this approach to the *CRP-GalS-GalE* feed-forward loop in *E. coli*, they analyzed how the relationship between *GalS* and *GalE* varies under different fucose concentrations and under the influence of *GalR* (26).

Although correlations at either mRNA or protein levels can reveal gene regulatory relationships, the two do not always perform equally well. To illustrate this scenario, Fig. 3, D and E, show scatter plots and cross-correlations between

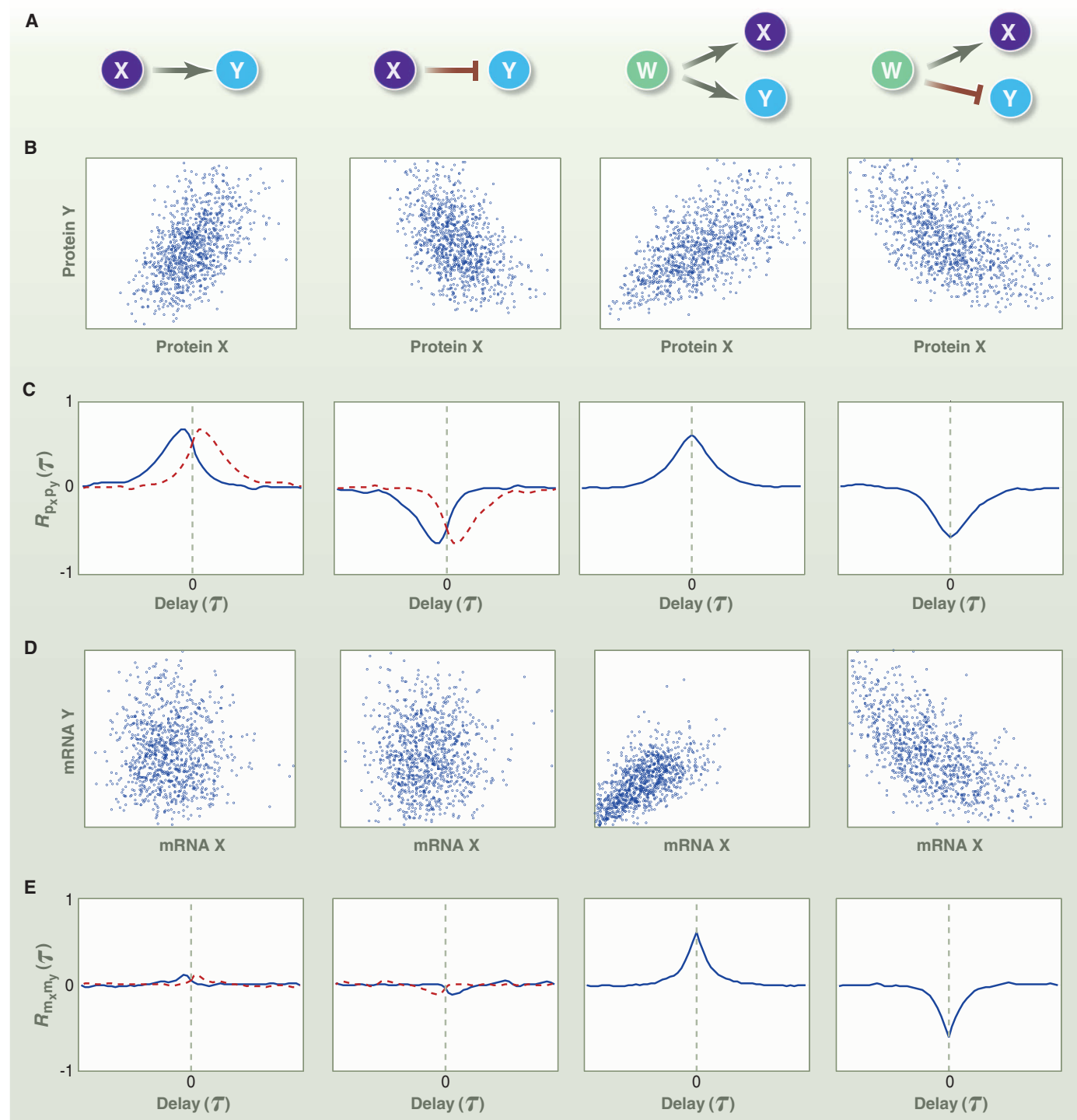


Fig. 3. Different regulatory motifs yield different steady-state correlations. **(A)** Schematics of four possible regulator motifs: X activates Y; X represses Y; W activates both X and Y; and W activates X but represses Y. For each motif, mRNA is produced according to the constitutive model; protein is translated from mRNA as a first-order reaction; and both mRNA and protein degrade as a first-order reaction. Regulation changes to the transcription rate are defined as $k_R(X) = \alpha X^4 / (M^4 + X^4)$ for activation and $k_R(X) = \alpha M^4 / (M^4 + X^4)$ for repression. **(B)** Scatter plots of the populations of protein X and protein Y at steady state. **(C)** Dynamic cross-

correlation functions of protein X and protein Y, versus the correlation time delay. The magnitude of $R_{XY}(\tau)$ indicates how strongly $X(t + \tau)$ is correlated (positive) or anticorrelated (negative) with $Y(t)$. For causal events, where X activates (or represses) Y, peaks (or dips) appear in $R_{XY}(\tau)$ at negative values of τ . Blue lines correspond to the motif in **(A)**, and red lines correspond to the same motif in which X and Y have been interchanged. **(D)** Scatter plots for mRNA X and mRNA Y populations. **(E)** Dynamic cross-correlation for mRNA X and mRNA Y. Simulations were conducted with the stochastic simulation algorithm (35).

the mRNA X and mRNA Y corresponding to protein X and protein Y, respectively. Although protein X and protein Y are coordinated for all four motifs in Fig. 3, this is not the case for their mRNA levels. This can be explained by the disparate time scales of mRNA and protein. Fast-degrading mRNA may exhibit fluctuations with a broad frequency bandwidth. Conversely, slow degradation of proteins filters out fast fluctuations but keeps slow fluctuations. Constitutively expressed mRNA X has both fast and slow fluctuations, but protein X only transmits the slow fluctuations downstream. The result is that the dynamics of mRNA X and mRNA Y are dominated by uncorrelated fast fluctuations, which overshadow their correlated slow fluctuations. On the other hand, protein X and protein Y only contain the better-correlated slow fluctuations. That is, two mRNA species can be mostly uncorrelated with one another, yet produce protein in a coordinated fashion. Gandhi *et al.* (18) observed such a circumstance in budding yeast, when they found very little correlation between pairs of transcripts that encode coordinated proteins of the same protein complex, including proteasome and RNA polymerase II subunits. They even found correlation lacking in two alleles of the same gene. In a related study, Taniguchi *et al.* (27) analyzed more than 1000 genes in *E. coli* and measured both mRNA and protein copy numbers in single cells. They found that for most genes, even the numbers of mRNA and protein molecules were uncorrelated. These studies suggest that understanding of regulatory phenomena requires one to consider regulation at both the mRNA and the protein level.

From these studies, it is now clear that variability in single-cell measurements contains a wealth of information that can reveal new insights into the regulatory phenomena of specific genes and the dynamic interplay of entire gene networks. As modern imaging techniques begin to beat the diffraction limitations of light (28) and flow cytometers become affordable for nearly any laboratory bench (29), we find ourselves in the midst of an explosion in single-cell research. With the advent of single-cell sequencing (30, 31), it might be possible to determine the full transcriptome of many single cells in the near future and to determine the full expression distributions and correlations for all genes in the genome. We expect that the approaches described in this review, which have been pioneered with the model microbial systems, will be readily applied to mammalian cells and tissues (32, 33).

References and Notes

1. G.-W. Li, X. S. Xie, *Nature* **475**, 308 (2011).
2. A. Raj, A. van Oudenaarden, *Cell* **135**, 216 (2008).
3. G. Balázs, A. van Oudenaarden, J. J. Collins, *Cell* **144**, 910 (2011).
4. A. Eldar, M. B. Elowitz, *Nature* **467**, 167 (2010).
5. M. E. Lidstrom, M. C. Konopka, *Nat. Chem. Biol.* **6**, 705 (2010).
6. B. Snijder, L. Pelkmans, *Nat. Rev. Mol. Cell Biol.* **12**, 119 (2011).
7. D. Zenklusen, D. R. Larson, R. H. Singer, *Nat. Struct. Mol. Biol.* **15**, 1263 (2008).
8. M. Thattai, A. van Oudenaarden, *Proc. Natl. Acad. Sci. U.S.A.* **98**, 8614 (2001).
9. A. M. Femino, F. S. Fay, K. Fogarty, R. H. Singer, *Science* **280**, 585 (1998).
10. A. Raj, P. van den Bogaard, S. A. Rifkin, A. van Oudenaarden, S. Tyagi, *Nat. Methods* **5**, 877 (2008).
11. I. Golding, J. Paulsson, S. M. Zawilski, E. C. Cox, *Cell* **123**, 1025 (2005).
12. J. Peccoud, B. Ycart, *Theor. Popul. Biol.* **48**, 222 (1995).
13. T. B. Kepler, T. C. Elston, *Biophys. J.* **81**, 3116 (2001).
14. J. M. Raser, E. K. O'Shea, *Science* **304**, 1811 (2004).
15. A. Raj, C. S. Peskin, D. Tranchina, D. Y. Vargas, S. Tyagi, *PLoS Biol.* **4**, e309 (2006).
16. V. Shahrezaei, P. S. Swain, *Proc. Natl. Acad. Sci. U.S.A.* **105**, 17256 (2008).
17. S. Iyer-Biswas, F. Hayot, C. Jayaprakash, *Phys. Rev. E Stat. Nonlin. Soft Matter Phys.* **79**, 031911 (2009).
18. S. J. Gandhi, D. Zenklusen, T. Lionnet, R. H. Singer, *Nat. Struct. Mol. Biol.* **18**, 27 (2011).
19. L.-H. So *et al.*, *Nat. Genet.* **43**, 554 (2011).
20. R. Z. Tan, A. van Oudenaarden, *Mol. Syst. Biol.* **6**, 358 (2010).
21. S. L. Bumgarner *et al.*, *Mol. Cell* **45**, 470 (2012).
22. L. M. Octavio, K. Gedeon, N. Maheshri, *PLoS Genet.* **5**, e1000673 (2009).
23. J. M. Pedraza, A. van Oudenaarden, *Science* **307**, 1965 (2005).
24. N. Rosenfeld, J. W. Young, U. Alon, P. S. Swain, M. B. Elowitz, *Science* **307**, 1962 (2005).
25. J. Stewart-Ornstein, J. S. Weissman, H. El-Samad, *Mol. Cell* **45**, 483 (2012).
26. M. J. Dunlop, R. S. Cox III, J. H. Levine, R. M. Murray, M. B. Elowitz, *Nat. Genet.* **40**, 1493 (2008).
27. Y. Taniguchi *et al.*, *Science* **329**, 533 (2010).
28. B. Huang, M. Bates, X. Zhuang, *Annu. Rev. Biochem.* **78**, 993 (2009).
29. L. Bonetta, *Nat. Methods* **2**, 785 (2005).
30. T. Kalisky, P. Blainey, S. R. Quake, *Annu. Rev. Genet.* **45**, 431 (2011).
31. F. Tang *et al.*, *Nat. Methods* **6**, 377 (2009).
32. S. Itzkovitz *et al.*, *Nat. Cell Biol.* **14**, 106 (2012).
33. P. Dalerba *et al.*, *Nat. Biotechnol.* **29**, 1120 (2011).
34. B. Munsky, M. Khammash, *J. Chem. Phys.* **124**, 044104 (2006).
35. D. T. Gillespie, *J. Phys. Chem.* **81**, 2340 (1977).

Acknowledgments: This work was funded by the National Science Foundation (ECCS-0835623) and a NIH Pioneer award (1DP10D003936).

10.1126/science.1216379

REVIEW

Computational Approaches to Developmental Patterning

Luis G. Morelli,^{1,2,3} Koichiro Uriu,^{1,4} Saúl Ares,^{2,5,6} Andrew C. Oates^{1*}

Computational approaches are breaking new ground in understanding how embryos form. Here, we discuss recent studies that couple precise measurements in the embryo with appropriately matched modeling and computational methods to investigate classic embryonic patterning strategies. We include signaling gradients, activator-inhibitor systems, and coupled oscillators, as well as emerging paradigms such as tissue deformation. Parallel progress in theory and experiment will play an increasingly central role in deciphering developmental patterning.

Animal and plant patterns amaze and perplex scientists and lay people alike. But how are the dynamic and beautiful patterns of developing embryos generated? Used appropriately, theoretical techniques can assist in the understanding of developmental processes (1–5). There is considerable art in this, and the key to success is an open dialogue between exper-

imentalist and theorist. The first step in this dialogue is to formulate a theoretical description of the process of interest that captures the properties and interactions of the most relevant variables of the system at a level of detail that is both useful and tractable. Once formulated, the second step is to analyze the theoretical model. If the model is sufficiently tractable, it may be possible

to understand its behavior with “pencil-and-paper” analysis and compare this analytical solution directly with experimental data. Very often, however, the number of variables and the complexity of their interactions preclude this approach, and the behavior of models must be solved or simulated by using computers in order to be understood and compared with data. This combined approach, which we refer to as computational biology, has become popular recently with the availability of powerful computers and increasingly sophisticated numerical algorithms.

¹Max Planck Institute of Molecular Cell Biology and Genetics, Pfotenhauserstrasse 108, 01307 Dresden, Germany. ²Max Planck Institute for the Physics of Complex Systems, Nöthnitzer Strasse 38, 01187 Dresden, Germany. ³Consejo Nacional de Investigaciones Científicas y Técnicas, Departamento de Física, Universidad de Buenos Aires, Ciudad Universitaria, 1428 Buenos Aires, Argentina. ⁴Theoretical Biology Laboratory, RIKEN Advanced Science Institute, Saitama 351-0198, Japan. ⁵Logic of Genomic Systems Laboratory, Centro Nacional de Biotecnología-Consejo Superior de Investigaciones Científicas (CSIC), Calle Darwin 3, 28049 Madrid, Spain. ⁶Grupo Interdisciplinar de Sistemas Complejos (GISC), Spain.

*To whom correspondence should be addressed. E-mail: oates@mpi-cbg.de

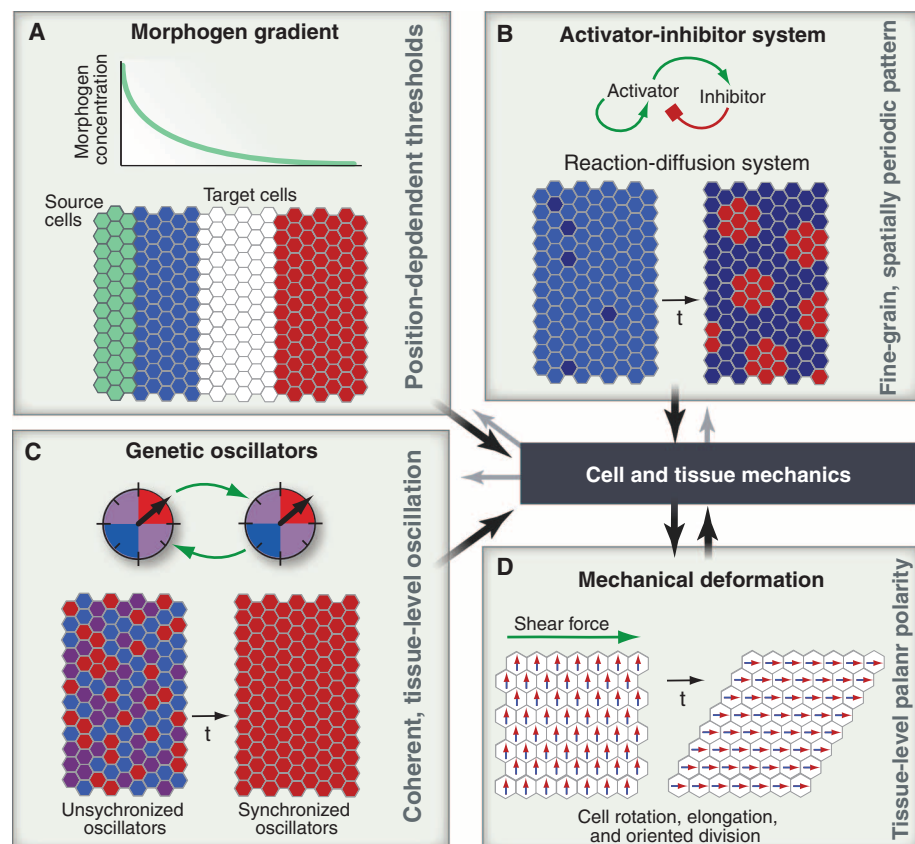


Fig. 1. Patterning strategies. **(A)** Signaling gradients supply global positional information. Horizontal axis is position within target tissue. Morphogen-producing cells are green; cells in tissue take identities (blue, white, and red) according to morphogen concentration. **(B)** Activator-inhibitor systems incorporate local positive and negative feedbacks to generate pattern. Distinct cell types are in red and blue. **(C)** Synchronization of genetic oscillators allows a tissue to generate a coherent temporal rhythm for patterning. In these snapshots, the phase of each oscillating cell is given by its color, which changes over time. **(D)** Tissue deformation can drive patterning reactions. Downstream of patterning information, the dynamic physical properties of tissues drive the morphogenesis of the embryo. *t*, time.

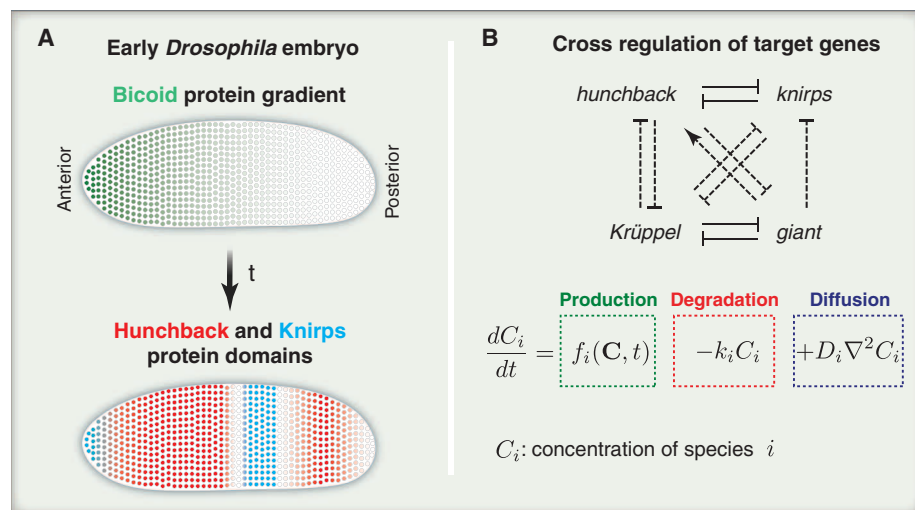


Fig. 2. Patterning with signaling gradients. **(A)** Schematic of early fruit fly embryo showing the maternal gradient of Bicoid protein at cycle 13 that directs the formation of precise target gene domains such as *hunchback* and *knirps*. **(B)** Proposed gene regulatory network showing cross-regulation of target genes (9). The four genes are also under control of Bicoid and other players. *t*, time.

In this Review, we hope to introduce scientists familiar with computational methods (geeks) to a selected set of interesting developmental problems (Fig. 1) and to illustrate to developmental biologists (nerds) a selected set of powerful tools. We focus on recent studies investigating four developmental patterning strategies: (i) gradients of signaling molecules released from localized source cells that guide global patterns across target cell populations (Fig. 1A). This external control contrasts with self-organizing strategies within the cell population that use local interactions, such as (ii) activator-inhibitor mechanisms (Fig. 1B) and (iii) the synchronization of cellular oscillations (Fig. 1C). (iv) Mechanical deformations can also change the pattern of a cellular population (Fig. 1D). Although models are often useful in explaining and predicting developmental phenomena, the eventual fate of a given model is to be proven wrong and then modified or replaced, as illustrated in the companion article on cell polarity by Mogilner and colleagues on page 175 of this special issue. Perhaps the greatest impact of computational approaches in developmental biology right now is to force hypotheses to be precisely stated and to stimulate corresponding new quantitative experiments to test them.

Patterning with Signaling Gradients

Morphogens are diffusible signaling molecules that can activate target genes in a concentration-dependent manner. During development, morphogen gradients are established across tissues, diffusing away from localized sources (Fig. 1A). It has been proposed that cells read morphogen levels to determine their position within the tissue and differentiate accordingly (6), and there is good evidence that morphogen gradients can direct cell differentiation in target cells. How these gradients are formed, and whether they are sufficient to control differentiation in very precise domains, are open questions that have benefited from computational approaches.

An important model system for studying these questions is the early embryo of the fruit fly *Drosophila*, in part because its geometry and symmetry simplify description and quantitation (Fig. 2A). One of the maternally deposited cues that breaks the symmetry along the embryo's long axis is *bicoid* mRNA, which is present only in the anterior pole. Bicoid protein is translated and transported (7), creating within an hour an exponentially decreasing concentration gradient over several hundred micrometers along the embryo's axis. This gradient directs the formation of precise domains of four target genes—among them *hunchback*—that establish the first segments of the future fly body (Fig. 2A). Given the stochastic nature of gene expression, discussed in the companion article by Munsky and colleagues on page 183 of this special issue, morphogen concentration is expected to fluctuate, both over developmental time and from one individual to another. The stunning precision in the position of the boundaries of the segmented out-

put pattern that is found despite these fluctuations puzzles both nerds and geeks. The field has wrestled with the issue of whether this precision can be achieved through the Bicoid gradient alone, or whether other mechanisms are required.

Contributing to this debate, recent papers by Manu *et al.* (8, 9) formulated the interactions between four target genes downstream of the maternal gradients in the early embryo using a gene regulatory network (GRN) model, in which each variable represents the quantity of a molecular species (Fig. 2B). One of the limitations of GRN models is that great experimental effort is often required to estimate relevant values of the model's many parameters in the embryo. Parameters for this *Drosophila* segmentation model were obtained computationally by finding those combinations that best reproduced a time series of quantitative spatial gene expression data from the embryo. The model hinted that cross-regulatory interactions between target genes in the GRN reduce the variability in the position of their expression domains.

One problem in understanding a model is that as the parameters vary, the general dynamic behavior of the system can change dramatically. These changes are called bifurcations, and using powerful tools from dynamical systems theory (10), Manu *et al.* (9) performed a bifurcation analysis of the model to identify the fundamental behaviors that the system can display over a given set of realistic parameter values. The model predicts that cells

in the anterior of the embryo select a stable state of the dynamics, and the concentrations of targets change as Bicoid levels drop. In the posterior of the embryo, the system never reaches a stable state because gastrulation happens first. Describing the simple behaviors of a complex regulatory network in this compact way is appealing because it makes similarities to other regulatory systems clearer and also makes falsifiable predictions about distinctive behaviors that can be experimentally tested.

Fluctuations in gene product levels generate molecular noise that limits the precision of signaling gradients and also degrades the targets' outputs. This problem can be formulated precisely by using the tools and concepts from information theory—originally used in engineering—which quantifies the flow of information through communication channels. A key concept is the mutual information between two variables, such as, for example, Bicoid and Hunchback levels. An elegant computation by Tkačik and Walczak used existing precise measurements of morphogen levels (11) to estimate the mutual information between Bicoid and Hunchback (12). On the basis of their result, they argued that if similar results hold for the other target genes under Bicoid control, the combined information conveyed by the four genes would be enough so that each of the roughly 100 rows of nuclei could unambiguously determine its position along the *Drosophila* embryo. To test this hypothesis, combined high-quality spatial expres-

sion data for the other target genes in the system will be necessary. Thus, information theory is emerging as a potentially powerful tool to quantify information transmission in developmental GRNs. As yet, it is unclear whether the *bicoid* gradient is sufficiently precise to instruct the precise boundaries of its target gene domains, or whether other mechanisms are necessary, but computational biology has a central role in this discussion.

Patterning with Activator-Inhibitor Systems

Cells in a morphogen gradient use the local level of an externally provided signal to produce patterns (Fig. 1A). However, patterns such as spots and stripes can arise spontaneously from entirely local interactions. In 1952, Alan Turing proposed a reaction-diffusion (RD) mechanism to explain spontaneous pattern formation without signaling gradients (13). Specifically, he considered two diffusing chemical components, an activator and an inhibitor (Figs. 1B and 3A). By self-activation, the activator can locally increase its concentration (Fig. 3A). The activator in that region produces the inhibitor, which suppresses the activator in surrounding space because of faster diffusion. As a result, local peaks of activator self-organize from the almost homogeneous starting state, leading to the spontaneous formation of spatial patterns, such as stripes and spots in a two-dimensional (2D) space (so-called Turing patterns) (Fig. 1B).

Subsequently, RD systems have been considered to play important roles in spontaneous pattern formation (14, 15). Although spatial structures very similar to simulated Turing patterns have been observed in development, until recently there was scant evidence showing that the Turing mechanism causes these structures. Indeed, conceptually elegant RD models of the *Drosophila* segmentation process introduced above proved to be entirely wrong (16), and this failure may even have left some developmental biologists wary of further theoretical efforts. However, identification of interaction rules and key molecular components in several putative RD systems (17, 18) now suggests the potential of a long-awaited experimental verification of these ideas.

Skin pattern formation in fish has long been a candidate for patterning by use of the Turing mechanism (19). To identify key interaction rules in the system, Nakamasu *et al.* studied stripe formation in zebrafish skin (20). These black and yellow stripes are self-organized over 3 weeks by local interactions between black and yellow pigment cells, which fulfill the condition for Turing patterns (Fig. 3B). To confirm that the experimentally observed interactions between pigment cells can generate stripes, the authors first used deterministic partial differential equations to model cellular dynamics. However, because the width of each stripe in zebrafish is only ~10 cells, Nakamasu *et al.* pointed out that stochastic effects caused by smaller cell numbers might prevent stable stripe formation. In that situation, it would

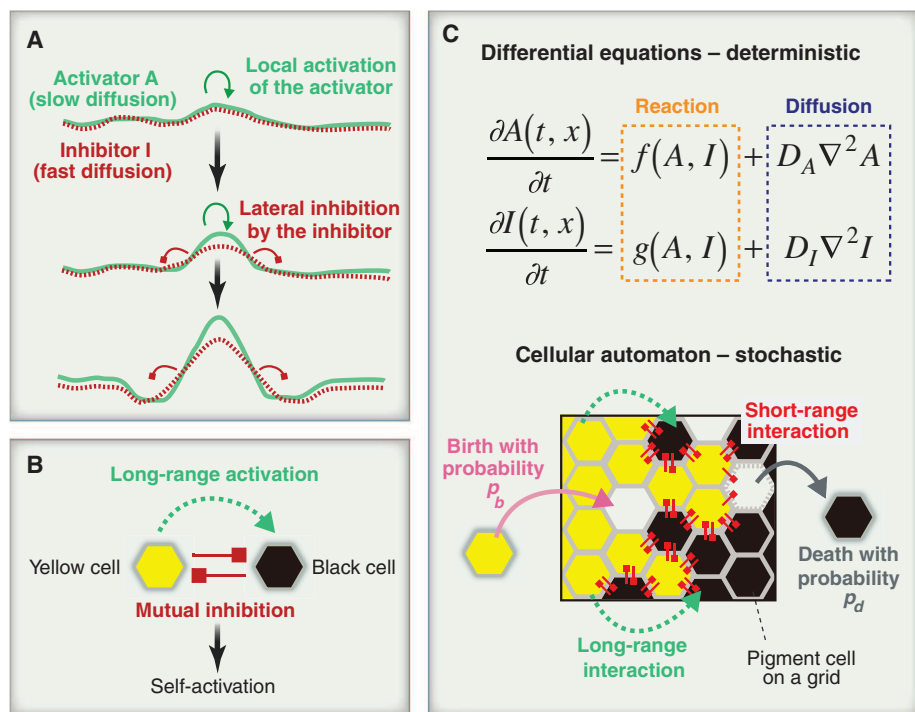


Fig. 3. Patterning with activator-inhibitor systems. (A) Local activation and lateral inhibition generates spatially heterogeneous patterns. (B) Interactions between black and yellow pigment cells produce Turing patterns in zebrafish skin. Mutual inhibition between them functions as self-activation for the yellow cells. Each yellow cell activates distant black cells. Therefore, inhibition of the yellow cell by the black cell works as a lateral inhibition. (C) Different modeling approaches to spontaneous pattern formation.

be a better formulation to explicitly describe stochastic behaviors of each single pigment cell, such as birth, movement, and cell death. The authors developed a cellular automaton-based model (Fig. 3C) that includes the observed pigment cell interactions to study the robustness of stripe patterns against stochastic effects. Although such detailed models usually include several parameters not measured experimentally, simulations of the cell-based model produced patterns similar to those obtained by the deterministic model and observed on the zebrafish skin. Combining investigations of the molecular and cellular basis of the cellular-level interaction rules (21) with further theoretical studies should reveal whether this is indeed a Turing system.

Gradient patterning strategies can also be formulated as RD systems because gradients can arise from diffusion of morphogens, and the pattern emerges due to reactions that involve these morphogens. However, the different length-scales involved in activator-inhibitor systems give rise to qualitatively different patterns, which are local in nature. This is an example of how very different developmental patterning strategies can be described by using similar model formulations.

Patterning with Genetic Oscillations

The growing body axis of all vertebrate embryos is rhythmically and sequentially subdivided into segments. For example, in the zebrafish embryo the multicellular segments are ~50 μm long and form with a periodicity of 30 min. Inspired by such clock-like regularity, Cooke and Zeeman proposed the Clock and Wavefront model in 1976 (22). In this model, a biological clock ticks at the posterior of the elongating embryo, and the distance advanced by a wavefront along the embryonic axis during a cycle of the clock sets the length of a forming segment. More than 20 years later, the model was revived with the discovery of genetic oscillations in the chick embryo (23). This segmentation clock appears to be a tissue-level rhythmic pattern generator (24), in which a population of progenitor cells behave as coupled oscillators, self-organizing a collective rhythm through mutual synchronization (Fig. 1C).

A clue to the existence of such a synchronized cell population came from zebrafish mutants that disrupt Delta-Notch intercellular signaling, in which coherent oscillations and segmental patterning are gradually lost (25). The current hypothesis is that in the wild-type embryo, Delta ligands under the control of a single-cell oscillator activate Notch receptors in the membrane of neighboring cells, and these receptors coordinate oscillating gene expression in the receiving cell (Fig. 4A). Without Delta-Notch signaling, the single cells' oscillations gradually lose synchrony. The plausibility

of this synchronization hypothesis has been studied by using GRN models showing that the Delta-Notch mechanism described above could keep neighboring cells oscillating in synchrony (26, 27).

Given the previously mentioned difficulty of determining GRN parameters from embryos (28), an alternative and complementary model formulation is to use an effective theory with variables that represent processes for which there is a particular interest or a possibility of experimental comparison. For the segmentation clock, this approach has been applied to investigate the synchronization hypothesis by using theories based on coupled phase oscillators (Fig. 4B). In a phase oscillator model, the variables corresponding to oscillating molecular species are substituted by a single variable: the phase of the oscillation cycle, which advances in time with a given intrinsic frequency. The effect of Delta-Notch signaling is captured by a coupling function that speeds up or slows down a cellular oscillator depending on the phase of neighboring cells. Phase oscillator models do not offer direct insight about dynamics of individual molecular species, but their simplicity allows powerful insights about system-level dynamics from paper-and-pencil analysis. Furthermore, they allow a direct fit to experimental data relying on a few coarse-grained parameters such as the period of the oscillations (29).

Using a phase oscillator model, the synchronization problem of the segmentation clock was formulated as a competition between noise and the intercellular coupling that keeps cells in synchrony (30). Together with quantitative experimental disruptions of Notch signaling in zebrafish, the model allowed estimation of the noise level and coupling strength relevant for the tissue-level synchrony of the clock. Coupling involves the new synthesis of Delta ligand every cycle (Fig. 4A), and to represent the anticipated duration of the ligand-receptor mechanism, Morelli *et al.* (29) included explicit

time delays in the coupling function of a phase oscillator model. This delayed coupling theory made the prediction that changing the coupling strength could change the clock period and motivated the study of the dynamics of Notch mutants. Quantitative time-lapse measurements of segmentation period and analysis of clock gene-expression patterns in mutants matched the theoretical predictions and so identified the first candidates for segmentation clock period mutants (31).

Although these studies have revealed some surprising insights into the segmentation clock's dynamics, most quantitative data used to test models have come from static images (28, 31), and the desynchronization of the clock has not been directly observed. The advent of new techniques to observe cyclic gene expression in vivo (32) will allow key assumptions of the existing models to be directly tested.

Patterning with Mechanical Deformations

We complete our roster of patterning mechanisms with a recently discovered case driven by tissue deformations. An apparently simple behavior for an epithelial sheet is to elongate along one axis while shrinking along the orthogonal axis. During *Drosophila* development, the wing blade epithelium stretches into the familiar elongate wing shape, and each of the hairs protruding from the wing cells points distally—an example of planar cell polarity (PCP) patterning (Fig. 5A). Although proximodistal gradients of PCP pathway components have been observed, they are not sufficient to produce the final wing hair polarity (33). Examination of cell shapes and trajectories from time-lapse movies shows that sharp contraction of the neighboring hinge region exerts anisotropic tension on the wing blade (34). Over a period of 15 hours, the blade deforms with a shear gradient arising from the cellular flow in the tissue.

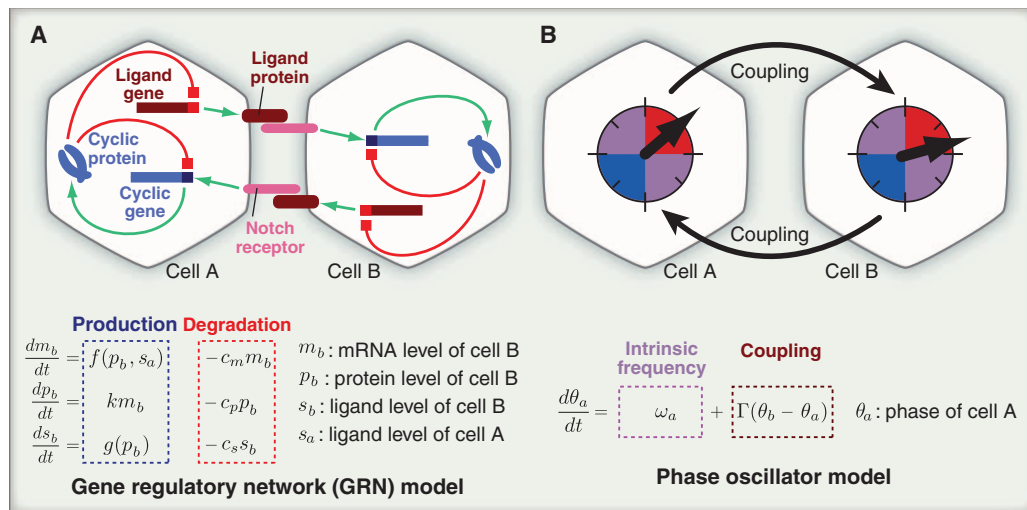


Fig. 4. Patterning with genetic oscillations. (A) Cyclic gene expression oscillates in individual cells because of a negative feedback loop, and oscillations are coupled to neighbor cells through the Notch pathway. **(B)** The mutual effects of cellular oscillators can be described by models of coupled phase oscillators.

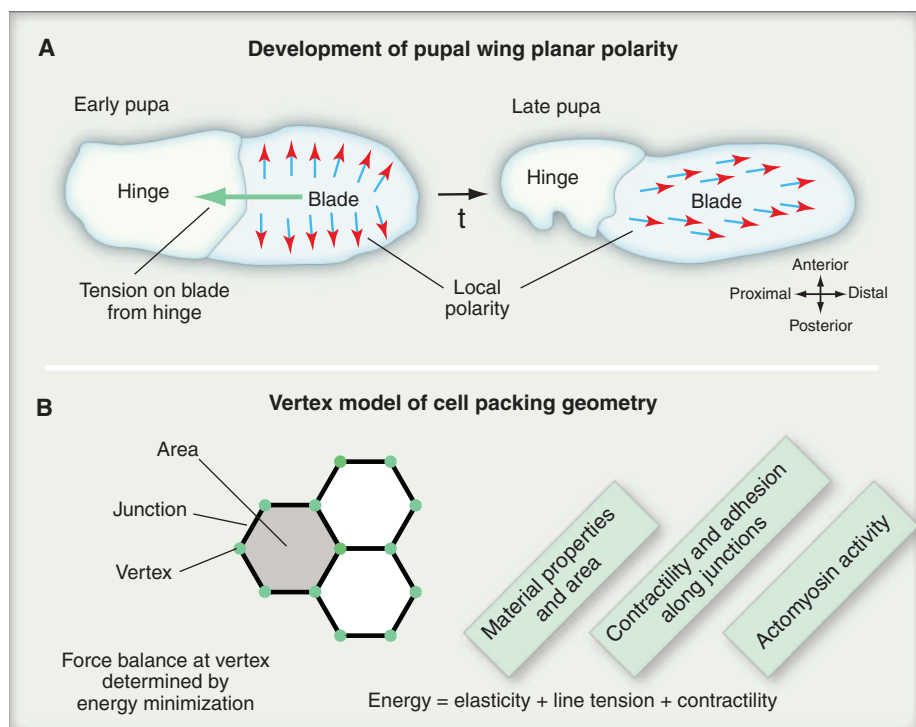


Fig. 5. Patterning by mechanical deformation. **(A)** Overview of *Drosophila* wing development during pupariation, when the wing blade elongates and proximo-distal planar polarity is established. **(B)** Schematic of the vertex model used to calculate stable cell-packing geometries.

Aigouy *et al.* explored the role of tissue shear in aligning the axis of cellular polarity with the proximo-distal axis of the wing blade by formulating a 2D vertex model of epithelial cell shape (Fig. 5B) (35), incorporating an effective description of the local recruitment of complementary PCP molecules to apposing cell boundaries (34). This new model predicts that polarity is reoriented by local rotation and cell flow-induced shear. Simulations show that shear associated with oriented cell division, proximo-distal cell elongation, and cell rearrangement also contribute to the alignment of cell polarity with the long axis of the wing. Future work can investigate how the 3D baso-lateral surfaces of the epithelial cells in the wing affect this description, and how the PCP protein complexes involved dynamically reorganize during cellular rearrangement. Thus, remarkably the final planar cell polarity of the completed wing may be a direct consequence of the externally applied stresses responsible for its extension, via simple physical rules such as those that determine molecular polarity in liquid crystals (36).

In this Review, we have mainly discussed chemical aspects of pattern formation as separate from downstream mechanics of morphogenesis (37, 38). Turing already wondered whether a closer linkage might be at work (13), and it seems timely to reconsider development as having integrated mechanochemical aspects (39). For example, motivated by recent findings on cell cortex dynamics in the nematode *Caenorhabditis* (40), Bois *et al.* studied pattern formation in an active fluid in which

mechanical contraction causes the flow of reactive chemical species (41). This theoretical analysis showed that an active fluid extends the parameter space in which classical Turing systems generate spatial patterns. To what extent continuous feedback between chemical and mechanical processes also underlies tissue-level phenomena in development is not yet clear, but it may be widespread.

Outlook

With the wide range of approaches in use, how should the developmental biologist select the appropriate modeling and computational methods? And where should the computational scientist dig for interesting problems in the vast field of developmental biology? Previous reviews have given multiple examples and advice (1–5). Here, we argue that the first step is key: The level of description and model type should be matched to the best available data. The data should be quantitative, accurate, and precise, and the model should make falsifiable predictions. Although some researchers are fluent in both domains, most often a successful computational approach to developmental biology will involve a long-term dialogue between experts across disciplinary boundaries. As advances in imaging and molecular methods increase experimental resolution and complexity, corresponding theoretical and computational developments will be required to assemble the puzzle. This co-dependence should generate a wealth of new opportunities for geeks and nerds alike.

References and Notes

1. A. C. Oates, N. Gorfinkel, M. González-Gaitán, C. P. Heisenberg, *Nat. Rev. Genet.* **10**, 517 (2009).
2. J. Lewis, *Science* **322**, 399 (2008).
3. G. T. Reeves, C. B. Muratov, T. Schüpbach, S. Y. Shvartsman, *Dev. Cell* **11**, 289 (2006).
4. C. J. Tomlin, J. D. Axelrod, *Nat. Rev. Genet.* **8**, 331 (2007).
5. S. Roth, *Dev. Genes Evol.* **221**, 255 (2011).
6. L. Wolpert, *J. Theor. Biol.* **25**, 1 (1969).
7. S. C. Little, G. Tkačik, T. B. Kneeland, E. F. Wieschaus, T. Gregor, *PLoS Biol.* **9**, e1000596 (2011).
8. Manu *et al.*, *PLoS Biol.* **7**, e1000049 (2009).
9. Manu *et al.*, *PLOS Comput. Biol.* **5**, e1000303 (2009).
10. S. H. Strogatz, *Nonlinear Dynamics and Chaos: With Applications to Physics, Biology, Chemistry, and Engineering* (Westview, Boulder, CO, 1994).
11. T. Gregor, E. F. Wieschaus, A. P. McGregor, W. Bialek, D. W. Tank, *Cell* **130**, 141 (2007).
12. G. Tkačik, A. M. Walczak, *J. Phys. Condens. Matter* **23**, 153102 (2011).
13. A. M. Turing, *Philos. Trans. R. Soc. London Ser. B* **237**, 37 (1952).
14. H. Meinhardt, *Models of Biological Pattern Formation* (Academic Press, London, 1982).
15. J. D. Murray, *Mathematical Biology* (Springer Verlag, Berlin, 2003).
16. M. Akam, *Nature* **341**, 282 (1989).
17. A. D. Economou *et al.*, *Nat. Genet.* **44**, 348 (2012).
18. M. V. Plikus *et al.*, *Science* **332**, 586 (2011).
19. A. Kondo, R. Asai, *Nature* **376**, 765 (1995).
20. A. Nakamasu, G. Takahashi, A. Kanbe, S. Kondo, *Proc. Natl. Acad. Sci. U.S.A.* **106**, 8429 (2009).
21. M. Inaba, H. Yamanaka, S. Kondo, *Science* **335**, 677 (2012).
22. J. Cooke, E. C. Zeeman, *J. Theor. Biol.* **58**, 455 (1976).
23. I. Palmerim, D. Henrique, D. Ish-Horowitz, O. Pourquie, *Cell* **91**, 639 (1997).
24. A. C. Oates, L. G. Morelli, S. Ares, *Development* **139**, 625 (2012).
25. Y. J. Jiang *et al.*, *Nature* **408**, 475 (2000).
26. J. Lewis, *Curr. Biol.* **13**, 1398 (2003).
27. K. Uriu, Y. Morishita, Y. Iwasa, *Proc. Natl. Acad. Sci. U.S.A.* **107**, 4979 (2010).
28. F. Giudicelli, E. M. Ozbudak, G. J. Wright, J. Lewis, *PLoS Biol.* **5**, e150 (2007).
29. L. G. Morelli *et al.*, *HFSP J.* **3**, 55 (2009).
30. I. H. Riedel-Kruse, C. Müller, A. C. Oates, *Science* **317**, 1911 (2007).
31. L. Herrgen *et al.*, *Curr. Biol.* **20**, 1244 (2010).
32. Y. Niwa *et al.*, *Genes Dev.* **25**, 1115 (2011).
33. D. Ma *et al.*, *Proc. Natl. Acad. Sci. U.S.A.* **105**, 18800 (2008).
34. B. Aigouy *et al.*, *Cell* **142**, 773 (2010).
35. R. Farhadifar, J. C. Röper, B. Aigouy, S. Eaton, F. Jülicher, *Curr. Biol.* **17**, 2095 (2007).
36. J. F. Joanny, F. Jülicher, K. Kruse, J. Prost, *New J. Phys.* **9**, 422 (2007).
37. N. Gorfinkel, S. Schamborg, G. B. Blanchard, *Genesis* **49**, 522 (2011).
38. S. M. Trier, L. A. Davidson, *Curr. Opin. Genet. Dev.* **21**, 664 (2011).
39. J. Howard, S. W. Grill, J. S. Bois, *Nat. Rev. Mol. Cell Biol.* **12**, 392 (2011).
40. M. Mayer, M. Depken, J. S. Bois, F. Jülicher, S. W. Grill, *Nature* **467**, 617 (2010).
41. J. S. Bois, F. Jülicher, S. W. Grill, *Phys. Rev. Lett.* **106**, 028103 (2011).

Acknowledgments: We thank F. Jülicher, C.-P. Heisenberg, S. Grill, P. R. ten Wolde, T. Bollenbach, P. Formosa-Jordan, and members of the Oates and Jülicher groups for discussion and critical comments. This work was supported by the Max Planck Society and the European Research Council (ERC) under the European Communities Seventh Framework Programme (FP7/2007-2013)/ERC grant 207634. K.U. is supported by the Japan Society for the Promotion of Science for Young Scientists. S.A. acknowledges funding from CSIC through the "Junta para la Ampliación de Estudios" program (JAEDOC014, 2010 call) co-funded by the European Social Fund, and from Ministerio de Ciencia e Innovación (Spain) through MOSAICO.

10.1126/science.1215478

A Fine-Scale Chimpanzee Genetic Map from Population Sequencing

Adam Auton,^{1,2*} Adi Fladel-Alon,^{3*} Susanne Pfeifer,^{4*} Oliver Venn,^{1*} Laure Ségurel,^{3,5} Teresa Street,⁴ Ellen M. Leffler,³ Rory Bowden,^{1,4,6} Ivy Aneas,³ John Broxholme,¹ Peter Humburg,¹ Zamin Iqbal,¹ Gerton Lunter,¹ Julian Maller,^{1,4} Ryan D. Hernandez,⁷ Cord Melton,³ Aarti Venkat,^{3,5} Marcelo A. Nobrega,³ Ronald Bontrop,⁸ Simon Myers,^{1,4} Peter Donnelly,^{1,4†} Molly Przeworski,^{3,5,9†} Gil McVean^{1,4‡}

To study the evolution of recombination rates in apes, we developed methodology to construct a fine-scale genetic map from high-throughput sequence data from 10 Western chimpanzees, *Pan troglodytes verus*. Compared to the human genetic map, broad-scale recombination rates tend to be conserved, but with exceptions, particularly in regions of chromosomal rearrangements and around the site of ancestral fusion in human chromosome 2. At fine scales, chimpanzee recombination is dominated by hotspots, which show no overlap with those of humans even though rates are similarly elevated around CpG islands and decreased within genes. The hotspot-specifying protein PRDM9 shows extensive variation among Western chimpanzees, and there is little evidence that any sequence motifs are enriched in hotspots. The contrasting locations of hotspots provide a natural experiment, which demonstrates the impact of recombination on base composition.

Multiple factors are likely to influence recombination rate, from the scales of individual hotspots to entire chromosomes. Evidence as to the nature and importance of such factors can potentially be obtained by studying the evolution of recombination rates at different scales (1). For example, previous studies of localized regions suggest that recombination hotspots are typically not shared between humans and chimpanzees (2–6), likely due to the function of the zinc-finger protein PRDM9 (2, 7, 8), which binds motifs associated with hotspot activity (7, 9) and is highly diverged between the human and chimpanzee reference genomes (2, 10). In humans, sequence variation within the PRDM9 zinc-finger array leads to differential activity at both allelic and nonallelic cross-over hotspots (7, 11, 12), and alleles found only in individuals of African ancestry lead to population-specific hotspots in patterns of both linkage disequilibrium (LD) and admixture (13).

However, to assess whether different classes of hotspot evolve in different ways, or to study recombination rate evolution over broader scales, requires genome-wide fine-scale genetic maps, which have only been generated for humans (13–16) and several distantly related model species including mice (17) and yeast (18, 19). Experimental techniques for identifying recombination events require either extensive pedigree data (15) or molecular characterization of meiotic cells (17–19), which are impractical for many species of interest. Methods for estimating recombination rates from single-nucleotide polymorphism (SNP) data (20, 21) have been validated at both broad and fine scales (14, 20), but there remains a gap for species without SNP arrays (i.e., most species). Hence, we set out to develop approaches based on sequence data, which, if successful, potentially open the possibility of producing genetic maps for many species.

Constructing a fine-scale chimpanzee genetic map from population sequencing. The genomes of 10 unrelated Western chimpanzees, *Pan troglodytes verus*, were sequenced (average $9.1\times$ coverage; table S1). Variants and haplotypes were inferred in a manner similar to that inferred for the 1000 Genomes Project (22, 23). Across the autosomes, we identified 5.3 million SNPs with a false-discovery rate of less than 3% (tables S2 and S3 and fig. S1). With 85% power to detect variant alleles present more than once in the sample (fig. S2) and >97% genotype accuracy (23), these data enable the construction of a high-resolution genetic map.

A major challenge in estimating genetic maps from sequence data is that erroneous, misassembled, or incorrectly genotyped genetic variants may mimic the effects of recombination. Initial maps estimated from variation data by existing meth-

ods (20) were dominated by large and artefactual increases in genetic distance (fig. S3) caused by clusters of false-positive SNP calls, often in large repeats that are systematically underrepresented in the chimpanzee reference genome (fig. S4). Most of these SNPs do not fail standard filters; hence, we developed regional filtering strategies (23). To validate the protocol and to estimate the sampling variance, we performed the same analyses on 10 human samples each from populations of European (CEU) and African (YRI) ancestry from the 1000 Genomes Project (22, 23). Genetic maps estimated for the human data sets showed strong correlations to previously generated LD-based maps, enabling us to quantify map quality (tables S4 and S5 and fig. S5) (16, 23). Hotspots estimated in the human data are concordant with previously described peaks in recombination rate (fig. S6). Moreover, we found a strong correlation between rates estimated in this study and from limited genomic regions in a larger sample of Western chimpanzees (5) ($r = 0.67$ at 20 kb; fig. S7). We conclude that sequencing data from only 10 individuals gives sufficient power to identify hotspots and estimate recombination rates at broad and even fine scales. For comparative analysis, we aligned genetic maps from human and chimpanzee over 2.5 Gb of synteny, 90% of the assembled genomes (fig. S8).

Broad-scale recombination rates. At the level of entire chromosomes, recombination rates were found to be very similar in humans and chimpanzees (fig. S9), with the exception of chromosome 2, discussed below. Even at the megabase scale, strong similarities emerge between human and chimpanzee rates, particularly driven by subtelomeric rate increase in both species (Fig. 1A). Yet we also found regions with substantial divergence (Fig. 1B). Notably, inverted regions showed a lower correlation in rate than noninverted regions (Fig. 1C and fig. S10), despite causing no systematic change in mean rate, indicating that chromosomal rearrangements often result in broad-scale changes in recombination rate. Change in distance to the telomere is a major significant factor (table S6; $P = 4 \times 10^{-9}$), with regions that move closer to the telomere increasing in rate. All except one of the inverted regions are pericentric; hence, the effect is not due to changes in proximity to the centromere.

The most notable change in broad-scale recombination rate is between the short arms of chimpanzee chromosome 2a and 2b and the orthologous regions in human chromosome 2, which originated from a telomeric fusion event in the human ancestral lineage (24) and which provides a natural experiment to explore the effect of chromosomal organization on recombination (Fig. 1D). We found that whereas the subtelomeric regions of chromosome 2a and 2b in chimpanzee show high recombination rates, the rate over the syntenic region in humans is suppressed by nearly threefold, and overall, the genetic map length of the fused chromosome is reduced by 20%. The

¹Wellcome Trust Centre for Human Genetics, Roosevelt Drive, Oxford OX3 7BN, UK. ²Department of Genetics, Albert Einstein College of Medicine, Bronx, New York, NY 10461, USA. ³Department of Human Genetics, University of Chicago, Chicago, IL 60637, USA. ⁴Department of Statistics, 1 South Parks Road, University of Oxford, Oxford OX1 3TG, UK. ⁵Howard Hughes Medical Institute, University of Chicago, Chicago, IL 60637, USA. ⁶Oxford Biomedical Research Centre, Nuffield Department of Medicine, University of Oxford, Oxford OX3 9DU, UK. ⁷Department of Bioengineering and Therapeutic Sciences, University of California, San Francisco, CA 94143–0912, USA. ⁸Department of Comparative Genetics and Refinement, Biomedical Primate Research Center, Lange Kleiweg 139 2288 GJ, Rijswijk, Netherlands. ⁹Department of Ecology and Evolution, University of Chicago, Chicago, IL 60637, USA.

*These authors contributed equally to the project.

†These authors jointly supervised the project.

‡To whom correspondence should be addressed. E-mail: mcvean@well.ox.ac.uk

extent to which recombination events are concentrated within the fused region is no different than in the unfused regions (fig. S11), indicating that the change in broad-scale rates was not ac-

complished by specifically eliminating cross-over events at hotspots. Although less pronounced, regions within structurally conserved chromosomes can also show

large changes in rate between species (Fig. 1E; 1-Mb correlation between human and chimpanzee maps in conserved regions is 0.60). Using a linear model, we found that the strongest deter-

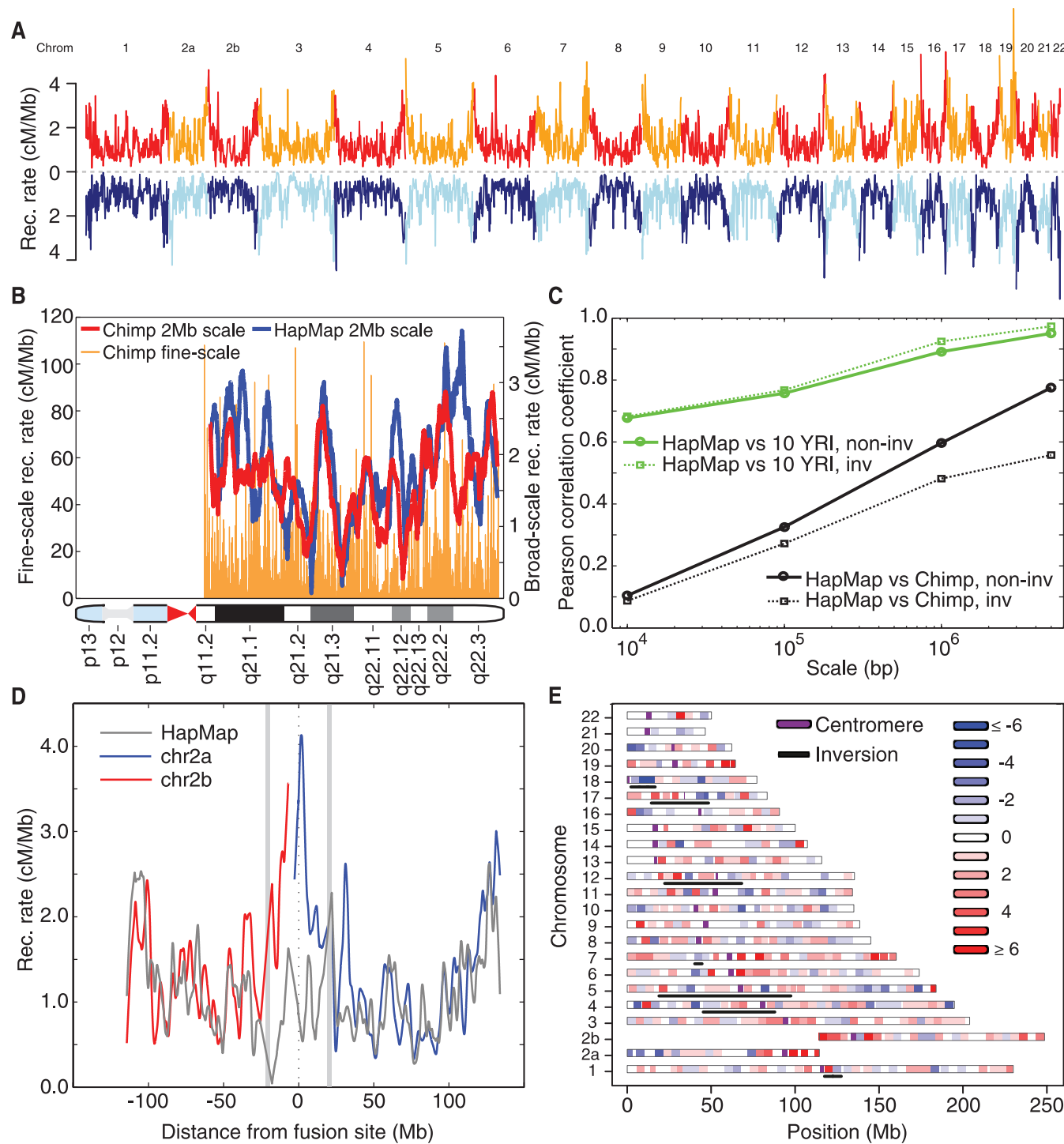


Fig. 1. Evolution of recombination rates between humans and chimpanzees. (A) Genome-wide comparison of recombination rates for chimpanzee (red and orange) and human (light and dark blue); rates were averaged over 1-Mb windows in regions of synteny. Unless otherwise stated, human rates are from the population-averaged HapMap genetic map (16). (B) Recombination rates estimated in human (blue) and chimpanzee (red) along chromosome 21q, averaged over 2-Mb intervals; fine-scale rates are shown behind. (C) Pearson correlation coefficients at different scales, estimated between the recombina-

tion rates of chimpanzee and HapMap YRI (black), and between HapMap YRI and ten 1000 Genomes YRI samples (green). Noninverted regions: solid lines; inverted regions: dotted lines. (D) Recombination rates in 2-Mb syntenic windows along chimpanzee chromosomes 2a and 2b (blue, red) and the corresponding syntenic region of human chromosome 2 (gray) derived from an ancient telomeric fusion. (E) Differences between chimpanzee and human recombination rates in 5-Mb syntenic windows across the genome. Regions involved in inversions are underlined.

minant of rate divergence in noninverted regions was base composition, such that although there is a substantial correlation between GC fraction and recombination rate in humans (partial $r = 0.51$ at 1Mb scale, with substantial variation between chromosomes, fig. S12), the correlation is much weaker in chimpanzees (partial $r = 0.11$; fig. S12). One consequence is that in low-GC regions (GC fraction <35%), the recombination rate in chimpanzees is more than 50% higher than in humans.

Fine-scale recombination rates. In humans, the PRDM9-bound 13–base pair (bp) motif is clearly detected only in a minority of hotspots (25), although activity at some hotspots with no clear match is PRDM9-dependent (7, 11). Nevertheless, there could exist different classes of hotspot in humans, some of which are PRDM9-independent and hence potentially shared between species. However, we found no evidence of sharing of recombination hotspots between species (Fig. 2, A and B, and fig. S13), even for human hotspots with no match to the PRDM9 motif (fig. S13).

Despite the absence of hotspot sharing, the landscape of recombination in the chimpanzee population is dominated by recombination hot-

spots to a similar extent as in African populations (Fig. 2C; though European populations show greater concentration of recombination). Moreover, the average fine-scale recombination rate profiles around genes and CpG islands are similar between species. Recombination increases on average by about 20% around transcription start and end sites and decreases on average by about 30% within the transcribed region (Fig. 3A). Such concordance suggests that features affecting chromatin state—for example, nucleosome occupancy, which is destabilized around CpG islands and promoters (26)—may similarly shape the propensity for recombination at these sites in humans and chimpanzees (17, 19, 27). Possibly reflecting a similar effect, we found recombination to be elevated around CpG islands in both species (Fig. 3B), although the effect is stronger in chimpanzees (increase of nearly 50% in rate relative to background compared to 15% in humans). The rate elevation around promoters in humans was found to be driven by genes that have a high rate of CpG methylation in sperm, but in chimpanzees it occurs around genes with low rates of sperm CpG methylation (fig. S14).

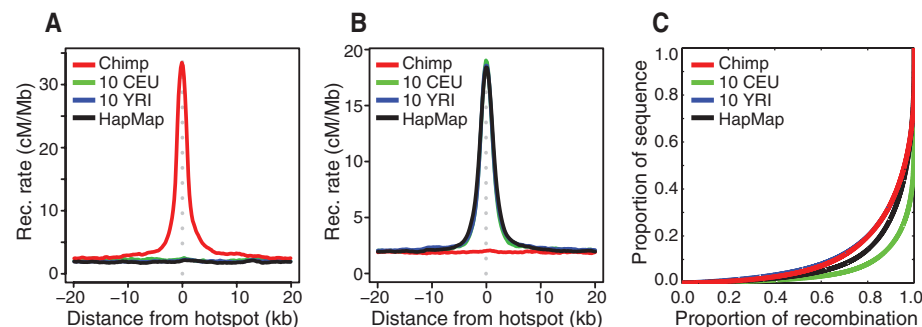


Fig. 2. (A) Recombination rates around hotspots identified in chimpanzee (red) at syntenic regions in CEU (green), YRI (blue), and HapMap (black). (B) As for (A) but around sites identified as recombination hotspots in 10 YRI; see also fig. S6. (C) The concentration of recombination rate in fine-scale genetic maps estimated from the chimpanzee and equivalent data from human populations of European (CEU) and African (YRI) ancestry (23). The higher degree of concentration seen in European relative to African populations likely reflects the lower diversity of PRDM9 alleles in the European population (11).

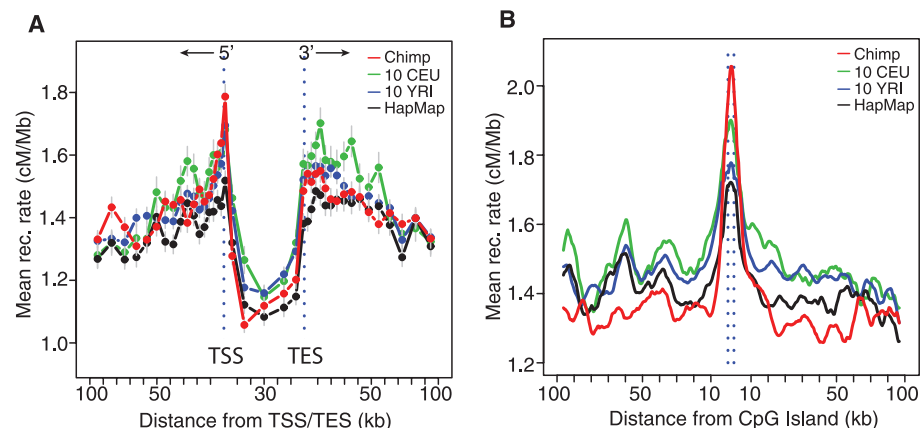


Fig. 3. The fine-scale profile of recombination rate variation around genomic features in chimpanzees and humans. (A) Average recombination rate as a function of distance to nearest transcription start site (TSS) and transcription end site (TES) in chimpanzee (red), YRI (blue), CEU (green), and HapMap (black). (B) Average recombination rate as a function of distance to nearest CpG island; colors as for (A). Dashed lines indicate start and end of elements; estimates were smoothed using a running average with a 7.5-kb window.

Extensive structural and sequence diversity in chimpanzee PRDM9. We sequenced 48 PRDM9 alleles from Western chimpanzees, including alleles from the 10 individuals for whom genome-wide data were collected. We found extensive variation in the number of zinc fingers and the identity of the DNA-contacting residues, with three common alleles of 6, 16, and 18 zinc fingers (Fig. 4A), a level of diversity greater than in human populations (Fig. 4A and fig. S15). Sequences from three Bonobo and one Eastern chimpanzee revealed a shared and hence potentially ancestral six-zinc-finger PRDM9 variant (Fig. 4A) not found in the Western samples, suggesting that Western allelic diversity may have arisen since the separation of the subspecies ~0.51 million years ago (28). Moreover, patterns of polymorphism among zinc fingers pointed to recurrent adaptive evolution of DNA-contacting residues, as seen in other mammalian species (10, 23).

In humans, using the same number of hotspots as detected in chimpanzees, we can identify the known motifs associated with hotspot activity (fig. S16). In Western chimpanzees, computationally predicted (23, 29) DNA-binding motifs for the different PRDM9 variants showed considerable overlap of submotifs (fig. S17). However, we found no evidence for local increases in recombination rate around any of the shared submotifs (Fig. 4C) or best matches to the predicted binding targets across the genome (23).

Moreover, a systematic analysis of repeat-element families showed no overall correlation in recombination-localizing activity between humans and chimpanzees (Fig. 5A). The strongest activating repeats in humans (LTR49, THE1A, and THE1B), which all contain the human PRDM9 A-allele 13-bp binding motif CCTCCCTNN-CCAC, suppress recombination in chimpanzees (Fig. 5B, top). A second class of elements, typically of low complexity (CT-rich, GA-rich, and G-rich), was found to be weakly activating in both species (Fig. 5B), whereas a few elements (e.g., LIPA2) suppress recombination in both species (Fig. 5b, middle right). Only a few elements [notably (GGAA)_n and MER92B elements] showed activation only in chimpanzees (Fig. 5b, bottom, and fig. S18). Among these and other repeats, we found that motifs with high GC fraction and CpG dinucleotide content lead to local rate increases in chimpanzees (table S7). For example, on Alu elements the motif CGGGCGC showed significant hotspot enrichment ($P_{\text{corrected}} = 2 \times 10^{-4}$, $RR = 1.2$), but the effect was better explained by CpG content (fig. S19).

We also carried out an exhaustive search for short DNA motifs enriched in nonrepeat DNA recombination hotspots relative to cold-spots, which identifies the known motifs CCTCCCT and CCCCACCC and related sequences in the samples of 10 humans (14) ($RR = 1.16$ and 1.28 , respectively; $P < 1 \times 10^{-10}$ after Bonferroni correction). In chimpanzees, the same approach only identifies two motifs, CGCG and CCCGGC, that are significantly enriched in chimpanzee hotspots

after Bonferroni correction (corrected $P = 0.0024$, $RR = 1.28$ and $P = 0.015$, $RR = 1.31$, respectively; table S8). Both motifs are typical of CpG islands. Overall, we could not identify any motif that was consistently activating in chimpanzees across multiple backgrounds (fig. S20).

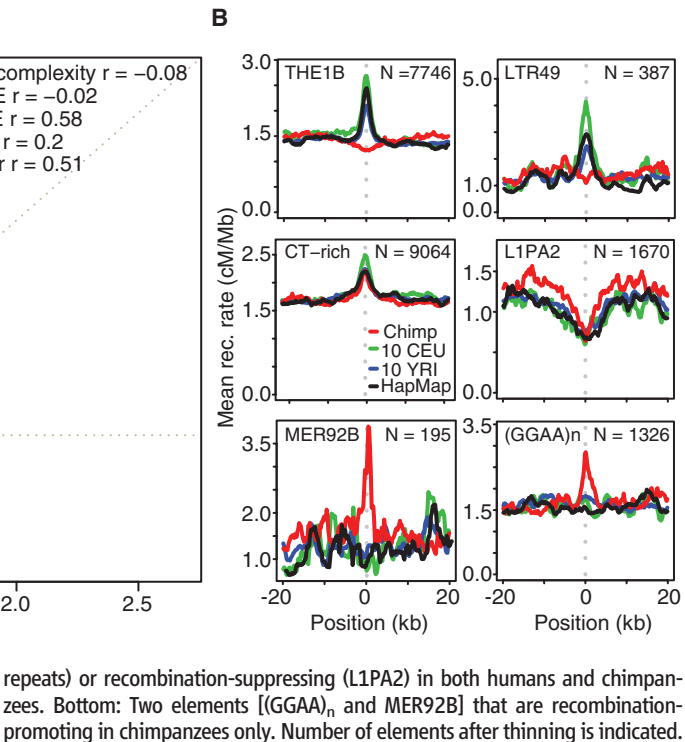
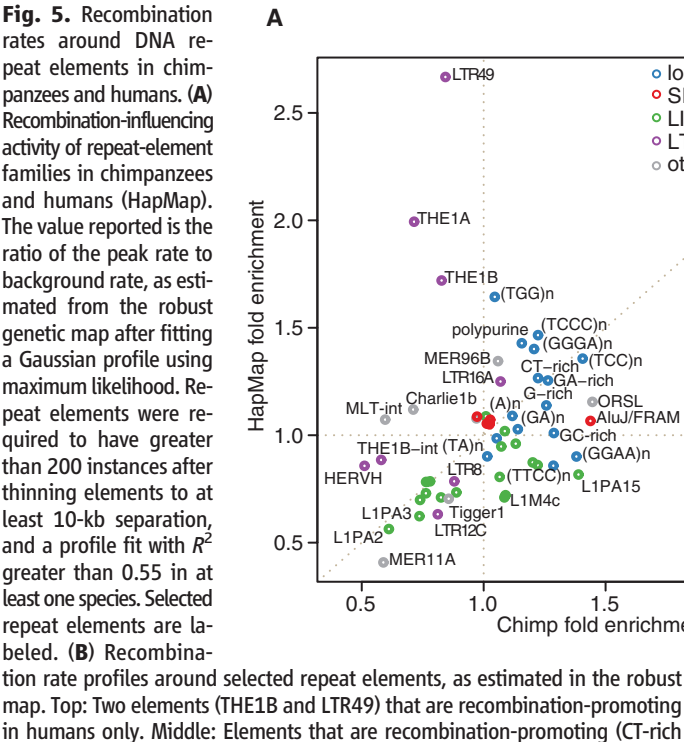
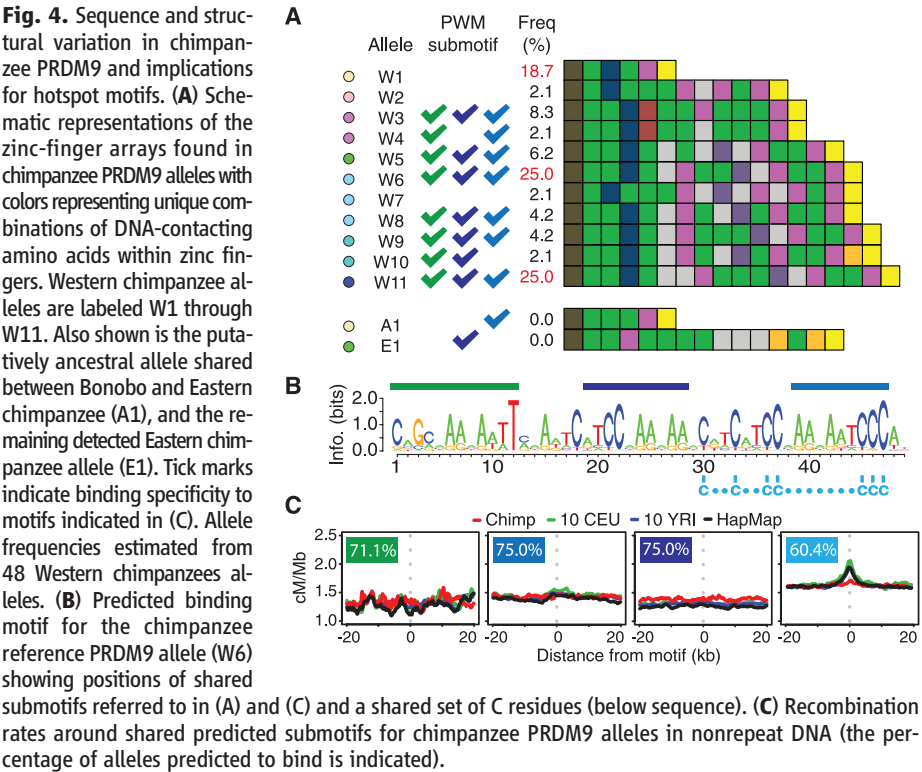
The influence of recombination on sequence evolution. Shifts in both local and broad-scale

patterns of recombination between humans and chimpanzees act as natural experiments that reveal the effect of recombination on patterns of molecular evolution while other factors, for example, gene density, remain similar. In particular, we can assess the ability of recombination to drive local increases in GC content through a preference for GC bases during mismatch repair within

gene conversion tracts (30, 31). Around human hotspots, we observed strong GC skew in both patterns of polymorphism (40% increase in GC skew at the hotspot center) and substitution (20% increase in GC skew), but only for mutations on the human lineage (Fig. 6A and fig. S21). In chimpanzees, we observed much weaker signals of GC bias (18% increase in GC skew at the hotspot center for polymorphisms compared to 10% increase for substitutions; Fig. 6B), despite comparable density and intensity for chimpanzee and human hotspots. These observations are consistent with a recent origin for hotspot locations in both species, and a more recent origin in chimpanzees.

At the megabase scale, we found that changes in the rate of recombination between species correlate with changes in GC bias in both substitutions and polymorphisms (Fig. 6C). The correlation was stronger in polymorphism ($r = 0.39$ in non-rearranged regions) than substitution ($r = 0.25$), consistent with the changes in broad-scale recombination being evolutionarily recent. We see stronger correlations in regions that have experienced chromosomal rearrangements, where the changes in recombination rate have typically been greater. The most pronounced changes are seen in the chromosome 2 fusion region, where the suppression of recombination in the regions syntenic to the short arms of chimpanzee chromosomes 2a and 2b has led to a large reduction in GC skew over megabase scales (32).

Discussion. Our study demonstrates how fine-scale genetic maps can be obtained by the analysis of patterns of genetic variation obtained from population sequencing. Studying humans and Western chimpanzees, we found no hotspot sharing between the two species, consistent with earlier



reports based on limited data (2–6). The complete lack of hotspot sharing is consistent with the hypothesis that in humans, PRDM9 plays a critical role in localizing cross-over activity at all hotspots, not just those that contain clear matches to previously identified motifs bound by PRDM9. Despite the marked shift in hotspot locations between the two species, we found that some fine-scale patterns, particularly the average profile of recombination rate around genes and CpG islands, remain similar, pointing to the importance of chromatin state in influencing where double-strand breaks occur (19) or to additional levels of control acting on broader scales (19, 33).

A notable difference between the species is that in chimpanzees no repeat elements, simple DNA motifs, or predicted PRDM9 binding sites are strongly or consistently associated with hot-

spot locations. There are three possible explanations. First, PRDM9 may have lost its role in specifying hotspot locations in chimpanzees, as has occurred in dogs, although we find no evidence for inactivating mutations (34). Second, PRDM9 alleles may each have similar specificity to target DNA sequences, but the substantial allelic diversity and their possibly recent origin may obscure signals for individual alleles. However, this hypothesis cannot explain why, when the density and strength of hotspots at the population level are similar in African populations and Western chimpanzees (Fig. 2c), we can recover known PRDM9-binding motifs in humans but no comparable motif in chimpanzees. Third, PRDM9 may play the same role as in humans and mice, but individual PRDM9 alleles may bind to a much greater variety of target sequences than do the pre-

dominant human alleles. If so, hotspot localization in chimpanzees may be more strongly driven by other factors, such as chromatin state. Whichever hypothesis is correct, one consequence is that, across the genome, no motif in chimpanzees will be strongly targeted for depletion by the inherent self-destructive drive of hotspots (though specific instances may be).

Our results also reveal the different processes that operate at fine and broad scales. At broad scales, we find substantial correlation in recombination rate between the species, which is disrupted by chromosomal rearrangement. However, even among conserved regions, less than 40% of the variance in chimpanzee recombination rate at 1 Mb can be explained by the human rate. Determining the factors that shape stasis and change in broad-scale recombination rates presents a key

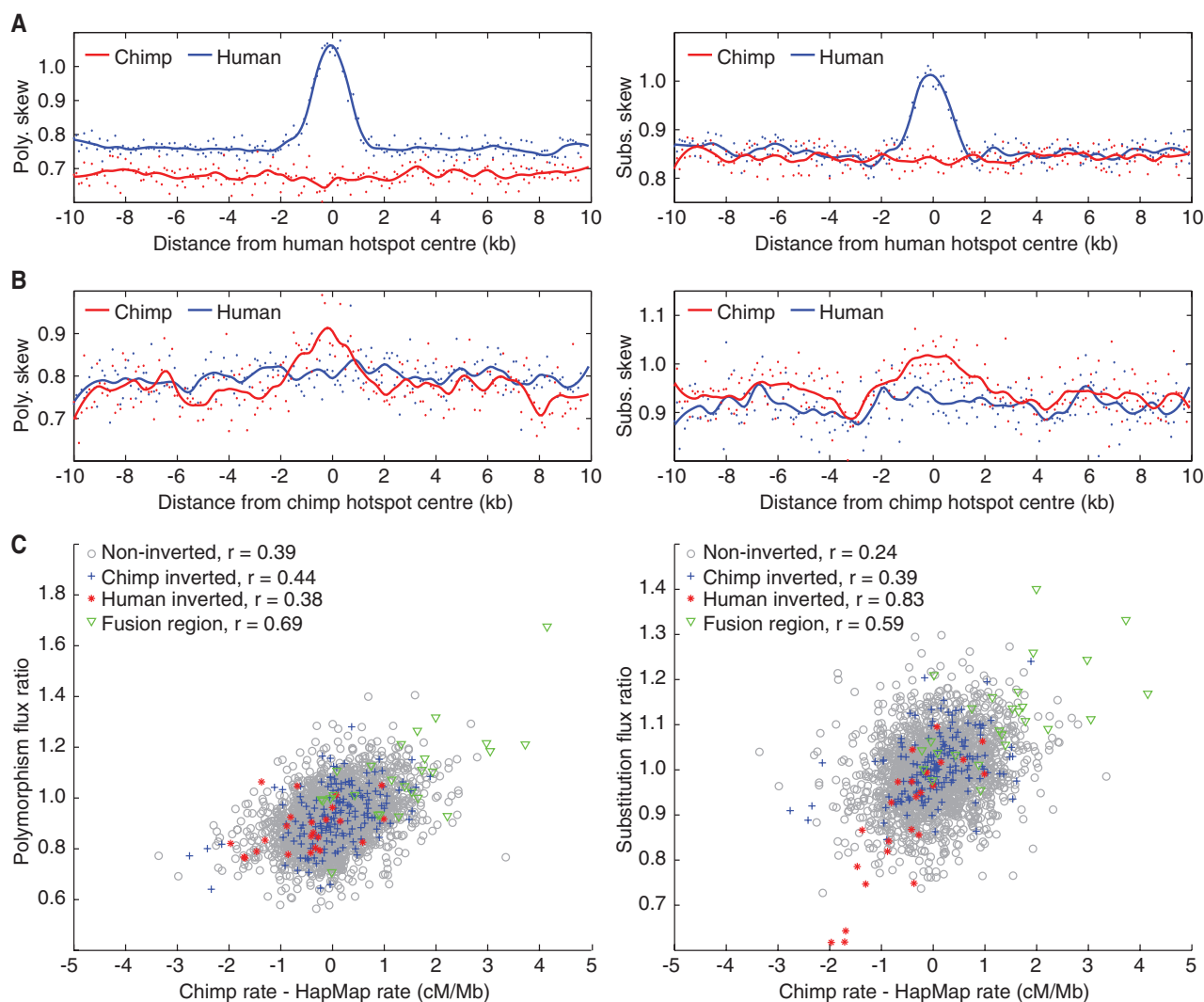


Fig. 6. The influence of broad- and fine-scale changes in recombination rate on GC-promoting mutations. **(A)** GC skew [defined as the ratio of the number of GC-increasing changes compared to GC-decreasing changes; see (23)] in both polymorphism (left) and substitutions (right). Estimates from mutations on the human lineage are indicated in blue, whereas those on the chimpanzee lineage are in red. Smoothed lines were estimated using loess. The observed increase in skew in humans is completely absent in chimpanzees. **(B)** As for (A), but around hotspots detected in chimpanzees. Although the

pattern of skew in chimpanzees is considerably weaker than for (A), no corresponding skew is observed in humans. **(C)** Broad-scale (1 Mb) effects of changes in recombination rate between chimpanzees and humans on patterns of GC skew in polymorphism (left) and substitution (right). Flux ratio is defined as the ratio of the GC skews in chimpanzees compared to humans. Chimpanzee recombination rate estimates are from the robust genetic map. Colors indicate different parts of the genome, with Pearson correlation coefficient indicated.

challenge in the study of recombination. A population sequencing approach, such as the one taken here, should enable further informative studies of recombination across a wide range of species.

References and Notes

- G. Coop, M. Przeworski, *Nat. Rev. Genet.* **8**, 23 (2007).
- S. Myers *et al.*, *Science* **327**, 876 (2010).
- S. E. Ptak *et al.*, *Nat. Genet.* **37**, 429 (2005).
- S. E. Ptak *et al.*, *PLoS Biol.* **2**, e155 (2004).
- W. Winckler *et al.*, *Science* **308**, 107 (2005).
- J. D. Wall, L. A. Frisse, R. R. Hudson, A. Di Rienzo, *Am. J. Hum. Genet.* **73**, 1330 (2003).
- F. Baudat *et al.*, *Science* **327**, 836 (2010).
- E. D. Parvanov, P. M. Petkov, K. Paigen, *Science* **327**, 835 (2010).
- C. Grey *et al.*, *PLoS Biol.* **9**, e1001176 (2011).
- P. L. Oliver *et al.*, *PLoS Genet.* **5**, e1000753 (2009).
- I. L. Berg *et al.*, *Nat. Genet.* **42**, 859 (2010).
- I. L. Berg *et al.*, *Proc. Natl. Acad. Sci. U.S.A.* **108**, 12378 (2011).
- A. G. Hinch *et al.*, *Nature* **476**, 170 (2011).
- S. Myers, L. Bottolo, C. Freeman, G. McVean, P. Donnelly, *Science* **310**, 321 (2005).
- A. Kong *et al.*, *Nature* **467**, 1099 (2010).
- International HapMap Consortium, *Nature* **449**, 851 (2007).
- F. Smagulova *et al.*, *Nature* **472**, 375 (2011).
- E. Mancera, R. Bourgon, A. Brozzi, W. Huber, L. M. Steinmetz, *Nature* **454**, 479 (2008).
- J. Pan *et al.*, *Cell* **144**, 719 (2011).
- G. A. McVean *et al.*, *Science* **304**, 581 (2004).
- M. P. Stumpf, G. A. McVean, *Nat. Rev. Genet.* **4**, 959 (2003).
- 1000 Genomes Project Consortium, *Nature* **467**, 1061 (2010).
- Detailed information on methods and analyses can be found in the supplementary materials available in Science Online.
- J. W. Ijdo, A. Baldini, D. C. Ward, S. T. Reeders, R. A. Wells, *Proc. Natl. Acad. Sci. U.S.A.* **88**, 9051 (1991).
- S. Myers, C. Freeman, A. Auton, P. Donnelly, G. McVean, *Nat. Genet.* **40**, 1124 (2008).
- V. R. Ramirez-Carrozzi *et al.*, *Cell* **138**, 114 (2009).
- T. D. Petes, *Nat. Rev. Genet.* **2**, 360 (2001).
- J. L. Caswell *et al.*, *PLoS Genet.* **4**, e1000057 (2008).
- A. V. Persikov, M. Singh, *Phys. Biol.* **8**, 035010 (2011).
- C. C. Spencer *et al.*, *PLoS Genet.* **2**, e148 (2006).
- S. Katzman, J. A. Capra, D. Haussler, K. S. Pollard, *Genome Biol. Evol.* **3**, 614 (2011).
- T. R. Dreszer, G. D. Wall, D. Haussler, K. S. Pollard, *Genome Res.* **17**, 1420 (2007).
- K. Paigen, P. Petkov, *Nat. Rev. Genet.* **11**, 221 (2010).
- E. Axelsson, M. T. Webster, A. Ratnakumar, C. P. Ponting, K. Lindblad-Toh; LUPA Consortium, *Genome Res.* **22**, 51 (2012).

Acknowledgments: This work was funded by NIH grants R01 GM83098 (to M.P.) and T32 GM007197 (to E.M.L.) and by Wellcome Trust grants 076113/E/04/Z (to P.D.), 086084/Z/08/Z (to G.M.), and 090532/Z/09/Z contribution to Core Facility. P.D. was supported in part by a Wolfson-Royal Society Merit Award. M.P. is supported by the Howard Hughes Medical Institute. O.V. is funded by a Wellcome Trust studentship (086786/Z/08/Z). We thank G. Sella, G. McVicker, members of the PPS labs, and reviewers for their comments and H. Thorogood and W. Czyz for assistance with *PRDM9* sequencing. Part of this work has been supported by EUPRIM-Net under the European Union contract RII3-026155 of the 6th Framework Programme. Data are available from <http://panmap.uchicago.edu>. Some primate samples used in this study are under a Material Transfer Agreement from the San Diego Zoo.

Supplementary Materials

www.sciencemag.org/cgi/content/full/science.1216872/DC1
Materials and Methods
Figs. S1 to S21
Tables S1 to S9
References (35–60)

21 November 2011; accepted 27 February 2012
Published online 15 March 2012;
10.1126/science.1216872

REPORTS

Observation of Skyrmions in a Multiferroic Material

S. Seki,^{1*} X. Z. Yu,² S. Ishiwata,¹ Y. Tokura^{1,2,3}

A magnetic skyrmion is a topologically stable particle-like object that appears as a vortex-like spin texture at the nanometer scale in a chiral-lattice magnet. Skyrmions have been observed in metallic materials, where they are controllable by electric currents. Here, we report the experimental discovery of magnetoelectric skyrmions in an insulating chiral-lattice magnet Cu_2OSeO_3 through Lorentz transmission electron microscopy and magnetic susceptibility measurements. We find that the skyrmion can magnetically induce electric polarization. The observed magnetoelectric coupling may potentially enable the manipulation of the skyrmion by an external electric field without losses due to joule heating.

Topological spin textures in solids are of great interest to future spin-electronic technology. One example is a magnetic skyrmion (1–3), a vortex-like spin-swirling object (Fig. 1H) with a typical size of 10 to 100 nm, recently observed in chiral-lattice magnets (4–7). Conduction electron flow with low current density can drive skyrmion motion, which in turn gives rise to the transverse electromotive force (8–10). Such electric controllability, as well as its particle-like nature with nanometric size, points

to potential application of skyrmions in high-density magnetic storage devices.

Another promising route to electric control of magnetism is through the usage of multiferroics, insulating materials characterized by both magnetic and dielectric orders (11). Recently, helical spin textures have been found to affect the symmetry of charge distribution and magnetically induce electric polarization (*P*) in compounds such as TbMnO_3 (12–14). Such coupling between ferroelectricity and magnetic structure enables versatile magnetoelectric response, such as the magnetic field (*H*) control of electric polarization direction (14) and the electric field (*E*) control of spin-chirality (15, 16), magnetic modulation vector (\vec{q}) (17), and magnetic domain distribution (18). Because the energy dissipation by applied *E* is negligible in insulators, this approach is energetically more efficient compared with the current-driven approach in metals or semiconductors.

In the noncentrosymmetric environment of a chiral lattice, the spin-exchange interactions are composed of two terms: symmetric $\vec{S}_i \cdot \vec{S}_j$ -like (e.g., ferromagnetic) and antisymmetric $\vec{S}_i \times \vec{S}_j$ -like, where \vec{S}_i and \vec{S}_j represent spins on neighboring sites. The antisymmetric exchange term, called Dzyaloshinskii-Moriya (D-M) interaction, stems from the relativistic spin-orbit interaction and tends to stabilize helical (mostly screwlike) spin texture with fixed handedness (spin chirality) against the simple ferromagnetic state. The skyrmions or their crystallized form are known to appear in a restricted window of magnetic fields and temperatures in chiral-lattice helimagnets as the intervening state between the helical and field-induced spin-collinear (ferromagnetic) states. The crystallized form of skyrmions has been experimentally detected in specific metallic alloys with B20 structure, such as MnSi (4), $\text{Fe}_{1-x}\text{Co}_x\text{Si}$ (5, 6), and FeGe (7). They all have a cubic crystal lattice with chiral space group $P2_13$, as well as the helimagnetic ground state formed as a result of the competition between the ferromagnetic exchange and D-M interactions (19). In bulk form, their magnetic phase diagram is characterized by the so-called A-phase, positioned within a narrow temperature (*T*) and magnetic field window just below the magnetic-ordering temperature (T_C) (20–22), where the formation of a triangular lattice of skyrmions is confirmed by small-angle neutron scattering experiments (4, 5). In each skyrmion, spins at the core (or edge) of the vortex orient antiparallel (or parallel) to the applied *H*. The real-space observation of skyrmion crystal (SkX) by Lorentz transmission electron microscopy (TEM) has been

¹Department of Applied Physics and Quantum Phase Electronics Center, University of Tokyo, Tokyo 113-8656, Japan.

²Cross-Correlated Materials Research Group and Correlated Electron Research Group, RIKEN Advanced Science Institute, Wako 351-0198, Japan. ³Multiferroics Project, Exploratory Research for Advanced Technology, Japan Science and Technology Agency, Tokyo 113-8656, Japan.

*To whom correspondence should be addressed. E-mail: seki@ap.t.u-tokyo.ac.jp

achieved for the thin-film form of the specimen (6, 7), in which SkX is found to be stabilized over a much wider T and H range than in bulk specimen. Because the existence of the SkX state has been confirmed only in conductive materials (4, 5, 7), the dielectric nature of this spin state remains unexplored.

The crystal structure of Cu_2OSeO_3 is characterized by the same space group (cubic and chiral) $P2_13$ as the B20 alloys, but with very different atom coordination (Fig. 1A) (23–25). Cu^{2+} (spin $S = 1/2$) sites are surrounded by either a square pyramid or a trigonal bipyramid of oxygen ligands, with the ratio of 3:1. Recent powder neutron diffraction (26) and nuclear magnetic resonance (27) studies suggested that a three-up, one-down type of ferrimagnetic spin arrangement is realized in the magnetic ground state below $T_c \sim 60$ K, where collinear spins align antiparallel among two inequivalent Cu^{2+} sites (Fig. 1B). The single crystal of Cu_2OSeO_3 has been grown by chemical vapor transport method (27).

To investigate the nanometric-scale modification of the magnetic structure, we performed

high-resolution Lorentz TEM imaging of a thin-film single crystal of Cu_2OSeO_3 with a thickness of ~ 100 nm. Combined with a magnetic transport-of-intensity equation calculation, this technique enables mapping the lateral magnetization distribution in real space (28). Under zero magnetic field for the (110) and (111) sample planes (Fig. 1, C and F, respectively), we observed the stripe patterns of the lateral magnetization, corresponding to a proper screw-spin order with a modulation period of ~ 50 nm, where spins rotate within a plane perpendicular to the magnetic modulation vector $q \parallel \langle 110 \rangle$. These results are consistent with the existence of a finite D-M interaction and reveal that the magnetic ground state of Cu_2OSeO_3 is helically modulated. Note that the modulation period (~ 50 nm) of the magnetic moment is long enough as compared with the Cu-Cu atomic distance, being compatible with the local ferrimagnetic spin arrangement. With $H \sim 800$ Oe applied normal to the sample plane, the formation of a triangular lattice of skyrmions is observed both for the (110) and (111) planes (Fig. 1, D and G). Here, the diameter of a skyrmion is identical to

the modulation period of the helical spin state. Every skyrmion in the SkX state has a uniform spin chirality (spin-swirling direction), and three magnetic modulation vectors always lie perpendicular to the applied H . These features are consistent with the recent report for the SkX state in B20 alloys (4, 6, 7). Based on these real-space observations, Fig. 2B shows the H - T phase diagram under $H \parallel [111]$ for thin-film Cu_2OSeO_3 determined through the measurement of skyrmion density. Skyrmions disappear for $H > 1800$ Oe, which implies transition into the collinear (ferrimagnetic) spin state. Typical spin textures for selected (T , H) points are displayed in Fig. 2, D to K.

In B20 alloys, the stability of the SkX state essentially depends on the dimensions of the system: Whereas the SkX is stable over a wide T and H range in the two-dimensional (2D) limit (thin film), it shrinks into the narrow A-phase region in the 3D limit (bulk) (6, 7). To investigate the effects of dimensionality in our system, we studied the magnetic behavior of a bulk single crystal of Cu_2OSeO_3 for $H \parallel [111]$. Figure 3, A and B, indicate the H -dependence of magnetization M and ac magnetic susceptibility χ' measured at 5 K. Around 600 Oe, the M profile shows a steplike anomaly, and χ' also exhibits a clear kink structure. Above 1800 Oe, M -value saturates at $M \sim 0.5\mu_B/\text{Cu}^{2+}$ (where μ_B is the Bohr magneton), which suggests the transition into the three-up, one-down ferrimagnetic state (Fig. 1B) (25, 26, 29). The same measurements are also performed at 55 (Fig. 3, D and E) and 57 K (Fig. 3, G and H), and the obtained χ' profiles indicate that the above two magnetic transitions still take place at both temperatures. Notably, we found an additional dip anomaly for $200 \text{ Oe} < H < 400 \text{ Oe}$ in the χ' profile at 57 K, which has not been identified previously. The H - T phase diagram for the bulk crystal of Cu_2OSeO_3 obtained through H and T scans of M and χ' is summarized in Fig. 2, A and C. The overall features of the magnetic phase diagram, including the existence of a narrow A phase characterized by the dip anomaly in the χ' profile, bear close resemblance to those reported for B20 alloys (21, 30). Considering the reported dimension dependence for the stability of the SkX state in B20 alloys (6, 7), we conclude that the observed A phase represents the SkX state in the bulk form of Cu_2OSeO_3 . The ground state of the bulk Cu_2OSeO_3 can be assigned to be helimagnetic, but with multiple q domains due to the high symmetry of the cubic lattice. Here, the application of H leads to the formation of a single q -domain state with $H \parallel q$ keeping the proper screw-spin texture, as antiferromagnetically aligned spins tend to lie perpendicular to the applied H . Such rearrangement of a q vector within the helimagnetic state explains the steplike anomaly of the M profile (Fig. 3A) and the enhancement of the χ' value (Fig. 3B) observed around 600 Oe at 5 K, as in the case of B20 (e.g., $\text{Fe}_{1-x}\text{Co}_x\text{Si}$) compounds (22).

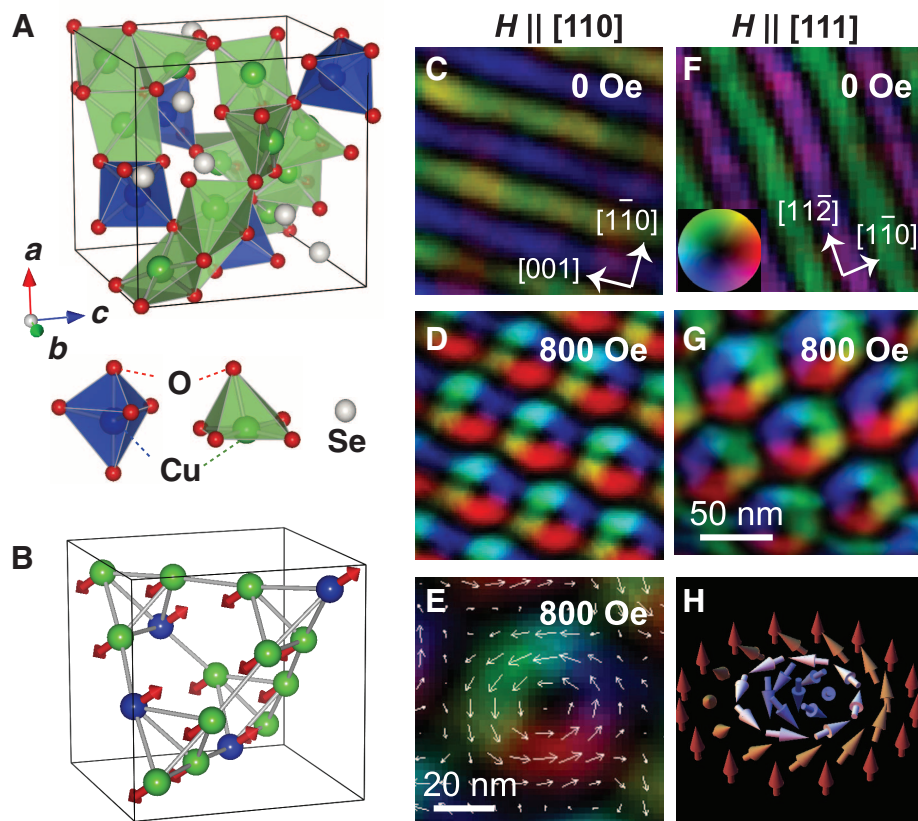


Fig. 1. (A) Crystal structure of Cu_2OSeO_3 , characterized by two inequivalent Cu^{2+} sites with different oxygen coordination. (B) Ferrimagnetic spin arrangement on Cu^{2+} sites. (C to G) Lateral magnetization distribution map for a thin-film (~ 100 -nm-thick) sample of Cu_2OSeO_3 , obtained through the analysis of Lorentz TEM data taken at 5 K. The color wheel in the bottom-left corner of (F) shows the direction (hue) and relative magnitude (brightness) of the lateral magnetization. Panels (C) and (D), as well as (F) and (G), represent images for the (110) and (111) plane, respectively, and a magnetic field is applied normal to the observed sample plane. In both cases, proper screw-spin texture appears for zero magnetic field, whereas a skyrmion lattice with the identical spin chirality is formed for $H = 800$ Oe. A magnified view of (D) is shown in (E), where white arrows represent the magnetization direction. (H) Schematic illustration of a single magnetic skyrmion.

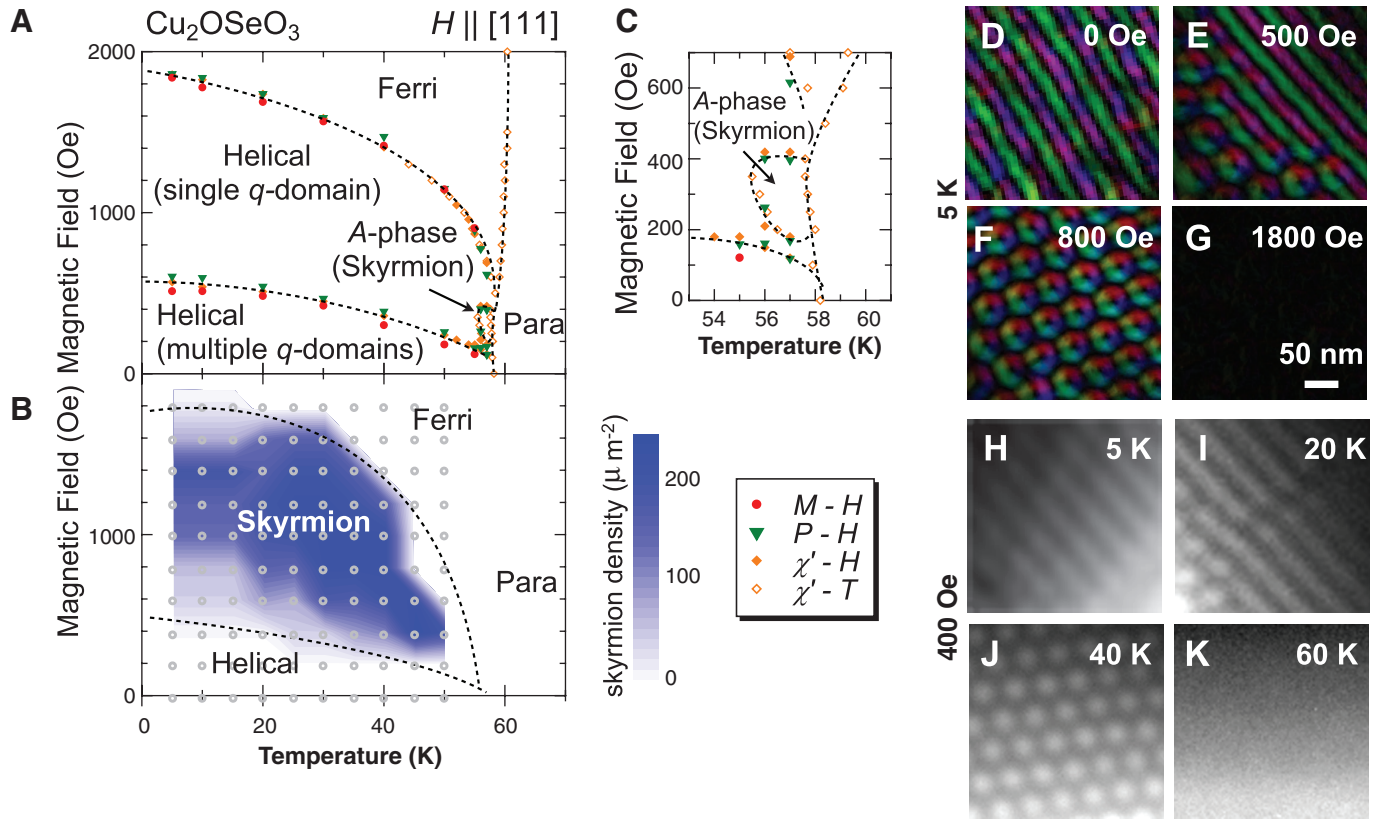


Fig. 2. Magnetic phase diagram under $H \parallel [111]$, deduced for (A) bulk and (B) thin-film forms of Cu_2OSeO_3 , respectively. The former is determined by temperature (T) and magnetic-field (H) scans of magnetization (M), electric polarization (P), and ac magnetic susceptibility (χ'), and the latter by the measurement of skyrmion density through Lorentz TEM imaging at selected data points (small gray circles). (C)

Magnified view of (A) near the A-phase (skyrmion crystal phase) region. (D to G) Magnetic field dependence of lateral magnetization distribution at 5 K with the same color wheel mapping as in Fig. 1, where a magnetic field is applied normal to the (111) thin film. (H to K) Temperature dependence of the magnetic domain configuration (underfocused Lorentz TEM images) with $H = 400$ Oe.

Cu_2OSeO_3 has recently been reported to show small anomalies in the dielectric constant accompanied with magnetic transitions (26, 31). To fully understand the magnetoelectric response in this material, we performed the electric polarization measurement for each magnetic phase, focusing on the $[111]$ component of the electric polarization ($P_{[111]}$) under $H \parallel [111]$. Figure 3C indicates the magnetic field dependence of $P_{[111]}$ at 5 K, measured after cooling at zero E and H . In the helimagnetic phase with multiple q domains (denoted as h'), $P_{[111]}$ remains zero even under finite H (<400 Oe). Upon the transition into the single q -domain helimagnetic state (denoted as h) around 600 Oe, $P_{[111]}$ first takes a nonzero negative value but then changes its sign as H is further increased. In the ferrimagnetic state (denoted as f), $P_{[111]}$ saturates at a positive value. The reversal of the H direction gives the same sign as that of $P_{[111]}$. In general, application of H induces the continuous deformation of spin texture from proper screw to conical, and finally to collinear (that is, ferrimagnetic) (Fig. 4A). The variation of $P_{[111]}$ with $H \parallel [111]$ appears to be well scaled with the relation that $P_{[111]} = P_0 + \beta M^2$ (where P_0 and β are the fitting parameters) (red dashed line in Fig. 3C), except for the low- H region where P remains zero probably due to the cancellation of P averaged over different q domains.

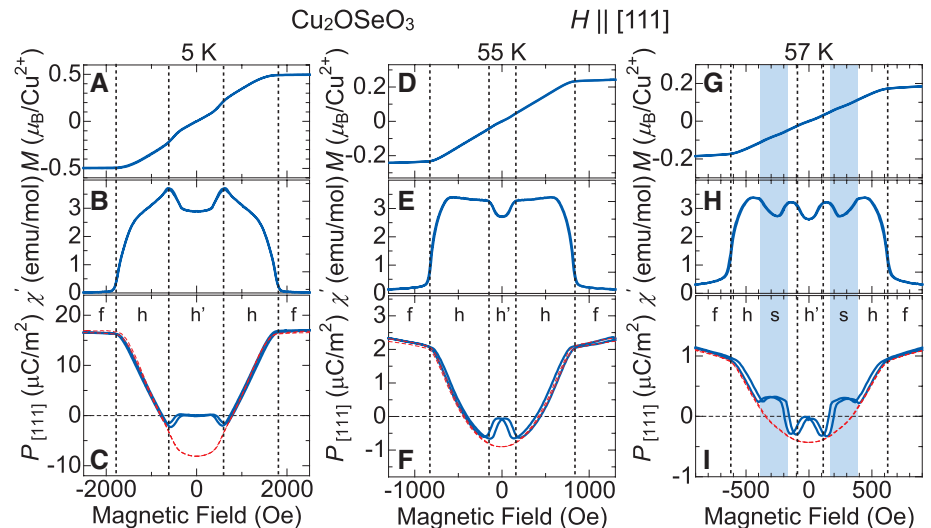


Fig. 3. Magnetic field ($H \parallel [111]$) dependence of magnetization M , ac magnetic susceptibility χ' , and $[111]$ -component of electric polarization ($P_{[111]}$) measured for bulk single crystal of Cu_2OSeO_3 at 5 (A to C), 55 (D to F), and 57 K (G to I), respectively. Red dashed lines in the $P_{[111]}$ -profiles indicate the numerical fit for the single-domain helimagnetic state with $P_{[111]} = P_0 + \beta M^2$. Letter symbols f, h, h' , and s denote ferrimagnetic, helimagnetic (single q domain), helimagnetic (multiple q domains), and skyrmion-crystal states, respectively.

Similar behavior is observed at elevated temperatures: 55 (Fig. 3F) and 57 K (Fig. 3I). However, when passing through the A phase—that

is, the bulk SkX phase (denoted as s) at 57 K— $P_{[111]}$ shows an abrupt change and takes a non-zero positive value. Each magnetic transition

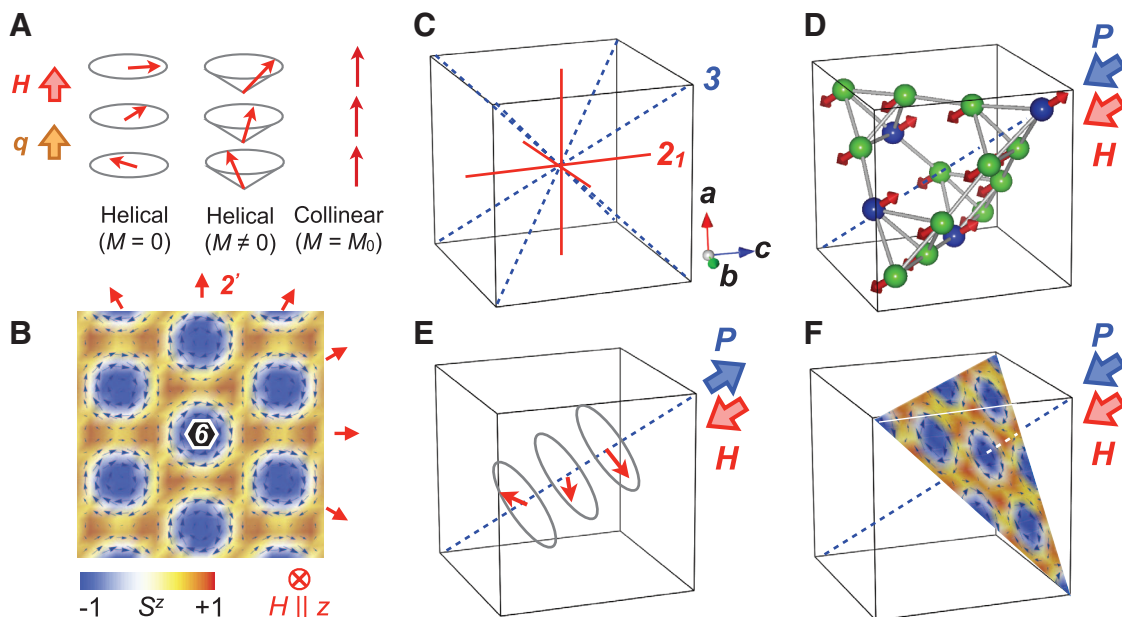


Fig. 4. (A) Development of helical spin order under an applied magnetic field. (B) Spin distribution for a magnetic skyrmion crystal, with background color representing the out-of-plane component of the magnetic moment (S^z). Compatible symmetry elements are also indicated: twofold rotation axes followed by time

reversal ($2'$) and a sixfold rotation axis along the out-of-plane direction (6). Red arrows indicate $2'$ axes. (C) Symmetry elements allowed for the crystal structure of Cu_2OSeO_3 with space group $P2_13$. (D to F) The P direction for ferrimagnetic, helimagnetic, and skyrmion-crystal states under $H \parallel [111]$, respectively.

coincides with the anomalies in the P - H profile (Fig. 2, A and C), suggesting a strong magnetoelectric coupling in this material. The above results indicate that all the magnetic phases (ferromagnetic, helimagnetic, and even the skyrmion lattice spin state) can magnetically induce non-zero electric polarization with varying sign and magnitude.

The emergence of $P \parallel H \parallel [111]$ in these magnetic phases can be justified from the viewpoint of magnetic symmetry. The crystal structure of Cu_2OSeO_3 belongs to the nonpolar (paraelectric) space group $P2_13$, which possesses threefold rotation axes along $\langle 111 \rangle$ and 2_1 -screw axes along $\langle 100 \rangle$ (Fig. 4C). The skyrmion lattice spin texture itself is also nonpolar, because it holds an orthogonal arrangement of a sixfold rotation axis (6) along H and twofold rotation axes followed by time reversal ($2'$) normal to H (Fig. 4B). When a skyrmion lattice is formed with $H \parallel [111]$ on the Cu_2OSeO_3 crystal lattice, however, most of symmetry elements are lost, and only the threefold rotation axis along the H direction survives. As a result, the system can become polar along the H direction, and the emergence of $P \parallel H \parallel [111]$ is allowed (Fig. 4F) (32). Likewise, the ferrimagnetic order with $H \parallel M \parallel [111]$ (Fig. 4D) or the helimagnetic order with $H \parallel q \parallel [111]$ (Fig. 4E) leaves only the threefold rotation axis or screw axis along H , and hence also allows the emergence of $P \parallel H \parallel [111]$. Because of the different magnetic-moment distributions, however, the M dependence of $P_{[111]}$ becomes distinct between the helimagnetic (conical) and SkX orders, thereby causing the nonmonotonous change of $P_{[111]}$ by way of the SkX state in the H -increasing/decreasing runs, as seen in Fig. 3I.

Cu_2OSeO_3 can be regarded as an insulating analog of B20 alloys, given the similarity in the crystal symmetry and a magnetic phase diagram characterized by the narrow A phase (SkX state) region; this might suggest that chiral-lattice cubic ferro/ferrimagnets ubiquitously host skyrmion spin texture regardless of metallic or insulating state. In insulators, the skyrmion can be accompanied by electric polarization, which may enable manipulation of skyrmions by an applied electric field. In B20 alloys (6), skyrmions can appear not only in crystallized form but also as independent particles, especially at the phase boundary between the collinear and SkX states. An individual skyrmion particle should locally carry a distinctive magnitude of electric dipole under the ferrimagnetic background in Cu_2OSeO_3 , which, in principle, allows the transport of skyrmions by the spatial gradient of an electric field as the process of minimizing electrostatic energy. Skyrmions in multiferroics may be a building block to design energy-efficient spintronic devices with unique magnetoelectric functions.

References and Notes

1. T. H. R. Skyrme, *Nucl. Phys.* **31**, 556 (1962).
2. U. K. Rößler, A. N. Bogdanov, C. Pfleiderer, *Nature* **442**, 797 (2006).
3. A. N. Bogdanov, D. A. Yablonskii, *Sov. Phys. JETP* **68**, 101 (1989).
4. S. Mühlbauer et al., *Science* **323**, 915 (2009).
5. W. Münzer et al., *Phys. Rev. B* **81**, 041203(R) (2010).
6. X. Z. Yu et al., *Nature* **465**, 901 (2010).
7. X. Z. Yu et al., *Nat. Mater.* **10**, 106 (2011).
8. P. Bruno, V. K. Dugaev, M. Taillefumier, *Phys. Rev. Lett.* **93**, 096806 (2004).
9. A. Neubauer et al., *Phys. Rev. Lett.* **102**, 186602 (2009).
10. F. Jonietz et al., *Science* **330**, 1648 (2010).
11. M. Fiebig, *J. Phys. D Appl. Phys.* **38**, R123 (2005).
12. S. W. Cheong, M. Mostovoy, *Nat. Mater.* **6**, 13 (2007).

13. Y. Tokura, S. Seki, *Adv. Mater.* **22**, 1554 (2010).
14. T. Kimura et al., *Nature* **426**, 55 (2003).
15. Y. Yamasaki et al., *Phys. Rev. Lett.* **98**, 147204 (2007).
16. S. Seki et al., *Phys. Rev. Lett.* **100**, 127201 (2008).
17. H. Murakawa, Y. Onose, Y. Tokura, *Phys. Rev. Lett.* **103**, 147201 (2009).
18. Y. Tokunaga et al., *Nat. Mater.* **8**, 558 (2009).
19. Y. Ishikawa, K. Tajima, D. Bloch, M. Roth, *Solid State Commun.* **19**, 525 (1976).
20. Y. Ishikawa, M. Arai, *J. Phys. Soc. Jpn.* **53**, 2726 (1984).
21. A. Bauer et al., *Phys. Rev. B* **82**, 064404 (2010).
22. S. V. Grigoriev et al., *Phys. Rev. B* **76**, 224424 (2007).
23. G. Meunier, M. Bertaud, *J. Appl. Cryst.* **9**, 364 (1976).
24. H. Effenberger, F. Pertlik, *Monatsh. Chem.* **117**, 887 (1986).
25. K. Kohn, *J. Phys. Soc. Jpn.* **42**, 2065 (1977).
26. J.-W. G. Bos, C. Colin, T. Palstra, *Phys. Rev. B* **78**, 094416 (2008).
27. M. Belesi et al., *Phys. Rev. B* **82**, 094422 (2010).
28. M. Uchida, Y. Onose, Y. Matsui, Y. Tokura, *Science* **311**, 359 (2006).
29. C. L. Huang et al., *Phys. Rev. B* **83**, 052402 (2011).
30. C. Thessieu, C. Pfleiderer, A. N. Stepanov, J. Flouquet, *J. Phys. Condens. Matter* **9**, 6677 (1997).
31. K. H. Müller et al., *Phys. Rev. B* **82**, 144107 (2010).
32. Based on the similar symmetry analysis, the emergence of $P \parallel [001]$ can be allowed in a skyrmion lattice spin state with $H \parallel [110]$, because only the $2_1'$ -axis normal to H remains unbroken.

Acknowledgments: We thank N. Nagaosa, T. Arima, M. Mochizuki, S. Miyahara, N. Furukawa, B.-J. Yang, F. Kagawa, Y. Shiomi, N. Kanazawa, T. Kurumaji, M. Shibata, M. Rikiso, and A. Nakao for enlightening discussions and experimental contributions. This work was partly supported by Grants-In-Aid for Scientific Research (grants 20340086 and 2010458) from the Ministry of Education, Culture, Sports, Science and Technology of Japan, and the FIRST Program by the Japan Society for the Promotion of Science.

Supplementary Materials

www.sciencemag.org/cgi/content/full/336/6078/198/DC1
Materials and Methods
References

19 September 2011; accepted 2 March 2012
10.1126/science.1214143

Demonstration of Entanglement of Electrostatically Coupled Singlet-Triplet Qubits

M. D. Shulman,^{1*} O. E. Dial,^{1*} S. P. Harvey,¹ H. Bluhm,^{1†} V. Umansky,² A. Yacoby^{1‡}

Quantum computers have the potential to solve certain problems faster than classical computers. To exploit their power, it is necessary to perform interqubit operations and generate entangled states. Spin qubits are a promising candidate for implementing a quantum processor because of their potential for scalability and miniaturization. However, their weak interactions with the environment, which lead to their long coherence times, make interqubit operations challenging. We performed a controlled two-qubit operation between singlet-triplet qubits using a dynamically decoupled sequence that maintains the two-qubit coupling while decoupling each qubit from its fluctuating environment. Using state tomography, we measured the full density matrix of the system and determined the concurrence and the fidelity of the generated state, providing proof of entanglement.

Singlet-triplet (S - T_0) qubits, a particular realization of spin qubits (*1–7*), store quantum information in the joint spin state of two electrons (*8–10*). The basis states for the S - T_0 qubit can be constructed from the eigenstates of a single electron spin, $|\uparrow\rangle$ and $|\downarrow\rangle$. We chose $|S\rangle =$

$(1/\sqrt{2})(|\uparrow\downarrow\rangle - |\downarrow\uparrow\rangle)$ and $|T_0\rangle = (1/\sqrt{2})(|\uparrow\downarrow\rangle + |\downarrow\uparrow\rangle)$ because these states are insensitive to uniform fluctuations in the magnetic field. The qubit can then be described as a two-level system with a representation on the so-called Bloch sphere (Fig. 1A). Universal quantum control is achieved using two physically distinct operations that drive rotations around the x and z axes of the Bloch sphere (*11*). Rotations around the z axis are driven by the exchange splitting, J , between $|S\rangle$ and $|T_0\rangle$, and rotations around the x axis are driven by a magnetic field gradient, ΔB_z , between the electrons.

We implemented the S - T_0 qubit by confining two electrons to a double quantum dot (QD) in a two-dimensional electron gas (2DEG) located

91 nm below the surface of a GaAs-AlGaAs heterostructure. We deposited local top gates using standard electron beam lithography techniques to locally deplete the 2DEG and form the QDs. We operated between the states $(0,2)$ and $(1,1)$, where (n_L, n_R) describes the state with $n_L(n_R)$ electrons in the left (right) QD. The $|S\rangle$ and $|T_0\rangle$ states, the logical subspace for the qubit, are isolated by applying an external magnetic field of 700 mT in the plane of the device such that the Zeeman splitting makes $T_+ = |\uparrow\uparrow\rangle$ and $T_- = |\downarrow\downarrow\rangle$ energetically inaccessible. The exchange splitting, J , is a function of the difference in energy, ϵ , between the levels of the left and right QDs. Pulsed DC electric fields rapidly change ϵ , allowing us to switch J on, which drives rotations around the z axis. When J is off, the qubit precesses around the x axis due to a fixed ΔB_z , which is stabilized to $\Delta B_z/2\pi = 30$ MHz by operating the qubit as a feedback loop between iterations of the experiment (*12*). Dephasing of the qubit rotations reflects fluctuations in the magnitude of the two control axes, J and ΔB , caused by electrical noise and variation in the magnetic field gradient, respectively. The qubit is rapidly (<50 ns) initialized in $|S\rangle$ by exchanging an electron with the nearby Fermi sea of the leads of the QD, by tuning the QD potentials so that only $|S\rangle$ lies below the Fermi energy. The qubit state is read out using standard Pauli blockade techniques, where ϵ is quickly tuned to the regime where S occupies $(0,2)$ and T_0 occupies $(1,1)$, allowing the qubit state to be determined by the proximal charge sensor. The charge state of the qubit is rapidly determined (~ 1 μ s) using standard radio frequency techniques (*13, 14*) on an adjacent sensing QD.

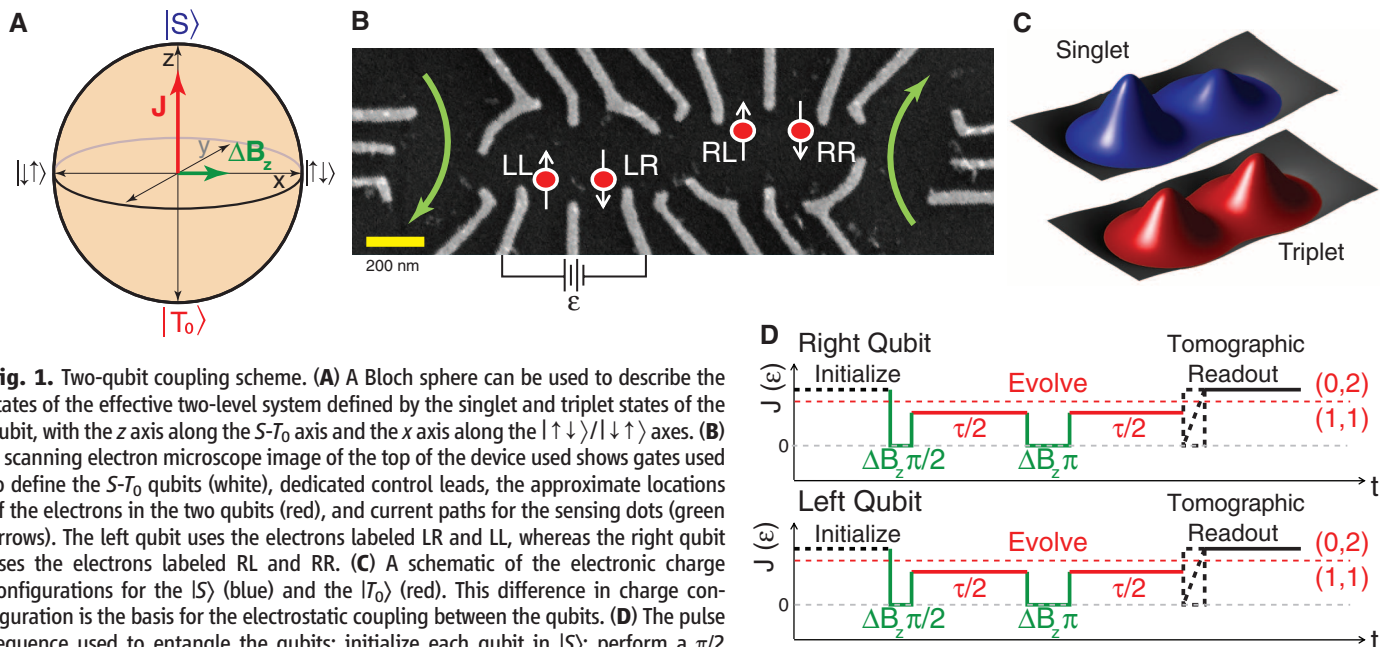


Fig. 1. Two-qubit coupling scheme. (A) A Bloch sphere can be used to describe the states of the effective two-level system defined by the singlet and triplet states of the qubit, with the z axis along the S - T_0 axis and the x axis along the $|\uparrow\downarrow\rangle/|\downarrow\uparrow\rangle$ axes. (B) A scanning electron microscope image of the top of the device used shows gates used to define the S - T_0 qubits (white), dedicated control leads, the approximate locations of the electrons in the two qubits (red), and current paths for the sensing dots (green arrows). The left qubit uses the electrons labeled LR and LL, whereas the right qubit uses the electrons labeled RL and RR. (C) A schematic of the electronic charge configurations for the $|S\rangle$ (blue) and the $|T_0\rangle$ (red). This difference in charge configuration is the basis for the electrostatic coupling between the qubits. (D) The pulse sequence used to entangle the qubits: initialize each qubit in $|S\rangle$; perform a $\pi/2$ rotation around the x axis; allow the qubits to evolve under exchange for a time $\tau/2$; perform a π rotation around the x axis, thereby decoupling the qubits from the environment but not each other; evolve under exchange for $\tau/2$; and perform state tomography to determine the resulting density matrix (fig. S3.)

To make use of the power of quantum information processing, it is necessary to perform two qubit operations in which the state of one qubit is conditioned on the state of the other (15). To investigate two-qubit operations, we fabricated two adjacent S - T_0 qubits such that they are capacitively coupled, but tunneling between them is suppressed (Fig. 1B). A charge-sensing QD next to each qubit allows for simultaneous and independent projective measurement of each qubit (see supplementary materials). We used the electrostatic coupling between the qubits to generate the two-qubit operation (16). When J is nonzero, the $|S\rangle$ and $|T_0\rangle$ states have different charge configurations in the two QDs because of the Pauli exclusion principle (Fig. 1C). This charge difference, which is a function of ϵ , causes the $|S\rangle$ and $|T_0\rangle$ states in one qubit to impose different electric fields on the other qubit. As J is a function of the electric field, the change in electric field imposed by the first qubit causes a shift in the precession frequency of the second qubit. In this way, the state of the second qubit may be conditioned on the state of the first qubit. More precisely, when a single qubit evolves under exchange, there exists a state-dependent dipole moment, \vec{d} , between $|S\rangle$ and $|T_0\rangle$, resulting from their difference in charge occupation of the QDs. Therefore, when simultaneously evolving both

qubits under exchange, they experience a capacitively mediated, dipole-dipole coupling that can generate an entangled state. The two-qubit Hamiltonian is therefore given by:

$$H_{2\text{-qubit}} = \frac{\hbar}{2} \left(J_1 (\sigma_z \otimes I) + J_2 (I \otimes \sigma_z) + \frac{J_{12}}{2} ((\sigma_z - I) \otimes (\sigma_z - I)) + \Delta B_{z,1} (\sigma_x \otimes I) + \Delta B_{z,2} (I \otimes \sigma_x) \right) \quad (1)$$

where $\sigma_{x,y,z}$ are the Pauli matrices, I is the identity operator, $\Delta B_{z,i}$, and J_i are the magnetic field gradients and the exchange splittings ($i = 1, 2$ respectively for the two qubits), and J_{12} is the two-qubit coupling, which is proportional to the product of the dipole moments in each qubit. For a two-level system with constant tunnel coupling, the dipole moment scales as $\vec{d}_i \propto \partial J_i / \partial \epsilon_i$. Empirically, we find that for experimentally relevant values of J_i , $\partial J_i / \partial \epsilon_i \propto J_i(\epsilon)$, so that $J_{12} \propto J_1 J_2$. As with the single qubit operations, this two-qubit operation requires only pulsed DC electric fields.

In principle, evolving both qubits under exchange produces an entangling gate. However, the time to produce this maximally entangled state exceeds the inhomogeneously broadened coherence times of each individual qubit, rendering

this simple implementation of the two-qubit gate ineffective. To mitigate this, we used a dynamically decoupled entangling sequence (17, 18) (Fig. 1D). In this sequence, each qubit is prepared in $|S\rangle$ and is then rotated by $\pi/2$ around the x axis ($J_i = 0$, $\Delta B_{z,i}/2\pi \approx 30$ MHz) to prepare a state in the x - y plane. The two qubits are subsequently both evolved under a large exchange splitting ($J_1/2\pi \approx 280$ MHz, $J_2/2\pi \approx 320$ MHz $\gg \Delta B_z$) for a time $\tau/2$, during which the qubits begin to entangle and disentangle. A π pulse around the x axis (ΔB_z) is then applied simultaneously to both qubits, after which the qubits are again allowed to exchange for a time $\tau/2$. This Hahn echo-like sequence (19) removes the dephasing effect of noise that is low frequency compared to $1/\tau$, and the π pulses preserve the sign of the two-qubit interaction. The resulting operation produces a controlled phase (CPhase) gate, which, in a basis of $\{|SS\rangle, |T_0S\rangle, |ST_0\rangle, |T_0T_0\rangle\}$, is an operation described by a matrix $\text{diag}(e^{-i\theta/2}, 1, 1, e^{-i\theta/2})$. For $\tau = \tau_{\text{ent}} = \frac{\pi}{(2J_{12})}$, the resulting state is a maximally entangled generalized Bell state $|\Psi_{\text{ent}}\rangle = e^{i\pi(I \otimes \sigma_y + \sigma_x \otimes I)/8} |\Psi_{-}\rangle$, which differs from the Bell state $|\Psi_{-}\rangle = (1/\sqrt{2})(|SS\rangle - |T_0T_0\rangle)$ by single-qubit rotations.

To characterize our two-qubit gate and verify that we produced an entangled state, we performed two-qubit state tomography and extracted

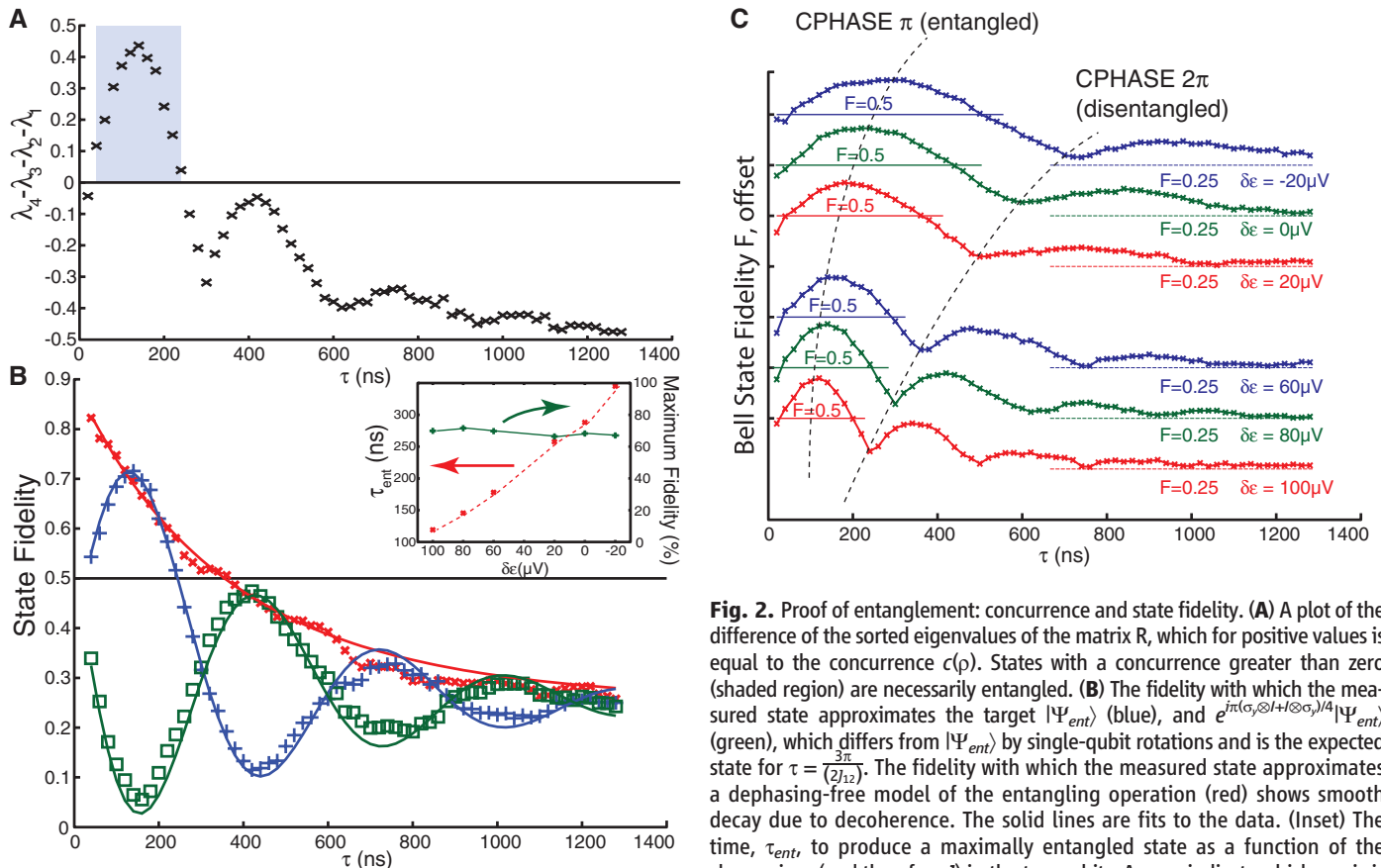


Fig. 2. Proof of entanglement: concurrence and state fidelity. **(A)** A plot of the difference of the sorted eigenvalues of the matrix R , which for positive values is equal to the concurrence $c(\rho)$. States with a concurrence greater than zero (shaded region) are necessarily entangled. **(B)** The fidelity with which the measured state approximates the target $|\Psi_{\text{ent}}\rangle$ (blue), and $e^{i\pi(\sigma_y \otimes I + I \otimes \sigma_y)/4} |\Psi_{\text{ent}}\rangle$ (green), which differs from $|\Psi_{\text{ent}}\rangle$ by single-qubit rotations and is the expected state for $\tau = \tau_{\text{ent}} = \frac{\pi}{(2J_{12})}$. The fidelity with which the measured state approximates a dephasing-free model of the entangling operation (red) shows smooth decay due to decoherence. The solid lines are fits to the data. (Inset) The time, τ_{ent} , to produce a maximally entangled state as a function of the change in ϵ (and therefore J) in the two qubits. Arrows indicate which y axis is

to be used. **(C)** The Bell state fidelity as a function of time for different values of J (offset for clarity), with guides to show where the fidelity exceeds 1/2 for each curve.

set (Fig. 3B), and we extracted a Bell state fidelity of 0.72, which demonstrates the production of an entangled state. For $\tau = \tau_{\text{ent}} = \frac{\pi}{(2J_{12})} = 160$ ns (Fig. 3C), we see a similar state to $\tau = 140$ ns, but with less weight in the single-qubit components of the Pauli set. This state corresponds to the intended CPhase of π , although the fidelity is slightly lower than at $\tau = 140$ ns due to additional decoherence. Finally, at $\tau = \pi/J_{12} = 320$ ns (Fig. 3D), where we expect the state to be unentangled, we again see large weight in the $\langle YI \rangle$, $\langle IY \rangle$, and $\langle YY \rangle$ components of the Pauli set, although the bars are shorter than the Pauli set for $\tau = 40$ ns because of dephasing of the qubits. We plotted the entire Pauli set as a function of time (Fig. 3E), which clearly shows the predicted oscillation (Eq. 2) between $\langle YI \rangle, \langle IY \rangle$ and $\langle XZ \rangle, \langle ZX \rangle$, with decays due to decoherence.

The two-qubit gate that we have demonstrated is an important step toward establishing a scalable architecture for quantum information processing in $S-T_0$ qubits. Although a Bell state fidelity of 0.72 is not as high as what has been reported in other solid state implementations of qubits (21, 27), there are easily implemented improvements to this two-qubit gate. State fidelity is lost to dephasing from electrical noise, and decreasing the ratio $\tau_{\text{ent}}/T_2^{\text{echo}}$, where T_2^{echo} is the single-qubit coherence time with an echo pulse, is therefore paramount to generating high-fidelity Bell states. Large improvements can be made by introducing an electrostatic coupler between the two qubits (28) to increase the two-qubit cou-

pling (J_{12}) and reduce τ_{ent} . We estimate that in the absence of other losses, if an electrostatic coupler were used, a Bell state with fidelity exceeding 90% could be produced. Other improvements can be made by studying the origins and properties of the charge noise that dephases the qubit and mitigating its adverse effects in order to increase T_2^{echo} . This would allow future tests of complex quantum operations, including quantum algorithms and quantum error correction. Finally, the addition of electrostatic couplers would allow the qubits to be spatially separated and is a path toward implementing surface codes for quantum computation.

References and Notes

1. D. Loss, D. P. DiVincenzo, *Phys. Rev. A* **57**, 120 (1998).
2. F. H. L. Koppens *et al.*, *Nature* **442**, 766 (2006).
3. M. Pioro-Ladriere *et al.*, *Nat. Phys.* **4**, 776 (2008).
4. K. C. Nowack, F. H. L. Koppens, Y. V. Nazarov, L. M. K. Vandersypen, *Science* **318**, 1430 (2007).
5. M. Pioro-Ladriere, Y. Tokura, T. Kubo, S. Tarucha, *Appl. Phys. Lett.* **90**, 024105 (2007).
6. H. O. H. Churchill *et al.*, *Phys. Rev. Lett.* **102**, 166802 (2009).
7. S. Nadj-Perge, S. M. Frolov, E. P. Bakkers, L. P. Kouwenhoven, *Nature* **468**, 1084 (2010).
8. J. Levy, *Phys. Rev. Lett.* **89**, 147902 (2002).
9. J. R. Petta *et al.*, *Science* **309**, 2180 (2005).
10. J. M. Taylor *et al.*, *Phys. Rev. B* **76**, 035315 (2007).
11. S. Foletti, H. Bluhm, D. Mahalu, V. Umansky, A. Yacoby, *Nat. Phys.* **5**, 903 (2009).
12. H. Bluhm, S. Foletti, D. Mahalu, V. Umansky, A. Yacoby, *Phys. Rev. Lett.* **105**, 216803 (2010).
13. D. J. Reilly, C. M. Marcus, M. P. Hanson, A. C. Gossard, *Appl. Phys. Lett.* **91**, 162101 (2007).
14. C. Barthel, D. J. Reilly, C. M. Marcus, M. P. Hanson, A. C. Gossard, *Phys. Rev. Lett.* **103**, 160503 (2009).

15. M. A. Nielsen, I. L. Chuang, *Quantum Computation and Quantum Information* (Cambridge Univ. Press, Cambridge, 2000).
16. J. M. Taylor *et al.*, *Nat. Phys.* **1**, 177 (2005).
17. L. Viola, E. Knill, S. Lloyd, *Phys. Rev. Lett.* **82**, 2417 (1999).
18. D. Leibfried *et al.*, *Nature* **422**, 412 (2003).
19. E. L. Hahn, *Phys. Rev.* **80**, 580 (1950).
20. F. V. Daniel, *Phys. Rev. A* **64**, 052312 (2001).
21. J. M. Chow *et al.*, *Phys. Rev. A* **81**, 062325 (2010).
22. S. Hill, W. Wootters, *Phys. Rev. Lett.* **78**, 5022 (1997).
23. C. A. Sackett *et al.*, *Nature* **404**, 256 (2000).
24. C. H. Bennett *et al.*, *Phys. Rev. Lett.* **76**, 722 (1996).
25. T. Yu, J. H. Eberly, *Opt. Commun.* **264**, 393 (2006).
26. L. Cywinski, R. M. Lutchyn, C. P. Nave, S. Das Sarma, *Phys. Rev. B* **77**, 174509 (2008).
27. M. Ansmann *et al.*, *Nature* **461**, 504 (2009).
28. L. Trifunovic *et al.*, *Phys. Rev. X* **2**, 011006 (2012).

Acknowledgments: This work is supported through the U.S. Army Research Office (ARO) Precision Quantum Control and Error-Suppressing Quantum Firmware for Robust Quantum Computing and the Intelligence Advanced Research Projects Activity (IARPA) Multi-Qubit Coherent Operations (MQCO) Program. This work was partially supported by the ARO under contract W911NF-11-1-0068. This work was performed in part at the Center for Nanoscale Systems (CNS), a member of the National Nanotechnology Infrastructure Network (NNIN), which is supported by the National Science Foundation under NSF award ECS-0335765. CNS is part of Harvard University. V.U. prepared the crystal; M.D.S. fabricated the sample; and M.D.S., O.E.D., H.B., S.P.H., and A.Y. carried out the experiment, analyzed the data, and wrote the paper. The authors declare no competing financial interests.

Supplementary Materials

www.sciencemag.org/cgi/content/full/336/6078/202/DC1
Materials and Methods
Figs. S1 to S5
References

9 December 2011; accepted 7 March 2012
10.1126/science.1217692

Topological Transitions in Metamaterials

Harish N. S. Krishnamoorthy,^{1,2*} Zubin Jacob,^{3*} Evgenii Narimanov,⁴
Ilona Kretschmar,⁵ Vinod M. Menon^{1,2†}

Light-matter interactions can be controlled by manipulating the photonic environment. We uncovered an optical topological transition in strongly anisotropic metamaterials that results in a dramatic increase in the photon density of states—an effect that can be used to engineer this interaction. We describe a transition in the topology of the iso-frequency surface from a closed ellipsoid to an open hyperboloid by use of artificially nanostructured metamaterials. We show that this topological transition manifests itself in increased rates of spontaneous emission of emitters positioned near the metamaterial. Altering the topology of the iso-frequency surface by using metamaterials provides a fundamentally new route to manipulating light-matter interactions.

Metamaterials are artificial media in which the subwavelength features of the designed unit cells and coupling between them governs the macroscopic electro-

magnetic properties (1). This control over material parameters has led to new applications (2–4) and also the ability to mimic and study physical processes, which is difficult by other methods (5–7). One specific design freedom afforded by metamaterials is the control over the iso-frequency surface, the surface of allowed wavevectors at constant frequency (8, 9). The topology of this surface governs wave dynamics inside a medium.

The ideas of mathematical topology play an important role in many aspects of modern physics, from phase transitions to field theory to nonlinear dynamics (10, 11). An important example of this is the Lifshitz transition (12), in which the transformation of the Fermi surface of a metal

from a closed to an open geometry (because of, for example, external pressure) leads to a dramatic effect on the electron magneto-transport (13). In optics, the role of the Fermi surface is played by the optical iso-frequency surface $\omega(\vec{k}) = \text{const}$, which can be engineered by tailoring the dielectric tensor, $\vec{\epsilon}(\vec{r})$. We use this to demonstrate the optical equivalent of the “Lifshitz transition”—the optical topological transition (OTT) in which the very nature of the electromagnetic radiation in the metamaterial undergoes a drastic change. Effects on the kinetic and thermodynamic properties, such as the dynamics of propagating waves supported by the system and the electromagnetic energy density, respectively, are modified at the transition point and can be probed by following the light-metamaterial interaction using a quantum emitter.

We considered a metamaterial structure that has a uniaxial form of the dielectric tensor $\vec{\epsilon}(\vec{r}) = \text{diag}(\epsilon_{xx}, \epsilon_{yy}, \epsilon_{zz})$, where $\epsilon_{xx} = \epsilon_{yy} = \epsilon_{\parallel}$ and $\epsilon_{zz} = \epsilon_{\perp}$. The iso-frequency surface for the extraordinary (TM-polarized) waves propagating in such a strongly anisotropic metamaterial is given by

$$\frac{k_x^2 + k_y^2}{\epsilon_{\perp}} + \frac{k_z^2}{\epsilon_{\parallel}} = \frac{\omega^2}{c^2} \quad (1)$$

Closed iso-frequency surfaces differing from a simple sphere (such as an ellipsoid) can occur in these metamaterials when $\epsilon_{\parallel}, \epsilon_{\perp} > 0$ and

¹Department of Physics, Queens College, City University of New York (CUNY) and Center for Photonic and Multiscale Nanomaterials, Flushing, NY 11367, USA. ²Department of Physics, Graduate Center, CUNY, New York, NY 10016, USA. ³Department of Electrical and Computer Engineering, University of Alberta, Edmonton T6G 2V4, Canada. ⁴Birk Nanotechnology Center, School of Electrical and Computer Engineering, Purdue University, West Lafayette, IN 47907, USA. ⁵Department of Chemical Engineering, City College, CUNY, New York, NY 10031, USA.

*These authors contributed equally to this work.

†To whom correspondence should be addressed. E-mail: vmenon@qc.cuny.edu

$\epsilon_{\parallel} \neq \epsilon_{\perp}$. On the other hand, an extreme modification of the iso-frequency surface into a hyperboloid occurs when the dielectric constants show opposite sign ($\epsilon_{\parallel} < 0$ and $\epsilon_{\perp} > 0$). We can design a metamaterial so that the dispersion of the dielectric constants leads to an OTT in the iso-frequency surface from an ellipsoid to a hyperboloid.

The photonic density of states (PDOS) in the metamaterial is related to the volume enclosed by the corresponding iso-frequency surface (14). Therefore, the topological transition from the closed (ellipsoid) iso-frequency surface for $\epsilon_{\parallel} > 0$ to an open (hyperboloid) iso-frequency surface for $\epsilon_{\parallel} < 0$ (Fig. 1) results in a nonintegrable singularity accompanied by a change in the density of states from a finite to an infinite value (in lossless effective medium limit). This optical analog of the Lifshitz transition in metamaterials is characterized by the appearance of additional

electromagnetic states in the hyperbolic regime, which have wave vectors much larger than those allowed in vacuum. Light-matter interaction is enhanced because of the presence of these additional electromagnetic states, resulting in a strong effect on related quantum-optical phenomena, such as spontaneous emission.

The decay rate near a half space of a metamaterial for a dipole-like emitter is given by (15–20)

$$\Gamma = \Gamma_{\text{vac}} + \Gamma_{\text{plasmon}} + \Gamma_{\text{high-k}} \quad (2)$$

where Γ_{vac} and Γ_{plasmon} are the decay rates due to propagating waves in vacuum and the surface plasmon polariton (SPP) modes supported by the metamaterial, respectively, and $\Gamma_{\text{high-k}}$ is the decay rate enhancement due to the high-wave vector states, which appear only beyond the OTT. In the near field of the metamaterial, when $d \ll \lambda$

the decay rate is dominated by the contribution from the high-wave vector states (21):

$$\Gamma_{\text{high-k}} \approx \frac{\mu_{\perp}^2 \text{Im}(r_p)}{8\hbar d^3} \quad (3)$$

where μ_{\perp} is the dipole moment of the perpendicularly oriented dipole, r_p is the plane wave reflection coefficient of p-polarized light (21), and d is the distance of the dipole from the interface. In a hyperbolic metamaterial half space where $\text{real}(\epsilon_{\parallel}) < 0$

$$\text{Im}(r_p) = \frac{2\sqrt{|\epsilon_{\parallel}||\epsilon_{\perp}|}}{1 + |\epsilon_{\parallel}||\epsilon_{\perp}|} \quad (4)$$

and for $[\text{real}(\epsilon_{\parallel}) > 0]$, we have an elliptical dispersion with $\text{Im}(r_p) = 0$ (assuming no losses). We thus introduce the topological transition parameter $\alpha = \text{Im}(r_p)$, which is proportional to the local density of electromagnetic modes and characterizes the emergence of high-k metamaterial states. The effect of dispersive and lossy effective medium dielectric constants on the topological transition parameter (proportional to the spontaneous emission rate) is shown in Fig. 2A. Although the losses reduce the sharp transition to a smooth crossover, the change in the iso-frequency surface topology still leads to an enhanced spontaneous emission rate.

Metamaterials with opposite signs of the dielectric constants can be realized by using metal-dielectric composites (22). We considered such a composite consisting of alternating layers of silver (9 nm) and titanium dioxide (TiO₂) (22 nm) corresponding to a 29% fill fraction of silver. Using the semiclassical theory of spontaneous

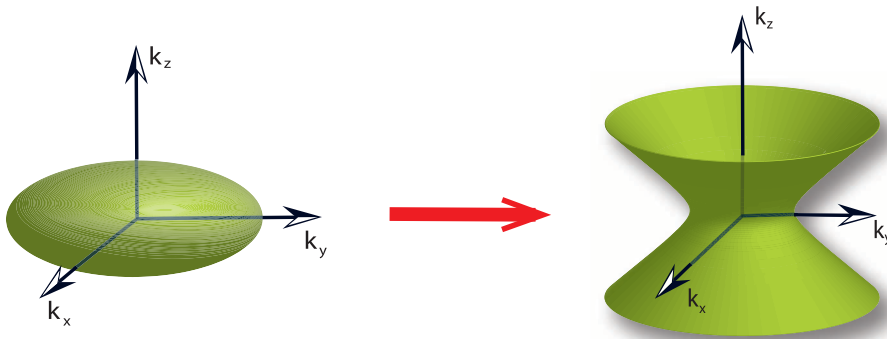


Fig. 1. OTT: The optical iso-frequency curve changes from a closed surface such as an ellipsoid to an open hyperboloid.

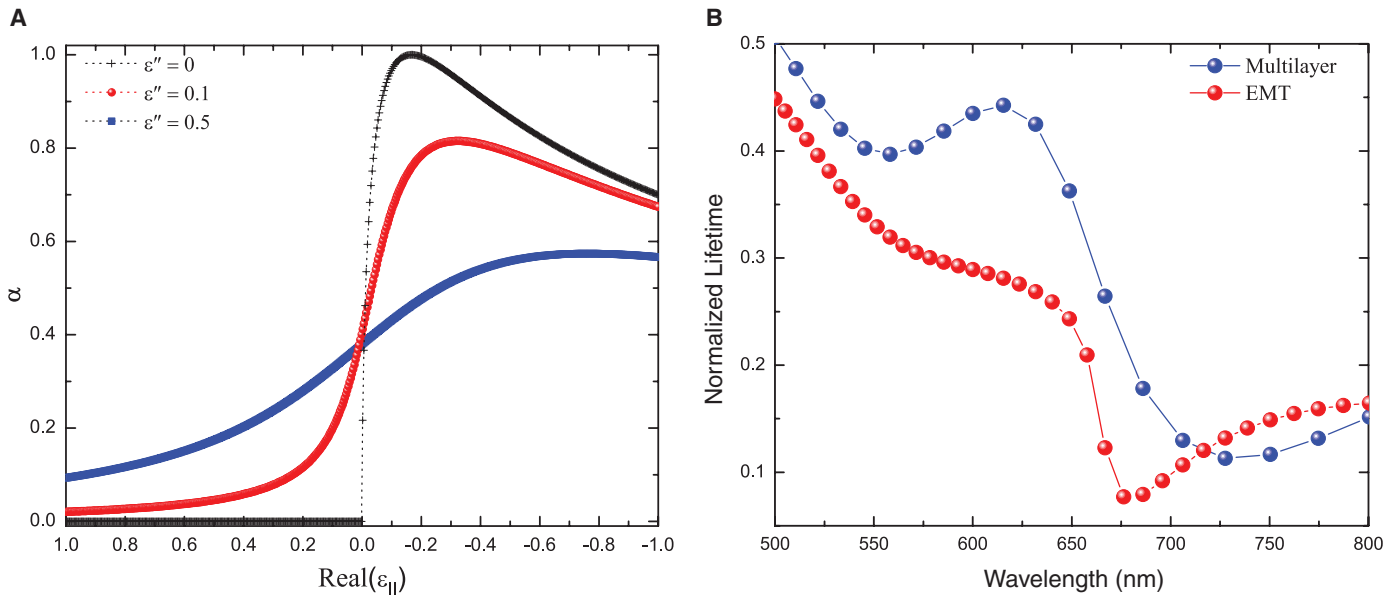


Fig. 2. (A) Topological transition parameter (proportional to the local density of states) near the topological transition wavelength as a function of the real part of ϵ_{\parallel} . The sharp transition becomes a smooth crossover as losses are increased. (B) Lifetime of emitters placed on a practical realization of the

metamaterial consisting of alternating layers of metal (silver, 9 nm) and dielectric (TiO₂, 22 nm) corresponding to the 29% fill fraction sample. A sharp reduction in the spontaneous emission lifetime is observed around the transition wavelength.

emission (23), we calculated the lifetime for quantum dots (QDs) placed in the near field of this metamaterial. Our simulation takes into account nonidealities arising because of realistic losses, dispersion, finite thickness of layers, sample size, and the substrate. Even in a practical structure (Fig. 2B), a clear modification in lifetime of the emitter is expected as the system transitions from elliptical to the hyperbolic dispersion regime over the spectral range of interest. The transition occurs because of the particular dispersion of coupled plasmons, which contribute to lifetime decrease only on the hyperbolic side of the transition (21).

Simulations carried out through effective medium theory (EMT) show good agreement with the prediction of numerical simulations (Fig. 2B).

To experimentally observe the signature of the predicted OTT manifested through enhancement in spontaneous emission rate, we investigated a metamaterial structure similar to that discussed above with multiple QD emitters positioned on its top surface (Fig. 3A) (21). The dielectric constants of the constituent thin films were extracted by using ellipsometry, and the effective medium parameters are shown in Fig. 3B. This structure is designed to have $\epsilon_{\parallel} \approx 0$ around

621 nm, which corresponds to the emission maximum of the CdSe/ZnS colloidal QDs used in the experiment. The photoluminescence (PL) from the QDs has a full width at half maximum (FWHM) of ~ 40 nm, which allows investigation of the phase space of both elliptical and hyperbolic dispersion regimes by use of the same sample. In order to isolate the effects of the nonradiative decay and SPP-based enhancement in the radiative rate due to the metal, we also measured the spontaneous emission rates of QDs on a control sample that consisted of one unit cell of the metamaterial (21).

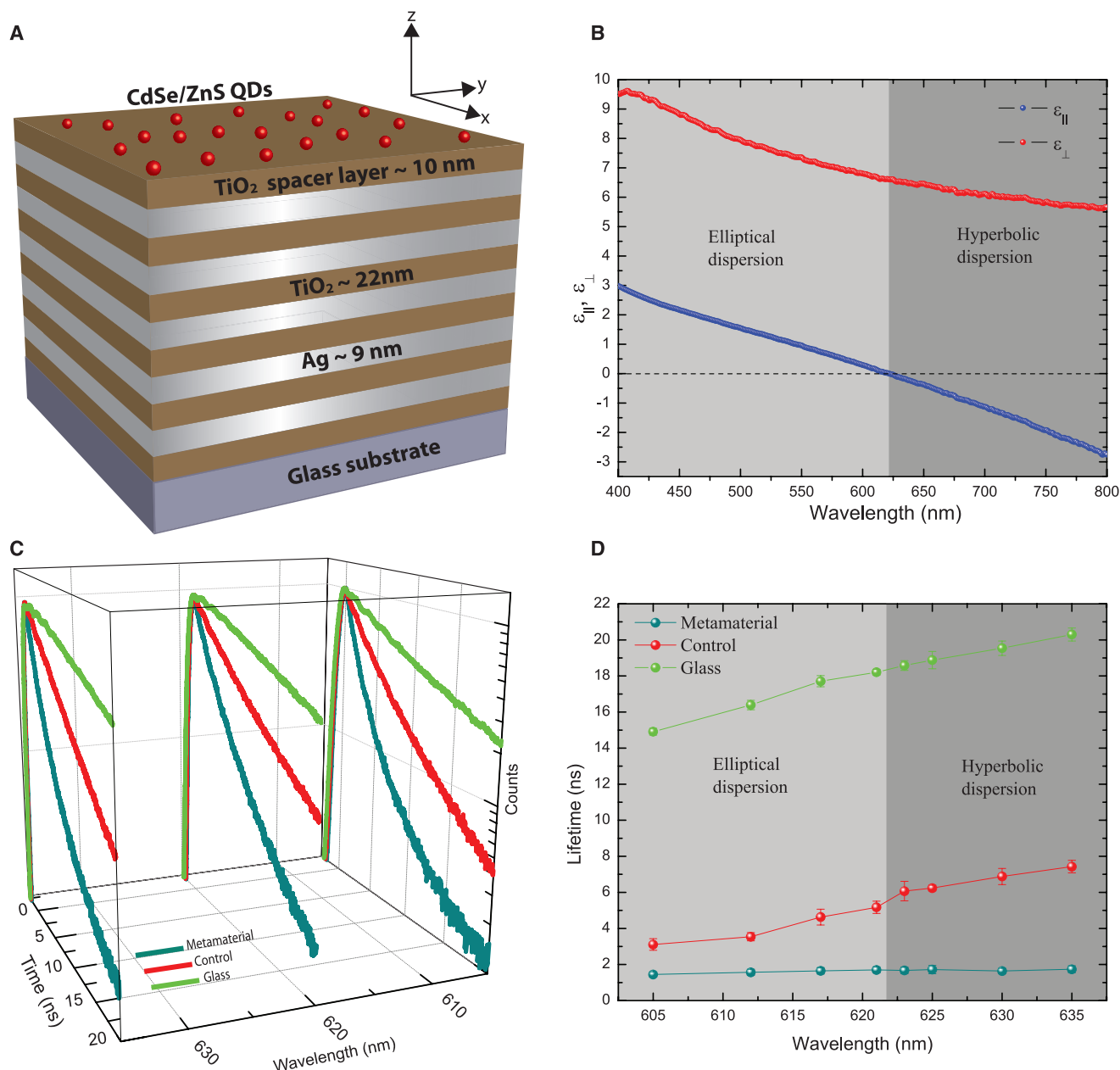
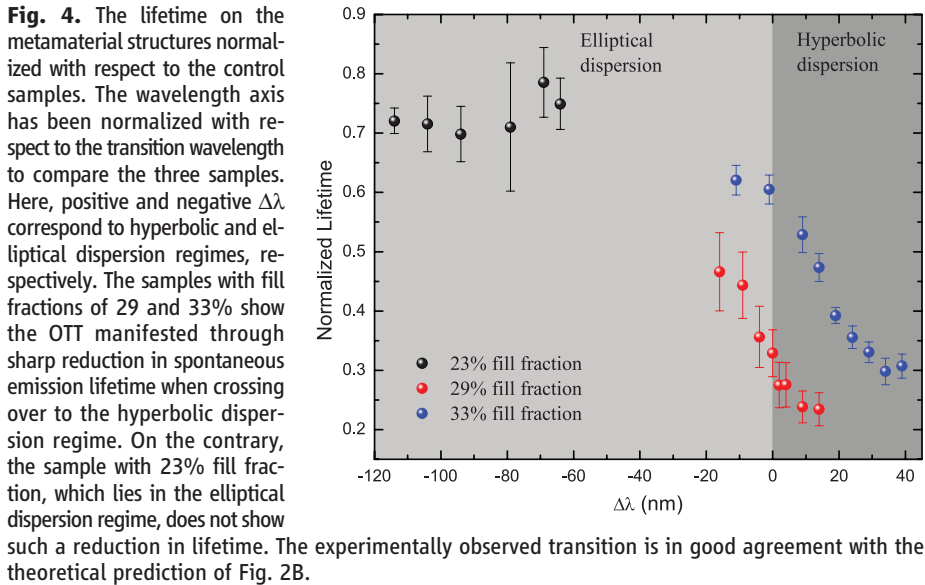


Fig. 3. (A) Schematic of the metamaterial structure. (B) Effective dielectric constants (real parts) of the structure determined with ellipsometry and effective medium theory. The transition from elliptical to hyperbolic dispersion occurs at 621 nm. (C) Time-resolved photoluminescence data from QDs deposited on the metamaterial, control sample, and glass substrate at 605, 621, and 635 nm.

Clear reduction in lifetime is observed over 30-nm spectral bandwidth when the emitter is placed on the metamaterial. (D) Lifetime of the QDs as a function of wavelength on metamaterial, control sample, and glass substrate. QDs on the control sample and glass shows an increase in the lifetime with wavelength, whereas on the metamaterial, a slight decrease in lifetime is observed.



Time-resolved PL measurements were carried out on the metamaterial sample, the control sample, and the glass substrate (Fig. 3C) at the anticipated transition wavelength (621 nm) and at spectral positions on either side (605 and 635 nm). The large change in the spontaneous emission lifetime of the QDs on the metamaterial compared with the glass substrate is due to the excitation of the high- k metamaterial states as well as the nonradiative contribution and the SPP modes of the metamaterial. When compared with the control sample, the metamaterial shows an enhancement in the spontaneous emission rate by a factor of ~ 3 at the transition wavelength and ~ 4.3 deeper in the hyperbolic regime (635 nm). These enhancements are attributed to the high- k metamaterial states. The overall reduction in the lifetime of the QDs when compared with those on a glass substrate is ~ 11 .

The lifetime of the QDs increases as a function of wavelength on both the glass substrate and the control sample (Fig. 3D). This is due to the size distribution of QDs and the dependence of the oscillator strength on the energy (24–26). On the contrary, the metamaterial sample shows a decrease in the lifetime as a function of wavelength and the shortest lifetime owing to coupling to the high- k metamaterial states (Fig. 3D). The coupling of the emission from the QDs into the metamaterial states was also verified by using steady-state PL measurements (fig. S6) in which a reduction in the PL intensity emitted in the direction away from the metamaterial sample was observed (21, 27).

To demonstrate the OTT, we studied the radiative lifetimes in three samples with differing volume ratio of metal to dielectric, which correspond to different transition wavelengths. We compared the lifetimes of the sample with 29% fill fraction of silver to one with 23% fill fraction, which lies deep in the elliptical phase, and to another sample that lies deeper in the hyperbolic

phase, with fill fraction of 33% (21). To make any conclusions regarding the effect of the OTT on the radiative lifetimes from the measurement of the total decay rates, the contribution of the high- k metamaterial states has to be distinguished from nonradiative decay and the SPP-assisted decay of the unit cell. Because the spacer and first-layer environment of the QDs is the same in the control and the metamaterial sample, we expected similar quantum yield dependence on wavelength owing to near-field interaction of the QDs and the metallic structure. Thus, to account for purely the contribution from the high- k metamaterial states to the overall lifetime change, we normalized the QD lifetime on the metamaterials with that on the control samples (Fig. 4). The controls for the three samples are different and correspond to the unit cell of each metamaterial sample. To compare these three samples, which have OTTs at different wavelengths, we normalized the wavelength with respect to the transition wavelength, with positive and negative $\Delta\lambda$ corresponding to the hyperbolic and elliptical dispersion regimes, respectively.

We clearly observed a sharp reduction in the normalized lifetime of the samples with 29 and 33% fill fractions that cross the transition wavelength, whereas the sample with 23% fill fraction, which lies in the elliptical regime, did not show this reduction. Whereas the combination of metal losses and finite thickness of layers leads to a smooth crossover, the signature of the transition is clear from the reduction in the normalized lifetime in the hyperbolic regime. The difference in the absolute value of the normalized lifetimes in the two samples that show the transitions is due to the differing fill fractions (29 versus 33%) and associated difference in the dielectric constants. Thus, the changes in the lifetime observed experimentally in these metamaterial structures can be attributed to the increase in the photonic density of states that manifests when the system goes

through the topological transition in its iso-frequency surface from an ellipsoid to a hyperboloid, which is in good agreement with the theoretical prediction of Fig. 2B.

We have established the occurrence of OTT in two metamaterial structures using spontaneous emission from a quantum emitter as the probe. Absence of OTT in a structure that lies solely in the elliptical dispersion phase has also been demonstrated. A host of interesting effects can transpire at the transition wavelength, such as the sudden appearance of resonance cones, which are characteristic of hyperbolic metamaterials (28), enhanced nonlinear effects, and abrupt changes in the electromagnetic energy density. We expect the OTT to be the basis for a number of applications of both fundamental and technological importance through use of metamaterial-based control of light-matter interaction.

References and Notes

- V. M. Shalaev, *Nat. Photonics* **1**, 41 (2007).
- J. B. Pendry, *Phys. Rev. Lett.* **85**, 3966 (2000).
- J. B. Pendry, D. Schurig, D. R. Smith, *Science* **312**, 1780 (2006).
- U. Leonhardt, *Science* **312**, 1777 (2006).
- D. A. Genov, S. Zhang, X. Zhang, *Nat. Phys.* **5**, 687 (2009).
- E. E. Narimanov, A. V. Kildishev, *Appl. Phys. Lett.* **95**, 041106 (2009).
- I. I. Smolyaninov, E. E. Narimanov, *Phys. Rev. Lett.* **105**, 067402 (2010).
- Z. Jacob, L. V. Alekseyev, E. Narimanov, *Opt. Express* **14**, 8247 (2006).
- Z. Liu, H. Lee, Y. Xiong, C. Sun, X. Zhang, *Science* **315**, 1686 (2007).
- M. Nakahara, *Geometry, Topology and Physics* (IOP Publishing, Bristol, UK, ed. 2, 2003).
- M. Monastyrskiy, *Riemann Topology and Physics* (Birkhäuser, Boston, ed. 2, 1999).
- I. M. Lifshitz, *Sov. Phys. JETP* **11**, 1130 (1960).
- A. M. Kosevich, *Low Temp. Phys.* **30**, 97 (2004).
- M. Born, E. Wolf, *Principles of Optics* (Cambridge Univ. Press, Cambridge, ed. 7, 2002).
- P. Yao et al., *Phys. Rev. B* **80**, 195106 (2009).
- Z. Jacob, I. Smolyaninov, E. Narimanov, arXiv:0910.3981v2 [physics.optics] (2009).
- M. A. Noginov et al., *Opt. Lett.* **35**, 1863 (2010).
- Z. Jacob et al., *Appl. Phys. B* **100**, 215 (2010).
- A. N. Poddubny, P. A. Belov, Y. S. Kivshar, *Phys. Rev. A* **84**, 023807 (2011).
- O. Kidwai, S. V. Zhukovsky, J. E. Sipe, *Opt. Lett.* **36**, 2530 (2011).
- A complete description of the fabrication, characterization, and modeling is available as supplementary materials on Science Online.
- A. J. Hoffman et al., *Nat. Mater.* **6**, 946 (2007).
- G. W. Ford, W. H. Weber, *Phys. Rep.* **113**, 195 (1984).
- M. D. Leistikow, J. Johansen, A. J. Kettler, P. Lodahl, W. L. Vos, *Phys. Rev. B* **79**, 045301 (2009).
- M. L. Andersen, S. Stobbe, A. S. Sørensen, P. Lodahl, *Nat. Phys.* **7**, 215 (2011).
- K. Okamoto, S. Vyawahare, A. Scherer, *J. Opt. Soc. Am. B* **23**, 1674 (2006).
- I. Contijo et al., *Phys. Rev. B* **60**, 11564 (1999).
- L. B. Felsen, N. Marcuvitz, *Radiation and Scattering of Waves* (IEEE, New York, 1994).

Acknowledgments: V.M.M. and H.N.S.K. acknowledge partial support through the Materials Research Science and Engineering Center program of the National Science Foundation through grant DMR 1120923 and the Army Research Office (ARO) grant W911NF0710397. V.M.M. and I.K. acknowledge support through Round 14 of the CUNY Collaborative Incentive Research Grant Program. E.N. was partially supported by ARO–Multidisciplinary University Research Initiative grants 50342-PH-MUR and W911NF-09-1-0539. Z.J. was partially

supported by Natural Sciences and Engineering Research Council of Canada/Discovery grant 402792 and Canadian School of Energy and Environment Proof of Principle Grant. The ellipsometric measurements were carried out at the Center for Functional Nanomaterials at Brookhaven National Laboratory, which is supported by the U.S. Department of

Energy, Office of Basic Energy Sciences, under contract DE-AC02-98CH10886.

Supplementary Materials

www.sciencemag.org/cgi/content/full/336/6078/205/DC1
Materials and Methods

Figs. S1 to S6
References (29, 30)

16 January 2012; accepted 7 March 2012
10.1126/science.1219171

Ferroelectric Columnar Liquid Crystal Featuring Confined Polar Groups Within Core–Shell Architecture

Daigo Miyajima,¹ Fumito Araoka,² Hideo Takezoe,^{2*} Jungeun Kim,³ Kenichi Kato,⁴ Masaki Takata,^{3,4} Takuzo Aida^{1*}

Ferroelectric liquid crystals are materials that have a remnant and electrically invertible polar order. Columnar liquid crystals with a ferroelectric nature have potential use in ultrahigh-density memory devices, if electrical polarization occurs along the columnar axis. However, columnar liquid crystals having an axial nonzero polarization at zero electric field and its electrical invertibility have not been demonstrated. Here, we report a ferroelectric response for a columnar liquid crystal adopting a core–shell architecture that accommodates an array of polar cyano groups confined by a hydrogen-bonded amide network with an optimal strength. Under an applied electric field, both columns and core cyano groups align unidirectionally, thereby developing an extremely large macroscopic remnant polarization.

Ferroelectric liquid crystals (FLCs) have potential application in lightweight, easy-processable electrical devices for fast-

switching displays, rewritable memories, and nonlinear optics (*1*). For liquid crystalline (LC) materials to operate ferroelectrically, a nonzero

polarization at zero electric field (E-field), together with its electrical invertibility, is a prerequisite. However, this goal is difficult to realize, particularly in dynamic molecular systems such as LC materials, as once oriented electrically, polar motifs reorganize spontaneously at zero E-field in such a way that their dipoles cancel each other either macroscopically or locally. Although FLCs with a smectic geometry (Fig. 1, A and B) have been reported (2–5), most require cell

¹Department of Chemistry and Biotechnology, School of Engineering, The University of Tokyo, 7-3-1 Hongo, Bunkyo-ku, Tokyo 113-8656, Japan. ²Department of Organic and Polymeric Materials, Tokyo Institute of Technology, 2-12-1 O-okayama, Meguro-ku, Tokyo 152-8552, Japan. ³Japan Synchrotron Radiation Research Institute (JASRI), 1-1-1 Kouto, Sayo-cho, Sayo-gun, Hyogo 679-5148, Japan. ⁴RIKEN SPring-8 Center, 1-1-1 Kouto, Sayo-cho, Sayo-gun, Hyogo 679-5148, Japan.

*To whom correspondence should be addressed. E-mail: takezoe.h.aa@m.titech.ac.jp (H.T.); aida@macro.t.u-tokyo.ac.jp (T.A.)

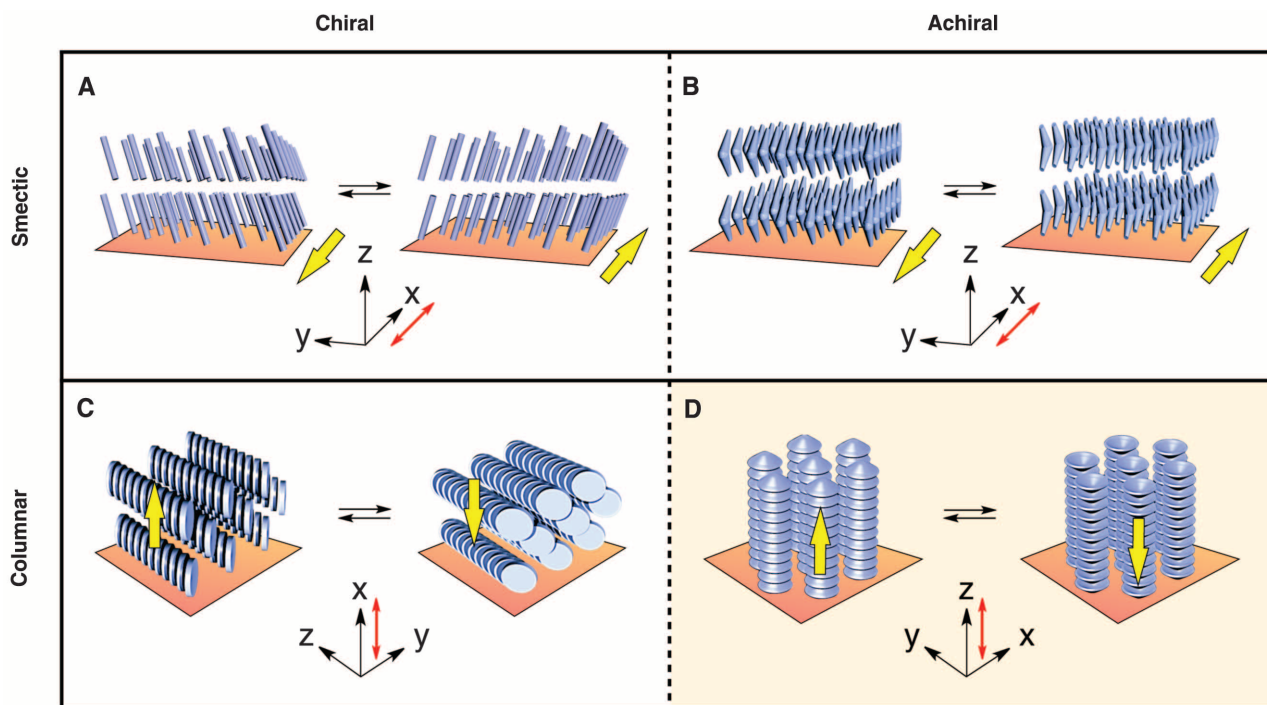


Fig. 1. Schematic illustrations of the electrical polarization behaviors of ferroelectric liquid crystals (FLCs) with four different geometries. (A) and (B) illustrate the behaviors of smectic-type FLCs consisting of chiral rod-shaped and achiral bent-shaped molecules, respectively, whereas (C) and (D) represent those of columnar FLCs composed of chiral discotic and achiral umbrella-shaped molecules, respectively. Red and yellow arrows denote the directions of an applied electric field (E-field) and the resulting polarization, respectively. Chiral rod-shaped molecules generate a layer polarization in the *x*-*y* plane. However, no macroscopic polarization develops because such a layer polarization is canceled owing to its helical orientation with the helical axis along the *z* direction. To develop a macroscopic polarization, a thin cell has been used so that an

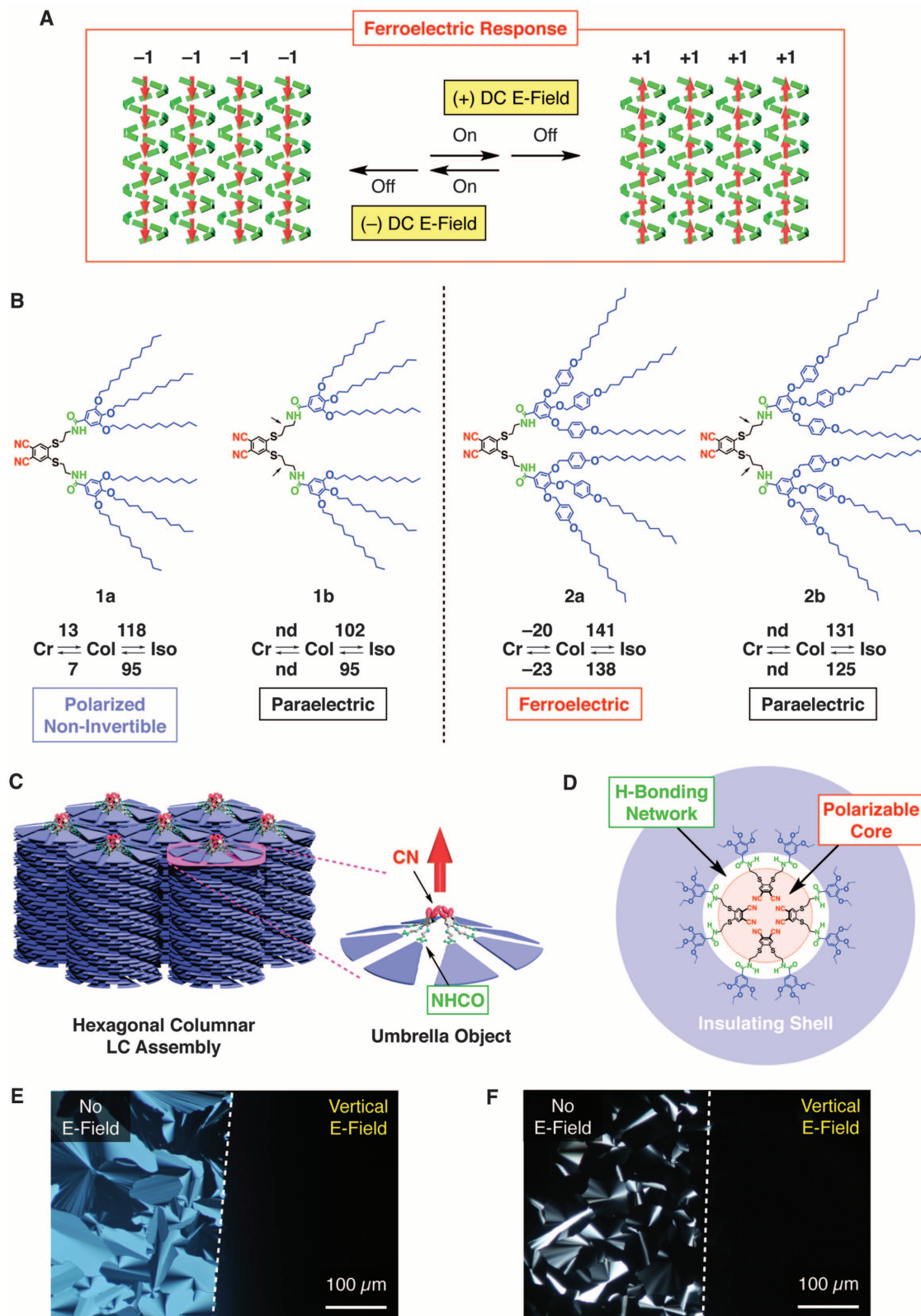
enhanced cell-surface effect unwinds the helical geometry as shown in (A). Achiral bent-shaped molecules, which likewise generate a layer polarization in the *x*-*y* plane, do not assemble in a helical geometry, so that a macroscopic polarization develops as shown in (B). Columnar assembled chiral discotic molecules adopt a helical geometry, which generates a polarization in a perpendicular direction (*x* direction) to the columnar axis when the helical geometry is unwound by means of a cell-surface effect as shown in (C). In contrast to (A) to (C), columnar assembled achiral umbrella-shaped molecules (this work) generate a polarization along the columnar axis (*z* direction). Therefore, unidirectional orientation of such columns results in the development of a macroscopic polarization as shown in (D).

surfaces to help maintain an electrically generated macroscopic polarization at zero E-field (6–8). To date, columnar FLCs, having a remnant and electrically invertible axial polarization (Fig.

1D), have not been demonstrated. Although some columnar LCs develop an electrically invertible axial polarization (9, 10), they lose the polarization within a millisecond (10, 11) when the

applied E-field is turned off. Even when the structural relaxation is observed to be slow, the polarization disappears only within ~100 s (12) after the E-field has been turned off. Further-

Fig. 2. Schematic illustration of (A) the ferroelectric response of electrically polarizable columns of **2a**. Red arrows and green squares represent an array of cyano groups and a hydrogen-bonded amide network, respectively. (B) Schematic illustrations of the molecular structures of compounds **1a** (14), **1b** (14), **2a**, and **2b** (arrows highlight the extra methylene group in **1b** and **2b**). Numerical values in phase diagrams represent phase-transition temperatures (°C), where Cr, Col, and Iso denote crystalline, hexagonal columnar, and isotropic phases, respectively (nd, not determined by DSC measurements). (C and D) Schematic illustrations of (C) columnar assembly of fan-shaped molecules and (D) a cross-section of their core-shell columnar assembly. (E and F) POM images of LC films of (E) **2a** at 120°C and (F) **2b** at 110°C under crossed polarizers. Samples were filled in a sandwich-type glass cell (thickness, 5 μm) equipped with patterned indium tin oxide (ITO) electrodes, which allowed an AC E-field (1.0 Hz, 20 $\text{V}_{\text{pp}} \mu\text{m}^{-1}$) to operate site-selectively from a vertical direction relative to the film sample. Dashed lines mark the border between E-field operating and nonoperating areas. In dark-view areas sandwiched by ITO electrodes, LC columns are oriented vertically.



more, unlike smectic FLCs, no columnar LCs are known to stabilize an electrically induced polarization along their columnar axes with the aid of cell surfaces. Here, we address a long-standing question of how to develop a ferroelectric response in a columnar architecture. Columnar FLCs having an axial nonzero polar-

ization at zero E-field and its electrical invertibility (Fig. 1D) are considered candidate materials for ultrahigh-density memory devices, as individual columns, when vertically aligned with respect to the electrodes, could ultimately serve as a one-bit memory (13, 14). If electrical polarization occurs in a direction perpendicu-

lar to the columnar axis (Fig. 1C) (15), such an ultrahigh-density memory device cannot be achieved. Thus, the goal of achieving columnar FLCs with an axial polarization (Fig. 1D) remains unresolved (16–20).

Here we report a columnar LC that can electrically develop a polarization along the columnar axis and maintain its polar order over a wide temperature range below the clearing temperature (Fig. 2A). Furthermore, this remnant polarization can be electrically inverted at a rather low coercive field (2.3 kV cm^{-1}), where the magnitude of spontaneous polarization is much larger ($P_s \sim 5.0 \text{ } \mu\text{C cm}^{-2}$) than those of current smectic FLCs ($P_s < 1.0 \text{ } \mu\text{C cm}^{-2}$). Our molecular design uses fan-shaped **2a** (Fig. 2B) carrying a polar phthalonitrile head group that anchors tapered paraffinic wedges via a hydrogen-bonding amide linker. This molecule self-assembles into an umbrella-shaped object (21, 22) with polar cyano groups inside, which stacks up columnar via hydrogen-bonding and van der Waals interactions at the amide and paraffinic parts, respectively (Fig. 2, C and D). The hydrogen-bonded amide network is developed along the columnar axis and ensures a core-shell architecture, where a large paraffinic shell wraps around a polarizable core domain accommodating an array of cyano groups. This core-shell architecture (Fig. 2D) was inspired by our recent work on E-field-responsive columnar LCs (23). We developed a particular type of “amide handle” that imparts an E-field-orientable nature to a variety of columnar LCs. In these cases, electrical orientation of the amide handles, by means of an alternating-current (AC) E-field, gives rise to large-area unidirectional orientation of LC columns along the field direction; however, none were ferroelectrically polarizable. Nevertheless, the LC mesophase of compound **1a** (Fig. 2B), which carries smaller paraffinic wedges than **2a**, has an intrinsic polarization, although its direction cannot be electrically inverted. We hypothesized that the inability to invert polarization may be due to a highly congested environment of the core part. Thus, compound **1b** (Fig. 2B), bearing amide linkers with one more carbon than **1a**, was synthesized in order to expand the core part appropriately. However, with such a small structural modification, the resulting columnar LC behaved paraelectrically.

In this study, we increased the shell volume of the core-shell architecture so that the hydrogen-bonded amide network, which confines the polarizable core, might become looser. We synthesized fan-shaped **2a** together with **2b** as a core-expanded reference (Fig. 2B) (24). By means of differential scanning calorimetry (DSC) (fig. S5), polarizing optical microscopy (POM; Fig. 2, E and F), and x-ray diffraction (XRD; fig. S7) analysis, we confirmed that both compounds self-assemble into a hexagonal columnar LC mesophase over a wide temperature range, including room temperature (phase diagrams in Fig. 2B). The intercolumnar distances,

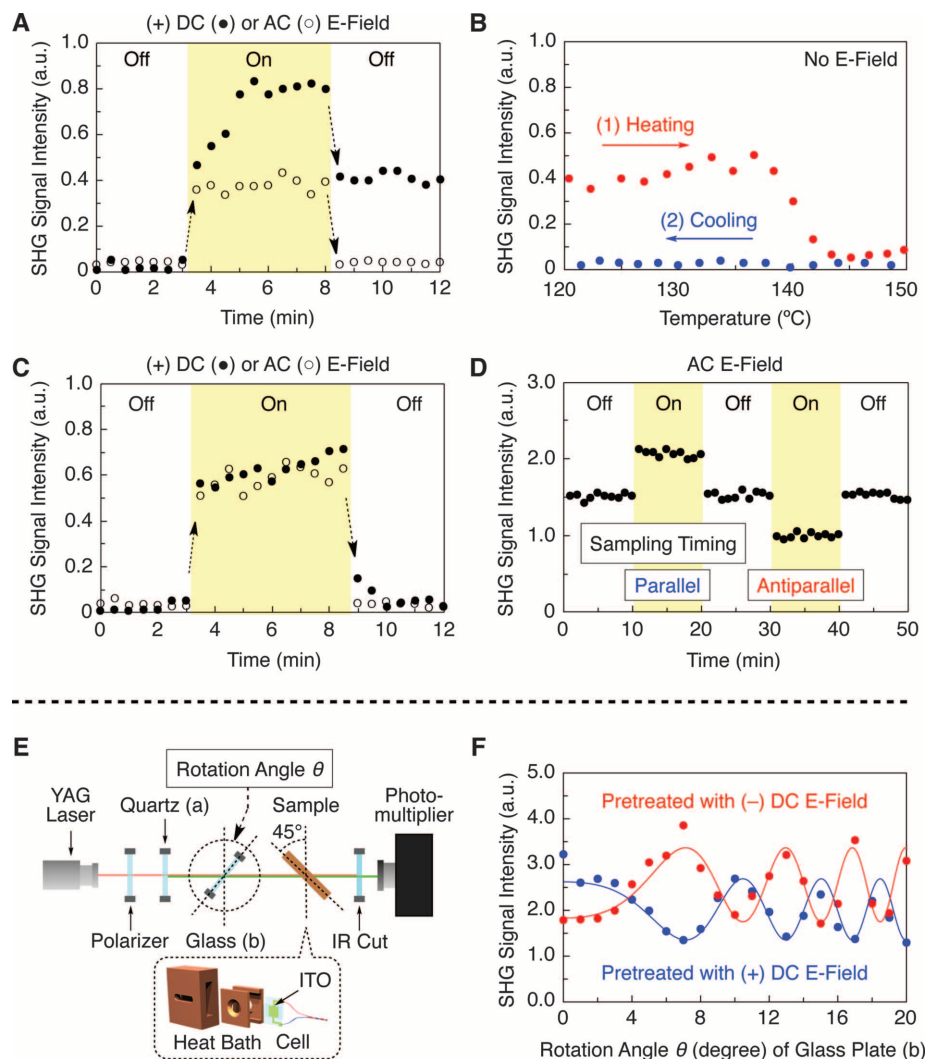


Fig. 3. (A and C) Effects of DC ($10 \text{ V } \mu\text{m}^{-1}$; filled circles) and AC (10 Hz , $20 \text{ V}_{\text{pp}} \mu\text{m}^{-1}$; open circles) E-fields on oriented LC films (thickness, $5 \text{ } \mu\text{m}$) of (A) **2a** at 120°C and (C) **2b** at 110°C , as observed by second-harmonic generation (SHG). (B) Thermal SHG profiles of a sample, obtained in (A) by use of a DC E-field ($10 \text{ V } \mu\text{m}^{-1}$), upon (1) heating up to an isotropic phase (red circles), followed by (2) cooling to the LC mesophase (blue circles) in the absence of an E-field. Once the LC sample lost its SHG activity on phase transition to the isotropic phase, macroscopic polar order did not emerge until the resulting material was allowed to transform back to the LC mesophase by cooling and polarized by applying a DC E-field. (D) Effect of an AC E-field (10 Hz , $20 \text{ V}_{\text{pp}} \mu\text{m}^{-1}$), as observed by SHG at 120°C , on an oriented LC film (thickness, $5 \text{ } \mu\text{m}$) of **2a**, polarized beforehand by applying a DC E-field ($10 \text{ V } \mu\text{m}^{-1}$) at 120°C . “Parallel” and “antiparallel” indicate that the data sampling was synchronously made when the switching AC E-field was directed parallel and antiparallel, respectively, to the DC E-field used for polarizing the sample. (E and F) SHG interferometry of an oriented LC film (thickness, $5 \text{ } \mu\text{m}$) of **2a**, polarized before the measurements by applying a DC E-field ($10 \text{ V } \mu\text{m}^{-1}$) at 120°C . (E) Schematic illustration of the optical setup for SHG interferometry. (F) SHG interferograms at different rotation angles (θ) of a glass plate (b) in (E) at 120°C . Samples that gave blue and red data points were polarized beforehand at 120°C with (+) and (–) DC E-fields, respectively. Solid curves were obtained by theoretical fitting. IR, infrared; YAG, yttrium-aluminum-garnet.

as determined from the observed XRD patterns, indicate that their columnar stacked elemental motifs are umbrella-shaped (25). Furthermore, when a 1.0-Hz square-shaped AC E-field [20 V peak-to-peak (V_{pp}) μm^{-1}] was applied site-selectively in a vertical direction, the LC films (thickness, $5 \mu\text{m}$) under crossed polarizers displayed a dark view in an E-field-operating area (Fig. 2, E and F). Thus, these columnar LCs can be electrically oriented.

FLCs should show a nonzero polarization at zero E-field, as well as electrical polarization switching. However, even nonferroelectric LCs, if contaminated with ionic species or if they relax slowly from an electrically polarized state, may display a switching profile that could be confused with ferroelectricity. Therefore, as in the case of **1a**, we investigated LC samples of **2a** and **2b** using second-harmonic generation (SHG), which provides a convenient and reliable method for optically demonstrating the existence of a polar order at zero E-field (26, 27). However, regardless of whether their columns were preoriented by an AC E-field, neither **2a** nor **2b** showed an intrinsic SHG activity (Figs. 3, A and C, 0 to 3 min). Hence, we decided to explore the effects of a direct-current (DC) E-field ($10 \text{ V } \mu\text{m}^{-1}$) on the polarization of these LC materials. Surprisingly a macroscopic polarization was electrically induced in a film sample (thickness, $5 \mu\text{m}$) of **2a** and was maintained after the applied E-field was turned off. The SHG signal appeared as soon as the DC E-field was applied to the sample (Fig. 3A, filled circles) then gradually intensified, reaching a plateau in 3 min. When the DC E-field was turned off, a certain amount of the SHG activity was lost. However, the material still remained SHG-active. By contrast, when an AC E-field (10 Hz , $20 \text{ V}_{\text{pp}} \mu\text{m}^{-1}$) was applied (Fig. 3A, open circles), SHG activity developed abruptly but was completely lost after the E-field was turned off. These observations allow us to conclude that the LC assembly of **2a** is macroscopically polarizable by a DC E-field. Notably, the induced polarization is thermally stable and maintained up to the clearing temperature for the LC mesophase (Fig. 3B, red circles).

We used SHG interferometry (28) to examine if the induced polarization in **2a** is electrically invertible. The optical setup (Fig. 3E) was configured so that SHG, if any, from a sample in question could interfere with that from a quartz plate (a). Thus, when a glass plate (b) is rotated, a phase shift is induced between the incident SHG beam from a quartz plate and the incident fundamental beam. Consequently, these SHG beams interfere constructively or destructively depending on the rotation angle, resulting in the development of a fringe pattern. Indeed, when the LC film of **2a** (thickness, $5 \mu\text{m}$) was polarized before the measurement by applying a DC E-field ($+10 \text{ V } \mu\text{m}^{-1}$) at 120°C , an interference fringe emerged (Fig. 3F). Notably, when the LC film was likewise pretreated in the opposite direction with the DC E-field ($-10 \text{ V } \mu\text{m}^{-1}$), a mirror-

image fringe pattern (Fig. 3F; blue and red lines) developed. Therefore, we conclude that **2a** gives rise to a ferroelectric response in its co-

lumnar assembly (Fig. 2A). By contrast, the SHG profiles of core-expanded **2b** under AC (Fig. 3C, open circles) and DC (Fig. 3C, filled circles)

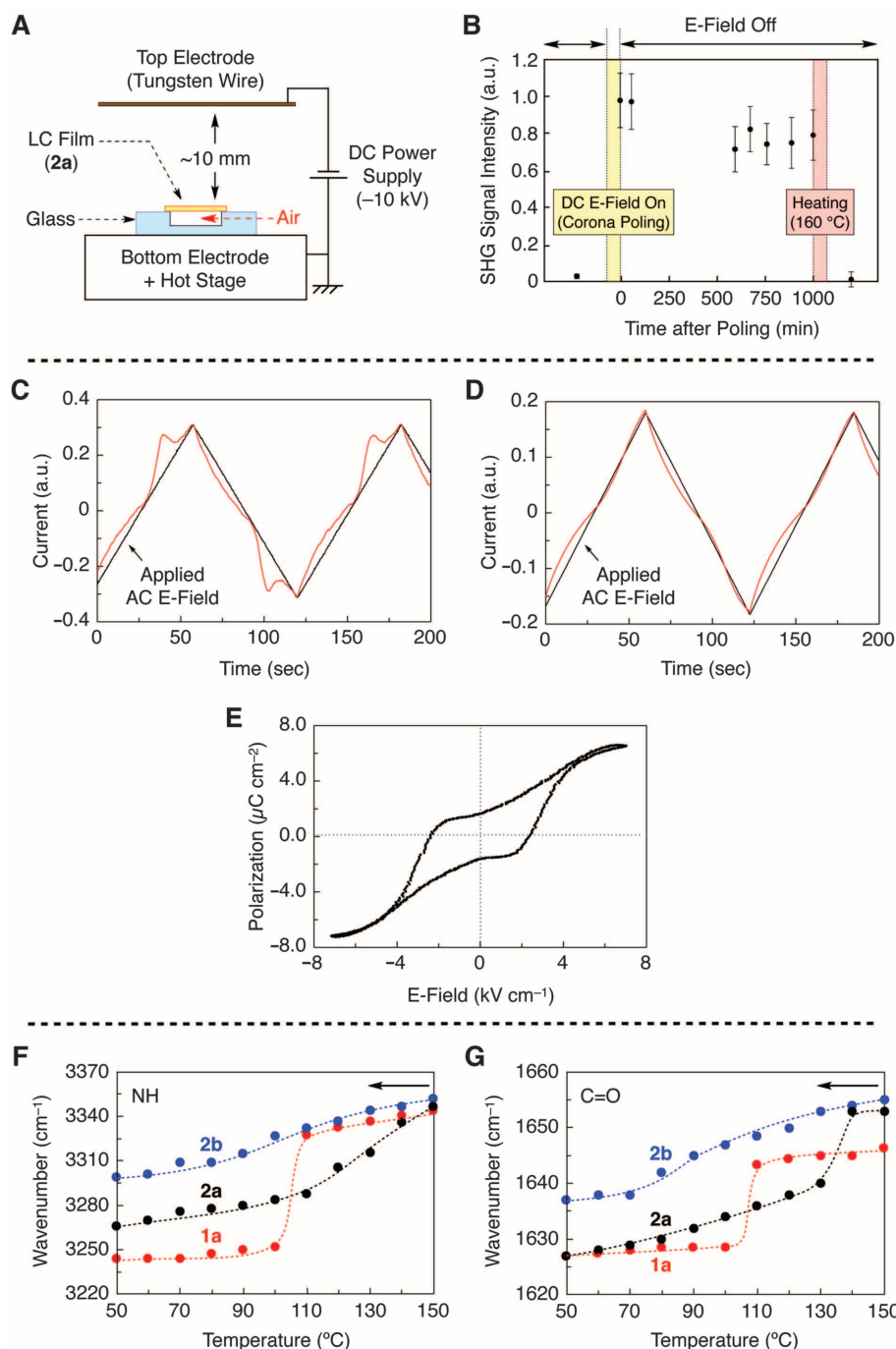


Fig. 4. (A and B) Effects of a DC E-field (corona poling; 1.0 kV mm^{-1}) on a free-standing LC film (thickness, $\sim 8 \mu\text{m}$) of **2a** at 120°C , as observed by SHG. (A) Schematic illustration of the optical setup for corona poling. (B) SHG profiles of the sample measured at 60°C before and after corona poling at 120°C for 30 min, followed by heating to 160°C for 15 min and then cooling to 60°C in the absence of an E-field. (C and D) Polarization reversal current profiles (red curves) of oriented LC films (thickness, $5 \mu\text{m}$) of (C) **2a** at 120°C and (D) **2b** at 110°C on application of a triangular-shaped AC E-field (0.008 Hz , $20 \text{ V}_{\text{pp}} \mu\text{m}^{-1}$, black lines). (E) P - E hysteresis loop of an oriented LC film (thickness, $5 \mu\text{m}$) of **2a** at 120°C , obtained by integration of the current profile in (C). (F and G) Infrared spectral change profiles at (F) 3370 to 3220 cm^{-1} (NH) and (G) 1660 to 1620 cm^{-1} (C=O) of **1a** (red circles), **2a** (black circles), and **2b** (blue circles) through the isotropic-to-LC phase transition.

E-fields indicated that the LC material in either case is polarized only temporarily, as in the case of **2a** under the influence of an AC E-field (Fig. 3A, open circles). Thus, the columnar LC assembly of **2b** is not ferroelectric but rather paraelectric. Unlike that of most smectic LCs, the ferroelectric nature observed for the columnar LC assembly of **2a** is “genuine” in that the electrically induced macroscopic polarization is maintained solely by its chemical architecture without the need for substrate-induced physical perturbations from cell surfaces. Indeed, when a DC E-field was applied to a free-standing LC film of columnarly assembled **2a** (corona poling, Fig. 4A), SHG activity emerged and was maintained unless the sample was heated above the clearing temperature for the LC mesophase (Fig. 4B).

For device applications, coercive electric field (E_c) and magnitude of polarization (P_s), together with remnant polarization (P_r), are important parameters (29, 30). For evaluating these parameters, a triangular-shaped AC E-field ($20 \text{ V}_{\text{pp}} \mu\text{m}^{-1}$) was applied at 120°C to an oriented LC film (thickness, $5 \mu\text{m}$) of **2a**. When the AC E-field frequency was in the range of 10 to 0.1 Hz, only featureless current profiles resulted (fig. S8), indicating that the electrical inversion of polarization is hardly induced. However, when the AC E-field frequency was further reduced (e.g., to 0.008 Hz), the sample started to display current peaks (Fig. 4C) as a result of the inversion of polarization. Integration of the observed current profile afforded a P - E loop with a clear hysteresis feature (Fig. 4E) typical of ferroelectric materials, where E_c , P_s , and P_r were evaluated as 2.3 kV cm^{-1} , $5.8 \mu\text{C cm}^{-2}$, and $1.7 \mu\text{C cm}^{-2}$, respectively. Notably, the E_c thus observed is much smaller than those of ferroelectric polymers. Furthermore, the observed P_s is larger than the highest P_s values ($<1.0 \mu\text{C cm}^{-2}$) so far reported for ferroelectric LC materials with a smectic geometry, although the value may contain a small margin of error due to a baseline fluctuation in Fig. 4C. By contrast, core-expanded **2b**, as expected from its paraelectric SHG response (Fig. 3C), displayed a nearly featureless current profile over a wide range of the applied E-field frequency (Fig. 4D).

Comparison of the structures of four fan-shaped LC molecules in Fig. 2B shows that the ferroelectric nature of **2a** results from a delicate balance between the structural factors involved in the core and shell domains of the columnar assembly. Namely, the polar cyano groups, which are confined in the core domain of the column, are congested in such a way that their E-field-induced orientation, leading to a polarization along the columnar axis, can be maintained after the E-field is turned off. The core environment in prototype **1a** seems to be too congested for the cyano groups to respond electrically, whereas those of core-expanded **1b** and **2b** are too flexible to main-

tain the induced orientation of the cyano groups. We consider that the ferroelectric columnar assembly of **2a** could possess a slightly looser hydrogen-bonded amide network than prototype **1a** because of the accommodation of larger paraffinic wedges in the shell domain. To support this hypothesis, we investigated the infrared spectral change profile of **2a** associated with the isotropic-to-LC phase transition, together with those of prototype **1a** and core-expanded **2b** as references. As expected from the three-dimensional structural order in its LC mesophase, prototype **1a** upon phase transition displayed an abrupt spectral change at the NH (Fig. 4F, red) and C=O (Fig. 4G, red) stretching vibrational bands. By contrast, the corresponding spectral change in core-expanded **2b** was quite gradual; the stretching vibrational bands due to C=O and NH shifted almost monotonically toward a lower wavenumber region (Fig. 4, F and G, blue dashed curves). Furthermore, the wavenumbers of these vibrational bands were obviously larger than those of **1a** in the LC mesophase. Therefore, the hydrogen-bonded amide network is much less developed and more labile than that in **1a**. Meanwhile, in agreement with our hypothesis, **2a** displayed a moderate spectral change profile between those of the two reference compounds (Fig. 4, F and G, black dashed curves), where the wavenumbers of its C=O and NH vibrational bands are present in-between those observed for **1a** and **2b**.

As discussed in Fig. 3A, the LC assembly of **2a** displays both ferroelectric and paraelectric properties, for which the cyano and amide groups, respectively, are responsible. It is interesting to consider whether these two polar components interfere with each other in their electrical operations. To clarify this point, we used an oriented LC film (thickness, $5 \mu\text{m}$) of **2a**, polarly pre-ordered using a (+) DC E-field ($10 \text{ V } \mu\text{m}^{-1}$), and an AC E-field (10 Hz, $10 \text{ V}_{\text{pp}} \mu\text{m}^{-1}$) was applied periodically (shaded areas in Fig. 3D; each 10 min). SHG signals were sampled when the switching AC E-field was directed parallel or antiparallel to the DC E-field used for the paraelectric polarization. Synchronous with the operation of the AC E-field, the signal intensity quickly changed either positively or negatively depending on the timing for data sampling (Fig. 3D), indicating that a paraelectric motion of the amide component was indeed activated. However, whenever the AC E-field operation was disabled, the SHG activity of the material returned to the original level. Therefore, the paraelectric motion of the amide groups, which allows for the unidirectional columnar orientation (Fig. 2E), does not deteriorate the orientation of the core cyano groups. Namely, in the core-shell columnar assembly of **2a** (Fig. 2, C and D), the hydrogen-bonded amide network with an optimal strength imparts to the polarizable core domain a remnant but electrically invertible axial polarization (Fig. 2A). This is a key

design strategy for the long-standing issue of how to realize columnar FLCs.

References and Notes

1. S. T. Lagerwall, *Ferroelectric and Antiferroelectric Liquid Crystals* (Wiley-VCH, Weinheim, 1999).
2. R. B. Meyer, L. Liebert, L. Strzelecki, P. Keller, *J. Phys. Lett.* **36**, 69 (1975).
3. H. Takezoe, Y. Takanishi, *Jpn. J. Appl. Phys.* **45**, 597 (2006).
4. R. A. Reddy, C. Tschierske, *J. Mater. Chem.* **16**, 907 (2006).
5. R. A. Reddy *et al.*, *Science* **332**, 72 (2011).
6. N. A. Clark, S. T. Lagerwall, *Appl. Phys. Lett.* **36**, 899 (1980).
7. F. Araoka, H. Hoshi, H. Takezoe, *Phys. Rev. E Stat. Nonlin. Soft Matter Phys.* **69**, 051704 (2004).
8. L. Guo *et al.*, *Phys. Rev. E Stat. Nonlin. Soft Matter Phys.* **84**, 031706 (2011).
9. E. Gorecka *et al.*, *J. Am. Chem. Soc.* **126**, 15946 (2004).
10. K. Kishikawa, S. Nakahara, Y. Nishikawa, S. Kohmoto, M. Yamamoto, *J. Am. Chem. Soc.* **127**, 2565 (2005).
11. Y. Okada *et al.*, *Phys. Rev. E Stat. Nonlin. Soft Matter Phys.* **76**, 041701 (2007).
12. C. F. F. Fitić, W. S. C. Roelofs, M. Kemerink, R. P. Sijbesma, *J. Am. Chem. Soc.* **132**, 6892 (2010).
13. H. Takezoe, K. Kishikawa, E. Gorecka, *J. Mater. Chem.* **16**, 2412 (2006).
14. D. Miyajima *et al.*, *J. Am. Chem. Soc.* **132**, 8530 (2010).
15. H. Bock, W. Helfrich, *Liq. Cryst.* **18**, 707 (1995).
16. A. Jákli, A. Saupe, *Liq. Cryst.* **22**, 309 (1997).
17. D. Kilian *et al.*, *Liq. Cryst.* **27**, 509 (2000).
18. E. Dalcanele, G. Antonoli, M. Riccò, H. Groothues, F. Kremer, *Liq. Cryst.* **27**, 1161 (2000).
19. W. Haase *et al.*, *Liq. Cryst.* **29**, 133 (2002).
20. D. Miyajima *et al.*, *J. Am. Chem. Soc.* **131**, 44 (2009).
21. C. Tschierske, *Chem. Soc. Rev.* **36**, 1930 (2007).
22. B. M. Rosen *et al.*, *Chem. Rev.* **109**, 6275 (2009).
23. D. Miyajima *et al.*, *Angew. Chem. Int. Ed.* **50**, 7865 (2011).
24. Materials and methods are available as supplementary materials on Science Online.
25. B. M. Rosen *et al.*, *J. Am. Chem. Soc.* **131**, 17500 (2009).
26. T. Watanabe *et al.*, *Jpn. J. Appl. Phys.* **35**, L505 (1996).
27. E. Gorecka *et al.*, *Phys. Rev. E Stat. Nonlin. Soft Matter Phys.* **73**, 031704 (2006).
28. Y. Okada *et al.*, *Phys. Rev. E Stat. Nonlin. Soft Matter Phys.* **72**, 020701 (2005).
29. S. Horiuchi, Y. Tokura, *Nat. Mater.* **7**, 357 (2008).
30. S. Horiuchi *et al.*, *Nature* **463**, 789 (2010).

Acknowledgments: D.M. thanks the Japan Society for the Promotion of Science for award of a Young Scientist Fellowship. The synchrotron radiation experiments were performed at BL02B2 and BL44B2 in Spring-8 under the Budding Researchers Support Programs and the Priority Nanotechnology Support Program administered by the Japan Synchrotron Radiation Research Institute (Proposal nos. 2008B1777, 2009A1651, and 2009A1699) and with the approval of RIKEN (Proposal no. 20090021).

Supplementary Materials

www.sciencemag.org/cgi/content/full/336/6078/209/DC1
Materials and Methods
Figs. S1 to S8
Reference (31)

15 December 2011; accepted 29 February 2012
10.1126/science.1217954

Gravity Field and Internal Structure of Mercury from MESSENGER

David E. Smith,¹ Maria T. Zuber,^{1*} Roger J. Phillips,² Sean C. Solomon,³ Steven A. Hauck II,⁴ Frank G. Lemoine,⁵ Erwan Mazarico,^{1,5} Gregory A. Neumann,⁵ Stanton J. Peale,⁶ Jean-Luc Margot,⁷ Catherine L. Johnson,^{8,9} Mark H. Torrence,^{10,5} Mark E. Perry,¹¹ David D. Rowlands,⁵ Sander Goossens,¹² James W. Head,¹³ Anthony H. Taylor¹⁴

Radio tracking of the MESSENGER spacecraft has provided a model of Mercury's gravity field. In the northern hemisphere, several large gravity anomalies, including candidate mass concentrations (mascons), exceed 100 milli-Galileos (mgal). Mercury's northern hemisphere crust is thicker at low latitudes and thinner in the polar region and shows evidence for thinning beneath some impact basins. The low-degree gravity field, combined with planetary spin parameters, yields the moment of inertia $C/MR^2 = 0.353 \pm 0.017$, where M and R are Mercury's mass and radius, and a ratio of the moment of inertia of Mercury's solid outer shell to that of the planet of $C_m/C = 0.452 \pm 0.035$. A model for Mercury's radial density distribution consistent with these results includes a solid silicate crust and mantle overlying a solid iron-sulfide layer and an iron-rich liquid outer core and perhaps a solid inner core.

The internal structure of a planet preserves substantial information regarding processes that have influenced thermal and tectonic evolution, and measuring a planet's gravity field provides fundamental information for understanding that body's internal mass distribution. Mapping Mercury's gravity field is consequently a primary objective of the MESSENGER Surface, Space ENvironment, GEochemistry, and Ranging (MESSENGER) mission (1).

On 18 March 2011, the MESSENGER spacecraft was inserted into a ~12-hour, near-polar orbit around Mercury, with an initial periaapsis altitude of 200 km, initial periaapsis longitude of 60°N, and apoapsis at ~15,200 km altitude in the southern hemisphere. This highly eccentric orbit permits the mapping of regional gravitational structure

in the northern hemisphere at the maximum resolution of a spherical harmonic model near periaapsis but limits the recoverability of the gravity field to long wavelengths at southern latitudes. At the ascending and descending nodes of the orbit (on the equator), the altitude of MESSENGER is about 4900 and 1200 km, respectively.

During the first few weeks after orbit insertion, MESSENGER was tracked extensively at X-band (8 GHz) by stations of NASA's Deep Space Network (DSN). After this initial period of nearly continuous tracking, the typical coverage was less frequent, limiting the number of direct periaapsis passages that were observed. We have processed data from 18 March through 23 August 2011, a tracking period that spans more than two Mercury sidereal days (2) (fig. S1). We lim-

ited our analysis to 1-day arcs to reduce the modeling errors from the nonconservative forces, which grow quadratically with time. The aggregated normal equations developed from daily arcs were used to develop solutions of the gravity field of Mercury (2) to degree (l) and order (m) in spherical harmonics, a compromise between data sensitivity and global resolution.

The gravity anomalies and gravitational potential (geoid) of the spherical harmonic solution, here termed HgM002, are depicted in Fig. 1, A and B, respectively. The northern lowlands, ~2 km lower in elevation than surrounding terrain and approximately centered over the north pole (3), correspond to a broad gravity low (Fig. 2). At mid-latitudes, a west-southwest-east-northeast-trending, discontinuous upland that extends for nearly half the circumference of Mercury is

¹Department of Earth, Atmospheric and Planetary Sciences, Massachusetts Institute of Technology, Cambridge, MA 02139–4307, USA. ²Planetary Science Directorate, Southwest Research Institute, Boulder, CO 80302, USA. ³Department of Terrestrial Magnetism, Carnegie Institution of Washington, Washington, DC 20015, USA. ⁴Department of Earth, Environmental, and Planetary Sciences, Case Western Reserve University, Cleveland, OH 44106, USA. ⁵NASA Goddard Space Flight Center, Greenbelt, MD 20771, USA. ⁶Department of Physics, University of California, Santa Barbara, CA 93106, USA. ⁷Department of Earth and Space Sciences, University of California, Los Angeles, CA 90095, USA. ⁸Department of Earth and Ocean Sciences, University of British Columbia, Vancouver, BC, V6T 1Z4 Canada. ⁹Planetary Science Institute, 1700 East Fort Lowell, Suite 106, Tucson, AZ 85719, USA. ¹⁰Stinger Ghaffarian Technologies, Inc., 7701 Greenbelt Rd., Greenbelt, MD 20770, USA. ¹¹Johns Hopkins University, Applied Physics Laboratory, Laurel, MD 20723, USA. ¹²University of Maryland, Baltimore County, Baltimore, MD 21250, USA. ¹³Department of Geological Sciences, Brown University, Providence, RI 02912, USA. ¹⁴KinetX, Inc., Tempe, AZ 85284, USA.

*To whom correspondence should be addressed. E-mail: zuber@mit.edu

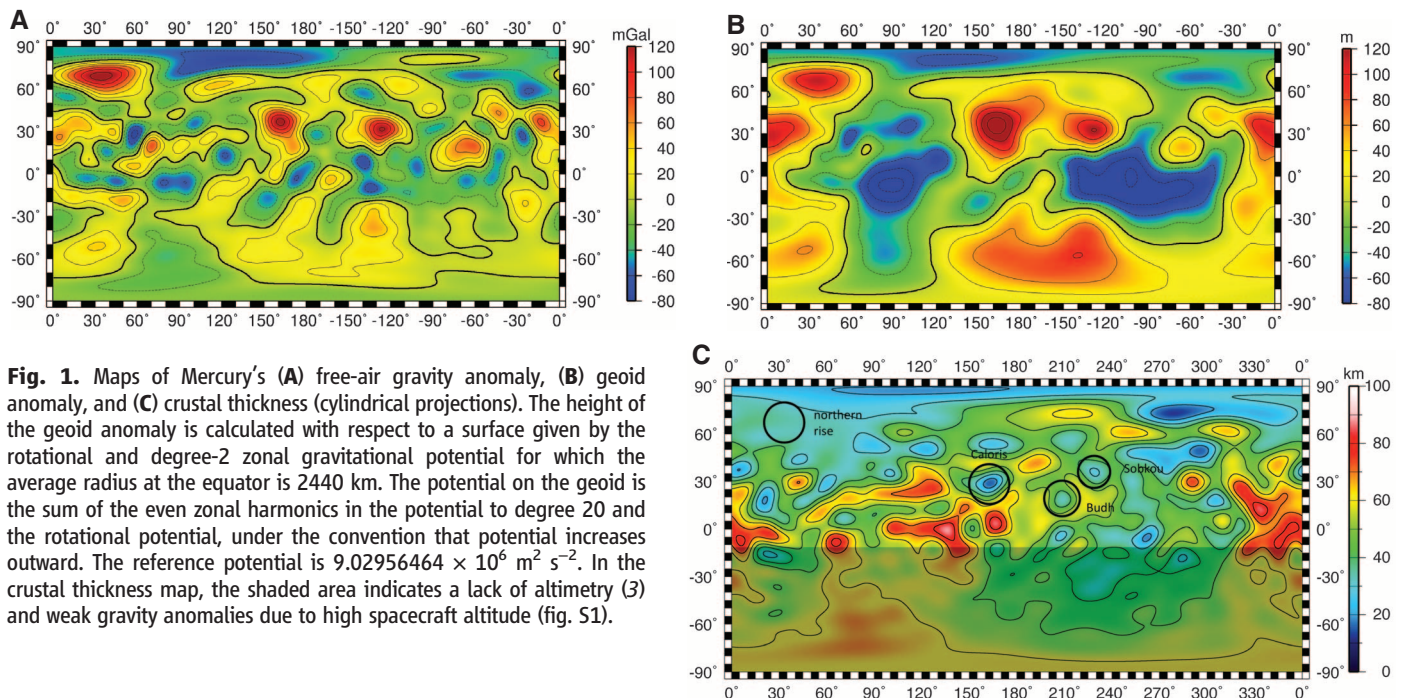


Fig. 1. Maps of Mercury's (A) free-air gravity anomaly, (B) geoid anomaly, and (C) crustal thickness (cylindrical projections). The height of the geoid anomaly is calculated with respect to a surface given by the rotational and degree-2 zonal gravitational potential for which the average radius at the equator is 2440 km. The potential on the geoid is the sum of the even zonal harmonics in the potential to degree 20 and the rotational potential, under the convention that potential increases outward. The reference potential is $9.02956464 \times 10^6 \text{ m}^2 \text{ s}^{-2}$. In the crustal thickness map, the shaded area indicates a lack of altimetry (3) and weak gravity anomalies due to high spacecraft altitude (fig. S1).

marked by weakly positive gravity anomalies and thus must be largely balanced at depth by thicker-than-average crust or lower-than-average densities. The gravity field in the northern hemisphere shows several regional anomalies that exceed 100 milli-Galileo (mgal) in amplitude. One such anomaly coincides with Mercury's northern rise, a locally elevated region (centered at 68°N, 33°E) (3) within the northern lowlands and north polar gravity low. Another is associated with the Caloris impact basin (31°N, 160°E), where some of the anomalous mass correlates with and can be attributed to regions of high topography on the basin floor (3). A third positive anomaly is near the Sobkou impact basin (36°N, 226°E), but the gravity anomaly is centered on the southeast rim of that basin, complicating the relation between gravity and topography. Other positive gravity anomalies are not obviously associated with mapped impact basins at the cur-

rent resolution of the gravity field. Attempts to resolve mass concentration (or mascon) anomalies similar to those seen at prominent basins on the Moon (4) and Mars (5) from tracking observations during MESSENGER's first two Mercury flybys (6) and the third Mariner 10 flyby (7) have not produced definitive results. From harmonic solution HgM002, the only large, positive free-air gravity anomaly that is spatially well-correlated with an impact basin, the classical definition of a mascon (4), is that associated with the Caloris basin.

The surface that represents Mercury's reference equipotential, or geoid (Fig. 1B), has a dynamic range of 200 m, and its largest anomaly is centered at Caloris. Because the spacecraft altitude over the southern hemisphere is much higher than in the northern hemisphere, the geoid error, projected from the full covariance of the HgM002 solution, is less than 20 m north of

the equator but reaches 40 to 50 m in regions of mid- to high latitudes in the southern hemisphere. The presence or absence of large geoid features in the south cannot be confirmed with the present data.

The gravity field has been combined with topography from MESSENGER's Mercury Laser Altimeter (MLA) (3) to produce a map of the crustal thickness of Mercury's northern hemisphere (Fig. 1C). On the basis of surface compositional measurements (8, 9) from MESSENGER's X-Ray Spectrometer (XRS) indicating that the crust is intermediate between basaltic and more ultramafic compositions, as well as melting experiments on candidate mantle compositions consistent with XRS measurements (10), we assume a density contrast between the crust and mantle of 200 kg m⁻³. On the basis of limits determined from flyby observations of gravity and topography (6, 11) and constraints from tectonic models for the depth extent of faulting (12), we adopt a mean crustal thickness of 50 km. The uncertainty in this mean value represents the largest uncertainty in the crustal thickness model. We also assume uniform values for the densities of the crust and mantle and that all signals in the gravity field not produced by topography are signatures of relief on the crust-mantle boundary. The resulting map of crustal thickness (Fig. 1C) indicates that the crust is generally thicker (50 to 80 km) near the equator and thins toward the north polar region (20 to 40 km), with the regionally thinnest crust located beneath the northern lowlands (3). The Caloris basin overlies an area of locally thin crust, consistent with the interpretation of mascon basins on the Moon (13) and Mars (14) that crustal thinning beneath basins contributes substantially to the observed gravity anomaly. The positive free-air gravity anomaly near Sobkou is associated with an adjacent topographic rise, and the anomaly extends in the directions of both the Sobkou and the Budh (17°N, 208°E) impact basins. If the gravitational effects of topography are removed from the free-air gravity anomaly map, the resulting Bouguer anomaly shows strong positive anomalies centered over the Sobkou and Budh basins and a weaker negative anomaly over the rise, indicating crustal thinning directly beneath the basins and thicker crust beneath the rise (Fig. 1C). Like Caloris, Sobkou and Budh also qualify as mascons on the basis of a crust-mantle boundary that is substantially elevated beneath these basins.

A comparison of gravity anomalies that would result from Mercury's shape alone with the gravity anomalies from the HgM002 solution is made in Fig. 2. High-standing terrain borders many parts of the northern lowlands (3), as is also evident in the broader-scale view of the equivalent gravity field (Fig. 2A). Mild gravity anomalies in this region (Fig. 2B) suggest a high degree of interior mass compensation. By contrast, the northern rise has a gravity anomaly nearly as strong as that due to shape alone (~150

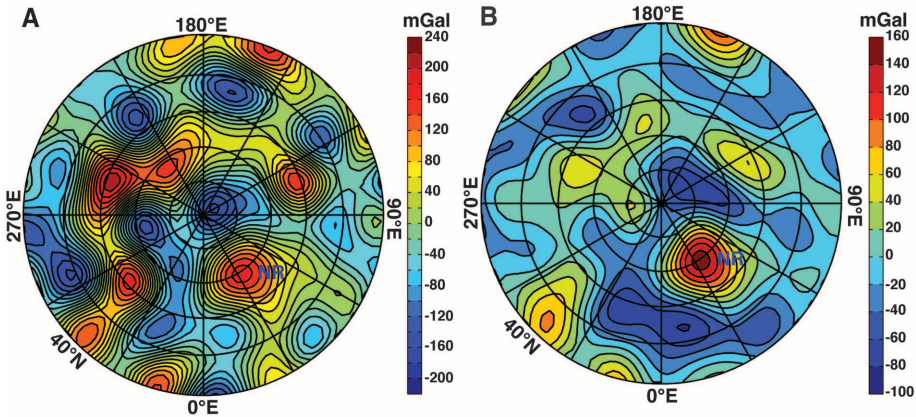


Fig. 2. (A) The radial component of the gravitational acceleration vector resulting from a 20 by 20 spherical harmonic expansion of Mercury's shape (3) given a density of upper crustal material of 3100 kg m⁻³. Results are shown in a polar stereographic projection north of 40°N. NR indicates the location of the northern rise. (B) The radial component of the gravitational acceleration vector resulting from the 20 by 20 HgM002 spherical harmonic gravity solution. In both plots, the solution shown has been limited to spherical harmonic terms with degrees 6 and greater to emphasize local- to regional-scale anomalies. The calculation demonstrates that gravity and shape are correlated and that the topography, except for the northern rise, is approximately compensated.

Table 1. Normalized* low-degree gravity coefficients in the HgM002 gravity model for Mercury.

Parameter	Value	Uncertainty†	Comments
GM , km ³ s ⁻²	22031.780	±0.02	No significant difference from HgM001.
$C_{20} \times 10^{-5}$	-2.25	±0.01	~20% smaller than Mariner 10 estimate of $(-2.68 \pm 0.89) \times 10^{-5}$.
$C_{21} \times 10^{-8}$	-4.64	±5	Consistent with coalignment of gravity field and angular momentum vector.
$S_{21} \times 10^{-8}$	1.35	±5	
$C_{22} \times 10^{-5}$	1.253	±0.01	Ratio of S_{22}/C_{22} is small, indicating that the equatorial major axis of the gravity field is aligned with Mercury's "hot-pole" longitudes.
$S_{22} \times 10^{-5}$	0.005	±0.01	
$C_{30} \times 10^{-6}$	-4.49	±0.3	Negative value indicates that a periapsis over the south pole is needed for a stable spacecraft orbit about Mercury.
$C_{40} \times 10^{-6}$	-6.5	±0.8	

*Normalizations follow those of Kaula (29).

†Uncertainties are best estimates rather than formal errors.

versus ~ 170 mGal), indicating little mass compensation and a thick lithosphere. We have estimated the thickness, T_e , of the effective elastic lithosphere beneath the northern rise by assuming that partial compensation takes place at the crust-mantle boundary and then finding model solutions that best fit the gravity anomaly in terms of crustal and elastic lithosphere thicknesses (Fig. 2). Over a crustal thickness range of 25 to 100 km, T_e is 70 to 90 km, and the downward flexural deflection of the crust-mantle boundary is minor (3 to 5 km), consistent with the lack of a discernible crustal thickness anomaly at the northern rise (Fig. 1C). An elastic lithosphere is a surrogate for one with more complex temperature-dependent strength, but temperatures at a given depth in the lower crust and uppermost mantle vary approximately inversely with T_e . The northern rise, part of the northern smooth plains volcanic complex (15), has been estimated from its impact crater size-frequency distribution to have a surface that formed ~ 3.7 to 3.8 billion years ago (Ga), substantially younger than that of the surrounding heavily cratered highlands (16). The greater level of apparent mass compensation of the highlands will yield, under similar assumptions, a thinner elastic lithosphere and higher crustal and mantle temperatures at the time of formation than the northern rise. The inference that Mercury's interior generally cooled with time is in keeping with thermal evolution models for the terrestrial planets. T_e estimates for Mars derived from gravity-topography relations for regions with ages of major topographic features similar to that of the northern rise, in contrast, are considerably smaller (17).

The major parameters of gravity field solution HgM002, including the product of the gravitational constant and Mercury's mass (GM), are given in Table 1. The GM value is close to that given by the most recent previous model of Mercury's gravitational field (HgM001), derived solely from the tracking of MESSENGER during its first two near-equatorial flybys (6).

The covariance matrix of solution HgM002 was used to generate clone models of the gravity field in order to analyze the error characteristics for the degree-2 coefficients and C_{30} (2) (fig. S5). The harmonic coefficients C_{20} and C_{22} are tightly bounded with small relative uncertainties, and C_{21} and S_{21} are small (Table 1).

The C_{20} and C_{22} terms provide important constraints on the interior structure of Mercury because they are directly relatable to the radial distribution of density. Earth-based radar measurements of Mercury's pole position confirm that the planet occupies a Cassini state in which the axis of rotation remains coplanar with the orbit normal and the normal to the Laplace plane as the spin vector and the orbit normal precess together about the latter with an $\sim 300,000$ -year period (18). Radar observations also show that the amplitude of the 88-day physical libration in longitude is so large that the mantle and crust must be librating independently of the core (18).

This state allows the determination of Mercury's normalized polar moment of inertia, C/MR^2 , where R is Mercury's mean radius, and a measurement of the ratio of the polar moment of inertia C_m of the solid outer portion of the planet (6, 18) to that of the entire planet (19, 20). The values of C_{20} and C_{22} (Table 1), combined with Earth-based radar measurements of the amplitude of Mercury's forced libration and obliquity (18) and ancillary data on the precession rate and pole position (21), provide the information necessary to estimate C/MR^2 and C_m/C . A libration amplitude of 35.8 ± 2 arcseconds and a slightly revised obliquity value of 2.06 ± 0.1 arcmin (22) yields internal structure parameters $C/MR^2 = 0.353 \pm 0.017$ and $C_m/C = 0.452 \pm 0.035$.

Resulting moment of inertia parameters for more than 1 million Monte Carlo models that include a silicate crust and mantle, as well as an Fe-rich core that may contain solid and liquid layers are shown in Fig. 3. These models are constrained only by the mean radius (2440 km) and bulk density of Mercury [5430 kg m^{-3} , e.g., (23)]. Comparison of the internal structure models with the measured moment of inertia parameters indicates that the outer radius of the liquid portion of the core under the adopted modeling assumptions is 2030 ± 37 km (1 SD), and the density of the outer shell overlying the liquid core is $3650 \pm 225 \text{ kg m}^{-3}$. The procedure does not provide a size estimate for any solid inner component of the core.

The large average bulk density inferred for Mercury's solid outer shell is surprising given that measurements by the MESSENGER XRS determined an upper bound on the average surface abundance of Fe of ~ 4 weight percent (8). Although uncertainty in the density of the solid shell permits a wide range of possibilities, the nominal value provides an important constraint on the planet's bulk composition. The low Fe abundance in volcanic rocks at Mercury's surface suggests that Mercury's silicate mantle is also low in iron and cannot account for the outer shell density. Relatively low surface abundances

of Ti and Al (8) are also inconsistent with substantial amounts of such high-density mantle minerals as ilmenite and garnet. A deeper reservoir of high-density material is therefore needed to account for the large solid-shell density and moment of inertia. One possibility is a dense silicate layer, possibly Fe-bearing, that has not substantively participated in the generation of Mercury's crust.

Alternatively, Mercury may have a solid layer of FeS at the top of the core. The highly reducing chemical conditions implied for Mercury's precursory materials by the low Fe and high S content of surface rocks (8, 9) suggest that Mercury's core likely contains substantial Si as well as S (24). Fe-S-Si alloys are subject to liquid immiscibility at pressures less than ~ 15 GPa (25), resulting in the buoyancy segregation of S-rich liquids at the top of the core. The density of solid FeS is sufficiently low that for a broad range of conditions the solid form would likely remain at the top of the core. There is a strong, albeit poorly constrained, trade-off between the thickness of a basal solid FeS layer and the density of the silicate mantle, although the basal layer could be a few tens of kilometers to as much as ~ 200 km in thickness. The thickness of the outer silicate portion of the planet would, under this interpretation, be thinner than the nominal 410-km depth to the solid-liquid boundary. A solid FeS layer at the base of the mantle would place strong constraints on the present thermal structure of Mercury. Moreover, a static, electrically conducting layer at the top of the core would act to decrease the overall strength of the field observable at or above the planetary surface and would attenuate harmonic components of the magnetic field increasingly strongly with increasing degree (26).

The gravity field results point to a much different interior structure for Mercury from that heretofore anticipated and from those of the other terrestrial planets. These results will require reconsideration of models for Mercury's interior thermal (27) and tectonic (28) evolution.

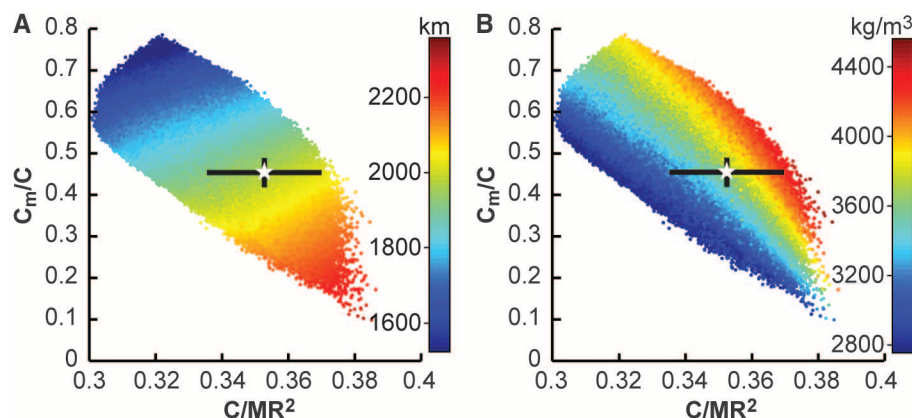


Fig. 3. (A) Outer radius of Mercury's liquid core. **(B)** Average density of the solid shell that overlies the liquid core. The stars represent the central values for C/MR^2 and C_m/C , and the black bars denote ± 1 SD.

References and Notes

1. S. C. Solomon, R. L. McNutt Jr., R. E. Gold, D. L. Domingue, *Space Sci. Rev.* **131**, 3 (2007).
2. Materials and methods are available as supporting material on Science Online.
3. M. T. Zuber *et al.*, *Science* **336**, 217 (2012); 10.1126/science.1218805.
4. P. M. Muller, W. L. Sjogren, *Science* **161**, 680 (1968).
5. D. E. Smith *et al.*, *J. Geophys. Res.* **98**, 20871 (1993).
6. D. E. Smith *et al.*, *Icarus* **209**, 88 (2010).
7. J. D. Anderson, J. Palguta, G. Schubert, Abstract P41A-1572, paper presented at the American Geophysical Union Fall Meeting, San Francisco, CA, 5 to 9 December 2011.
8. L. R. Nittler *et al.*, *Science* **333**, 1847 (2011).
9. L. R. Nittler *et al.*, Abstract 142-3, paper presented at the Geological Society of America Annual Meeting, Minneapolis, MN, 9 to 12 October 2011.
10. B. Charlier, T. L. Grove, M. T. Zuber, *Lunar Planet. Sci.* **43**, abstract 1400 (2012).
11. M. T. Zuber *et al.*, *Science* **321**, 77 (2008).
12. F. Nimmo, T. R. Watters, *Geophys. Res. Lett.* **31**, L02701 (2004).
13. G. A. Neumann, M. T. Zuber, D. E. Smith, F. G. Lemoine, *J. Geophys. Res.* **101** (E7), 16841 (1996).
14. M. T. Zuber *et al.*, *Science* **287**, 1788 (2000).
15. J. W. Head *et al.*, *Science* **333**, 1853 (2011).
16. R. G. Strom, G. Neukum, in *Mercury*, F. Villas, C. R. Chapman, M. S. Matthews, Eds. (Univ. of Arizona Press, Tucson, 1988), pp. 363–373.
17. P. J. McGovern *et al.*, *J. Geophys. Res.* **109**, E07007 (2004).
18. J.-L. Margot, S. J. Peale, R. F. Jurgens, M. A. Slade, I. V. Holin, *Science* **316**, 710 (2007).
19. S. J. Peale, *Nature* **262**, 765 (1976).
20. S. J. Peale, R. J. Phillips, S. C. Solomon, D. E. Smith, M. T. Zuber, *Meteorit. Planet. Sci.* **37**, 1269 (2002).
21. M. Yseboodt, J.-L. Margot, *Icarus* **181**, 327 (2006).
22. J.-L. Margot, S. Padovan, S. J. Peale, S. C. Solomon, Abstract P41A-1573, paper presented at the American Geophysical Union Fall Meeting, San Francisco, CA, 5 to 9 December 2011.
23. S. A. Hauck II, S. C. Solomon, D. A. Smith, *Geophys. Res. Lett.* **34**, L18201 (2007).
24. V. Malavergne, M. J. Toplis, S. Berthet, J. Jones, *Icarus* **206**, 199 (2010).
25. G. Morard, T. Katsura, *Geochim. Cosmochim. Acta* **74**, 3659 (2010).
26. U. R. Christensen, *Nature* **444**, 1056 (2006).
27. S. A. Hauck II, A. J. Dombard, R. J. Phillips, S. C. Solomon, *Earth Planet. Sci. Lett.* **222**, 713 (2004).
28. M. T. Zuber *et al.*, *Icarus* **209**, 88 (2010).
29. W. M. Kaula, *Theory of Satellite Geodesy* (Blaisdell, Waltham, MA, 1966).

Acknowledgments: The MESSENGER project is supported by the NASA Discovery Program under contracts NASS-97271 to The Johns Hopkins University Applied Physics Laboratory and NASW-00002 to the Carnegie Institution of Washington. We acknowledge the contributions of the MESSENGER spacecraft team and the radio science and MLA instrument teams in acquiring the observations used herein. We are also grateful to three anonymous reviewers for comments that improved the manuscript.

Supporting Online Material

www.sciencemag.org/cgi/content/full/science.1218809/DC1

Materials and Methods

Figs. S1 to S7

References (30–37)

6 January 2012; accepted 5 March 2012

Published online 21 March 2012;

10.1126/science.1218809

Topography of the Northern Hemisphere of Mercury from MESSENGER Laser Altimetry

Maria T. Zuber,^{1*} David E. Smith,¹ Roger J. Phillips,² Sean C. Solomon,³ Gregory A. Neumann,⁴ Steven A. Hauck II,⁵ Stanton J. Peale,⁶ Olivier S. Barnouin,⁷ James W. Head,⁸ Catherine L. Johnson,⁹ Frank G. Lemoine,⁴ Erwan Mazarico,^{1,4} Xiaoli Sun,⁴ Mark H. Torrence,^{4,10} Andrew M. Freed,¹¹ Christian Klimczak,³ Jean-Luc Margot,¹² Jürgen Oberst,¹³ Mark E. Perry,⁷ Ralph L. McNutt Jr.,⁷ Jeffrey A. Balcerski,⁵ Nathalie Michel,⁵ Matthieu J. Talpe,¹ Di Yang¹

Laser altimetry by the MESSENGER spacecraft has yielded a topographic model of the northern hemisphere of Mercury. The dynamic range of elevations is considerably smaller than those of Mars or the Moon. The most prominent feature is an extensive lowland at high northern latitudes that hosts the volcanic northern plains. Within this lowland is a broad topographic rise that experienced uplift after plains emplacement. The interior of the 1500-km-diameter Caloris impact basin has been modified so that part of the basin floor now stands higher than the rim. The elevated portion of the floor of Caloris appears to be part of a quasi-linear rise that extends for approximately half the planetary circumference at mid-latitudes. Collectively, these features imply that long-wavelength changes to Mercury's topography occurred after the earliest phases of the planet's geological history.

The topography of a planet provides fundamental information about its internal structure and geological and thermal evolution. Ranging observations made from orbit by the Mercury Laser Altimeter (MLA) (1) on the MErcury Surface, Space ENvironment, GEochemistry, and Ranging (MESSENGER) (2) spacecraft have provided a precise, geodetically referenced topographic model of the northern hemisphere of the planet as well as a characterization of slopes and surface roughness over a range of spatial scales.

From MESSENGER's eccentric, near-polar orbit (2), the MLA (3) illuminates surface areas averaging between 15 and 100 m in diameter, spaced ~400 m apart along the spacecraft ground track. The range from the spacecraft to the surface is converted to a measurement of radius from the planet's center of mass via the deter-

mination of MESSENGER's orbit. Radius is then converted to topography (Fig. 1A) by subtracting the radius of the gravitational equipotential or geoid obtained from Doppler tracking of MESSENGER (4). The radial precision of individual measurements is <1 m, and the accuracy with respect to Mercury's center of mass is better than 20 m (Table 1). MLA can successfully range at distances up to 1500 km from Mercury's surface when operating at nadir, and from ~1000 km at angles up to 40° from the vertical (5). As of 2 December 2011, more than 4.3 million independent measurements of surface elevation had been obtained.

Elevations in Mercury's northern hemisphere exhibit an approximately symmetric, unimodal hypsometric distribution and a dynamic range of 9.85 km (Fig. 2), considerably less than the global dynamic range for the Moon (19.9 km)

or Mars (30 km) (6, 7). Mercury contains numerous large impact structures (8, 9) that influence the hemispheric shape but do not markedly affect the hypsometry.

Mercury's high bulk density, presumably the result of an iron-rich core that constitutes an unusually large mass fraction of the planet (10), yields a surface gravitational acceleration comparable to that of Mars for a body intermediate in size between Mars and the Moon. For at least some topography-producing forces, a higher gravitational acceleration results in less variation in elevation, which can account for the difference in topographic dynamic range between Mercury and the Moon. However, Mercury's shallow core-mantle boundary, at a depth of <400 km below the surface (4), could have affected viscous flow in Mercury's mantle and may have influenced the growth and relaxation of the largest structures (11). Shield-building volcanism and large-scale extension contribute substantially to the dynamic range of topography on Mars but have no evident counterparts on Mercury. Indeed,

¹Department of Earth, Atmospheric and Planetary Sciences, Massachusetts Institute of Technology, Cambridge, MA 02139, USA. ²Planetary Science Directorate, Southwest Research Institute, Boulder, CO 80302, USA. ³Department of Terrestrial Magnetism, Carnegie Institution of Washington, Washington, DC 20015, USA. ⁴NASA Goddard Space Flight Center, Greenbelt, MD 20771, USA. ⁵Department of Earth, Environmental and Planetary Sciences, Case Western Reserve University, Cleveland, OH 44106, USA. ⁶Department of Physics, University of California, Santa Barbara, CA 93106, USA. ⁷Johns Hopkins University Applied Physics Laboratory, Laurel, MD 20723, USA. ⁸Department of Geological Sciences, Brown University, Providence, RI 02912, USA. ⁹Department of Earth and Ocean Sciences, University of British Columbia, Vancouver, BC V6T 1Z4, Canada. ¹⁰Stinger Ghaffarian Technologies Inc., 7701 Greenbelt Road, Greenbelt, MD 20770, USA. ¹¹Department of Earth and Atmospheric Sciences, Purdue University, West Lafayette, IN 47907, USA. ¹²Department of Earth and Space Sciences, University of California, Los Angeles, CA 90095, USA. ¹³Institute of Planetary Research, German Aerospace Center, Berlin D-12489, Germany.

*To whom correspondence should be addressed. E-mail: zuber@mit.edu

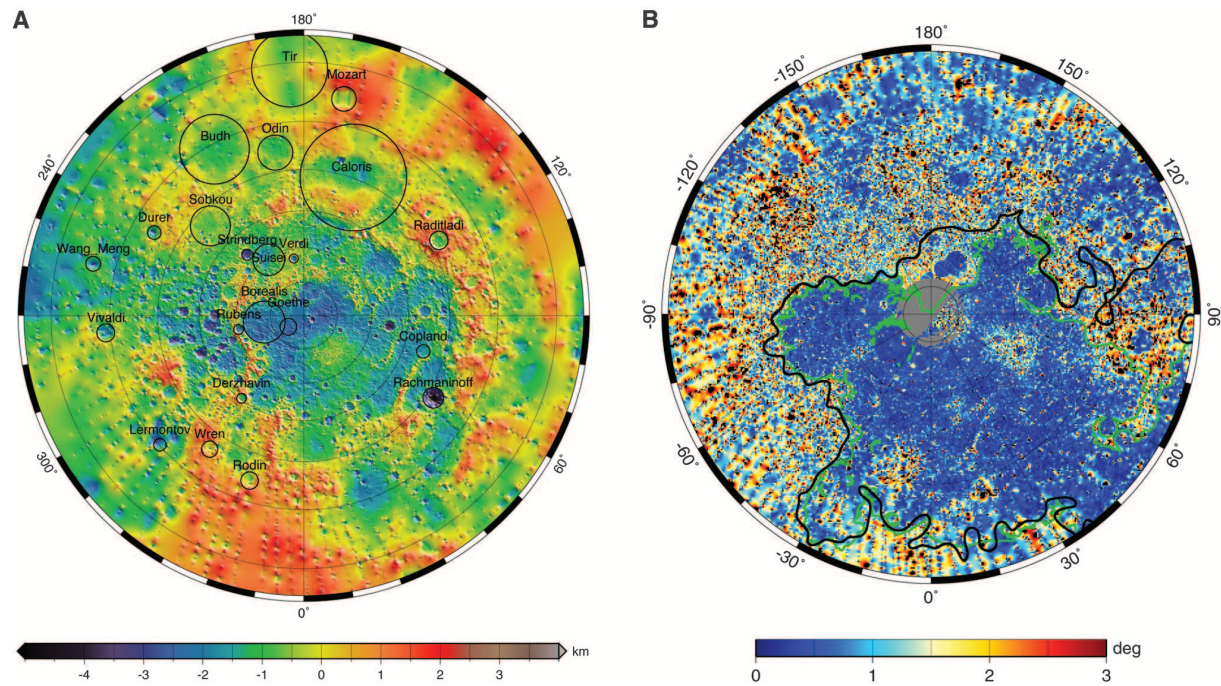


Fig. 1. (A) Polar stereographic projection of topography (local radius minus the radius of the HgM002 geoid, the gravitational equipotential referenced to the mean equatorial radius) (4) from the north pole to 5°S. The locations of selected major impact structures are shown as black circles. (B) Polar stereographic

projection of median differential slope (15) on a baseline of length 3.2 km, from the north pole to 50°N latitude. The green line shows the mapped boundary of the northern smooth plains (16); the black line corresponds to the topographic contour of −1.24 km. Both maps include data collected through 24 October 2011.

if the topography associated with Tharsis and Valles Marineris is excluded, the dynamic range of the remaining topography on Mars can be approximated by the rim-to-floor depth of the Hellas basin. This figure is comparable to the dynamic range of topography on Mercury and is consistent with a gravitational influence on topographic relief for terrestrial planetary bodies.

A spherical harmonic fit of planetary shape (12) (table S1) confirms an elliptical form of the equator, with a long axis close to the prime meridian (12) (fig. S1), as well as an offset between the center of mass and center of figure in the equatorial plane (5, 13). This distinctive feature of the planetary shape reflects a hemispheric difference in internal structure that could potentially arise from large-scale variations in crustal thickness or density, mantle density, or topography along Mercury’s core-mantle boundary.

A north-polar projection of topography (Fig. 1A) shows irregular lowlands at high northern latitudes that are ~2 km deeper than the surrounding terrain. Portions of the boundary of the northern lowlands appear to follow segments of rims of degraded impact basins, but the large extent of the lowlands and the irregular shape of the remainder of the boundary suggest that additional processes were involved in the formation of relief. The northern lowlands are marked by a negative free-air gravity anomaly and are in a state of approximate local compensation (e.g., underlain by thinner than average crust) (4), although the area is likely not in strict local mass balance because of contributions to

Table 1. Geodetic parameters for Mercury derived from MLA topography.

Parameter	Value
Reference radius (km)	2440
North polar radius (km)*	2437.57 ± 0.01
Equatorial mean radius (km)†	2439.83 ± 0.05
Northern hemisphere mean radius (km)‡	2439.59 ± 0.05
Shape dynamic range (km)	9.848
Shape accuracy (m)	±25
High point (km)§ 11.222°N, 164.752°E	+4.024
Low points (km)§	
Rachmaninoff, 27.417°N, 57.215°E	−5.815
Polar crater, 85.446°N, 62.440°E	−5.824
Hypsometric mean (km)§	−0.589
Hypsometric median (km)§	−0.616
Hypsometric mode (km)§	−0.700
(a − b)/a	(514 ± 52) × 10 ^{−6}
φ ₂ (°E)#	−18.6 ± 4
CoF-CoM x (km)**	0.133 ± 0.052
CoF-CoM y (km)**	0.193 ± 0.051

*Average of all MLA observations within 10° of north pole. †Average of all MLA observations within 15° of equator. ‡Mean planetary radius from a spherical harmonic least-squares fit to all observations with a Kaula constraint applied. §Relative to the reference radius. ||a and b are, respectively, the semimajor and semiminor axes of the ellipse fit to shape measurements within 15° of the equator. #Longitude of the equatorial semimajor axis of the ellipse fit to near-equatorial shape. Longitude 0° coincides with one of the hot poles of Mercury, which is on the axis of minimum moment of inertia, and 90° on the equator is in the direction of the intermediate axis of inertia. **CoF-CoM is the offset of the center of figure (CoF) from the center of mass (CoM), the origin of the coordinate system for gravity and topography; x and y are the components of offset in Mercury’s equatorial plane in the direction of 0° and 90°E, respectively.

topographic support from flexural and membrane stresses. Barring some sort of offsetting structure near the south pole, the large area of low topography at high latitudes raises the prospect that the region may have migrated to the pole during a reorientation of the planet’s prin-

cipal inertia axes driven by the shallow mass deficit (14). If the present location of the northern lowlands is a consequence of polar wander, then the implied planet-scale reorientation must have occurred at a time when the outer portions of Mercury were sufficiently cool and mechanical-

topographic model, in contrast, is precisely controlled and enables confident characterization of long-wavelength topography. MLA observations confirm that the northern floor of Caloris is elevated relative to other parts of the basin interior, so much so that in places the floor lies above the basin rim (Fig. 3). This portion of the floor of Caloris appears to be part of a quasi-linear rise that trends generally west-southwest–east-northeast and extends over approximately half the circumference of Mercury at mid-latitudes (Fig. 1A). The floors of younger impact craters within and near Caloris (Fig. 3) display departures from the horizontal that generally correlate with regional tilts imparted by the long-wavelength topography of the region and are consistent with modification of Mercury's long-wavelength topography some time after the formation of Caloris and the emplacement of its interior and exterior volcanic plains.

The changes in long-wavelength topography within the Caloris basin and northern plains, and perhaps elsewhere on Mercury, occurred after both the end of heavy impact bombardment and the emplacement of the largest expanses of volcanic plains on the planet. One possible source of long-wavelength topography is the isostatic response to variations in crustal thickness. However, the oldest terrains on Mercury display crater size-frequency distributions at large crater diameters similar to those on the most densely cratered parts of the Moon (24). Thus, crustal formation substantially predated long-wavelength topographic change and cannot explain the observations. A second possible source of such long-wavelength change in topography is mantle convection (25). However, recent mantle convection simulations (26) constrained by internal structure models consistent with Mercury's long-wavelength gravity field (4) and by the latitudinal distribution of surface insolation do not produce surface deformation of the magnitude required to explain the observed topography. Another contribution to topographic change is volcanic and magmatic loading of the lithosphere along with its flexural response, which has a predictable pattern. Finally, long-wavelength changes in topography could be a deformational response to interior planetary cooling and contraction (27). Evidence for topographic changes during Mercury's evolution is consistent with evidence from the geometry of ridges and lobate scarps that these features accommodated surface strain over a substantial fraction of Mercury's geological history (28). Observations of the topography add to the growing body of evidence that Mercury was a tectonically, volcanically, and dynamically active planet for much of its evolution.

References and Notes

- J. F. Cavanaugh *et al.*, *Space Sci. Rev.* **131**, 451 (2007).
- S. C. Solomon, R. L. McNutt Jr., R. E. Gold, D. L. Domingue, *Space Sci. Rev.* **131**, 3 (2007).
- The MLA is a time-of-flight laser rangefinder that uses direct detection and pulse-edge timing to determine precisely the range from the MESSENGER spacecraft to Mercury's surface. MLA's laser transmitter emits 5-ns-wide pulses at an 8-Hz rate with 20 mJ of energy at a wavelength of 1064 nm. Return echoes are collected by an array of four refractive telescopes and are detected with a single silicon avalanche photodiode detector. The timing of laser pulses is measured with a set of time-to-digital converters and counters and a crystal oscillator operating at a frequency that is monitored periodically from Earth.
- D. E. Smith *et al.*, *Science* **336**, xxx (2012); 10.1126/science.1218809.
- M. T. Zuber *et al.*, *Science* **321**, 77 (2008).
- M. T. Zuber, D. E. Smith, F. G. Lemoine, G. A. Neumann, *Science* **266**, 1839 (1994).
- D. E. Smith *et al.*, *Science* **284**, 1495 (1999).
- P. D. Spudis, J. E. Guest, in *Mercury*, F. Vilas, C. R. Chapman, M. S. Matthews, Eds. (Univ. of Arizona Press, Tucson, AZ, 1988), pp. 118–164.
- S. C. Solomon *et al.*, *Science* **321**, 59 (2008).
- S. A. Hauck II, S. C. Solomon, D. A. Smith, *Geophys. Res. Lett.* **34**, L18201 (2007).
- S. Zhong, M. T. Zuber, *J. Geophys. Res.* **105**, 4153 (2000).
- See supplementary materials on Science Online.
- D. E. Smith *et al.*, *Icarus* **209**, 88 (2010).
- P. Goldreich, A. Toomre, *J. Geophys. Res.* **74**, 2555 (1969).
- Median differential slope (29) removes the effect of larger-scale tilts from the elevation difference at a given baseline length. At each location x , half the difference in elevations between points one baseline length ahead and one behind along the altimetry ground track is subtracted from the difference in elevation between points one-half baseline length ahead and one-half behind, as $\tan \alpha = \{h[x + (l/2)] - h[x - (l/2)] - 0.5[h(x + l) - h(x - l)]\}/l$, where h is elevation, l is the baseline length, and α is the differential slope.
- J. W. Head *et al.*, *Science* **333**, 1853 (2011).
- L. R. Nittler *et al.*, *Science* **333**, 1847 (2011).
- L. R. Nittler *et al.*, abstr. 142-3, paper presented at the Geological Society of America annual meeting, Minneapolis, 9 to 12 October 2011; http://gsa.confex.com/gsa/2011AM/finalprogram/abstract_193666.htm.
- C. I. Fassett *et al.*, abstr. 142-6, paper presented at the Geological Society of America annual meeting, Minneapolis, 9 to 12 October 2011; http://gsa.confex.com/gsa/2011AM/finalprogram/abstract_196331.htm.
- C. Klimczak *et al.*, abstr. 142-10, paper presented at the Geological Society of America annual meeting, Minneapolis, 9 to 12 October 2011; http://gsa.confex.com/gsa/2011AM/finalprogram/abstract_195048.htm.
- S. L. Murchie *et al.*, *Science* **321**, 73 (2008).
- J. W. Head *et al.*, *Space Sci. Rev.* **131**, 41 (2007).
- J. Oberst *et al.*, *Icarus* **209**, 230 (2010).
- C. I. Fassett, S. J. Kadish, J. W. Head, S. C. Solomon, R. G. Strom, *Geophys. Res. Lett.* **38**, L10202 (2011).
- S. D. King, *Nat. Geosci.* **1**, 229 (2008).
- N. Michel *et al.*, P41A-1581, paper presented at the American Geophysical Union fall meeting, San Francisco, 5 to 9 December 2011.
- A. J. Dombard, S. A. Hauck II, S. C. Solomon, *Lunar Planet. Sci.* **32**, abstr. 2035 (2001).
- M. T. Zuber *et al.*, *Icarus* **209**, 247 (2010).
- M. A. Kreslavsky, J. W. Head III, *J. Geophys. Res.* **105**, 26695 (2000).

Acknowledgments: The MESSENGER project is supported by the NASA Discovery Program under contracts NAS5-97271 to the Johns Hopkins University Applied Physics Laboratory and NASW-00002 to the Carnegie Institution of Washington. We are grateful for the myriad contributions from the MLA instrument and MESSENGER spacecraft teams, and we appreciate three helpful reviews of an earlier version of the paper.

Supplementary Materials

www.sciencemag.org/cgi/content/full/science.1218805/DC1
Materials and Methods
Figs. S1 and S2
Table S1
Reference (30)

6 January 2012; accepted 2 March 2012
Published online 21 March 2012;
10.1126/science.1218805

ESCRT-III Governs the Aurora B–Mediated Abscission Checkpoint Through CHMP4C

Jeremy G. Carlton,* Anna Caballe, Monica Agromayor, Magdalena Kloc, Juan Martin-Serrano†

The endosomal sorting complex required for transport (ESCRT) machinery plays an evolutionarily conserved role in cytokinetic abscission, the final step of cell division where daughter cells are physically separated. Here, we show that charged multivesicular body (MVB) protein 4C (CHMP4C), a human ESCRT-III subunit, is involved in abscission timing. This function correlated with its differential spatiotemporal distribution during late stages of cytokinesis. Accordingly, CHMP4C functioned in the Aurora B–dependent abscission checkpoint to prevent both premature resolution of intercellular chromosome bridges and accumulation of DNA damage. CHMP4C engaged the chromosomal passenger complex (CPC) via interaction with Borealin, which suggested a model whereby CHMP4C inhibits abscission upon phosphorylation by Aurora B. Thus, the ESCRT machinery may protect against genetic damage by coordinating midbody resolution with the abscission checkpoint.

The final separation of daughter cells during cytokinesis is the ancestral function of the endosomal sorting complex required for transport (ESCRT) machinery (1–5) which also acts to resolve equivalent membrane scission events in multivesicular body (MVB) forma-

tion (6, 7) and human immunodeficiency virus–1 (HIV-1) budding (8, 9). Midbody recruitment of ESCRT-III, the filament-forming scission machinery, is an essential event in cytokinesis that is thought to provide constrictive force during abscission (2, 10–12). An Aurora B–dependent

abscission checkpoint (NoCut) is thought to retard abscission to prevent damage of lagging chromosomes that are trapped in the midbody (13–15) and may function more generally as an abscission timer (13). However, mechanisms that modulate abscission timing remain poorly understood and the involvement of the core abscission machinery in this process is unclear.

Here, we investigated the function of charged MVB proteins CHMP4A, -B, and -C, human homologs of the yeast ESCRT-III subunit Snf7p. For this purpose, specific small interfering RNAs (siRNAs) and antibodies against each of the CHMP4s were developed (16) (fig. S1). We then analyzed ESCRT-dependent endosomal down-regulation of class I major histocompatibility complex (MHC-I) molecules in HeLa cells stably expressing the K3 ubiquitin ligase from Kaposi's

sarcoma-associated herpes virus (KSHV) (17). Similarly to depletion of tumor susceptibility gene 101 (TSG101), depletion of CHMP4B prevented MHC-I degradation, whereas depletion of CHMP4A or CHMP4C had little effect on this process (fig. S2, A and B). As expected (18), depletion of CHMP4A or CHMP4C did not inhibit HIV-1 release, and only depletion of CHMP4B inhibited this ESCRT-dependent process (fig. S3). Furthermore, CHMP4A and CHMP4C were dispensable for completion of cytokinesis, whereas CHMP4B was again the sole paralog required (Fig. 1, A and B). However, in asynchronous cultures of CHMP4C-depleted HeLa cells, fewer cells were connected by midbodies (Fig. 1C), which led us to question whether midbodies were resolved faster in cells lacking CHMP4C.

We then imaged live HeLa cells stably expressing mCherry-tubulin (HeLa mCh-Tub) (19) to examine mitotic dynamics. CHMP4C-depleted cells (Fig. 1D) showed normal duration of early mitotic phases and centrosome amplification (Fig. 1E and fig. S4A). We next monitored tubulin disassembly at the midbody as a marker that cor-

relates strongly with abscission (15). Cells treated with control siRNAs resolved their midbodies with similar kinetics and depletion of CHMP4C reduced abscission time by ~30 min (Fig. 1F, fig. S4A, and movies S1 to S4). Abscission was also faster in cells codepleted of CHMP4C and Spastin, an adenosine triphosphatase involved in destabilization of midbody microtubules (20, 21), which suggested that CHMP4C and Spastin regulate distinct stages of abscission (fig. S4B). We next used cell lines stably expressing mCh-tubulin and comparable levels of green fluorescent protein (GFP)-tagged CHMP4B or CHMP4C (22) (Fig. 1G) for simultaneous imaging of abscission and midbody recruitment of ESCRT-III. Early phases of mitosis and abscission (Fig. 1, H and I) were similar in control and GFP-CHMP4B-expressing cells. However, expression of GFP-CHMP4C resulted in an abscission delay that could be explained by increased levels of intracellular CHMP4C (Fig. 1I; fig. S5, A to D; and movies S5 and S6). As expected (12), GFP-CHMP4B localized transiently to the midbody arms immediately (21 ± 7 min) before abscission, whereas GFP-CHMP4C

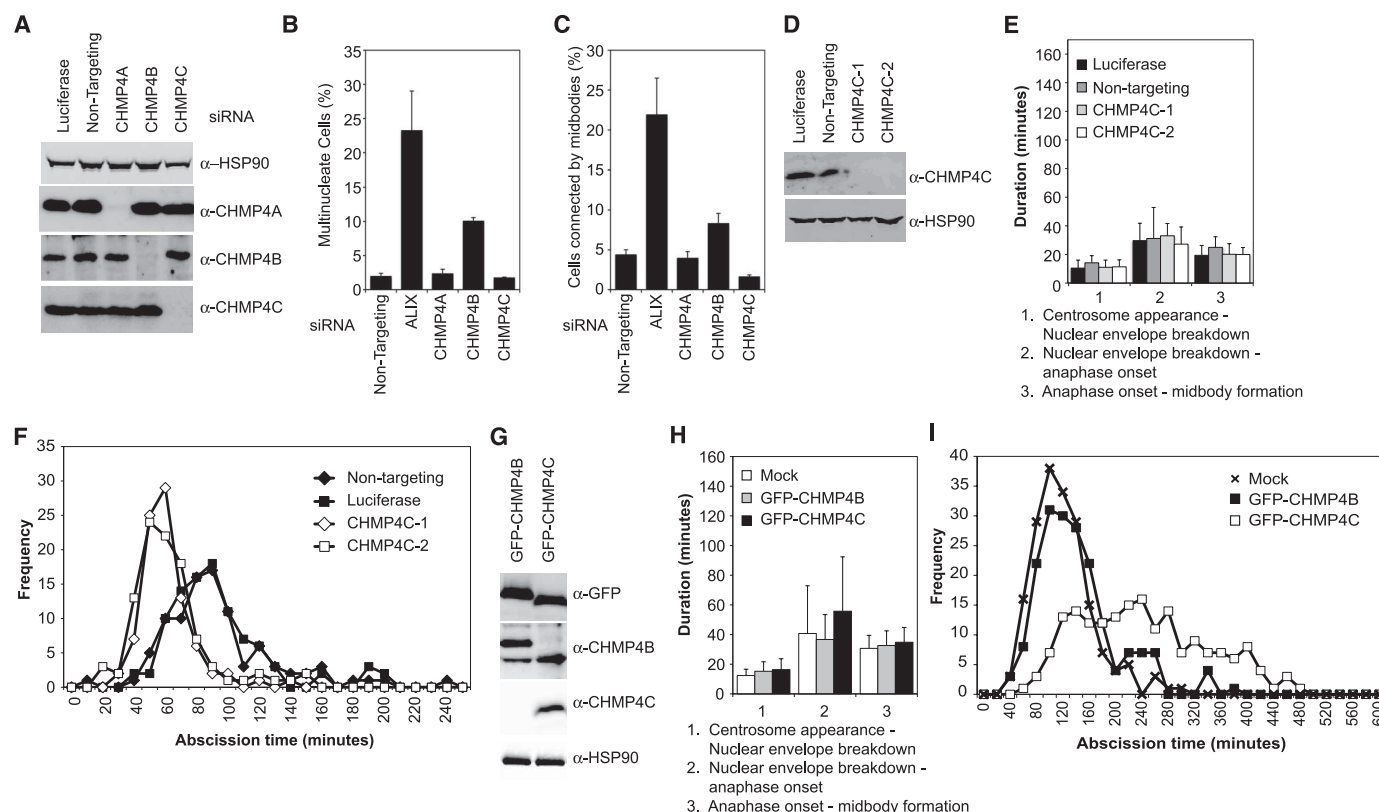


Fig. 1. CHMP4C negatively regulates cytokinesis. (A) Resolved HeLa cell lysates were examined by blotting with antibodies against CHMP4A, CHMP4B, CHMP4C, or heat shock protein 90 kD (HSP90). (B and C) siRNA-transfected HeLa cells were fixed and stained with α -tubulin. (B) Multinucleate cells ($n = 3$, \pm SD) or (C) cells connected by midbodies ($n = 7$, \pm SD) were scored visually. (D) Resolved lysates from siRNA-transfected HeLa mCh-Tub cells were examined by blotting with antibodies against CHMP4C or HSP90. (E and F) Asynchronous cultures of HeLa mCh-Tub cells were transfected with the indicated siRNA and imaged live, and mitotic durations were quantified. Abscission time was calculated across four independent experiments (Luciferase:

93 ± 38 min, $n = 96$; nontargeting: 94 ± 36 min, $n = 94$; CHMP4C-1: 59 ± 17 min, $n = 88$; CHMP4C-2: 61 ± 25 min, $n = 100$). (G) Resolved cell lysates from HeLa cells stably expressing mCh-Tub and either GFP-CHMP4B or GFP-CHMP4C were examined by blotting with antibodies against HSP90, GFP, CHMP4B, or CHMP4C. (H and I) Cells from (G) were imaged live, and mitotic durations were quantified. The more intense imaging (16) resulted in general abscission delays to 116 ± 45 and 137 ± 61 min for control or GFP-CHMP4B-expressing cells, whereas GFP-CHMP4C-expressing cells took 240 ± 103 min to complete abscission. Data comprise 185 cells per condition from three independent experiments.

localized earlier to the midbody, arriving 176 ± 19 min before abscission (Fig. 2, A to D). During its recruitment, GFP-CHMP4C localized initially to the midbody arms, before being directed to the central region (Flemming body) (Fig. 2, A to D; fig. S5, A to D; and movies S5 and S6). Thus, CHMP4B and CHMP4C exhibit differential spatiotemporal distribution during late cytokinesis.

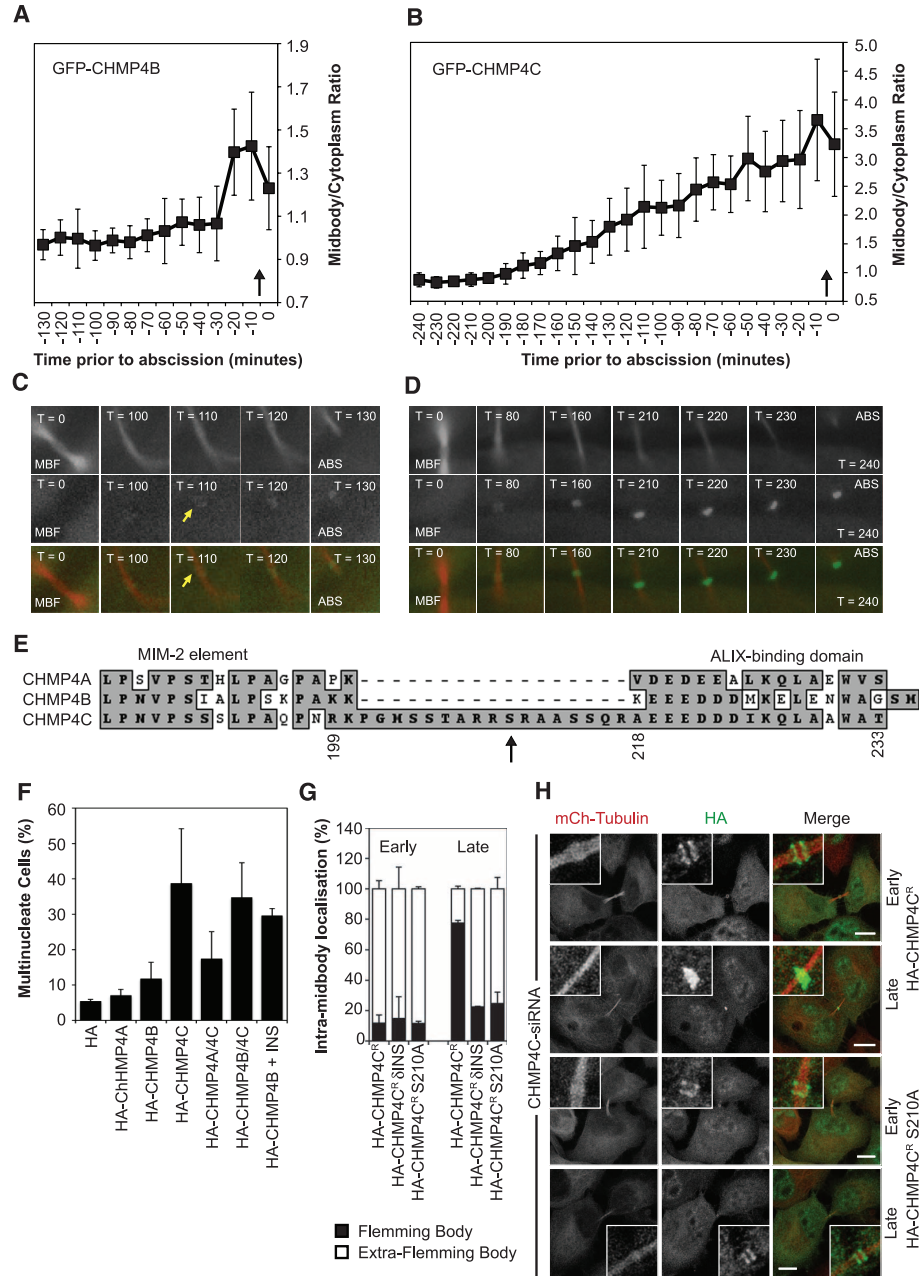
We sought differences between CHMP4 paralogs that could explain their differential behavior. Alignment of the regulatory region at the C termini of CHMP4s revealed a CHMP4C-specific insertion (INS) at residues 201 to 217 (Fig. 2E). This insertion is expanded in mammals (fig. S6) and contains numerous serine (S) and threonine (T) residues. Transiently overexpressed CHMP4 chimeras containing CHMP4C's C terminus were more potent inhibitors of cell division

(Fig. 2F), and grafting INS into the corresponding region of CHMP4B produced a chimera that inhibited cell division (Fig. 2F), which suggested that INS may be a platform for phosphorylation that inhibits abscission. We next determined the spatial distribution of CHMP4C during abscission by analyzing hemagglutinin (HA)-tagged CHMP4C expressed stably at near-endogenous levels. In early midbodies, HA-CHMP4C localized to the midbody arms, whereas in late midbodies, as observed for GFP-CHMP4C in living cells (Fig. 2B), HA-CHMP4C localized to the Flemming body in an INS-dependent manner (Fig. 2, G and H). In contrast, CHMP4A and CHMP4B were only observed on midbody arms (fig. S5E). We speculated that phosphorylation of residues within INS may have directed CHMP4C's localization and mapped the determinant of

Flemming body localization in late cytokinesis to S210, a residue conforming to the consensus sequence for Aurora B ([R/K]₍₁₋₃₎-X-[S/T] (23) (Fig. 2, G and H, and fig. S5F).

We next wondered whether CHMP4C participated in the Aurora B-dependent NoCut abscission checkpoint. This checkpoint can be activated by partial depletion of nucleoporin 153 kD (NUP153) and is evidenced by an accumulation of cells unable to complete abscission and arrested at the midbody stage (24). NoCut activation was prevented by codepletion of CHMP4C with NUP153 (Fig. 3, A and B), despite phosphorylated Aurora B persisting at midbodies (Fig. 3C). Chromosomes trapped at the midbody may provide an alternative NoCut activation route. We found that HA-CHMP4C preferentially localized to intercellular chromatin bridges illuminated with yellow

Fig. 2. Differential spatiotemporal recruitment of CHMP4 paralogs during cytokinesis. (A to D) GFP fluorescence intensities of midbody-localized (A and C) GFP-CHMP4B ($n = 14$, \pm SD) or (B and D) GFP-CHMP4C ($n = 9$, \pm SD) during abscission. Abscission indicated by arrow, time in minutes. (C and D) Selected frames are presented. Initial recruitment of GFP-CHMP4C to midbody arms is marked (arrowhead). (E) ClustalW alignment of the C-terminal regions of CHMP4A, CHMP4B, and CHMP4C, S210 indicated by arrow. MIM2, a motif that binds microtubule interaction and trafficking (MIT) domains. (F) HeLa cells transfected with plasmids encoding the indicated HA-CHMP4 constructs were fixed and stained with antibodies against tubulin and HA. Multinucleate cells were scored ($n = 5$, \pm SD). (G and H) HeLa mCh-Tub cells stably expressing HA-CHMP4C^R, HA-CHMP4C^RINS, or HA-CHMP4C^R S210A were treated with CHMP4C siRNA, fixed, and stained with HA-specific antibody. The HA-CHMP4C location was scored ($n = 3$, \pm SD). Scale bar is 10 μ m.



fluorescent protein (YFP)-tagged lamin-associated protein 2 β (LAP2 β) (Fig. 3D and fig. S7, A and B). Moreover, HA-CHMP4C colocalized with activated Aurora B at these chromatin bridges (Fig. 3E). We examined intercellular DNA-bridge resolution in CHMP4C-depleted cells and observed that YFP-LAP2 β -positive bridge formation and cellular viability were normal (fig. S7, C and D) and also found, similarly to Aurora B-inhibited cells (15), faster resolution of YFP-LAP2 β -positive chromatin bridges (Fig. 3F; fig. S7, E to G; and movies S7 to S9). Consequently, stable depletion of CHMP4C resulted in increased levels of histone H2AX phosphorylation (Fig. 3G and fig. S7H), which suggested that deregulation of the abscission checkpoint in these cells results in the accumulation of genetic damage (25).

Given the essential role of CHMP4C in the regulation of abscission timing and its participation in the Aurora B-dependent abscission checkpoint, we searched for links between components of the chromosomal passenger complex (CPC) and ESCRT-III by yeast two-hybrid screening. We found interactions between Borealin and CHMP2A, CHMP4B, CHMP4C, and CHMP6 (Fig. 4, A and B) and mapped these interactions to the C terminus of Borealin (fig. S8A), a region that recruits adaptor proteins to the CPC. CHMP4C was the strongest interactor with Borealin, and we could coprecipitate CHMP4C with Aurora B (fig. S8B), which confirmed that the ESCRT machinery is able to engage the CPC. Colocalization of HA-CHMP4C and members of the CPC was observed in early, but not late, midbodies (Fig. 4C and fig. S8, C and D). Accordingly,

a λ -phosphatase-sensitive, mobility-shifted form of HA-CHMP4C was detected in mitotic lysates and was enriched on a phospho-affinity resin (Fig. 4D and fig. S8E). Similar to centrosomal protein of 55 kD (CEP55) (26, 27), CHMP4C phosphorylation occurred at mitotic onset and reverted in a phosphatase-dependent manner as mitosis progressed (Fig. 4E). An Aurora B inhibitor reduced CHMP4C phosphorylation (Fig. 4F), and the epitope detected by α -CHMP4C, which recognizes INS, was masked in the mobility-shifted fraction and revealed upon λ -phosphatase treatment (Fig. 4D), which suggested that residues within CHMP4C's insertion were phosphorylated during mitosis. Finally, Aurora B could specifically phosphorylate CHMP4C on S210 within INS, the residue required for Flemming body localization (Fig. 4, G and H, and fig. S8, F and G).

To investigate the role of Aurora B phosphorylation of CHMP4C on abscission timing, we used HeLa mCh-Tub cell lines stably expressing HA-tagged, siRNA-resistant versions of CHMP4C (HA-CHMP4C^R, HA-CHMP4C^R δ INS, or HA-CHMP4C^R S210A) expressed at similar, near-endogenous levels (Fig. 4I). Interaction of these mutants with known CHMP4C-binding proteins (fig. S8H) was maintained, and early mitotic phases were completed normally in cells depleted of endogenous CHMP4C and reliant on these proteins (fig. S8I). Note that HA-CHMP4C^R rescued the faster abscission induced by CHMP4C depletion (Fig. 4J), whereas cells reliant on HA-CHMP4C^R δ INS and HA-CHMP4C^R S210A could not (Fig. 4K). We propose that Aurora B-dependent phosphorylation of S210 allows

CHMP4C localization to the Flemming body and acts as a brake on the late stages of cytokinesis. Furthermore, cells stably expressing YFP-LAP2 β and HA-CHMP4C^R S210A were unable to delay abscission in response to intracellular chromatin bridges, despite the presence of these proteins at the chromatin bridge (fig. S9A), which indicated deregulation of the NoCut checkpoint in these cells (Fig. 4L).

Here, we found that CHMP4C acts as an essential regulator of the Aurora B-mediated abscission checkpoint. In the absence of CHMP4C, cells complete abscission faster. We suggest that Aurora B-dependent phosphorylation of CHMP4C on S210 directs its Flemming body localization and delays abscission through activation of NoCut, possibly by preventing assembly of a productive abscission complex. A phosphomimetic mutation (S210D) had no apparent effect on known CHMP4C interactions (fig. S9B), which suggested that phosphoregulation of abscission timing may involve as-yet-unknown CHMP4C binding partners. That the S210 consensus site is conserved only in mammals suggests that this mechanism might have emerged late in evolution as a safety belt in addition to the interactions of the CPC with CHMP2A and CHMP6. CHMP4C depletion circumvents the NoCut abscission checkpoint, allows faster resolution of chromatin bridges, and induces the accumulation of phosphorylated H2AX. These observations are consistent with a role of CHMP4C in protection against DNA damage accumulation. In this context, as well as being charged MVB proteins (28), CHMPs were originally reported as chromatin-modifying proteins (29) that could associate with condensed

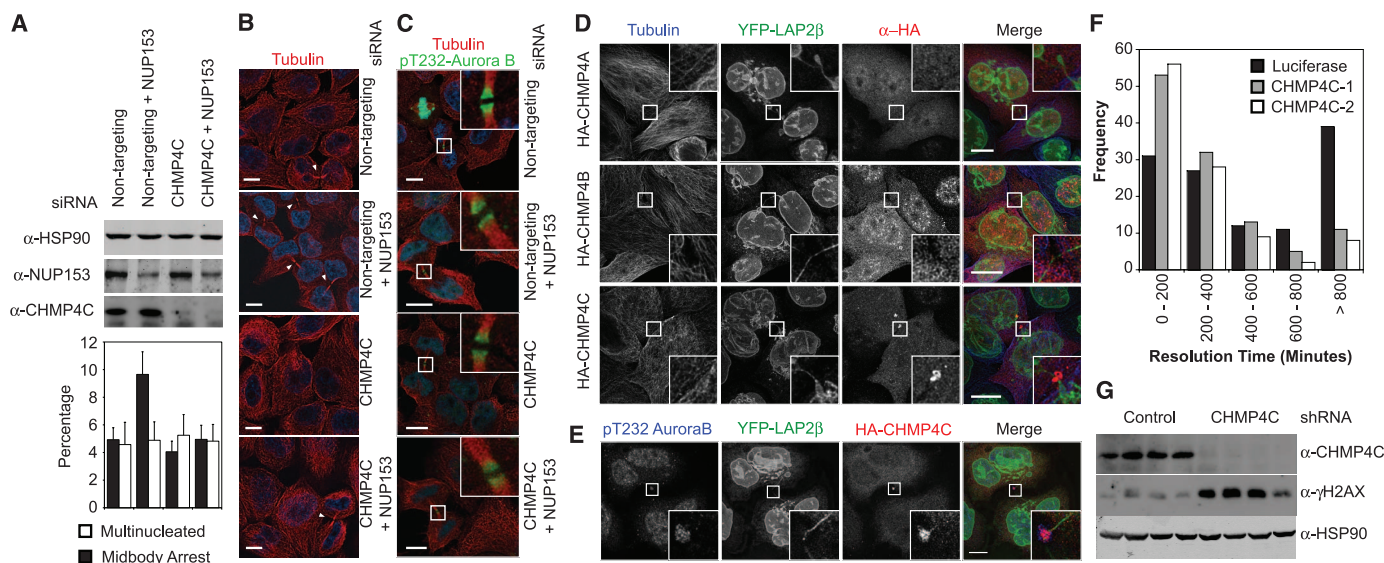


Fig. 3. CHMP4C regulates the abscission checkpoint. (A to C) (A) Cell lysates from siRNA-transfected HeLa cells were examined by blotting with antibodies against NUP153, CHMP4C, HA, and HSP90. Multinucleate and midbody-connected cells were scored visually ($n = 6$, ± 5 D). Alternatively, cells were fixed and stained with antibodies against (B) tubulin or (C) tubulin and pT232 Aurora B. Scale bar is 10 μ m. (D and E) HeLa cells stably expressing YFP-LAP2 β were transfected with plasmids encoding the indicated HA-CHMP4 constructs. Cells were fixed and stained with antibodies against (D)

tubulin and HA or (E) pT232 Aurora B and HA. Scale bar is 10 μ m. (F) HeLa cells stably expressing YFP-LAP2 β were transfected with the indicated siRNA and imaged live; the duration of LAP2 β -bridge resolution was quantified across six independent experiments (luciferase: 576 ± 454 min, $n = 116$; CHMP4C-1: 321 ± 308 min, $n = 112$; CHMP4C-2: 291 ± 278 min, $n = 103$). (G) Cell lysates from clonal short hairpin RNA (shRNA)-transduced HeLa cells were examined by blotting with antibodies against γ H2AX, CHMP4C, or HSP90.

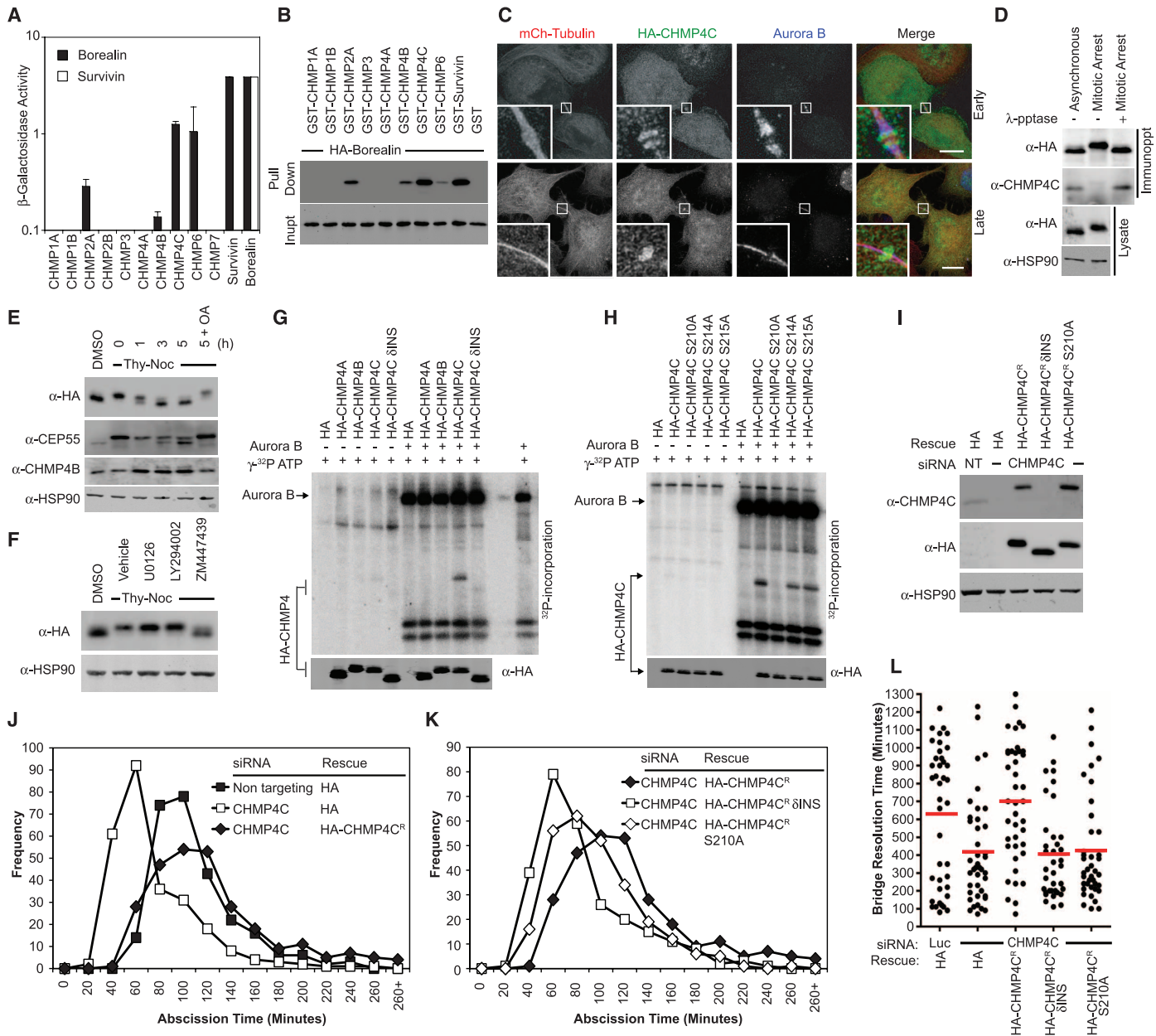


Fig. 4. Aurora B–dependent phosphorylation of CHMP4C S210 activates the NoCut abscission checkpoint. **(A)** β -Galactosidase assay from yeast co-transformed with the indicated VP16- and GAL4-fused constructs ($n = 3$, \pm SD). **(B)** Cell lysates and glutathione-bound fractions from human embryonic kidney (HEK) 293T cells transfected with the indicated fusion proteins were examined by Western blotting with antibody against HA. **(C)** HeLa mCh-Tub cells stably expressing HA-CHMP4C^R were fixed and stained with antibodies against HA and Aurora B. **(D)** Asynchronous and mitotic lysates of HeLa mCh-Tub cells stably expressing HA-CHMP4C^R were immunoprecipitated with HA-specific antibody and treated as indicated, then examined by blotting with antibodies against HA, CHMP4C, CHMP4B, CEP55, and HSP90. **(E and F)** Asynchronous or mitotically arrested HeLa mCh-Tub cells stably expressing HA-CHMP4C^R were either **(E)** released into media containing dimethyl sulfoxide (DMSO) or the phosphatase inhibitor okadaic acid (OA) for the indicated times or **(F)** treated overnight during the nocodazole arrest with inhibitors of mitogen-activated protein kinase (MEK) (U0126), phosphatidylinositol 3-kinase (LY294002) or Aurora B (ZM447439). Cell lysates were examined by blotting with antibodies against HA and HSP90. **(G and H)** Proteins were immunoprecipitated from HEK 293T cells with antibody against

HA and subjected to an in vitro kinase assay with recombinant Aurora B. Incorporated 32 P was visualized by phosphorimaging; blotting with HA-specific antibody allowed detection of immunoprecipitates. **(I to K)** Asynchronous cultures of HeLa mCh-Tub cells stably expressing HA, HA-CHMP4C^R, HA-CHMP4C^R δ INS, or HA-CHMP4C^R S210A were transfected with the indicated siRNA. **(I)** Resolved cell lysates were examined by blotting with antibodies against CHMP4C, HA, and HSP90. **(J and K)** Alternatively, cells were imaged live. Abscission times were quantified across seven independent experiments (luciferase, 104 ± 35 min, $n = 244$; CHMP4C siRNA, 71 ± 37 min, $n = 260$; CHMP4C siRNA and HA-CHMP4C^R, 118 ± 52 min, $n = 269$; CHMP4C siRNA and HA-CHMP4C^R δ INS, 81 ± 40 min, $n = 264$; CHMP4C siRNA and HA-CHMP4C^R S210A, 91 ± 38 min, $n = 268$). **(L)** HeLa cells stably expressing YFP-LAP2 β and HA or HA-CHMP4C^R, HA-CHMP4C^R δ INS, or HA-CHMP4C^R S210A were treated with the indicated siRNA and imaged live. The timing of YFP-LAP2 β bridge resolution was quantified from two independent experiments (luciferase, 628 ± 382 min, $n = 41$; CHMP4C siRNA, 413 ± 292 min, $n = 41$; CHMP4C siRNA and HA-CHMP4C^R, 698 ± 332 min, $n = 41$; CHMP4C siRNA and HA-CHMP4C^R δ INS, 402 ± 259 min, $n = 36$; CHMP4C siRNA and HA-CHMP4C^R S210A, 421 ± 295 min, $n = 40$).

chromatin, which suggests that the physical interaction of lagging chromosomes and ESCRT-III at the midbody may trigger activation of NoCut.

References and Notes

- J. G. Carlton, J. Martin-Serrano, *Science* **316**, 1908 (2007).
- E. Morita *et al.*, *EMBO J.* **26**, 4215 (2007).
- R. Y. Samson, T. Obata, S. M. Freund, R. L. Williams, S. D. Bell, *Science* **322**, 1710 (2008).
- H. H. Lee, N. Elia, R. Ghirlando, J. Lippincott-Schwartz, J. H. Hurley, *Science* **322**, 576 (2008).
- A. Caballe, J. Martin-Serrano, *Traffic* **12**, 1318 (2011).
- C. Raiborg, H. Stenmark, *Nature* **458**, 445 (2009).
- W. M. Henne, N. J. Buchkovich, S. D. Emr, *Dev. Cell* **21**, 77 (2011).
- E. R. Weiss, H. Göttlinger, *J. Mol. Biol.* **410**, 525 (2011).
- J. Martin-Serrano, S. J. D. Neil, *Nat. Rev. Microbiol.* **9**, 519 (2011).
- J. G. Carlton, M. Agromayor, J. Martin-Serrano, *Proc. Natl. Acad. Sci. U.S.A.* **105**, 10541 (2008).
- J. Guizetti *et al.*, *Science* **331**, 1616 (2011).
- N. Elia, R. Sougrat, T. A. Spurlin, J. H. Hurley, J. Lippincott-Schwartz, *Proc. Natl. Acad. Sci. U.S.A.* **108**, 4846 (2011).
- C. Norden *et al.*, *Cell* **125**, 85 (2006).
- M. Mendoza *et al.*, *Nat. Cell Biol.* **11**, 477 (2009).
- P. Steigemann *et al.*, *Cell* **136**, 473 (2009).
- Materials and methods are available as supporting material on *Science* Online.
- E. W. Hewitt *et al.*, *EMBO J.* **21**, 2418 (2002).
- E. Morita *et al.*, *Cell Host Microbe* **9**, 235 (2011).
- M. Agromayor *et al.*, *Mol. Biol. Cell* **20**, 1374 (2009).
- J. W. Connell, C. Lindon, J. P. Luzio, E. Reid, *Traffic* **10**, 42 (2009).
- D. Yang *et al.*, *Nat. Struct. Mol. Biol.* **15**, 1278 (2008).
- N. Jouvencet, M. Zhadina, P. D. Bieniasz, S. M. Simon, *Nat. Cell Biol.* **13**, 394 (2011).
- P. Meraldi, R. Honda, E. A. Nigg, *Curr. Opin. Genet. Dev.* **14**, 29 (2004).
- D. R. Mackay, M. Makise, K. S. Ullman, *J. Cell Biol.* **191**, 923 (2010).
- O. Fernandez-Capetillo, A. Lee, M. Nussenzweig, A. Nussenzweig, *DNA Repair (Amst.)* **3**, 959 (2004).
- R. N. Bastos, F. A. Barr, *J. Cell Biol.* **191**, 751 (2010).
- M. Fabbro *et al.*, *Dev. Cell* **9**, 477 (2005).
- T. L. Howard, D. R. Stauffer, C. R. Degnin, S. M. Hollenberg, *J. Cell Sci.* **114**, 2395 (2001).
- D. R. Stauffer, T. L. Howard, T. Nyun, S. M. Hollenberg, *J. Cell Sci.* **114**, 2383 (2001).

Acknowledgments: We thank P. Bieniasz for kind gifts of GFP-CHMP4-expressing cells. J.M.-S. was funded by the Medical Research Council (G0802777), the Lister Institute for Preventative Medicine and the EMBO Young Investigators Program. J.M.-S. and M.A. were funded by Wellcome Trust grant (WT093056MA). J.G.C. was funded by Wellcome Trust Value in People award (092429/Z/10/Z). We acknowledge the U.K. National Institute for Health Research Comprehensive Biomedical Research Centre at Guy's and St. Thomas's National Health Service Foundation Trust and King's College London for an equipment grant.

Supporting Online Material

www.sciencemag.org/cgi/content/full/science.1217180/DC1
Materials and Methods

Figs. S1 to S9
References (30–32)
Movies S1 to S9

28 November 2011; accepted 2 March 2012

Published online 15 March 2012;

10.1126/science.1217180

Atg7 Modulates p53 Activity to Regulate Cell Cycle and Survival During Metabolic Stress

In Hye Lee,¹ Yoshichika Kawai,¹ Maria M. Fergusson,¹ Ilsa I. Rovira,¹ Alexander J. R. Bishop,² Noboru Motoyama,³ Liu Cao,^{4*} Toren Finkel^{1*}

Withdrawal of nutrients triggers an exit from the cell division cycle, the induction of autophagy, and eventually the activation of cell death pathways. The relation, if any, among these events is not well characterized. We found that starved mouse embryonic fibroblasts lacking the essential autophagy gene product Atg7 failed to undergo cell cycle arrest. Independent of its E1-like enzymatic activity, Atg7 could bind to the tumor suppressor p53 to regulate the transcription of the gene encoding the cell cycle inhibitor p21^{CDKN1A}. With prolonged metabolic stress, the absence of Atg7 resulted in augmented DNA damage with increased p53-dependent apoptosis. Inhibition of the DNA damage response by deletion of the protein kinase Chk2 partially rescued postnatal lethality in Atg7^{-/-} mice. Thus, when nutrients are limited, Atg7 regulates p53-dependent cell cycle and cell death pathways.

Cell cycle progression and autophagic flux are both sensitive to nutrient availability. Furthermore, with prolonged nutrient deprivation, cell death pathways and autophagy are simultaneously activated (1). However, our understanding of how autophagy intersects with cell cycle progression or apoptotic cell death is incomplete. We demonstrate that in the setting of low nutrients, cells lacking Atg7 have impaired p53-mediated cell cycle arrest, whereas with continued metabolic stress, cells and tissues

lacking Atg7 display increased p53-mediated cell death.

To address whether cell cycle progression and autophagy are linked, we examined the effects of acute nutrient withdrawal on subsequent S-phase entry in either wild-type or Atg7^{-/-} mouse embryonic fibroblasts (MEFs). In wild-type MEFs, S-phase entry, as assessed by bromodeoxyuridine (BrdU) incorporation, decreased by about 60% in the first 3 hours after acute withdrawal of serum and amino acids (Fig. 1A and fig. S1). In contrast, only about 20% of Atg7^{-/-} MEFs successfully exited the cell cycle under the same conditions ($P < 0.001$, $n = 4$). The withdrawal from the cell cycle under starved conditions is often mediated by accumulation of cyclin-dependent kinase inhibitors (CKIs) such as p27^{CDKN1B} or p21^{CDKN1A} (2–7). Although early-passage wild-type MEFs rapidly accumulated p21^{CDKN1A} protein after being shifted to starvation media, this response was

largely absent in Atg7^{-/-} MEFs (Fig. 1B). In contrast, the abundance of p27^{CDKN1B} was not appreciably different between the two cell types. Similarly, metabolic stress induced the accumulation of p21^{CDKN1A} mRNA in wild-type but not Atg7^{-/-} MEFs (Fig. 1C). Consistent with previous observations (8), the starvation-induced increase in p21^{CDKN1A} expression was largely absent in human or mouse cells lacking p53 (fig. S2). Transcription from a p21^{CDKN1A} promoter linked to a luciferase reporter was increased in wild-type but not Atg7^{-/-} MEFs deprived of nutrients (Fig. 1D). Chromatin immunoprecipitation (ChIP) analysis demonstrated that under starved conditions, endogenous Atg7, along with p53, was present at the p21 promoter (Fig. 1E).

Similar analysis in human cells in which Atg7 expression was decreased with small interfering RNA (siRNA) confirmed the impaired expression of p21^{CDKN1A} in nutrient-deprived cells (Fig. 1F). In contrast, depletion of Beclin 1 (Atg6) had no effect on the starvation-induced increase in either p21^{CDKN1A} protein or mRNA expression (Fig. 1G and fig. S3). A similar analysis in Atg5^{-/-} MEFs again revealed no alteration in expression of p21^{CDKN1A} (fig. S4) or other cell cycle parameters (9). Thus, the observed defects in cell cycle arrest and the lack of p21^{CDKN1A} accumulation after nutrient withdrawal appear to be specific for Atg7. This defect was not confined to nutrient withdrawal, as Atg7-deficient cells also appeared to have impaired confluence-dependent growth arrest (Fig. 1, H and I).

We used epitope-tagged proteins to demonstrate that p53 and Atg7 are present in a single complex (Fig. 2A). Analysis of endogenous proteins revealed a similar interaction that was enhanced after nutrient withdrawal (Fig. 2B). Complexes containing Atg7 and p53 complex were evident in both the cytosol and the nucleus (fig. S5). Using p53 glutathione *S*-transferase (GST) constructs, we showed that the region corresponding

¹Center for Molecular Medicine, National Heart, Lung, and Blood Institute, Bethesda, MD 20892, USA. ²University of Texas Health Science Center, San Antonio, TX 78229, USA. ³Department of Cognitive Brain Sciences, Research Institute, National Center for Geriatrics and Gerontology, Aichi 474-8511, Japan. ⁴Key Laboratory of Medical Cell Biology, China Medical University, Shenyang 110001, China.

*To whom correspondence should be addressed. E-mail: finkelt@nih.gov (T.F.); caoliu@mail.cmu.edu (L.C.)

ly strong to preserve a nonhydrostatic response to topographic stresses, as well as the present configuration of inertial axes.

A map of median differential slope (15) derived from the topographic measurements (Fig. 1B) illustrates that kilometer-scale slopes are generally much lower within the northern lowlands than in the surrounding areas. The lowlands are partially filled with a smooth plains unit that occupies more than 6% of Mercury's surface (16). On the basis of its geological characteristics, the plains have been interpreted as a product of flood volcanism early in Mercury's history marked by high rates of eruption of high-temperature lavas (16). Elemental composition measurements made with MESSENGER's X-Ray

Spectrometer (XRS) indicate that the northern plains are similar in composition to basalts on other terrestrial bodies (17, 18). The diameters of partially to fully buried craters on the plains unit imply that plains thicknesses, at least locally, exceed 1 to 2 km (16). The black curve in Fig. 1B shows that the boundary of the smoothed plains and of the area of low differential slope is reasonably well matched along a substantial portion of its length by a constant elevation relative to the geoid. These relationships suggest that the flood volcanism that created the northern plains involved highly fluid lavas.

At present, however, the northern smooth plains deviate from a level surface. In partic-

ular, the northern lowlands host a regional topographic rise (centered near 68°N, 33°E) that is ~950 km in diameter and is elevated by ~1.5 km above its surroundings. This northern rise is characterized by a large (~150 mGal) positive gravity anomaly (4). This value is only slightly less than the magnitude of the anomaly that would be predicted by topography alone and suggests at most limited compensation (e.g., by thickened crust) (4). The northern rise does not display kilometer-scale slopes distinguishable from the rest of the northern plains (Fig. 1B), and the size-frequency distributions of superposed impact craters indicate that the age of the rise surface is indistinguishable from that of the surrounding plains (19). Moreover, topographic profiles through volcanically buried craters on the rise indicate that the flooded floors tilt away from the highest point on the rise (20). These observations indicate collectively that at least a portion of the rise topography postdates the emplacement of the plains. The implied vertical motions following plains emplacement could be the result of lithospheric deformation, magmatic intrusion, or mantle dynamic uplift.

The Caloris basin (centered at 31°N, 160°E), 1550 km in diameter (21), is the best preserved and presumably youngest of the large impact basins on Mercury (8, 22). A terrain model of the Caloris region derived from stereo images acquired during MESSENGER's first Mercury flyby (23) displayed basin-concentric rings and suggested long-wavelength undulations of the basin interior surface, but the lack of long-wavelength geodetic control in the model rendered these undulations uncertain. The MLA

Fig. 2. Histogram of northern hemisphere elevations, relative to a sphere of radius 2440 km, projected onto an equal-area grid from 4°S to 83.5°N. The red line is a smooth curve fit to the observations; the red bar indicates ± 1 standard deviation from the mean.

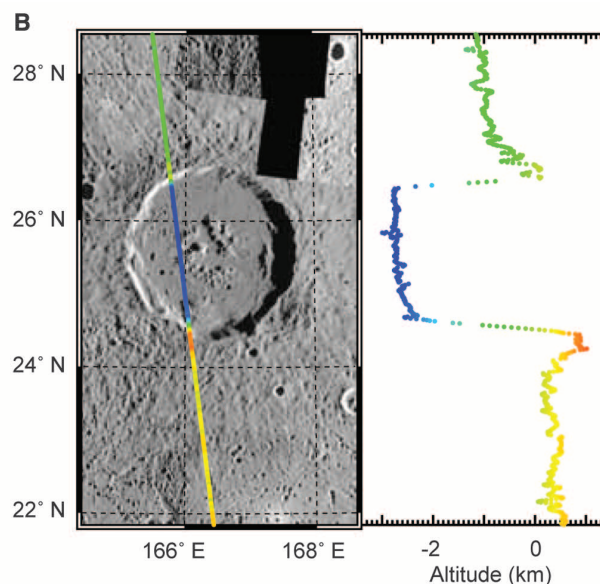
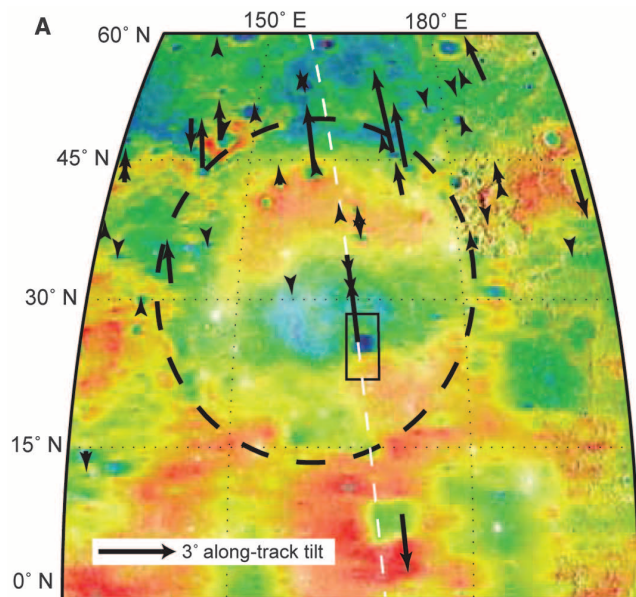
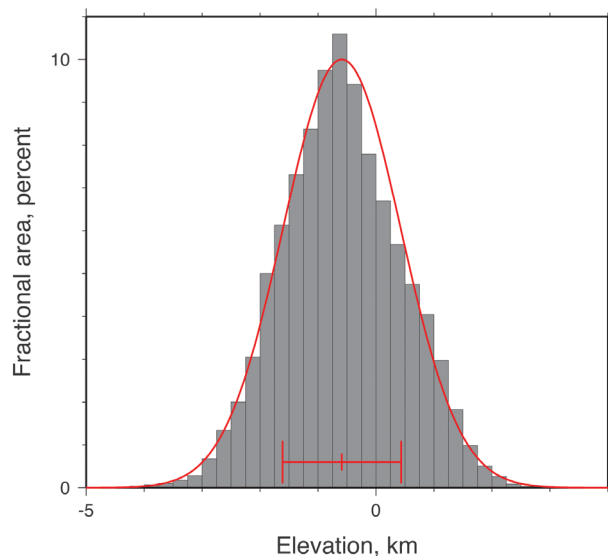


Fig. 3. (A) Average along-track tilts of the floors of impact craters (arrows) within and in the vicinity of the Caloris basin superimposed on regional topography. Tilts are obtained from representative MLA tracks across each crater and constitute the projection of total tilt onto the

vertical plane containing the track. Arrow length is proportional to tilt. Dashed line shows the ground track of the profile in (B). (B) Profile MLASCIRD1107292041 across the 100-km-diameter crater Atget demonstrates northward tilt of the crater floor.

topographic model, in contrast, is precisely controlled and enables confident characterization of long-wavelength topography. MLA observations confirm that the northern floor of Caloris is elevated relative to other parts of the basin interior, so much so that in places the floor lies above the basin rim (Fig. 3). This portion of the floor of Caloris appears to be part of a quasi-linear rise that trends generally west-southwest–east-northeast and extends over approximately half the circumference of Mercury at mid-latitudes (Fig. 1A). The floors of younger impact craters within and near Caloris (Fig. 3) display departures from the horizontal that generally correlate with regional tilts imparted by the long-wavelength topography of the region and are consistent with modification of Mercury's long-wavelength topography some time after the formation of Caloris and the emplacement of its interior and exterior volcanic plains.

The changes in long-wavelength topography within the Caloris basin and northern plains, and perhaps elsewhere on Mercury, occurred after both the end of heavy impact bombardment and the emplacement of the largest expanses of volcanic plains on the planet. One possible source of long-wavelength topography is the isostatic response to variations in crustal thickness. However, the oldest terrains on Mercury display crater size-frequency distributions at large crater diameters similar to those on the most densely cratered parts of the Moon (24). Thus, crustal formation substantially predated long-wavelength topographic change and cannot explain the observations. A second possible source of such long-wavelength change in topography is mantle convection (25). However, recent mantle convection simulations (26) constrained by internal structure models consistent with Mercury's long-wavelength gravity field (4) and by the latitudinal distribution of surface insolation do not produce surface deformation of the magnitude required to explain the observed topography. Another contribution to topographic change is volcanic and magmatic loading of the lithosphere along with its flexural response, which has a predictable pattern. Finally, long-wavelength changes in topography could be a deformational response to interior planetary cooling and contraction (27). Evidence for topographic changes during Mercury's evolution is consistent with evidence from the geometry of ridges and lobate scarps that these features accommodated surface strain over a substantial fraction of Mercury's geological history (28). Observations of the topography add to the growing body of evidence that Mercury was a tectonically, volcanically, and dynamically active planet for much of its evolution.

References and Notes

- J. F. Cavanaugh *et al.*, *Space Sci. Rev.* **131**, 451 (2007).
- S. C. Solomon, R. L. McNutt Jr., R. E. Gold, D. L. Domingue, *Space Sci. Rev.* **131**, 3 (2007).
- The MLA is a time-of-flight laser rangefinder that uses direct detection and pulse-edge timing to determine precisely the range from the MESSENGER spacecraft to Mercury's surface. MLA's laser transmitter emits 5-ns-wide pulses at an 8-Hz rate with 20 mJ of energy at a wavelength of 1064 nm. Return echoes are collected by an array of four refractive telescopes and are detected with a single silicon avalanche photodiode detector. The timing of laser pulses is measured with a set of time-to-digital converters and counters and a crystal oscillator operating at a frequency that is monitored periodically from Earth.
- D. E. Smith *et al.*, *Science* **336**, xxx (2012); 10.1126/science.1218809.
- M. T. Zuber *et al.*, *Science* **321**, 77 (2008).
- M. T. Zuber, D. E. Smith, F. G. Lemoine, G. A. Neumann, *Science* **266**, 1839 (1994).
- D. E. Smith *et al.*, *Science* **284**, 1495 (1999).
- P. D. Spudis, J. E. Guest, in *Mercury*, F. Vilas, C. R. Chapman, M. S. Matthews, Eds. (Univ. of Arizona Press, Tucson, AZ, 1988), pp. 118–164.
- S. C. Solomon *et al.*, *Science* **321**, 59 (2008).
- S. A. Hauck II, S. C. Solomon, D. A. Smith, *Geophys. Res. Lett.* **34**, L18201 (2007).
- S. Zhong, M. T. Zuber, *J. Geophys. Res.* **105**, 4153 (2000).
- See supplementary materials on Science Online.
- D. E. Smith *et al.*, *Icarus* **209**, 88 (2010).
- P. Goldreich, A. Toomre, *J. Geophys. Res.* **74**, 2555 (1969).
- Median differential slope (29) removes the effect of larger-scale tilts from the elevation difference at a given baseline length. At each location x , half the difference in elevations between points one baseline length ahead and one behind along the altimetry ground track is subtracted from the difference in elevation between points one-half baseline length ahead and one-half behind, as $\tan \alpha = \{h[x + (l/2)] - h[x - (l/2)] - 0.5[h(x + l) - h(x - l)]\}/l$, where h is elevation, l is the baseline length, and α is the differential slope.
- J. W. Head *et al.*, *Science* **333**, 1853 (2011).
- L. R. Nittler *et al.*, *Science* **333**, 1847 (2011).
- L. R. Nittler *et al.*, abstr. 142-3, paper presented at the Geological Society of America annual meeting, Minneapolis, 9 to 12 October 2011; http://gsa.confex.com/gsa/2011AM/finalprogram/abstract_193666.htm.
- C. I. Fassett *et al.*, abstr. 142-6, paper presented at the Geological Society of America annual meeting, Minneapolis, 9 to 12 October 2011; http://gsa.confex.com/gsa/2011AM/finalprogram/abstract_196331.htm.
- C. Klimczak *et al.*, abstr. 142-10, paper presented at the Geological Society of America annual meeting, Minneapolis, 9 to 12 October 2011; http://gsa.confex.com/gsa/2011AM/finalprogram/abstract_195048.htm.
- S. L. Murchie *et al.*, *Science* **321**, 73 (2008).
- J. W. Head *et al.*, *Space Sci. Rev.* **131**, 41 (2007).
- J. Oberst *et al.*, *Icarus* **209**, 230 (2010).
- C. I. Fassett, S. J. Kadish, J. W. Head, S. C. Solomon, R. G. Strom, *Geophys. Res. Lett.* **38**, L10202 (2011).
- S. D. King, *Nat. Geosci.* **1**, 229 (2008).
- N. Michel *et al.*, P41A-1581, paper presented at the American Geophysical Union fall meeting, San Francisco, 5 to 9 December 2011.
- A. J. Dombard, S. A. Hauck II, S. C. Solomon, *Lunar Planet. Sci.* **32**, abstr. 2035 (2001).
- M. T. Zuber *et al.*, *Icarus* **209**, 247 (2010).
- M. A. Kreslavsky, J. W. Head III, *J. Geophys. Res.* **105**, 26695 (2000).

Acknowledgments: The MESSENGER project is supported by the NASA Discovery Program under contracts NAS5-97271 to the Johns Hopkins University Applied Physics Laboratory and NASW-00002 to the Carnegie Institution of Washington. We are grateful for the myriad contributions from the MLA instrument and MESSENGER spacecraft teams, and we appreciate three helpful reviews of an earlier version of the paper.

Supplementary Materials

www.sciencemag.org/cgi/content/full/science.1218805/DC1
Materials and Methods
Figs. S1 and S2
Table S1
Reference (30)

6 January 2012; accepted 2 March 2012
Published online 21 March 2012;
10.1126/science.1218805

ESCRT-III Governs the Aurora B-Mediated Abscission Checkpoint Through CHMP4C

Jeremy G. Carlton,* Anna Caballe, Monica Agromayor, Magdalena Kloc, Juan Martin-Serrano†

The endosomal sorting complex required for transport (ESCRT) machinery plays an evolutionarily conserved role in cytokinetic abscission, the final step of cell division where daughter cells are physically separated. Here, we show that charged multivesicular body (MVB) protein 4C (CHMP4C), a human ESCRT-III subunit, is involved in abscission timing. This function correlated with its differential spatiotemporal distribution during late stages of cytokinesis. Accordingly, CHMP4C functioned in the Aurora B-dependent abscission checkpoint to prevent both premature resolution of intercellular chromosome bridges and accumulation of DNA damage. CHMP4C engaged the chromosomal passenger complex (CPC) via interaction with Borealin, which suggested a model whereby CHMP4C inhibits abscission upon phosphorylation by Aurora B. Thus, the ESCRT machinery may protect against genetic damage by coordinating midbody resolution with the abscission checkpoint.

The final separation of daughter cells during cytokinesis is the ancestral function of the endosomal sorting complex required for transport (ESCRT) machinery (1–5) which also acts to resolve equivalent membrane scission events in multivesicular body (MVB) forma-

tion (6, 7) and human immunodeficiency virus–1 (HIV-1) budding (8, 9). Midbody recruitment of ESCRT-III, the filament-forming scission machinery, is an essential event in cytokinesis that is thought to provide constrictive force during abscission (2, 10–12). An Aurora B-dependent

abscission checkpoint (NoCut) is thought to retard abscission to prevent damage of lagging chromosomes that are trapped in the midbody (13–15) and may function more generally as an abscission timer (13). However, mechanisms that modulate abscission timing remain poorly understood and the involvement of the core abscission machinery in this process is unclear.

Here, we investigated the function of charged MVB proteins CHMP4A, -B, and -C, human homologs of the yeast ESCRT-III subunit Snf7p. For this purpose, specific small interfering RNAs (siRNAs) and antibodies against each of the CHMP4s were developed (16) (fig. S1). We then analyzed ESCRT-dependent endosomal down-regulation of class I major histocompatibility complex (MHC-I) molecules in HeLa cells stably expressing the K3 ubiquitin ligase from Kaposi's

sarcoma-associated herpes virus (KSHV) (17). Similarly to depletion of tumor susceptibility gene 101 (TSG101), depletion of CHMP4B prevented MHC-I degradation, whereas depletion of CHMP4A or CHMP4C had little effect on this process (fig. S2, A and B). As expected (18), depletion of CHMP4A or CHMP4C did not inhibit HIV-1 release, and only depletion of CHMP4B inhibited this ESCRT-dependent process (fig. S3). Furthermore, CHMP4A and CHMP4C were dispensable for completion of cytokinesis, whereas CHMP4B was again the sole paralog required (Fig. 1, A and B). However, in asynchronous cultures of CHMP4C-depleted HeLa cells, fewer cells were connected by midbodies (Fig. 1C), which led us to question whether midbodies were resolved faster in cells lacking CHMP4C.

We then imaged live HeLa cells stably expressing mCherry-tubulin (HeLa mCh-Tub) (19) to examine mitotic dynamics. CHMP4C-depleted cells (Fig. 1D) showed normal duration of early mitotic phases and centrosome amplification (Fig. 1E and fig. S4A). We next monitored tubulin disassembly at the midbody as a marker that cor-

relates strongly with abscission (15). Cells treated with control siRNAs resolved their midbodies with similar kinetics and depletion of CHMP4C reduced abscission time by ~30 min (Fig. 1F, fig. S4A, and movies S1 to S4). Abscission was also faster in cells codepleted of CHMP4C and Spastin, an adenosine triphosphatase involved in destabilization of midbody microtubules (20, 21), which suggested that CHMP4C and Spastin regulate distinct stages of abscission (fig. S4B). We next used cell lines stably expressing mCh-tubulin and comparable levels of green fluorescent protein (GFP)-tagged CHMP4B or CHMP4C (22) (Fig. 1G) for simultaneous imaging of abscission and midbody recruitment of ESCRT-III. Early phases of mitosis and abscission (Fig. 1, H and I) were similar in control and GFP-CHMP4B-expressing cells. However, expression of GFP-CHMP4C resulted in an abscission delay that could be explained by increased levels of intracellular CHMP4C (Fig. 1I; fig. S5, A to D; and movies S5 and S6). As expected (12), GFP-CHMP4B localized transiently to the midbody arms immediately (21 ± 7 min) before abscission, whereas GFP-CHMP4C

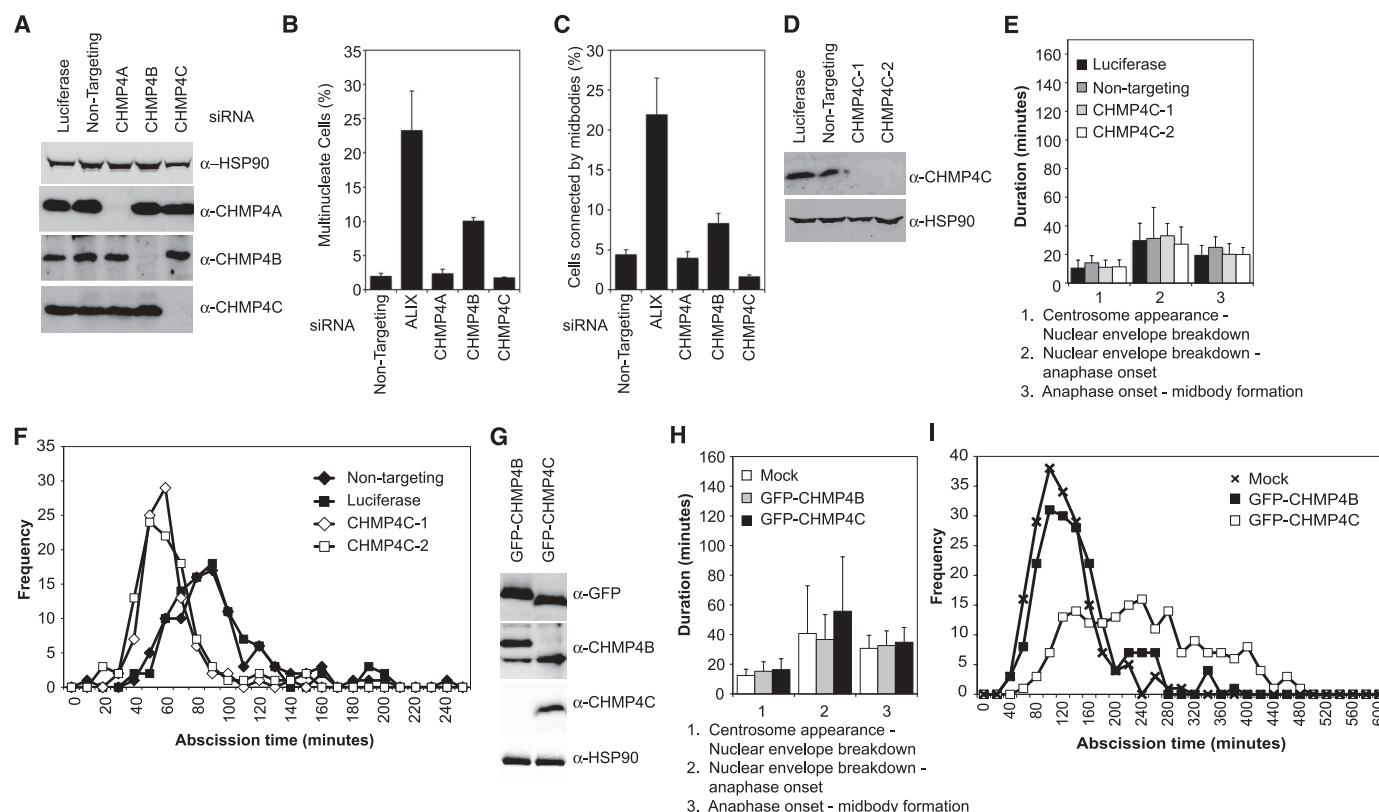


Fig. 1. CHMP4C negatively regulates cytokinesis. (A) Resolved HeLa cell lysates were examined by blotting with antibodies against CHMP4A, CHMP4B, CHMP4C, or heat shock protein 90 kD (HSP90). (B and C) siRNA-transfected HeLa cells were fixed and stained with α -tubulin. (B) Multinucleate cells ($n = 3$, \pm SD) or (C) cells connected by midbodies ($n = 7$, \pm SD) were scored visually. (D) Resolved lysates from siRNA-transfected HeLa mCh-Tub cells were examined by blotting with antibodies against CHMP4C or HSP90. (E and F) Asynchronous cultures of HeLa mCh-Tub cells were transfected with the indicated siRNA and imaged live, and mitotic durations were quantified. Abscission time was calculated across four independent experiments (Luciferase:

93 ± 38 min, $n = 96$; nontargeting: 94 ± 36 min, $n = 94$; CHMP4C-1: 59 ± 17 min, $n = 88$; CHMP4C-2: 61 ± 25 min, $n = 100$). (G) Resolved cell lysates from HeLa cells stably expressing mCh-Tub and either GFP-CHMP4B or GFP-CHMP4C were examined by blotting with antibodies against HSP90, GFP, CHMP4B, or CHMP4C. (H and I) Cells from (G) were imaged live, and mitotic durations were quantified. The more intense imaging (16) resulted in general abscission delays to 116 ± 45 and 137 ± 61 min for control or GFP-CHMP4B-expressing cells, whereas GFP-CHMP4C-expressing cells took 240 ± 103 min to complete abscission. Data comprise 185 cells per condition from three independent experiments.

localized earlier to the midbody, arriving 176 ± 19 min before abscission (Fig. 2, A to D). During its recruitment, GFP-CHMP4C localized initially to the midbody arms, before being directed to the central region (Flemming body) (Fig. 2, A to D; fig. S5, A to D; and movies S5 and S6). Thus, CHMP4B and CHMP4C exhibit differential spatiotemporal distribution during late cytokinesis.

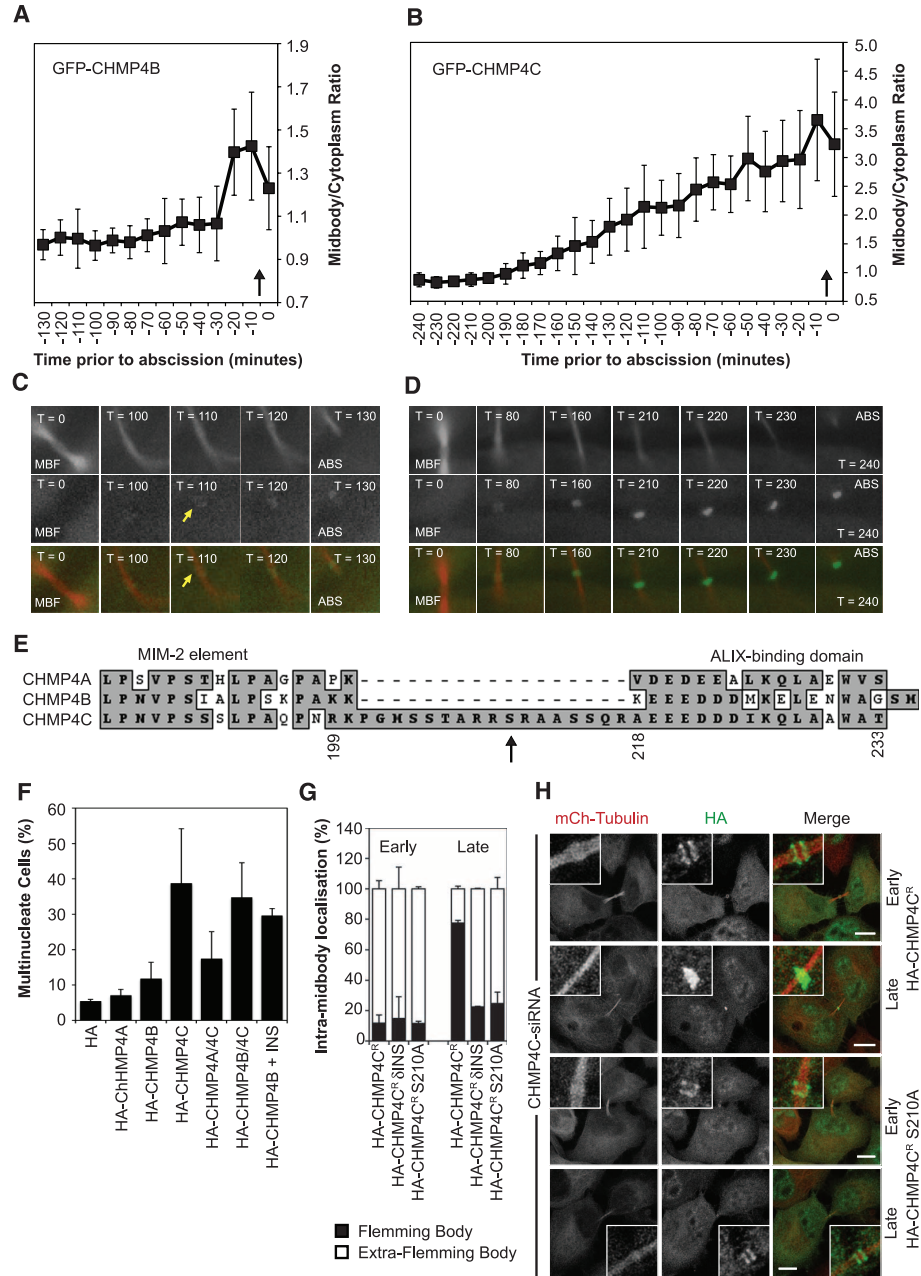
We sought differences between CHMP4 paralogs that could explain their differential behavior. Alignment of the regulatory region at the C termini of CHMP4s revealed a CHMP4C-specific insertion (INS) at residues 201 to 217 (Fig. 2E). This insertion is expanded in mammals (fig. S6) and contains numerous serine (S) and threonine (T) residues. Transiently overexpressed CHMP4 chimeras containing CHMP4C's C terminus were more potent inhibitors of cell division

(Fig. 2F), and grafting INS into the corresponding region of CHMP4B produced a chimera that inhibited cell division (Fig. 2F), which suggested that INS may be a platform for phosphorylation that inhibits abscission. We next determined the spatial distribution of CHMP4C during abscission by analyzing hemagglutinin (HA)-tagged CHMP4C expressed stably at near-endogenous levels. In early midbodies, HA-CHMP4C localized to the midbody arms, whereas in late midbodies, as observed for GFP-CHMP4C in living cells (Fig. 2B), HA-CHMP4C localized to the Flemming body in an INS-dependent manner (Fig. 2, G and H). In contrast, CHMP4A and CHMP4B were only observed on midbody arms (fig. S5E). We speculated that phosphorylation of residues within INS may have directed CHMP4C's localization and mapped the determinant of

Flemming body localization in late cytokinesis to S210, a residue conforming to the consensus sequence for Aurora B ([R/K]₍₁₋₃₎-X-[S/T]) (23) (Fig. 2, G and H, and fig. S5F).

We next wondered whether CHMP4C participated in the Aurora B-dependent NoCut abscission checkpoint. This checkpoint can be activated by partial depletion of nucleoporin 153 kD (NUP153) and is evidenced by an accumulation of cells unable to complete abscission and arrested at the midbody stage (24). NoCut activation was prevented by codepletion of CHMP4C with NUP153 (Fig. 3, A and B), despite phosphorylated Aurora B persisting at midbodies (Fig. 3C). Chromosomes trapped at the midbody may provide an alternative NoCut activation route. We found that HA-CHMP4C preferentially localized to intercellular chromatin bridges illuminated with yellow

Fig. 2. Differential spatiotemporal recruitment of CHMP4 paralogs during cytokinesis. (A to D) GFP fluorescence intensities of midbody-localized (A and C) GFP-CHMP4B ($n = 14$, \pm SD) or (B and D) GFP-CHMP4C ($n = 9$, \pm SD) during abscission. Abscission indicated by arrow, time in minutes. (C and D) Selected frames are presented. Initial recruitment of GFP-CHMP4C to midbody arms is marked (arrowhead). (E) ClustalW alignment of the C-terminal regions of CHMP4A, CHMP4B, and CHMP4C, S210 indicated by arrow. MIM2, a motif that binds microtubule interaction and trafficking (MIT) domains. (F) HeLa cells transfected with plasmids encoding the indicated HA-CHMP4 constructs were fixed and stained with antibodies against tubulin and HA. Multinucleate cells were scored ($n = 5$, \pm SD). (G and H) HeLa mCh-Tub cells stably expressing HA-CHMP4C^R, HA-CHMP4C^RINS, or HA-CHMP4C^R S210A were treated with CHMP4C siRNA, fixed, and stained with HA-specific antibody. The HA-CHMP4C location was scored ($n = 3$, \pm SD). Scale bar is 10 μ m.



fluorescent protein (YFP)-tagged lamin-associated protein 2 β (LAP2 β) (Fig. 3D and fig. S7, A and B). Moreover, HA-CHMP4C colocalized with activated Aurora B at these chromatin bridges (Fig. 3E). We examined intercellular DNA-bridge resolution in CHMP4C-depleted cells and observed that YFP-LAP2 β -positive bridge formation and cellular viability were normal (fig. S7, C and D) and also found, similarly to Aurora B-inhibited cells (15), faster resolution of YFP-LAP2 β -positive chromatin bridges (Fig. 3F; fig. S7, E to G; and movies S7 to S9). Consequently, stable depletion of CHMP4C resulted in increased levels of histone H2AX phosphorylation (Fig. 3G and fig. S7H), which suggested that deregulation of the abscission checkpoint in these cells results in the accumulation of genetic damage (25).

Given the essential role of CHMP4C in the regulation of abscission timing and its participation in the Aurora B-dependent abscission checkpoint, we searched for links between components of the chromosomal passenger complex (CPC) and ESCRT-III by yeast two-hybrid screening. We found interactions between Borealin and CHMP2A, CHMP4B, CHMP4C, and CHMP6 (Fig. 4, A and B) and mapped these interactions to the C terminus of Borealin (fig. S8A), a region that recruits adaptor proteins to the CPC. CHMP4C was the strongest interactor with Borealin, and we could coprecipitate CHMP4C with Aurora B (fig. S8B), which confirmed that the ESCRT machinery is able to engage the CPC. Colocalization of HA-CHMP4C and members of the CPC was observed in early, but not late, midbodies (Fig. 4C and fig. S8, C and D). Accordingly,

a λ -phosphatase-sensitive, mobility-shifted form of HA-CHMP4C was detected in mitotic lysates and was enriched on a phospho-affinity resin (Fig. 4D and fig. S8E). Similar to centrosomal protein of 55 kD (CEP55) (26, 27), CHMP4C phosphorylation occurred at mitotic onset and reverted in a phosphatase-dependent manner as mitosis progressed (Fig. 4E). An Aurora B inhibitor reduced CHMP4C phosphorylation (Fig. 4F), and the epitope detected by α -CHMP4C, which recognizes INS, was masked in the mobility-shifted fraction and revealed upon λ -phosphatase treatment (Fig. 4D), which suggested that residues within CHMP4C's insertion were phosphorylated during mitosis. Finally, Aurora B could specifically phosphorylate CHMP4C on S210 within INS, the residue required for Flemming body localization (Fig. 4, G and H, and fig. S8, F and G).

To investigate the role of Aurora B phosphorylation of CHMP4C on abscission timing, we used HeLa mCh-Tub cell lines stably expressing HA-tagged, siRNA-resistant versions of CHMP4C (HA-CHMP4C^R, HA-CHMP4C^R δ INS, or HA-CHMP4C^R S210A) expressed at similar, near-endogenous levels (Fig. 4I). Interaction of these mutants with known CHMP4C-binding proteins (fig. S8H) was maintained, and early mitotic phases were completed normally in cells depleted of endogenous CHMP4C and reliant on these proteins (fig. S8I). Note that HA-CHMP4C^R rescued the faster abscission induced by CHMP4C depletion (Fig. 4J), whereas cells reliant on HA-CHMP4C^R δ INS and HA-CHMP4C^R S210A could not (Fig. 4K). We propose that Aurora B-dependent phosphorylation of S210 allows

CHMP4C localization to the Flemming body and acts as a brake on the late stages of cytokinesis. Furthermore, cells stably expressing YFP-LAP2 β and HA-CHMP4C^R S210A were unable to delay abscission in response to intracellular chromatin bridges, despite the presence of these proteins at the chromatin bridge (fig. S9A), which indicated deregulation of the NoCut checkpoint in these cells (Fig. 4L).

Here, we found that CHMP4C acts as an essential regulator of the Aurora B-mediated abscission checkpoint. In the absence of CHMP4C, cells complete abscission faster. We suggest that Aurora B-dependent phosphorylation of CHMP4C on S210 directs its Flemming body localization and delays abscission through activation of NoCut, possibly by preventing assembly of a productive abscission complex. A phosphomimetic mutation (S210D) had no apparent effect on known CHMP4C interactions (fig. S9B), which suggested that phosphoregulation of abscission timing may involve as-yet-unknown CHMP4C binding partners. That the S210 consensus site is conserved only in mammals suggests that this mechanism might have emerged late in evolution as a safety belt in addition to the interactions of the CPC with CHMP2A and CHMP6. CHMP4C depletion circumvents the NoCut abscission checkpoint, allows faster resolution of chromatin bridges, and induces the accumulation of phosphorylated H2AX. These observations are consistent with a role of CHMP4C in protection against DNA damage accumulation. In this context, as well as being charged MVB proteins (28), CHMPs were originally reported as chromatin-modifying proteins (29) that could associate with condensed

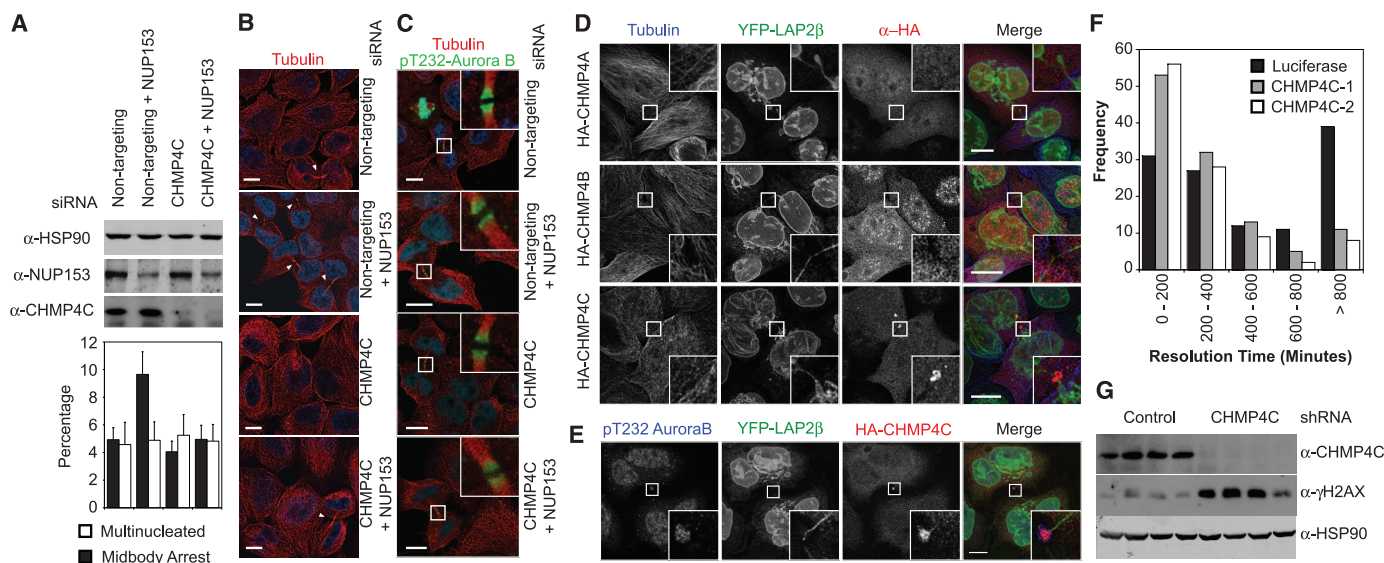


Fig. 3. CHMP4C regulates the abscission checkpoint. (A to C) (A) Cell lysates from siRNA-transfected HeLa cells were examined by blotting with antibodies against NUP153, CHMP4C, HA, and HSP90. Multinucleate and midbody-connected cells were scored visually ($n = 6$, ± 5 D). Alternatively, cells were fixed and stained with antibodies against (B) tubulin or (C) tubulin and pT232 Aurora B. Scale bar is 10 μ m. (D and E) HeLa cells stably expressing YFP-LAP2 β were transfected with plasmids encoding the indicated HA-CHMP4 constructs. Cells were fixed and stained with antibodies against (D)

tubulin and HA or (E) pT232 Aurora B and HA. Scale bar is 10 μ m. (F) HeLa cells stably expressing YFP-LAP2 β were transfected with the indicated siRNA and imaged live; the duration of LAP2 β -bridge resolution was quantified across six independent experiments (luciferase: 576 ± 454 min, $n = 116$; CHMP4C-1: 321 ± 308 min, $n = 112$; CHMP4C-2: 291 ± 278 min, $n = 103$). (G) Cell lysates from clonal short hairpin RNA (shRNA)-transduced HeLa cells were examined by blotting with antibodies against γ H2AX, CHMP4C, or HSP90.

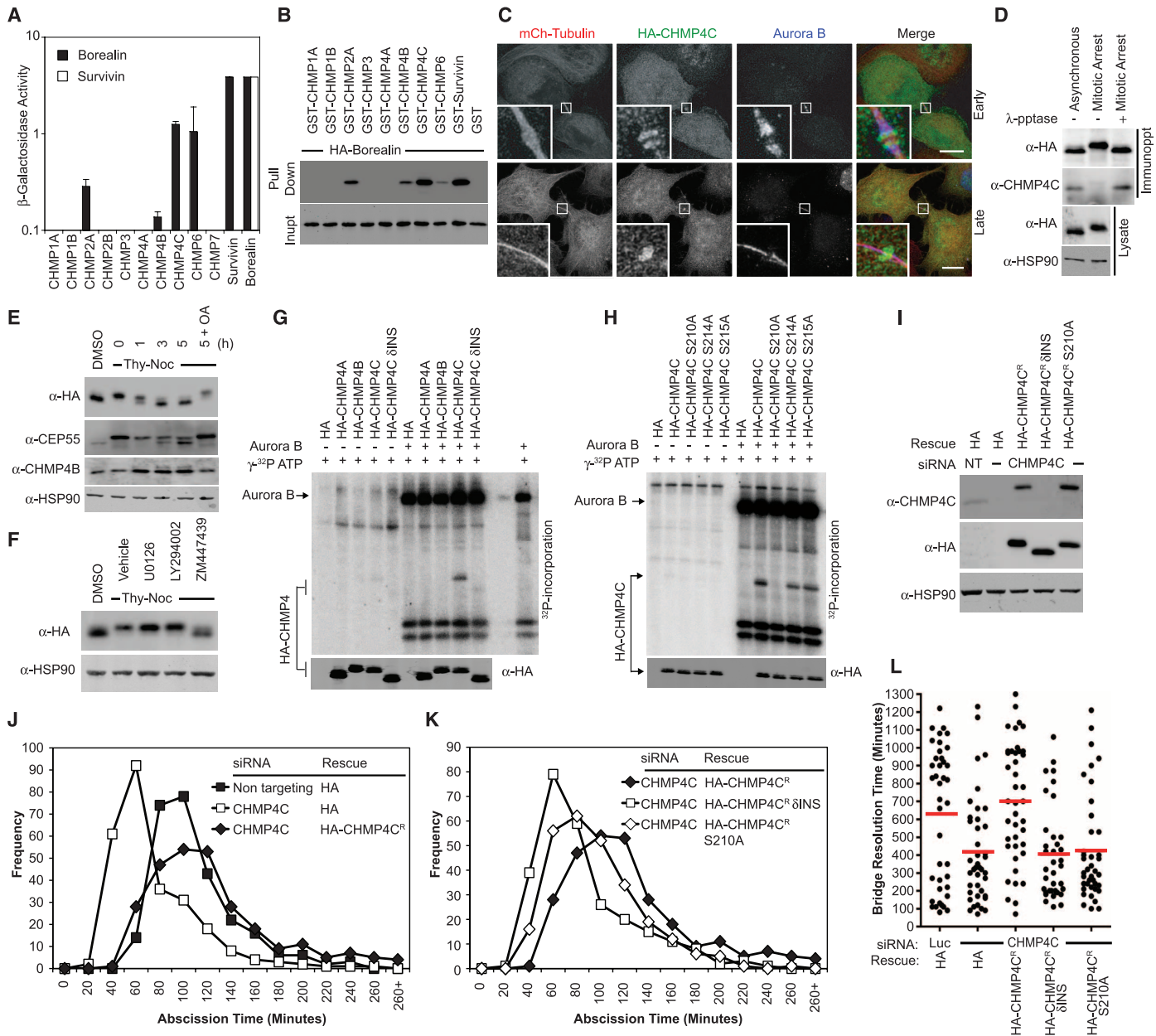


Fig. 4. Aurora B-dependent phosphorylation of CHMP4C S210 activates the NoCut abscission checkpoint. **(A)** β -Galactosidase assay from yeast co-transformed with the indicated VP16- and GAL4-fused constructs ($n = 3$, \pm SD). **(B)** Cell lysates and glutathione-bound fractions from human embryonic kidney (HEK) 293T cells transfected with the indicated fusion proteins were examined by Western blotting with antibody against HA. **(C)** HeLa mCh-Tub cells stably expressing HA-CHMP4C^R were fixed and stained with antibodies against HA and Aurora B. **(D)** Asynchronous and mitotic lysates of HeLa mCh-Tub cells stably expressing HA-CHMP4C^R were immunoprecipitated with HA-specific antibody and treated as indicated, then examined by blotting with antibodies against HA, CHMP4C, CHMP4B, CEP55, and HSP90. **(E and F)** Asynchronous or mitotically arrested HeLa mCh-Tub cells stably expressing HA-CHMP4C^R were either **(E)** released into media containing dimethyl sulfoxide (DMSO) or the phosphatase inhibitor okadaic acid (OA) for the indicated times or **(F)** treated overnight during the nocodazole arrest with inhibitors of mitogen-activated protein kinase (MEK) (U0126), phosphatidylinositol 3-kinase (LY294002) or Aurora B (ZM447439). Cell lysates were examined by blotting with antibodies against HA and HSP90. **(G and H)** Proteins were immunoprecipitated from HEK 293T cells with antibody against

HA and subjected to an in vitro kinase assay with recombinant Aurora B. Incorporated ³²P was visualized by phosphorimaging; blotting with HA-specific antibody allowed detection of immunoprecipitates. **(I to K)** Asynchronous cultures of HeLa mCh-Tub cells stably expressing HA, HA-CHMP4C^R, HA-CHMP4C^R δ INS, or HA-CHMP4C^R S210A were transfected with the indicated siRNA. **(I)** Resolved cell lysates were examined by blotting with antibodies against CHMP4C, HA, and HSP90. **(J and K)** Alternatively, cells were imaged live. Abscission times were quantified across seven independent experiments (luciferase, 104 ± 35 min, $n = 244$; CHMP4C siRNA, 71 ± 37 min, $n = 260$; CHMP4C siRNA and HA-CHMP4C^R, 118 ± 52 min, $n = 269$; CHMP4C siRNA and HA-CHMP4C^R δ INS, 81 ± 40 min, $n = 264$; CHMP4C siRNA and HA-CHMP4C^R S210A, 91 ± 38 min, $n = 268$). **(L)** HeLa cells stably expressing YFP-LAP2 β and HA or HA-CHMP4C^R, HA-CHMP4C^R δ INS, or HA-CHMP4C^R S210A were treated with the indicated siRNA and imaged live. The timing of YFP-LAP2 β bridge resolution was quantified from two independent experiments (luciferase, 628 ± 382 min, $n = 41$; CHMP4C siRNA, 413 ± 292 min, $n = 41$; CHMP4C siRNA and HA-CHMP4C^R, 698 ± 332 min, $n = 41$; CHMP4C siRNA and HA-CHMP4C^R δ INS, 402 ± 259 min, $n = 36$; CHMP4C siRNA and HA-CHMP4C^R S210A, 421 ± 295 min, $n = 40$).

chromatin, which suggests that the physical interaction of lagging chromosomes and ESCRT-III at the midbody may trigger activation of NoCut.

References and Notes

1. J. G. Carlton, J. Martin-Serrano, *Science* **316**, 1908 (2007).
2. E. Morita *et al.*, *EMBO J.* **26**, 4215 (2007).
3. R. Y. Samson, T. Obata, S. M. Freund, R. L. Williams, S. D. Bell, *Science* **322**, 1710 (2008).
4. H. H. Lee, N. Elia, R. Ghirlando, J. Lippincott-Schwartz, J. H. Hurley, *Science* **322**, 576 (2008).
5. A. Caballe, J. Martin-Serrano, *Traffic* **12**, 1318 (2011).
6. C. Raiborg, H. Stenmark, *Nature* **458**, 445 (2009).
7. W. M. Henne, N. J. Buchkovich, S. D. Emr, *Dev. Cell* **21**, 77 (2011).
8. E. R. Weiss, H. Göttlinger, *J. Mol. Biol.* **410**, 525 (2011).
9. J. Martin-Serrano, S. J. D. Neil, *Nat. Rev. Microbiol.* **9**, 519 (2011).
10. J. G. Carlton, M. Agromayor, J. Martin-Serrano, *Proc. Natl. Acad. Sci. U.S.A.* **105**, 10541 (2008).
11. J. Guizetti *et al.*, *Science* **331**, 1616 (2011).
12. N. Elia, R. Sougrat, T. A. Spurlin, J. H. Hurley, J. Lippincott-Schwartz, *Proc. Natl. Acad. Sci. U.S.A.* **108**, 4846 (2011).
13. C. Norden *et al.*, *Cell* **125**, 85 (2006).
14. M. Mendoza *et al.*, *Nat. Cell Biol.* **11**, 477 (2009).
15. P. Steigemann *et al.*, *Cell* **136**, 473 (2009).
16. Materials and methods are available as supporting material on *Science* Online.
17. E. W. Hewitt *et al.*, *EMBO J.* **21**, 2418 (2002).
18. E. Morita *et al.*, *Cell Host Microbe* **9**, 235 (2011).
19. M. Agromayor *et al.*, *Mol. Biol. Cell* **20**, 1374 (2009).
20. J. W. Connell, C. Lindon, J. P. Luzio, E. Reid, *Traffic* **10**, 42 (2009).
21. D. Yang *et al.*, *Nat. Struct. Mol. Biol.* **15**, 1278 (2008).
22. N. Jouvencet, M. Zhadina, P. D. Bieniasz, S. M. Simon, *Nat. Cell Biol.* **13**, 394 (2011).
23. P. Meraldi, R. Honda, E. A. Nigg, *Curr. Opin. Genet. Dev.* **14**, 29 (2004).
24. D. R. Mackay, M. Makise, K. S. Ullman, *J. Cell Biol.* **191**, 923 (2010).
25. O. Fernandez-Capetillo, A. Lee, M. Nussenzweig, A. Nussenzweig, *DNA Repair (Amst.)* **3**, 959 (2004).
26. R. N. Bastos, F. A. Barr, *J. Cell Biol.* **191**, 751 (2010).
27. M. Fabbro *et al.*, *Dev. Cell* **9**, 477 (2005).
28. T. L. Howard, D. R. Stauffer, C. R. Degnin, S. M. Hollenberg, *J. Cell Sci.* **114**, 2395 (2001).
29. D. R. Stauffer, T. L. Howard, T. Nyun, S. M. Hollenberg, *J. Cell Sci.* **114**, 2383 (2001).

Acknowledgments: We thank P. Bieniasz for kind gifts of GFP-CHMP4-expressing cells. J.M.-S. was funded by the Medical Research Council (G0802777), the Lister Institute for Preventative Medicine and the EMBO Young Investigators Program. J.M.-S. and M.A. were funded by Wellcome Trust grant (WT093056MA). J.G.C. was funded by Wellcome Trust Value in People award (092429/Z/10/Z). We acknowledge the U.K. National Institute for Health Research Comprehensive Biomedical Research Centre at Guy's and St. Thomas's National Health Service Foundation Trust and King's College London for an equipment grant.

Supporting Online Material

www.sciencemag.org/cgi/content/full/science.1217180/DC1
Materials and Methods

Figs. S1 to S9

References (30–32)

Movies S1 to S9

28 November 2011; accepted 2 March 2012

Published online 15 March 2012;

10.1126/science.1217180

Atg7 Modulates p53 Activity to Regulate Cell Cycle and Survival During Metabolic Stress

In Hye Lee,¹ Yoshichika Kawai,¹ Maria M. Fergusson,¹ Ilsa I. Rovira,¹ Alexander J. R. Bishop,² Noboru Motoyama,³ Liu Cao,^{4*} Toren Finkel^{1*}

Withdrawal of nutrients triggers an exit from the cell division cycle, the induction of autophagy, and eventually the activation of cell death pathways. The relation, if any, among these events is not well characterized. We found that starved mouse embryonic fibroblasts lacking the essential autophagy gene product Atg7 failed to undergo cell cycle arrest. Independent of its E1-like enzymatic activity, Atg7 could bind to the tumor suppressor p53 to regulate the transcription of the gene encoding the cell cycle inhibitor p21^{CDKN1A}. With prolonged metabolic stress, the absence of Atg7 resulted in augmented DNA damage with increased p53-dependent apoptosis. Inhibition of the DNA damage response by deletion of the protein kinase Chk2 partially rescued postnatal lethality in Atg7^{-/-} mice. Thus, when nutrients are limited, Atg7 regulates p53-dependent cell cycle and cell death pathways.

Cell cycle progression and autophagic flux are both sensitive to nutrient availability. Furthermore, with prolonged nutrient deprivation, cell death pathways and autophagy are simultaneously activated (1). However, our understanding of how autophagy intersects with cell cycle progression or apoptotic cell death is incomplete. We demonstrate that in the setting of low nutrients, cells lacking Atg7 have impaired p53-mediated cell cycle arrest, whereas with continued metabolic stress, cells and tissues

lacking Atg7 display increased p53-mediated cell death.

To address whether cell cycle progression and autophagy are linked, we examined the effects of acute nutrient withdrawal on subsequent S-phase entry in either wild-type or Atg7^{-/-} mouse embryonic fibroblasts (MEFs). In wild-type MEFs, S-phase entry, as assessed by bromodeoxyuridine (BrdU) incorporation, decreased by about 60% in the first 3 hours after acute withdrawal of serum and amino acids (Fig. 1A and fig. S1). In contrast, only about 20% of Atg7^{-/-} MEFs successfully exited the cell cycle under the same conditions ($P < 0.001$, $n = 4$). The withdrawal from the cell cycle under starved conditions is often mediated by accumulation of cyclin-dependent kinase inhibitors (CKIs) such as p27^{CDKN1B} or p21^{CDKN1A} (2–7). Although early-passage wild-type MEFs rapidly accumulated p21^{CDKN1A} protein after being shifted to starvation media, this response was

largely absent in Atg7^{-/-} MEFs (Fig. 1B). In contrast, the abundance of p27^{CDKN1B} was not appreciably different between the two cell types. Similarly, metabolic stress induced the accumulation of p21^{CDKN1A} mRNA in wild-type but not Atg7^{-/-} MEFs (Fig. 1C). Consistent with previous observations (8), the starvation-induced increase in p21^{CDKN1A} expression was largely absent in human or mouse cells lacking p53 (fig. S2). Transcription from a p21^{CDKN1A} promoter linked to a luciferase reporter was increased in wild-type but not Atg7^{-/-} MEFs deprived of nutrients (Fig. 1D). Chromatin immunoprecipitation (ChIP) analysis demonstrated that under starved conditions, endogenous Atg7, along with p53, was present at the p21 promoter (Fig. 1E).

Similar analysis in human cells in which Atg7 expression was decreased with small interfering RNA (siRNA) confirmed the impaired expression of p21^{CDKN1A} in nutrient-deprived cells (Fig. 1F). In contrast, depletion of Beclin 1 (Atg6) had no effect on the starvation-induced increase in either p21^{CDKN1A} protein or mRNA expression (Fig. 1G and fig. S3). A similar analysis in Atg5^{-/-} MEFs again revealed no alteration in expression of p21^{CDKN1A} (fig. S4) or other cell cycle parameters (9). Thus, the observed defects in cell cycle arrest and the lack of p21^{CDKN1A} accumulation after nutrient withdrawal appear to be specific for Atg7. This defect was not confined to nutrient withdrawal, as Atg7-deficient cells also appeared to have impaired confluence-dependent growth arrest (Fig. 1, H and I).

We used epitope-tagged proteins to demonstrate that p53 and Atg7 are present in a single complex (Fig. 2A). Analysis of endogenous proteins revealed a similar interaction that was enhanced after nutrient withdrawal (Fig. 2B). Complexes containing Atg7 and p53 complex were evident in both the cytosol and the nucleus (fig. S5). Using p53 glutathione *S*-transferase (GST) constructs, we showed that the region corresponding

¹Center for Molecular Medicine, National Heart, Lung, and Blood Institute, Bethesda, MD 20892, USA. ²University of Texas Health Science Center, San Antonio, TX 78229, USA. ³Department of Cognitive Brain Sciences, Research Institute, National Center for Geriatrics and Gerontology, Aichi 474-8511, Japan. ⁴Key Laboratory of Medical Cell Biology, China Medical University, Shenyang 110001, China.

*To whom correspondence should be addressed. E-mail: finkelt@nih.gov (T.F.); caoliu@mail.cmu.edu (L.C.)

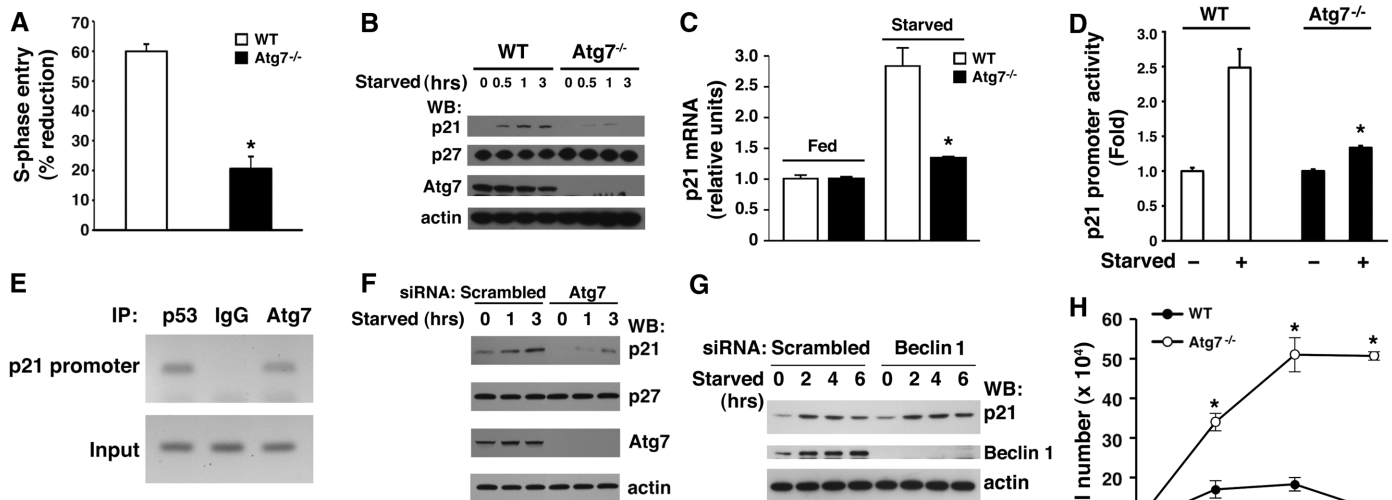
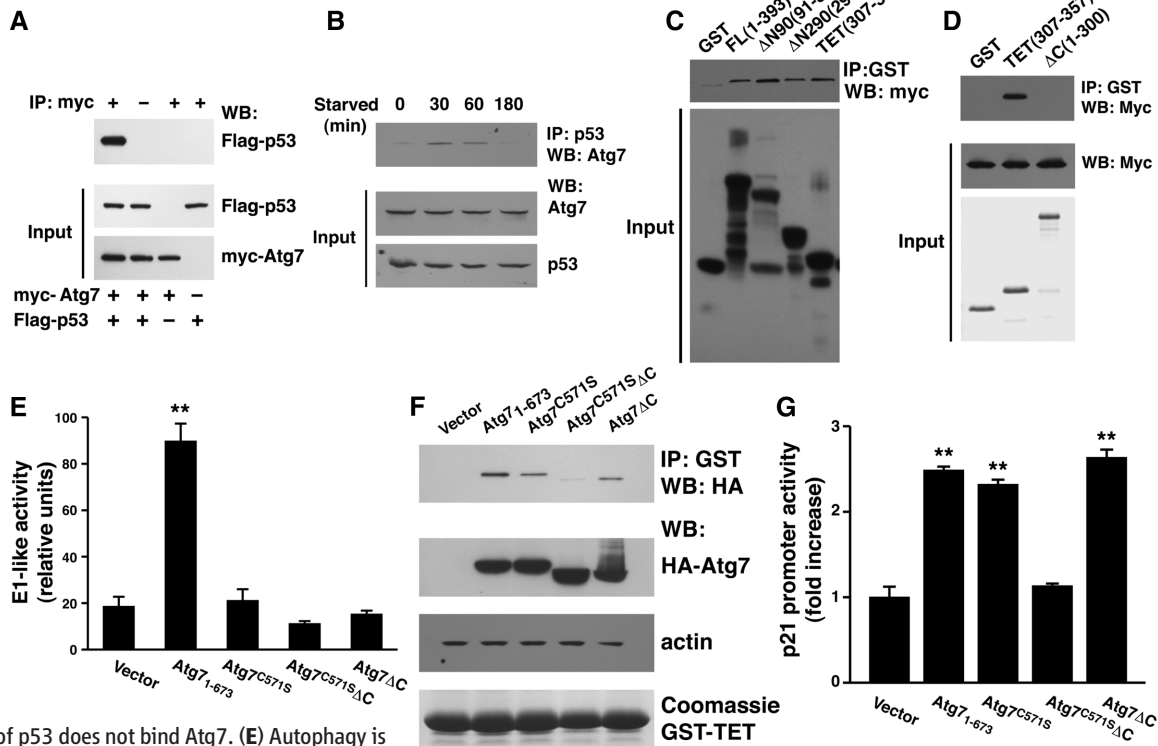


Fig. 1. Requirement of Atg7 for p21^{CDKN1A} expression and for cell cycle arrest. **(A)** Percentage reduction in S-phase entry as measured by BrdU incorporation during starved versus fed conditions for early-passage primary wild-type (WT) or Atg7^{-/-} MEFs. Shown is one representative experiment performed in triplicate with greater than 200 individual cells assessed per condition. **(B)** Protein immunoblot assessment of p21^{CDKN1A} and p27^{CDKN1B} expression in WT and Atg7^{-/-} MEFs after withdrawal of nutrients. Actin is used as a loading control. **(C)** Abundance of p21^{CDKN1A} mRNA after starvation in WT and Atg7^{-/-} MEFs. **(D)** Activity of the p21^{CDKN1A} promoter containing a p53 binding element in WT or Atg7^{-/-} MEFs under fed and starved conditions. **(E)** ChIP of the p21^{CDKN1A} promoter prepared from starved HCT116 cells with antibodies to endogenous p53, Atg7, or an irrelevant immunoglobulin G (IgG) control. **(F)** Starvation-induced p21^{CDKN1A} protein expression in the human HCT116 cell line after transfection with a scrambled control siRNA or after depletion of Atg7. **(G)** p21^{CDKN1A} protein after depletion of Beclin 1 (Atg6). **(H)** Confluent density achieved by either WT or Atg7^{-/-} primary MEFs seeded initially at a high but equal density. **(I)** Corresponding expression of p21^{CDKN1A} as a function of confluent density in WT or Atg7^{-/-} MEFs. **P* < 0.01 (Student *t* test between WT and Atg7^{-/-} MEFs, *n* ≥ 3).

Fig. 2. Interaction of Atg7 with p53. **(A)** Protein-protein interaction in transfected HCT116 cells assessed by protein immunoblot (WB) analysis with myc-tagged Atg7 and Flag-tagged p53. Immunoprecipitation (IP) was performed using an antibody to the myc epitope or, where indicated (–), an irrelevant IgG isotype control serum. IP was performed using 2 mg of protein lysate; the input represents 50 μg of lysate. **(B)** Interaction between endogenous Atg7 and p53 in HCT116 cells under fed conditions (*t* = 0) and after withdrawal of nutrients. **(C)** In vitro interaction between full-length myc-tagged Atg7 and various GST full-length (FL) or truncation mutants of p53. **(D)** A GST-p53 construct (ΔC) consisting of the first 300 amino acids of p53 does not bind Atg7. **(E)** Autophagy is stimulated by full-length Atg7 (1–673), whereas constructs lacking either the active cysteine (Cys⁵⁷¹), the C terminus (ΔC), or both of these alterations lack E1-like enzymatic activity. A minimum of 300 cells per sample were counted using quadruplicate samples per construct (***P* < 0.01, full-length Atg7 compared to other conditions). **(F)** In vitro binding of hemagglutinin (HA)–tagged Atg7 constructs to the GST-p53 tetramerization domain. **(G)** p21^{CDKN1A} promoter activity in fed Atg7^{-/-} MEFs transfected with WT Atg7 or Atg7 constructs with and without E1-like enzymatic activity (*n* = 4 per condition, ***P* < 0.01 compared to vector control).



to the p53 tetramerization (TET) domain mediated the interaction with Atg7 (Fig. 2, C and D, and fig. S6) and that Atg7 could promote the formation of p53 tetramers (fig. S7).

In yeast Atg7, a specific C-terminal active-site cysteine residue and the C-terminal 40 amino acids are required for full enzymatic activity (10). We therefore analyzed the biological activity of mammalian Atg7 mutants containing a serine residue at the active-site cysteine (Atg7^{C571S}), a deletion of the C terminus (Atg7 Δ C), or a combination of the two (Atg7^{C571S} Δ C). Increased Atg7 expression can stimulate autophagic flux (11, 12). The overexpression of wild-type Atg7 but not the mutant proteins caused an increase in the conversion of light chain 3 form I (LC3-I) to LC3-II. This posttranslational modification of LC3 is indicative of the E1-like ubiquitin-conjugating activity of Atg7 (Fig. 2E and figs. S8 and S9). However, full-length Atg7, as well as the enzymatically deficient Atg7^{C571S} and Atg7 Δ C constructs, all appeared to bind to GST-p53 (Fig. 2F). This interaction was lost with the combined Atg7^{C571S} Δ C construct. When assayed in Atg7^{-/-} MEFs, the combined Atg7^{C571S} Δ C mutant failed to stimulate transcription of the

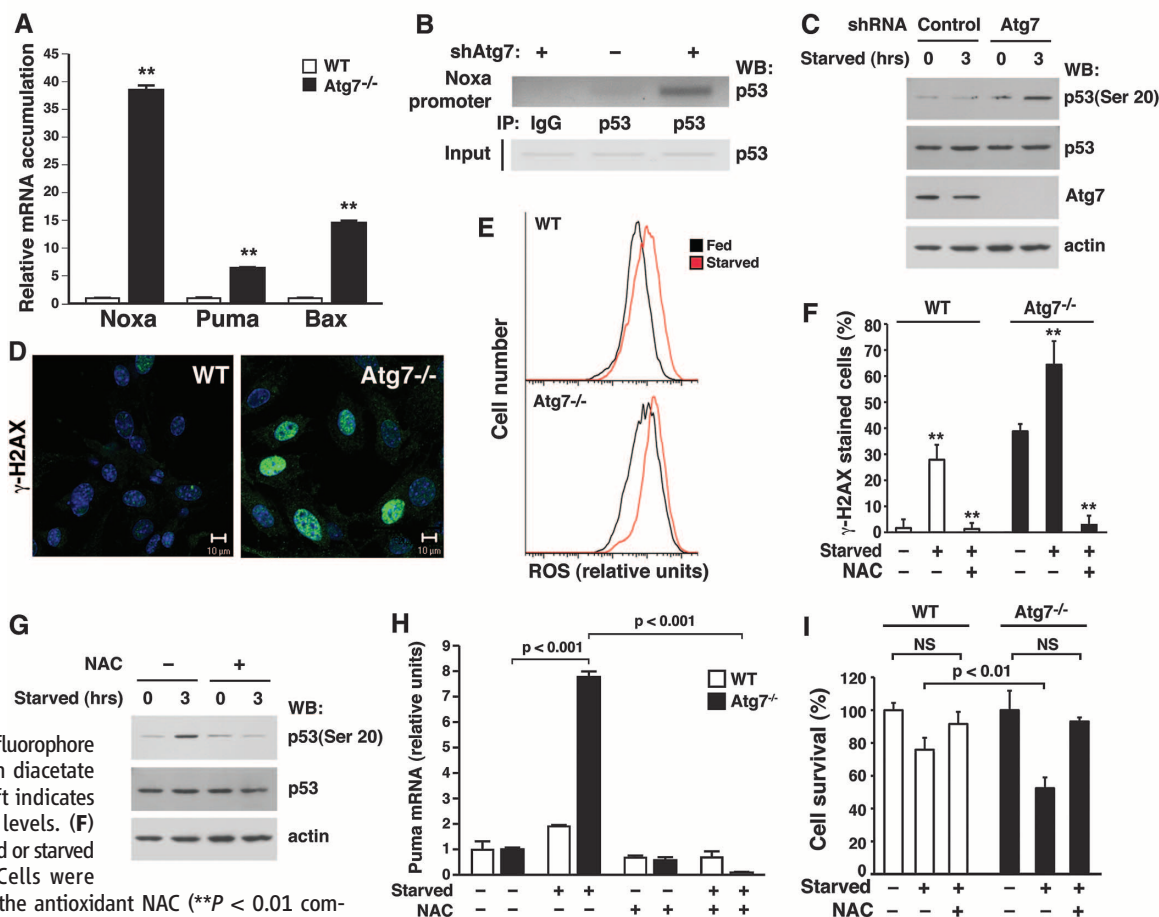
p21^{CDKN1A} gene (Fig. 2G), consistent with the absence of an *in vitro* interaction. In contrast, the autophagy-deficient Atg7^{C571S} and Atg7 Δ C constructs were indistinguishable from wild-type Atg7 in stimulating transcription at the p21^{CDKN1A} promoter. As such, the ability of Atg7 to bind p53 and regulate transcription of p21^{CDKN1A} appears separable from its E1-like enzymatic function.

Taken together, our data indicate that under conditions of metabolic stress, Atg7 is required for the p53-dependent expression of p21^{CDKN1A}. Analysis of several other known p53-regulated genes revealed no significant differences in expression between wild-type and Atg7^{-/-} MEFs (fig. S10). In contrast, analysis of a subset of p53-regulated proapoptotic genes—most notably Noxa, Bax, and Puma—demonstrated increased expression of mRNA and protein in starved Atg7-deficient cells (Fig. 3A and fig. S11A). ChIP analysis revealed that Atg7-deficient cells deprived of nutrients had increased p53 binding at promoters of proapoptotic target genes (Fig. 3B and figs. S11B and S12). Thus, the absence of Atg7 reciprocally regulates p53-dependent cell cycle and cell death pathways.

In other contexts such as exogenous γ -irradiation, activation of p53-dependent apoptosis occurs in conjunction with DNA damage and the phosphorylation of p53 on specific N-terminal residues such as Ser²⁰ (13). When deprived of nutrients, cells lacking Atg7 had increased phosphorylation of p53 at Ser²⁰ (Fig. 3C) along with other parameters indicating increased activation of the DNA damage response pathway (Fig. 3D). Cells deficient in other essential autophagy gene products including Beclin 1 and Atg5 also exhibit increased activation of the DNA damage response (14–16), along with an increase in reactive oxygen species (ROS) (14, 17). We similarly found that Atg7^{-/-} MEFs had higher levels of ROS under basal and starved conditions (Fig. 3E) that were reduced by addition of the cell-permeant antioxidant *N*-acetylcysteine (NAC) or a mitochondrial uncoupler (fig. S13).

Treatment of wild-type or Atg7^{-/-} MEFs with NAC reduced the number of cells with DNA damage foci and starvation-induced phosphorylation of p53 Ser²⁰ (Fig. 3, F and G). Nutrient depletion-induced expression of Puma and other proapoptotic genes was also abrogated by antioxidant treatment of wild-type or Atg7^{-/-} MEFs

Fig. 3. The absence of Atg7 increases mitochondrial ROS, augments DNA damage, and activates p53. (A) Relative mRNA expression in starved WT or Atg7^{-/-} MEFs for a panel of proapoptotic p53-responsive genes (***P* < 0.01 compared to WT MEFs). (B) ChIP assay 3 hours after the induction of nutrient stress, demonstrating increased p53 binding to the Noxa promoter in HCT116 cells depleted of Atg7. (C) Ser²⁰ phosphorylation in control or Atg7-depleted cells. (D) Images of DNA damage in WT and Atg7^{-/-} MEFs as assessed by γ -H2AX staining. (E) Fluorescence-activated cell sorter analysis of WT and Atg7^{-/-} MEFs under fed (black) or starved (red) conditions, using the redox-dependent fluorophore dichlorodihydrofluorescein diacetate (DCFDA). A rightward shift indicates higher intracellular ROS levels. (F) γ -H2AX foci formation in fed or starved WT and Atg7^{-/-} MEFs. Cells were treated as indicated with the antioxidant NAC (***P* < 0.01 compared to starved cells not treated with NAC). (G) NAC treatment inhibits starvation-induced p53 Ser²⁰ phosphorylation in Atg7-depleted cells. (H) Puma expression in WT and Atg7^{-/-} MEFs under fed (–) or starved (+) conditions, in the presence or absence of the cell permeant antioxidant



N-acetylcysteine (NAC). (I) Cell death during fed or starved conditions in WT or Atg7^{-/-} MEFs in the presence or absence of NAC. Unless specified, all results are from at least triplicate determinations.

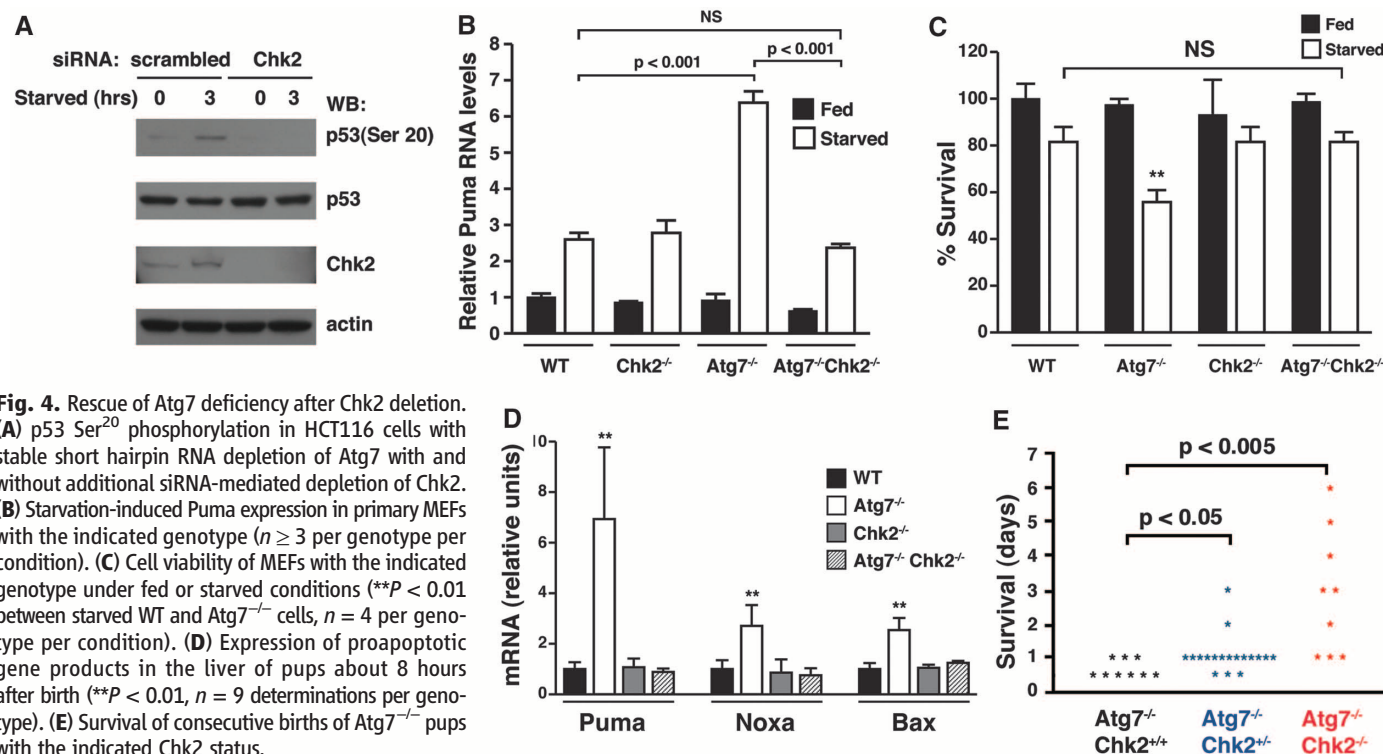


(Fig. 3H and fig. S14). Underscoring the difference between the p53-mediated growth arrest and p53-mediated cell death pathways, NAC treatment had no effect on p53-dependent expression of p21^{CDKN1A} during metabolic stress (fig. S15). Finally, consistent with the augmented DNA damage and increased activation of proapoptotic genes, Atg7^{-/-} MEFs were significantly more sensitive to starvation (fig. S16). Nonetheless, treatment with NAC largely protected these cells from starvation-induced cell death (Fig. 3I).

After DNA damage induced by γ -irradiation, activation of Chk2 activation is required for p53 Ser²⁰ phosphorylation and subsequent p53-dependent cell death (18). In certain genetic models such as the absence of the Polycomb gene product Bmi-1, a rise in mitochondrial oxidants is sufficient to induce DNA damage and Chk2 activation (19). Thus, we analyzed the effect of depletion of Chk2 on p53 Ser²⁰ phosphorylation induced by metabolic stress. In Atg7-deficient cells, depletion of Chk2 reduced starvation-induced phosphorylation of p53 Ser²⁰ (Fig. 4A and fig. S17). The increase in proapoptotic gene expression observed in Atg7-deficient cells was not observed in Atg7^{-/-}Chk2^{-/-} MEFs (Fig. 4B and figs. S18 and S19). Similarly, the reduced viability observed in starved Atg7^{-/-} MEFs was also absent in Atg7^{-/-}Chk2^{-/-} MEFs (Fig. 4C).

Mice lacking Atg7 are born with the expected Mendelian frequency but rapidly succumb in the first few hours of life (20). The basis for this lethality is incompletely understood (21). We wondered whether oxidative stress and the activation of the DNA damage response played a role. Metabolically active tissues of Atg7^{-/-} mice

demonstrated augmented expression of p53-dependent proapoptotic genes (Fig. 4D and fig. S20), but this was not observed in Atg7^{-/-}Chk2^{-/-} mice. Fewer than 5% of ATG7^{-/-} pups survived more than 24 hours and none survived more than 48 hours. Deletion of one or both alleles of Chk2, however, significantly extended survival of Atg7-deficient animals (Fig. 4E). Long-term survival of double-knockout mice appeared to be limited by persistent neurological defects (fig. S21).

Our data demonstrate that Atg7 and p53 bind each other directly, that starvation increases this interaction, and that in the absence of Atg7, cells fail to properly induce p21^{CDKN1A} expression. This cell cycle defect is specific for Atg7 and is not observed in Atg5- or Atg6-deficient cells, nor does it require the E1-like enzymatic activity of Atg7. In the absence of Atg7, prolonged metabolic stress leads to augmented p53 proapoptotic activity. The increase in p53 proapoptotic activity appears to be similarly dysregulated in Atg7^{-/-} and Atg5^{-/-} cells (figs. S22 and S23). The physiological importance of this shared ROS-Chk2-p53-dependent pathway is underscored by the rescue of Atg7^{-/-} postnatal lethality by Chk2 deletion. Previous results suggest that p53 can regulate autophagy (22–25). Our observations suggest that an additional and reciprocal regulation also exists whereby Atg7 can regulate p53.

References and Notes

1. J. D. Rabinowitz, E. White, *Science* **330**, 1344 (2010).
2. J. W. Harper, G. R. Adams, N. Wei, K. Keyomarsi, S. J. Elledge, *Cell* **75**, 805 (1993).
3. L. Delavaine, N. B. La Thangue, *Oncogene* **18**, 5381 (1999).
4. P. Perucca *et al.*, *Cell Cycle* **8**, 105 (2009).

5. N. Rivard, G. L'Allemain, J. Bartek, J. Pouyssegur, *J. Biol. Chem.* **271**, 18337 (1996).
6. M. H. Ladhak, K. Y. Lee, T. M. Upton, M. F. Reed, M. E. Ewen, *Mol. Cell. Biol.* **18**, 6605 (1998).
7. Y. H. Kwon, A. Jovanovic, M. S. Serfas, H. Kiyokawa, A. L. Tyner, *J. Biol. Chem.* **277**, 41417 (2002).
8. W. S. El-Deiry *et al.*, *Cell* **75**, 817 (1993).
9. M. Valentin, E. Yang, *Cell Cycle* **7**, 2762 (2008).
10. M. Komatsu *et al.*, *J. Biol. Chem.* **276**, 9846 (2001).
11. L. Yang, P. Li, S. Fu, E. S. Calay, G. S. Hotamisligil, *Cell Metab.* **11**, 467 (2010).
12. J. S. Pattison, H. Osinska, J. Robbins, *Circ. Res.* **109**, 151 (2011).
13. A. Vazquez, E. E. Bond, A. J. Levine, G. L. Bond, *Nat. Rev. Drug Discov.* **7**, 979 (2008).
14. R. Mathew *et al.*, *Cell* **137**, 1062 (2009).
15. R. Mathew *et al.*, *Genes Dev.* **21**, 1367 (2007).
16. V. Karantz-Wadsworth *et al.*, *Genes Dev.* **21**, 1621 (2007).
17. M. C. Tal *et al.*, *Proc. Natl. Acad. Sci. U.S.A.* **106**, 2770 (2009).
18. A. Hirao *et al.*, *Science* **287**, 1824 (2000).
19. J. Liu *et al.*, *Nature* **459**, 387 (2009).
20. M. Komatsu *et al.*, *J. Cell Biol.* **169**, 425 (2005).
21. S. Schiaffino, C. Mammucari, M. Sandri, *Autophagy* **4**, 727 (2008).
22. D. Crighton *et al.*, *Cell* **126**, 121 (2006).
23. Z. Feng, H. Zhang, A. J. Levine, S. Jin, *Proc. Natl. Acad. Sci. U.S.A.* **102**, 8204 (2005).
24. R. K. Amaravadi *et al.*, *J. Clin. Invest.* **117**, 326 (2007).
25. E. Tasdemir *et al.*, *Cell Cycle* **7**, 3006 (2008).

Acknowledgments: We thank M. Komatsu for providing the Atg7^{-/-} mice. Supported by National Natural Science Foundation of China grants 81130042 and 31171323 (L.C.), NIH intramural funds, and a grant from the Ellison Medical Foundation (T.F.).

Supplementary Materials

www.sciencemag.org/cgi/content/full/336/6078/225/DC1
Materials and Methods
Figs. S1 to S23
References (26–31)

23 December 2011; accepted 6 March 2012
10.1126/science.1218395

Mechanism of Voltage Gating in Potassium Channels

Morten Ø. Jensen,^{1*} Vishwanath Jogini,¹ David W. Borhani,¹ Abba E. Leffler,¹ Ron O. Dror,¹ David E. Shaw^{1,2*}

The mechanism of ion channel voltage gating—how channels open and close in response to voltage changes—has been debated since Hodgkin and Huxley's seminal discovery that the crux of nerve conduction is ion flow across cellular membranes. Using all-atom molecular dynamics simulations, we show how a voltage-gated potassium channel (KV) switches between activated and deactivated states. On deactivation, pore hydrophobic collapse rapidly halts ion flow. Subsequent voltage-sensing domain (VSD) relaxation, including inward, 15-angstrom S4-helix motion, completes the transition. On activation, outward S4 motion tightens the VSD–pore linker, perturbing linker–S6-helix packing. Fluctuations allow water, then potassium ions, to reenter the pore; linker–S6 repacking stabilizes the open pore. We propose a mechanistic model for the sodium/potassium/calcium voltage-gated ion channel superfamily that reconciles apparently conflicting experimental data.

Hodgkin and Huxley discovered that voltage-regulated ion flow underlies nerve conduction (1). Only decades later were voltage-sensing domains (VSDs) identified as controlling the activity of voltage-gated K⁺, Na⁺, and Ca²⁺ channels (2–4), shifting these proteins between activated and deactivated states in response to changes in transmembrane voltage (5–7). Different mechanistic models have been proposed to describe how conserved arginine and lysine gating-charge residues on a VSD transmembrane helix (S4) couple with the electric field to gate ion channel conduction (8–10). Some experiments suggest substantial S4 motion during gating (11), others far less (12). Also unresolved has been whether S4 moves through a largely static electric field or whether the VSD instead reshapes the field around S4 during gating. Even less clear has been how S4 triggers the attached channel pore domain to gate conduction. Finally, it has been unknown whether other motions, either subtle or large-scale, are involved in voltage gating (6, 13), largely because, unlike the open state, no crystal structure of a fully deactivated, closed-state voltage-gated channel exists.

To study the voltage-gated transition at the atomic level, we subjected the open conformation of the K_V1.2/K_V2.1 “paddle chimera” (10, 14) voltage-gated K⁺ channel to molecular dynamics (MD) simulations at both hyperpolarizing ($V < 0$ mV) and depolarizing ($V > 0$ mV) voltages over experimentally determined channel-gating time scales. Our all-atom system comprises the channel, either with (T1⁺) or without (T1[−]) the modulatory, but functionally nonessential cytoplasmic T1 domain (15, 16), in a symmetric, neutral phospholipid bilayer [omitting modulatory, negatively charged lipids (17)], hydrated with 0.5 M KCl (18). The simulations were performed using a special-purpose machine designed for high-speed MD simulations (19).

At depolarizing voltages, the channel exhibited steady outward conduction through a fully hydrated pore cavity (fig. S1); K⁺ current and H₂O/K⁺ permeation ratio (~1) broadly agree with experiment (20) and pore domain-only simulations (21). No noticeable conformational changes occurred, suggesting that the crystal structure (10) represents a fully activated, open state.

In marked contrast, at hyperpolarizing voltages the channel went from an open, inwardly conducting state to a closed, nonconducting state—the resting state. The channel exhibited a transient inward “tail” current, but conduction halted upon water leaving the hydrophobic pore cavity (dewetting) and concurrent pore closure (cavity collapse) at ~20 μs (Fig. 1A and fig. S1); the observed dewetting, as also seen in pore-only simulations (21), explains the osmotic sensitivity of the overall gating process (21, 22). Subsequent inward S4 translation and lateral loosening of the VSDs from the pore domain completed the transition over ~100 to 200 μs (Fig. 1A). Overall, the gating transition thus consists of the channel moving from a VSD-up, (VSD–pore apposed) conformation to a VSD-down (VSD–pore loosened) conformation (Fig. 1A, fig. S2, and movies S1 to S3). The T1⁺ resting state exhibited less VSD–pore separation than T1[−].

The activated-state VSDs delay channel closure by preventing pore hydrophobic collapse into the intrinsically more stable closed state (21, 23). The time at which pore closure occurred (determined by the pore cavity hydration level) and the tail current persistence time observed here—both ~20 μs—are in line with the 20 μs experimental tail current time constant [temperature-corrected *Shaker* data (18, 24) (see fig. S1 and table S1)]. This closure time is ~10 times as long as what we found in pore domain-only simulations (21), indicative of a VSD-imposed delay on the closure. A control simulation with a different water model (18) also exhibited dewetting, after ~30 μs, with little gating-charge transfer (fig. S4). The ~100 to 200 μs taken to complete the activated-to-resting transition—including full gating-charge displacement (Fig. 1)—compares well with the ~300 μs

observed experimentally for the slow off-gating component (25).

The S4 helix—bearing gating-charge residues R1 [neutral Gln in the chimera: R1(Q)], R2, R3, R4, and K5—is the main VSD moving part. S4 translated ~15 Å overall across the membrane in sequential steps while rotating ~120°, moving in a groove formed by the largely stationary S1 to S3a helices (Fig. 1, B and C, and movies S4 to S6). S3b, while more mobile than S1 to S3a, did not translate inward to a notable extent. R4—centrally located in the activated state at the point of strongest transmembrane electric field (Fig. 1, B and D, inset)—initiated gating-charge movement; Phe²³³, a central hydrophobic residue, separated the VSD extracellular and intracellular hydrated lumens throughout. R3 and R2 moved in turn, and inward S4 motion typically stopped when R1(Q) reached Phe²³³. These observations support a recent gating model that emphasizes sequential motion of S4 gating-charge residues past Phe²³³ (26).

As the gating-charge residues filed past Phe²³³, their side chains faced the aqueous VSD lumens, not the hydrophobic membrane or VSD core; transient salt bridges formed by the gating-charge residues with acidic residues on S1 and S2 and with lipid negatively charged phosphodiester groups facilitated the transition. Relative to the activated state, the resting state had fewer intra-VSD salt bridges but more S4-phosphate interactions (fig. S2). Our findings are consistent with VSD–phosphodiester group interactions being functionally critical, whereas anionic lipids are modulatory, perhaps by interacting with gating charges or the T1 domain (17, 27).

In line with experimental gating-charge values of 12 to 14 elementary charges (e) (28), the complete transition into the fully relaxed state—all four VSDs “down” with all the gating-charge residues (R2 to R4) inward of Phe²³³—yielded a calculated gating charge of $13.3 \pm 0.4 e$ (Fig. 1D and table S1). This VSD gating charge was solely accounted for by the ~15 Å translation of the S4 helices through an electric field, focused over ~15 Å, that we found to be similar in activated and resting VSD conformations (Fig. 1D and fig. S3). Our data indicate that limited motion of a single VSD (S4) toward the resting state suffices to close the pore. Charge displacements tied to early S4 motion—typically ~1 to 7 e with at least one R4 inward of Phe²³³ (table S1)—preceded pore closure, yet the pore always closed before all four VSDs were fully down. Experimentally, it is known that ~25% charge displacement suffices to close the channel (29).

Initial S4 inward motion disrupted the extracellular VSD–pore domain interface, resulting in domain separation: ~14 Å for T1[−] and ~5 Å for T1⁺, measured as the R1(Q)–Ala351 distance parallel to the membrane plane. VSD–pore separation contributed to a whole-protein root mean square deviation (RMSD) of >14 Å (C_α atoms, relative to the x-ray structure) for the T1[−] resting state and ~9 Å for that of T1⁺ (Fig. 1E); the linker between the T1 domain and the VSD—an

¹D. E. Shaw Research, New York, NY 10036, USA. ²Center for Computational Biology and Bioinformatics, Columbia University, New York, NY 10032, USA.

*To whom correspondence should be addressed. E-mail: morten.jensen@DEShawResearch.com (M.Ø.); david.shaw@DEShawResearch.com (D.E.S.)

additional constraint not present in $T1^-$ —serves to reduce $T1^+$ VSD mobility within the membrane plane (movies S5 and S6). By contrast, the tetrameric pore domain exhibited, relative to the open-state crystal structure, only a modest, ~ 3 Å RMSD increase, due to pore closure at ~ 20 to 30 μ s. Translation of S4 alone, or as the main moving part of the S3b to S4 paddle, resulted in large, >10 Å RMSDs for S4 relative to the mostly stationary S1 to S3a helices (RMSD <3 Å).

Additional simulations revealed the major steps of channel activation (simulations 10 to 14) (table S1). We studied the first step of the resting-to-activated transition by subjecting the computationally determined $T1^+$ resting state, obtained above (simulation 9), to depolarizing voltages. Experimentally, $T1^+$ channels activate faster than $T1^-$ deletion mutant channels (16), presumably due to restraint of VSD mobility by the T1 domain.

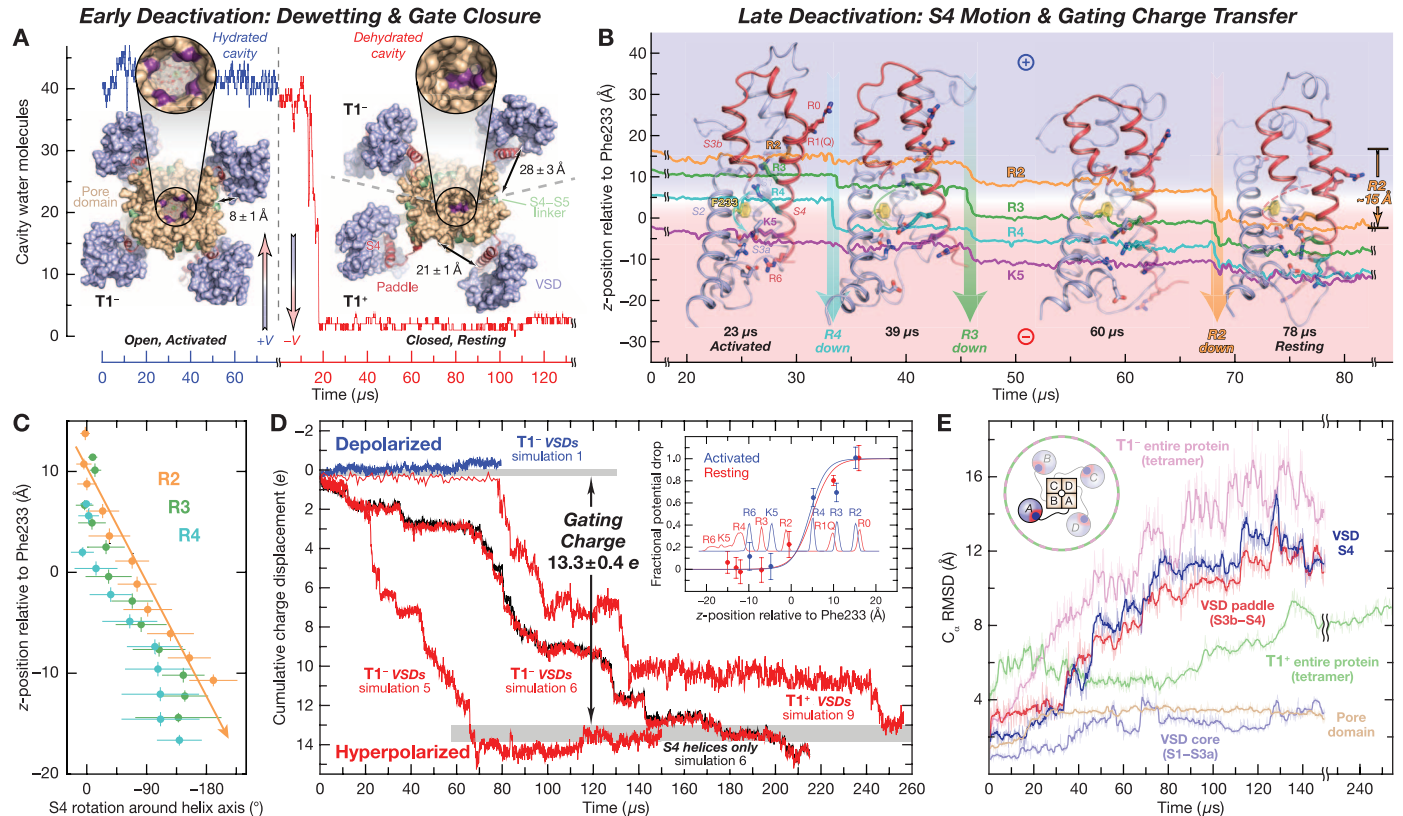
Upon depolarization, helix S4 immediately moved ~ 5 to 10 Å outward, transferring $\sim 50\%$ of the total gating charge in ~ 75 μ s (Fig. 2, A and B). Initially, gating-charge transfer is fast because most

salt bridges between S4 and the rest of the VSD are disrupted in the resting state; as S4 moved outward, these salt bridges began transiently to reform, leading to a gradual slowing of S4 motion and gating-charge transfer. As S4 movement neared completion, the VSDs reapproached the activated state, with RMSDs of ~ 3 Å and ~ 4 Å for S1 to S3a and S3b to S4 in the VSD returning closest to the crystal structure (Fig. 2A and movie S7). Experimentally, gating-charge transfer must be complete, in all four subunits, for the pore to open (8, 28). In line with these experimental observations, full S4 outward movement (and gating-charge transfer) in one or two VSDs was insufficient to open the pore in our simulations (table S1).

We simulated the second, and perhaps most enigmatic (6, 7, 13), activation step—the final cooperative transition (30, 31) to the open state—by starting from a computationally determined $T1^-$ configuration in which all VSDs, save one, were “up” (S4 helices fully outward, as in the activated state) but for which the pore remained fully or partially closed. [The partially closed pore

cavity contains ~ 20 water molecules (table S1, simulations 10 to 12, and fig. S4); the fully closed state resembles that observed in Na_vAb (32)]. These simulations, at depolarizing voltages, led to a fully activated and conducting state within a few tens of microseconds (Fig. 2, C to H).

Experiments have shown that a single, cooperative transition precedes conduction; this final transition, which contributes only $\sim 5\%$ of total gating charge, occurs after all VSDs have moved fully up (8). In our simulations, little or no additional gating-charge transfer occurred after the final outward motion of the S4 helix brought the S4-S5 linker into a tense conformation (table S1). This final motion perturbed the packing between the S4-S5 linker and the pore domain S6 helix, leading to packing fluctuations, as shown by the linker-S6 interaction energies (Fig. 2, F and G). This weakened and fluctuating packing enabled partial pore opening and rapid partial rehydration—water molecules reentered the pore cavity in less than 1 μ s—allowing subsequent K^+ entry and initial slow, outward conduction (Fig. 2, C to E).



The partially open, partially hydrated, and slowly conducting pore persisted for a few microseconds before reaching the fully conducting state (Fig. 2, C and E). The presence of ions in the cavity, which subsequently were driven outward through the selectivity filter (SF) by the depolarizing voltage, further increased pore rehydration (Fig. 2, C and D). As the hydrostatic pressure within the cavity thereby increased, the lower gate, at the pore Pro-Val-Pro (PVP) motif, fully opened, with the Leu³³¹ (S5) and Pro⁴⁰⁵ (S6) side chains interchanging positions (2I). This interchange caused S6 to kink at the PVP motif, widening the cavity and allowing it to finally become fully hydrated (Fig. 2C). Concurrent opening of the upper (hydrophobic) gate, at Ile⁴⁰² (Fig. 2H), enabled SF site S5 to become populated with K⁺, thus increasing the cavity ion occupancy by one (Fig. 2, D and E). K⁺ presence in S5 allowed

formation of the critical knock-on conduction mechanism intermediate [S5,(S4,S2)] (Fig. 2E) (2I), causing the channel to assume a fully conducting state (20.7 ± 2.7 pA) (Fig. 2, C and E). Early conduction occasionally slowed as Leu³³¹ and Pro⁴⁰⁵ transiently back-interchanged; after the final Leu³³¹/Pro⁴⁰⁵ interchange took place, however, S6 and the S4-S5 linker settled into a closely packed configuration that stabilized the open pore, and thus the activated, conducting state (Fig. 2, C, F, and G).

Interaction of the S4-S5 linker and helix S6 is central to gating. In K_V1.5, for instance, pairs of interacting linker and C-terminal S6 residues have been identified (33). Mapped onto K_V1.2, these interactions are between residues Ile³¹⁶ and Thr³²⁰ (linker) and Asn⁴¹², Phe⁴¹³, Phe⁴¹⁶, and Tyr⁴¹⁷ (S6). These pairs, and linker residue Ala³²³, all stand out in residue contact maps (Fig. 2G),

highlighting linker-S6 interaction as central to activation. Substitution of the K_V2.1 linker and S6 C terminus into K_V1.5, moreover, has been shown to confer K_V2.1 activation and deactivation kinetics to this K_V1.5 chimera, while preserving K_V1.5 voltage dependency (33). This and similar findings (34) suggest, in line with our results, that the linker and S6 C terminus together ultimately govern pore gating, irrespective of the details of the VSD structural machinery that moves up or down during voltage sensing.

We propose a mechanistic model for voltage gating (Fig. 3) that integrates our analysis of atomic-level observations of both the activated-to-resting-state transition and key steps of the resting-to-activated-state transition (table S1). Our model incorporates Hodgkin and Huxley's observations (I) that voltage-gated K⁺ channel opening requires the motion of four independent membrane-

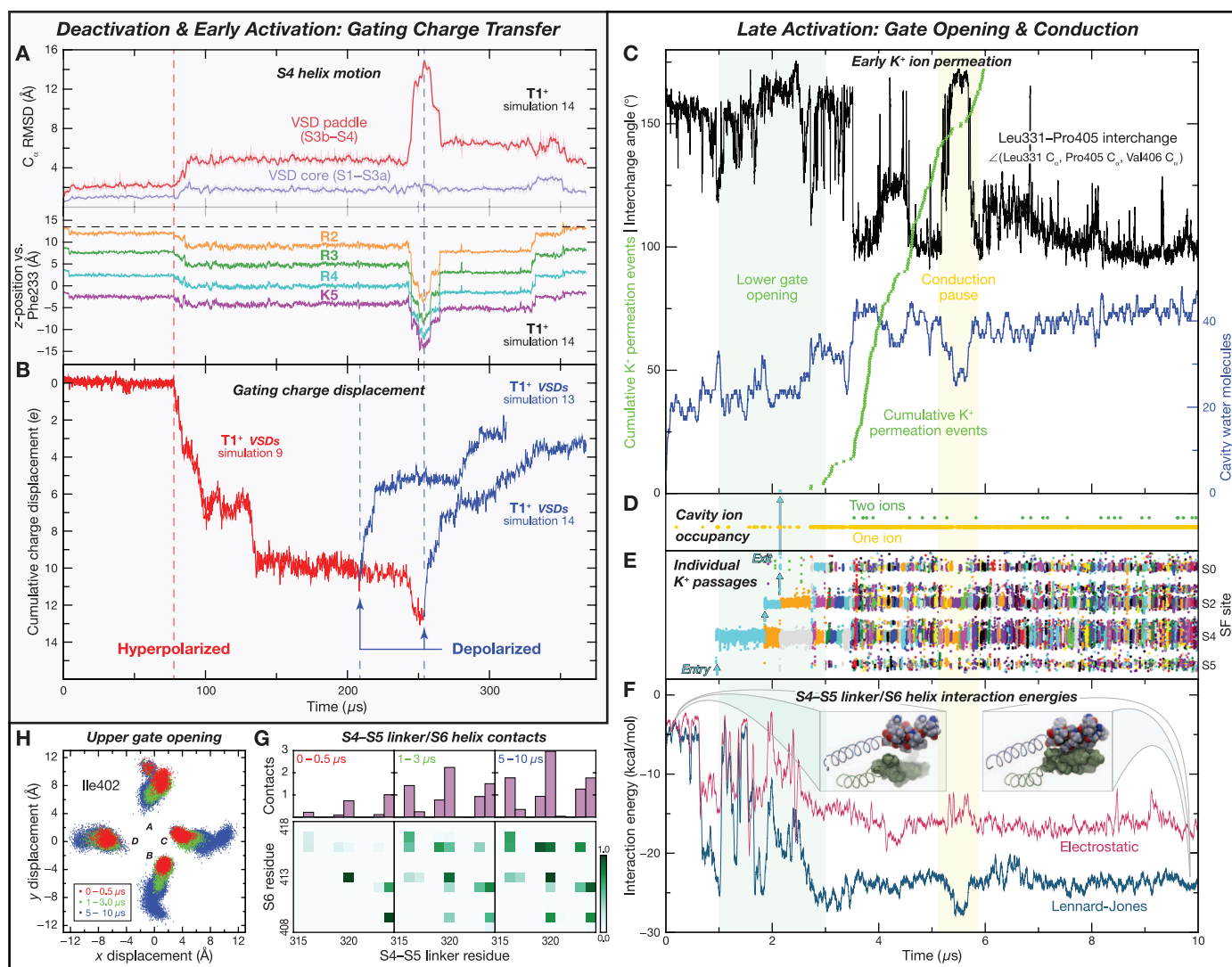


Fig. 2. Key steps of voltage-gated K⁺ channel activation. (A and B) Deactivation (red), then early activation (blue; first ~120 μ s). Paddle C _{α} RMSD relative to the initial structure, inward and outward S4 gating-charge residue movement, and total gating-charge transfer. (C to H) Late activation (final ~10 μ s, after essentially complete gating-charge transfer). (C) Pore cavity

rewetting, Leu³³¹ (S5)–Pro⁴⁰⁵ (S6) side-chain interchange, and cumulative outward K⁺ permeation events. (D and E) K⁺ population of pore cavity and SF. (F) S4-S5 linker/S6 helix interaction energies. (Insets) S5 and S6 (ribbons), S4-S5 linker (spheres), and S6 (surface) before and after repacking. (G) S4-S5 linker/S6 contacts. (H) Upper gate (Ile⁴⁰²/SF site S5) lateral opening.

bound charged particles, whereas channel closing requires the motion of only one.

Beginning with the activated state (Fig. 3, state 1), ion depletion, hydrophobic dewetting, and closure of the pore cavity, with concurrent early gating-charge inward movement, halt ionic conduction. Subsequent full VSD relaxation—inward S4 translation by ~ 15 Å relative to a largely rigid S1 to S3a VSD core coupled with $\sim 120^\circ$ S4 rotation that keeps the gating-charge residues pointed toward the VSD lumens, and lateral VSD-pore loosening due to VSD rotation and translation relative to the pore—permits the pore to remain closed (Fig. 3, state 4). Translation of S4 gating-charge residues accounts for the gating charge. Channel activation reverses these steps. The key difference is that all four VSDs must be up before the closed pore can reopen; a fully outward S4 perturbs the S4-S5 linker/S6 packing, thereby allowing water, and hence ion, reentry and subsequent conduction, stabilized by linker/S6 repacking.

Our observed gating mechanism and resting-state structure may help reconcile the many apparently conflicting measures of voltage-gated K^+ channel conformation. Given natural sequence variability in functionally critical regions (S3b-S4 paddle and the interacting S4-S5 linker and S6), certain details of gating likely vary between channels, including between wild-type $K_v1.2$ and the $K_v1.2/K_v2.1$ chimera that we used in our simulations. Yet, the fact that the S3b-S4 paddle can be swapped between channels to yield chimeras that retain voltage-gating function (35, 36) suggests that the key mechanistic aspects are broadly shared across the voltage-gated ion channel superfamily.

Our results suggest that channel opening and closing are energetically asymmetric processes. Because the intrinsically most stable state of the pore in isolation is dewetted and closed (21, 23), due to the hydrophobic lining of the pore cavity (21), S4 need not actively push the S4-S5 linker down to close the pore. Channel activation does, however, require depolarization-driven work—the forcing of S4 back across the membrane—to ultimately pull the S4-S5 linker tight, which perturbs its interaction with S6, leading to pore opening. Only when all gating-charge residues and S4-S5 linkers are fully up does the closed pore become sufficiently destabilized that fluctuations of the lower gate, through perturbed linker-S6 packing, allow partial and then—as the last conformational transition during activation—complete cavity rewetting (Figs. 2 and 3). The S4-S5 linker is tense in the activated state but relaxed in the resting state, perhaps explaining conservation of linker length: A shorter linker would inhibit channel closing, because S4 could not translate inward far enough, and a longer linker would inhibit opening, because even full S4 outward translation could not lead to an effective pull on the pore through the linker.

Our atomic-level computational determination of a resting-state conformation may be useful in guiding the development of drugs to treat those

human channelopathies associated with the resting state (37). VSDs normally are impermeable to ions, but certain inherited S4 gating-charge mutations permit abnormal cation conduction through resting state omega pores (38), leading to, for example, cardiac long-QT syndromes, various

paralyses, and migraine (37, 39, 40). VSD residues accessible from the intracellular and extracellular sides (41, 42) and residues thought to line the omega pore (43) map well onto our resting-state conformation (Fig. 4A). This resting-state VSD should thus exhibit omega currents, once an

Fig. 3. Mechanistic model for voltage gating. Subjecting the activated state (1) to hyperpolarizing voltage initiates S4 inward movement and VSD-pore loosening. Ion depletion of the pore cavity (2)—coupled to inward motion of a single S4—leads to pore hydrophobic collapse. Closure of upper (Ile⁴⁰² in $K_v1.2$) and lower gates [PVP motif; Leu³³¹ (S5)—Pro⁴⁰⁵ (S6) side-chain interchange (21)] halts conduction (3). S4 continues inward; as S4 completes its inward motion, the S4-S5 linker helix moves fully down and the VSDs loosen from the pore, consolidating the resting state (4). Subjecting the resting state to depolarizing voltage drives S4 outward. When all four S4 and S4-S5 linker helices are fully up (5) and all VSDs repack against the pore, the lower gate becomes destabilized; the 4 → 5 transition constitutes the rate-limiting step in the activation process. Lower gate fluctuation triggers pore opening and partial pore rehydration (water molecules cooperatively enter the cavity) that allow ion entry and initial outward conduction (6); the 5 → 6 transition is essentially voltage-independent. The presence of ions drives complete pore rehydration that pushes fully open the upper and lower gates, returning the channel to the activated state (1). The lateral position of the VSDs (circles) relative to the pore domain (squares) is shown schematically (extracellular view).

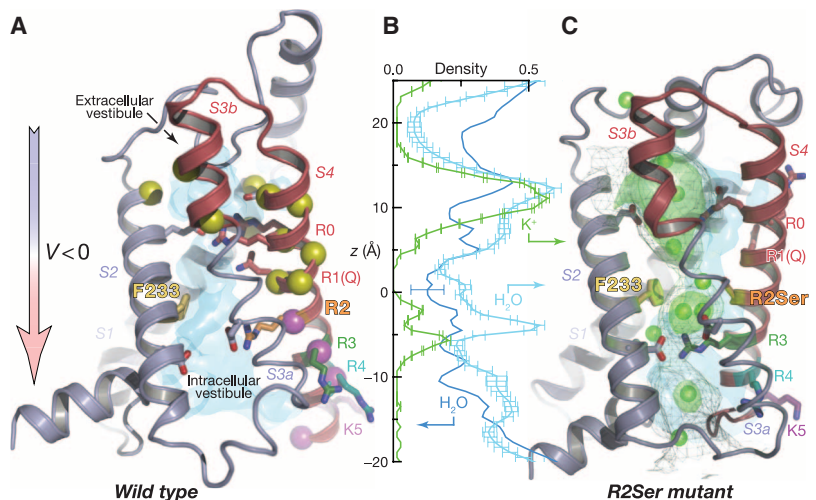
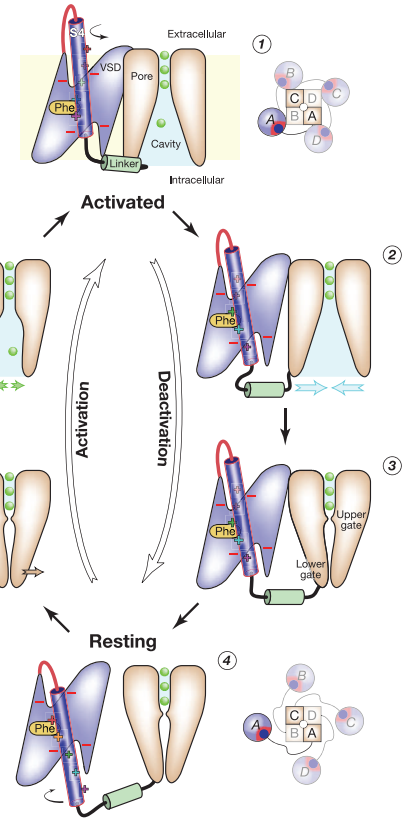


Fig. 4. The omega pore. (A and C) Resting-state conformations of chimera and R2Ser mutant VSDs. Spheres in (A) mark residues accessible to chemical modification from the extracellular (yellow) and intracellular (purple) sides in the resting state (42), consistent with ~ 15 Å S4 inward motion (Fig. 2A). (B) Water and K^+ (R2Ser) densities (arbitrary units). The R2Ser mutation increases hydration at Phe²³³ by $\sim 50\%$, facilitating K^+ permeation. The ion permeation pathway (the omega pore) in the R2Ser mutant is shown as a gray mesh in (C). The green surface and spheres indicate predominant K^+ sites and actual positions from a single permeation event; the blue surfaces represent VSD hydration.

S4 gating-charge residue is appropriately mutated to a smaller, polar, uncharged residue (37, 44, 45). Such mutation of *Shaker* R1 to histidine or serine permits H^+ or alkali cation and guanidium currents (38, 46).

We introduced an R2Ser mutation (37) into the resting-state conformation (R2 to R4 down) (18, 38). The mutant VSD exhibited significant inward K^+ current (no Cl^- current) (movie S8, table S2, and fig. S5). This current arises because apposition of Phe²³³ with the mutated residue, which lacks the large, positive guanidinium group of the gating-charge residues, leads to increased hydration of the VSD hydrophobic constriction and thereby permits permeation of cations (Fig. 4, B and C). Depolarization halted the current and transferred $\sim 2 e$ of gating charge (table S2).

The transition into the resting state, as well as the conformation of the state itself, demonstrates that the VSD omega and gating-permeation pathways are one and the same. Mutation of gating-charge residues enables pathological cation leaks through the VSD along the identical pathway taken by the physiological gating-charge guanidinium groups. We thus provide a structural explanation for hyperpolarization-induced (as well as depolarization-induced) cationic leak currents associated with channelopathies in certain human voltage-gated ion channels.

References and Notes

1. A. L. Hodgkin, A. F. Huxley, *J. Physiol.* **117**, 500 (1952).
2. M. Noda et al., *Nature* **312**, 121 (1984).
3. B. L. Tempel, D. M. Papazian, T. L. Schwarz, Y. N. Jan, L. Y. Jan, *Science* **237**, 770 (1987).
4. R. D. Nelson, G. Kuan, M. H. Saier Jr., M. Montal, *J. Mol. Microbiol. Biotechnol.* **1**, 281 (1999).

5. F. Bezanilla, *Physiol. Rev.* **80**, 555 (2000).
6. K. J. Swartz, *Nature* **456**, 891 (2008).
7. F. J. Sigworth, *Nature* **423**, 21 (2003).
8. N. E. Schoppa, K. McCormack, M. A. Tanouye, F. J. Sigworth, *Science* **255**, 1712 (1992).
9. S. K. Aggarwal, R. MacKinnon, *Neuron* **16**, 1169 (1996).
10. S. B. Long, X. Tao, E. B. Campbell, R. MacKinnon, *Nature* **450**, 376 (2007).
11. V. Ruta, J. Chen, R. MacKinnon, *Cell* **123**, 463 (2005).
12. M. M. Pathak et al., *Neuron* **56**, 124 (2007).
13. W. A. Catterall, *Neuron* **67**, 915 (2010).
14. X. Tao, R. MacKinnon, *J. Mol. Biol.* **382**, 24 (2008).
15. A. M. VanDongen, G. C. Frech, J. A. Drew, R. H. Joho, A. M. Brown, *Neuron* **5**, 433 (1990).
16. W. R. Kobertz, C. Miller, *Nat. Struct. Biol.* **6**, 1122 (1999).
17. D. Schmidt, Q. X. Jiang, R. MacKinnon, *Nature* **444**, 775 (2006).
18. Materials and methods are available as supplementary materials on Science Online.
19. D. E. Shaw et al., *Proc. Conf. High Performance Computing, Networking, Storage and Analysis (SC09)* (ACM Press, New York, 2009).
20. H. Ando, M. Kuno, H. Shimizu, I. Muramatsu, S. Oiki, *J. Gen. Physiol.* **126**, 529 (2005).
21. M. Ø. Jensen et al., *Proc. Natl. Acad. Sci. U.S.A.* **107**, 5833 (2010).
22. J. Zimmerberg, F. Bezanilla, V. A. Parsegian, *Biophys. J.* **57**, 1049 (1990).
23. O. Yifrach, R. MacKinnon, *Cell* **111**, 231 (2002).
24. B. M. Rodríguez, F. Bezanilla, *Neuropharmacology* **35**, 775 (1996).
25. B. M. Rodríguez, D. Sigg, F. Bezanilla, *J. Gen. Physiol.* **112**, 223 (1998).
26. X. Tao, A. Lee, W. Limapichat, D. A. Dougherty, R. MacKinnon, *Science* **328**, 67 (2010).
27. Y. Xu, Y. Ramu, Z. Lu, *Nature* **451**, 826 (2008).
28. L. D. Islas, F. J. Sigworth, *J. Gen. Physiol.* **114**, 723 (1999).
29. A. Loboda, C. M. Armstrong, *Biophys. J.* **81**, 905 (2001).
30. N. E. Schoppa, F. J. Sigworth, *J. Gen. Physiol.* **111**, 313 (1998).
31. J. L. Ledwell, R. W. Aldrich, *J. Gen. Physiol.* **113**, 389 (1999).
32. J. Payandeh, T. Scheuer, N. Zheng, W. A. Catterall, *Nature* **475**, 353 (2011).
33. A. J. Labro et al., *J. Gen. Physiol.* **132**, 667 (2008).
34. K. McCormack et al., *Proc. Natl. Acad. Sci. U.S.A.* **88**, 2931 (1991).
35. A. A. Alabi, M. I. Bahamonde, H. J. Jung, J. I. Kim, K. J. Swartz, *Nature* **450**, 370 (2007).
36. F. Bosmans, M. F. Martin-Eauclaire, K. J. Swartz, *Nature* **456**, 202 (2008).
37. S. Sokolov, T. Scheuer, W. A. Catterall, *Nature* **446**, 76 (2007).
38. F. Tombola, M. M. Pathak, E. Y. Isacoff, *Neuron* **45**, 379 (2005).
39. S. Sokolov, T. Scheuer, W. A. Catterall, *Neuron* **47**, 183 (2005).
40. S. C. Cannon, *J. Physiol.* **588**, 1887 (2010).
41. A. Banerjee, R. MacKinnon, *J. Mol. Biol.* **381**, 569 (2008).
42. H. P. Larsson, O. S. Baker, D. S. Dhillon, E. Y. Isacoff, *Neuron* **16**, 387 (1996).
43. F. Tombola, M. M. Pathak, P. Gorostiza, E. Y. Isacoff, *Nature* **445**, 546 (2007).
44. L. Delemotte, W. Treptow, M. L. Klein, M. Tarek, *Biophys. J.* **99**, L72 (2010).
45. F. Khalili-Araghi, E. Tajkhorshid, B. Roux, K. Schulten, *Biophys. J.* **102**, 258 (2012).
46. D. M. Starace, F. Bezanilla, *Nature* **427**, 548 (2004).
47. M. Lainé et al., *Neuron* **39**, 467 (2003).
48. K. H. Hong, C. Miller, *J. Gen. Physiol.* **115**, 51 (2000).
49. F. V. Campos, B. Chanda, B. Roux, F. Bezanilla, *Proc. Natl. Acad. Sci. U.S.A.* **104**, 7904 (2007).

Acknowledgments: We thank R. MacKinnon for useful discussions; K. Lindorff-Larsen, S. Piana, and K. Palmo for their help with force-field modifications; A. Philippsen and J. Gullingsrud for creating the animations; E. Chow, K. Mackenzie, and D. Scarpazza for developing simulation software; and R. Kastleman and M. Kirk for editorial assistance.

Supplementary Materials

www.sciencemag.org/cgi/content/full/336/6078/229/DC1
Materials and Methods
Figs. S1 to S5
Tables S1 to S4
References (50–66)
Movies S1 to S8

31 January 2011; accepted 29 February 2012
10.1126/science.1216533

Ribosome Profiling Shows That miR-430 Reduces Translation Before Causing mRNA Decay in Zebrafish

Ariel A. Bazzini,^{1*} Miler T. Lee,^{1*} Antonio J. Giraldez^{1,2†}

MicroRNAs regulate gene expression through deadenylation, repression, and messenger RNA (mRNA) decay. However, the contribution of each mechanism in non-steady-state situations remains unclear. We monitored the impact of miR-430 on ribosome occupancy of endogenous mRNAs in wild-type and *dicer* mutant zebrafish embryos and found that miR-430 reduces the number of ribosomes on target mRNAs before causing mRNA decay. Translational repression occurs before complete deadenylation, and disrupting deadenylation with use of an internal polyadenylate tail did not block target repression. Lastly, we observed that ribosome density along the length of the message remains constant, suggesting that translational repression occurs by reducing the rate of initiation rather than affecting elongation or causing ribosomal drop-off. These results show that miR-430 regulates translation initiation before inducing mRNA decay during zebrafish development.

MicroRNAs (miRNAs) control multiple processes, including development, physiology, and disease. These ~22-nucleotide (nt) RNAs regulate gene expression through translational repression and mRNA de-

adenylation and decay. The contribution and timing of these effects remain unclear (1, 2). Although some studies show translational repression without mRNA decay (3–7), others point to decay as a primary effect (8–11). Ribosome-

profiling experiments, which quantify the number of ribosomes bound to a message (12), and polysome profiling (13) have suggested that the main effect of miRNAs is to accelerate decay, with only a minor (8) or moderate (13) contribution from translational repression. This disparity may stem from the steady-state conditions used to assess the molecular effects of miRNAs, resulting in insufficient temporal resolution to identify the first step in miRNA-mediated repression (2).

To dissect the temporal effects of miRNA-mediated regulation and to distinguish between translational repression and mRNA decay, we have analyzed the ribosome profiles and RNA levels of endogenous messages in zebrafish embryos (fig. S1) (14). At the onset of zygotic transcription, zebrafish express a predominant miRNA (miR-430) that facilitates clearance of maternal mRNAs (15, 16) (Fig. 1, A and B). By comparing the ribosome profile of wild-type embryos

¹Department of Genetics, Yale University School of Medicine, New Haven, CT 06510, USA. ²Yale Stem Cell Center, Yale University School of Medicine, New Haven, CT 06520, USA.

*These authors contributed equally to this work.

†To whom correspondence should be addressed. E-mail: antonio.giraldez@yale.edu

with maternal and zygotic *dicer* mutants (*MZdicer*) before [2 hours postfertilization (hpf)] and after (4 and 6 hpf) miR-430 expression (fig. S1), we can analyze the dynamics of translational repression and mRNA decay in vivo. We sequenced 54 million reads generated by ribosome profiling, which predominately map to ribosomes, tRNAs, and coding sequences (CDS) compared with untranslated regions (UTRs), and 59 million reads generated by polyadenylated [poly(A)⁺] selection (input RNA), which map equally to CDS and UTRs (Fig. 1C, table S1, and figs. S1 and S2). We focused our analysis on 4476 genes that are present and translated at 2 hpf before miR-430 is expressed (≥ 15 reads per kilobase, per million reads, RPKM) (fig. S2).

We reasoned that, if mRNA decay is the main effect of miR-430 on their targets, a reduction in ribosome-protected fragments (RPFs) should parallel the loss of input reads. Alternatively, if translation repression precedes decay, RPF loss should precede loss of input (fig. S1). Before miR-430 is expressed (2 hpf), we found no significant reduction of either RPFs or mRNA in wild-type compared to *MZdicer* embryos for known miR-430

targets (15) or nontargets (Figs. 1D and 2A). At 4 hpf, once miR-430 is expressed, we observed a significant decrease in RPF number for miR-430 targets in wild type compared with *MZdicer* ($P = 1.3 \times 10^{-24}$, Wilcoxon rank-sum test), without a corresponding decrease in mRNA (Figs. 1E and 2A). Thus, translation repression by miR-430 is occurring independent of RNA decay. However, at 6 hpf, we observed a significant reduction in the number of RPFs that coincided with a reduction in input reads ($P < 1 \times 10^{-43}$), suggesting that, by 6 hpf, miR-430 targets have undergone mRNA decay with a mild contribution from additional translational repression (Figs. 1F and 2A). These results show that, for targets experimentally identified by their miR-430-dependent decay (15), translation repression occurs before the decay.

To determine the predominant effect of miR-430-mediated regulation independent of these experimentally identified targets, we asked whether translational repression or mRNA decay is (i) more associated with miRNA target sites and (ii) better correlated with miRNA seed strength. First, we found that miR-430 target sites are enriched in both transcripts with lower RPF at

4 hpf ($P = 1.6 \times 10^{-19}$ for septamers, Fisher's exact test) and transcripts with lower input at 6 hpf ($P = 8.9 \times 10^{-41}$) in wild type compared with *MZdicer*, but not those with lower input at 4 hpf ($P > 0.33$) (figs. S3 and S4). Second, when we identified all putative miR-430 targets that contain 3'UTR and CDS seed matches, the level of regulation followed the order of seed strength (multiple sites > octamer > septamer > hexamer) for both translational repression at 4 hpf ($P = 1.2 \times 10^{-6}$, Kruskal-Wallis) and mRNA decay at 6 hpf ($P = 2.0 \times 10^{-10}$) (Fig. 2, B and C, and figs. S5 and S6). Further analysis confirmed that targets that are first translationally repressed predominantly coincide with those that undergo mRNA decay later, suggesting that most targets undergo both regulatory effects (Fig. 3A). These mRNAs correspond to the most strongly regulated targets ($P = 5.0 \times 10^{-10}$, Kruskal-Wallis) (Fig. 3B), are the most significantly enriched for miR-430 target sites ($P < 2.2 \times 10^{-16}$, χ^2 test, 4 df) (Fig. 3C), and are correlated with various 3'UTR sequence characteristics (fig. S8).

It has been postulated that loss of the poly(A) tail may be the underlying cause of miRNA-

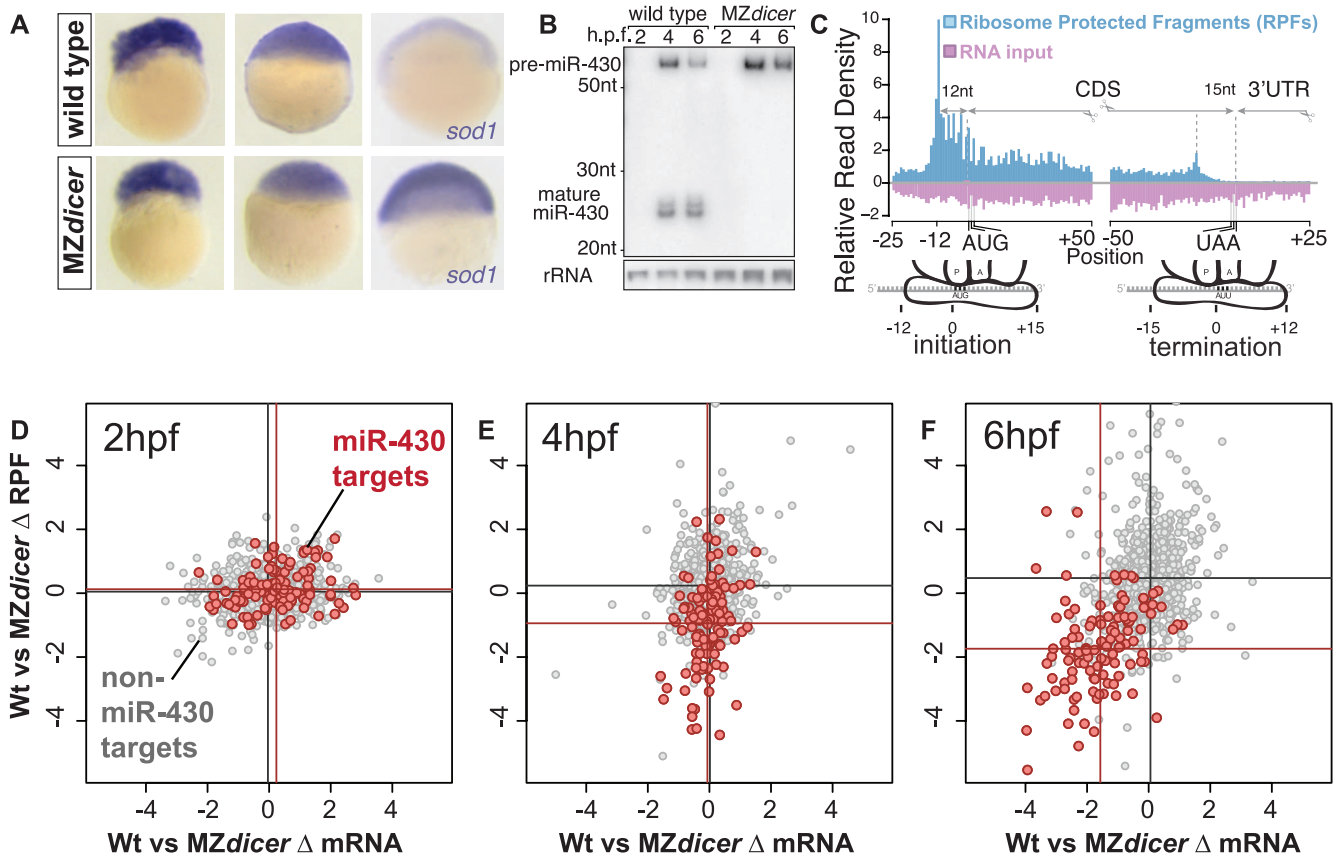


Fig. 1. Temporal analysis of miR-430-mediated translational repression in zebrafish. (A) In situ hybridization (purple) for the miR-430 target gene *sod1* in wild-type and *MZdicer* embryos at 2, 4, and 6 hpf. Decay of the target is observed at 6 hpf in a miRNA-dependent manner. (B) Northern blot showing miR-430 expression in wild type and *MZdicer*. (C) RPF and input reads mapped to a composite transcript. RPFs mainly map to the CDS. Input reads map to both the UTRs and CDS. (D to F) Biplots show \log_2 -fold RPKM

differences of RPFs (y axis) and mRNA (x axis) between wild type and *MZdicer* at 2 (D), 4 (E), and 6 (F) hpf. Known miR-430 targets are in red (15), nontargets lacking miR-430 seeds in gray. Mean values per group are indicated as lines. Mean difference between targets and nontargets are as follows: (E) RPF 2.26-fold, $P = 1.3 \times 10^{-24}$; RNA, 1.05-fold, $P = 0.12$; (F) RPF 4.6-fold, $P = 1.5 \times 10^{-44}$; RNA 3.1-fold, $P = 8.1 \times 10^{-44}$, by two-sided Wilcoxon rank sum test.

mediated repression (1, 2, 15, 17, 18). Because the input was poly(A)⁺-selected, lower mRNA levels for miR-430 targets at 6 hpf could arise from mRNA deadenylation or decay (14) (fig S3). Conversely, the similar mRNA levels at 4 hpf between wild type and MZ*dicer* suggest that full deadenylation has not occurred by the onset of translational repression. To analyze the dynamics of deadenylation of individual endogenous mRNAs, we first combined poly(A) tail analysis with high-resolution gel electrophoresis (Fig. 4A and fig. S9). We found that the endogenous miR-430 target *rhotein2* (repressed ~80% in wild type) is fully deadenylated by 6 hpf but is still polyadenylated at 4 hpf in wild type and MZ*dicer* (albeit

slightly shorter in wild-type embryos). There was no difference in poly(A) tail length at 2 hpf, before miR-430 is expressed, nor for a nontarget between wild type and MZ*dicer* (Fig. 4B and fig. S10). Second, when we analyzed *adipor1a*, which undergoes translational repression at 4 and 6 hpf without decay, we found no apparent deadenylation by 6 hpf (fig. S10). Although these results indicate that loss of RPFs occur before complete deadenylation, they cannot exclude that initial deadenylation might be responsible for the translational repression observed. Next, to determine whether repression requires deadenylation, we disrupted deadenylation of a green fluorescent protein (GFP)-zgc:63829-3'UTR reporter mRNA by

using an internal poly(A) tail followed by 10C (A₉₈C₁₀) (19, 20) and compared repression of this reporter with one containing a polyadenylation signal (Fig. 4, C and D). We observed repression of both reporters compared with versions where the miR-430 site was mutated GCACTT to GGTCTT, even when deadenylation was reduced (Fig. 4C). These results indicate that translational repression by miR-430 observed at 4 hpf occurs before and independently of complete deadenylation.

miRNAs have been proposed to influence protein translation by either reducing the rate of translation initiation, reducing elongation, or accelerating ribosome drop-off (1, 2, 18). Ribosome

Fig. 2. miR-430 induces translation repression before RNA decay. (A) Cumulative distributions of mRNA, RPF, and translation efficiency differences (Δ) between wild type and MZ*dicer* for known miR-430 targets (red), all genes with 3'UTR miR-430 seed sites (blue), and nontargets (gray), with number of genes in parentheses. *P* values for rank-sum tests are shown for nontargets versus known targets (red) and versus all predicted targets (blue). (B and C) Cumulative distribution plots with predicted targets separated by seed type as indicated.

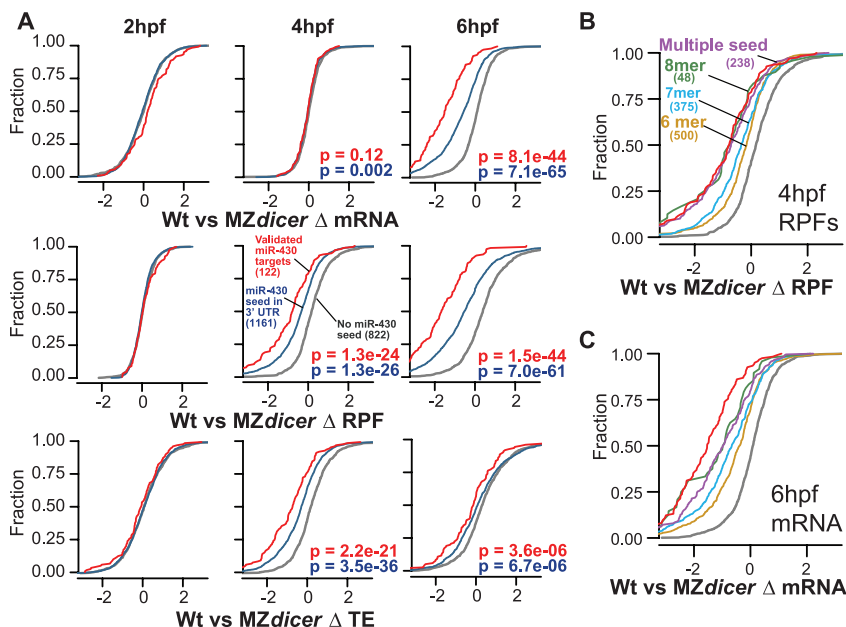
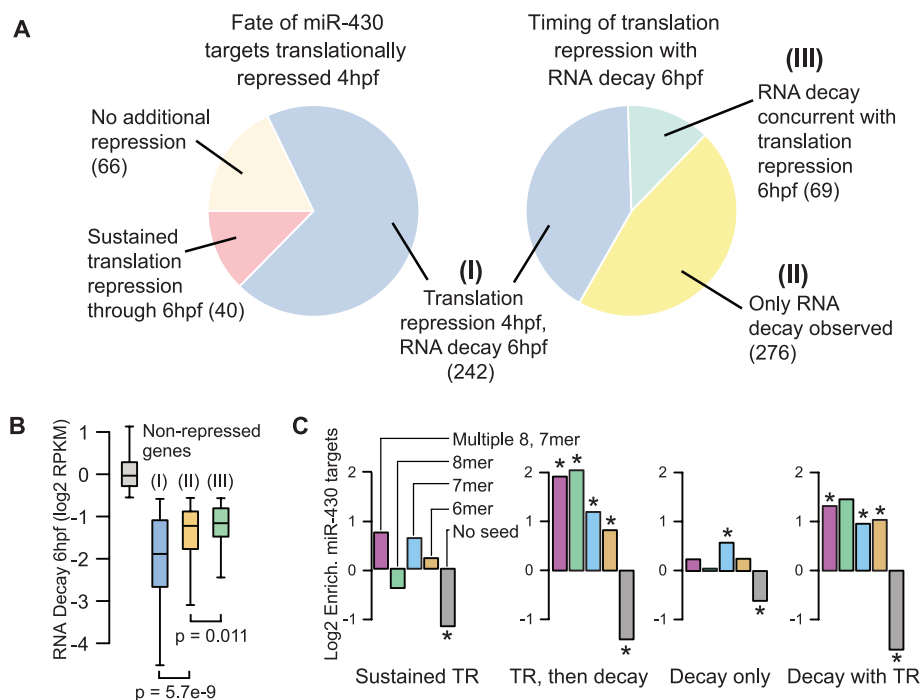


Fig. 3. miR-430 induces translation repression followed by RNA decay. (A) Pie charts of different repression categories (cutoffs defined in fig. S7). Seventy percent of the targets translationally repressed at 4 hpf go on to be deadenylated or degraded at 6 hpf (group I). Among transcripts decayed at 6 hpf, 41% were translationally repressed at 4 hpf (I), 47% were not observed to be translationally repressed (II), and the remainder experienced concurrent translation repression at 6 hpf not explained by the decay (III). (B) Box and whisker plot showing that the level of RNA decay at 6 hpf is highest among genes that are translationally repressed early. (C) The different modes of translation repression (TR) induce significant enrichment in miR-430 target seeds ($*P < 0.05$, Fisher's exact test). See table S2 for counts.



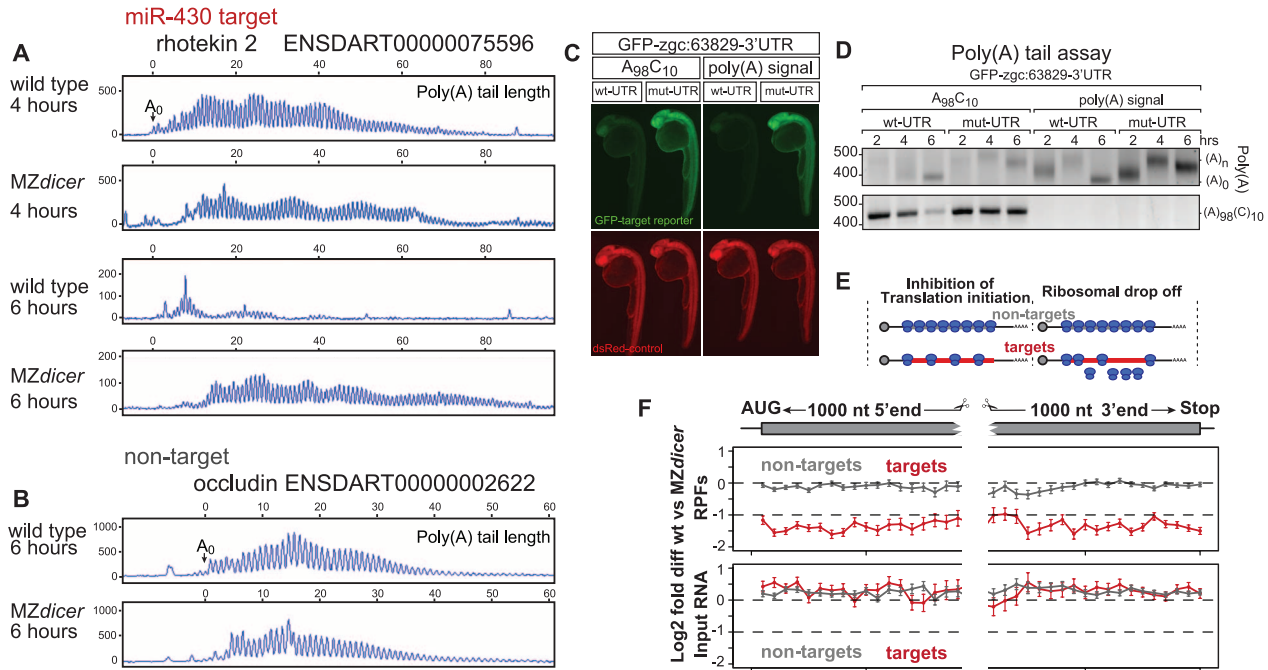


Fig. 4. Poly(A) length and ribosome distribution. **(A and B)** Single nucleotide resolution electrophoresis for poly(A) length for a target **(A)** and nontarget **(B)** in wild type and *MZdicer* (14). A_0 represents the polyadenylation site confirmed by DNA sequencing (fig. S9). **(C)** GFP expression (green) from an injected miR-430 reporter mRNA containing the 3'UTR for *zgc:63829* with wild-type (wt-UTR) or mutated (mut-UTR) miR-430 sites. The 3'UTRs are followed by an internal poly(A) tail (A_{98C10}) or a polyadenylation signal. Expression of a co-injected dsRed control mRNA is shown in red. Note the repression of the wild-type reporter compared to the mutant reporter when an internal poly(A) tail is used. **(D)** Gel electrophoresis of a PCR to determine the length of the poly(A) tail (ending in A, top) and A_{98C10} (bottom). Note the polyadenylation by 2 hpf

and deadenylation by 6 hpf, but deadenylation of the mRNA with the internal poly(A) tail (A_{98C10}) is delayed. Deadenylated product size is shown (A_0). **(E)** Two models for translational repression are shown: reducing translation initiation (left) or causing ribosome drop-off and slower elongation rate (right). **(F)** Plot showing relative RPF read density (top) and mRNA density (bottom) along the length of miR-430 targets (red) undergoing >1.5-fold translation repression at 4 hpf and those for nontargets (gray). Points show mean \pm SEM \log_2 -fold differences between wild-type and *MZdicer* expression in 50-nt bins spanning the first and last 1000 nts of the genes (13). Bins represent $41 \geq N \geq 277$ genes for targets, $107 \geq N \geq 906$ genes for nontargets. Bin values do not significantly differ ($P = 0.53$, Friedman rank sum test).

profiling allows us to quantify ribosome position by examining the RPF distribution along the length of the message. If miR-430 functions primarily by reducing translation initiation, then we would expect lower ribosome occupancy but uniform density along repressed messages. In contrast, if miR-430 causes ribosomal drop-off or reduced translation elongation with the same initiation rate, we would expect a graded distribution of ribosomes, with fewer RPFs in the 3' end than the 5' end (Fig. 4E). When we aggregated the reads of miR-430 targets translationally repressed at 4 hpf, we found uniform loss of RPF density along the length of the target mRNAs, suggesting that miR-430 inhibits translation initiation (Fig. 4F).

We show that miR-430 first induces translational repression by reducing the rate of translation initiation and then induces mRNA decay through deadenylation (fig. S11). Our results reconcile observations in vitro (6, 7, 21–23), which typically used short time courses and observed repression before deadenylation, with observations in vivo (8–11, 24), which are carried out over longer time scales after perturbing miRNA function, where the strongest effect appears to be deadenylation and decay. Most of the miR-430-regulated genes undergo translational repression followed by decay. A small group of targets appear

to be primarily regulated only at the level of translation; however, because of the limited number of time points analyzed, it is possible that those targets could undergo decay at later time points (15).

Previously, several laboratories, including ours, identified deadenylation as a main effect of miRNA-mediated regulation (15, 17, 24, 25), leading to our initial hypothesis that complete deadenylation (at 6 hpf) disrupts the interaction between the poly(A)-binding protein and the cap through eukaryotic translation initiation factor 4 γ , thus reducing translation of the message (15, 18). Although it is clear that deadenylation contributes to the rate of decay and overall level of repression, our findings show that, in the case of miR-430, initial repression can occur before complete deadenylation and that reducing deadenylation does not block translational repression. These data align with the observation that miRNAs can induce repression in transcripts that lack a poly(A) but include instead a histone tail or a self-cleaving ribozyme (17, 24). Recent studies have reported that the CCR4-NOT complex is recruited by GW182/TNRC6 to target mRNAs (26–28) and can repress translation independent of its deadenylase activity (26–29). Furthermore, it appears that GW182 has two distinct domains that are independently required to elicit repres-

sion and deadenylation (19, 20). These results suggest that repression can occur independent of deadenylation in vivo and that miRNAs trigger these two mechanisms in parallel to ensure maximum target mRNA repression and decay. Yet, the degree by which each mechanism regulates different genes may vary depending on the 3'UTR context [as shown in *Caenorhabditis elegans* (30)], the miRNA, or even the cell type.

References and Notes

1. M. R. Fabian, N. Sonenberg, W. Filipowicz, *Annu. Rev. Biochem.* **79**, 351 (2010).
2. S. Djuranovic, A. Nahvi, R. Green, *Science* **331**, 550 (2011).
3. R. S. Pillai *et al.*, *Science* **309**, 1573 (2005).
4. P. H. Olsen, V. Ambros, *Dev. Biol.* **216**, 671 (1999).
5. R. C. Lee, R. L. Feinbaum, V. Ambros, *Cell* **75**, 843 (1993).
6. G. Mathonnet *et al.*, *Science* **317**, 1764 (2007).
7. R. Thermann, M. W. Hentze, *Nature* **447**, 875 (2007).
8. H. Guo, N. T. Ingolia, J. S. Weissman, D. P. Bartel, *Nature* **466**, 835 (2010).
9. D. Baek *et al.*, *Nature* **455**, 64 (2008).
10. L. P. Lim *et al.*, *Nature* **433**, 769 (2005).
11. S. Bagga *et al.*, *Cell* **122**, 553 (2005).
12. N. T. Ingolia, S. Ghaemmaghami, J. R. Newman, J. S. Weissman, *Science* **324**, 218 (2009).
13. D. G. Hendrickson *et al.*, *PLoS Biol.* **7**, e1000238 (2009).
14. See supporting material on Science Online.
15. A. J. Giraldez *et al.*, *Science* **312**, 75 (2006).
16. A. J. Giraldez *et al.*, *Science* **308**, 833 (2005).

17. L. Wu, J. Fan, J. G. Belasco, *Proc. Natl. Acad. Sci. U.S.A.* **103**, 4034 (2006).
18. E. Huntzinger, E. Izaurralde, *Nat. Rev. Genet.* **12**, 99 (2011).
19. T. Fukaya, Y. Tomari, *EMBO J.* **30**, 4998 (2011).
20. Y. Mishima *et al.*, *Proc. Natl. Acad. Sci. U.S.A.* **109**, 1104 (2012).
21. M. R. Fabian *et al.*, *Mol. Cell* **35**, 868 (2009).
22. M. R. Fabian, Y. V. Svitkin, N. Sonenberg, *Methods Mol. Biol.* **725**, 207 (2011).
23. A. Zdanowicz *et al.*, *Mol. Cell* **35**, 881 (2009).
24. A. Eulalio *et al.*, *RNA* **15**, 21 (2009).
25. T. H. Beilharz *et al.*, *PLoS ONE* **4**, e6783 (2009).
26. M. Chekulaeva *et al.*, *Nat. Struct. Mol. Biol.* **18**, 1218 (2011).
27. M. R. Fabian *et al.*, *Nat. Struct. Mol. Biol.* **18**, 1211 (2011).
28. J. E. Braun, E. Huntzinger, M. Fauser, E. Izaurralde, *Mol. Cell* **44**, 120 (2011).
29. A. Cooke, A. Prigge, M. Wickens, *J. Biol. Chem.* **285**, 28506 (2010).
30. E. Wu *et al.*, *Mol. Cell* **40**, 558 (2010).

Acknowledgments: We thank S. Wolin and the Wolin laboratory for vital intellectual and technical support and access to equipment and reagents; N. Ignolia, J. Weissman, D. Schoenberg, D. Patil, A. Staton, C. Takacs, and Y. Mishima for reagents and discussions; and S. Baserga, D. Cazalla, D. Cifuentes, and S. Moxon for discussions. Supported by the Pew Fellows Program in Biomedical Sciences (A.A.B.), the Pew Scholars Program in the Biomedical Sciences, the Yale Scholar Program, and NIH grants R01GM081602-05 (A.J.G.). Contributions: A.A.B. and A.J.G. designed the project. A.A.B. performed the experiments. A.A.B. and M.T.L. performed

data analysis. A.A.B., M.T.L., and A.J.G. interpreted the data and wrote the manuscript. Sequencing data are deposited in the Gene Expression Omnibus (GEO) database with accession number GSE34743.

Supporting Online Material

www.sciencemag.org/cgi/content/full/science.1215704/DC1
Materials and Methods
SOM Text
Figs. S1 to S11
Tables S1 and S2
Reference (31)
Database S1

24 October 2011; accepted 5 March 2012

Published online 15 March 2012;

10.1126/science.1215704

miRNA-Mediated Gene Silencing by Translational Repression Followed by mRNA Deadenylation and Decay

Sergej Djuranovic, Ali Nahvi, Rachel Green*

microRNAs (miRNAs) regulate gene expression through translational repression and/or messenger RNA (mRNA) deadenylation and decay. Because translation, deadenylation, and decay are closely linked processes, it is important to establish their ordering and thus to define the molecular mechanism of silencing. We have investigated the kinetics of these events in miRNA-mediated gene silencing by using a *Drosophila* S2 cell-based controllable expression system and show that mRNAs with both natural and engineered 3' untranslated regions with miRNA target sites are first subject to translational inhibition, followed by effects on deadenylation and decay. We next used a natural translational elongation stall to show that miRNA-mediated silencing inhibits translation at an early step, potentially translation initiation.

MicroRNAs (miRNAs) are short endogenous RNAs that regulate protein expression from targeted genes by pairing to sites in the 3' untranslated region (3'UTR) (1). Although some studies showed a strong correlation between the diminution of protein and mRNA levels of miRNA-targeted genes (2–6), other

studies showed that miRNAs principally affect protein expression of miRNA-targeted genes without obvious effects on mRNA abundance (7–10). By simultaneously measuring translational efficiencies (thus indirectly levels of protein synthesis) and mRNA abundance, global analyses have shown evidence of significant mRNA destabili-

zation and translational repression (11, 12). Because only slightly more translational repression is observed than mRNA destabilization, it is possible that most of the loss in protein synthesis could directly result from effects on mRNA stability. Most of these studies have not, however, evaluated the kinetics of the miRNA-related cellular processes (5, 10, 13, 14). Exceptions include several analyses of in vitro systems that concluded that the effects of miRNAs on translational repression precede effects on mRNA target deadenylation or decay (15–17), but concerns remain that the in vitro reactions may not fully recapitulate the in vivo situation.

We used an in vivo luciferase-based reporter system in *Drosophila melanogaster* S2 cells under the control of an inducible metallothionein promoter (Mtn) (18). The reporter constructs consist of one of the luciferase reporter genes [Firefly (F-Luc) or Renilla (R-Luc)] fused at its 5' end to the Mtn promoter and at its 3' end to synthetic or

Howard Hughes Medical Institute (HHMI) and Department of Molecular Biology and Genetics, Johns Hopkins University School of Medicine, Baltimore, MD 21205, USA.

*To whom correspondence should be addressed. E-mail: ragreen@jhmi.edu

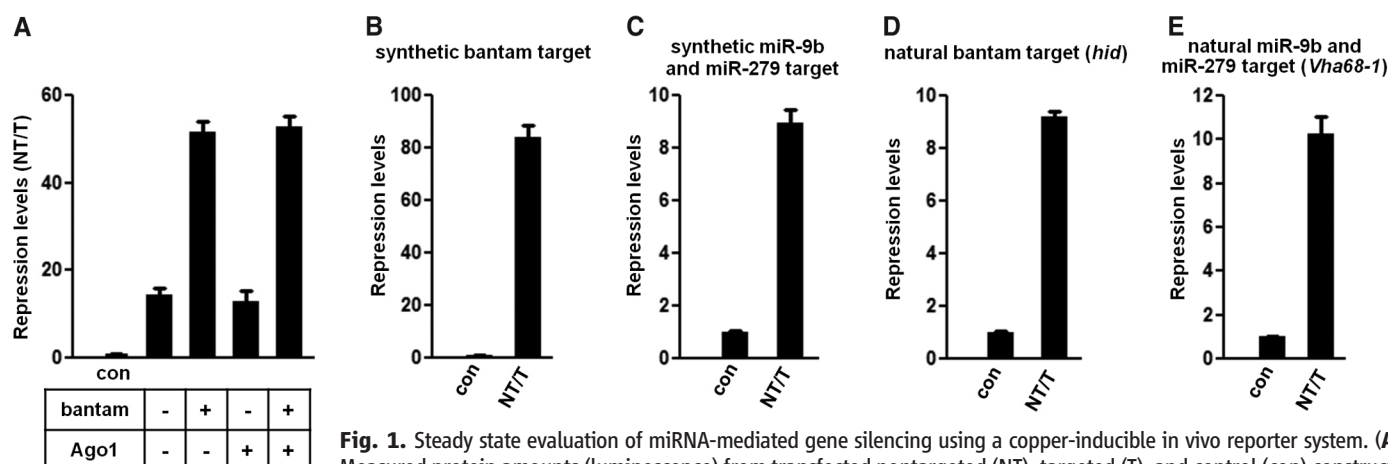


Fig. 1. Steady state evaluation of miRNA-mediated gene silencing using a copper-inducible in vivo reporter system. **(A)** Measured protein amounts (luminescence) from transfected nontargeted (NT), targeted (T), and control (con) constructs 24 hours after induction. Additional expression of bantam miRNA, not Argonaute 1, results in increased repression for synthetic bantam targeted constructs (fig. S1). **(B to E)** Ratios of steady-state protein amounts for synthetic and natural miRNA-targeted constructs 48 hours after induction. In each case, mean values \pm SD from three independent triplicate experiments are shown as a normalized ratio of protein amounts (NT/T).

synthetic bantam targeted constructs (fig. S1). **(B to E)** Ratios of steady-state protein amounts for synthetic and natural miRNA-targeted constructs 48 hours after induction. In each case, mean values \pm SD from three independent triplicate experiments are shown as a normalized ratio of protein amounts (NT/T).

natural 3'UTRs that contain miRNA binding sites responsive to either endogenously expressed (bantam and miR-279) or ectopically introduced miRNAs (miR-9b) (fig. S1); control constructs not subject to miRNA-mediated gene regulation are detailed in fig. S1. We first asked whether miRNA-mediated responsiveness is limited by endogenous components of the microRNA-induced silencing complex (miRISC) (Argonaute protein or miRNAs). By using a previously characterized bantam-responsive synthetic construct and ectopically expressed additional miRISC components (bantam and Ago1), we followed repression levels of the target mRNAs 24 hours after induction (Fig. 1A) (19). The results indicate that Ago1 is not limiting for repression in *Drosophila* S2 cells, whereas bantam is limiting because greater repression was observed when it was overexpressed (Fig. 1A). In the remaining experiments, we expressed additional amounts of endogenously present miRNAs (bantam and miR-279) from plasmids under the constitutive *actin* promoter.

We next used a set of synthetic and natural 3'UTRs with miRNA binding sites responding to either bantam or miR-9b and miR-279 and their corresponding controls (fig. S1 and tables S1 and S2). We chose natural (endogenous) 3'UTRs from *hid* and *Vha68-1* and a pair of synthetic 3'UTR targets that contain six natural tandem sites for either bantam or miR-9b and miR-279 miRNAs (19, 20). After transfection and constitutive induction, luciferase expression levels were measured after 48 hours and normalized to assess the end-point effects of miRNA-mediated repression (Fig. 1, B to E). The synthetic bantam 3'UTR exhibited repression levels up to 80-fold when compared with the control (Fig. 1B); the reporter containing the 3'UTR of the *hid* gene with as many as eight miRNA binding sites exhibited ~ninefold repression (Fig. 1D) (19). Additionally, both synthetic and natural (20) 3'UTRs responding to ectopically expressed miR-9b and miR-279 exhibited strong repression 48 hours after induction (Fig. 1, C and E). The addition of

antagomirs to the cell cultures induced levels of derepression for the reporter constructs similar to those observed when comparing reporter protein expression from constructs with intact and altered miRNA binding sites (fig. S2). For regulated induction, transcriptional shut-off of the Mtn promoter was accomplished by using a specific copper chelator, bathocuproine disulphonate (BCS). Although BCS chelates any residual copper in the S2 cell medium, it does not penetrate the cell membrane and thus does not affect normal cellular homeostasis (21). A 90-min pulse induction by copper (II) sulfate induced expression of the various reporter constructs to levels that could be monitored over the subsequent 48 hours. By using this optimized pulse-induction protocol (fig. S3), we determined how our reporter pairs with synthetic and natural 3'UTRs respond to miRNAs during an extended period of time. Normalized levels of luciferase luminescence for both miRNA-targeted and nontargeted constructs were used to assess miRNA-mediated gene silencing at

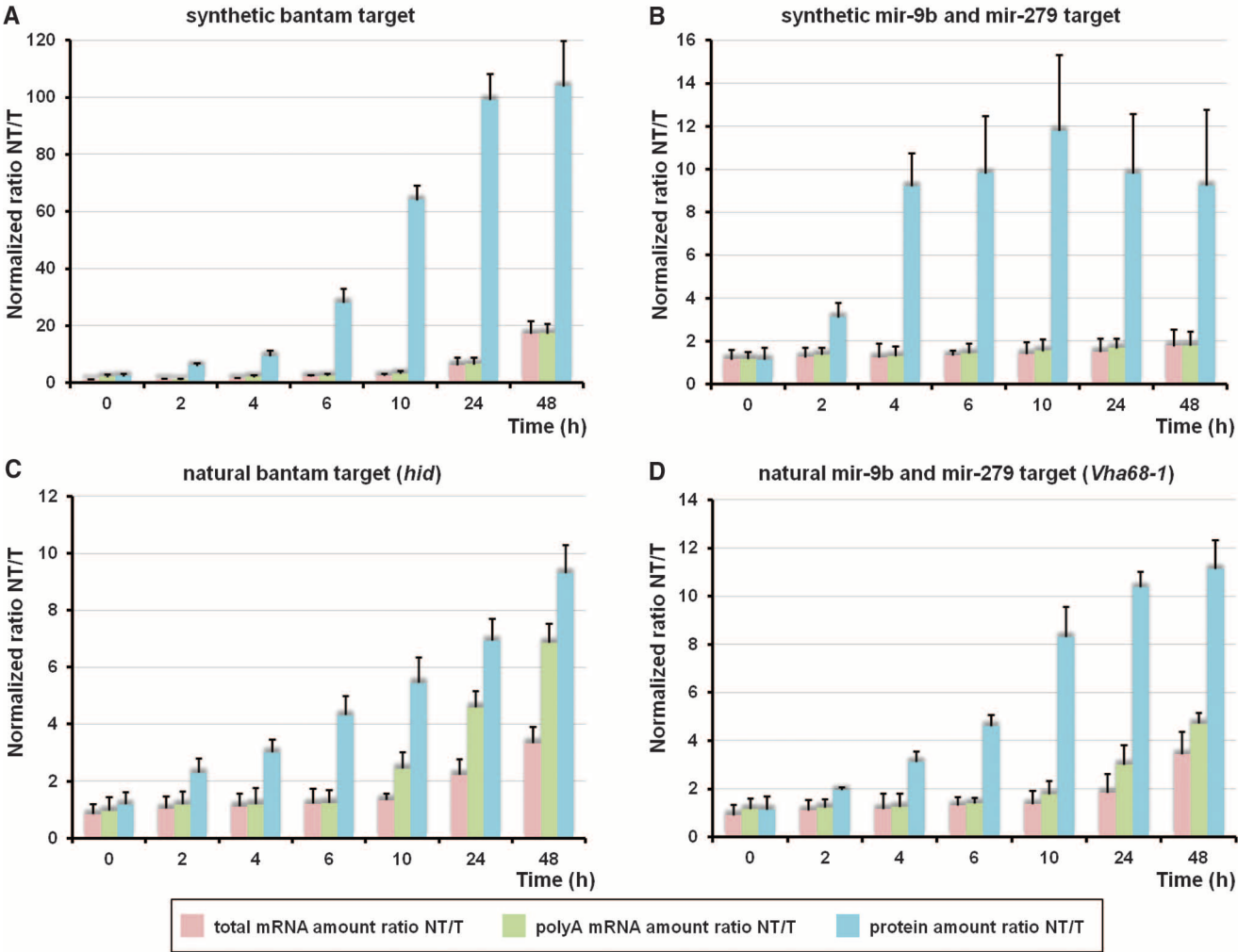


Fig. 2. Time-resolved progression of miRNA-mediated gene silencing establishes that repression of protein synthesis precedes mRNA deadenylation and decay. (A to D) Normalized levels of protein amounts for both miRNA-targeted (T) and nontargeted (NT) constructs; normalized mRNA levels for

reporter genes from oligo(dT)₂₅ resin precipitation or from total RNA presented as ratios of poly(A) and total mRNA, respectively. Each data point represents the mean value \pm SD calculated from three independent experiments.

the protein level. mRNA levels for reporter and control genes were determined by using quantitative reverse transcription polymerase chain reaction (qRT-PCR) from RNA samples isolated with oligo (dT)₂₅ resin, as well as from total RNA. Both values were normalized with respect to the parallel transfected control genes and were used to calculate repression ratios between miRNA-targeted and nontargeted constructs (Fig. 2). We emphasize that there is substantial mRNA degradation (for all reporters) during the experiment (fig. S4), but here we are interested in the relative amount of decay of the targeted and nontargeted mRNAs. The results of the pulse-induction experiments were consistent and show that the repressive effects of miRNAs on synthesis of all four proteins precede any effects on mRNA deadenylation or decay (Fig. 2).

These four examples include effects on protein and mRNA levels that are both well cor-

related and poorly correlated (5, 10–12, 19, 20). For reporters with natural 3' UTRs, the repression effects on protein and mRNA levels are correlated at later (but not early) time points (Fig. 2, C and D), consistent with global studies on miRNA-mediated silencing (11, 12). For reporters with synthetic 3' UTRs, the repression effects on protein and mRNA levels are uncorrelated at both early and late time points (Fig. 2, A and B) (5, 10, 19, 20). The differences in overall stability of the mRNAs likely reflect the complexity of RNA degradation as specified by various 3' UTR-located sequence motifs. In all experiments here, repression of protein synthesis is consistently seen just 2 hours after induction, whereas mRNA destabilization comes later. Additionally, in experiments where less bantam miRNA was present (by not supplying an exogenous source), the observed timing of protein repression and mRNA dead-

enylation and decay were unaffected (fig. S5, A and B).

We performed a similar set of experiments with use of actinomycin D to more rapidly shut off transcription (fig. S6, A to D). At a single time point after induction, all constructs showed a substantial reduction in protein production but no reduction in mRNA abundance (Fig. 2). Consistent with BCS shut-off data, translation rates for targeted constructs are substantially reduced with respect to nontargeted ones (fig. S6, A to D).

mRNA polyadenylate [poly(A)] tails are involved in translation initiation and thus in determining translational efficiency (22, 23). Potential subtle changes in poly(A) tail length not detectable using an oligo(dT)₂₅ isolation procedure were analyzed for the complete set of RNA samples by using a poly(A) tail-length assay that allows

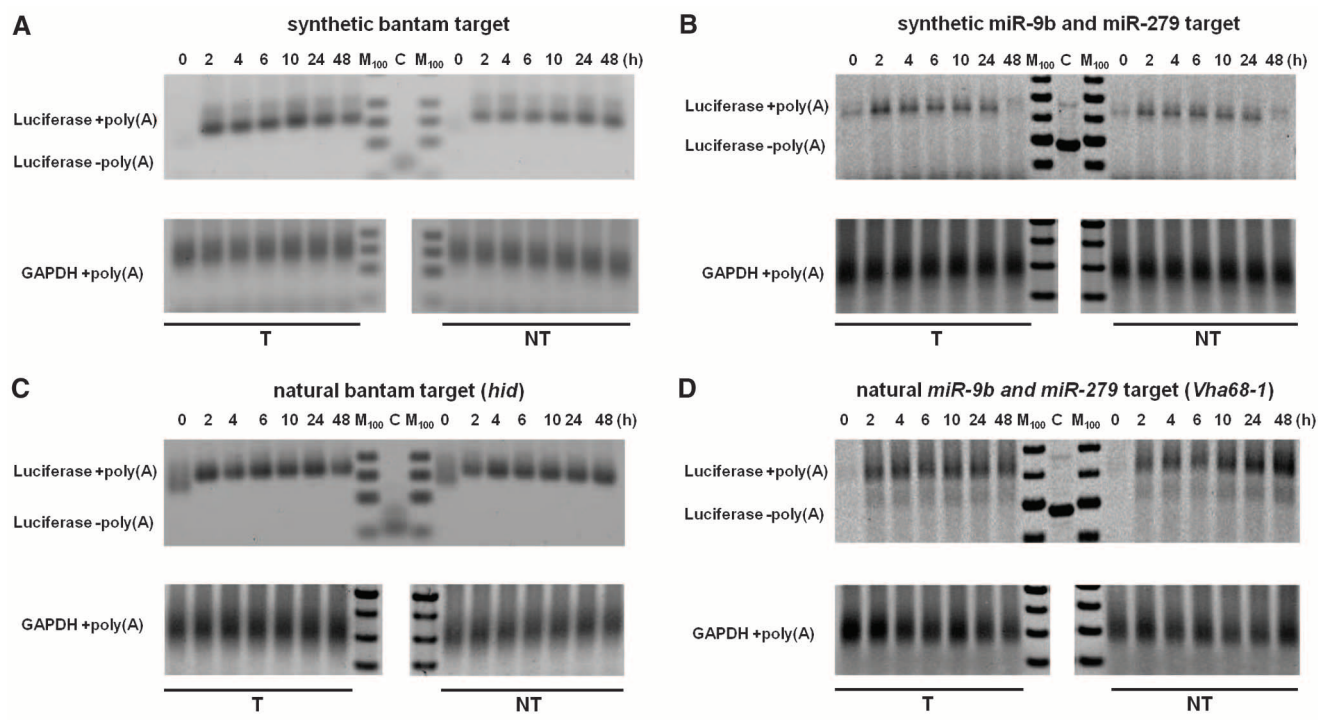


Fig. 3. mRNA deadenylation is not required for miRNA-mediated translational repression. (A to D) Length of poly(A) tail was determined by using G/I tailing PCR-based amplification (materials and methods). Positions of overamplified products with or without (C) poly(A) tail are indicated. Glyceraldehyde-3-phosphate dehydrogenase (GAPDH) mRNA poly(A) tail length is shown as a control. M lane represents 100-base pair markers. (E) Time-resolved progression of miRNA-mediated gene silencing for histone H3 constructs. Normalized levels of protein and mRNA amounts for miRNA-targeted (T) and nontargeted (NT) constructs are shown. Each data point represents an average value \pm SD from three independent experiments.

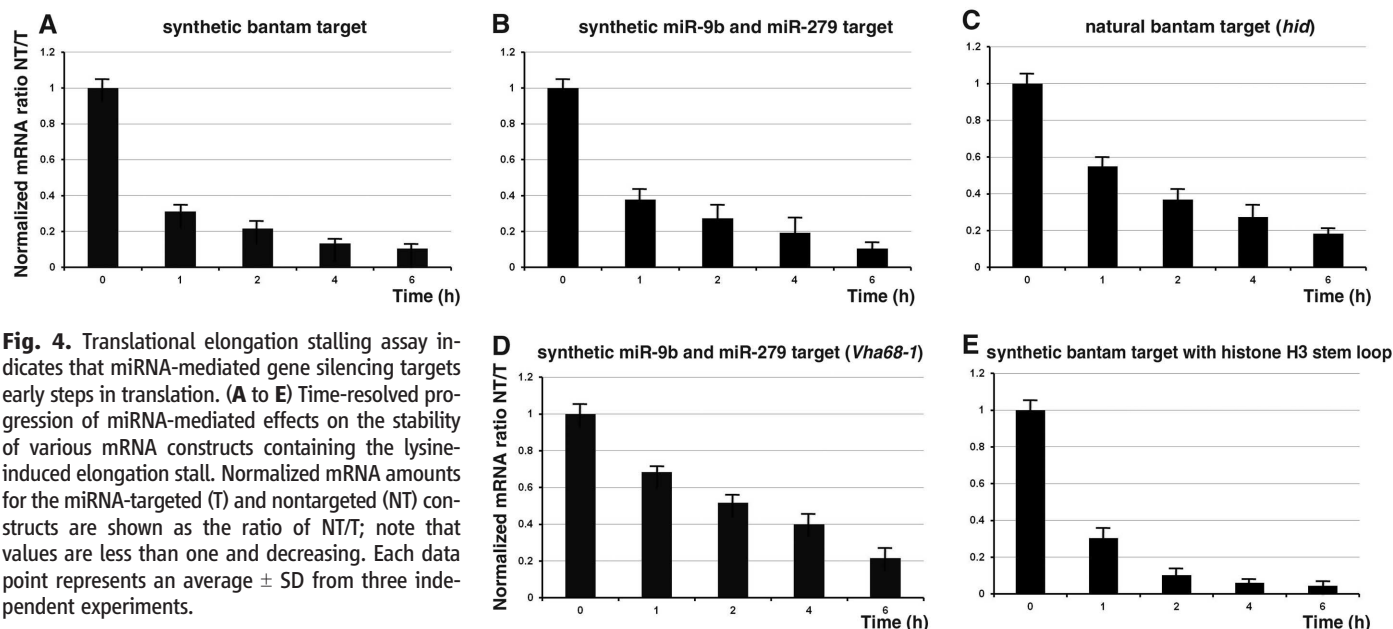


Fig. 4. Translational elongation stalling assay indicates that miRNA-mediated gene silencing targets early steps in translation. (**A** to **E**) Time-resolved progression of miRNA-mediated effects on the stability of various mRNA constructs containing the lysine-induced elongation stall. Normalized mRNA amounts for the miRNA-targeted (T) and nontargeted (NT) constructs are shown as the ratio of NT/T; note that values are less than one and decreasing. Each data point represents an average \pm SD from three independent experiments.

for specific amplification of poly(A)-containing mRNAs. Subtle changes in poly(A) tail length could be documented with this assay when cells were treated with puromycin (fig. S7) (24). However, we did not observe any shortening of poly(A) tails in reporter constructs responding to bantam or mir-9b and mir-279 (Fig. 3, A to D). Because no intermediates are observed, these data suggest that deadenylation *in vivo* is processive and closely coupled to mRNA decay. These data argue that translational inhibition is not triggered by deadenylation, either partial or complete, in the system that we have established [in contrast with earlier studies (6, 12, 25)].

We also evaluated the timing and extent of silencing of reporter gene pairs carrying histone H3 terminal stem loops [and no poly(A) tail] (26) (fig. S8). This reporter pair is translationally repressed rapidly (Fig. 3E) and at levels comparable to those observed with equivalent constructs carrying a poly(A) tail (Fig. 2A versus Fig. 3E). These data provide further support for the idea that deadenylation is not required for translational repression by miRNAs (5). However, deadenylases may play a direct role in translational repression independent of their deadenylation activity (27–29), and deadenylation may consolidate the observed translational repression.

To define where in the translation cycle the miRNA-mediated stalling occurs, we developed an approach that uses as a read-out the specific cleavage of mRNAs when ribosomes stall during translation elongation (30) (fig. S9). We inserted 12 lysine codons at position 6 in both the natural and synthetic reporters; as a control, we inserted 12 arginines and 12 more neutral glutamine residues (fig. S10). By using qRT primers that encompassed the predicted cleavage site as well as the stall sequence, we determined the extent of cleavage of both targeted and nontargeted report-

er mRNAs over time (Fig. 4, A to D, and fig. S11, A to C). Ratios of the targeted and nontargeted proteins and mRNAs were normalized to the amount of a parallel control reporter. In all cases, mRNAs of nontargeted reporters were rapidly cleaved and degraded, whereas mRNAs of the targeted reporters were relatively stabilized. Similar results were obtained in a stalling experiment with histone H3 constructs, confirming that the poly(A) tail is not essential for miRNA-mediated translational repression (Fig. 4E). These data establish that miRNA-mediated translational silencing happens in the *Drosophila* system during the initiation or early elongation phase of protein synthesis.

We find that miRNA-mediated gene silencing in *Drosophila* S2 cells is first manifested through effects on translation, and in particular the early events thereof, and is subsequently consolidated by mRNA deadenylation and decay. Although it is possible that the order of events is different in other systems or in a fashion that is mRNA-specific, our data in *Drosophila* are consistent. Moreover, these observations are consistent with earlier studies on miRNA-mediated silencing *in vitro* (15, 17) and with previous studies of translation as affected by iron levels (24). With these insights into the relative timing of the events involved in miRNA-mediated gene silencing, we can now focus subsequent molecular mechanistic analysis on these earliest triggering steps.

References and Notes

1. D. P. Bartel, *Cell* **136**, 215 (2009).
2. S. Bagga *et al.*, *Cell* **122**, 553 (2005).
3. L. P. Lim *et al.*, *Nature* **433**, 769 (2005).
4. A. J. Giraldez *et al.*, *Science* **312**, 75 (2006); 10.1126/science.1122689.
5. A. Eulalio *et al.*, *RNA* **15**, 21 (2009).
6. T. H. Beilharz *et al.*, *PLoS ONE* **4**, e6783 (2009).
7. P. H. Olsen, V. Ambros, *Dev. Biol.* **216**, 671 (1999).

8. R. S. Pillai *et al.*, *Science* **309**, 1573 (2005); 10.1126/science.1115079.
9. C. P. Petersen, M. E. Bordeleau, J. Pelletier, P. A. Sharp, *Mol. Cell* **21**, 533 (2006).
10. X. C. Ding, H. Grosshans, *EMBO J.* **28**, 213 (2009).
11. D. G. Hendrickson *et al.*, *PLoS Biol.* **7**, e1000238 (2009).
12. H. Guo, N. T. Ingolia, J. S. Weissman, D. P. Bartel, *Nature* **466**, 835 (2010).
13. L. Wu, J. Fan, J. G. Belasco, *Proc. Natl. Acad. Sci. U.S.A.* **103**, 4034 (2006).
14. M. Wakiyama, K. Takimoto, O. Ohara, S. Yokoyama, *Genes Dev.* **21**, 1857 (2007).
15. G. Mathonnet *et al.*, *Science* **317**, 1764 (2007).
16. A. Zdanowicz *et al.*, *Mol. Cell* **35**, 881 (2009).
17. M. R. Fabian *et al.*, *Mol. Cell* **35**, 868 (2009).
18. H. Johansen *et al.*, *Genes Dev.* **3**, 882 (1989).
19. A. Nahvi, C. J. Shoemaker, R. Green, *RNA* **15**, 814 (2009).
20. I. Behm-Ansmant *et al.*, *Genes Dev.* **20**, 1885 (2006).
21. A. Selvaraj *et al.*, *Genes Dev.* **19**, 891 (2005).
22. D. R. Gallie, *Genes Dev.* **5**, 2108 (1991).
23. T. H. Beilharz, T. Preiss, *RNA* **13**, 982 (2007).
24. M. Muckenthaler, N. Gunkel, R. Striepecke, M. W. Hentze, *RNA* **3**, 983 (1997).
25. S. Iwasaki, T. Kawamata, Y. Tomari, *Mol. Cell* **34**, 58 (2009).
26. W. F. Marzluff, E. J. Wagner, R. J. Duronio, *Nat. Rev. Genet.* **9**, 843 (2008).
27. J. E. Braun, E. Huntzinger, M. Fauser, E. Izaurralde, *Mol. Cell* **44**, 120 (2011).
28. M. Chekulaeva *et al.*, *Nat. Struct. Mol. Biol.* **18**, 1218 (2011).
29. M. R. Fabian *et al.*, *Nat. Struct. Mol. Biol.* **18**, 1211 (2011).
30. K. Kuroha *et al.*, *EMBO Rep.* **11**, 956 (2010).

Acknowledgments: We thank K. Wehner, J. Doudna, M. Jinek, N. Guydosh, and J. Collier for helpful comments. Funding is from HHMI.

Supplementary Materials

www.sciencemag.org/cgi/content/full/336/6078/237/DC1
Materials and Methods
Figs. S1 to S11
Tables S1 to S4
References

24 October 2011; accepted 13 March 2012
10.1126/science.1215691

A Memory Retrieval-Extinction Procedure to Prevent Drug Craving and Relapse

Yan-Xue Xue,^{1*} Yi-Xiao Luo,^{1*} Ping Wu,^{1*} Hai-Shui Shi,^{1,2} Li-Fen Xue,¹ Chen Chen,¹ Wei-Li Zhu,¹ Zeng-Bo Ding,¹ Yan-ping Bao,¹ Jie Shi,¹ David H. Epstein,³ Yavin Shaham,³ Lin Lu^{1†}

Drug use and relapse involve learned associations between drug-associated environmental cues and drug effects. Extinction procedures in the clinic can suppress conditioned responses to drug cues, but the extinguished responses typically reemerge after exposure to the drug itself (reinstatement), the drug-associated environment (renewal), or the passage of time (spontaneous recovery). We describe a memory retrieval-extinction procedure that decreases conditioned drug effects and drug seeking in rat models of relapse, and drug craving in abstinent heroin addicts. In rats, daily retrieval of drug-associated memories 10 minutes or 1 hour but not 6 hours before extinction sessions attenuated drug-induced reinstatement, spontaneous recovery, and renewal of conditioned drug effects and drug seeking. In heroin addicts, retrieval of drug-associated memories 10 minutes before extinction sessions attenuated cue-induced heroin craving 1, 30, and 180 days later. The memory retrieval-extinction procedure is a promising nonpharmacological method for decreasing drug craving and relapse during abstinence.

Conditioning plays a major role in drug addiction, and responses to drug-associated cues persist during prolonged abstinence (1, 2). These findings led to the development of cue-exposure therapies to extinguish the craving-

and relapse-provoking effects of drug cues (1, 3). However, cue-exposure therapy in clinical settings does not usually prevent relapse when former drug addicts return to their previous drug environments (4). Animal learning studies predict that extinction responding is susceptible to renewal, reinstatement, and spontaneous recovery. Respectively, these terms refer to resumption of original learned responses after change of environmental context, acute exposure to the unconditioned stimulus (such as food or drug), or passage of time (5).

More recently, preclinical investigators have been able to decrease behavioral effects of drug-

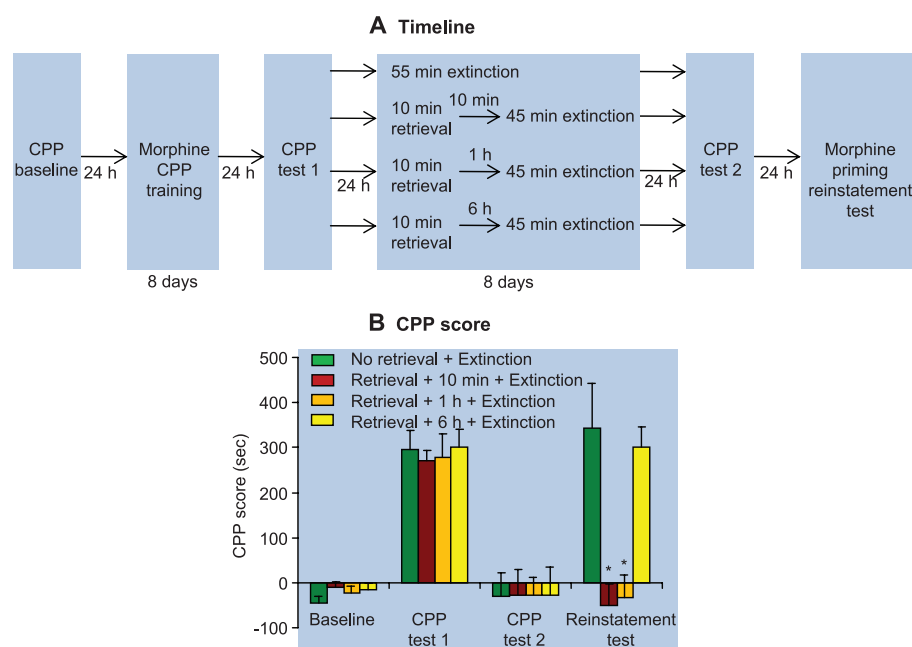
associated cues by pharmacologically interfering with reconsolidation of drug-cue memories (6–9). Reconsolidation refers to a time-dependent process in which consolidated memory items are rendered transiently unstable shortly after their reactivation (10–12). However, with the exception of the beta-adrenoceptor antagonist propranolol (13, 14), which is approved for human use, the other pharmacological compounds used in these studies are not suitable for human use (15–18). Consequently, the results from rat reconsolidation studies have not yet “translated” to clinical use in addiction treatment.

A nonpharmacological alternative may be possible: the “memory retrieval-extinction” behavioral procedure to interfere with reconsolidation of fear cues in rats and humans (19, 20). Reinstatement, renewal, and spontaneous recovery of fear responding are prevented by acute exposure to cues previously paired with foot-shock (a retrieval manipulation) if that exposure is followed 10 min or 1 hour later (but not 6 hours later) by repeated exposure to the same cues in extinction sessions. Thus, extinction experience within the timeframe of the “reconsolidation window” after cued retrieval of the fear memories mimicked the behavioral effect of a pharmacological manipulation on suppression of fear conditioning (19, 20).

We used an extinction-reinstatement procedure in rats [an animal model of drug relapse (21)] and a cue-induced-craving procedure in humans (1) to assess whether the memory retrieval-extinction procedure can decrease drug- and cue-induced drug preference and relapse in rats and cue-induced drug craving in humans.

We first assessed the effect of the memory retrieval-extinction manipulation on drug-priming-

Fig. 1. In rats, retrieval of drug-cue memories 10 min or 1 hour before extinction sessions prevented drug-priming-induced reinstatement of morphine CPP. **(A)** During CPP training, rats learned to associate one environmental context with the effect of morphine injections (10 mg/kg, subcutaneous) and to associate another context with saline injections. Next, all rats were tested for their place preference (CPP test 1). Twenty-four hours later, rats were divided into four groups and given different memory retrieval-extinction manipulations: 55-min extinction training (in one group), or 10-min memory retrieval + 45 min extinction training (in the other three groups—with either a 10-min, 1-hour, or 6-hour delay between memory retrieval and extinction training). All rats were tested for reinstatement of morphine CPP induced by a priming injection of morphine (5 mg/kg, subcutaneous). **(B)** Effect of the experimental manipulations on the CPP score. Data are mean \pm SEM of preference score in seconds (time spent in the morphine-paired chamber minus time spent in the saline-paired chamber) during the CPP tests. Asterisk indicates different from the “no memory retrieval” condition; $P < 0.05$; $n = 9$ to 11 rats per experimental condition.



induced reinstatement of drug conditioned place preference (CPP) and spontaneous recovery of drug CPP (details are available in the supplementary material). In the Pavlovian CPP version of the reinstatement model, CPP is induced by a drug, extinguished, and then reinstated by priming injections of the drug (21); like other conditioned responses (22), the extinguished CPP response can reemerge after the passage of time (spontaneous recovery).

In experiment 1 (cocaine CPP) (fig. S1A) and experiment 2 (morphine CPP) (Fig. 1A), we used four groups of rats: (i) no memory retrieval + extinction; (ii) memory retrieval + 10-min delay + extinction; (iii) memory retrieval + 1-hour delay + extinction; and (iv) memory retrieval + 6-hour delay + extinction. We analyzed the data with the between-subjects factor of group and the within-subjects factor of CPP test (test 2, after extinction; test 3, drug-induced reinstatement or spontaneous recovery test). Brief (10 min) cued retrieval of the drug memories 10 min or 1 hour but not 6 hours before the longer 45-min daily extinction sessions impaired drug-priming-induced reinstatement of drug CPP for cocaine (table S1, statistical results, and fig. S1) and morphine (group \times test interaction, $F_{3,25} = 9.5$, $P < 0.01$) (Fig. 1). In experiment 3, we used an identical experimental procedure to demonstrate that the memory retrieval-extinction manipulation also impaired spontaneous recovery of cocaine CPP (fig. S2).

We next assessed the effect of the memory retrieval-extinction manipulation on drug-

priming-induced reinstatement of the drug self-administration behavior, spontaneous recovery, and context-induced reinstatement of drug seeking [a renewal manipulation (23)]. These experiments used the operant self-administration version of the reinstatement model, in which animals are trained to respond for drug infusions, given daily extinction sessions until operant responding ceases, and then tested for reinstatement of (nonreinforced) pressing on the drug-associated device (such as a lever or nosepoke operandum) after acute noncontingent exposure to drug-priming injections or exposure to drug-associated cues (24, 25). A selective increase in nonreinforced responding on the device previously associated with drug infusions (but not on the inactive device) is interpreted to indicate relapse to drug seeking (26). Like drug CPP, the extinguished drug-reinforced conditioned response undergoes spontaneous recovery after the completion of extinction training (27).

In experiments 4 and 5, we used rats that had been trained to self-administer cocaine or heroin to demonstrate the inhibitory effect of the memory retrieval-extinction manipulation on drug-priming-induced reinstatement (Fig. 2 and fig. S3). The statistical analysis included the between-subjects factor of group (no memory retrieval + extinction, memory retrieval + 10-min delay + extinction, and memory retrieval + 6-hour delay + extinction for cocaine; or no memory retrieval + extinction and memory retrieval + 10-min delay + extinction for heroin) and the within-subjects factor of reinstatement condition (last extinc-

tion session, reinstatement test session). Brief (15 min) cued retrieval of the drug memories 10 min but not 6 hours before the long 180-min daily extinction sessions impaired drug-priming-induced reinstatement of cocaine (fig. S3) or heroin (Fig. 2) seeking. There were significant group \times reinstatement condition interactions for both cocaine (table S2) and heroin ($F_{1,10} = 6.9$, $P < 0.05$). No group differences were seen in responding on the inactive nosepoke operandum ($P > 0.1$). Additionally, the memory retrieval-extinction manipulation accelerated extinction responding in the cocaine-trained rats (table S2 and fig. S3) but not the heroin-trained rats ($P > 0.05$) (Fig. 2).

In experiments 6 and 7, we used rats that had been trained to self-administer cocaine to demonstrate the inhibitory effect of the memory retrieval-extinction manipulation on spontaneous recovery (experiment 6) and renewal (context-induced reinstatement; experiment 7) of cocaine seeking (figs. S4 and S5). In the renewal experiment, the rats were trained to self-administer cocaine in a distinct context (context A). Then, the operant responding was extinguished in a different, nondrug context (context B). During the subsequent tests, reinstatement of cocaine seeking was assessed after exposure to context A (28). Brief (15 min) cued retrieval of the cocaine memories 10 min before the long 180-min daily extinction sessions impaired spontaneous recovery (fig. S4) and renewal (fig. S5) of cocaine seeking. The statistical analyses, which included the between-subjects factor of group

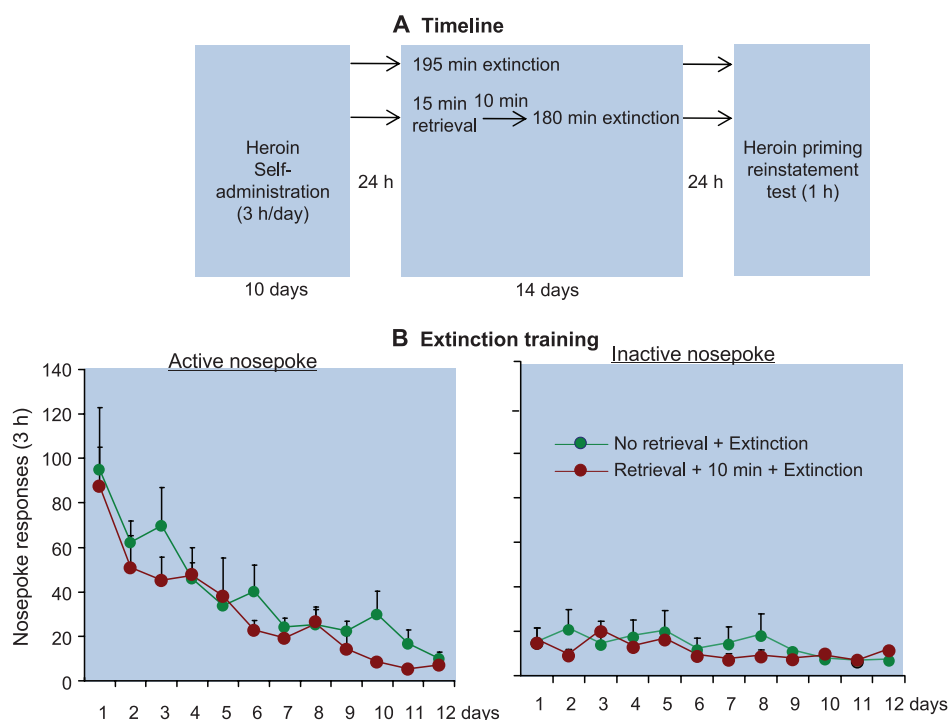


Fig. 2. In rats, retrieval of drug-cue memories 10 min before extinction sessions attenuated heroin-priming-induced reinstatement of drug seeking. (A) Timeline of the experimental procedure. Rats were trained to self-administer intravenous heroin during three 1-hour daily sessions over 10 days. Twenty-four hours later, the rats were divided into two groups and given different memory retrieval-extinction manipulations: 195-min extinction training or 15-min memory retrieval + 180-min extinction training, with 10 min between memory retrieval and extinction

training. The rats were then tested for reinstatement of nosepoke responding after noncontingent priming injections of heroin (0.25 mg/kg, subcutaneous). (B and C) Number of responses (mean \pm SEM) on the active and inactive nosepoke devices during the extinction sessions and the heroin-priming test. Asterisk indicates different from the "no memory retrieval" condition; $P < 0.05$; $n = 6$ to 7 rats per experimental condition.

(no memory retrieval + extinction and memory retrieval + 10-min delay + extinction) and the within-subjects factor of test condition (last extinction session, spontaneous recovery, or renewal test session), showed significant interactions between group \times test condition (table S2). No group differences were seen in responding on the inactive nosepoke operandum ($P > 0.1$). Additionally, the memory retrieval-extinction manipulation modestly accelerated extinction responding in experiment 6 (fig. S4) but not experiment 7 (fig. S5).

In experiment 8, we assessed the effect of the memory retrieval-extinction manipulation on the protein expression of protein kinase M ζ (PKM ζ) in medial prefrontal cortex (mPFC; infralimbic and prelimbic subregions) and amygdala (basolateral and central subregions). PKM ζ is a constitutively active atypical isoenzyme of protein kinase C that mediates long-term maintenance of aversive and appetitive memories (29, 30), including drug-associated memories (31, 32). We found that extinction training alone increased PKM ζ expression in infralimbic (but not prelimbic) cortex and decreased PKM ζ expression in basolateral (but not central) amygdala (fig. S6). Furthermore, the memory retrieval-extinction manipulation with a 10-min but not 6-hour delay potentiated extinction-induced increases in PKM ζ expression in infralimbic cortex and extinction-induced decreases in PKM ζ expression in basolateral amygdala (table S2 and fig. S6). There was no group effect on the levels of β -actin (a control protein).

Next, we assessed the clinical relevance of the memory retrieval-extinction procedure in inpatient detoxified heroin addicts. Heroin craving was assessed by using a visual analog scale (VAS) on which the participants had to rate their current craving for heroin, before and immediately after exposure to a neutral cue and a heroin cue. Neutral and heroin cues were both 5-min videotapes. Heart rate (HR) and blood pressure were monitored before and after cue exposure as additional measures of cue reactivity. The heroin addicts were assigned to three groups: (i) no memory retrieval + extinction, (ii) memory retrieval + 10-min delay + extinction, or (iii) memory retrieval + 6-hour delay + extinction. The memory retrieval-extinction manipulation with a 10-min but not 6-hour delay inhibited both cue-induced craving (Fig. 3) and cue-induced increases in blood pressure, but not heart rate (Fig. 4). Craving reactivity to cues was assessed by using change scores from preexposure baseline (33).

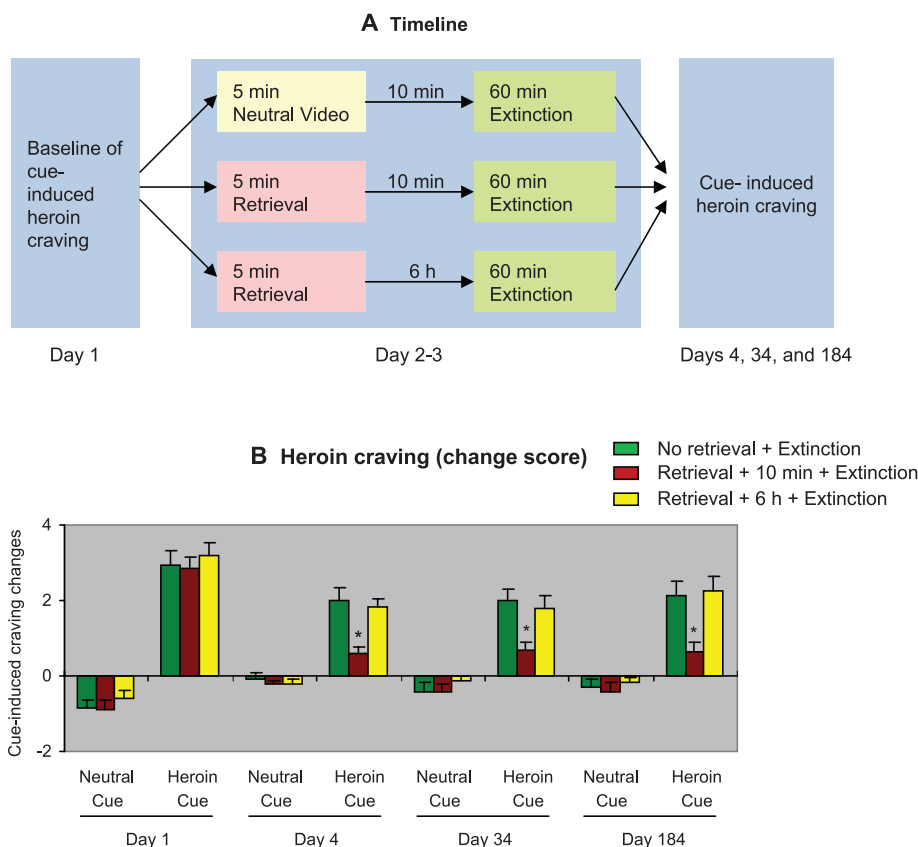
For cue-induced craving, the statistical analysis [SAS PROC MIXED, Satterthwaite method for denominator degrees of freedom that takes into account missing cells in repeated-measures analysis of variance (ANOVA)], which included baseline (day 1) as the covariate, the between-subjects factor of group, and the within-subjects factors of test day (posttreatment tests on days 4, 34, and 184) and cue type (neutral cue and heroin cue), showed a significant interaction between group \times cue type ($F_{2,23.75} = 9.0$, $P < 0.01$). For systolic and diastolic blood pressure, the analyses showed a trend

toward an interaction between group \times cue type ($F_{2,343.25} = 2.38$, $P = 0.094$ and $F_{2,374.46} = 2.42$, $P = 0.09$, respectively). No group differences were observed for heart rate.

In 2009, Monfils and colleagues introduced a memory retrieval-extinction procedure whose application to both rats (19) and humans (20) led to long-lasting blockade of shock-conditioned fear responses. Here, we introduce an appetitive-conditioning version of the memory retrieval-extinction procedure whose application caused long-lasting attenuation of conditioned drug effects and drug seeking (in rats) and drug craving (in detoxified heroin users). The behavioral effects of our procedure were also associated with changes in the expression of the memory-maintenance-related molecule PKM ζ in infralimbic cortex and basolateral amygdala. As in the fear-conditioning studies, a key determinant of effectiveness was the interval between the shorter memory-retrieval sessions and the longer extinction sessions or the interval between short reexposure to the drug-associated cues (memory retrieval) and subsequent longer nonreinforced reexposure to the same cues (extinction).

The development of the memory retrieval-extinction fear-conditioning procedure was inspired by theoretical accounts of memory retrieval and reconsolidation (34) and studies of pharmacological manipulations of reconsolidation of fear memories (11, 35). The latter body of work has since been extended to appetitive memories (6), including memories of drug-associated cues

Fig. 3. In humans, retrieval of drug-cue memories 10 min before extinction sessions caused long-lasting attenuation of cue-induced heroin craving. **(A)** Timeline of the experimental procedure. Neutral- and heroin-cue-induced drug craving (see supplementary materials) in abstinent heroin addicts was measured with VAS on day 1. Twenty-four hours later, the participants were divided into three groups and given different memory retrieval-extinction manipulations for 2 consecutive days: neutral cue exposure + 10-min delay + 60-min extinction training (in one group), or 5-min heroin-cue exposure (memory retrieval) + 60-min extinction training (in the other two groups—with 10 min or 6 hours between memory retrieval and extinction training). During the extinction sessions, the participants were given four consecutive sessions of repeated exposures to three different heroin-related cues (supplementary material). Measures of subjective craving and sympathetic activation (heart rate and blood pressure) were obtained after the extinction sessions. Cue-induced heroin craving was assessed again on days 4, 34, and 184 by using a procedure identical to that used on day 1. **(B)** Cue-induced heroin craving (mean \pm SEM) on day 1 (baseline), days 4, 34, and 184 (1, 30, and 180 days after the memory retrieval-extinction sessions). Asterisk indicates different from “no memory retrieval” group; $P < 0.05$; $n = 22$ human subjects per group for day 1, 4, and 34; $n = 16$ to 18 human subjects per group for day 184.



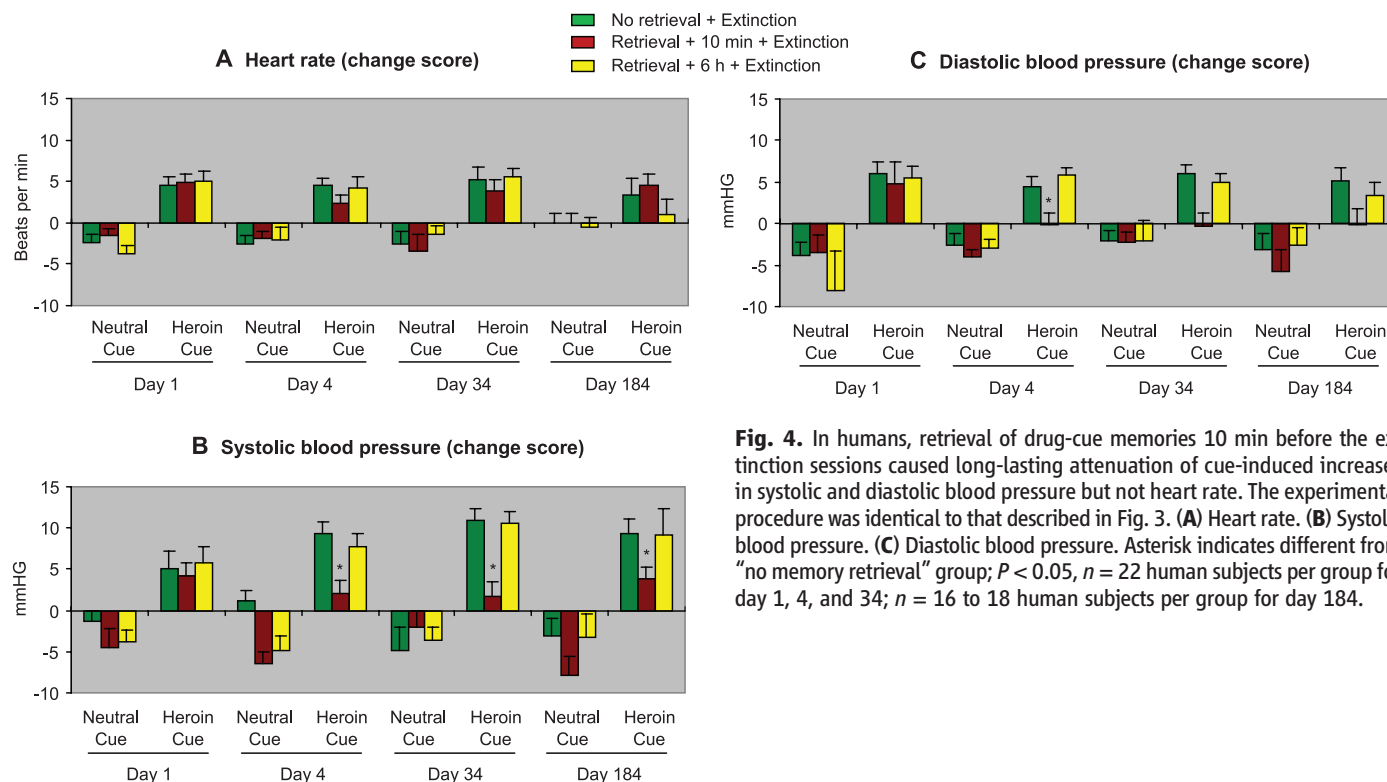


Fig. 4. In humans, retrieval of drug-cue memories 10 min before the extinction sessions caused long-lasting attenuation of cue-induced increases in systolic and diastolic blood pressure but not heart rate. The experimental procedure was identical to that described in Fig. 3. **(A)** Heart rate. **(B)** Systolic blood pressure. **(C)** Diastolic blood pressure. Asterisk indicates different from “no memory retrieval” group; $P < 0.05$, $n = 22$ human subjects per group for day 1, 4, and 34; $n = 16$ to 18 human subjects per group for day 184.

(7, 36). In those studies, investigators inferred that memory reconsolidation was disrupted on the basis of findings that post-retrieval systemic or intracranial injections of pharmacological agents within a specific time interval (up to 2 hours after retrieval)—often termed a “reconsolidation window”—disrupted the expression of responses to aversive or appetitive cues (6, 12, 37). Accordingly, results from studies of memory retrieval-extinction manipulations have been taken to reflect interference with reconsolidation (19, 20, 38). The findings that the memory retrieval-extinction manipulation is ineffective when the extinction sessions are given at delays that are longer than the reconsolidation window (19, 20, 38) supports this interpretation. The retrieval-extinction manipulation also blocks shock-induced reinstatement, spontaneous recovery, and renewal of conditioned-fear expression [phenomena that are otherwise reliably observed after extinction training (5)] in some studies (19, 20, 38), but not others (39, 40). On the basis of the above findings, a plausible interpretation of our data is that the memory retrieval-extinction manipulation interfered with reconsolidation of memories for drug cues. This hypothesis is supported by two sets of observations. First, across the different experiments in both rats and humans, the memory retrieval-extinction manipulation was effective only within the time window of reconsolidation. Second, in the CPP experiments the memory retrieval-extinction manipulation completely blocked drug-priming-induced reinstatement and spontaneous recovery.

However, a reconsolidation account of the data should be made with some caution in the case of

the drug self-administration experiments. In those experiments, nosepoke responding was significantly lower during the last extinction session than during the tests for drug-priming-induced reinstatement, spontaneous recovery, and renewal in the 10-min or 1-hour memory retrieval-extinction condition. Additionally, the effect of the memory retrieval-extinction manipulation on nosepoke responding during extinction training—a behavior induced in part by exposure to the drug-associated cues (26)—was modest and inconsistent across experiments. Together, these observations suggest that our memory retrieval-extinction manipulation only weakened the memories of the drug cues (or decreased their motivational effects) rather than completely preventing the expression of the conditioned response, as would have been predicted by a reconsolidation account of the data.

What might account for the attenuation but not blockade of drug seeking in the self-administration experiments? One possibility is that the memory retrieval-extinction manipulation preferentially disrupted reconsolidation of stimulus-response Pavlovian-based memories that mediate drug CPP in rats and cue-induced drug craving in humans, while having less impact on reconsolidation of response-outcome operant-based memories that play a role in reinstatement of drug seeking in the drug self-administration procedure. Operant drug seeking is controlled by a complex interplay between operant and Pavlovian conditioning processes (7, 26), and there is evidence that reconsolidation of operant memories is more difficult to disrupt than reconsolidation of Pavlovian memories (41).

Another issue to consider in interpreting the present data is that the memory-retrieval manipulations were performed under extinction conditions, and therefore, a given manipulation could have affected reconsolidation of cue memories, consolidation of extinction memory, or both (6). Our retrieval manipulation in the self-administration experiments was 15 min of daily non-reinforced operant responding in the presence of the drug-associated cues. Thus, an alternative interpretation could be that intermittent exposure to extinction training within the consolidation window of extinction memory may have strengthened the extinction memory, rendering the original appetitive memory less susceptible to reinstatement, spontaneous recovery, or renewal. Indeed, results from fear-conditioning studies demonstrate that pharmacological manipulations that promote consolidation of extinction memory, decrease reinstatement, spontaneous recovery, and renewal of fear memories (42–44).

It is also possible that our memory retrieval-extinction manipulation both facilitated extinction consolidation and disrupted reconsolidation. Two lines of evidence from published reports support this hypothesis. The first is our recent finding that post-training PKM ζ activity in basolateral amygdala is critical for memories of morphine reward and morphine withdrawal aversion but not extinction memory, whereas PKM ζ activity in infralimbic cortex is critical for extinction memory but not reward or withdrawal memories (31). The second is that plasticity in basolateral amygdala is critical for reconsolidation of memories for both aversive and appetitive cues (6, 7) and

for the effects of the retrieval-extinction manipulation on fear memories (38), whereas infralimbic plasticity is critical for maintenance of aversive and appetitive extinction memories (44, 45). In the experiments reported here, we found that repeated cocaine-cue retrieval 10 min before daily extinction sessions potentiated the opposite effects of extinction training alone on PKM ζ in the infralimbic cortex (increased expression) versus basolateral amygdala (decreased expression) (fig. S6). These findings are consistent with a “dual” effect of the memory retrieval-extinction manipulation on both consolidation of extinction memory and reconsolidation of cue memories.

Investigators have identified several ways to disrupt cue-memory reconsolidation or strengthen extinction learning (7, 46). However, their potential as preventive treatments for addiction is limited because they often rely on pharmacological agents that are either not approved for human use or that can cause problematic side effects. We used established animal models of drug relapse and a standard human laboratory procedure for drug-induced craving to assess a purely behavioral procedure to decrease the motivational effects of drug cues during abstinence. The memory retrieval-extinction procedure decreased cue-induced drug craving and (extrapolating from our rat data) perhaps could reduce the likelihood of cue-induced relapse during prolonged abstinence periods. If our procedure weakens the original drug-cue memories rather than solely facilitating extinction, it may overcome the contextual renewal problems that have limited the clinical effectiveness of traditional extinction procedures (4), although this possibility needs empirical evaluation in human addicts. Last, although the cellular mechanisms and brain circuits underlying the long-lasting effects of the retrieval-extinction procedure on drug relapse and craving

remain to be elucidated, our data point to a role for PKM ζ activity in the infralimbic cortex and basolateral amygdala.

References and Notes

- C. P. O'Brien, R. N. Ehrman, J. W. Ternes, in *Behavioral Analysis of Drug Dependence*, S. Goldberg, I. Stolerman, Eds. (Academic Press, Orlando, FL, 1986), pp. 329–356.
- J. Stewart, H. de Wit, R. Eikelboom, *Psychol. Rev.* **91**, 251 (1984).
- G. A. Marlatt, *Addict. Behav.* **15**, 395 (1990).
- C. A. Conklin, S. T. Tiffany, *Addiction* **97**, 155 (2002).
- M. E. Bouton, *Biol. Psychiatry* **52**, 976 (2002).
- N. C. Tronson, J. R. Taylor, *Nat. Rev. Neurosci.* **8**, 262 (2007).
- A. L. Milton, B. J. Everitt, *Eur. J. Neurosci.* **31**, 2308 (2010).
- J. L. Lee, P. Di Ciano, K. L. Thomas, B. J. Everitt, *Neuron* **47**, 795 (2005).
- C. A. Miller, J. F. Marshall, *Eur. J. Neurosci.* **21**, 1385 (2005).
- K. Nader, G. E. Schafe, J. E. Le Doux, *Nature* **406**, 722 (2000).
- Y. Dudai, *Curr. Opin. Neurobiol.* **16**, 174 (2006).
- C. M. Alberini, *Trends Neurosci.* **28**, 51 (2005).
- A. L. Milton, J. L. Lee, B. J. Everitt, *Learn. Mem.* **15**, 88 (2008).
- J. A. Wouda *et al.*, *Front. Behav. Neurosci.* **4**, 179 (2010).
- F. Q. Li *et al.*, *J. Neurosci.* **30**, 10351 (2010).
- H. Sanchez, J. J. Quinn, M. M. Torregrossa, J. R. Taylor, *J. Neurosci.* **30**, 4401 (2010).
- M. H. Milekic, S. D. Brown, C. Castellini, C. M. Alberini, *J. Neurosci.* **26**, 3010 (2006).
- J. L. Lee, A. L. Milton, B. J. Everitt, *J. Neurosci.* **26**, 5881 (2006).
- M. H. Monfils, K. K. Cowansage, E. Klann, J. E. LeDoux, *Science* **324**, 951 (2009).
- D. Schiller *et al.*, *Nature* **463**, 49 (2010).
- Y. Shaham, U. Shalev, L. Lu, H. De Wit, J. Stewart, *Psychopharmacology (Berl.)* **168**, 3 (2003).
- M. E. Bouton, D. Swartzentruber, *Clin. Psychol. Rev.* **11**, 123 (1991).
- H. S. Crombag, J. M. Bossert, E. Koya, Y. Shaham, *Philos. Trans. R. Soc. London Ser. B Biol. Sci.* **363**, 3233 (2008).
- R. E. See, *Eur. J. Pharmacol.* **526**, 140 (2005).
- H. de Wit, J. Stewart, *Psychopharmacology (Berl.)* **75**, 134 (1981).
- U. Shalev, J. W. Grimm, Y. Shaham, *Pharmacol. Rev.* **54**, 1 (2002).
- Y. Shaham, L. K. Adamson, S. Grocki, W. A. Corrigall, *Psychopharmacology (Berl.)* **130**, 396 (1997).
- H. S. Crombag, Y. Shaham, *Behav. Neurosci.* **116**, 169 (2002).
- T. C. Sacktor, *Nat. Rev. Neurosci.* **12**, 9 (2011).
- R. Shema, T. C. Sacktor, Y. Dudai, *Science* **317**, 951 (2007).
- Y. Y. He *et al.*, *Neuropsychopharmacology* **36**, 1972 (2011).
- Y. Q. Li *et al.*, *J. Neurosci.* **31**, 5436 (2011).
- R. Sinha, T. Fuse, L. R. Aubin, S. S. O'Malley, *Psychopharmacology (Berl.)* **152**, 140 (2000).
- M. Eisenberg, T. Kobilo, D. E. Berman, Y. Dudai, *Science* **301**, 1102 (2003).
- K. Nader, G. E. Schafe, J. E. LeDoux, *Nat. Rev. Neurosci.* **1**, 216 (2000).
- L. Diergaarde, A. N. Schoffeleer, T. J. De Vries, *Eur. J. Pharmacol.* **585**, 453 (2008).
- K. Nader, O. Hardt, *Nat. Rev. Neurosci.* **10**, 224 (2009).
- R. L. Clem, R. L. Huganir, *Science* **330**, 1108 (2010).
- M. Soeter, M. Kindt, *Learn. Mem.* **18**, 357 (2011).
- W. Y. Chan, H. T. Leung, R. F. Westbrook, G. P. McNally, *Learn. Mem.* **17**, 512 (2010).
- P. J. Hernandez, A. E. Kelley, *Learn. Mem.* **11**, 748 (2004).
- B. M. Graham, R. Richardson, *Behav. Neurosci.* **124**, 337 (2010).
- M. Davis, K. Ressler, B. O. Rothbaum, R. Richardson, *Biol. Psychiatry* **60**, 369 (2006).
- G. J. Quirk, D. Mueller, *Neuropsychopharmacology* **33**, 56 (2008).
- J. Peters, P. W. Kalivas, G. J. Quirk, *Learn. Mem.* **16**, 279 (2009).
- J. R. Taylor, P. Olausson, J. J. Quinn, M. M. Torregrossa, *Neuropharmacology* **56** (suppl. 1), 186 (2009).

Acknowledgments: This work was supported in part by the National Basic Research Program of China (No 2009CB522000 and 2011CB707800) and the Natural Science Foundation of China (No 91132716 and 31070958). The preparation of the manuscript was also supported in part by the Intramural Research Program of the National Institute on Drug Abuse. The authors declare that they do not have any conflicts of interest related to the data presented in this manuscript.

Supplementary Materials

www.sciencemag.org/cgi/content/full/336/6078/241/DC1
Materials and Methods
Figs. S1 to S6
Tables S1 and S2
References (47–61)

10 October 2011; accepted 23 February 2012
10.1126/science.1215070

Orthographic Processing in Baboons (*Papio papio*)

Jonathan Grainger,* Stéphane Dufau, Marie Montant, Johannes C. Ziegler, Joël Fagot

Skilled readers use information about which letters are where in a word (orthographic information) in order to access the sounds and meanings of printed words. We asked whether efficient processing of orthographic information could be achieved in the absence of prior language knowledge. To do so, we trained baboons to discriminate English words from nonsense combinations of letters that resembled real words. The results revealed that the baboons were using orthographic information in order to efficiently discriminate words from letter strings that were not words. Our results demonstrate that basic orthographic processing skills can be acquired in the absence of preexisting linguistic representations.

Reading is a complex process that starts with the extraction of detailed visual information, which is used to access the sounds (phonology) and the meanings (semantics) of words. Before they process the pho-

nological and semantic information, readers of languages that use an alphabetic script must first process the elementary visual features of the word's constituent letters and assign these different letter identities to specific positions in the

word. The computation of letter identities and their relative positions is referred to as orthographic processing, and there is a large consensus today that such processing represents the first “language-specific” stage of the reading process that follows the operations involved in the control of eye movements (bringing words into the focus of central vision) and early visual processing (enabling visual feature extraction; Fig. 1A) (1–4). In the present study, we examined whether the ability to efficiently process orthographic information can operate in the absence of prior linguistic knowledge.

Orthographic processing lies at the interface between the visual processing and the linguistic processing involved in written language

CNRS and Aix-Marseille University Laboratoire de Psychologie Cognitive, Fédération de Recherche 3C, Brain and Language Research Institute, Aix-Marseille University and CNRS, 3 Place Victor Hugo, 13331 Marseille, France.

*To whom correspondence should be addressed. E-mail: jonathan.grainger@univ-amu.fr

comprehension. The vast majority of research on visual word recognition, however, has ignored the status of printed words as visual objects, focusing mainly on how letter-level information maps onto higher-level linguistic properties (phono-

logical, morphological, semantic, and syntactic) (5). The discovery that orthographic processing is achieved by neural structures in the left ventral occipitotemporal cortex (6, 7), a region that is bilaterally associated with object and face pro-

cessing, has encouraged a reconsideration of the role of basic object identification processes in visual word recognition. In the light of this finding, Dehaene and colleagues proposed that skilled reading involves an adaptation of general object-

Fig. 1. Teaching baboons to recognize words. (A) Skilled readers use an orthographic code to recognize words, mapping elementary visual features, such as lines of different orientation (here features contained in the word “WASP”), onto whole-word orthographic representations via some form of letter-level code (1–4, 9). (B and C) While maintained in their social group, the baboons had free access to computer-controlled operant conditioning setups with touch screen technology (13). (C) The baboons were trained to recognize four-letter English words and distinguish them from strings of letters that are not English words, such as “STOD.” Baboons responded by touching either the cross or the oval shape presented immediately after the word or nonword. After a correct response, a blank screen was presented and baboons received a food reward (dry wheat). A green screen was presented for 3 s after an incorrect response. We asked whether baboons would use an orthographic code, as described in (A), in order to discriminate words from nonwords.

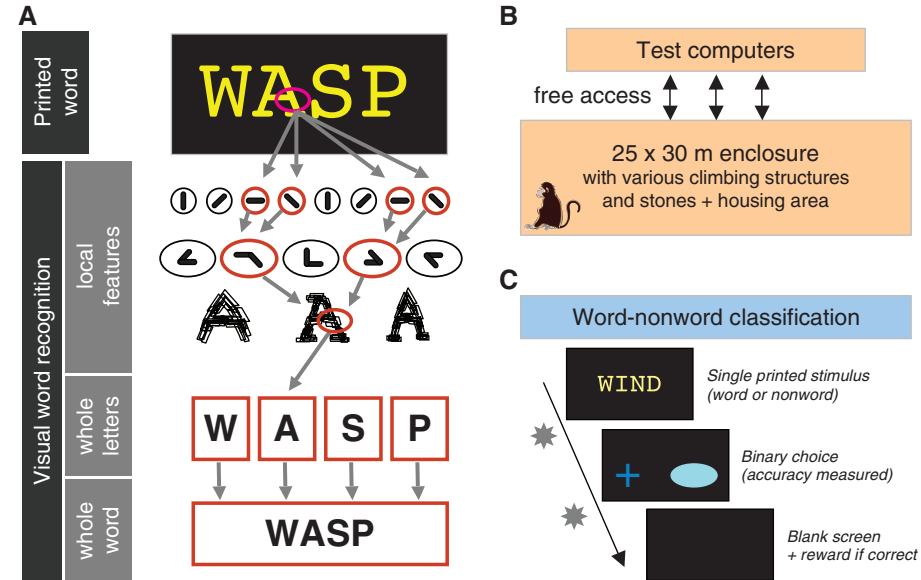
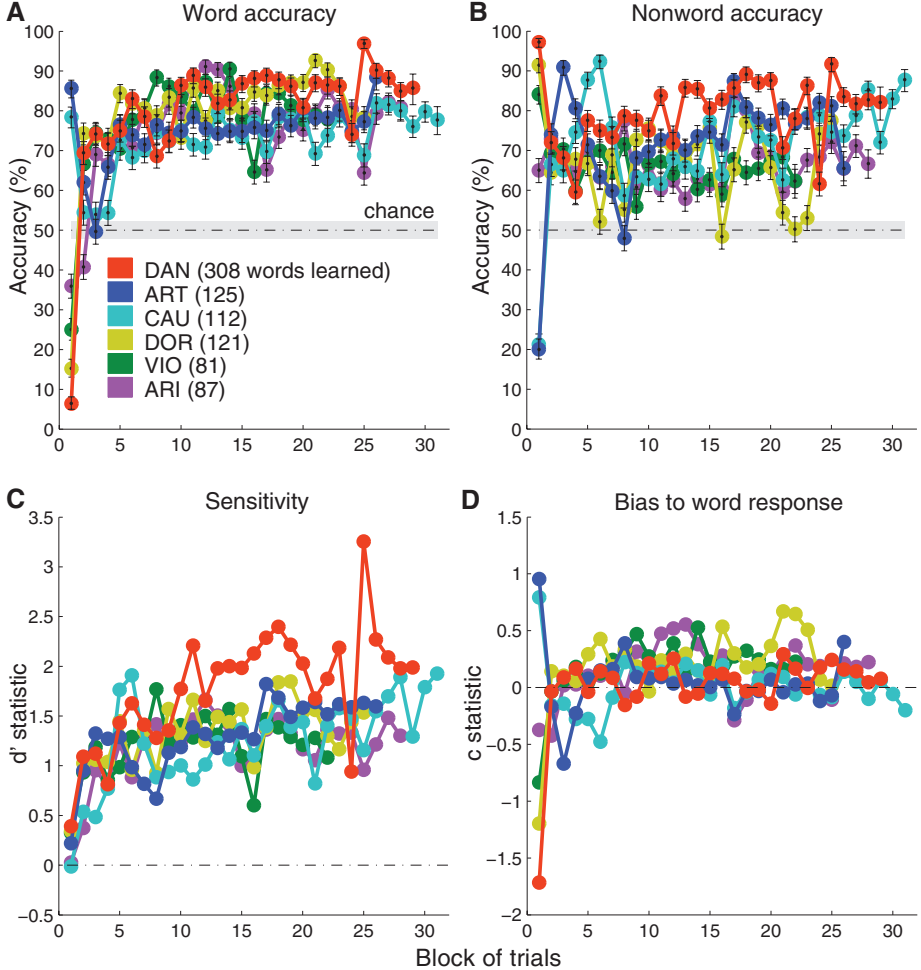


Fig. 2. Successful word-nonword discrimination in baboons. (A) Accuracy for words (e.g., DONE, LAND, THEM, VAST) and (B) nonwords (e.g., DRAN, LONS, TELK, VIRT) was calculated for blocks of 2000 consecutive trials (except for the last block) separately for each baboon (here and in Figs. 3 and 4, baboons are indicated by their abbreviated names: DAN, ART, CAU, DOR, VIO, and ARI). The results of a signal detection analysis are shown in (C) (sensitivity: baboons’ ability to discriminate words from nonwords) and (D) (bias: baboons’ inclination to answer “word” or “nonword”). During the first block of 2000 trials, numerical estimates of bias show that each baboon predominantly chose one of the two possible responses resulting in a “word” or “nonword” bias and low sensitivity. After 2000 trials, the baboons started to perform accurate word-nonword classification by responding “word” to repeated stimuli and “nonword” to novel stimuli as shown by above-zero sensitivities and bias values close to zero. Baboons attained an accuracy level of about 75%. Error bars in (A) and (B) correspond to the 95% binomial confidence interval, which are also displayed in gray for chance performance (see supplementary materials for more details).



identification processes in ventral occipitotemporal brain areas to the specific characteristics of printed words (8, 9).

However, according to the dominant theories of reading, orthographic processing is still primarily considered to be an extension of already established linguistic skills in the domain of spoken language processing (or sign language processing in hearing-impaired persons). Indeed,

the task of learning to read a language with an alphabetic script is facilitated by the fact that individual letters and letter clusters (graphemes) can be associated with the elementary sounds of the language (phonemes) in order to recover a phonological representation of the word being read, and from there to understand its meaning (5). Such phonological recoding operations could well be a major constraint that forces the be-

ginning reader to process individual letters rather than the word as a whole (10). Thus, it has typically been argued that orthographic processing is a predominantly linguistic skill, requiring the same cerebral predisposition as thought to be required for spoken and sign language processing, or at the least, prior exposure to the language in question.

We challenged the hypothesis that learning an orthographic code depends on preexisting linguistic knowledge by investigating whether nonhuman primates can learn this skill. Humans and nonhuman primates from the cercopithecidae family, such as macaques or baboons, have similar visual systems (11). However, the communicative system of cercopithecidae arguably lacks the structural complexity of human language (12) and certainly does not include any phonological representation of English words that could be associated with the printed forms of these words. Using a new testing procedure in which socially housed monkeys had free access to computer-controlled operant conditioning setups with touch screens (Fig. 1B) (13), we trained six baboons to discriminate randomly selected real English words four letters in length from artificially generated four-letter strings of letters that were not real English words [henceforth, nonwords (Fig. 1C)]. All nonwords were formed of a vowel and three consonants and contained letter combinations (bigrams) that occurred in real words. Bigram frequency was minimized in the list of nonwords and maximized in the list of words (14), so that the word versus nonword discrimination could be made implicitly on the basis of statistical dependencies between letters. Words and nonwords were presented randomly in blocks of 100 trials. The 100-trial sessions were composed of 25 presentations of a novel word to learn, 25 presentations of words randomly selected from already learned words, and 50 nonword trials. Each new word was added to the ever-increasing pool of already learned words, once responses to that word exceeded 80% correct within the preceding session. Thus, in terms of explicit information available to the baboons, a word was defined as a string of letters that was repeatedly presented, whereas a nonword was rarely repeated. The baboons responded by touching one of two shapes shown on the touch screen and were given a food reward after a correct response (Fig. 1C) (see the supplementary materials for more details).

Over a period of a month and a half, baboons learned to discriminate dozens of words (the counts ranged from 81 words for baboon VIO to 308 words for baboon DAN) from among a total of 7832 nonwords at nearly 75% accuracy (Fig. 2 and table S1). This in itself is a remarkable result, given the level of orthographic similarity between the word and nonword stimuli. More detailed analyses revealed that baboons were not simply memorizing the word stimuli but had learned to discriminate words from nonwords on the basis of differences in the frequency of letter combinations in the two categories of stimuli

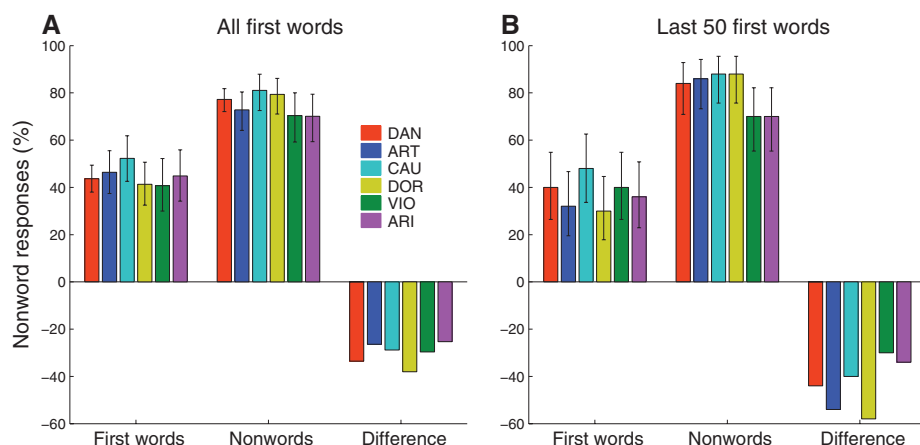


Fig. 3. Percentage of nonword responses on trials corresponding to words seen for the first time as compared to the first nonword stimuli after these particular trials. Performance on trials corresponding to the first presentation of words is of particular interest, because any divergence from performance to nonword stimuli is an indication that the baboons have learned general statistical properties of the two classes of stimuli. All six baboons showed such a divergence for both the total number of first word trials (A) and the last 50 first word trials (B), as revealed in the differences in the percentage of nonword responses to first words and nonwords (all P values < 0.01).

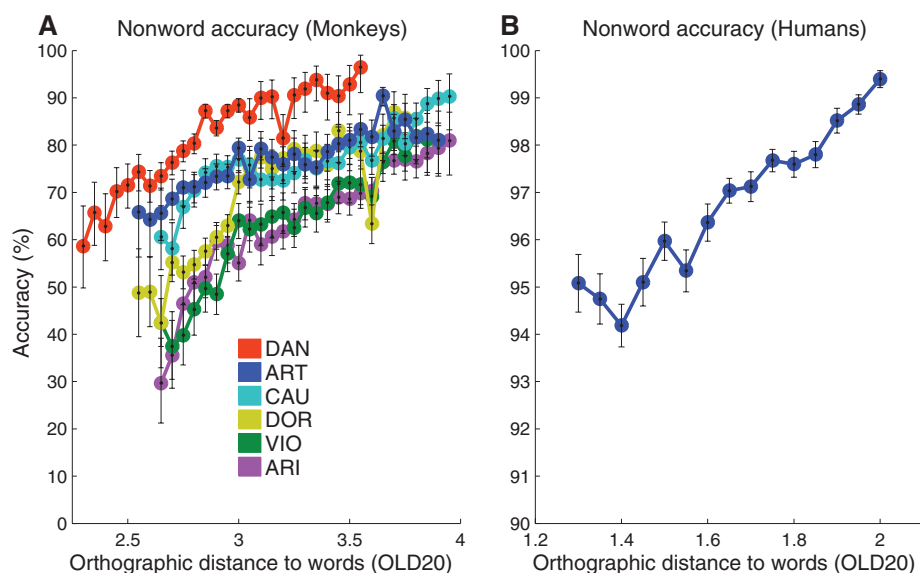


Fig. 4. Performance in response to nonwords depends on their orthographic similarity to learned words for both monkeys and humans. (A) For each of the last 20,000 nonword trials, the orthographic Levenshtein distance (OLD20) (15, 16) was computed between the corresponding nonword and each of the words learned at that time, separately for each baboon. The average accuracy corresponding to each unique value of OLD20 was then calculated. The graph shows that baboons responded less accurately to more wordlike nonwords (smaller OLD20 values). Error bars correspond to the 95% binomial confidence interval. (B) For comparison, humans show a similar sensitivity to orthographic distance to known words when responding to nonwords (see supplementary text).

(i.e., statistical learning). Indeed, there was a significant correlation between mean bigram frequency and word accuracy [correlation coefficients (r) ranged from 0.51 for baboon VIO to 0.80 for baboon DAN, all P values < 0.05 ; see supplementary materials]. More importantly, words that were seen for the first time triggered significantly fewer “nonword” responses than did the nonword stimuli (Fig. 3). This implies that the baboons had extracted knowledge about what statistical properties characterize words and nonwords and used this information to make their word versus nonword decision without having seen the specific examples before. In the absence of such knowledge, words seen for the first time should have been processed like nonwords. Figure 3 shows that this was clearly not the case.

Even more striking is the strong linear relation, shown in Fig. 4, between accuracy in response to nonword stimuli and their orthographic similarity to words that the baboons had already learned. The more similar a nonword was to a known word, the more false positive responses it produced. Orthographic similarity was measured with a standard edit distance used in information theory and computer science (15). For each nonword we counted the number of letter insertions, letter deletions, and letter substitutions required to transform the nonword into a known word, and we retained the average of the 20 lowest values as the OLD20 value of that nonword (16). Thus, the smaller the OLD20 value, the greater the orthographic similarity between the nonword and the set of known words. This standard measure of orthographic similarity was found to have a quasi-linear relationship with the accuracy of responses to nonwords [explained variance (R^2) ranged from 0.76 for baboon DOR to 0.91 for baboon VIO; see supplementary materials]. Exactly the same quasi-linear relationship was found in an analysis of the accuracy of human responses to nonwords in a large-scale lexical decision experiment (17). This finding implies that the baboons were sensitive to the orthographic characteristics of word and nonword stimuli in a way that mimics the sensitivity to orthographic similarity seen in skilled human readers.

Our results indicate that baboons were coding the word and nonword stimuli as a set of letter identities arranged in a particular order. Baboons had learned to discriminate different letters from each other (letter identity) and to associate those letter identities with positional information. Their coding of the statistical dependencies between position-coded letters is reflected in (i) their ability to discriminate novel words from nonwords (i.e., generalization), (ii) the significant correlation between bigram frequency and the accuracy of responses to words, and (iii) the increase in errors in response to nonword stimuli that were orthographically more similar to known words. Thus, our results support the conclusion that the baboons were computing an orthographic code in order to accurately discriminate words from nonwords. Prior linguistic knowledge is therefore not a necessary prerequisite in order to achieve humanlike orthographic processing.

Our findings have two important theoretical implications. First, they suggest that statistical learning is a powerful universal (i.e., cross-species) mechanism that might well be the basis for learning higher-order (linguistic) categories that facilitate the evolution of natural language (18, 19). Second, our results suggest that orthographic processing may, at least partly, be constrained by general principles of visual object processing shared by monkeys and humans. One such principle most likely concerns the use of feature combinations to identify visual objects (20), which would be analogous to the use of letter combinations in recent accounts of orthographic processing (4, 9, 21). Given the evidence that baboons process individual features or their combinations in order to discriminate visual objects (22), we suggest that similar mechanisms were used to distinguish words from nonwords in the current study. Our study may therefore help explain the success of the human cultural choice of visually representing words using combinations of aligned, spatially compact, ordered sequences of symbols. The primate brain might therefore be better prepared than previously thought to process printed words, hence facilitating the initial steps toward mastering one of the most complex of human skills: reading.

References and Notes

1. J. L. McClelland, D. E. Rumelhart, *Psychol. Rev.* **88**, 375 (1981).
2. S. Dehaene, *Reading in the Brain* (Penguin Viking, New York, 2009).
3. J. Grainger, A. M. Jacobs, *Psychol. Rev.* **103**, 518 (1996).
4. J. Grainger, J. C. Ziegler, *Front. Psychology* **2**, 54 (2011).
5. J. C. Ziegler, U. C. Goswami, *Psychol. Bull.* **131**, 3 (2005).
6. L. Cohen *et al.*, *Brain* **123**, 291 (2000).
7. S. Dehaene, L. Cohen, *Trends Cogn. Sci.* **15**, 254 (2011).
8. S. Dehaene, L. Cohen, *Neuron* **56**, 384 (2007).
9. S. Dehaene, L. Cohen, M. Sigman, F. Vinckier, *Trends Cogn. Sci.* **9**, 335 (2005).
10. K. Nation, *Q. J. Exp. Psychol.* **61**, 1121 (2008).
11. J. L. Fobes, L. E. King, in *Primate Behavior*, J. L. Fobes, J. E. King, Eds. (Academic Press, New York, 1982), pp. 219–243.
12. R. M. Seyfarth, D. L. Cheney, *Brain Lang.* **115**, 92 (2010).
13. J. Fagot, E. Bonté, *Behav. Res. Methods* **42**, 507 (2010).
14. Materials and methods are available as supplementary materials on Science Online.
15. V. I. Levenshtein, *Sov. Phys. Dokl.* **10**, 707 (1966).
16. T. Yarkoni, D. A. Balota, M. J. Yap, *Psychon. Bull. Rev.* **15**, 971 (2008).
17. E. Keuleers, P. Lacey, K. Rastle, M. Brysbaert, *Behav. Res. Methods* **44**, 287 (2012).
18. F. Ramus, M. D. Hauser, C. Miller, D. Morris, J. Mehler, *Science* **288**, 349 (2000).
19. J. R. Saffran, R. N. Aslin, E. L. Newport, *Science* **274**, 1926 (1996).
20. S. L. Brincat, C. E. Connor, *Neuron* **49**, 17 (2006).
21. C. Whitney, *Psychon. Bull. Rev.* **8**, 221 (2001).
22. C. Parron, J. Fagot, *Learn. Behav.* **38**, 374 (2010).

Acknowledgments: J.G. was supported by the European Research Council (ERC grant 230313). J.F. was supported by research grant Volet Exploratoire 2008 from the Provence regional council. This research was conducted at the Rousset-sur-Arc primate center (CNRS-UPS846), France. The authors thank its staff for technical support. Data are available at (dryad/science Supporting Online Material). J.G., J.F., and J.C.Z. conceived the study and designed the experiment; J.F., M.M., and S.D. implemented the experiment; S.D. analyzed the data; J.F. wrote the test program and conducted the experiment; J.G. wrote the first draft; and all authors contributed equally to latter versions of this article.

Supplementary Materials

www.sciencemag.org/cgi/content/full/336/6078/245/DC1
Materials and Methods
Supplementary Text
Tables S1 and S2
Reference (23)

19 December 2011; accepted 28 February 2012
10.1126/science.1218152

New Products

UV-VIS SPECTROPHOTOMETERS

The compact UV-2600 and UV-2700 UV-Vis spectrophotometers feature advanced optical systems and “Lo-Ray-Ligh” diffraction gratings. The new spectrophotometers substantially reduce stray light, enabling confident and convenient use for routine analysis and demanding research applications. With its double monochromator design and Lo-Ray-Ligh diffraction gratings, the UV-2700 achieves ultralow stray light of 0.00005%T at 220 nm. Its photometric performance range has been expanded to 8 Abs, with a transmittance value of 0.000001%. This eliminates the need to dilute samples and allows the measurement of low transmittance samples. Equipped with a single monochromator, the UV-2600 features a measurement wavelength range to 1,400 nm, using the ISR-2600Plus two-detector integrating sphere. This ultrawide range permits measurements in the near-infrared region, and expanded research of photovoltaics and other materials. The UV-2600 also features the Lo-Ray-Ligh gratings for high efficiency and low stray light levels.

Shimadzu Scientific Instruments

For info: 800-477-1227 | www.ssi.shimadzu.com



BENCHTOP XRD INSTRUMENT

The new fifth generation MiniFlex is a general purpose X-ray diffractometer that can perform qualitative and quantitative analysis of polycrystalline materials. MiniFlex is now available in two variations. Operating at 600 watts (X-ray tube), the MiniFlex 600 is twice as powerful as other benchtop models, enabling faster analysis and improved overall throughput. Running at 300 watts (X-ray tube), the new MiniFlex 300 does not require an external heat exchanger and thus requires even less space. The new MiniFlex delivers speed and sensitivity through innovative technology enhancements such as the optional D/teX Ultra high speed detector coupled with the new 600 W X-ray source. The optional graphite monochromator, coupled with the standard scintillation counter, maximizes sensitivity by optimizing peak-to-background ratios. If resolution is paramount, incident and diffracted beam slits can be selected to provide the desired resolution. For high sample throughput, MiniFlex is the only benchtop XRD system with an available sample changer.

Rigaku

For info: 281-362-2300 | www.rigaku.com

3-D HIGH CONTENT IMAGING PLATFORM

Designed for demanding high content assays and cell biology challenges, the new ArrayScan Infinity HCS Reader has 3-D imaging capability and features the latest in variable pin-hole confocal technology, solid-state LED illumination, live-cell and label-free capabilities, coupled with best-in-class image analysis and bioinformatics software. The instrument's integrated confocal module features the latest high speed Nipkow spinning disk technology and a variable pinhole to give finer control over image acquisition across a range of objectives (magnifications), compared to traditional confocal (fixed pin-hole) technology. The confocal module has a four-color LED Light Engine, bringing robust, laser-like performance without the complications and cost of lasers or the need for alignment of camera, confocal, and laser. The ArrayScan Infinity HCS Reader is also coupled with enhanced Thermo Scientific iDev Workflow software for multidimensional analysis. Multiple projection options for image analysis and the ability to save the stack of images to create 3-D movies enable complex 3-D structures to be imaged more clearly.

Thermo Fisher Scientific

For info: 800-432-4091 | www.thermoscientific.com

CRYOGENIC STORAGE RACK

The durably constructed, thick-walled Arctic Rack-24 is a new rack and cover that enables high integrity sample storage at ultralow (cryogenic) temperatures over extended periods of time. The Arctic Rack-24 is designed to accommodate 24 high volume (6.00 mL or 7.50 mL) Micronic storage tubes in an automation-friendly SBS footprint. A special cover enables the Arctic Rack-24 to be securely locked ensuring high sample security during transport or storage. The Arctic Rack-24 may be autoclaved several times providing considerable cost savings over consumable sample storage products. Absolute traceability and reproducibility on the Arctic Rack-24 are ensured through alphanumeric visual location aids and laser engraved barcodes on two sides of the rack plus rack foot mounting points. The open bottom design of the Arctic Rack-24 facilitates quick defrosting of samples. The Arctic Rack-24 with covers are stackable, enabling conservation of valuable storage space within freezers or during transport.

Micronic

For info: +31-320-277070 | www.micronic.com

MICROPLATE WASHER

The new 405 Touch Microplate Washer has a high resolution, LED backlit touchscreen interface that provides intuitive and flexible protocol creation and implementation and instrument maintenance, and supports all gloved environments. Additionally, two integrated flash drives enable convenient file storage, transfer, and operation. Instructional videos provide clear direction on instrument setup and basic use, and the context-sensitive help system, complete with recommendations, diagrams and images is available at the touch of a finger. The 405 Touch maintains the same features as the ELx405 washers, including 96- and 384-well compatibility, Dual-Action manifold, patent-pending Ultrasonic Advantage and vacuum filtration and biomagnetic separation for bead-based assays. All models include automated internal buffer switching, quick release manifolds, and optimized cell washing with gentle, low-flow rates ideal for loosely adherent cell monolayers. The 405 Touch is powered by Liquid Handling Control software, and can be coupled with the BioStack Microplate Stacker for unattended batch processing.

BioTek Instruments

For info: 888-451-5171 | www.biotek.com

Electronically submit your new product description or product literature information! Go to www.sciencemag.org/products/newproducts.dtl for more information. Newly offered instrumentation, apparatus, and laboratory materials of interest to researchers in all disciplines in academic, industrial, and governmental organizations are featured in this space. Emphasis is given to purpose, chief characteristics, and availability of products and materials. Endorsement by *Science* or AAAS of any products or materials mentioned is not implied. Additional information may be obtained from the manufacturer or supplier.

Over 7000 antibodies to popular pathways ►

Autophagy



Atg3
Cat.#: 3580-1

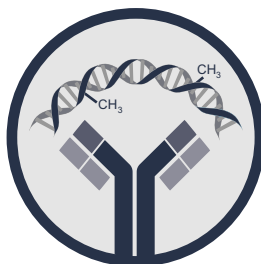


Atg5
Cat.#: 3167-1

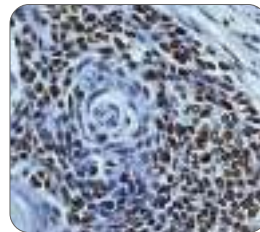


AMPK Alpha 1 (pS487)
Cat.#: 2802-1

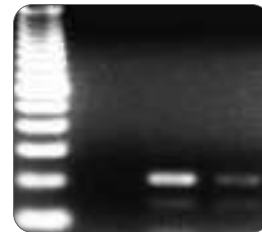
Epigenetics



Histone H3 (pS10)
Cat.#: 1173-1

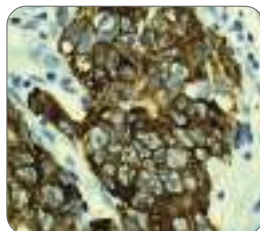
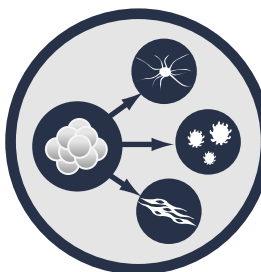


Histone H4 (K8)
Cat.#: 1796-1

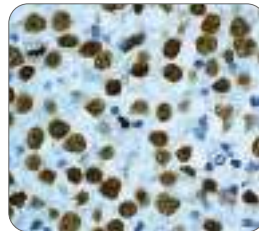


5-Methylcytosine
Cat.#: 3913-1

Stem Cells



LIN28A
Cat.#: 3533-1



Nanog
Cat.#: 3369-1



SOX2
Cat.#: 2683-1



View over 30 interactive pathway maps @ www.epitomics.com/pathways



Antibody Satisfaction Guarantee

www.epitomics.com

US & Canada | 1-877-772-2622
Outside NA | 650-583-6688
info@epitomics.com



PNAS Congratulates **2011** Cozzarelli Prize Recipients

The *Proceedings of the National Academy of Sciences* (PNAS) has selected six outstanding articles for the 2011 Cozzarelli Prize, in recognition of their scientific excellence and originality. Winners were selected from the 3,500 research articles published in PNAS in 2011 and represent exceptional contributions to the six broadly defined classes under which the National Academy of Sciences is organized.

2011 Cozzarelli Prize Recipients

CLASS I: PHYSICAL AND MATHEMATICAL SCIENCES

Microaerobic steroid biosynthesis and the molecular fossil record of Archean life

Jacob R. Waldbauer, Dianne K. Newman, and Roger E. Summons
(2011) PNAS 108:13409–13414

CLASS II: BIOLOGICAL SCIENCES

Mild hyperthermia inhibits homologous recombination, induces BRCA2 degradation, and sensitizes cancer cells to poly (ADP-ribose) polymerase-1 inhibition

Przemek M. Krawczyk, Berina Eppink, Jeroen Essers, Jan Stap, Hans Rodermond, Hanny Odijk, Alex Zelensky, Chris van Bree, Lukas J. Stalpers, Marrije R. Buist, Thomas Soullié, Joost Rens, Hence J. M. Verhagen, Mark J. O'Connor, Nicolaas A. P. Franken, Timo L. M. ten Hagen, Roland Kanaar, and Jacob A. Aten
(2011) PNAS 108:9851–9856

CLASS III: ENGINEERING AND APPLIED SCIENCES

The Voronoi Implicit Interface Method for computing multiphase physics

Robert I. Saye and James A. Sethian
(2011) PNAS 108:19498–19503

CLASS IV: BIOMEDICAL SCIENCES

Masking the 5' terminal nucleotides of the hepatitis C virus genome by an unconventional microRNA-target RNA complex

Erica S. Machlin, Peter Sarnow, and Selena M. Sagan
(2011) PNAS 108:3193–3198

CLASS V: BEHAVIORAL AND SOCIAL SCIENCES

The long shadow cast by childhood physical and mental problems on adult life

Alissa Goodman, Robert Joyce, and James P. Smith
(2011) PNAS 108:6032–6037

CLASS VI: APPLIED BIOLOGICAL, AGRICULTURAL, AND ENVIRONMENTAL SCIENCES

Conditions associated with protected area success in conservation and poverty reduction

Paul J. Ferraro, Merlin M. Hanauer, and Katharine R. E. Sims
(2011) PNAS 108:13913–13918

Mix it up.

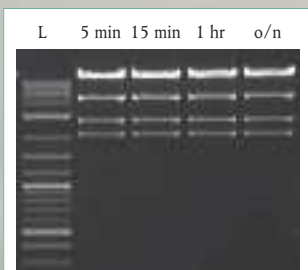
RE-Mix[™] Restriction Enzyme Master Mixes

Restriction enzyme digests are now even easier! The same high quality restriction enzymes that you have come to trust from New England Biolabs are now available in master mix format, including enzyme, buffer and loading dye; simply add your DNA and digest.

With RE-Mix Master Mixes take advantage of:

- Simplified and shortened protocols
- Fast digestion in 15 minutes (Time-Saver qualified)
- High product quality with reproducible results

RE-Mix Master Mixes – just add your DNA and mix



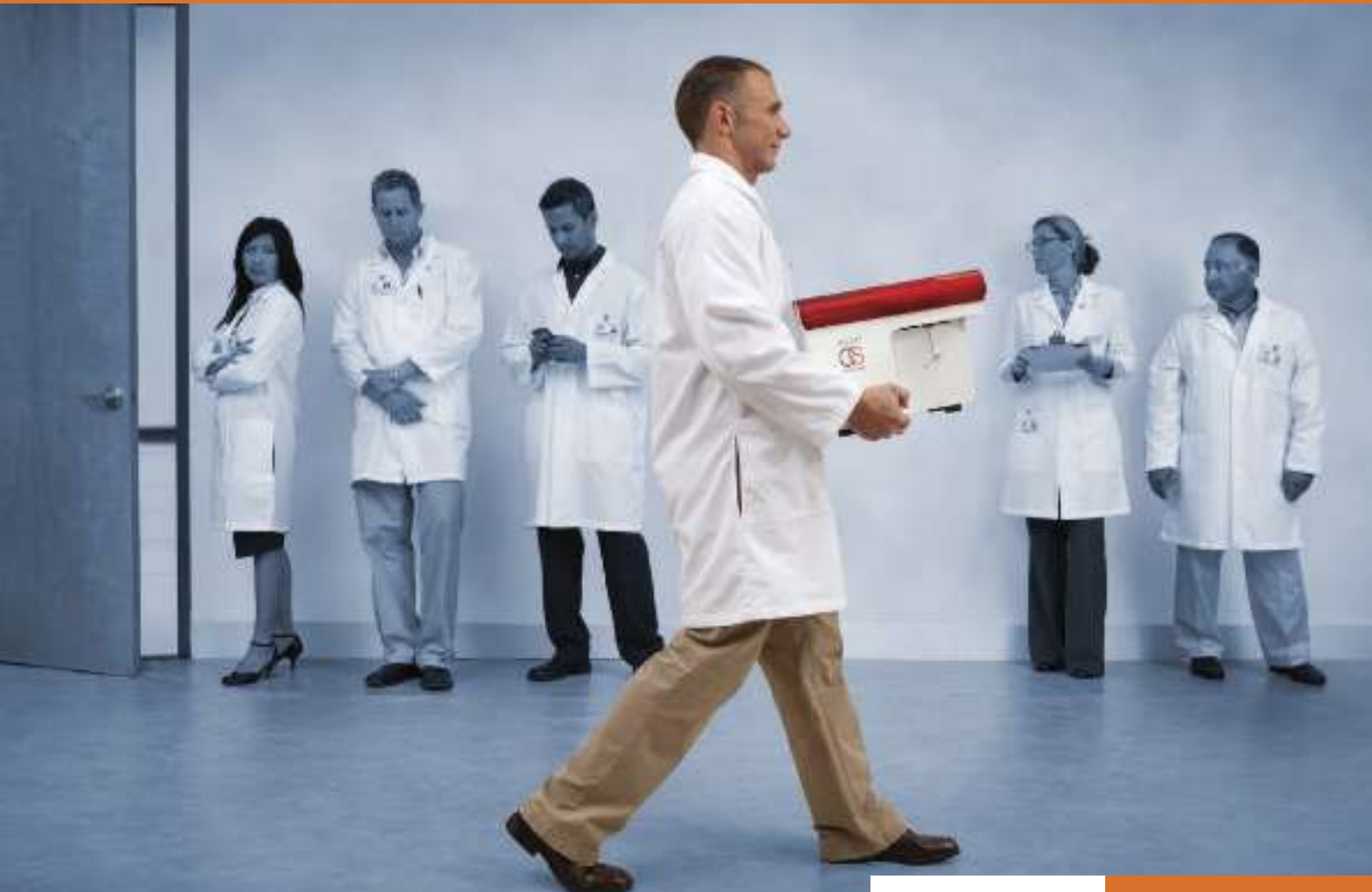
pXba DNA was digested with EcoRV-HF[™] RE-Mix[™] according to the recommended protocol. Lane L is the TriDye[™] 2-Log DNA Ladder (NEB #N3270). The same results are obtained whether incubated for 5–15 minutes, 1 hour or overnight.

GTAGCCT
TCUTGAAT
AGTITC
GTOUTT
GACTACG

To experience the new restriction enzyme challenge from NEB, visit www.NEBcutitout.com

For more information, visit
www.NEBREMIX.com

The BD Accuri™ personal flow cytometer



Flow cytometry within reach.™



The BD Accuri™ Cytometer is a personal flow cytometer that puts flow cytometry within reach. It gives you 4-color cell analysis in an affordable, transportable, and easy-to-use format.

Measuring just 11 x 14.75 x 16.5 inches (27.9 x 37.5 x 41.9 centimeters) and weighing just 30 pounds (13.6 kilograms), the BD Accuri Cytometer gives both novice and experienced researchers the power of multicolor analysis, when and where you need it. The software's intuitive interface guides you through workflows, making it easy to begin collecting and analyzing data—even if you have little flow cytometry knowledge or know-how.



Helping all people
live healthy lives

Setup and maintenance are also simplified to increase availability and up-time. In the event service is required, just pack up the system and return it. A loaner system will be provided while your system is serviced.

For more information about how you can more easily access the power of flow cytometry in your lab, visit bdbiosciences.com/go/accuri.

Flow cytometry within reach.™



Reagent Proteins

A DIVISION OF Pfenex Inc.

source

Go to the



The Protein Source

Reagent Proteins is *the source* for high quality reagent, pre-clinical and cGMP proteins.

Order now to experience cost-effective, rapid delivery of high quality proteins to enable your R&D efforts.

Vaccine Components
Bacterial and Viral Antigens
Cytokines
Chemokines
Growth Factors
Antibodies
Custom Reagents

Visit our website for a complete listing of over 5,000 high quality reagent proteins, specialized products and vaccine components.



Reagent Proteins

A DIVISION OF Pfenex Inc.

phone 858 • 352 • 4400

reagentproteins.com

fax 858 • 352 • 4602

Quantify, verify,

In science there are always essential steps in any workflow. Accurate measurements of DNA, RNA and protein samples are critical for confidence in qPCR, sequencing, microarrays or bioproduction, but there's a better alternative to the time and complexity of conventional methods. Using minimal sample (0.5 – 2.0 μ L), **Thermo Scientific NanoDrop** instruments make concentration and purity analysis so incredibly easy, and so much faster, you won't notice this step on the way to your ultimate discovery.

simplify

• Realize the difference.
Try any NanoDrop instrument for FREE.
www.thermoscientific.com/nanodrop



NEW!

NanoDrop™ Lite
Basic microvolume
measurements



NanoDrop™ 2000C
Full-spectrum microvolume
and cuvette measurements
in a single instrument



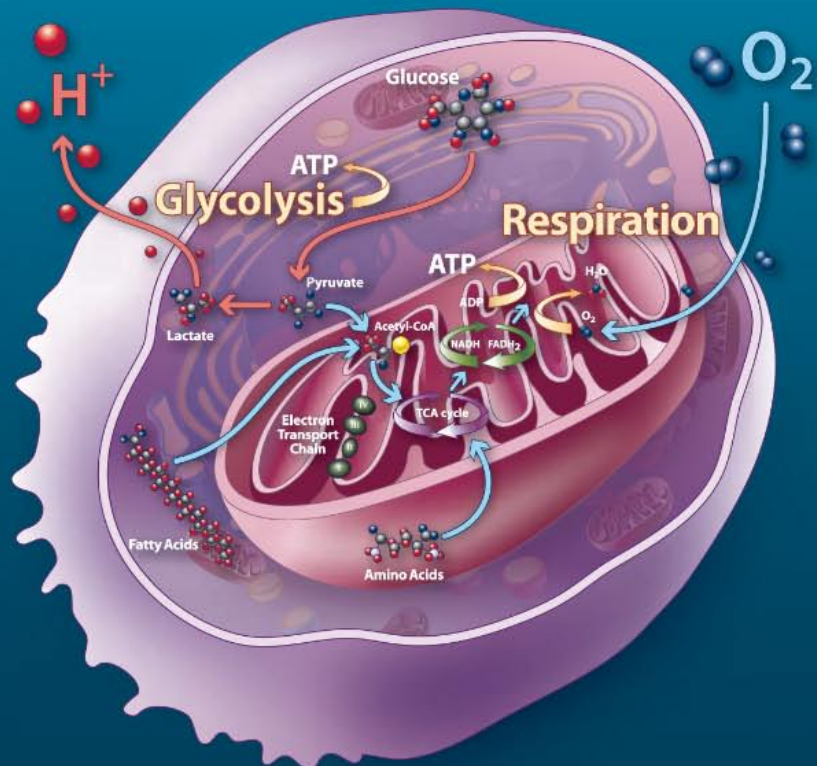
NanoDrop™ 2000
Full-spectrum microvolume
measurements



NanoDrop 8000
Higher throughput, full-spectrum
microvolume measurements



NanoDrop 3300
Full-spectrum microvolume
fluorescence measurements



Develop a new understanding of THE ROLE OF MITOCHONDRIAL DYSFUNCTION in cancer and age-related diseases



The Seahorse XF Extracellular Flux Analyzer

The XF Analyzer, and XF Stress Test Kits, make cellular bioenergetic studies simple, efficient and user-friendly. The first new in vitro metabolic measurement in 50 years, XF Analyzers non-invasively profile the metabolic activity of cells in minutes, offering scientists a physiologic cell based assay for determination of basal oxygen consumption, glycolysis rates, ATP turnover and respiratory capacity in a single experiment to assess mitochondrial dysfunction.



See what's possible.

Scan this QR code to view videos and see what the XF Analyzer can achieve.
Visit www.seahorsebio.com/science for more information!

Seahorse Bioscience



FASEB

Federation of American Societies
for Experimental Biology

Proudly celebrating 100 years of service to the biological and biomedical sciences community

Stand Up for Science!

We Support Scientists By:

- Advocating for funding for biological research
- Advancing policies that facilitate research and reduce regulatory burden
- Improving the environment for science training and education

FASEB, the voice of biological and biomedical researchers, represents 26 scientific societies and over 100,000 scientists and engineers.

Join our e-Action Alert

Help us communicate with Congress on key research issues by visiting www.faseb.org/StandUp to join our e-Action list and keep up with the latest policy news.

Join a FASEB Member Society

Benefits include reduced fees for scientific meetings, conferences, and journals; access to continuing education, professional development and career resources; and opportunities to contribute to science policy, advocacy, and public education.

The American Physiological Society
American Society for Biochemistry and Molecular Biology
American Society for Pharmacology and Experimental Therapeutics
American Society for Investigative Pathology
American Society for Nutrition
The American Association of Immunologists
American Association of Anatomists
The Protein Society

Society for Developmental Biology
American Peptide Society
Association of Biomolecular Resource Facilities
The American Society for Bone and Mineral Research
American Society for Clinical Investigation
Society for the Study of Reproduction
Teratology Society
The Endocrine Society
The American Society of Human Genetics

Environmental Mutagen Society
International Society for Computational Biology
American College of Sports Medicine
Biomedical Engineering Society
Genetics Society of America
American Federation for Medical Research
The Histochemical Society
Society for Pediatric Research
Society for Glycobiology

PICTURE YOURSELF AS A AAAS SCIENCE & TECHNOLOGY POLICY FELLOW

Make a Difference.

Help give science a greater voice in Washington, DC! Since 1973, AAAS Fellows have applied their skills to federal decision-making processes that affect people in the U.S. and around the world, while learning first-hand about the government and policymaking.

Join the Network.

Year-long fellowships are available in the U.S. Congress and federal agencies. Applicants must hold a PhD or equivalent doctoral-level degree in any behavioral/social, biological, computational/mathematical, earth, medical/health, or physical science, or any engineering discipline. Individuals with a master's degree in engineering and three years of post-degree professional experience also may apply. Federal employees are not eligible and U.S. citizenship is required.

Apply.

The application deadline for the 2013-2014 AAAS Fellowships is 5 December. Fellowships are awarded in the spring and begin in September. Stipends range from \$74,000 to \$97,000.

Note: Additional fellowships are available through approximately 30 scientific society partners. Individuals are encouraged to apply with AAAS as well as with any scientific societies for which they qualify.

Full details at: **fellowships.aaas.org**



*Enhancing Public Policy,
Advancing Science Careers*

Sabrina McCormick, PhD

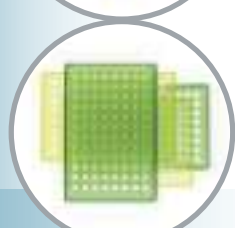
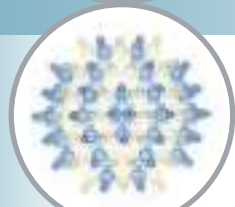
Sociology and Environmental
Sciences, Brown University

2009-11 S&T Policy Fellow,
Environmental Protection
Agency, Office of Research
and Development

Now president,
Evidence Based Media



ADVANCING SCIENCE. SERVING SOCIETY



eppendorf® and eppendorf Biopur® are registered trademarks of Eppendorf AG.
All rights reserved, including graphics and images.

Absolute Certainty!

Get peace of mind with Eppendorf

Experience peace of mind with Eppendorf
guaranteed quality and order your free sample
on www.eppendorf.com/consumables

Don't leave your results to chance –
count on Eppendorf consumables

- Unique features to make every day routines faster and easier
- Minimized risk of chemical leaching from our consumables
- Purity grades tailored to even the highest requirements

eppendorf
In touch with life



8 trusted brands. 600,000 citations. lifetechnologies.com

One curated website to easily find what you need

Now you can find all the products you need from the most cited brands on one website, as well as through our automated Supply Centers and B2B catalogs. Choices to suit how you prefer to buy.

lifetechnologies.com



©2012 Life Technologies Corporation. All rights reserved. The trademarks mentioned herein are the property of Life Technologies Corporation or their respective owners. TaqMan® is a registered trademark of Roche Molecular Systems, Inc., used under permission and license. C025005 0312

Invitrogen™

Applied Biosystems®

Gibco®

Molecular Probes®

Novex®

TaqMan®

Ambion®

Ion Torrent™



Expanding research on a shrinking budget

Introducing the QuantStudio™ 12K Flex system, the only all-in-one real-time PCR solution designed to scale with your lab. With five interchangeable thermal blocks supporting a variety of TaqMan® and SYBR® Assays, the system allows you to analyze from 1 to over 12,000 data points per run in the format that's right for your project. For ultimate flexibility and gold-standard performance in a single instrument, it's a perfect fit.

Expand your research at lifetechnologies.com/quantstudio

LOCATION: Jackson Park Health Club
ARTICLE: *An Electronic Second Skin*
DATE: Sep 21, 7:43am

LOCATION: University Faculty Lounge
ARTICLE: *The Visual Impact of Gossip*
DATE: Sep 21, 4:22pm

LOCATION: Gyro King
ARTICLE: *Cavemen Craved Carbs, Too*
DATE: Sep 21, 1:13pm

LOCATION: Hemlock Bar
ARTICLE: *Quantum Simulation of Frustrated Classical Magnetism in Triangular Optical Lattices*
DATE: Sep 21, 9:21pm

LOCATION: Bed
ARTICLE: *Consciousness: What, How and Why*
DATE: Sep 21, 10:56pm



A new way to look at science

The new *Science* Reader app for iPad® from AAAS puts *Science* in your hands, wherever you go. Read abstracts, career advice, and highlights from our newest journals, *Science Signaling* and *Science Translational Medicine*. Plus, AAAS members can access full text articles from *Science*. Visit [iTunes App StoreSM](#) or content.aaas.org/ipad for details.



Research can cost millions of dollars.

Fortunately, you could save right now with GEICO'S SPECIAL DISCOUNT.

Get a free quote.

GEICO®

1-800-368-2734

geico.com/sci/aaas



Mention your AAAS membership to see how much you could save.

Some discounts, coverages, payment plans and features are not available in all states or all GEICO companies. Discount amount varies in some states. One group discount applicable per policy. Coverage is individual. In New York a premium reduction may be available. GEICO is a registered service mark of Government Employees Insurance Company, Washington, D.C. 20076; a Berkshire Hathaway Inc. subsidiary. © 2012 GEICO

LAMBDA DG-4/DG-5 PLUS

High Speed
Wavelength Switcher

This complete illumination system with improved digital servo technology allows 30% greater light output and switching times of up to 0.5msec. The unique optical design uses modern interference filters, providing integral blocking characteristics 1000 times better than typical monochromators.

FEATURES

- Complete system for wavelength switching
- Switches in 0.5msec
- Integral shuttering
- Integral neutral density filtering
- Two outputs for monitoring filter position
- Turbo blanking
- Video sync pulsed ring buffer

SUTTER INSTRUMENT

PHONE: 415.883.0128 | FAX: 415.883.0572
EMAIL: INFO@SUTTER.COM | WWW.SUTTER.COM

Produced by the Science/AAAS Custom Publishing Office

LIFE SCIENCE TECHNOLOGIES

Innovation in Japan Results from Reforms

In This Issue

Japanese academic reforms over the last decade have encouraged entrepreneurship and technology transfer from universities to industry. These reforms are now yielding results. Science and business leaders hope these changes push Japan into the next phase of innovation development, with increased flexibility and transparency, a more global focus, and more national and international collaboration. Although recovery and reconstruction are priorities, the long-term goals of developing sustainable energy sources and solving the health challenges of an aging population continue to be major focus areas.

See full story on page 245.

Upcoming Features

Proteomics: Protein Chip Arrays—May 11

Digital Imaging—June 8

Nanotechnology—July 6

Innovation in Japan

Results from Reforms

Japanese academic reforms over the last decade have encouraged entrepreneurship and technology transfer from universities to industry. These reforms are now yielding results. Science and business leaders hope these changes push Japan into the next phase of innovation development, with increased flexibility and transparency, a more global focus, and more national and international collaboration. Japanese scientists are ready. After delays caused by the March 2011 triple disaster of earthquake, tsunami, and nuclear power plant failure, the lights are on again in Japanese research laboratories. Although recovery and reconstruction are priorities, the long-term goals of developing sustainable energy sources and solving the health challenges of an aging population continue to be major focus areas. **By Chris Tachibana**

“We have many good engineers working on photovoltaics. And people are even more concerned about energy after the Fukushima nuclear power plant disaster.”

The Japanese government wants practical, globally useful applications from its science programs, and the sooner the better. “We intend to have societal or economic impact more clearly and more quickly—that is our aim,” says Michiharu Nakamura, president of the **Japan Science and Technology Agency (JST)**, an independent organization within the **Ministry of Education, Culture, Sports, Science and Technology (MEXT)**. “We’re trying to find new capabilities from basic research as soon as possible, and transfer technology sooner.”

Using science and technology to address societal challenges is the theme of the Fourth Basic Plan for Science and Technology, a roadmap for Japanese science in 2011–2015 from Japan’s Council on Science and Technology Policy. The plan was passed by the Japanese cabinet in August 2011 after revisions to include reconstruction and recovery strategies for the March 2011 earthquake and its consequences. However, a core focus on addressing the need for sustainable energy and the medical issues of an aging population remains unchanged. The sense that science and technology could drive a return to global economic competitiveness is clear.

“Japan is moving toward exploiting innovations more efficiently, and the earthquake is not going to stop that,” says Richard B. Dasher. He is director of the **Stanford University US-Asia Technology Management Center** and knows both Japan and earthquakes. He was the first non-Japanese person in senior university governance, at Tohoku University, and remembers the decade of rebuilding at Stanford after the 1989 Loma Prieta earthquake. Dasher says true innovation means bringing an idea into real-world practice, but turning a research breakthrough into a global application requires the combined efforts of industry and university research, typically funded by the government. However, after World War II, Japanese universities and industry had an aloof relationship. Industry researchers maintained personal

contacts with their former university mentors, but professors were civil employees, which limited their entrepreneurial possibilities and hindered technology transfer. Until recently, funding for academics and industry was siloed in separate government agencies, MEXT and the Ministry of Economy, Trade and Industry (METI). However, a 1998 law created technology-licensing organizations—essentially technology transfer departments—to move basic research results into applications. In 2004, a change in intellectual property law freed professors to start companies. Educational and research institutions, industry, and government are still adjusting, but Dasher believes Japan is on the brink of a more mature phase in innovation development, saying, “It feels like a glacier about to calve: you can see the cracks and splits and see it is just about to go.”

THE NEW INNOVATION MODELS

Satoshi Kawata is a professor at **Osaka University** and director of the Photonics Advanced Research Center, and a chief scientist at **RIKEN**, a MEXT research institute. He took advantage of the new laws to found **Nanophoton**, with 13 full-time employees, including eight Ph.D.s. Nanophoton produces laser Raman microscopes, which generate images based on energy shifts that occur in laser photons when they interact with molecular bonds. The technique identifies molecules based on distinct laser-scattering patterns and creates images of biological **continued>**

UPCOMING FEATURES

Proteomics: Protein Chip Arrays—May 11

Digital Imaging—June 8

Nanotechnology—July 6

Astellas Pharma-Kyoto University Project (the AK Project)

The Center for Innovation in Immunoregulative Technology and Therapeutics

Supported by the “Formation of Innovation Center for Fusion of Advanced Technologies Program”

“The Center for Innovation in Immunoregulative Technology and Therapeutics (AK Project)” established in 2007 by Kyoto University and Astellas Pharma and supported by the Ministry of Education, Culture, Sports, Science and Technology (MEXT) aims to make innovative therapeutics to overcome intractable diseases in immunology area, that is, allergy, autoimmune diseases, chronic inflammation, cancer and infection. We have the Fusion Laboratory in Kyoto University Medical School Campus, where 16 young principal investigators work independently under the leadership of three key researchers, Professors Shuh Narumiya, Nagahiro Minato and Shimon Sakaguchi. A prominent feature of the AK Project is integration of clinical science in drug discovery and development. To synergize each expertise interdisciplinary, basic scientists, clinicians and Astellas scientists form clusters in the Fusion Laboratory for each of target diseases. They share clinical information and sample, knowledge of molecular mechanism and drug discovery skills. Our purpose in the project is to carry out excellence of science and drug discovery at the same time, which is facilitated by IP managers of the AK Project. We have successfully discovered 15 drug targets, filed 19 patent applications and published more than 150 scientific papers in four years. We welcome participation of young scientists in our Project.



Best Drugs on Best Science



Contact: E-mail: akpro@ak.med.kyoto-u.ac.jp URL: <http://www.ak.med.kyoto-u.ac.jp/>

Medical Innovation Center at Kyoto University School of Medicine

~Opportunities to Open Innovation for Drug Discovery~

The Kyoto University Medical Innovation Center (MIC) established in 2010 offers the pharmaceutical company an opportunity for a one-to-one institution-level collaboration for drug discovery and development in a specific disease area. MIC aims to identify drug targets that are truly useful in clinical practice, using various technology platforms to analyze the highly accurate patient information and clinical samples available through the university's medical school and university hospital, and linking the clarification of the basic structure and mechanism of living organisms—a tradition at the Kyoto University Medical School—with the analysis of human disease mechanisms. Under our alliance with a company, we assign appropriate professor(s) of our Medical School as a project leader, recruit young distinguished scientists worldwide, and provide a laboratory where basic medical scientists, company scientists and clinicians work together by sharing clinical samples and information and the company's technology for drug discovery. We can also conduct Phase I and IIa clinical trials for proof of concept at the Translational Research Center of our hospital. Each project is managed under the equal partnership between academia and company, and scientific inputs, outputs, knowledge and intellectual properties are shared with both parties. In addition to the forgoing AK Project, we started three projects of alliance with Japanese pharmaceutical companies in 2011 at MIC; the TK Project with Takeda Pharmaceuticals on obesity and schizophrenia, the DSK Project with Dainippon-Sumitomo Pharmaceuticals on cancer, and the TMK Project with Mitsubishi-Tanabe Pharmaceuticals on chronic kidney disease. We welcome proposals from any pharmaceutical companies on new areas.



MIC building will be completed in March, 2013, supported by the Ministry of Economy, Trade and Industry (METI).



Contact: The Office of Promotion for Medical Innovation

E-mail: kumbl-mi@office.med.kyoto-u.ac.jp URL: <http://www.med.kyoto-u.ac.jp/mic/>



The WPI-AIMR Main Building



The 2012 WPI-AIMR Annual Workshop

WPI-Advanced Institute for Materials Research **ADVANCING MATERIALS TO BUILD A BETTER FUTURE**

The top-class international researchers at WPI-AIMR are adding new dimensions to the rapidly growing field of materials science – developing innovative functional materials and devices.

WPI-AIMR was established at Tohoku University in 2007 under the Japanese Ministry of Education, Culture, Sports, Science and Technology (MEXT)' s World Premier International Research Center Initiative (WPI).

The interdisciplinary research vigorously conducted there is based on atomic and molecular control.

Currently, interdisciplinary fusion research is accelerated with mathematics as a catalyst so as to elucidate common principles.



New Director From April 2012 Motoko Kotani

Mathematician; leader of the interdisciplinary research between math and materials science in Japan.

**WPI-AIMR
Research Groups**

- Bulk Metallic Glasses (BMG)
- Materials Physics
- Mathematics
- Soft Materials
- Device /System

**WPI-AIMR
Tohoku University**

Administrative Office : wpi-int@wpi-aimr.tohoku.ac.jp
<http://www.wpi-aimr.tohoku.ac.jp/>

Open Positions : <http://www.wpi-aimr.tohoku.ac.jp/en/modules/staff/>

NO PERMIT REQUIRED



COSMO BIO CO., LTD.
Inspiration for Life Science



NON-RADIOACTIVE

2DG Glucose Uptake Assay

Sensitive, accurate, and safe measurement of glucose uptake (2DG) by cultured cells is now available to any laboratory. No radiation permit required !
The Glucose Uptake Assay Kit from Cosmo Bio features:

- Picomole sensitivity
- Advanced recycling enzymatic amplification
- Photometric detection (420nm)
- No wash, automation friendly assay protocol
- Optimized for 96-well culture plates
- Needs no correction for extracellular 2DG



New •

www.cosmobio.com

Innovation in Japan

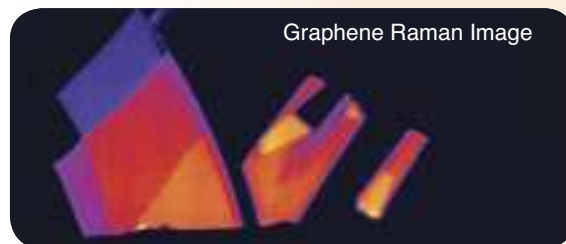
samples that show both structure and molecular composition. Nanophoton's microscopes are used in pharmaceutical research to study small molecules and in materials science to analyze polymers and semiconductors.

A recent collaboration with Mikiko Sodeoka, chief scientist and director of the Synthetic Organic Chemistry Laboratory, RIKEN Advanced Science Institute, and director of the JST ERATO Live Cell Chemistry Project shows the technique's potential. In a 2011 *Journal of the American Chemical Society* article, the group showed that an alkyne—just two carbon atoms in a triple bond—acted as a Raman tag. The alkyne could replace bulky fluorescent tags or proteins currently used for imaging, whose large size can change the properties, localization, and function of smaller biomolecules. “We looked for a method using a tiny tag that does not affect the biological profile of the small molecule,” says Sodeoka. “We had the idea that we could detect the alkyne directly by Raman microscopy.” Putting an alkyne on a nucleotide analog allowed visualization of chromosomes in unfixed, unstained living cells without interference from untagged endogenous proteins and other biomolecules. Sodeoka says the ultimate goal is real-time continuous imaging, for example for detecting transient interactions between receptors and ligands.

Policy changes that encouraged professors to commercialize innovations are the reason his company exists, says Kawata, adding that he wants Nanophoton “to be an example of success.” Nanophoton, which rents space on campus, gives students hands-on entrepreneurial experience. “Students are happy to earn money here doing development, English translation, and product assembly rather than working at McDonald's, because they learn things about running a company,” says Kawata.

In contrast to Nanophoton's nano-sized innovation model is a collaboration between electronics and communications giant **Fujitsu** and the **University of Tokyo's Research Center for Advanced Science and Technology (RCAST)**. Their drug discovery project shows how the resources of a large industry partner can be applied to basic research. Drug discovery begins with a target protein that might be regulated through small molecule binding. For example, statin drugs bind and inhibit an enzyme in cholesterol production to lower blood cholesterol. Traditionally, small molecule drugs are found by wet-lab screening of chemical libraries for compounds that bind and regulate the target. This can be a hit-or-miss process that takes years. Sophisticated computer simulations can design molecules that interact with the target, accelerating this process and expanding candidate possibilities. However, they require tremendous computer power. In 2004, Fujitsu began efforts in information technology (IT)-based drug development, based on 20 years of creating computational chemistry software. In 2010, a supercomputer for IT-based drug discovery was built at RCAST.

The project is funded by Fujitsu, and its goals, says Shunji Matsumoto of the Fujitsu Bio-IT Business Development Unit, are “building the platform, training our team, and getting highly available compounds as drug candidates.” Fujitsu will have the intellectual property license for potential drug candidates. Matsumoto says that IT-based drug design requires supercomputer power because even highly specific compound-target interactions can be transient, dissociating in nanoseconds, and are complicated by the water-based physiological environ-



“We had the idea that we could detect the alkyne directly by Raman microscopy.”

ment. The Fujitsu-RCAST supercomputer overcomes these challenges by rapidly modeling thousands of compounds in various bound and unbound states to find the most promising candidates. The first targets of the project are in diabetes and cancer.

Academic-industry relationships are not new in Japan, although the old-school style is a professor handing off a basic research idea to a company. The new model, encouraged by JST and other funding agencies, is much more collaborative. An example is the AK project between **Astellas Pharma** and **Kyoto University**, started in 2007 and funded by MEXT and Astellas. The budget was 600 million yen (\$7.8 million) in the first three years, with 4 of 10 initial projects selected to continue with 1,400 million yen in support annually. Although Kyoto University's most famous discovery might be the 2006 publication of induced pluripotent stem (iPS) cells, immunology and antibody therapy have long been a research focus in Japan, particularly at Kyoto University. The AK project builds on this tradition. After just three years, the project had discovered 14 potential drug targets in B cell development, immune tolerance, and atopic dermatitis, and filed 18 patent applications.

Shuh Narumiya, professor of pharmacology and director of the Medical Innovation Center and the AK Project, Kyoto University Graduate School of Medicine, says that in addition to seeking scientific innovations, the project employs a novel research strategy for Japan, giving young investigators autonomy to try a variety of approaches. From the company side, the level of integration with the university is unusually extensive, says Toichi Takenaka, professor, Graduate School of Pharmaceutical Sciences, Chemical Biology, University of Tokyo, and Astellas Pharma president and board chair until his retirement in 2011. “The AK project has its own research laboratories on the medical school campus, with basic research scientists from the university and drug discovery scientists from Astellas working with clinical research scientists from clinical departments,” says Takenaka. He says advantages of the collaboration are fast decision-making, a focus on the most important projects, an uninterrupted pipeline from target discovery to drug development, and productive management of intellectual property.

FIGHTING CHERRY PICKING AND THE GALAPAGOS EFFECT

A problem with exclusive company-university partnerships such as the AK project or the Fujitsu-RCAST collaboration is that potential innovations are controlled by a single **continued**

Bringing...

Stem Cell

science & technology



Mesoscopic

science & technology

Shinya Yamanaka
Prof & CiRA Director



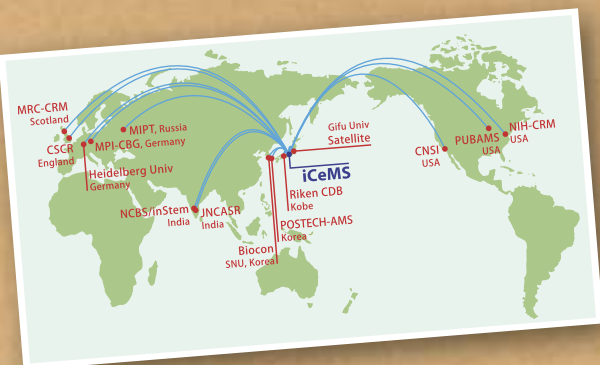
Director
Norio Nakatsuji



Deputy Director
Susumu Kitagawa



and a
growing network of global partners



the Institute for Integrated Cell-Material Sciences

at **Kyoto University**
in the cultural heart of Japan



...together in

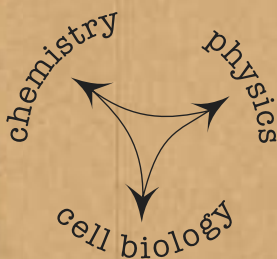
World-Class
facilities

& with...



World-Class
scientists

in an open, cross-disciplinary environment
with ample opportunities for
young researchers to collaborate
across borders & boundaries



Part of the Japanese science
ministry's World Premier
International Research Center
(WPI) Initiative

Find us at
www.icems.kyoto-u.ac.jp
and on Facebook, Twitter,
and YouTube



Innovation in Japan

FEATURED PARTICIPANTS

Astellas Pharma
www.astellas.us

Fujitsu
www.fujitsu.com/global

Japan External Trade Organization (JETRO)
www.jetro.org

Japan Science and Technology Agency
www.jst.go.jp/EN/index.html

Japan Society for the Promotion of Science
www.jsps.go.jp/english/index.html

Kyoto University
www.kyoto-u.ac.jp/en

Ministry of Education, Culture, Sports, Science and Technology (MEXT)
www.mext.go.jp/english

Nanophoton
www.nanophoton.jp/eng/index.html

Osaka University
www.osaka-u.ac.jp/en

RCAST, University of Tokyo
www.rcast.u-tokyo.ac.jp/en

RIKEN
www.riken.jp/eng/index.html

Sharp Solar
www.sharpsolar.com/SolarElectricity.aspx

Smart Solar International
www.smart-solar-inc.com

Stanford US-Asia Technology Management Center
www.asia.stanford.edu

company, which might develop only a few, rather than the range of applications possible from basic research, says Robert Kneller of RCAST, who has written extensively on this issue. Although Narumiya says the AK project allows outside licensing of intellectual property that Astellas is not interested in developing, Kneller says that exclusive partnerships tend to cut projects that don't show tangible results early, hindering blue-sky research that takes longer to develop. The arrangement results in cherry picking of a few ideas by industry. "Big companies might develop one aspect of a discovery, but not the full panoply of applications, and discoveries can get lost," says Kneller. Another issue in Japanese innovation is the Galapagos effect: discoveries are often adapted only for the island nation of 127 million people. Those that are successful globally—for example in electronics—are useful to other countries incidentally rather than by design.

Technology analysts think that both the limitations of exclusive partnerships and the Galapagos effect can be overcome if Japanese research and development embraces openness and flexibility. Changing the old attitudes and infrastructure might increase the productivity and efficiency of innovation development. Examples include encouraging job market mobility, foreign exchange programs, expanded interdisciplinary and international collaborations, and education in global entrepreneurial thinking.

A global technology field with a natural opening for Japan is photovoltaic cells, the units of solar panels that convert light energy into electricity. Renewable energy is needed worldwide and Japan has strengths in materials science and a commitment to green technology, with government support for sustainable energy development since the 1970s. More recently, the **Japan Society for the Promotion of Science**, an independent organization under MEXT that promotes scientific programs, gave \$40 million through its \$1.5 billion Funding Program for World-Leading In-

novative R&D on Science and Technology (FIRST) program to Hiroshi Segawa of RCAST for a project on photovoltaics that use organic molecules and polymers as light-absorbing components. These have a high capacity to absorb light, although they are currently less stable and less efficient than inorganic materials such as silicon.

Organic photovoltaics may or may not be the future, but solar energy remains a high priority in Japan, says Toshiro Matsuyama, who was the manager, Corporate Advanced Technology Planning Corporate Research and Development Group at **Sharp**. "We have many good engineers working on photovoltaics. And people are even more concerned about energy after the Fukushima nuclear power plant disaster," Matsuyama is currently technical advisor at **Smart Solar**, a three-year-old spin-off company from the University of Tokyo that is developing concentrated photovoltaic systems that convert optically concentrated solar light to electricity. Current solar energy systems tend to be made for huge spaces like U.S. deserts, or on a small scale, for Japanese rooftops. However, solar panels are a scalable technology, so Japanese advances can be applied to big systems. Japan could also lead in developing sophisticated, application-specific systems to optimize solar power use, says Matsuyama, because "extending the power from a rooftop to a household, or from a desert to a city is different. This is the direction solar is going, partly in developing materials, partly in how you use the power." Matsuyama says he hopes the next innovations come from Japan. The country has large corporations with a history of spending for decades, if necessary, to develop new technology, he says, citing Sharp's 30-year development of liquid-crystal display (LCD) television, starting with applying the technology to small-screen electronics.

TRANSFORMATIONS LEADING TO THE NEXT INNOVATION PHASE

The push to redefine industry-academic partnerships and increase technology transfer comes as the labor market is transforming. Unlike previous generations, young people no longer expect lifetime employment at a single institution. As Japan's population ages, the number of immigrant students and workers is expected to rise, which could add diversity and new ideas to research and corporate teams. This feels unsettling, but is ultimately beneficial, says Stanford's Dasher, who thinks research and development in Japan "has been a little too stable. We should see changes over the next 10 to 20 years as pressure for these changes is applied."

For those seeking calm after the 2011 disasters though, Kenichi Kawamoto, executive director of the **Japanese External Trade Organization (JETRO)** New York has a reassuring message. "The earthquake was a tragic event," he says, "but I'm proud of the Japanese people for recovering quickly. It shows that they should be confident that they can make a contribution to the global market and society." The earthquake itself might have created the path for these contributions. Says JST's Nakamura, "We received very warm sympathy and support from other countries. We will never forget that support."

Chris Tachibana is a science writer based in Seattle, USA, and Copenhagen, Denmark.

DOI: 10.1126/science.opms.p1200064



INTERNATIONAL INSTITUTE FOR CARBON-NEUTRAL ENERGY RESEARCH

The International Institute for Carbon-Neutral Energy Research (I²CNER) at Kyushu University, Japan is actively seeking candidates for open-rank faculty and post-doctoral research associates.

OUTLINE

The International Institute for Carbon-Neutral Energy Research (I²CNER) is a member of the World Premier International Research Center Initiative established by the Japanese Ministry of Education, Culture, Science and Technology (MEXT). Faculty members and researchers associated with I²CNER are dedicated to the Institute's mission to contribute to the creation of a sustainable and environmentally friendly society by advancing fundamental science to reduce CO₂ emissions and the realization of a hydrogen economy. The ITO Campus of the Kyushu University houses extensive state-of-the-art experimental and computational facilities.

QUALIFICATIONS & CURRENT OPENINGS

All faculty members are expected to initiate and sustain vigorous research programs that both advance and are relevant to the I²CNER's mission. Candidates for senior faculty positions must have achieved national and international recognition for their research accomplishments. Post-doctoral research associates will join research groups relevant to their field of expertise and education.

1. I²CNER is seeking candidates with experimental or computational expertise in the physics, chemistry, mechanics, and materials science aspects of:
 - Hydrogen embrittlement (Mechanics, Fatigue and Fracture, Materials, Tribology)
 - Chemistry for efficient material transformation
 - Basic science issues underlying CO₂ separation/concentration
 - Applied (and/or basic) science issues underlying geologic/sub-seabed/ocean CCS (CO₂ capture and storage)
 - Thermophysical properties, heat and mass transfer, thermal engineering for highly efficient energy utilization
 - Solar/Chemical hydrogen production (including steam electrolysis)
2. I²CNER is also accepting applications in the Energy Analysis research area. Emphasis will be given to the potential costs and use of low carbon energy systems to meet the future energy demand.

REQUIRED APPLICATION MATERIALS*

1. Cover Letter
2. Application Form (located on website)
3. Curriculum vitae that details research experience and interests
4. Research Proposal
 - a. NOTE: Proposal templates vary depending upon interest area. Specifically, use template #1 for all interest areas except Energy Analysis and #2 for Energy Analysis.
5. List of publications
 - a. Separate lists for refereed journal and conference proceedings.
6. Names and contact information of four references

****All materials must be submitted in English.***

SALARY & STARTING DATE

Salary will be commensurate with qualifications and experience. The starting date will be as soon as possible after the closing date.

APPLICATION DEADLINE

- Wednesday, June 6, 2012, 17:00 (Japan)
- Interviews may take place prior to closing date; however, no final decisions will be made until after this time.

APPLICATION SUBMISSION

Please email your application via email attachment to: **wpi-office@i2cner.kyushu-u.ac.jp**

QUESTIONS?

Please contact the I²CNER Administrative Office at: **wpi-office@i2cner.kyushu-u.ac.jp**

International Institute for Carbon-Neutral Energy Research (I²CNER)
Kyushu University
744 Motoooka, Nishi-ku, Fukuoka
Postal Code 819-0395, JAPAN
TEL: +81-(0)92-802-6932 FAX: +81-(0)92-802-6939

FOR MORE INFORMATION

<http://i2cner.kyushu-u.ac.jp/en/recruit/recruit.php>

Kyushu University is an Equal Opportunity/Affirmative Action Employer. The administration, faculty and staff embrace diversity and are committed to attracting qualified candidates who also embrace and value diversity and inclusivity.

New Products

UV-VIS SPECTROPHOTOMETERS

The compact UV-2600 and UV-2700 UV-Vis spectrophotometers feature advanced optical systems and “Lo-Ray-Ligh” diffraction gratings. The new spectrophotometers substantially reduce stray light, enabling confident and convenient use for routine analysis and demanding research applications. With its double monochromator design and Lo-Ray-Ligh diffraction gratings, the UV-2700 achieves ultralow stray light of 0.00005%T at 220 nm. Its photometric performance range has been expanded to 8 Abs, with a transmittance value of 0.000001%. This eliminates the need to dilute samples and allows the measurement of low transmittance samples. Equipped with a single monochromator, the UV-2600 features a measurement wavelength range to 1,400 nm, using the ISR-2600Plus two-detector integrating sphere. This ultrawide range permits measurements in the near-infrared region, and expanded research of photovoltaics and other materials. The UV-2600 also features the Lo-Ray-Ligh gratings for high efficiency and low stray light levels.

Shimadzu Scientific Instruments

For info: 800-477-1227 | www.ssi.shimadzu.com



BENCHTOP XRD INSTRUMENT

The new fifth generation MiniFlex is a general purpose X-ray diffractometer that can perform qualitative and quantitative analysis of polycrystalline materials. MiniFlex is now available in two variations. Operating at 600 watts (X-ray tube), the MiniFlex 600 is twice as powerful as other benchtop models, enabling faster analysis and improved overall throughput. Running at 300 watts (X-ray tube), the new MiniFlex 300 does not require an external heat exchanger and thus requires even less space. The new MiniFlex delivers speed and sensitivity through innovative technology enhancements such as the optional D/teX Ultra high speed detector coupled with the new 600 W X-ray source. The optional graphite monochromator, coupled with the standard scintillation counter, maximizes sensitivity by optimizing peak-to-background ratios. If resolution is paramount, incident and diffracted beam slits can be selected to provide the desired resolution. For high sample throughput, MiniFlex is the only benchtop XRD system with an available sample changer.

Rigaku

For info: 281-362-2300 | www.rigaku.com

3-D HIGH CONTENT IMAGING PLATFORM

Designed for demanding high content assays and cell biology challenges, the new ArrayScan Infinity HCS Reader has 3-D imaging capability and features the latest in variable pin-hole confocal technology, solid-state LED illumination, live-cell and label-free capabilities, coupled with best-in-class image analysis and bioinformatics software. The instrument's integrated confocal module features the latest high speed Nipkow spinning disk technology and a variable pinhole to give finer control over image acquisition across a range of objectives (magnifications), compared to traditional confocal (fixed pin-hole) technology. The confocal module has a four-color LED Light Engine, bringing robust, laser-like performance without the complications and cost of lasers or the need for alignment of camera, confocal, and laser. The ArrayScan Infinity HCS Reader is also coupled with enhanced Thermo Scientific iDev Workflow software for multidimensional analysis. Multiple projection options for image analysis and the ability to save the stack of images to create 3-D movies enable complex 3-D structures to be imaged more clearly.

Thermo Fisher Scientific

For info: 800-432-4091 | www.thermoscientific.com

CRYOGENIC STORAGE RACK

The durably constructed, thick-walled Arctic Rack-24 is a new rack and cover that enables high integrity sample storage at ultralow (cryogenic) temperatures over extended periods of time. The Arctic Rack-24 is designed to accommodate 24 high volume (6.00 mL or 7.50 mL) Micronic storage tubes in an automation-friendly SBS footprint. A special cover enables the Arctic Rack-24 to be securely locked ensuring high sample security during transport or storage. The Arctic Rack-24 may be autoclaved several times providing considerable cost savings over consumable sample storage products. Absolute traceability and reproducibility on the Arctic Rack-24 are ensured through alphanumeric visual location aids and laser engraved barcodes on two sides of the rack plus rack foot mounting points. The open bottom design of the Arctic Rack-24 facilitates quick defrosting of samples. The Arctic Rack-24 with covers are stackable, enabling conservation of valuable storage space within freezers or during transport.

Micronic

For info: +31-320-277070 | www.micronic.com

MICROPLATE WASHER

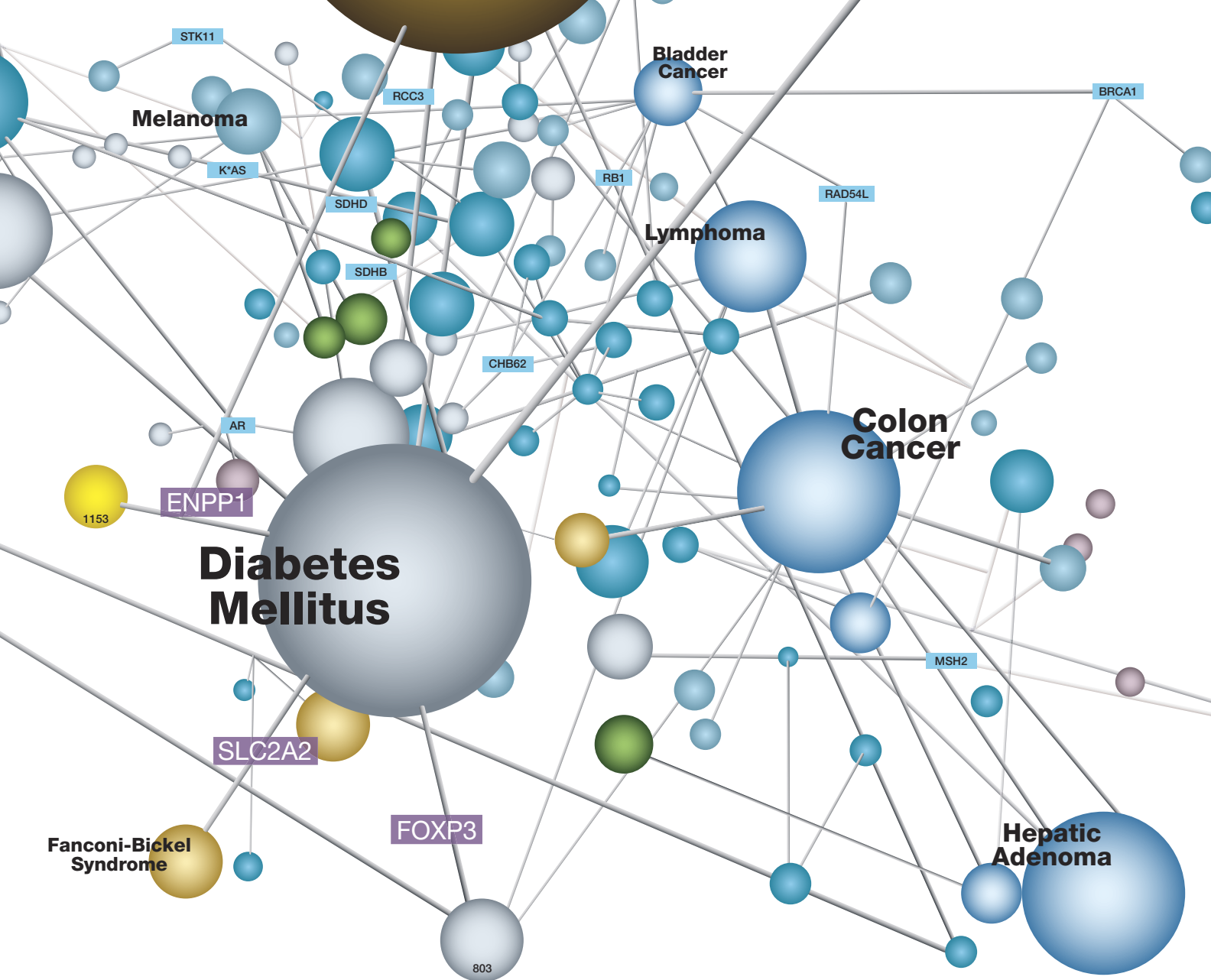
The new 405 Touch Microplate Washer has a high resolution, LED backlit touchscreen interface that provides intuitive and flexible protocol creation and implementation and instrument maintenance, and supports all gloved environments. Additionally, two integrated flash drives enable convenient file storage, transfer, and operation. Instructional videos provide clear direction on instrument setup and basic use, and the context-sensitive help system, complete with recommendations, diagrams and images is available at the touch of a finger. The 405 Touch maintains the same features as the ELx405 washers, including 96- and 384-well compatibility, Dual-Action manifold, patent-pending Ultrasonic Advantage and vacuum filtration and biomagnetic separation for bead-based assays. All models include automated internal buffer switching, quick release manifolds, and optimized cell washing with gentle, low-flow rates ideal for loosely adherent cell monolayers. The 405 Touch is powered by Liquid Handling Control software, and can be coupled with the BioStack Microplate Stacker for unattended batch processing.

BioTek Instruments

For info: 888-451-5171 | www.biotek.com

Electronically submit your new product description or product literature information! Go to www.sciencemag.org/products/newproducts.dtl for more information.

Newly offered instrumentation, apparatus, and laboratory materials of interest to researchers in all disciplines in academic, industrial, and governmental organizations are featured in this space. Emphasis is given to purpose, chief characteristics, and availability of products and materials. Endorsement by *Science* or AAAS of any products or materials mentioned is not implied. Additional information may be obtained from the manufacturer or supplier.



FIND THE CONNECTIONS AND YOU'LL FIND THE SOLUTIONS

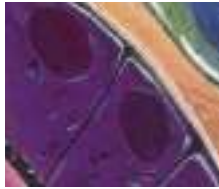
Mapping the genetic linkages among diseases can advance whole categories of medical research—just one example of how Northeastern University's world-leading Center for Complex Network Research connects the dots on the global challenges of our time.

Our broad range of interdisciplinary research turns discoveries into practical solutions, with a focus on global challenges in health, security, and sustainability.

northeastern.edu/research



Northeastern University



Proteins

Antibodies

ELISAs

Assay Services

MultiAnalyte Profiling

Activity Assays

Stem Cells

ELISpot Kits

Flow Cytometry

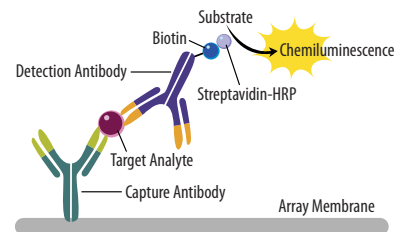
Cell Selection

R&D Systems Proteome Profiler™ Antibody Arrays

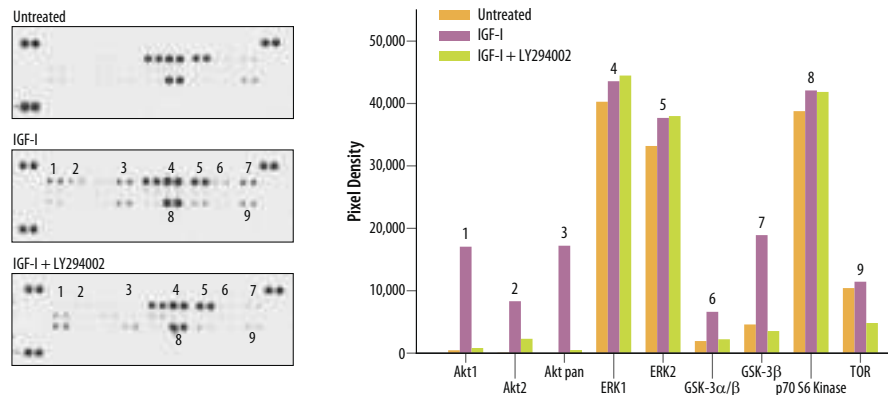
Tired of Western Blots for Signal Transduction?

Arrays are comprised of a nitrocellulose membrane pre-spotted in duplicate with a series of capture antibodies. Simply incubate the membrane with cell lysates, then detect phospho-proteins as you would a Western blot using the included detection antibody and chemiluminescence.

- ✓ No gel to run and no proteins to transfer
- ✓ Simultaneously measure up to 59 phospho-proteins
- ✓ Only 2.5 hours of hands-on assay time
- ✓ Chemiluminescence detection
- ✓ No specialized equipment is required



IGF-I-Induced Kinase Phosphorylation



Kinase phosphorylation measured using the Proteome Profiler MAPK Array (Catalog # ARY002B). MCF-7 cells were treated with IGF-I (Catalog # 291-G1). The PI 3-Kinase inhibitor LY294002 (Catalog # 1130) suppresses the phosphorylation of kinases in the PI 3-K/Akt signaling pathway.

For more information, visit our website at www.RnDSystems.com/ProteomeProfiler

For research use only. Not for use in diagnostic procedures.

R&D Systems, Inc. www.RnDSystems.com

R&D Systems Europe, Ltd. www.RnDSystems.com

R&D Systems China Co., Ltd. www.RnDSystemsChina.com.cn

R&D
SYSTEMS®

There's only one Science

Science Careers Advertising

For full advertising details, go to
ScienceCareers.org and click
For Employers, or call one of
our representatives.

Tracy Holmes

Worldwide Associate Director
Science Careers
Phone: +44 (0) 1223 326525

UNITED STATES & CANADA

E-mail: advertise@sciencecareers.org
Fax: 202-289-6742

Tina Burks

Midwest/West Coast/
South Central/Canada
Phone: 202-326-6577

Elizabeth Early

East Coast & Corporate
Phone: 202-326-6578

Marci Gallun

Sales Administrator
Phone: 202-326-6582

Online Job Posting Questions

Phone: 202-312-6375

EUROPE & REST OF WORLD

E-mail: ads@science-int.co.uk
Fax: +44 (0) 1223 326532

Simone Jux

Phone: +44 (0)1223 326529

Lucy Nelson

Phone: +44 (0)1223 326527

Kelly Grace

Phone: +44 (0) 1223 326528

JAPAN

Yuri Kobayashi

Phone: +81-6-6627-9250
E-mail: ykobayas@aaas.org

CHINA & TAIWAN

Ruolei Wu

Phone: +86-1367-1015-294
E-mail: rwu@aaas.org

All ads submitted for publication must comply with applicable U.S. and non-U.S. laws. *Science* reserves the right to refuse any advertisement at its sole discretion for any reason, including without limitation for offensive language or inappropriate content, and all advertising is subject to publisher approval. *Science* encourages our readers to alert us to any ads that they feel may be discriminatory or offensive.

Science Careers

From the journal *Science*



DREXEL UNIVERSITY
COLLEGE OF MEDICINE

DEPARTMENT OF PHARMACOLOGY & PHYSIOLOGY

Tenure Track Faculty Positions Cardiovascular and/or Renal Physiology

The Department of Pharmacology and Physiology at Drexel University College of Medicine invites applications for tenure-track positions at the Assistant or Associate Professor level. This initiative continues our effort to attract an exceptional and diverse faculty to contribute to the overall scientific and translational growth of the University. We are particularly interested in outstanding candidates with strong research interests in cardiovascular and/or renal physiology. Candidates are expected to establish or continue active extramurally-funded research programs and to participate in the teaching of medical and graduate students. Competitive start-up packages will be available to facilitate transition and productivity.

Candidates for these positions should possess primary and focused expertise in the designated areas, but are expected to embrace a broad, integrative focus with a range of skills, technical expertise and a spirit of collaboration. The Department of Pharmacology and Physiology is one of four basic science departments within the College of Medicine. Collaborative efforts are strongly encouraged within Pharmacology and Physiology, with other basic science and clinical departments, the School of Biomedical Engineering and across the University, as well as with other institutions and organizations within the Greater Philadelphia Area.

The Department of Pharmacology and Physiology is in the process of renovating substantial laboratory and support space to accommodate new and existing faculty as part of the overall initiative to enhance the research infrastructure and educational strengths. Additionally, a M.S. program in Drug Discovery and Development has been established to provide advanced graduate-level training and to encourage future collaborations between academia and industry.

For more information please consult the following the Departmental website (<http://www.drexelmed.edu/Home/AboutTheCollege/DepartmentsCentersandInstitutes/BasicScienceDepts/PharmacologyandPhysiology.aspx>). Applicants should submit a curriculum vitae, a statement describing their current research and future research directions, and the names of three references to Carolann.Imbesi@Drexelmed.edu. Review of applications will begin immediately with the intent of hiring by the fall of 2012.

max-planck-institut für
neurobiologie



The Max Planck Institute of Neurobiology (MPIN) in Martinsried near Munich, Germany, is one of the leading neuroscience research institutes with about 10 groups conducting cutting-edge basic research in molecular, cellular and systems neurobiology. The institute houses state-of-the-art facilities and has a lively, highly international atmosphere.

Scientist & Head of the Microscopy Core Facility

The MPIN invites applications for the position of head of the microscopy facility.

The core facility currently houses four microscopes for multi-spectral confocal laser scanning. It provides high quality service and training for a wide range of users and applications. Research groups here employ multi-photon microscopy, time-lapse imaging and optogenetics.

The prospective head of the facility will be responsible for the general management and development of the facility in accordance with the needs of the MPIN research groups. Main duties include training and advising both new and experienced users in a variety of imaging methods and assisting the scientists in developing suitable experimental setups. Extensive hands-on experience in image acquisition and data processing and outstanding interpersonal skills are essential. The head of the facility is expected to develop new and adapt emerging microscopy techniques, potentially also as leader of a research unit. A competitive budget will be provided to expand the existing instrumentation and support innovative research.

The Max Planck Society is committed to employing more handicapped individuals and especially encourages them to apply. The Max Planck Society seeks to increase the number of women in those areas, where they are underrepresented, and therefore explicitly encourages women to apply.

Applications can be sent to

Max Planck Institute of Neurobiology
Verwaltung
Am Klopferspitz 18
82152 Martinsried



MAX-PLANCK-GESELLSCHAFT

CHINA RETURNEES

ACCELERATE YOUR CAREER

AT LIFE TECHNOLOGIES CHINA.

Life Technologies is the world's most innovative biotechnology company formed with the merger of Applied Biosystems and Invitrogen. If you're thinking about accelerating your career, there's no better place to do that than in China, the world's fastest growing economy, with a fast growing company. A company of people working together to shape discovery and improve life.

For more information, visit lifetechnologies.com/careers/cn

life
technologies™

Invitrogen™

Applied Biosystems®

Gibco®

Molecular Probes®

Novex®

TaqMan®

Ambion®

Ion Torrent™



**Director, Centre for Psychiatry and Neuroscience (CPN)
in Sainte-Anne Hospital, Paris, France**

Inserm, University Paris Descartes (recently identified and funded as one of the 8 French Universities of excellence) and Sainte-Anne hospital invite applications for the position of Director of CPN.

The CPN provides an excellent scientific environment that allows neuroscientists and clinicians to work in close proximity to each other, facilitating the path from bench to bedside. It is located in Sainte-Anne hospital which has a long record of excellence in psychiatry and clinical neurosciences and attracts clinical and basic science students and visiting scholars from around the world. Sainte-Anne hospital drains the largest clinical population for psychiatry in France, and for cerebrovascular diseases in the Paris area. The CPN is currently home to 80 scientists and investigators, 30 technical support staff and 40 trainees, spanning the spectrum from basic to clinical research, particularly in translational and biological psychiatry, cerebrovascular sciences, and cognitive neuroscience. Laboratory-based research programmes are currently located in a 2,800 Sq-meter building, with in-house molecular and cellular biology, imaging, and behavioural facilities and animal house. Laboratories are planned to move into a new building of 5,000 Sq Meters, scheduled for occupancy in 2014. Clinical research facilities (including biobank, clinical research centre, human brain imaging (1.5 and 3T MR)) are also available.

The Director will be an eminent scientist, MD, PhD or both, with a track record of excellence in fields relevant to psychiatry and/or translational neurosciences, and documented leadership credentials in an academic research setting. He/She will serve as Chief Scientific and Executive Officer, with a mandate to expand the Centre's existing strengths, and enhance the international stature of the CPN. He/she will be expected in parallel to carry out his/her own research in the Centre, whose facilities will be made available.

Applicants should send an expression of interest, research statement (not exceeding 5 pages), curriculum vitae and three letters of recommendation or names of references to maurice.nakache@inserm.fr, at **Centre for Psychiatry & Neuroscience, 2 ter rue d'Alésia 75014, Paris, France**. To receive full consideration, applications should be submitted by **June 3rd, 2012**. Salary and position will be tailored to the qualifications of the successful applicant.



Energy and Environment Hire

Tenure-track position in the field of Energy and Environment at **assistant, associate, or full professor** level.

As part of Duke University's new Energy Initiative, the Division of Earth and Ocean Sciences in the Nicholas School of the Environment invites applicants for a tenure-track faculty position at the assistant, associate or full professor level in the field of Energy and Environment. The candidate should have a strong science or engineering background, an understanding of energy issues beyond his/her area of technical training, and the ability and interest to interact with colleagues from a wide spectrum of fields on interdisciplinary energy problems. We are particularly interested in candidates who have expertise in energy systems, i.e. the integrative use of energy by humans, including energy resources, power generation and distribution, energy technologies, and the connection between energy use and climate change. The candidate's work will ideally reflect a long temporal (decadal and greater) and large spatial (regional to global) scale perspective on energy systems.

If a senior candidate is hired, he/she will assume Directorship of the Nicholas School's Energy & Environment Program, which encompasses leadership of the Energy and Environment Concentration in the School's Professional Masters of Environmental Management Program, and leadership roles in Duke University's Undergraduate Certificate in Energy and Environment and in the University's Gendell Center for Engineering, Energy & Environment, the latter two of which are jointly administered by the Nicholas School and Duke's Pratt School of Engineering. The successful candidate will also join the Faculty Advisory Council of Duke's new Energy Initiative. This Council consists of energy experts from across the University and is responsible for developing, coordinating, and promoting a shared set of energy courses and programs, and energy faculty hiring at Duke. More on the Initiative can be found at energy.duke.edu. The Nicholas School focuses on leadership in education, research, and service to understand basic earth and environmental processes, to understand human behavior related to the environment, and to inform society about the conservation and management of the environment and its natural resources. Research interests within Earth and Ocean Sciences and the Nicholas School that will complement this position include climate dynamics, water resources, land-use change, and environmental science and policy. Additional interactions with respect to energy are possible with the Pratt School of Engineering, Trinity College of Arts & Sciences, the Fuqua School of Business, the Sanford School of Public Policy, the Law School, and the Nicholas Institute of Environmental Policy Solutions.

Letters of interest should include a curriculum vitae, a statement describing the candidate's research interests and goals as they relate to energy systems, and names of three references. All materials should be sent electronically as a single PDF file to **Mrs. Mary Anne Perez** at maryanne@duke.edu. The search will remain open until the position is filled, with a target start date of September 1, 2012.

Duke University is an Affirmative Action/ Equal Opportunity Employer.



**VIROLOGY, CANCER VIROLOGY
ASSISTANT PROFESSOR POSITIONS
Department of Molecular Biology
and Microbiology**

The Department of Molecular Biology and Microbiology at CWRU School of Medicine is continuing its expansion under our Chair, Dr. Jonathan Karn. We are currently seeking applications for **Assistant Professor** level positions. We encourage applications from highly qualified individuals with demonstrated experience in the areas of:

- **Molecular Virology:** Fundamental aspects of Virology (e.g. molecular mechanisms in viral replication; virus assembly and maturation; control of latency; host cell interactions; virus entry mechanisms; viral diversity and immune evasion).
- **Cancer Virology:** Basic virology leading to a fundamental understanding of the molecular basis for tumorigenesis. This includes interests in the discovery of new human pathogens, viral etiology of cancer, viral models for cancer.

Successful candidates will establish a vigorous research program, participate in teaching activities, and interact productively with a nationally-ranked team of basic and clinical scientists interested in the overall areas of HIV/AIDS and host-pathogen interactions, microbiology and infectious diseases.

We stress excellence in research and in teaching. Candidates at the Assistant Professor level should have a Ph.D., and have completed at least 3 years of postdoctoral training, have demonstrated a capacity for independent research and an ability to attract Federal funding.

In addition to newly refurbished laboratory space and a generous start-up package, we offer a highly interactive environment with exceptional intellectual, infrastructural, and administrative support. All candidates should have a Ph.D. and relevant post-doctoral experience, a record of funding, an active research program and a national reputation. Salary will be commensurate with experience.

Please submit an online application including a letter of application, curriculum vitae, brief statement of research goals and accomplishments, and 3 references as PDF files to: **Jonathan Karn, Ph.D., Chair; Virology Search Committee** at: <http://sunshine.case.edu/vassistantsearch/index.htm>.

In employment, as in education, Case Western Reserve University is committed to Equal Opportunity and Diversity. Women, veterans, members of underrepresented minority groups, and individuals with disabilities are encouraged to apply. Case Western Reserve University provides reasonable accommodations to applicants with disabilities. Applicants requiring a reasonable accommodation for any part of the application and hiring process should contact the Office of Inclusion, Diversity and Equal Opportunity at 216-368-8877 to request a reasonable accommodation. Determinations as to granting reasonable accommodations for any applicant will be made on a case-by-case basis.



Increased opportunities

We are now considering applications **three times a year** for Senior Research Fellowships to support outstanding researchers wishing to build up their own independent research groups.

Candidates may undertake research across the Trust's scientific remit, from laboratory-based basic research to clinical, population and public health studies.

wellcometrust

- Senior Research Fellowships in Basic Biomedical Science
- Senior Research Fellowships in Clinical Science
- International Senior Research Fellowships
- Senior Fellowships in Public Health and Tropical Medicine

Support provided includes the Fellow's salary and direct research costs for a period of five years in the first instance.

This year's deadlines for preliminary applications: 13 May, 24 September and 10 December 2012.

For further details and links to the individual Senior Research Fellowship schemes:
www.wellcome.ac.uk/seniors

Sickle-cell anaemia. EM Unit, UCL Medical School, Royal Free Campus/Wellcome Images



Call for Application to the ESPCI-ParisTech Director position

ESPCI-ParisTech is seeking to appoint a new Director General ("Directeur Général") starting January 1st 2014. The application procedure will be open until October 31st 2012.

ESPCI is committed, on the one hand, to educate students in physics, chemistry and biology preparing high-level professions, on the other hand to support world-class research laboratories.

The call for applications is international, but the candidates should have a good knowledge of the French system and language. They should also have strong education and research experiences at a world level, with industrial collaboration and a marked interest in innovation. They should furthermore have shown their ability to take on research or teaching responsibilities. Finally, they should be able to understand the education and research domains of ESPCI.

During a five-year mandate, renewable once, the "Directeur Général" heads the different services of ESPCI, the administrative status of which is a "Régie Administrative". He or she chooses, with the agreement of the President of the Board, a Director for Education and a Research Director. With their help, the "Directeur Général" leads on education and research policies, in the context of the institution rules. For administrative matters, he or she is being helped by an Administrative Director. Furthermore he or she is the representative of ESPCI in its different projects. In particular he or she will have to contribute to the creation of the "Paris Sciences et Lettres" school of engineering.

By the end of November 2012 the International Scientific Committee of ESPCI (ISC) will select a short list of at most five candidates.

The application may be in French or in English and should contain a curriculum vitae as well as a letter of intent showing

that the candidate has a good knowledge of the institution and has a vision for it. It should be sent by e-mail before October 31st 2012 to DG2014@espci.fr.

The candidate names will be confidential until the end of April 2013. Between December 2012 and the end of April 2013 an appropriate hiring package will be discussed with each candidate. In any case, the position includes the use of an apartment on the site of ESPCI.

The first week of May 2013 (May 6th–7th) the candidates will be interviewed by the ISC, which will then provide the President of the Board of ESPCI with a ranked list of three names. Subsequently, the President, after consulting the Board, will propose one name to the Paris City Mayor and the Minister of Research and Higher Education of France for an appointment starting January 1st 2014.

More information on ESPCI may be found at www.espci.fr

Get a Career Plan that Works.

An exceptional career requires insightful planning and management. That's where *Science Careers* comes in. From job search to career enhancement, *Science Careers* has the tools and resources to help you achieve your goals. Get yourself on the right track today and get a real career plan that works. Visit ScienceCareers.org.

Science Careers

From the journal *Science*



ScienceCareers.org

Find My Job

Develop My Career

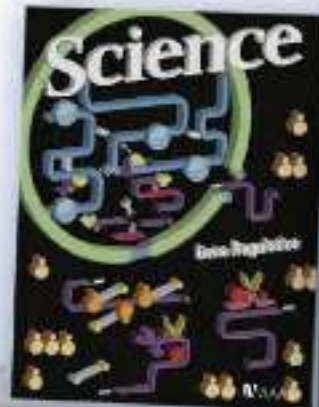
Navigate

Network

Research

Search

Track





Epigenomics Researcher – Center for Individualized Medicine

Heal the sick, advance the science, share the knowledge.

The Center for Individualized Medicine at Mayo Clinic is seeking an exceptional Applied Research Scientist (MD and/or PhD) in the field of Epigenomics. This “collaborative scientist” position is a permanent investigator position with sustained intramural funding support. The Epigenomics Researcher will be expected to develop commercializable epigenetic/epigenomic methodology relevant to the diagnosis, prognosis and prevention of human disease. The candidate will be expected to lead and facilitate innovations in his/her area that have commercial value, contribute to collaborative, extramurally funded academic research, and support the overall mission and specific research efforts of Mayo Clinic’s Epigenomics Translational Program. The candidate will benefit from collaboration with colleagues to utilize the rapidly growing, very large body of genomic, transcriptomic, proteomic and metabolomic data from a larger patient population to enhance and complement existing strengths in diagnostic test development. Mayo is an ideal environment to build this type of research program as it houses a wide variety of specialists who collectively serve a large patient population that offers strong validation and clinical translation opportunities.

Credentials of a successful candidate will include national recognition and experience in the field, and a strong track record of publication. The ideal candidate will have significant experience in intellectual property generation demonstrated by formally issued patent(s), familiarity with both regulatory and clinical laboratory processes, and the ability to collaborate successfully with industry, academia and clinical laboratory medicine.

Mayo Clinic is a premier academic medical center with over 3,800 physicians and scientists in a unified multi-campus system. This unique environment brings together the best in patient care, groundbreaking research and innovative medical education. Mayo Clinic offers a highly competitive compensation package with sustained intramural funding, outstanding laboratory facilities, capital equipment funding, technical and computational resources, and exceptional benefits.

To apply and learn more, please visit www.mayoclinic.org/scientist-jobs/ and reference job posting number **11168BR**. Applications should include a CV and a statement of research interests. Specific questions related to the posting should be directed to:

Jennifer Schilbe, Scientist Recruiter
Center for Individualized Medicine
Mayo Clinic
Email: schilbe.jennifer@mayo.edu

Mayo Foundation is an affirmative action and equal opportunity educator and employer. Post-offer/pre-employment drug screening is required.

Scan this QR code with your smartphone and begin your job search.



Pharmacoepigenomics – Center for Individualized Medicine

Heal the sick, advance the science, share the knowledge.

The Center for Individualized Medicine at Mayo Clinic is seeking an exceptional junior to mid-career investigator in the field of Pharmacoepigenomics.

This “career scientist” position is an institutionally funded investigator position. The Pharmacoepigenomics Researcher will be expected to maintain a nationally/internationally recognized, extramurally funded program of pharmacoepigenomics research. The candidate will benefit from collaboration with colleagues in the Pharmacogenomics and Epigenomics Translational Programs of the Center for Individualized Medicine and access to a rapidly growing body of drug-related genomic, transcriptomic, proteomic and metabolomic data from Mayo Clinic’s large and exceptionally diverse patient population. Other major resources available at the Mayo Clinic include one of the NIH-funded Pharmacogenomics Research Network Centers, an NIH-funded CTSA and an NIH-funded Comprehensive Cancer Center.

Credentials of a successful candidate will include a doctoral degree in biomedical sciences (MD and/or PhD, PharmD or equivalents), national recognition and experience in the field and a strong track record of publication. Preference will be given to applicants with established research programs in any aspect of pharmacoepigenomics including, but not limited to, epigenomics of interindividual variability in drug response, epigenetic mechanisms of drug actions and adverse effects, discovery of predictive biomarkers for pharmacotherapy, and epigenetic pharmacology. Early-stage investigators with exceptional accomplishments and rigorous training in these areas will also be considered.

Mayo Clinic is a premier academic medical center with over 3,800 physicians and scientists in a unified multi-campus system. This unique environment brings together the best in patient care, groundbreaking research and innovative medical education. Mayo Clinic offers a highly competitive compensation package with sustained intramural funding, outstanding laboratory facilities, capital equipment funding, technical and computational resources, and exceptional benefits.

To apply and learn more, please visit www.mayoclinic.org/scientist-jobs/ and reference job posting number **11746BR**. Applications should include a CV and a statement of research interests. Specific questions related to the posting should be directed to:

Jennifer Schilbe, Scientist Recruiter
Center for Individualized Medicine
Mayo Clinic
Email: schilbe.jennifer@mayo.edu

Mayo Foundation is an affirmative action and equal opportunity educator and employer. Post-offer/pre-employment drug screening is required.

Scan this QR code with your smartphone and begin your job search.





AAAS is here – helping scientists achieve career success.

Every month, over 400,000 students and scientists visit ScienceCareers.org in search of the information, advice, and opportunities they need to take the next step in their careers.

A complete career resource, free to the public, *Science* Careers offers a suite of tools and services developed specifically for scientists. With hundreds of career development articles, a grants and scholarships database, webinars and downloadable booklets filled with practical advice, a community forum providing real-time answers to career questions, and thousands of job listings in academia, government, and industry, *Science* Careers has helped countless individuals prepare themselves for successful careers.

As a AAAS member, your dues help AAAS make this service freely available to the scientific community. If you're not a member, join us. Together we can make a difference.

To learn more, visit aaas.org/plusyou/sciencecareers





The EGL Foundation invites you to apply to the
**Gruss Lipper Post-Doctoral
Fellowship Program**

Eligibility

- Israeli citizenship
- Candidates must have completed PhD and/or MD/PhD degrees in the Biomedical Sciences at an accredited Israeli University/Medical School or be in their final year of study
- Candidates must have been awarded a postdoctoral position in the U.S. host research institution.

Details regarding the fellowship are available
at www.eglc.org

NW210508R

CAREER TRENDS Running Your Lab

Science Careers
ScienceCareers.org/booklets

Download your free copy today at
ScienceCareers.org/booklets

MEETINGS



iubmb&febs
Sevilla 2012

○
Congress
22nd
37th **IUBMB
FEBS**
○
From Single Molecules
To Systems Biology



International Union
of Biochemistry
and Molecular Biology



Federation of European
Biochemical Societies



Sociedad Española
de Bioquímica y
Biología Molecular

Early Fee Registration Deadline
30 April 2012



www.iubmb-febs-2012.org

September 4 - 9, 2012
Sevilla, Spain

POSITIONS OPEN

UT SOUTHWESTERN MEDICAL CENTER

DEAN

Graduate School of Biomedical Sciences

Applications are invited for Dean of the UT Southwestern Graduate School of Biomedical Sciences. The successful candidate will be an experienced academic and accomplished scientist with a documented commitment to graduate and post-graduate education in biological sciences. The Dean will be responsible for enhancing all aspects of the Graduate School, including admissions, curriculum, student development, and the formation of new interdisciplinary doctoral programs that reflect advances in modern research. The Dean provides administrative guidance to a staff of Associate Deans, Graduate Program Directors, and administrators. The Dean of the Graduate School will report to the Vice Provost.

The UT Southwestern Graduate School of Biomedical Sciences is ranked in the top 20 programs in the nation for biological research by U.S. News & World Report. The Graduate School comprises twelve graduate programs and currently enrolls over 600 doctoral students, 1100 postdoctoral fellows and approximately 100 undergraduate summer interns. An outstanding faculty of Nobel Laureates, members of the National Academy, Howard Hughes Medical Institute investigators, and distinguished researchers and teachers hold appointments in the Graduate School.

Applications should be submitted electronically to e-mail: dionne.ware@utsouthwestern.edu and include a two-page letter stating the candidate's qualifications and vision for the position, curriculum vitae, and the names and contact information of five references. Review of the applications will begin immediately.

UT Southwestern Medical Center is an Affirmative Action/Equal Opportunity Employer.

POSTDOCTORAL FELLOWSHIP Brain Plasticity and Metaplasticity

The Haas Lab in the Brain Research Centre at the University of British Columbia in Vancouver CANADA is seeking a PDF immediately to identifying and test novel molecular mechanisms underlying brain neural network structural and functional plasticity and metaplasticity. Techniques include molecular and genomic strategies for identifying novel candidates and their testing using targeted in vivo transfection, in vivo two-photon rapid time-lapse imaging of brain neuronal growth and calcium imaging of network function. Applications with a Ph.D., a strong background in molecular techniques, and a publication record in high impact international journals should send curriculum vitae and names of three references to: **Dr. Kurt Haas, e-mail: kurt.haas@ubc.ca.**

FACULTY POSITIONS Medical School

The Saint James School of Medicine, an international medical school ([website: http://www.sjsm.org](http://www.sjsm.org)), invites applications from candidates with teaching and/or research experience in any of the basic medical sciences for its Caribbean campuses. Senior faculty positions are currently available in Pathology. Applicants must be M.D., D.O., and/or Ph.D.

Teaching experience in the U.S. system is desirable but not required. Retired persons are encouraged to apply. Attractive salary and benefits. Submit curriculum vitae electronically to e-mail: mjansen@mail.sjsm.org or mail to: **HRDS Inc., 1480 Renaissance Drive, Suite 300, Park Ridge, IL 60068.**

CAREER OPPORTUNITY—Doctor of Optometry (O.D.) degree in 27 months for Ph.D.s in science and M.D.s. Excellent career opportunities for O.D./Ph.D.s and O.D./M.D.s in research, education, industry, and clinical practice. This unique program starts in March of each year, features small classes, and 12 months devoted to clinical care.

Contact the Admissions Office, telephone: 800-824-5526 at the New England College of Optometry, 424 Beacon Street, Boston, MA 02115. Additional information at [website: http://www.neco.edu](http://www.neco.edu), e-mail: admissions@neco.edu.

POSITIONS OPEN

TWO POSTDOCTORAL FELLOWS Department of Pharmacology Tulane University

(1) **Dr. Prasad V.G. Katakam's** research will focus on ischemia-reperfusion injury of heart and the impact of insulin resistance on vascular dysfunction. The applicant should have significant experience in performing ischemia-reperfusion studies of heart involving occlusion of coronary arteries in rats and mice.

(2) **Dr. Milton Hamblin's** research will focus on abdominal aortic aneurysms, diabetes-associated cardiovascular complications, and vascular remodeling-related pathophysiology. The applicant should have experience in performing procedures on animals, including mini-pump implantation, animal tissue dissection/collection, administering anesthesia and analgesics, blood collection, and some small animal surgery. Experience in mouse colony breeding is highly desirable. Also, the applicant should have some expertise with immunohistochemical/morphological staining and tissue sectioning. Preference will be given to the applicant with experience in conducting standard laboratory techniques, including immunoblotting, PCR genotyping, RNA extraction, RT-PCR, the use of adenovirus and RNA interference methods, and cell culture (isolation and culture of primary vascular cells-endothelial cells, smooth muscle cells, and fibroblasts).

Requirements: M.D., D.V.M., Ph.D., or equivalent degree with a strong background in cardiovascular biology and diabetes research.

Additional Information: Salary and benefits are commensurate with NIH guidelines. Applications should include a brief cover letter highlighting the applicant's research experience and interests, along with full curriculum vitae and the names and contact information of three references.

Please submit full curriculum vitae and names of three references via e-mail to: **Dr. Prasad V.G. Katakam, M.D., Ph.D., Assistant Professor, Department of Pharmacology, Tulane University School of Medicine, 1430 Tulane Avenue, SL 83, New Orleans, LA 70112; e-mail: pkatakam@tulane.edu; website: <http://tulane.edu/som/departments/pharmacology/katakam.cfm>.** Please also include a letter that summarizes your future research plans. Review of applications will begin immediately and will continue until the positions are filled.

Tulane University is an Affirmative Action/Equal Opportunity Employer. We invite Women and Minorities to apply.

DIVISION CHIEF for the Advanced Network Technologies Division Information Technology Laboratory The National Institute of Standards and Technology

The National Institute of Standards and Technology (NIST), Information Technology Laboratory (ITL) is seeking a highly qualified candidate for the position of Division Chief for the Advanced Network Technologies Division. The Division carries out interdisciplinary collaborations with industry, academia, and other government agencies on the application of measurement science for advanced network technologies focused on critical national needs including Internet interoperability, scalability, performance and reliability, wireless communications, complex systems and trusted networks, public safety communication infrastructure, smart grid, and cloud computing.

Title of Position: Supervisory Computer Scientist, ZP-1550-V; Supervisory Electronics Engineer, ZP-0850-V; or Supervisory Mathematician, ZP-1520-V. Salary Range: \$123,758–\$155,500. Geographic Location: Gaithersburg, Maryland. Tenure: Permanent. Work Schedule: Full Time. Relocation Expenses: Relocation expenses are authorized.

For further information and to apply for this position, visit the website at [website: http://www.usajobs.gov/GetJob/ViewDetails/313012300](http://www.usajobs.gov/GetJob/ViewDetails/313012300). The job announcement number associated with this position is NISTITL-2012-0019. The vacancy opens March 29, 2012 and closes April 25, 2012. U.S. citizenship is required. *The Department of Commerce is an Equal Opportunity Employer.*

POSITIONS OPEN

ASSISTANT/ASSOCIATE PROFESSOR in Chemical Biology Medicinal Chemistry

The Division of Chemical Biology and Medicinal Chemistry in the UNC Eshelman School of Pharmacy in cooperation with the Lineberger Comprehensive Cancer Center and University Cancer Research Fund (UCRF) is seeking to fill a 12-month tenure-track position at the rank of Assistant Professor or Associate Professor without tenure. The ideal candidate will have research interest in the broad area of chemical biology and medicinal chemistry with the emphasis on cancer-related research. The successful candidate is expected to attract NIH funds and develop a research program with a national reputation.

The selected candidate will have appointments in the Division of Chemical Biology and Medicinal Chemistry and the Center for Integrative Chemical Biology and Drug Discovery, and be eligible for membership in the Lineberger Comprehensive Cancer Center.

The qualified candidate must have a Ph.D. degree in organic chemistry, medicinal chemistry, biochemistry, or a closely related discipline with postdoctoral research experience. Individuals with interest in chemical epigenetics are encouraged to apply. The successful candidate must have a strong track record of publications that demonstrates creativity and breadth of experience in cancer research.

Review of applications will begin May 15, 2012. Applications should be in PDF format including the following items: (1) a cover letter, (2) curriculum vitae, (3) the statement of research plan (limited to three pages), and (4) the names and contact information of four references. Interested applicants should apply directly to [website: http://jobs.unc.edu/2502676](http://jobs.unc.edu/2502676). Questions about the position should be directed to **Gwendolyn Ricks** by e-mail.

CB# 7360, Search Committee, UNC Eshelman School of Pharmacy, Gwendolyn Ricks, University of North Carolina, Chapel Hill, NC 27599-7360, E-mail gricks@unc.edu.

The University of North Carolina at Chapel Hill is an Equal Opportunity Employer. Women, minorities, and individuals with disabilities are encouraged to apply.

THE JOHN CALDWELL MEEKER POSTDOCTORAL FELLOW

Applications are invited for the position of the John Caldwell Meeker Postdoctoral Researcher in the Department of Geology at The Field Museum. The successful candidate will be expected to complement, and/or participate in any one of the ongoing research programs in the Department of Geology. Research projects are being pursued in the areas of Vertebrate Paleontology, Invertebrate Paleontology, and Meteoritics. Individual Curators and their research programs are featured on the Field Museum [website: http://fieldmuseum.org/explore/departments/geology](http://fieldmuseum.org/explore/departments/geology). Applications will be reviewed both for merit and suitability with the research and collections strengths of the department. Applicants are strongly encouraged to contact relevant curators prior to application.

A Ph.D. in a field of research represented in the Department of Geology is required. The term for this position is for a maximum of two years. The appointment is anticipated to begin in the summer of 2012.

Please send a statement of research interests and experience, curriculum vitae including publications list, and names of three references (with e-mail addresses) to: **Peter J. Makovicky, Chair, Department of Geology, The Field Museum, 1400 S. Lake Shore Drive, Chicago, IL 60605-2496 USA; e-mail: pmakovicky@fieldmuseum.org; telephone: 312-665-7633.** Applications must be received by May 15, 2012. *The Field Museum is an Equal Opportunity/Affirmative Action Employer.*

MARKETPLACE

Widely
Recognized
Original &
Guaranteed

KlenTaq1

8¢/u
Truncated
Taq DNA
Polymerase

Withstand 99°C

US Pat #5,436,149

Call: **Ab Peptides**

Fax: 314•968•8988

e-mail: abpeps@msn.com

1•800•383•3362

www.abpeps.com